NANOSTRUCTURES: PHYSICS AND TECHNOLOGY

28th International Symposium

Minsk, Republic of Belarus, September, 2020

PROCEEDINGS

Ioffe Institute, RAS
St Petersburg, 2020

The International Symposium "Nanostructures: Physics and Technology" is held annually since 1993. The first Symposium was initiated by Prof. Zh. Alferov and Prof. L. Esaki. More detailed information on the Symposium is presented on the World Wide Web **http://www.ioffe.ru/NANO2020/**

The Proceedings include extended abstracts of invited talks and contributed papers to be presented at the Symposium.
By tradition this book is published before the beginning of the meeting.

The volume was composed at the Ioffe Instutute from electronic files submitted by the authors.
When necessary these files were converted into the Symposium LaTeX 2_ε style. Only minor technical corrections were made by the composers.

Desk editing, design and layout: N. Vsesvetskii
Proof reader: E. Savostyanova

Published by the Ioffe Institute
26 Politekhnicheskaya, St Petersburg 194021, Russia
http://www.ioffe.ru/

ISBN 978-5-93634-066-6

Printed in the Republic of Belarus

The Symposium is held under the auspices of
the National Academy of Sciences of Belarus

Organizers

National Academy of Sciences of Belarus

B.I. Stepanov Institute of Physics NASB, Belarus

Ioffe Institute, RAS

НТЦ РАН
Submicron Heterostructures for Microelectronics
Research and Engineering Center of the RAS

Location and Date

Symposium is held in Minsk, Republic of Belarus, September, 2020.

Advisory Committee

G. Abstreiter (*Germany*)
Y. Arakawa (*Japan*)
A. Aseev (*Russia*)
G. Bastard (*France*)
D. Bimberg (*Germany*)
L. Eaves (*United Kingdom*)
L. Esaki (*Japan*)
S. Gaponov (*Russia*)
E. Gornik (*Austria*)
Yu. Gulyaev (*Russia*)
N. Holonyak, Jr. (*USA*)
J. Merz (*USA*)
M. Shur (*USA*)
M. Skolnick (*United Kingdom*)
R. Suris (*Russia*)
V.V. Ustinov (*Russia*)

Program Committee

R. Suris, Co-Chair, (*Russia*)
S. Kilin, Co-Chair, (*Belarus*)
V. Evtikhiev, Secretary (*Russia*)
A. Andronov (*Russia*)
N. Bert (*Russia*)
M. Bogdanovich (*Belarus*)
C. Chang-Hasnain (*USA*)
A. Chaplik (*Russia*)
V. Dneprovskii (*Russia*)
A. Egorov (*Russia*)
A. Gippius (*Russia*)
L. Golub (*Russia*)
S. Gurevich (*Russia*)
S. Ivanov (*Russia*)
P. Kop'ev (*Russia*)
Z. Krasil'nik (*Russia*)
V. Kulakovskii (*Russia*)
M. Kupriyanov (*Russia*)
D. Mogilevtsev (*Belarus*)
V. Panov (*Russia*)
O. Pchelyakov (*Russia*)
N. Poklonski (*Belarus*)
H. Sakaki (*Japan*)
N. Sibeldin (*Russia*)
M. Stutzmann (*Germany*)
V. Timofeev (*Russia*)
V. Volkov (*Russia*)
L. Vorobjev (*Russia*)
V.M. Ustinov (*Russia*)
A. Zhukov (*Russia*)

Organizing Committee

S. Kilin, Co-Chair
(*B.I. Stepanov Institute of Physics, NASB*)
P. Kop'ev, Co-Chair
(*Ioffe Institute, RAS*)
G. Ryabtsev, Vice-Chair
(*B.I. Stepanov Institute of Physics, NASB*)
A. Ryabtsev, Secretary
(*B.I. Stepanov Institute of Physics, NASB*)
E. Batura (*B.I. Stepanov Institute of Physics, NASB*)
Ya. Bogdanovich (*B.I. Stepanov Institute of Physics, NASB*)
A. Danilchyk (*B.I. Stepanov Institute of Physics, NASB*)
N. Denisenko (*B.I. Stepanov Institute of Physics, NASB*)
E. Evmenenko (*B.I. Stepanov Institute of Physics, NASB*)
A. Kot (*B.I. Stepanov Institute of Physics, NASB*)
E. Kruplevich (*B.I. Stepanov Institute of Physics, NASB*)
M. Leanenia (*B.I. Stepanov Institute of Physics, NASB*)
M. Sudenkova (*Ioffe Institute, RAS*)
I. Sulim (*B.I. Stepanov Institute of Physics, NASB*)
G. Yablonskii (*B.I. Stepanov Institute of Physics, NASB*)

Contents

Lasers and Optoelectronic Devices

Graphene

Microcavity and Photonic Crystals

Nanostructure Devices

Plasmonics

Nanostructure Technology

Si-Ge Based Nanostructures

Nanostructures for Life Sciences

Nanostructure Characterization

Excitons in Nanostructures

Spin Related Phenomena in Nanostructures

Quantum Wells and Quantum Dots

Wide Band Gap Nanostructures

Transport in Nanostructures

28th Int. Symp. "Nanostructures: Physics and Technology"
Minsk, Belarus, September 2020

Quantum-cascade ring resonator laser with 7–8 μm wavelength and surface radiation output

A.V. Babichev[1], E.S. Kolodeznyi[2], A.G. Gladyshev[1], D.V. Denisov[3], G.V. Voznyuk[2,4], D.I. Kuritsyn[5], M.I. Mitrofanov[4], S.O. Slipchenko[4], A.V. Lyutetskii[4], V.P. Evtikhiev[4], L.Ya. Karachinsky[1,2,4], I.I. Novikov[1,2,4], N.A. Pikhtin[4], S.V. Morozov[5], A.Y. Egorov[2]

[1] Connector Optics LLC, St Petersburg, 194292 Russia
[2] ITMO University, St Petersburg, 197101 Russia
[3] St Petersburg Electrotechnical University "LETI", St Petersburg, 197376 Russia
[4] Ioffe Institute, St Petersburg, 194021 Russia
[5] Institute for Physics of Microstructures of the RAS, Nizhny Novgorod, 603950 Russia

Abstract. We have created a quantum-cascade ring resonator laser with 7–8 μm wavelength and surface radiation output through windows formed by focused ion beam etching of the upper cladding layer of the waveguide. The active area of the quantum-cascade laser heterostructure was formed on the basis of the solid alloy heteropair $In_{0.53}Ga_{0.47}As/Al_{0.48}In_{0.52}As$ with two-phonon depletion of the cascade lower level. The studies of the generation spectra for the temperatures in 8–77 K range have shown, that the mode spacing in the generation spectra of these lasers correspond to the whispering-gallery modes.

1. Introduction

A big progress has been recently achieved in forming surface-radiating quantum-cascade lasers (QCL) with selective ring resonators [1–10]. Moreover, Mahler *et al*. [11] and Mujagic *et al*. [12] have constructed the surface-radiating QCL with selective ring resonators that radiate in the THz range. The surface radiation output is realized through forming the second-order lattice in the layers of the upper cladding layer of the waveguide. Mahler *et al*. [13,14] have also shown existence of the "enhancement areas" (in the double-segment configuration) between the segments of the second-order lattice. Finally, Liang *et al*. [15] have realized surface radiation in the ring QCL for the THz emission range through arranging second-order concentric rings.

In this paper we present results on formation and properties of the surface-radiating ring resonator QCL with radiation wavelengths in the 7.5–8.0 μm range.

2. Experiment

The QCL heterostructure has been grown on the InP substrate with (001) orientation by the "Connector Optics LLC" company with the Riber 49 MBE system [16,17]. The waveguide we used has thick upper cladding layer (3.9 μm) and is based on indium phosphide (with doping $n = 1.0 \cdot 10^{17}$ cm^{-3}). The active area is formed on the basis of the solid alloy heteropair $In_{0.53}Ga_{0.47}As/Al_{0.48}In_{0.52}As$ with two-phonon depletion of the cascade lower level [18,19]. For the contact layers we have used layers of $In_{0.53}Ga_{0.47}As$ that are 100 nm and 20 nm thick and had doping levels $1.0 \cdot 10^{17}$cm^{-3} and $1.0 \cdot 10^{19}$ cm^{-3}, correspondingly. The QCL crystal formation was done according to the methodic suggested in [20]. We have used deep-mesa construction with etching inside the substrate. The outer radius of the ring resonator is 201 μm, and its width near the surface is 20 μm. The laser crystal was mounted with the indium solder with substrate soldered to the copper heat sink.

The windows was etched in the super high vacuum with focused beam of gallium ions with the energy 30 keV and working current 490 pA, focused in the spot that was 40 nm in diameter [21]. The radiation dose during the etching was $4.5 \cdot 10^{10}$ pC/cm^2. We have etched the windows in the right trapezoid form with the 18.9° period in the polar coordinates. The etching depth was 800±100 nm (see Fig. 1a) and includes the upper metallization with the Ti-Pt-Au layers with total thickness around 605 nm. We present SEM images of QCL with ring resonator and 9 etched dashes on the Fig. 1b,1c.

The especially rough etching by ion beam formed on the base of upper cladding layer the coarse layer that worked as an effective media and provided the laser radiation output. The pulse length was 100ns with 10 kHz frequency. The QCL crystal was put inside closed-cycle helium cryostat, with temperature varying in the 8–77 K range. The waveguide for the emitted radiation was a pipe 100 mm long and 8 mm in diameter, and was located 1 mm away from the QCL crystal butt with the laser located at a slight angle to the waveguide axis. The waveguide exit was located close to the focus entrance of the Fourier spectrometer.

On the Fig. 2a we present surface radiation spectra of the QCL we studied. The spectra were measured in the 8–77 K temperature range with fixed current pumping level 1.7 A. At the 8 temperature the spectrum features 8 optical modes that are about $\Delta\lambda = 13$ nm away from each other. This value of $\Delta\lambda$ agrees well with the mode spacing of the whispering-gallery modes found according to the formula $\Delta\lambda = \lambda^2/2(2\pi R_{out})n_{eff}$, where R_{out} is the outer radius and $n_{eff} = 3.28$ is the effective refraction index [22]. Increasing temperature to 77 K leads to the modes shift to the higher-wavelength area, which may be due to the decrease of the zone break on the heteroboundary with the temperature increase.

On Fig. 2b we present the surface radiation laser generation spectra that were measured at 77 K temperature with various levels of pumping current. The generation spectra feature whispering-gallery modes that are 13 nm away from each other. The lasers we studied didn't have broadening of the generation spectrum after increasing the pumping current to $10\times I_{th}$. This is different from the half-ring lasers of the similar radii, for which increasing the pumping current to $10\times I_{th}$ led to the significant broadening of the generation spectrum (up to 435 nm) [22].

3. Conclusions

To sum up, we have demonstrated laser generation in a QCL with selective ring resonator in the 8–77 K temperature range. The active area of the QCL heterostructure was formed on the basis of the $In_{0.53}Ga_{0.47}As/Al_{0.48}In_{0.52}As$ solid solution heteropair with two-phonon depletion of the cascade lower level. We have realized the surface output of the radiation through the windows that was formed in the upper cladding layer of the waveguide by the focused ion

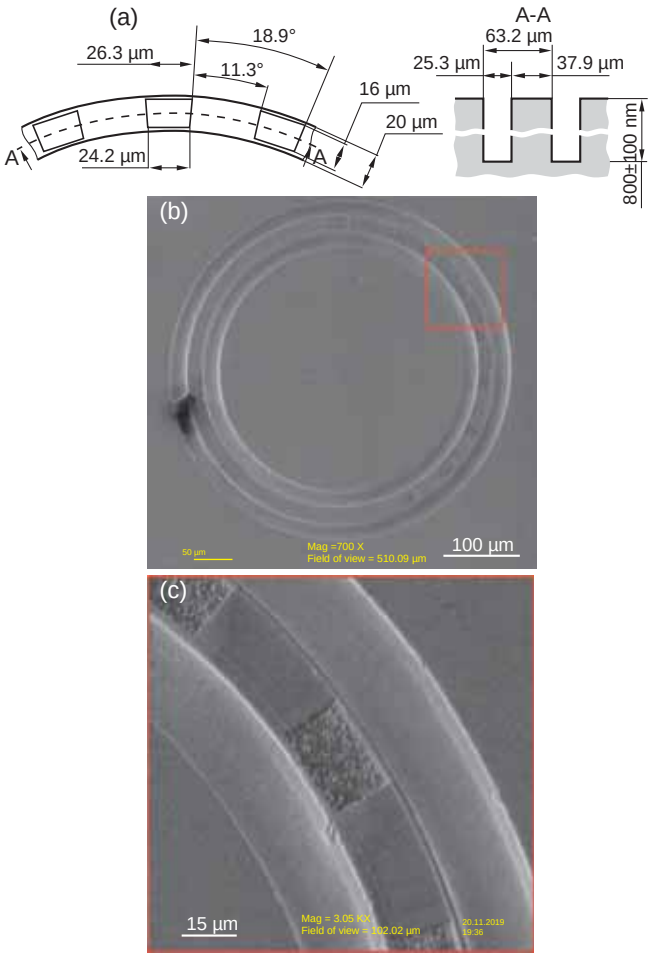

Fig. 1. (a) Schematic view of the lattice segment. The lattice was formed in the layers of the upper cladding layer of the QCL waveguide, the section (left) and the view from above. (b) SEM image of QCL with a ring resonator (view from above). (c) Enlarged SEM image of the ring resonator area with the etched lattice (view from above)

beam etching. We have observed the generation at 78 K temperature near 7.5 μm wavelength. The intermodal distance corresponds to the whispering-gallery modes.

Acknowledgement

The study was supported by a grant from the Russian Science Foundation (project No. 20-79-10285).

Conflict of interest

The authors claim no conflict of interests.

References

[1] R. Szedlak, C. Schwarzer, T. Zederbauer, *et al*, *Appl. Phys. Lett.* **104**, 15. 151105 (2014).
[2] R. Szedlak, M. Holzbauer, D. MacFarland, *et al*, *Sci. Rep.* **5**, 1, 16668 (2015).
[3] E. Tütüncü, V. Kokoric, R. Szedlak, *et al*, *Analyst.* **141**, 22, 6202–6207 (2016).
[4] H. Moser, A. Genner, J. Ofner, *et al*, *Opt. Express.* **24**, 6, 6572 (2016).
[5] R. Szedlak, M. Holzbauer, P. Reininger, *et al*, *Vib. Spectrosc.* **84**, 101–105 (2016).
[6] D.H. Wu and M. Razeghi, *APL Mater.* **5**, 3, 035505 (2017).
[7] R. Szedlak, J. Hayden, P. Martín-Mateos, *et al*, *Opt. Eng.* **57**, 01, 1 (2017).

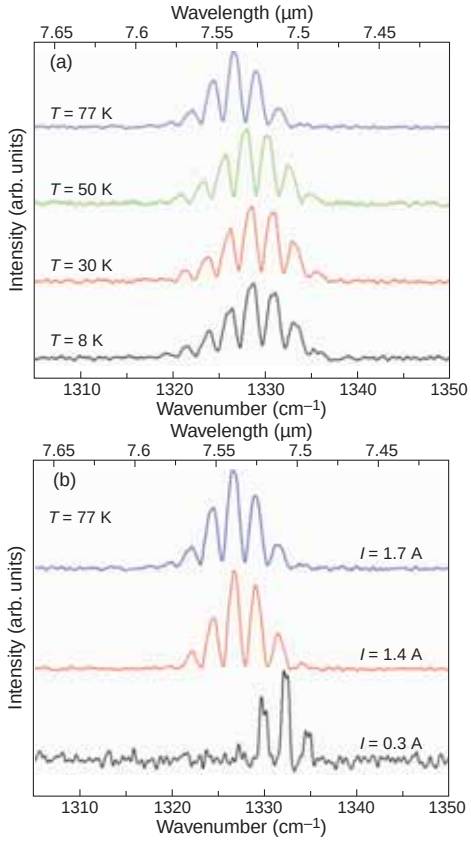

Fig. 2. (a) Normalized spectra of QCL surface generation, measured in 8–77 K temperature range with 1.7 A pumping current. (b) Normalized spectra of QCL surface generation, measured at 77 K with various levels of pumping current

[8] M. Holzbauer, R. Szedlak, H. Detz, *et al*, *Appl. Phys. Lett.* **111**, 17, 171101 (2017).
[9] R. Szedlak, T. Hisch, B. Schwarz, *et al*, *Sci. Rep.* **8**, 1, 7998 (2018).
[10] B. Hinkov, J. Hayden, R. Szedlak, *et al*, *Opt. Express.* **27**, 10, 14716 (2019).
[11] L. Mahler, A. Tredicucci, F. Beltram, *et al*, *Nat. Photonics.* **3**, 1, 46–49 (2008).
[12] E. Mujagic, C. Deutsch, H. Detz, *et al*, *Appl. Phys. Lett.* **95**, 1, 011120 (2009).
[13] L. Mahler, M.I. Amanti, C. Walther, *et al*, *Opt. Express* **17**, 15, 13031 (2009).
[14] L. Mahler, A. Tredicucci, F. Beltram, *et al*, *Appl. Phys. Lett.* **96**, 19, 191109 (2010).
[15] G. Liang, H. Liang, Y. Zhang, *et al*, *Appl. Phys. Lett.* **102**, 3, 031119 (2013).
[16] A.V. Babichev, G.A. Gusev, A.N. Sofronov, *et al*, *Tech. Phys.* **63**, 10, 1511–1515 (2018).
[17] A.V. Babichev, A.S. Kurochkin, E.C. Kolodeznyi, *et al*, *Semiconductors* **52** 6, 745–749 (2018).
[18] A.V. Babichev, A.G. Gladyshev, A.S. Kurochkin, *et al*, *Semiconductors* **52**, 8, 1082–1085 (2018).
[19] A.V. Babichev, A.G. Gladyshev, A.S. Kurochkin, *et al*, *Tech. Phys. Lett.* **45**, 4, 398–400 (2019).
[20] V.V. Dudelev, D.A. Mikhailov, A.V. Babichev, *et al*, *Quantum Electron.* **50**, 2, 141–142 (2020).
[21] A.V. Babichev, D.A. Pashnev, A.G. Gladyshev, *et al*, *Tech. Phys. Lett.* **46**, 4, 312–315 (2020).
[22] A.V. Babichev, D.A. Pashnev, A.G. Gladyshev, *et al*, *Opt. Spectrosc.*, in press.

28th Int. Symp. "Nanostructures: Physics and Technology"
Minsk, Belarus, September 2020

Electroluminescence in heterostructures GaSb/AlSb/InAsSb due to the tunneling mechanism of radiative recombination

L.V. Danilov, M.P. Mikhailova, E.V. Ivanov, Yu.P. Yakovlev, P.S. Kop'ev
Ioffe Institute, 26 Politekhnicheskaya, St Petersburg 194021, Russia

Abstract. We report on the unusually large blue shift of electroluminescence spectrum with increase of the drive current at 77 K in a double-barrier nanoheterostructure with a deep AlSb/$InAs_{0.83}Sb_{0.17}$/AlSb quantum well grown by MOVPE on *n*-GaSb: Te substrate. The rise of drive current from 20 to 220 mA led to shift of the electroluminescence spectrum maximum towards higher photon energies by 100 meV. It was shown that this effect is due to indirect (tunnelling) radiative transitions between electrons in InAsSb quantum well and heavy holes localized near AlSb/*p*-GaSb heterointerface. Energy of radiative transition was linearly dependent on applied voltage. In the drive current range of 50–220 mA electroluminescence blue shift was accompanied by the spectrum narrowing by 40 meV and noticeable change of the spectrum shape. With rise in drive current superlinear increase of electroluminescence intensity caused by the nonlinear dependence of tunneling radiative recombination rate on transition energy was observed at 300 and 77 K.

Double asymmetric *n*-GaSb/AlSb/$InAs_{0.83}Sb_{0.17}$/AlSb/*p*-GaSb heterostructures were grown by MOVPE on *n*-GaSb: Te (100) substrate with GaSb buffer layers, single InAsSb QW with 5–6 nm thickness and *p*-GaSb: Zn cap layer of 0.4 μm thick. Electrical and electroluminescent properties of the structures were studied at forward bias in the temperature range of 77–300 K.

For the first time unusually large blue shift of electroluminescence spectrum was observed at $T = 77$ K: current change from 20 to 220 mA led to displacement of the spectrum maximum towards higher photon energies by 100 meV. This phenomenon manifested the photon-assisted tunneling nature of the radiative transition. The photon energy at maximum of electroluminescence spectrum was linearly dependent on applied voltage and the rate of blue shift $d(h\nu_{77\mathrm{K}})/dU$ is inversely proportional to the nonideality factor $\beta_{77\mathrm{K}}$ of I–V characteristic.

The observed effect is determined by indirect (tunneling) radiative transitions between the electrons localized at the E_1 level in InAsSb QW and heavy holes localized in the valence band offset at the interface of AlSb barrier and *p*-GaSb cap layer.

It is shown that superlinear dependence of electroluminescence intensity on the drive current observed at room and cryogenic temperatures is caused by the nonlinear dependence of the rate of tunneling radiative recombination on the transition energy.

Double asymmetric *n*-GaSb/AlSb/$InAs_{0.83}Sb_{0.17}$/AlSb/*p*-GaSb heterostructures grown by MOVPE are potentially applicable to fabricate the tunable light sources and quantum-cascade emitting heterostructures for the near and middle IR range.

Acknowledgement

We are grateful to colleagues from MOVPE laboratory at Institute of Physics of the Czech Academy of Sciences (Prague, Czech Republic) for growing GaSb-based nanoheterostructures.

References

[1] M. Mikhailova, N. Stoyanov, I. Andreev, *et al*, Proc. SPIE **6585**, 658526 (2007).
[2] S.V. Ivanov and P.S. Kopev, in *Optoelectronic Properties of Semiconductors and Superlattices, Vol. 3 Antimonide-Related Stained-Layer Heterostructures*, ed. by M.O. Manasreh (Gordon and Breach Science Publishers, Amsterdam, 1997), Chap. 4, p. 109.
[3] S.V. Ivanov, K.D. Moiseev, A.M. Monakhov, *et al*, in *Proc. of 8th Int. Symp. Nanostructures: Physics and Technology*, St Petersburg, Russia, 19–23 June 2000, p. 109.
[4] D. Barate, R. Teissier, Y. Wang and A.N. Baranov, *Appl. Phys. Lett.* **87**, 051103 (2005).
[5] B.M. Nguyen, S.A. Pour, M. Razeghi, Appl. Phys. Lett. **95**, 183502 (2009).
[6] Zh.I. Alferov *Nobel Lecture*, Stockholm, Sweden, 8 December 2000 [*in Russian:* Uspekhi Fiz. Nauk **172** (9), 1068 (2002)].
[7] A.N. Baranov, B.E. Zhurtanov, A.N. Imenkov, etal, *Sov. Phys. Semicond.*, **20**, 1385 (1986).
[8] B. Wilson, J. Quantum Electr., **24** (8), 1763 (1988).
[9] V.N. Abakumov, V.I. Perel, and I.N. Yassievich, *Non-Radiative Recombination in Semiconductors*, Series Modern Problems in Condensed Matter Sciences, Vol. 33, ed. by V.M. Arganovich and A.A. Maradudin (North-Holland, Amsterdam, 1991).
[10] G.G. Zegrya, in *Optoelectronic Properties of Semiconductors and Superlattices, Vol. 3 Antimonide-Related Stained-Layer Heterostructures*, ed. by M.O. Manasreh (Gordon and Breach Science Publishers, Amsterdam, 1997), Chap. 7, p. 273.
[11] M.P. Mikhailova, E.V. Ivanov, L.V. Danilov, *et al*, *J. Appl. Phys.*, **112**, 023108 (2012).

28th Int. Symp. "Nanostructures: Physics and Technology"
Minsk, Belarus, September 2020

QCL design engineering: automatization vs classical approaches

A.S. Dashkov[1] and L.I. Goray[1,2]

[1] Alferov University, Khlopin str. 8/3, St Petersburg, 194021, Russia
[2] ITMO University, Kronverkskiy pr. 49, St Petersburg, 197101, Russia

Abstract. In this work, we applied automatic design generation techniques to obtain the most efficient QCL structures for the MIR range. For simulations, the transfer matrix, Ensemble Monte Carlo and density matrix techniques, accelerated with CUDA computation technology, were utilized. As a result, several designs were created using the modification of the genetic algorithm. These structures were compared with manually created designs based on a rule of thumb. The work provides a first-time combination of the most efficient techniques of QCL simulation and an optimization method for their generation. The difference between the two types of designs is analyzed.

Introduction

Quantum cascade laser (QCL) has already become an irreplaceable type of mid-infrared (MIR) and terahertz light source. Their foundation was established in 1971 by R.A. Suris and R.F. Kazarinov [1]. It was only 20 years later when a group of researchers with F. Capasso managed to manufacture the first implementation of QCL [2]. Such devices have a variety of applications in different areas of modern science and technology: medical diagnostics, high-speed communication, etc. All these results in the fact that nowadays QCLs and their improvement are in high demand.

To obtain the most efficient device, one has to create a rather complicated QCL design. This can be achieved via optimization methods. Though there are many QCL designs, yet the fully automated design creation of these devices is a matter of question.

Recently, researchers introduced several methods of QCL simulation and outlined the features of an automatic laser design generator. However, there were only several attempts to apply optimization techniques in such laser design simulation [3,4]. In this work, we applied the most efficient simulation techniques and the most reliable optimization algorithm to obtain several QCL designs. We also compared obtained designs with existing ones to acquire insights on ways of creating more efficient devices.

1. Experimental

The QCL designs were generated based on InGaAs/InAlAs material system. This material system was chosen as it is the most convenient for MIR QCL creation [5]. Optimization methods aimed to obtain the most efficient designs emitting in the 4–10 μm spectral range. The modified genetic algorithm is used as a core of optimization. The wallplug efficiency and emitting wavelength were merit factors of the algorithm, i.e. reward functions.

The entire generation scheme consists of three parts. At first, the best QCL designs generated based on the results of a previous step via the genetic algorithm. Then, the simulation procedures are applied to obtain designs' characteristics. Finally, simulation results are fed to the genetic algorithm and then the whole step repeats. On the initial stage, the sample of designs generated randomly based on the initial design.

During the simulation process one needs to solve three distinct problems:

- The Schrodinger–Poisson equation — to obtain energy levels;
- The Maxwell equation for determining electromagnetic field distribution in the structure;
- The rate equations for optical gain computation.

The first and second tasks solved using a transfer matrix approach as the most efficient one. The dynamic characteristics were obtained via Ensemble Monte Carlo (EMC) and density matrix techniques [6,7]. Simulation techniques were also accelerated using CUDA computation technology [8]. This acceleration increased performance up to five times on our workbench. The workbench consisted of PC with an Intel® Core® i5-3570 K 3.40 3.80 GHz processor operating on Windows®7 Pro 64 bit OS, 16 GB of RAM and NVIDIA GeForce GTX 660 GPU. The average time measured by two hundred simulations in different applied biases is approximately 270 ms per simulation. Such limited enhancement was connected with CPU-GPU data transfer bottlenecks.

2. The generated designs analysis

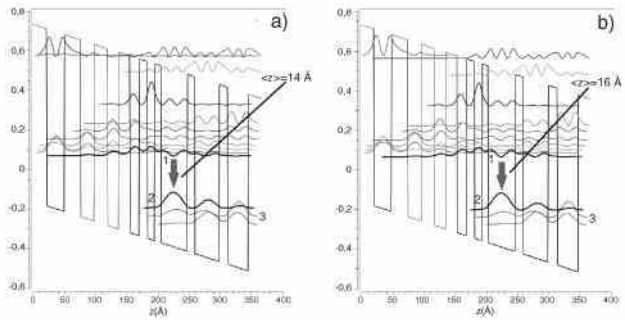

Fig. 1. The comparison of the initial manually created (a) and optimized (b) MIR QCL structures. The optimized structure has narrowed barriers and broadened wells in the active region, whilst the injector barriers were simply narrowed. The lower lasing levels (2,3) resemble a staircase shape, similar to diagonal QCL design.

These generated structures were compared with manually created designs based on a rule of thumb. Here we present analysis for the MIR QCLs emitting at 4.5 μm.

Initially, the variation parameters were layer thicknesses and doping concentrations. For some reason, such a set of parameters didn't converge in a reasonable time. Hence the

variation was restricted to thickness varying only. The dopping concentrations still influence the optical gain, but more simply than the layer thicknesses and can be considered separately. Its variation may lead to unnecessary optimization complications, which might explain the absence of fast convergence in the first case. As a result, the optimization generated a large number of designs with increased wallplug efficiency for needed wavelengths.

The most notable and systematic changes were the shrinking of injector layers which we can interpret as an attempt to increase the electron tunneling effect. Also, the shrinking and expanding of the active region layers are evident (Fig. 1), which led to better electron confinement in the active region wells. Applied changes increased dipole matrix elements and revealed a trade-off between vertical and diagonal types of design.

3. Conclusions

We have applied the most efficient techniques of QCL simulations in combination with the genetic algorithm to obtain MIR QCL designs. Utilized methods were accelerated using the CUDA technology on GPU. Achieved acceleration allows one to use optimization tools for time-efficient automatic device generation. Structures obtained via the optimization method were compared with the initial designs. The comparison showed changes in the device thicknesses for both active and injector regions. Observed changes altered the lasing scheme of QCLs towards a different type of designs. Obtained insights can help with the manufacturing of new more efficient QCL devices.

References

[1] R.F. Kazarinov and R.A. Suris, *Soviet Physics Semiconductors* **5**, 707 (1971).
[2] J. Faist, F. Capasso, D.L. Sivco *et al*, *Science* **264**, 553 (1994).
[3] A. Bismuto, R. Terazzi, B. Hinkov *et al*, *Applied Physics Letters* **101**, 021103 (2012).
[4] A. Mirčetić, D. Indjin, Z. Ikonić *et al*, *J. of Applied Physics* **97**, 084506 (2005).
[5] M. Fischer, G. Scalari C. Walther *et al*, *J. of Crystal Growth* **311**, 1939 (2009).
[6] C. Jirauschek. C. Kubis, *Applied Physics Reviews* **1**, 011307 (2014).
[7] A.S. Dashkov. L.I. Goray, *J. of Physics: Conference Series* **1410**, 012085 (2019).
[8] *What is CUDA?* (n.d.). NVIDIA. Retrieved March 04, 2020, from https://www.nvidia.com/object/io_69526.html

28th Int. Symp. "Nanostructures: Physics and Technology"
Minsk, Belarus, September 2020

High power quantum-cascade lasers emitting at 8 µm wavelength

V.V. Dudelev[1], D.A. Mikhailov[1], E.D. Cherotchenko[1], A.V. Babichev[2,3], A.G. Gladyshev[3], S.N. Losev[1], I.I. Novikov[1,2,3], A.V. Lyutetskiy[1], S.O. Slipchenko [1], N.A. Pikhtin[1], L.Ya. Karachinsky[1,2,3], A.Yu. Egorov[3], D.V. Denisov[4], V.I. Kuchinskii[1], G.S. Sokolovskii[1]

[1] Ioffe Institute, Saint Petersburg, Russia
[2] ITMO University, Saint Petersburg, Russia
[3] Connector Optics LLC, Saint Petersburg, Russia
[4] ETU "LETI", Saint Petersburg, Russia

Abstract. We study high power quantum-cascade lasers emitting near 8 μm. In the regime of pulsed electrical pumping the peak optical power exceeding 13 W (> 6.5 W/facet) is demonstrated at room temperature.

Introduction

The spectral range near 8 μm contains both a window of transparency of the atmosphere and absorption lines of gases and explosives that makes it very useful for many applications. Therefore, high-power quantum cascade lasers (QCLs) for the spectral range of 8 μm are considered as the key components for wireless optical communication, security systems, and environmental monitoring. In this work we study the characteristics of high-power quantum-cascade lasers emitting near 8 μm.

1. Experimental results

At first we fabricated 4 sets of QCL samples, varying the stripe width and cavity length [1]. Lasers with a stripe width of 20 μm and 50 μm were fabricated from a heterostructure containing 50 quantum cascades in the active region. The studied cavity lengths were 3 and 4.7 mm. The QCL characteristics were investigated in the regime of pulsed electrical pumping with a pulse duration of 70 ns and a repetition rate of 48 kHz. For the efficient active region cooling the QCL samples were mounted epi-side down to the heat sink. The measurement technique is described in detail in [2,3]. Typical QCL threshold currents with a cavity length of 3 mm and 4.7 mm were 2.7 and 4 A respectively for samples with a stripe width of 20 μm, 6 and 8 A respectively for samples with a stripe width of 50 μm.

Figure 1a represents a typical QCL generation spectrum. The maximum of the lasing spectrum for these samples typically lies in the spectral range of 7.8–8.1 μm and varies from sample to sample depending on the cavity length and the amplitude of the pump current.

Figure 1b shows the typical L-I curve of a QCL with 50 μm stripe and resonator lengths 4.7 mm. The maximum optical power from one facet of QCLs with a cavity length of 4.7 mm exceeded 13 W (>6.5 from/facet) for 50 μm stripe widths. The achieved powers are currently record-high for a QCL in a spectral range of 8 μm [4,5].

2. Conclusion

In conclusion, we study high-power QCLs lasing in spectral range of 8 μm with an active region based on the $In_{0.53}Ga_{0.47}As/Al_{0.48}In_{0.52}As$ heterostructures lattice-matched to the substrate. Record-high peak optical power exceeding 13 W (> 6.5 W/facet) is demonstrated at room temperature.

Acknowledgement

This research is supported by the Ministry of Science and Higher Education of Russian Federation (project identifier RFMEFI60719X0318)

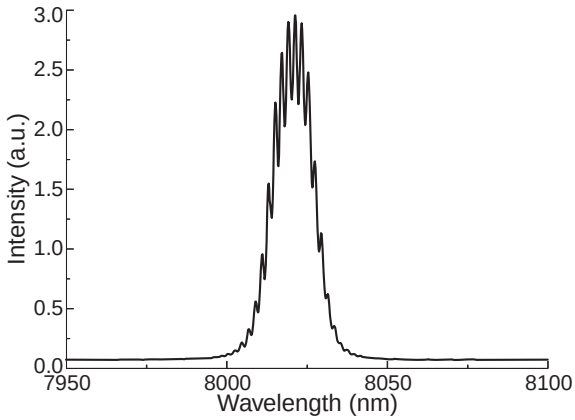

Fig. 1. Typical spectrum of QCL with stripe width of 50 μm and cavity length of 4.7 mm at 10 A pump current.

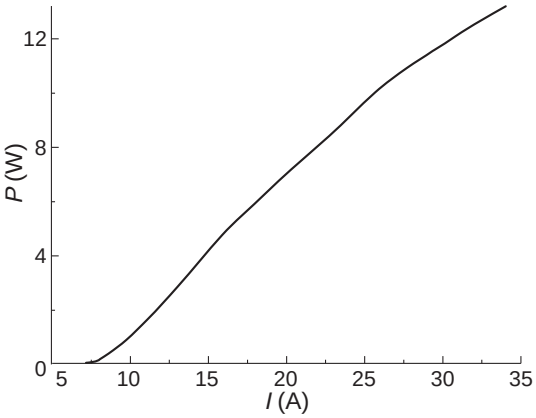

Fig. 2. L-I curve of QCL with stripe width 50 μm.

References

[1] A.V. Babichev, A.G. Gladyshev, A.V. Filimonov, *et al*, *Technical Physics Letters* **43**, 666–669 (2017).
[2] A.V. Babichev, V.V. Dudelev, A.G. Gladyshev, *et al*, *Technical Physics Letters* **45**(7), 735–738 (2019).
[3] V.V. Dudelev, S.N. Losev, V.Yu. Mylnikov, *et al*, *Opt.ics and Spectroscopy* **125**, 402–404 (2018).
[4] B. Schwarz, C.A. Wang, L. Missaggia, *et al*, *ACS Photonics* **4**, 1225–1231 (2017).
[5] D. Botez, J.D. Kirch, C. Boyle, *et al*, *Opt. Mat. Exp.* **8**, 1378–1398 (2018).

28th Int. Symp. "Nanostructures: Physics and Technology"
Minsk, Belarus, September 2020

Towards far and mid IR lasers based on HgCdTe QW heterostructures

V.I. Gavrilenko[1,2], S.V. Morozov[1,2], V.V. Rumyantsev[1,2], M.A. Fadeev[1,3], K.E. Kudryavtsev[1], V.V. Utochkin[1,2], N.S. Kulikov[1,2], A.A. Razova[1,2], A.A. Dubinov[1,2], V.Ya. Aleshkin[1,2], N.N. Mikhailov[4,5], S.A. Dvoretckiy[4], F. Teppe[3] and C. Sirtori[6]

[1] Institute for Physics of Microstructures, 603950, N.Novgorod, Russia
[2] Lobachevsky State University of Nizhny Novgorod, 603950, N.Novgorod, Russia
[3] Laboratoire Charles Coulomb, UMR CNRS 5221, Montpellier University, 34095 Montpellier, France
[4] A.V.Rzhanov Institute of Semiconductor Physics, Siberian Branch of Russian Academy of Sciences, 630090, Novosibirsk, Russia
[5] Novosibirsk State University, Novosibirsk, 630090, Russia
[6] Laboratoire de Physique de l'Ecole Normale Supèurieure, Paris, 75005, France

Abstract. Stimulated emission (SE) at wavelengths up to 24 μm (12.5 THz) and down to 2.8 μm is demonstrated from HgCdTe quantum well (QW) heterostructures. Non-radiative Auger recombination is shown to be mitigated due to relativistic energy spectrum. Pump-probe carrier lifetime measurements show that further increase in SE wavelength is feasible up to 60 μm (5 THz). In the short wavelength range SE down to 2.8 μm is demonstrated at temperatures available with Peltier coolers.

Introduction

Far IR spectral range still lacks compact and efficient radiation sources. Quantum cascade lasers (QCLs) demonstrate remarkable performance in the range 1 to 5 THz and above 15 THz [1]. In between 5 and 15 THz their characteristics drop because of phonon absorption. The interband lasers are a straightforward alternative, but it requires narrow-gap materials (with low optical phonon frequencies), in which the Auger recombination is expected to be very effective. However Auger processes can be suppressed in $Hg_{1-x}Cd_xTe/Cd_yHg_{1-y}Te$ QWs due to a "symmetry" of electron and hole energy-momentum laws that greatly in-creases the threshold energy of the intrawell Auger recombination [2]. It is worth mentioning that quasirelativistic electron-hole dispersion in PbSnSe and PbSnTe compounds results in Auger processes suppression in these materials [3]. As a consequence, leadtin salt diodes operate at wavelengths up to 50 μm [4] despite high residual carrier concentration resulting from impurities and defects. However, the figures of merit for such lasers are limited by the growth technology. The paper presents recent results on SE in long wavelength end of mid IR/ far IR range as well as on the SE in the opposite short wavelength end of mid IR range obtained at nearly room temperatures.

1. Methods and approaches

The structures under study were MBE-grown on semi-insulating GaAs(013) substrates with ZnTe and CdTe buffers with in situ ellipsometric control of the layer content and thickness [5]. Ex situ characterization of the structures was performed by measuring interband photoconductivity and photoluminescence spectra at different temperatures. The temperature dependence of the bandgap was extracted from the PC and PL spectra and then compared to the band diagrams calculated in the framework of Kane 8×8 Hamiltonian axial model, allowing us to determine the width and Cd content for each QW. The structures under study were designed so as to effectively confine light to in-plane direction; therefore the "active" region (5–10 QWs) was placed at the antinode position of TE_0 mode of the dielectric waveguide [2] — Fig.1. They have no cleaved facets, so, the SE results from single-pass amplification. QW parameters of structures are as follows:

#1: $d_{QW} = 7.9$ nm (10 QWs), $x_{QW} = 0.078$, $y_{barr} = 0.7$;
#2: $d_{QW} = 5.4$ nm (5 QWs), $x_{QW} = 0.09$, $y_{barr} = 0.6$;
#3: $d_{QW} = 1.9$ nm (10 QWs), $x_{QW} = 0.09$, $y_{barr} = 0.65$;
#4: $d_{QW} = 2.5$ nm (10 QWs), $x_{QW} = 0.08$, $y_{barr} = 0.65$
#5: $d_{QW} = 2.7$ nm (10 QWs), $x_{QW} = 0.08$, $y_{barr} = 0.75$.

The structures were not intentionally doped; the residual carrier density is several 10^{10} cm^{-2} and the typical dislocation density determined from the etch pits density was of $\sim 10^6$ cm^{-2}. The samples were mounted either on the cold finger of a closed-cycle helium cryostat ($T = 8-200$ K) or in a Peltier cooler ($T = 200-300$ K). Pulsed (100 ns, 10 Hz) CO_2 laser ($\lambda_{exc} = 10.6$ μm) was used for the optical excitation of the sample #1, c.w. semiconductor laser ($\lambda_{exc} = 0.9$ μm) for that of the sample #2, the pulsed (10 ns, 10 Hz) optical parametric oscillator (SOLAR OPO, $\lambda_{exc} = 1.5-1.6$ μm) pumped with Nd:YAG laser — for the samples #3, #4 and Nd:YAG laser ($\lambda_{exc} = 1.06$ μm) — for the sample #5. SE was collected from the sample's facet and guided to the FTIR spectrometer Bruker Vertex 80v operating in the step scan mode [2,6]. Liquid-helium-cooled silicon bolometer and liquid-nitrogen-cooled MCT photodiodes were used as detectors.

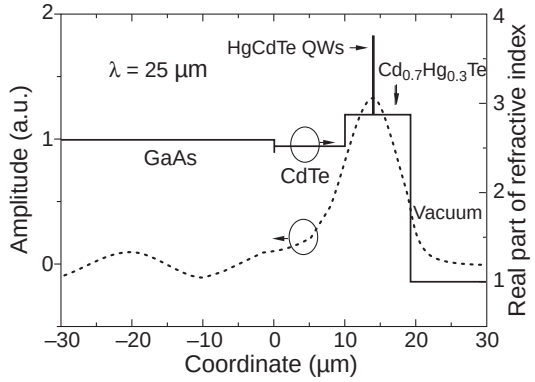

Fig. 1. The refractive index distribution throughout structure #1 and the calculated TE mode localization for $\lambda = 25$ μm.

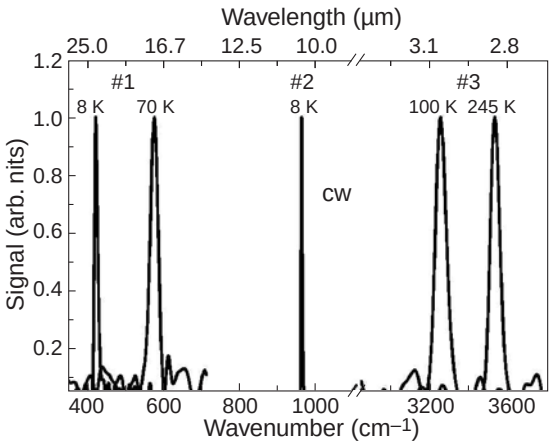

Fig. 2. SE spectra at different temperatures (solid curves) obtained under pulsed (sample #1, $\lambda_{exc} = 10.6$ μm; sample #3, $\lambda_{exc} = 1.5$ μm) and CW (sample #2, $\lambda_{exc} = 0.9$ μm) optical excitation.

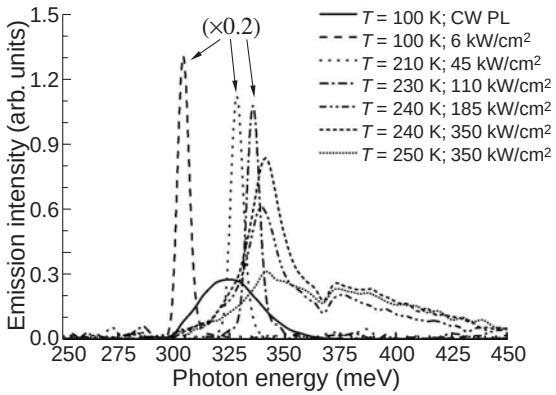

Fig. 3. SE spectra in the sample #5 obtained under pulsed optical excitation (λ_{exc} =1.06 μm) at different temperatures.

2. Results and discussions

Typical SE spectra are given in Fig. 2. In the long wavelength range the best results were achieved at a "cold" excitation with CO_2 laser that provide the lower effective temperature of the photoexcited thus preventing from the nonradiative Auger recombination [7]. As a result, SE was obtained at a record wavelength 24 μm (Fig. 2, sample #1). The threshold excitation power was 10 kW/cm^2 and it could be decreased by growing a structure with pure HgTe (without Cd) QW keeping the same bandgap. At shorter wavelengths λ10 μm the excitation threshold power ($\lambda_{exc} \sim 2$ μm) proved to be as low as 120 W/cm^2 [2] and the SE was obtained even at CW excitation ($\lambda_{exc} \sim 0.9$ μm, 7 W/cm^2, Fig. 2, sample #2).

Direct pump-probe lifetime measurements in HgTe QW with bandgap of 20 meV (4.8 THz) give a figure of 100 ps that corresponds to threshold pumping intensity for SE again of 10 kW/cm^2 [2] thus paving the way towards HgTe QW based interband lasers operating up to wavelength of 60 μm (5 THz).

In narrow (1.9–2.7 nm) HgCdTe/CdHgTe QWs the SE was obtained in 2.8–3.7 μm wavelength range at temperatures available with thermoelectric cooling [6] (see e.g. Fig. 2, sample #3). In such QWs intended for the SE in the spectral range 3 to 5 μm a new type of Auger processes could arise, namely thresholdless electron-hole recombination when the third electron/hole is driven to the continuum of the conduction/valence band in the barriers [8]. Such processes are switched-on when the band gap in a QW exceeds the conduction/valence band offset at the QW interfaces. The only way to avoid this thresholdless Auger recombination seems to enhance the band gap in $CdyHg_{1-y}Te$ barriers, i.e. to increase the y. In doing so we have increased the Cd content in the sample #5 up to y =0.75 if compares to $y = 0.65$ in the sample #4, the gap being approximately the same. According to our calculations this leads to a larger conduction band offset exceeding the gap in the QW (though this is not the case for the valence band offset). This immediately has resulted in the increase of the SE threshold temperature $T_{th} = 230-240$ K at $\lambda = 3.7$ μm in the sample #5 (see Fig. 3) compared with $T_{th} = 210$ K in the sample #4 at even shorter wavelength $\lambda = 3.55$ μm [6]. So, such QW structures seem prospective for the lasers operating in the atmospheric transparency window 3 to 5 μm at room temperature or at thermoelectric cooling ($T = 200$ to 300 K) which are demanded for numerous spectroscopy applications

Acknowledgements

The work was performed as part of the state assignment of IPM RAS (#0035-2019-0020) and under the support of the Russian Foundation for Basic Research (grants No. 18-52-16013, and No. 19-02-00827) and the Ministry of Science and Education of the Russian Federation (MK-1430.2020.2). The work was done using equipment of the Center "Physics and technology of micro- and nanostructures" at IPM RAS.

References

[1] M.S. Vitiello *et al*, *Opt. Express* **23**, 5167 (2015).
[2] S. Ruffenach *et al*, *APL Materials* **5**, 035503 (2017).
[3] J. Dimmock *et al*, *Phys. Rev. Lett.* **16**, 1193 (1966).
[4] K.V. Maremyanin *et al*, *Semiconductors* **52**, 1590 (2018).
[5] N.N. Mikhailov *et al*, *Int. J. Nanotechnol.* **3**, 120 (2006).
[6] M.A. Fadeev *et al*, *Optics Express* **26**, 12755 (2018).
[7] V.V. Rumyantsev *et al*, *Semiconductors* **52**, 1375 (2018).
[8] A.S. Polkovnikov, G.G. Zegrya. *Phys. Rev. B* **58**, 4039 (1998).

28th Int. Symp. “Nanostructures: Physics and Technology”
Minsk, Belarus, September 2020

Nonlinear optical properties of epitaxial quantum dot semiconductor lasers on silicon

F. Grillot[1,4], W.W. Chow[2], J. Duan[1], J.C. Norman[3], S. Liu[3], and J.E. Bowers[3]

[1] LTCI, Télécom Paris, Institut Polytechnique de Paris, 19 place Marguerite Perey, 91120 Palaiseau, France
[2] Sandia National Laboratories, Albuquerque, NM 87185, USA
[3] Materials and Electrical and Computer Engineering Departments, University of California, Santa Barbara, California 93106, USA
[4] Center for High Technology Materials, University of New Mexico, Albuquerque, NM 87106, USA

Abstract. This work features the nonlinear optical properties in semiconductor quantum dot lasers grown on silicon. Here, we measure, discuss and analyze the wave-mixing contributions resulting in mode competition, gain saturation, carrier-induced refractive index and creation of combination tones, all of which have roles for self-mode-locking. Using a microscopic level model including the quantum mechanical electron-hole polarization, we show that such optical nonlinearities in epitaxial quantum dot lasers on silicon can provide a strong mechanism of self-mode-locking. Overall, we believe that these results are promising not only for integrated technologies on silicon but also for entangled photon creation in future quantum information systems.

Introduction

When two co-polarized fields at different frequencies copropagate within a nonlinear gain media having a third-order nonlinear susceptibility, the beating between them leads to the occurrence of wave-mixing and the generation of two new fields. Here, we investigate optical nonlinearities in a semiconductor quantum-dot (QD) active medium directly grown on silicon substrate. Prior works concentrated on on QD semiconductor optical amplifiers (SOA) [1–2] and lasers [3–4] grown on natural substrates. In the former, it was found that SOAs have a larger linear gain providing higher conversion efficiency, while also generating stronger amplified spontaneous emission noise, thus limiting the optical signal-to-noise ratio. This work is motivated by indications that QD optical nonlinearities can provide the mechanism of self-mode-locking, which will significantly reduce complexity and energy requirement in wavelength division multiplex (WDM) systems [5]. To do so, we measure and analyze the wave-mixing contributions resulting in mode competition, gain saturation, carrier-induced refractive index and creation of combination tones, all of which have roles self-mode-locking. Our approach constitutes a first-principles determination four-wave-mixing coefficients in a semiconductor QD active medium. In particular, we extract relevant four-wave-mixing coefficients from pump-probe laser measurements and connect to multimode semiclassical laser theory for understanding the underlying physics of QDs [6]. We show that optical nonlinearities in such epitaxial QD lasers on silicon do provide a strong mechanism of self-mode-locking. Overall, these results are promising not only to develop optical wavelength converters for integrated WDM communication systems that can be employed in future photonic integrated circuits but also for entangled photon creation in future quantum information systems [7,8].

1. Device description

The QD laser material was grown on pieces from a 300 mm on-axis (001) GaP/Si template. The laser structure shown in Fig. 1 consists of 1400 nm $Al_{0.4}Ga_{0.6}As$ upper (p-type) and lower (n-type) cladding to provide electrical and optical confinement.

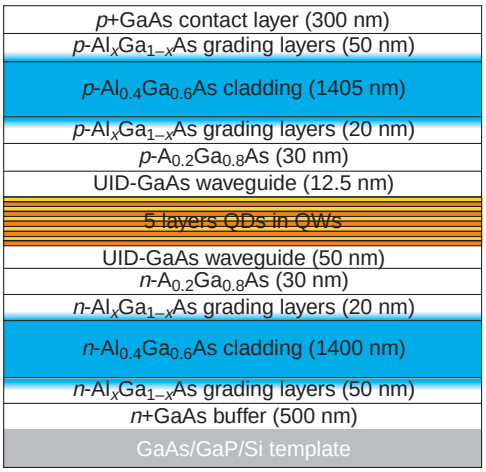

Fig. 1. Epitaxial structure of the FP QD laser on silicon

The active region consists of five periods.

2. Theory

Fig. 2(a) shows a schematic of frequencies involved in the intracavity four-wave mixing experiment. The laser injection are at the pump and probe modes, labeled 0 and p, respectively. The signal appears in the mode labeled s. Also present are lasing or non lasing modes, collectively labeled as n. Fig. 2(b) displays the QD active region inside cavity of length L and facets with transmissions T_1 and T_2. The injected intensities are $I_0^{\rm inj}$ and $I_p^{\rm inj}$, the measured 4-wave mixing signal intensity is $I_s^{\rm out}$, and the corresponding intracavity intensities are I_0, I_p and I_s, respectively. Intensities of the other modes are labeled I_n.

Using the semiclassical laser theory [6], the laser intensities in the different cavity modes are obtained by solving the following equations of motion:

$$I_0(t) = \left[G_0^{\rm sat}(N) - \frac{\nu}{Q}\right] I_0(t) + \frac{c}{2Ln_B}\sqrt{T_1 I_0(t) I_0^{\rm inj}} + S \quad (1)$$

$$I_p(t) = \left[G_0^{\rm sat}(N) - \frac{\nu}{Q}\right] I_p(t) + \frac{c}{2Ln_B}\sqrt{T_1 I_p(t) I_p^{\rm inj}} + S \quad (2)$$

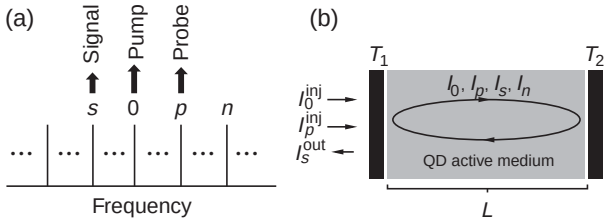

Fig. 2. (a) Sketch showing frequencies involved in the intracavity four-wave mixing experiment. (b) Sketch of laser showing quantum dot active region with the injected intensities $I_0^{\rm inj}$ and $I_p^{\rm inj}$, the measured 4-wave mixing signal intensity is $I_s^{\rm out}$, and the corresponding intracavity intensities are I_0, I_p and I_s, respectively.

$$I_s(t) = \Big[G_0^{\rm sat}(N) - \frac{\nu}{Q}\Big] I_s(t) + |2\theta s_0 p_0(N)| \sqrt{I_p(t) I_s I_0(t) + S} \tag{3}$$

$$I_n(t) = \Big[G_n^{\rm sat}(N)\Big] I_n(t) + S \tag{4}$$

$$N(t) = \frac{\eta J}{e}\Big[1 - \frac{N(t)}{2N_{QD}}\Big] - \gamma_{nr} N(t) - BN^2(t) - \frac{2n_B d}{\nu c}\sum_n G_n^{\rm sat}(N) I_n(t) \tag{5}$$

where ν/Q is the passive mode linewidth, ν is the average mode frequency, c is the speed of light in vacuum, L is the laser cavity length, n_B is the background refractive index and $S = \beta BN^2$ accounts for the spontaneous emission into a cavity mode. β is the spontaneous emission factor, B is the bimolecular carrier recombination rate coefficient and N is the two-dimensional (2d) saturated carrier density. The subscripts 0, p and s label the pump, probe and signal modes. External injection is via the cavity mirror with transmission T_1, with pump and probe intensities $I_0^{\rm inj}$ and $I_p^{\rm inj}$, respectively. In Eq. (5), the pump term consists the current density J, injection efficiency from electrodes to QD states η, and carrier blocking due to the Exclusion Principle $1 - \frac{N}{2N_{QD}}$, where N_{QD} is the 2D QD density. The QD gain medium properties appear in the equations in the form of the saturated gain $G_n^{\rm sat}$ and the relative phase angle coefficient $\theta_{s0p0}(N)$.

From the derivation of active medium polarization, the saturated gain is

$$G_n^{\rm sat}(N) = \frac{G_n(N)}{1 + \sum_m^I m^{\varepsilon} nm(N)} \tag{6}$$

which contains a linear gain contribution

$$G_n(N) = \frac{\nu_n \wp^2 N_{QD}\Gamma}{\sqrt{2}\pi\epsilon_B \Delta_{\rm inh} d} n_{\rm inv}(\nu_n, N)\Lambda_n \tag{7}$$

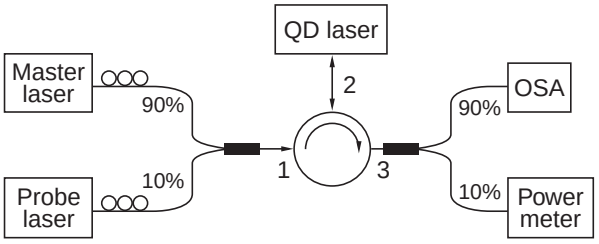

Fig. 3. Optical injection locking setup used for the four-wave mixing experiments. OSA: optical spectrum analyzer

where

$$\Lambda_n = \int_{-\infty}^{\infty} d\omega \exp\Big[\Big(\frac{\omega - \omega_0}{\sqrt{2}\Delta_{\rm inh}}\Big)^2\Big] L(\omega - \nu_n) \tag{8}$$

where ϵ_B is the permittivity in vacuum, $\Delta_{\rm inh}$ is the QD inhomogeneous width, d is the thickness of a QD layer, Γ is the confinement factor, $\wp$ is the dipole matrix element, $L(x) = \big[1 + \big(\frac{x}{y}\big)^2\big]^{-1}$ and γ is the dephasing rate. Also, in Eq. (7) are contributions from the active medium nonlinearities. They give rise to gain saturation and mode competition. To evaluate the coefficients ε_{nm}, we use the general 4-wave mixing expression:

$$\theta nn'mm' = D(\nu_m - \nu m') \int_{-\infty}^{\infty} d\omega \exp\Big[\Big(\frac{\omega - \omega_0}{\sqrt{2}\Delta_{\rm inh}}\Big)^2\Big] \times D(\omega - \nu_{n'} + \nu_m - \nu_{m'})[D(\nu_m - \omega) + D(\omega - \nu_{m'})] \tag{9}$$

where $D(x) = \big(1 + i\frac{x}{y}\big)^{-1}$. As for the self-saturation coefficient, it can be expressed as

$$\varepsilon_{nn} = \frac{1}{\epsilon_B c\gamma}\Big(\frac{\wp}{2\gamma}\Big)^2 \frac{\theta_{nnnn}}{\Lambda_n} \tag{10}$$

and for the cross-saturation coefficient,

$$\varepsilon_{nm} = \frac{1}{\epsilon_B c\gamma}\Big(\frac{\wp}{2\gamma}\Big)^2 \frac{\theta_{nnmm} + \theta_{nmmn}}{\Lambda_n} \tag{11}$$

for $n \neq m$. The QD optical nonlinearities can also lead to self-mode-locking via the relative phase angle term in Eq. (3). The relevant 4-wave mixing susceptibility is then defined such as

$$\chi^{(3)}(N) = \frac{2}{\nu_o}\Big(\frac{\wp}{2\gamma}\Big)^2 |\theta_{s0p0}(N)| \tag{12}$$

The experiment starts with injecting only the pump field. Fig. 3 shows the optical injection locking experimental setup used for the four-wave mixing experiment. The light from two external tunable lasers are combined using a 90/10 coupler and injected into the QD laser through an optical circulator. The master laser is used to lock the gain peak mode of the FP modes while the probe laser is used to generate the four-wave mixing with the locked FP modes. The optical spectrum at the output of the QD laser is then measured by an optical spectrum analyzer with a 20 pm resolution. Figure 4(a) shows the computed suppression of side modes with increasing injected pump power, for a laser operating

Figure 4(a) shows the computed suppression of side modes with increasing injected pump power, for a laser operating at $T = 300$ K with a 1.4 mm$\times$6 μm$\times$0.5 μm GaAs cavity and an active region consisting of 5 $In_{0.15}Ga_{0.85}As$ QWs, each 7 nm thick and embedding a density of 2×10^{10} cm^{-2} InAs QDs. We use background refractive index $n_B = 3.66$, dipole matrix element $\wp = e\times0.6$ nm and central transition energy $\omega_0 = 0.943$ eV. The dephasing rate is $\gamma = 2\times10^{12}$ s^{-1} and the nonradiative decay rate is γnr $= 10^9$ s^{-1}. We assume a carrier injection efficiency of $\eta = 0.35$ with lasing at around 1.315 μm. The figure indicates a sideband suppression ratio of approximately 103 with an injected intensity of $I_0^{\rm inj} = 0.04$ mW, with the laser operating three times above threshold. This is where the four-wave mixing experiments are conducted (see data point in Fig. 4(b)).

With the injection of a laser field at the probe mode, one sees the rise of a signal intensity, as depicted in Fig. 5(a). The

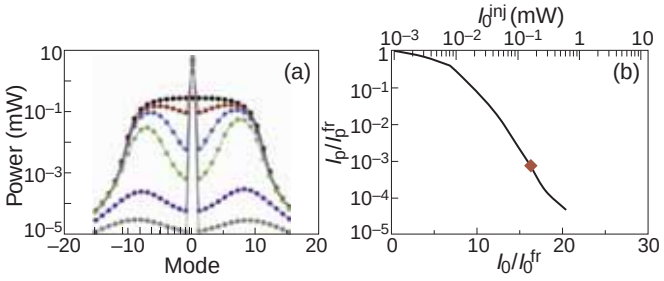

Fig. 4. (a) Intracavity power versus mode number for injection intensity $I_0^{\text{inj}} = 0$ (black), 0.01 mW (red), 0.05 mW (blue), 0.10 mW (green), 0.2 mW (purple) and 0.40 mW (grey). (b) Suppression of intracavity probe intensity versus amplification of intracavity pump intensity (bottom axis) and injected pump intensity (top axis). The reference are the corresponding free-running (fr) intensities and the red data point is from experiment. For (a) and (b), the FP QD laser is operated at twice its threshold current

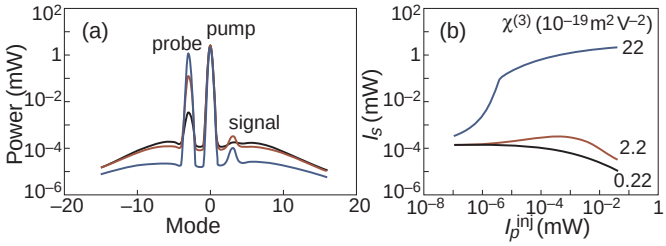

Fig. 5. (a) Intracavity power versus mode number for injection intensity $I_0^{inj} = 0.04$ mW and injected probe intensities $I_p^{inj} = 10^{-6}$ mW (black), 10^{-4} mW (red) and 10^{-2} mW (blue). The curves are computed assuming 4-wave mixing susceptibility $\chi^{(3)} = 2.2\times10^{-19}$ m^{2}V^{-2}. (b) Signal power versus injected probe power for 4-wave mixing susceptibility $\chi^{(3)} = 2.2\times10^{-20}$ m^{2}V^{-2} (black), $\chi^{(3)} = 2.2\times10^{-18}$ m^{2}V^{-2} (blue)

laser experiments yield some differences from the amplifier ones, as illustrated in Fig. 5(b). The differences arise because of gain saturation by the pump and probe intracavity fields. For small four-wave mixing susceptibility, mode competition can dominate the generation of the signal. Then, increasing the probe intensity will depress the signal intensity as shown by the black curve in Fig. 5(b), for $\chi^{(3)} = 2.2\times10^{-20}$ m^{2}V^{-2}. With a higher four-wave mixing susceptibility, e.g. $\chi^{(3)} = 2.2\times10^{-19}$ m^{2}V^{-2}, there is a range of injected probe intensities where the four-wave mixing gain exceeds the attenuation from mode competition and one sees an increase in signal intensity with increasing injected probe power. Eventually, the signal power drops, when the four-wave mixing gain can no longer overcome the mode competition (red curve). In the rare situation of a larger four-wave mixing susceptibility, one may even encounter the situation of four-wave mixing gain to exceed the cavity losses. Then lasing by four-wave mixing can occur, as depicted by the 'S' shape blue curve for $\chi^{(3)} = 2.2\times10^{-18}$ m^{2}V^{-2}. The experiments are conducted in the regime represented by the red curve where $D(x) = \gamma/(\gamma + ix)$. The attractiveness of the ratio given by Eq. (4) is the drastic reduction in device variables. The relevant material parameters are, Δ_{inh} describing QD inhomogeneous broadening [4], and the carrier scattering rates, γ and γ_{ab} for dephasing and population relaxation, respectively. Laser resonator configuration enters via the mode frequencies Ω_n and spatial-hole burning as given by the integral over the passive cavity eigenfunctions $u_n(z)$. Important is that the ratio applies to lasers with different lasing threshold, excitation above threshold, confinement factor, active layer thickness and QD density. Also, it does not depend on less precisely known parameters, such as the dipole matrix element, background refractive index, nonradiative carrier loss and absorption.

To sum, we calculated four-wave-mixing coefficients from pump-probe laser measurements and connect to multimode semiclassical laser theory. We discovered that there is a range of injected probe intensities where the four-wave mixing gain exceeds the attenuation from mode competition and one sees an increase in signal intensity with increasing injected probe power. Thus, lasing by four-wave mixing occurs for $\chi^{(3)} = 2.2\times10^{-18}$ m^{2}V^{-2}. These initial results are promising for controlling optical nonlinearities in epitaxial QD lasers with the view of using them for integrated technologies on silicon and quantum information systems and to better understand so-called self mode-locking.

Acknowledgements

This work is supported in part by the Center for Integrated Nanotechnologies (CINT) through a Rapid Access proposal (2019BRA0032). Authors also acknowledge the financial support of Advanced Research Projects Agency — Energy contract DE-AR0001039, and the Institut Mines-Télécom.

References

[1] T. Akiyama, *et al*, *IEEE J. Quantum Electron.* **60**, 1059 (2001).
[2] H. Ishikawa *et al*, *Semiconductor and Semimetals*, **60**, 287 (1999).
[3] H. Su *et al*, *IEEE Photonics Tech. Lett.*, **17**, 1686 (2005).
[4] T. Sadeev *et al*, *App. Phys. Lett.*, **107**, 191111 (2005).
[5] J.C. Norman *et al*, *APL Photonics*, **3**, 030901 (2018).
[6] W.W. Chow *et al*, *Semiclassical Laser Physics*, Springer (1994).
[7] W.W. Chow *et al*, *Progr. Quantum Electron.*, **37**, 109 (2013).
[8] J.C. Norman *et al*, *IEEE J. Quantum Electron.*, **55**, 2000511 (2019).

28th Int. Symp. "Nanostructures: Physics and Technology"
Minsk, Belarus, September 2020

Inelastic scattering of carriers by LO-phonons in pumped semiconductors lasers

V.G. Popov[1,2], V.G. Krishtop[1,2] and S.A. Tarelkin[3]

[1] Center of scientific research and perspective development, JSC Infotecs, Stariy Petrovskii-Razumovskii proezd, 1/23 bd. 1, Moscow, 127287.
[2] Institute of Microelectronics Technology of RAS, Academician Osipyan st., 6, Chernogolovka Moscow region, 142432.
[3] The All-Russian Research Institute for Optical and Physical Measurements, Federal State Unitary Enterprise, Ozernaya st., 46, Moscow, 119361.

Abstract. Inelastic scattering of carriers by LO-phonons is considered theoretically in the case of a non-equilibrium distribution of the LO-phonons. The distribution appears due to the raman scattering of the pump light in the laser active region. It is interesting to note that the pumping can be used in the Stokes regime to increase the number of the LO-phonons and in anti-Stokes regime to decrease the LO-phonons number. Thus the pumping gives a possibility to adjust the occupancy of the LO-phonons in the laser active region and change of the probability of the carriers inelastic scattering. As a result a turn-on delay of the semiconductor lasers can be decreased.

Introduction

Carriers scattering is crucial process responsible for a turn-on delay of semiconductor lasers [1] that is in its turn crucial for the speed of the information exchange in telecommunications. To management of this process gives the possibility to further decrease of the delay and finally increase the information exchange. In this report we have considered an inelastic scattering of the carriers in the presence of the pumping light that is expected to produce or reduce the non-equilibrium LO-phonons in the active region of the laser. The study of the LO-phonon scattering has a very long history in semiconductors. This scattering is also responsible for the drift-velocity saturation in the MOSFETs [2]. LO-phonons were thoroughly investigated in semiconductors nanostructures taking in to consideration size-quan-tization effect [3]. It was shown that scattering rate is increased on interface modes of the LO-phonons in the quantum wells (QW) and wires. From the first point of view the rate increase should decrease the turn-on delay. However since phonons becomes localized they continue to interact with carriers even after the scattering and hence it can restore the energy of the carriers. As a result the overall turn-on delay is observed to increase that is called the phonon bottleneck effect. Thus the dynamics of the phonon subsystem becomes very crucial for the problem of the turn-on delay in semiconductor lasers. To overcome the phonon bottleneck there are some techniques such as resonant-tunneling injection of the carriers [4] or preliminary heating of the laser active region. The phonon bottleneck is also crucial when the semiconductor lasers is used as optical amplifiers or transformers in telecommunications.

Recently a new tasks appear dealt with quantum key distribution (QKD) [5]. In particularly the promising single-photon source is a N-V center in the diamond since it operates in room temperateure [6]. However it emits light of 637 nm wavelength and conversion is required to the telecommunication wavelengths [7]. The semiconductor laser can be also considered as a such kind transformer. In this case the photon emitted by the N-V center can be absorbed by an electron-hole pair in the laser active region and after relaxation in to the QW can emit photon of the telecommunication wavelength. Thus increase the rate of the relaxation should increase the efficiency of the conversion.

In the next section we consider the inelastic scattering rate and their dependence upon the phonon number and consider the conditions of the phonon bottleneck effect after that the dependence of the turn-on delay up on the pump power will be discussed when the phonon bottleneck is negligible and the pumping takes place in the stokes regime. In the section 2 we will discussed the phonon bottleneck effect thoroughly and consider the pumping in anti-stokes regime. Finally we conclude our results and acknowledge.

1. Scattering in Stokes regime

Usually the probability of the inelastic scattering or more accurately a rate can be estimated via Fermi golden role and Fröhlich Hamiltonian [3] as follows:

$$W_{if}^{e,a} = \frac{|C|^2}{4\pi\hbar^2 q^2}\left(n_q + \{{}^1_0\}\right)\delta\left(E_i - E_f \mp \hbar\omega_0\right), \qquad (1)$$

where the C is the Fröhlich constant of interaction, q, n_q, ω_0 are a wave vector, occupation and frequency of the LO-phonon. In this case the transition takes place assisted by LO-phonon emission (superscript "e", sign "-" and "1" are chosen) or absorption (superscript "a", sign "+" and "0" are chosen) between initial carrier state with energy E_i and final state with E_f. The key parameter is the phonon occupation n_q. In the equilibrium the $n_q = 1/(\exp(\hbar\omega_0/kT) - 1) \ll 1$ here k is Boltzmann constant, T is temperature. At room temperature the $kT = 26$ meV is less than LO-phonon energy $\hbar\omega_0 = 36$ meV for GaAs and the phonon emission overcomes the absorption. At non-equilibrium condition $n_q \gg 1$ emission and absorption times $\tau_{e,a} = 1/W^{e,a}$ becomes very short and equals and carrier energy relaxation takes place only if the LO-phonons disappear between sequent processes of its emission and absorption. The time of LO-phonons disappearance τ_d is determined by the interaction of the LO-phonons with acoustic those [8]. Thus a condition for the energy relaxation is the following:

$$\tau_d < 2\tau_e. \qquad (2)$$

When the condition (2) is broken one can expect the phonon bottleneck effect. In the case of the GaAs τ_d is about 5 ps [9] thus one can decrease τ_e up to 2 ps.

To increase the LO-phonon occupation one can used a Raman scattering of the pump light in the active region of the laser. In this case the energy of the light $\overline{h}\omega$ can be chosen below the laser bandgap E_g to prevent carriers interband absorption. The Raman inelastic light scattering by LO-phonons can also be of two types. The first one is called Stokes one followed by the LO-phonon emission and the second is called anti-Stokes one dealt with the phonon absorption [9]. The dominant type of the Raman scattering can be adjust with a cascade of fiber Bragg grates like it is used in Raman amplifiers [10]. In this case the external Bragg grates should have period correspond to the wave length of the pump light but the internal grates should have the period correspond to the length of the Stokes wave. In this case the intensity of the Stoke wave will be proportional to the occupancy n_q.

2. Scattering in anti-Stokes regime

When the phonon occupancy n_q is high enough or the interaction of the phonons is weak the condition (2) is broken and the phonon bottleneck effect takes place. To decrease the phonon occupancy one can change the wave length of the pump or the internal Bragg grates period in the Raman cascade to fit its reflection to the anti-Stokes wave. In this case the inelastic light scattering will dominate with the LO-phonon absorption. Thus the phonon occupancy will be decreased on a value proportional to the intensity of the anti-Stokes wave. As a result the minimal value for the inelastic scattering time of the carriers can determined from the condition (2) as follows: $\tau_{e\min} = \tau_d/2$.

Conclusion

Finally we have proposed a new method to manage the inelastic scattering of the carriers by the LO-phonons. This method based on the Raman inelastic light scattering of the pump light. This light scattering increases the LO-phonon occupancy at the Stokes regime and decreases it when the Raman fiber cascade provides the anti-Stokes regime. This cascade can be made outside the laser cavity in the fibers coupled to the semiconductor laser. This method give the possibility to reach a minimal time $\tau_{e\min}$ for carriers inelastic scattering and minimal turn-on delay.

Acknowledgement

The work was carried out with the financial support of the Ministry of education and science of the Russian Federation in the framework of applied scientific research (unique identifier RFMEFI62419X0052), grant Agreement dated 29.11. 2020 05.624.21.0052.

References

[1] S.M. Sze, K.K. Ng *Physics of Semiconductor Devices*, 3-d Ed. (Hoboken, New Jersey: John Wiley & Sons, Inc.) 646, 2007.

[2] S. A. Schwarz, S. E. Russek, *IEEE Trans. Electron Devices*, ED-**30**, 1629 (1983).

[3] M.A. Stroscio, M. Dutta *Phonons in Nanostructures*, (Cambridge: Cambridge University Press) 131, (2004).

[4] X. Zhang, A.L. Gutierrez-Aitken, D. Klotzkin *et al*, *Electronics Letters* **32**, 1715 (1996).

[5] K.A. Balygin, V.I. Zaitsev, A.N. Klimov *et al*, *JETP Letters* **105**, 606 (2017) (in English); *Pis'ma v ZETF* **105**, 570 (2017) (in Russian).

[6] A. Gruber, A. Drabenstedt, C. Tietz *et al*, *Science* **276**, 2012 (1997).

[7] R. Ikuta, T. Kobayashi, S. Yasui *et al*, *Optics express* **22**, 11205 (2014).

[8] M.A. Stroscio, M. Dutta *Phonons in Nanostructures*, (Cambridge: Cambridge University Press) 45 (2004).

[9] A.R. Bhatt, K.W. Kim, and M.A. Stroscio, *J. Appl. Phys.* **76**, 3905 (1994).

[10] G.P. Agrawal, *Nonlinear Fiber Optics* 5-th Ed. (Oxford: Academic Press is an imprint of Elsevier) 295 (2013).

28th Int. Symp. "Nanostructures: Physics and Technology"
Minsk, Belarus, September 2020

Diffraction focusing of electromagnetic radiation by transmission through sub-wavelength nanoapertures

V. M. Serdyuk[1], S.V. von Gratovski[2] and V.V. Koledov[2]

[1] Institute of Applied Physical Problems, Belarusian State University, Minsk, Belarus
[2] Kotel'nikov Institute of Radioengineering and Electronics, Russian Academy of Sciences, Moscow, Russia

Abstract. It is shown theoretically, that the phenomenon of radiation focusing in a small region of the near zone inside a dielectric film can present due to electromagnetic wave transmission through sub-wavelength nanoapertures. The confirmation is based on the rigorous theory of plane wave diffraction by a slot in a perfectly conducting screen of finite thickness in the presence of a plane dielectric film on a substrate, which plays the role of a radiation detector.

Introduction

It was established experimentally, that at light transmission through sub-wavelength apertures with dimensions of the order of the wavelength, one can observe anomalous phenomena in the near zone, for example, great intensity of transmitted field [1,2]. It is appeared that in the case of a small aperture, one more anomalous phenomenon can exist, and it is the focusing of transmitted radiation in a small region behind the aperture. One knows, that the smaller dimension of an aperture in an opacus screen, the greater divergence of radiation behind that. In empty space at great distances, so it occurs, but in special cases, in a thin closely-spaced dielectric film (target), the dimension of light spot from an aperture can be smaller than the dimension of the latter. In the present work, the theoretical confirmation of this phenomenon is presented.

1. Results of simulation

Until recent time, the sub-wavelength aperture phenomena have described on the basis of approximate methods like the Kirchhoff's method and its modifications [2], although in the case of diffraction obstacles with dimension of the order of the wavelength, one should use only rigorous methods. That is why one can meet with incorrect statements in modern works, like that the main features of sub-wavelength transmission in conducting screens are caused by excitation of surface plasmons in the volume of a screen.

One further disadvantage of most theoretical works on this topic lies in the fact that the transmitted field is considered in empty space behind the aperture without regard for material objects, on which it effects and in which it is registered. Meanwhile, in the case of sub-wavelength spatial dimensions, for adequate estimation of real electromagnetic effect on material objects, one should take into account the distorting exposure of a radiated object as itself on the exciting field, just as in quantum mechanics one cannot neglect the reciprocal effect of an apparatus on microparticles and fields under study.

The main features of radiation transmission through sub-wavelength apertures can be explained fully without the concept of any quasi-particles in conductor, on the bases of the usual mode-matching technique of exact diffraction theory, for which a slot in a perfectly conducting screen serves as an elementary two-dimensional model of an aperture [3–5]. These features are explained by character of the field in small scale inside a slot and immediately behind that in the near zone. They are described by the solution of plane-wave diffraction problem, obtained for a slot in a perfectly conducting screen of finite thickness, which is placed before a plane dielectric film [5]. In order to study the phenomenon of focusing, we have used this model with amendment, that a thin dielectric layer (film), exposed to radiation, is placed on a thick substrate (see Fig. 1). Computations on the basis of such model confirm the possibility of presence of light focusing by a sub-wavelength aperture. The results of these computations are presented below for two field polarizations, H and E, the first of which is characterized by orthogonality of its electric vector to the plane of incidence, and the second one is determined by its parallelism to that.

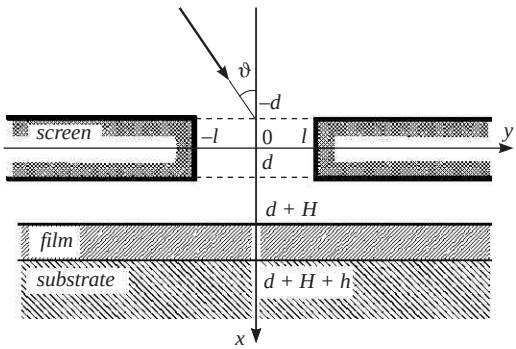

Fig. 1. Geometry of the diffraction problem.

We have considered the incidence of a plane wave at the perfectly conducting screen with the thickness $2d = 1.6\lambda$ at the angle of incidence $\vartheta = 30^\circ$, which has a slot of the width $2l = 3.2\lambda$; it has assumed that behind the screen, at the distance $H = 0.2\lambda$, the plane transparent dielectric film is located, which has the thickness $h = 1.5\lambda$ and the refractive index $n = 1.62$, and placed on the transparent substrate of very large thickness with the refractive index $n_s = 1.46$.

Some of computation results are presented on Fig. 2a for spatial distribution of electric field energy density $W(y)$ along the surface of thin film, arranged on its thickness and computed relative to the energy density W_0 of incident wave. For the radiation of E polarization, the field pattern turns out fully expected: light spot in a dielectric with dimension of more than the slot width, represents interchange of several light and dark zones with the maximal amplitude of field of the order of incident wave amplitude. However, the case of H polarization demonstrates appearance of narrow peak of intensity, whose value is greater by several fold than field intensity in another maximums, and which is more than 3 times smaller in effective width than the width of the slot itself. Thereby, for H polariza-

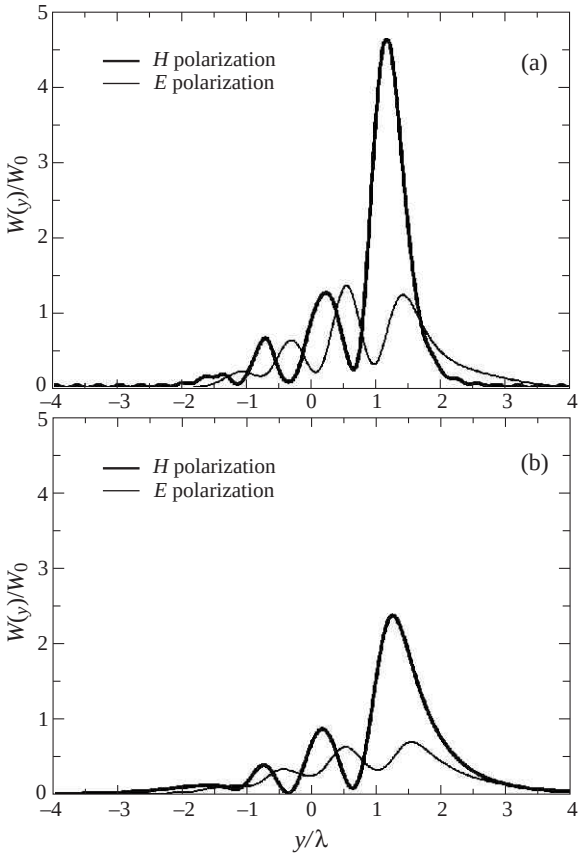

Fig. 2. Spatial distribution of relative energy density of electric field at diffraction of the H-polarized and E-polarized plane wave by a slot (a) in the presence of dielectric film on a substrate behind the screen and (b) in the absence of that.

tion there is the effect of focusing high intensity light radiation into a narrow spot with the width less than wavelength. For comparison, Fig. 2b demonstrates such pattern of spatial distribution of energy density in the same region, but of empty space, in the absence of a dielectric film behind the screen [4]. Hear, the main peak of intensity for the field of H polarization slightly wider and almost 2 times lower than in the film (Fig. 2a). It turns out that the appearance of the film behind the aperture cannot result to additional spreading of the field away from the aperture, as would be expected, but can cause an even greater concentration of light energy in a small spatial region of this layer.

2. Conclusion

Thus, as a result of the transition of light radiation through the sub-wavelength slot, the effect of focusing this radiation can take place, which is manifested in the appearance of narrow peaks of high intensity, the width of which is several times less than its wavelength. This effect is very sensitive to changes in the geometric parameters of the propagation scheme and displays explicitly only for linear polarization of the light field with an electric vector orthogonal to the plane of incidence of the wave on the screen with a slot.

References

[1] T.W. Ebbesen *et al*, *Nature* **391**, 667 (1998).
[2] F.J. Garcia-Vidal *et al*, *Rev. Modern Phys.*, **82**, 729 (2010).
[3] V.M. Serdyuk, *Technical Physics* **50**, 1076 (2005).
[4] V.M. Serdyuk *et al*, *Progr. In Electrom. Research M* **69**, 15 (2018).
[5] V.M. Serdyuk, *Progr. In Electrom. Research B* **83**, 129 (2019).

28th Int. Symp. "Nanostructures: Physics and Technology"
Minsk, Belarus, September 2020

Lateral mode tuning in coupled ridge waveguides using focused ion beam

A.A. Serin[1], A.S. Payusov[1], M.M. Kulagina[1], M.I. Mitrofanov[1], G.V. Voznyuk[1], M.V. Maximov[2] and N.Yu. Gordeev[1]

[1] Ioffe Institute, Politekhnicheskaya 26, 194021, St Petersburg, Russia
[2] Alferov University, St Petersburg, Russia

Abstract. We present an approach for treatment of coupled-ridge lasers using focused ion beam (FIB) etching. We show experimentally that the FIB etching allows post-processing lateral mode tuning without deterioration of the main laser parameters.

Introduction

Laterally coupled semiconductor lasers have been studied both theoretically and experimentally during last decades due to interesting effects which may occur in coupled active waveguides, such as bistability, mode selectivity [1], chaotic mode behavior [2] and possible modulation rates beyond the relaxation oscillation frequency [3,4]. Besides, phase-locked arrays of the optically coupled lasers allow broadening waveguides in the lateral direction which results in high optical power in spatially single-mode regime [5].

Optical coupling of the index guided lasers requires precise control of the waveguide parameters, namely the width, etch depth, distance between the waveguides and taking into account the lateral current spreading. Uncertainty of the post-growth techniques often leads to creation of slightly different devices which complicates the effects under study. In this paper, we show that the lateral modes of the coupled ridge lasers are affected by FIB [6] etching of the region between the two ridges, hence the technique is considered to allow post-processing fine tuning of the lateral optical modes without deterioration of the main laser parameters.

1. Experiment details

For our experiments, we have chosen an MBE-grown laser structure with ten layers of InAs quantum dots (QD) capped with InGaAs and separated by 35 nm GaAs which were sandwiched between 1.5 μm $Al_{0.35}Ga_{0.65}As$ claddings. The coupled ridge waveguide consisted of two ridges placed at a distance of 4 μm formed by reactive-ion etching. One ridge had 10 μm width (active ridge), another ridge had 2.5 μm width (passive ridge). The laser wafer except the active ridge was covered by 100 nm Si_3N_4 that also provided electrical isolation of the passive ridges. The idea of using coupled passive waveguides is to promote fundamental mode lasing in broadened multi-mode active waveguide [7]. The Cr/Au metal layer with a thickness of ~ 0.5 μm was used as a p-contact. Reference single stripe devices were made with the same process.

All studied devices where mounted p-side up on copper heatsinks using indium solder. The FIB etching was performed in ultra-high vacuum with custom-designed Ga^+ FIB lithography system after lasers were processed, tested and mounted. Ultra-high vacuum prevents unwanted oxidation during the etching process. Ion dose for etching was 1.25×10^{17} ions/cm^2. The ion beam current was 500 pA. During the etching, metal and dielectric layers between the ridges were completely removed. The width of the etched region was 3.5 μm. The inset in Fig. 1 schematically shows the layout of the etched region.

2. Near-field measurements

Both single and coupled-ridge devices with 1 mm long cavities demonstrated the threshold current density of 250 A/cm^2 and the lasing wavelength of 1.26 μm in the pulse regime, which corresponds to the lasing via the QD ground state. We did not detect any changes in threshold currents after the FIB etching whatsoever, however, several samples demonstrated a minor decrease of the differential efficiency.

Fig. 1 shows light intensity profiles on laser facets (near-fields) of different devices. All measurements were carried out in the pulse regime to reduce overheat. Even though the single-stripe device demonstrates single lobe near-field profile (dashed curve in Fig. 1) it operates on several lateral modes. It was confirmed by spectral and spectrally resolved near-field measurements. High-order modes tend to have larger intensity outside the ridge waveguide than the fundamental one which is consistent with our observations.

The coupled-ridge device (dash-dot curve in Fig. 1) demonstrates a complex near-field pattern. Our numerical simulations suggest that it operates on several composite modes typical for two coupled waveguides. This is in agreement with the spec-

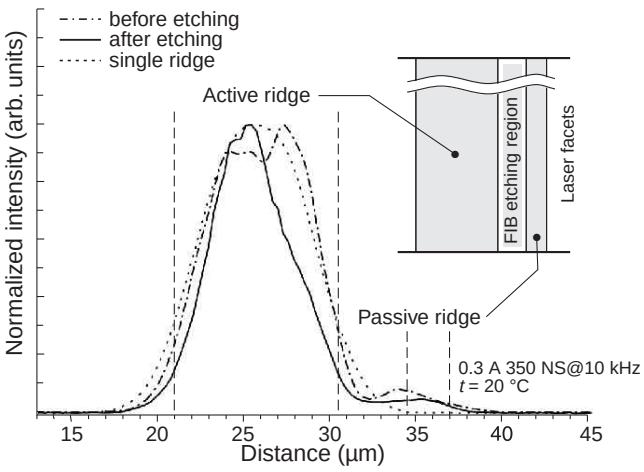

Fig. 1. Lateral intensity profiles of the coupled-ridge laser before (dash-dot line) and after (solid line) FIB etching. The dashed curve corresponds to the reference single-ridge device. The inset schematically shows the layout of the etched region.

tral measurements, where we observed the lasing lines not presented in the spectrum of the single-ridge device. The emission from the passive ridge indicates that it is not completely isolated and is electrically pumped due to the current spreading effect.

It is seen that the near-field pattern after the FIB etching (solid curve in Fig. 1) has narrowed down. We attribute this to the suppressed lasing of one of the composite modes caused by a reduced current spreading and partial etching of the residual cladding layer. This is consistent with a decrease in the emission intensity from the passive ridge and narrowed lasing spectrum. We believe that current spreading was suppressed due to ion-induced lattice defects generated during the FIB etching which, in turn, decrease the carrier mobility.

Conclusion

We presented the approach for post-processing lateral mode tuning in coupled-ridge lasers using focused ion beam (FIB) etching. We showed experimentally that the FIB etching allows suppressing lateral modes and reducing current spreading effects without deterioration of the main laser parameters.

Further practical implementation of the technique proposed requires additional experiments and optimization.

Acknowledgement

The reported study was funded by RFBR, project number 19-32-90219.

References

[1] E. Kapon, J. Katz and A. Yariv, *Opt. Lett.* **9**, 125 (1984).
[2] R. Santos and H. Lamela, *IEEE J. Quantum Electron*, **45** 1940 (2009)
[3] G.A. Wilson, R.K. DeFreez and H.G. Winful, *Opt. Commun.* **82**, 239 (1991).
[4] N. Nair, E. Bochove and Y. Braiman, *Opt. Express* **26**, 20040 (2018).
[5] D. Botez, *Proc. of SPIE* **4533**, 78 (2001).
[6] C.A. Volkert and A.M. Minor, *MRS Bull.* **32**, 389 (2007).
[7] A.S. Payusov, Yu.M. Shernyakov, M.M. Kulagina *et al*, *2018 International Conference Laser Optics (St Petersburg, Russia)* IEEE 140 (2018).

28th Int. Symp. “Nanostructures: Physics and Technology”
Minsk, Belarus, September 2020

10 W quantum-cascade lasers for the spectral range 4.6 µm

V.V. Dudelev[1], D.A. Mikhailov[1], A.V. Babichev[2,3], E.D. Cherotchenko[1], A.G. Gladyshev[3], S.N. Losev[1], I.I. Novikov[1,2,3], A.V. Lyutetskiy[1], S.O. Slipchenko[1], N.A. Pikhtin[1], L.Ya. Karachinsky[1,2,3], A.Yu. Egorov[3], D.V. Denisov[4], V.I. Kuchinskii[4], and *G.S. Sokolovskii*[1]

[1] Ioffe Institute, Saint Petersburg, Russia
[2] ITMO University, Saint Petersburg, Russia
[3] Connector Optics LLC, Saint Petersburg, Russia
[4] ETU “LETI”, Saint Petersburg, Russia

Abstract. In this work we characterize fabricated stripe quantum cascade lasers emitting in the 4.6μm spectral range and study their power and spectral properties under pulsed electrical pumping. In the measurements we show stable lasing with peak optical power exceeding 10 W (> 5 W per facet) at room temperature

Introduction

Currently, quantum cascade lasers (QCL) appear to be the most compact and effective light sources emitting in the mid-infrared wavelength range from 3 to 20 μm [1–4] that are extremely useful in modern gas sensing technologies, security systems, and environmental monitoring [5–6]. At present, there is an active development of different QCL constructions that emit near 4.6 μm [6–11] as this range includes carbon monoxide and silane absorption lines. There are works, showing the effective high-power generation both in a single wide stripe geometry [7] and in the array of narrow stripe lasers [8–9]. Apart from that, the dependence of QCL characteristics on the temperature and carrier transport is actively studied [10–11].

1. Experimental structures and measurement techniques

QCL heterostructures were fabricated by the MBE technique. The active region consists of 30 cascades based on strained quantum wells and barriers $In_{0.669}Ga_{0.331}As/In_{0.362}Al_{0.638}As$. The detailed description of the structure is given in [12]. Lasers with a stripe width of 20 μm and 50 μm were fabricated with cavity length varying from 2 to 5 mm. The facets were formed by cleaving without application of any reflecting and anti-reflecting coatings. In order to prevent the overheating of the active region, QCL samples were mounted epi-side down to the heat sink. In spectral measurements we used the monochromator with a diffraction grating of 150 mm^{-1} and a photodetector Vigo Systems PVI-4TE-10.6. The power was measured with calibrated power meter Thorlabs PM100 with a thermoelectric detector head S401C. The detailed measurement technique is described in elsewhere [13,14].

2. Experimental results

In our experiments the fabricated QCL samples were subject to the pulsed electrical pumping with 75 ns pulse length and 0.3% duty-cycle. The threshold current densities were in the range of 1.5–2.5 kA/cm^2. Fig. 1 demonstrates the typical L-I dependence measured from one facet. The maximum reached peak power exceeded 10 W (> 5 W per facet).

Fig. 2 depicts a typical QCL spectrum of a sample with a 3 mm cavity and 50 μm stripe. The lasing is in the region of the designed maximum value (4.6 μm). The spectrum full width at half maximum reaches 100 nm. The intermodal distance is 1.04 nm, which corresponds to the laser waveguide refractive index value of 3.28. The observed threshold current values and maximum peak power prove the high quality of fabricated heterostructures and good gain properties of the lasers’ active region

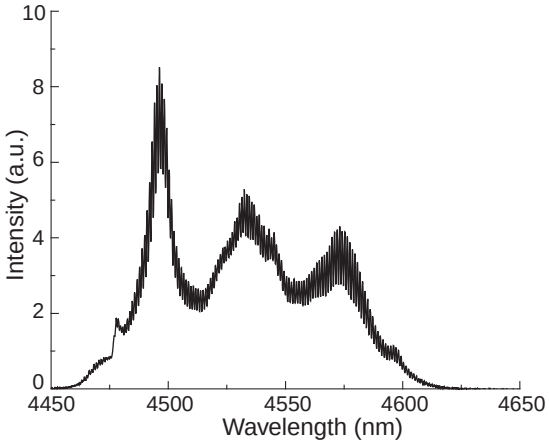

Fig. 1.
Typical spectrum of QCL with stripe width of 50 μm and cavity length of 3 mm at room temperature.

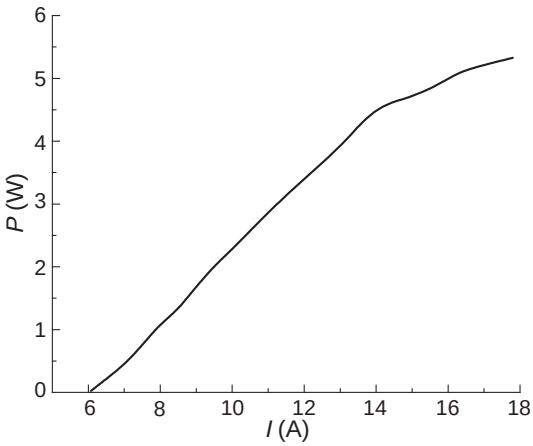

Fig. 2.
L-I curve of QCL with stripe width 50μm and 5 mm cavity at room temperature

3. Conclusion

In conclusion, we report the results of fabrication and characterization of QCLs and demonstrate lasing peak power in excess of 10 W. The lasing spectrum has maximum near 4.6 μm and full width at half maximum of about 100 nm.

Acknowledgement

This research is supported by the Ministry of Science and Higher Education of Russian Federation (project identifier RFMEFI61619X0111)

References

[1] F. Capasso, *et al*. *IEEE Journal of Selected Topics of Quantum Electronics* **5**, 31 (2000).
[2] D. Botez, *et al*. *J. Phys. D: Appl. Phys.* **49**, 043001 (2016).
[3] Dudelev V.V. *et al*, *Quantum Electronics* **50**, 141 (2020).
[4] Babichev A.V. *et al*, *Tech. Phys. Lett.* **45**, 735 (2019).
[5] Curl R.F., Capasso F., Gmachl C., *et al*, *Chemical Physics Letters* **487**, 1 (2010).
[6] van Helden J.H., Lopatik D., Nave A., *et al*, *J. of Quantitative Spectroscopy and Radiative Transfer* **151**, 287 (2015).
[7] Liu P.Q., Hoffman A.J., Escarra M.D, *et al*, *Nat. Photonics* **4**, 95 (2010).
[8] Yan F.-L., Zhang J.-C., Jia Z.-W., *et al*, *AIP Advances* **6**, 035022 (2016).
[9] Lyakh A.,Maulini R., Tsekoun A., *et al*, *Opt. Express* **106**, 619 (2012).
[10] Lee H.K., Yu J.S. *Appl. Phys. B* **106**, 619 (2012).
[11] Jonasson O, *et al*, *Photonics* **3**, 38 (2016).
[12] Babichev A.V. *et al*, *Tech. Phys. Lett.* **46**, 35 (2020).
[13] Dudelev V.V., Losev S.N., Myl'nikov V.Yu., *et al*, *Technical Physics* **63**, 1656 (2018).
[14] Dudelev V.V., Losev S.N., Myl'nikov V.Yu., *et al*, *Optics and Spectroscopy* **125**, 402 (2018).

28th Int. Symp. "Nanostructures: Physics and Technology"
Minsk, Belarus, September 2020

Raman studies of graphene films grown on 4*H*-SiC after the deposition of Ni

I.A. Eliseyev[1], V.Yu. Davydov[1], A.N. Smirnov[1], S.V. Belov[1], A.V. Zubov[2], S.P. Lebedev[1], and A.A. Lebedev[1]

[1] Ioffe Institute, 194021, St Petersburg, Russia
[2] ITMO University, 197101, St Petersburg, Russia

Abstract. In order to develop the process of separating the graphene film from a 4*H*-SiC substrate and transferring it to a dielectric substrate of different type, Raman spectroscopy is used to evaluate the structural perfection of the graphene films after deposition of a Ni thin layer to their surface by magnetron sputtering. Two deposition modes with different gas pressures and deposition times were investigated. It is found that Ni deposition under low pressure combined with long deposition time does not lead to the separation of graphene/Ni film. On the other hand, higher pressure and shorter deposition time results in successful but uncontrollable exfoliation of the upper graphene layer together with the Ni film. The results obtained will serve as the basis for the optimization of Ni deposition modes, in order to acheive complete exfoliation of the graphene film from the SiC substrate without damaging the graphene layer.

Introduction

The development of a process for separating of graphene films grown on semi-insulating silicon carbide from the substrate is an important technological task. This will make it possible to repeatedly use the same expensive silicon carbide substrate for growing graphene layers. Thus, the devices obtained on the basis of such graphene should be significantly cheaper compared to the ones fabricated on a single-use SiC substrate. Another benefits of such technology are the ability to control the number of layers in the graphene film, and, last but not least, to transfer a uniform monolayer film grown on SiC onto other substrates. One of the methods for separating graphene films from the substrates is the deposition of metal layers (including Ni) on graphene and the subsequent removal of graphene layers together with the metal from the substrate. This process is based on the difference in graphene-substrate and graphene-metal binding enegries and occurrence of stresses induced by the presence of a layer of metal on top of the film [1]. The goal of this study was to investigate by means of Raman spectroscopy the influence of Ni deposition on the structural perfection and composition of graphene films grown on 4*H*-SiC and to determine the optimal Ni sputtering conditions for successful and controllable exfoliation of graphene/Ni film from the surface of SiC.

1. Experimental

The graphene films coated with a Ni layer were studied by Raman spectroscopy on a Horiba Jobin-Yvon T64000 spectrometer. To excite the spectra, an Nd: YAG laser with a wavelength of 532 nm was used. The beam diameter on the sample was $\sim 1\mu$m. The power of the laser beam on the sample was chosen so that there was no local heating of the film and was limited to 4 mW.

Graphene films were obtained by sublimation of the Si face of a semi-insulating 4*H*-SiC substrate in an argon atmosphere at a temperature of $\sim$ 1745 °C with preliminary etching in a nitrogen atmosphere (at 1600 °C for 1 min.).

The Ni films were deposited on top of the graphene layers using the magnetron sputtering method. For this task, two main technological modes were used.

- Mode 1: Anode voltage 550 V, anode current 125 mA, gas pressure $6.6 \cdot 10^{-5}$ mm Hg, spray time 20 min. Sample 1.
- Mode 2: Anode voltage 540 V, anode current 125 mA, gas pressure $1.5 \cdot 10^{-4}$ mm Hg, spray time 10 min. Sample 2.

2. Results and discussion

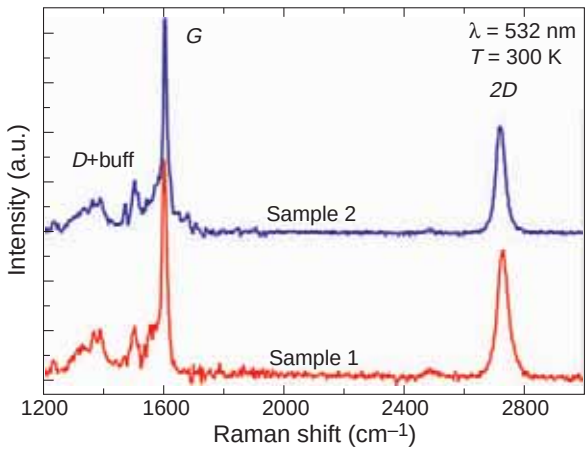

Fig. 1. Typical Raman spectra of the samples under study before Ni deposition. Hereinafter the spectra are given after subtraction of the second-order SiC spectrum contribution.

Figure 1 shows typical Raman spectra of the as-grown graphene films (before Ni deposition). The spectra show the *G* and 2*D* Raman lines characteristic of graphene [2]. In addition to these lines, there are bands in the 1300–1500 cm^{-1} frequency region associated with the buffer layer [3].

An analysis of the spectra shows that the grown layers are of high quality. This is evidenced by the low intensity of the *D* line which appears in the presence of defects, and which is invisible in these spectra in comparison to the buffer layer bands. Analysis of large areas (10×10 μm^2) of the as-grown films by Raman and Kelvin-probe force microscopy mapping

showed that both graphene films were mainly monolayers with a small fraction of bilayer inclusions.

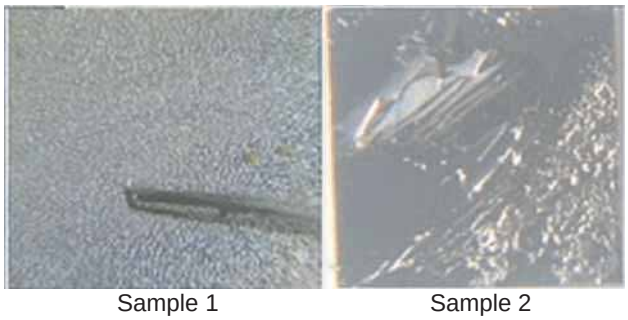

Fig. 2. Optical images of the samples under study.

Figure 2 shows images of the surfaces of samples after applying a Ni metal film. It is clearly seen that the metal film covers almost the entire surface of the samples; however, in some areas of sample 1, the Ni film exfoliates from the surface.

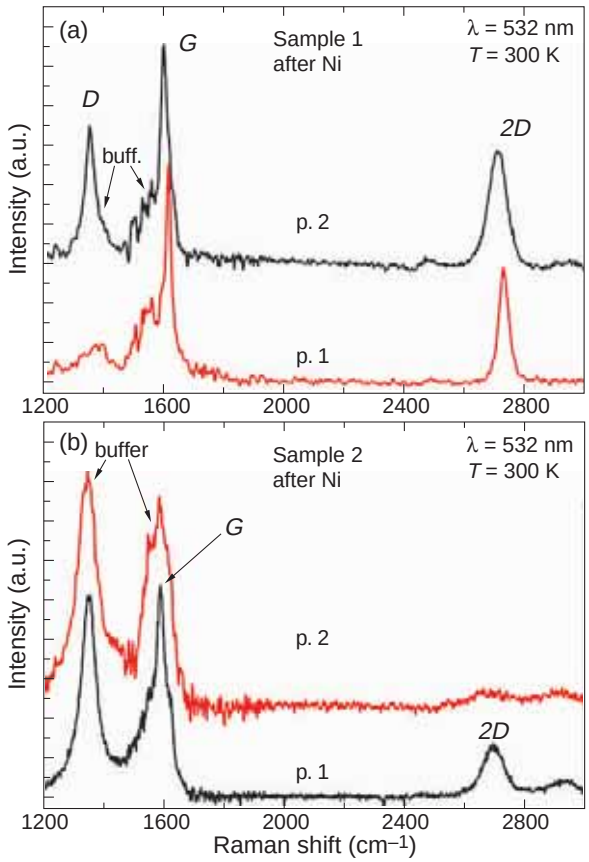

Fig. 3. Raman spectra of samples 1(a) and 2(b) after Ni deposition.

Figure 3(a,b) shows the characteristic Raman spectra of graphene films after the deposition of Ni layers in different modes measured in two different points (p.1 and p.2). Due to the fact that the metal layers are not transparent for a given wavelength, the phonon spectrum of graphene films was excited through the transparent SiC substrate from the back side. Fig. 3(a) shows two characteristic types of spectra of graphene films after Ni deposition under the conditions of Mode 1. Under these deposition conditions, no regions in which the Ni film separated from the substrate were observed. In most of the spectra (Fig. 3(a), p.1), no *D*-line was present, and the *G* and 2*D* lines did not demonstrate any significant shift or broadening compared to the spectra of the as-grown sample. An increase in the *D*-line intensity is observed in some of the spectra (Fig. 3(a), p.2), which is accompanied by broadening of the *G* and 2*D* lines. According to the model proposed in [4], observation of broadening of the *G*-line from 15 to 29 cm^{-1} together with the I(*D*)/I(*G*) lines intensity ratio of 0.7 indicates presence of defects associated with grain boundaries. The average crystalline size in this case can be evaluated from the formula introduced in [5] as 27 nm. Thus, it can be argued that during Ni deposition under the conditions of Mode 1, most of the graphene film remains untouched, and the remaining areas demonstrate structural degradation of the graphene film with the appearance of defects associated with grain boundaries.

In case of sample 2, the spectra shown on Fig. 3(b) were taken from the area where the Ni film exfoliated from the sample. Both spectra demonstrate strong contribution of the buffer layer bands similar to those observed in the spectra of the buffer layer without graphene on top in [6], and a weak contribution of graphene is present in case of p.1. This is an evidence that the topmost graphene layer has exfoliated from the surface together with the Ni film.

3. Conclusion

Based on Raman spectroscopy data, it was found that Ni deposition under low gas pressure and long deposition times does not allow separation of the graphene/Ni film from the surface of graphene/SiC sample, resulting only in appearance of small regions of damaged graphene layer. Ni deposition under higher gas pressure with shorter metal deposition time resulted in successful exfoliation of large areas of Ni film together with the topmost graphene layer. On the other hand, self-exfoliation of the Ni film from the sample surface, which was observed in this case, is unwanted for the further graphene transfer process. The results obtained will serve as the basis for the optimization of nickel deposition modes, in which the possibility of controllable exfoliation of the Ni film together with defect-free graphene from the SiC substrate is created.

References

[1] J. Kim *et al*, *Science*, **342(6160)**, 833–836 (2013).
[2] A.C. Ferrari *et al*, *Nat. Nanotechnol.* **8**, 235–246 (2013).
[3] F. Fromm *et al*, *New. J. Phys.*, **15**, 1 (2013).
[4] L. Cancado *et al*, *2D Mater.*, **4**, 025309 (2017).
[5] L. Cancado *et al*, *Appl. Phys. Lett.*, **88**, 163106 (2006).
[6] T. Wang *et al*, https://hal.archives-ouvertes.fr/hal-02417876 (2020).

28th Int. Symp. "Nanostructures: Physics and Technology"
Minsk, Belarus, September 2020

Magnetic properties of the electrons in unmodulated bilayer graphene

V.V. Karpunin
Mordovian State Pedagogical Institute, 430007 Saransk, Russia

Abstract. The magnetic moment of the unmodulated bilayer graphene is calculated in the presence of a perpendicular magnetic field **B**. The oscillatory character of the magnetic moment dependences on the magnetic field is investigated.

Introduction

The investigation of electrons properties of nanostructures has allowed the direct observation of quantum behaviors in their electron system. In [1] magnetotransport in bilayer graphene in the presence of a weak and periodic potential modulation and of a perpendicular magnetic field B was studied.

In [2] the four-band Dirac–Weyl Hamiltonian, vicinity of both K and $K^{'}$ valleys, obtained analytically the energy levels and the corresponding wave functions of a bilayer graphene quantum dot is solving.

In [3] the effect of valley-dependent orbital magnetic moment on the transmission of quasiparticles through biased bilayer graphene npn and pnp junctions in the presence of out-of-plane magnetic field was investigated.

In [4] the structural, electronic, magnetic and adsorption properties of Bernal stacked bilayer graphene (DLG) on MnO(111) surface terminated by an oxygen atom, as a function of nonstoichiometric composition of the BLG/MnOx (111) interface is investigated systematically.

The electronic and thermodynamic properties of simple stacked bilayer graphene have been studied in [5].

In [6] the optical properties and quantum Hall effect in bilayer graphene in a strong magnetic field have been described.

In [7] electronic and optical properties of monolayer and bilayer graphene are investigated to verify the effects of interlayer interactions and external magnetic field.

In [8] authors review recent experimental and theoretical work addressing the quantum oscillatory magnetization M(B) in 2DESs subject to SOI.

The microscopic mechanism of magnetization and polarization owing to the strong spin-orbital coupling of the electron gas in multiferroics was examined in [9].

In [10] was found the absorption coefficient of the electromagnetic radiation by free carriers in a phosphorene single layer. Both a nondegenerate and degenerate electron gas are considered.

One particle Hamiltonian for unmodulated bilayer graphene is given by [1]

$$H_0 = \begin{pmatrix} 0 & \pi & t & 0 \\ \pi^{\dagger} & 0 & 0 & 0 \\ t & 0 & 0 & \pi^{\dagger} \\ 0 & 0 & \pi & 0 \end{pmatrix}, \quad (1)$$

where $t \approx 400$ meV is the interlayer coupling, $(\overline{h}/eB)^{1/2} = l_B$, v_F is the Fermi velocity, π and $\pi^{\dagger}$ are the momentum operators,
$\pi = -i\overline{h}v_F[d/dx + id/dy - (eB/\overline{h})x]$,
$\pi^{\dagger} = -i\overline{h}v_F[d/dx - id/dy + (eB/\overline{h})x]$.

The energy spectrum of the eigenstates electrons in this system can be written as [1]

$$\varepsilon = s_1(k^2/2 + 2n + 1 + s_2\sqrt{k^4/4 + (2n+1)k^2 + 1})^{1/2}, \quad (2)$$

where $n = 0, 1, 2...$, $k = (l_B/\overline{h}v_F)t$, $\varepsilon = (l_B/\overline{h}v_F)E$, and $s_1 = \pm 1$, $s_2 = \pm 1$ denoting the energy bands. We will consider electrons in the conduction band

We can write this formula in a convenient form for us

$$E = t(1/2 + (2n+1)k^{-2} + \sqrt{1/4 + (2n+1)k^{-2} + k^{-4}})^{1/2}. \quad (3)$$

The thermodynamic potential can be determined with the use of the classical partition function Z [9,11]. In our case that is

$$Z = \sum_{n=0}^{\infty} \exp\left(-\frac{E}{T}\right). \quad (4)$$

Here the temperature T is expressed in the unit of energy. Let us introduce $\xi = t/T$ and formula (4) will be written in the form

$$Z = \sum_{n=1}^{\infty} \exp\left(-\xi\varepsilon_n\right), \varepsilon_n = E/t. \quad (5)$$

1. Thermodinamic potential Ω and magnetic moment

Thermodinamic potential Ω can be obtained from the dependence $\Omega(Z)$ [9,11]. Then we obtain

$$\Omega = \frac{1}{2\pi i}\int_{\alpha-i\infty}^{\alpha+i\infty} \frac{Z(\xi)d\xi}{\xi^2} \int_0^{\infty} \exp(E\xi)\frac{\partial f_0}{\partial E}dE, \quad (6)$$

where $f_0(E)$ is the Fermi distribution function and $\alpha \leq 1/T$.

We use the approach [9,11] in order to find Ω. Let us introduce the notation $z(\varepsilon_F)$.

$$z(\varepsilon) = \frac{1}{2\pi i}\int_{\alpha-i\infty}^{\alpha+i\infty} \frac{\exp(\varepsilon\xi)Z(\xi)d\xi}{\xi^2}. \quad (7)$$

We rewrite magnetic moment of the nanorings $\mathbf{M} = -\partial\Omega/\partial\mathbf{B}$ in the convenient form

$$M = -\frac{\partial k}{\partial B}\frac{\partial\Omega}{\partial k} = \frac{1}{2}\left(\frac{1}{e\overline{h}}\right)^{1/2}\frac{tB^{-3/2}}{v_F}\frac{\partial\Omega}{\partial k}. \quad (8)$$

It should be noted that from the formula (7) one must introduce the expression for dz/dk

$$\frac{dz(\varepsilon)}{dk} = \frac{1}{2\pi i}\int_{\alpha-i\infty}^{\alpha+i\infty} \exp(\varepsilon\xi)\frac{1}{\xi^2}\frac{dZ}{dk}d\xi, \quad (9)$$

where

$$\frac{dZ}{dk} = -\xi \sum_n \exp(-\varepsilon_n \xi) \times$$

$$\frac{1}{2}\left(1/2 + (2n+1)k^{-2} + \sqrt{1/4 + (2n+1)k^{-2} + k^{-4}}\right)^{-1/2} \times$$

$$\left[(2n+1)(-2)k^{-3} + \frac{1}{2}\left(\frac{1}{4} + (2n+1)k^{-2} + k^{-4}\right)^{-1/2} \times \left(\frac{(2n+1)(-2)}{k^3} - \frac{4}{k^5}\right)\right]. \quad (10)$$

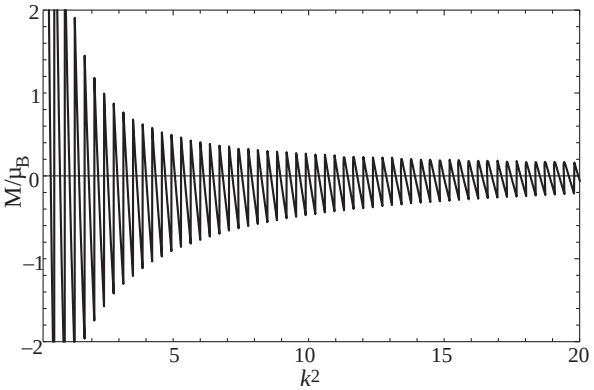

Fig. 1. Dependence of the magnetic moment on the reverse magnetic field. $T = 0K$.

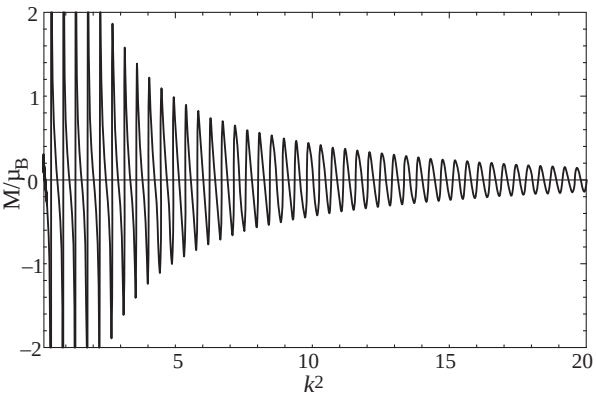

Fig. 2. Dependence of the magnetic moment on the reverse magnetic field. $T = 0.1K$.

We obtain the case $T \neq 0$ from (8)

$$\frac{M_{T\neq 0}}{\mu_B} = -\frac{1}{2\mu_B}\left(\frac{1}{e\hbar}\right)^{1/2} \frac{tB^{-3/2}}{v_F} t \int_0^\infty \sum_n \frac{\partial f_0}{\partial E} \times \quad (11)$$

$$\frac{1}{2}\left(1/2 + (2n+1)k^{-2} + \sqrt{1/4 + (2n+1)k^{-2} + k^{-4}}\right)^{-1/2} \times$$

$$\left[(2n+1)(-2)k^{-3} + \frac{1}{2}\left(\frac{1}{4} + (2n+1)k^{-2} + k^{-4}\right)^{-1/2} \times \left(\frac{(2n+1)(-2)}{k^3} - \frac{4}{k^5}\right)\right] dE.$$

From (11) we can obtain the limiting case for the magnetic moment at $T = 0$.

$$\frac{M_{T=0}}{\mu_B} = -\frac{1}{4\mu_B}\frac{k}{B} t \times$$

$$\sum_n \left(1/2 + (2n+1)k^{-2} + \sqrt{1/4 + (2n+1)k^{-2} + k^{-4}}\right)^{-1/2}$$

$$\left[(2n+1)(-2)k^{-3} + \frac{1}{2}\left(\frac{1}{4} + (2n+1)k^{-2} + k^{-4}\right)^{-1/2} \times \left(\frac{(2n+1)(-2)}{k^3} - \frac{4}{k^5}\right)\right], \quad (12)$$

here μ_B is the Bohr magneton.

Next, we use the classic expression of the thermodynamic potential [12]

$$\Omega = -T \sum_{n=0}^{\infty} \ln\left[1 + \exp\left(\frac{\mu - E}{T}\right)\right], \quad (13)$$

μ is chemical potential.

For the magnetic moment we get

$$-M = \sum_{n=0}^{\infty} \frac{dE}{dB}\left[1 + \exp\left(\frac{E-\mu}{T}\right)\right]^{-1}. \quad (14)$$

Finally we get

$$-M = \frac{1}{2}\frac{k}{B} t \sum_{n=0}^{\infty} \frac{1}{2}\left(1/2 + (2n+1)k^{-2} + \sqrt{1/4 + (2n+1)k^{-2} + k^{-4}}\right)^{-1/2} \times$$

$$\left[(2n+1)(-2)k^{-3} + \frac{1}{2}\left(\frac{1}{4} + (2n+1)k^{-2} + k^{-4}\right)^{-1/2} \times \left(\frac{(2n+1)(-2)}{k^3} - \frac{4}{k^5}\right)\right]\left[1 + \exp\left(\frac{E-\mu}{T}\right)\right]^{-1}. \quad (15)$$

2. Conclusion

The m agnetic moment of electrons of the bilayer graphene has an oscillatory dependence on the magnetic field, this is clearly seen in Fig. 1 and follows from formula (12). It was obtained under the condition of zero temperature, the oscillation peaks in Fig. 1 are sharp and not smoothed by temperature. Temperature smoothes the peaks in Fig. 2.

References

[1] M. Zarenia *et al*, *Phys. Rev. B.* **85**, 245426 (2012).
[2] D.R. da Costa, *et al*, *Carbon* **78**, 392 (2014).
[3] Chang-Soo Park. *Phys. Lett. A* **382**, 121 (2018).
[4] Victor V.Ilyasov, *et al*, *Superlatt. Microstr.* **117**, 72 (2018).
[5] S. Karimi, *et al*, *Chem. Phys.* **525**, 110417 (2019).
[6] V.I. Fal'ko *Phil. Trans. R. Soc. A* **366**, 205 (2008).
[7] Y.H. Ho, *et al*, *Phil. Trans. R. Soc. A* **368**, 5445 (2010).
[8] M.A. Wilde, *et al*, *Phys. Status Solidi B* **251**, 1710 (2014).
[9] V.A. Margulis. *Low Temp. Phys.* **40**, 363 (2014).
[10] V.A. Margulis, V.V. Karpunin. *Semiconductors* **53**, 458 (2019).
[11] V.A. Margulis, *et al*, *Sol. St. Commun.* **269**, 108 (2018).
[12] L.D. Landau, E.M. Lifshitz, Statistical Physics, Part 1, 3rd ed., Pergamon Press, Oxford (1980).

28th Int. Symp. "Nanostructures: Physics and Technology"
Minsk, Belarus, September 2020

Comparative study of conventional and quasi-freestanding epitaxial graphene grown on 4H-SiC substrate

S.P. Lebedev[1], I.A. Eliseyev[1], V.N. Panteleev[1], P.A. Dementev[1], V.V. Shnitov[1], M.K. Rabchinskii[1], D.A. Smirnov[2], A.A. Lebedev[1]

[1] Ioffe Institute, 194021, St Petersburg, Russia
[2] Institut für Festkörper und Materialphysik, Technische Universität Dresden, 01062 Dresden, Germany

Abstract. The structural characteristics of quasi-freestanding single-layer graphene obtained by annealing of buffer layer in the flow of hydrogen are studied in comparison with those of conventional epitaxial graphene. The high structural quality and good lateral uniformity of the thus-obtained graphene film are checked and confirmed by use of such techniques as Raman spectroscopy, atomic-force and Kelvin-probe force microscopy. The confirmation of its single-layer and freestanding character is obtained via the analysis of the X-ray photoelectron spectroscopy data.

Introduction

Thermal decomposition of the silicon (Si) face of $4H$-SiC substrates is currently one of the most popular technologies of the epitaxial graphene (EG) growth. This technology allows transforming the top layer of an insulating SiC substrate into large-area homogeneous single-layer graphene (SLG). However, due to the presence of a buffer layer between the SiC substrate and SLG, the electron mobility of the latter turns out to be much lower than in the case of free-standing graphene [1]. The buffer layer has a graphene-like honeycomb structure ($(6\sqrt{3}\times 6\sqrt{3})R30^\circ$ superstructure) consisted of carbon (C) atoms, some of which are covalently bonded to the Si atoms of the substrate. One of the ways to exclude the buffer layer effect on the electron mobility of graphene is to anneal the sample in the hydrogen atmosphere. At sufficiently high temperatures, the hydrogen intercalation under a buffer layer causes the breaking of bonds between this layer and SiC substrate and concurrent forming of Si–H bonds which terminate the SiC surface. As a result, the SiC + buffer layer structure transforms to SiC + quasi-freestanding graphene [1]. The term "quasi-freestanding" reflects the absence of chemical bonding of the graphene layer to the substrate. Thus, to obtain the quasi-freestanding single-layer graphene (QFSLG), it is necessary to anneal the SiC substrates covered by the single buffer layer in hydrogen. Since the applicability of such QFSLG for the manufacturing of various electronic devices strongly depends on its structural perfection and uniformity, this work was aimed at the comparative study of the structural and electronic properties of QFSLG and EG samples including the uniformity of hydrogen termination of the SiC substrate in the case of QFSLG sample.

1. Experimental

Graphene films were grown by using the method of thermal decomposition of the SiC surface in an inert gas (argon). High-resistivity $4H$-SiC wafers with the $\{0001\} \pm 0.25^\circ$ orientation (Si-face) were used as substrates. EG sample was grown with the following technological parameters: growth temperature of 1750 ± 20 °C, growth time of 5 min, the heating rate of the SiC substrate of 250 °C/min and argon pressure in the chamber of 730 ± 10 Torr. The buffer layer was grown on the Si-face of 4H-SiC substrate at 1580 ± 20°C. QFSLG sample was obtained by annealing the buffer layer/SiC structure in a flow of molecular hydrogen at 800 °C. Comparison of EG and QFSLG properties were carried out by using several measurement techniques: atomic-force microscopy (AFM), Kelvin-probe force microscopy (KPFM), Raman spectroscopy, and X-ray photoelectron spectroscopy (XPS). Investigations by AFM and KPFM were performed using a scanning probe microscope NtegraAURA (NT-MDT) in ambient conditions. Raman measurements were performed at room temperature in the backscattering geometry using a Horiba Jobin-Yvon T64000 spectrometer installation equipped with a confocal microscope, which allowed us to obtain information from a spot of 1 μm in diameter. The XPS spectra were measured at the Russian-German beamline of electron storage ring BESSY-II (Helmholtz-Zentrum Berlin) using the beamline ultrahigh vacuum experimental station.

2. Results and discussion

In order to get information on structural and electronic properties of the samples, Raman spectroscopy mapping within 10×10 μm^2 areas of each sample was employed. Fig. 1a demonstrates the array obtained by Raman mapping of the EG sample. The spectra exhibit the features characteristic of high-quality single-layer EG: G($\sim$1600 cm^{-1}) and $2D$ ($\sim$2700 cm^{-1}) lines originating from the vibrations of the graphene lattice and wide bands in the 1300–1550 cm^{-1} range corresponding to the buffer layer [2].

In case of QFSLG sample, G and $2D$ lines, as well as a very weak defect-related D($\sim$ 1350 cm^{-1}) line can be observed in its Raman spectra (Fig. 1b). Absence of the buffer layer bands in all the spectra of the array shown on Fig. 1b confirms that transformation of the buffer layer into graphene took place. Another important evidence of successful transformation is the ratio of G and $2D$ lines intensity — for the EG sample this ratio is smaller than for QFSLG sample, which may indicate smaller charge carrier concentration in QFSLG compared to EG [3]. The symmetric Lorentzian shape of the $2D$ Raman line in most of the spectra pointed to the predominantly single-layer nature of the graphene layer. The spectra taken from the rest of the sample's surface ($\sim$15% of the total surface) demonstrated the $2D$ line with an asymmetric shape that could be approximated by four Lorentzians, which pointed to the presence of bilayer graphene in the corresponding area [4].

The surface morphology and surface potential of QFSLG sample were studied by AFM and KPFM techniques before and after annealing in hydrogen. A comparison of AFM sur-

face topography maps (not shown here) confirmed the absence of significant influence of annealing on the surface morphology of EG sample. The distribution of the surface potential also did not exhibit significant changes. However, the value of the surface potential contrast, depending on the electrons work function, changed from the value characteristic of buffer layer — single-layer graphene pair ($\Delta U \sim 300$ mV) to the value of $\sim$100 mV, which corresponds to the difference between single-layer and bilayer graphene [5]. It can be concluded that hydrogen intercalation was uniform and the buffer layer was transformed into graphene over the entire area. 3

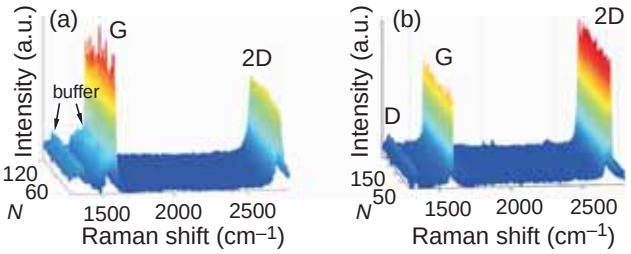

Fig. 1. Arrays of Raman spectra for samples 1 (a) and 2 (b). All spectra are presented after subtraction of the second-order SiC substrate contribution.

The chemical composition and electronic properties of the samples were determined by measuring and analysis of their XPS spectra presented in the Fig. 2 in the scale of binding energy (BE). Analysis of the survey XPS spectra shows that, unlike the EG sample, the QFSLG sample contains a noticeable amount of oxygen that is chemically bonded to the SiC substrate presumably during its annealing in hydrogen.

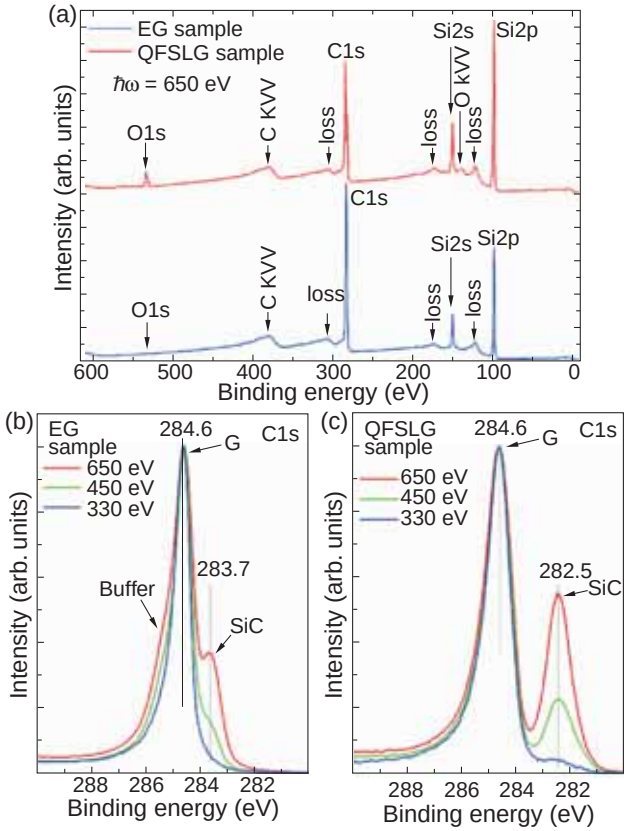

Fig. 2. Survey (a) and C1s (b and c) XPS spectra of the EG and QFSLG samples. The photon energies at which the measurements were performed are denoted for each spectrum.

A comparison of the ratios either between intensity of C1s and Si_2p lines in the survey spectra (Fig. 2a) or between the areas of graphene and SiC components in the C1s spectra (Fig. 2b and 2c) clearly evidences that in case of the EG sample, the thickness of carbon layer (buffer+SLG) is significantly larger than in case of QFSLG sample, where this layer is predominantly formed by single-layer graphene with only a small fraction of bilayer.

The analysis of the shape of C1s spectra related to EG allow us to distinguish three components which can be assigned to the buffer layer (BE = 285.3 eV), graphene layer (BE = 284.6 eV) and SiC substrate (BE = 283.7 eV) [6]. The last one reveals itself as weak left shoulder of the main C1s peak. At the same time, only two components can be resolved in the C1s spectra of QFSLG sample. The first one (BE = 284.6 eV) can be assigned to the graphene single-layer, while the second (BE = 282.5 eV) to the SiC. The absence of the third component with BE $\sim$ 285.3 eV in these spectra confirms the absence of the buffer layer in the QFSLG sample. The substantial 1.2 eV downshift of the SiC-related C1s, Si2p and Si_2s peaks clearly visible in the XPS spectra of this sample can be explained by the presence of the interface dipole layer between the graphene and SiC substrate [6]. This layer forms between the SiC and buffer layer due to hydrogen intercalation of the latter during its annealing in hydrogen. Its formation goes via formation of Si-H bonds and is accompanied by complete destruction of the sp^3 bonds connecting the SiC and buffer layer.

3. Conclusion

Structural properties and chemical composition of the QFSLG film obtained by the annealing of the buffer layer in a flow of hydrogen were studied using a number of probing techniques. Raman spectroscopy together with AFM and KPFM confirmed that the structural quality and lateral uniformity of the obtained QFSLG film can be very high and quite comparable to those of the best samples of epitaxial graphene. The analysis of the acquired survey and C1s XPS spectra confirmed that the EG film is noticeably thicker than the QFSLG one. The substantial 1.2 eV downshift of all the SiC-related features in the XPS spectra of QFSLG sample clearly evidences for the formation of a dipole layer between the buffer and substrate. This fact indicates the complete detachment of the buffer layer from the SiC substrate and confirms its conversion into quasi-freestanding SLG.

Acknowledgements

The authors thank Helmholtz-Zentrum Berlin for the allocation of synchrotron radiation beamtime and the German-Russian Laboratory at BESSY II for the support of the XPS measurements. S.P. Lebedev and I.A. Eliseyev acknowledge the support from RFBR (Project 18-02-00498).

References

[1] J.D. Emery *et al*, *Appl. Phys. Lett.*, **105**, 161602 (2014).
[2] F. Fromm *et al*, *New J. Phys.* **8**, 043031 (2013).
[3] A. Das *et al*, *Nat. Nanotech.*, **3**, 210–215 (2008).
[4] A.C. Ferrari *et al*, *Phys. Rev. Lett.*, **97**, 187401 (2006).
[5] V. Panchal *et al*, *Sci. Rep.*, **3**, 2597 (2013).
[6] S. Watcharinyanon *et al*, *Surf. Sci.*, **605**, 1662–1668 (2011).

28th Int. Symp. "Nanostructures: Physics and Technology"
Minsk, Belarus, September 2020

Quantum chemical calculations of nanoscroll energy rolled from zigzag graphene nanoribbon

A.I. Siahlo. S.A. Vyrko. S.V. Ratkevich, *N.A. Poklonski*, and A.T. Vlassov
Physics Department, Belarusian State University, 220030 Minsk, Belarus

Abstract. The geometry of nanoscroll rolled from flat zigzag graphene nanoribbon (nzGNR) into Archimedean spiral is defined by the set of parameters: nanoscroll inner radius, the length of the nzGNR, the nanoscroll width, the distance between the layers in the nanoscroll, and the bond length between the nzGNR atoms. Using the semi-empirical quantum chemical PM3 method the energies of nanoscrolls formed from 46zGNR and 70zGNR are calculated. The dependence of the energy of the nanoscrolls relative to the energy of corresponding flat nanoribbon on the inner nanoscroll radius obtained using quantum chemical calculations qualitatively agrees with the semi-classical analytical results.

Carbon nanoscroll is a rectangular graphene fragment (nanoribbon) rolled into a scroll [1,2]. A semi-classical analytical model for calculating of the energy of a carbon nanoscroll was proposed [2]. The model includes the following parameters of the nanoscroll: the inner radius R_{in}, the length L of the nanoribbon, which forms the nanoscroll, the nanoscroll width W, the distance $h = 0.335$ nm between the layers in the nanoscroll, the area $S_a = 3\sqrt{3}a_{\text{CC}}^2/4$ per atom in graphene (where $a_{\text{CC}} = 0.142$ nm is the bond length), the elastic constants $C = 2.01$ eV·Å^2/ atom and $p = 2$, connecting elastic energy with the radius R of curvature of the graphene layer ($E_{\text{el}} = C/R^p$) and the interaction energy $\varepsilon = 35$ meV/atom of graphene layers associated with the van der Waals interaction. The dependences of the nanoscroll energy on the geometric parameters of nanoscrolls in [2] are presented and the conclusions about the stability of the nanoscroll are made.

It is known that the energy and electromechanical characteristics of a system of not too many atoms can be calculated using the quantum chemical methods [3]. For example, the calculations of the electronic band structure and the magnetic

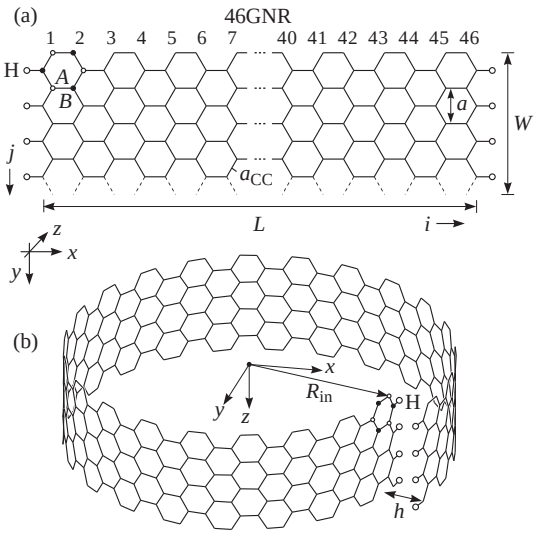

Fig. 1. Structure of a computational cell of width W for 46zGNR nano-ribbon of length L(a) and for a nanoscroll formed from the nanoribbon with the inner radius $R_{\text{in}} = 1.35$ nm (b). Here $n = 46$ *zigzag* chains of carbon atoms constituting the 46zGNR are enumerated; a_{CC} is the C–C bond length in the nanoribbon, a is the translational period, and h is the distance between the layers of the scroll.

states of *zigzag* graphene nanoribbons using the semiempirical method of molecular orbitals PM3 [4], implemented in the MOPAC2016 program [5], were provided in [6]. The atom coordinates in [6] were obtained after full geometry optimization. In the present work we propose the algorithm to define the Cartesian coordinates of the atoms of a carbon nanoscroll by the parameters R_{in}, L, W, h and the interatomic distance between the carbon atoms a_{CC} using the analytical expressions. We use the same values of the parameters $a_{\text{CC}} = 0.142$ nm and $h = 0.335$ nm as in [2]. The coordinates of carbon nanoscroll atoms can be then used in the programs for the quantum chemical calculations of nanoscroll energy. The energy of nanoscroll as a function of nanoscroll parameters (for example, R_{in} for fixed L, a_{CC} and h) can be found. Thus, the set of parameters, corresponding to the minimum energy of the nanoscroll, can be obtained.

The purpose of this work is to define the geometry of nanoscrolls by a few number of parameters using the analytical expressions and to compare the results of nanoscroll energy calculations by the semi-classical analytical model and by the quantum chemical method. This will allow, on the one hand, to select of parameters for the analytical models of multimolecular systems, and on the other hand, to assess the correctness of quantum chemical calculation methods.

Figure 1 shows the structures of carbon nanoribbon 46zGNR (a) and carbon nanoscroll (b) with inner radius $R_{\text{in}} = 1.35$ nm formed from carbon nanoribbon 46zGNR.

The length of a *zigzag* nanoribbon nzGNR, that forms a nanoscroll, is equal to $L = (3n/2 - 1)a_{\text{CC}}$, where n is the number of zigzag chains along the length of the nanoribbon (along the x axis in Fig. 1(a)). For 46zGNR ($n = 46$)$L =$ 9.66 nm and for 70zGNR ($n = 70$)$L = 14.77$ nm.

The coordinates of carbon atom of a zigzag nanoribbon, which is rolled into a nanoscroll, are determined by three indices: the first index q takes the values A or B in accordance with the sublattices A and B, the second index i is the number of the cell along the length of the nanoribbon, the third index j is the number of the cell along the width of the nanoribbon, see Fig. 1(a). The coordinates of carbon atom of the nanoribbon are given by the formulae:

$$\begin{aligned} x_{Aij} &= (3/2)(i-1)a_{\text{CC}} \qquad x_{Bij} = x_{Aij} + a_{\text{CC}}, \\ y_{qij} &= (a/2)(j-1) \quad \text{for odd } i, \\ y_{qij} &= (a/2)(j-1) + a/4 \quad \text{for even } i, \\ z_{qij} &= 0\,, \end{aligned} \tag{1}$$

where $a = \sqrt{3}a_{CC}$ is the period of translation (along the y axis).

The free *zigzag* edges of the nanoribbon are passivated by the hydrogen atoms, which are positioned at the distances of $a_{CH} = 0.1091$ nm from the carbon atoms along the x axis.

A nanoribbon rolled up around the axis that is perpendicular to the nanoribbon length (around the y axis in Fig. 1(a)) forms a carbon nanoscroll, as it is shown in Fig. 1(b). The cross-section of the nanoscroll is the Archimedean spiral with the distance between the turns $h = 0.335$ nm. Note that in the proposed model of the nanoscroll geometry the distance between carbon atoms is not equal to a_{CC} (Fig. 1(b)). The coordinates for nanoscroll atoms $(x_{qij}\, y_{qij}\, z_{qij})$ are given by the following expressions:

$$\begin{aligned} x_{qij} &= R_{qij}\sin(\varphi_{qij}), \\ y_{qij} &= R_{qij}\cos(\varphi_{qij}), \\ z_{qij} &= (j-1)(a/2) \quad \text{for odd } i, \\ z_{qij} &= (j-1)(a/2) - a/4 \quad \text{for even } i\,, \end{aligned} \tag{2}$$

where $R_{qij} = h\varphi_{qij}/2\pi$ is the curvature radius of the nanoscroll surface at the point corresponding to the angle φ_{qij} in radians, which is found from the equation $X_{qij} = \lambda(\varphi_{\text{in}}, \varphi_{qij})$, here $X_{Aij} = (3/2)(i-1)a_{CC}$ and $X_{Bij} = X_{Aij} + a_{CC}$ are the coordinates of carbon atoms along x axis of the corresponding nanoribbon, and

$$\begin{aligned} \lambda(\varphi_{\text{in}}, \varphi_{qij}) &= \sum_{\varphi_{\text{in}}}^{\varphi_{qij}} \frac{h}{2\pi}\sqrt{1+\varphi^2}\,d\varphi = \\ &= \frac{h}{4\pi}\Big[\varphi_{qij}\sqrt{1+\varphi_{qij}^2} - \varphi_{\text{in}}\sqrt{1+\varphi_{\text{in}}^2} + \\ &+ \ln\left(\varphi_{qij}+\sqrt{1+\varphi_{qij}^2}\right) - \ln\left(\varphi_{\text{in}}+\sqrt{1+\varphi_{\text{in}}^2}\right)\Big] \end{aligned}$$

is the length of Archimedean spiral with the distance between the adjacent scroll turns h, the inner angle φ_{in} and the outer angle φ_{qij}. The inner angle φ_{in} of the nanoscroll is expressed via inner radius R_{in} as $\varphi_{\text{in}} = 2\pi R_{\text{in}}/h$. Note that we used the different systems of coordinates for the carbon nanoscroll and for the carbon nanoribbon. For the nanoribbon the x axis is directed along the nanoribbon length L, while for the nanoscroll the xy plane is perpendicular to the axis of the nanoscroll.

In the quantum chemical calculations the periodic boundary conditions that translate the computational cell to infinity along the zigzag axis of the nanoscroll (z axis in Fig. 1(b)) were used. The width W of the computational cell (nanoribbon or nanoscroll) was set to four translation periods $a = \sqrt{3}a_{CC} = 0.246$ nm along the axis of the nanoscroll, thus $W = 4a = 4\sqrt{3}a_{CC} = 0.984$ nm.

Figure 2 shows the total energy of the nanoscrolls formed from the carbon nanoribbons 46zGNR (points a) and 70zGNR (points b) with the coordinates of carbon atoms defined by Eq. (2) relative to the total energy of the corresponding flat nanoribbon with coordinates defined by Eq. (1), calculated in MOPAC2016 program, as the function of the nanoscroll inner radius R_{in}. The PM3 method was used in MOPAC2016; the optimization of the geometry of the structures was not carried out. For comparison, the calculations of the potential energy

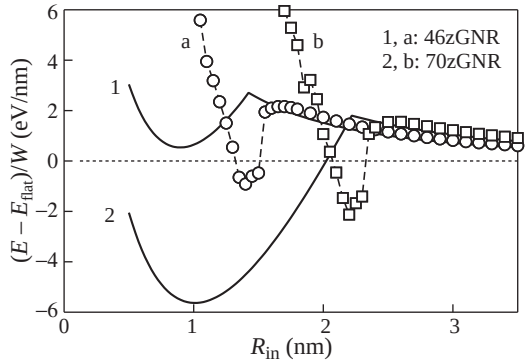

Fig. 2. The energy of nanoscroll E with respect to the energy E_{flat} of the corresponding flat nanoribbon of length $L = 10$ nm (46zGNR: 1, a) and 15 nm (70zGNR: 2, b), as a function of the inner radius R_{in} of the nanoscroll. Calculations are performed using the PM3 quantum chemical method (points a and b) and using the semi-classical analytical model [2] (curves 1 and 2). The energies are shown per width W of the computational cell.

of the nanoscrolls according to the semi-classical analytical model [2] are also presented in Fig. 2 (curves 1 and 2).

The semi-classical analytical and quantum chemical calculations show a similar behavior of the nanoscroll energy as a function of R_{in}. For both calculation methods, at large R_{in} the scroll energy converges to the energy of the flat nanoribbon. During nanoscroll rolling (moving along the horizontal axis in Fig. 2 from right to left) the energy increases, can have a maximum value, can have a minimum value and then increases at further decreasing of R_{in}.

The calculations by the PM3 method show that the nanoscrolls have a minimum energy at the specific inner radius $R_{\text{in}} \approx 1.35$ nm for 46zGNR and $R_{\text{in}} \approx 2.2$ nm for 70zGNR. The calculations by the semi-classical analytical model give the minimum energy at the inner radius $R_{\text{in}} \approx 0.9$ nm for $L = 10$ nm and $R_{\text{in}} \approx 1.0$ nm for $L = 15$ nm.

In conclusions, the structure of *zigzag* nanoscrolls was defined by a small length of the nzGNR, the nanoscroll width, the distance between the layers in nanoscroll, the bond length between the nzGNR atoms). Using the semi-empirical quantum chemical method of molecular orbitals PM3, the energy is calculated in the process of the nanoribbon folding into nanoscroll. The results of energy calculations are compared with the similar results obtained by the semi-classical analytical model.

Acknowledgements

The work has been supported by the Belarusian Republican Foundation for Fundamental Research (grant Nos. F18R-253 and F20R-301) and the Belarusian National Research Program "Convergence-2020".

References

[1] E. Perim and D.S. Galvão, *Nanotechnology*, **20**, 335702 (2009).
[2] A.I. Siahlo, N.A. Poklonski, A.V. Lebedev, *et al*, *Phys. Rev. Materials.*, **2**, 036001 (2018).
[3] N.A. Poklonski, S.A. Vyrko, A.I. Siahlo, *et al*, *Mater. Res. Express.*, **6**, 042002 (2019).
[4] J.J.P. Stewart, *J. Comp. Chem.*, bf10, 209 (1989).
[5] J.J.P. Stewart, MOPAC2016 (Colorado Springs, CO, USA, Stewart Computational Chemistry, 2012) [http://openmopac.net].
[6] N.A. Poklonski, E.F. Kislyakov, S.A. Vyrko, *et al*, *J. Nanophotonics*, **6**, 061712 (2012).

28th Int. Symp. "Nanostructures: Physics and Technology"
Minsk, Belarus, September 2020

Supersymmetry and stable Dirac sea in carbon nanotubes

E.L. Rumyantsev, P.E. Kunavin, A.V. Germanenko
Institute of Natural Science, Ural Federal University, 620000 Ekaterinburg, Russia

Abstract. We consider the construction of exactly solvable models of twisted carbon nanotubes by applying Darboux transformation to the square of the Dirac-like Hamiltonian, describing the low-energy dynamics of charge carriers. It is shown that obtained two pseudo-Schrodinger expressions are intertwined, demonstrating supersymmetry structure. It is proved, that for the considered class of scalar external perturbations, the unitary disentanglement of negative/positive states as within Foldy–Wouthuysen (FW) approach, so by Eriksen or SU(2) methods, can be carried out exactly, thus demonstrating the stability of the Dirac sea. The necessity of introduction of the probability density operator into the theory in Foldy–Wouthuysen representation is discussed.

Introduction

The role of exactly solvable models in physics is unquestionably of great importance. More so if they can be realized and tested experimentally. The broad class of the solvable problems is presented by the (1+1) Dirac-like equations. It can be shown that the following set of unitary equivalent one-dimensional Dirac-like Hamiltonians ($i \neq j$)

$$\hat{H} = \upsilon p_y \sigma_i + W(y)\sigma_j \tag{1}$$

demonstrate supersymmetric properties, due to specific introduction of static pseudo-scalar potential into the theory. Such Hamiltonians find its use for the description of the systems ranging from quantum field theory (e.g. (1+1) version of Nambu–Jona–Lasino model [1]) to solid state physics (so called "twisted" single wall carbon nanotubes (CNT) [2]). In what follows, we restrict our consideration to the Hamiltonian of the form

$$\hat{H}_{\mathrm{CNT}} = \upsilon_{\mathrm{CNT}} p_y \sigma_y + W(y)\sigma_x, \tag{2}$$

which describes dynamics of the low-energy charge carriers in CNT within $k \cdot p$ theory at K point of the Brillouin zone [3] in presence of magnetic field or as a consequence of mechanical deformations (twisted CNT [4]). One of the widely known examples of such Hamiltonian is the famous Dirac oscillator [5].

1. Schrodinger-like SUSY approach

In order to establish hidden supersymmetry (SUSY) properties of $\hat{H}_{\mathrm{CNT}}$ we reformulate the problem in more formal language, following [6]. To this end we define two fermionic operators Q, and its adjoint Q^+, such that $Q^2 = (Q^+)^2 = 0$

$$Q = A\sigma_-, \quad Q^+ = A^+\sigma_+, \tag{3}$$

$$A = i\upsilon_{\mathrm{CNT}} p_y + W(y), \quad \sigma_+ = \sigma_x + i\sigma_y. \tag{4}$$

$\hat{H}_{\mathrm{CNT}}$ can be written in these operators as $\hat{H}_{\mathrm{CNT}} = Q + Q^+$, and $\hat{H}^2_{\mathrm{CNT}}$, which is of prime interest for us, as

$$\hat{H}^2_{\mathrm{CNT}} = \mathcal{H}_{\mathrm{CNT}} = \{Q, Q^+\} = \begin{pmatrix} \mathcal{H}^{(1)}_{\mathrm{CNT}} & 0 \\ 0 & \mathcal{H}^{(2)}_{\mathrm{CNT}} \end{pmatrix}. \tag{5}$$

The operators $\mathcal{H}^{(1)}_{\mathrm{CNT}}, \mathcal{H}^{(2)}_{\mathrm{CNT}}$ are formally of Schrodinger second-order Hamiltonian form and are SUSY intertwined partners. It is important, that notwithstanding formal diagonal form of $\hat{H}^2_{\mathrm{CNT}}$, the solutions $\varphi^{(1)}(y)$ and $\varphi^{(2)}(y)$ of $\mathcal{H}^{(1)}_{\mathrm{CNT}}$ and $\mathcal{H}^{(2)}_{\mathrm{CNT}}$ are not independent, as they must compose pseudospinor $\Psi^T(y) = (\varphi^{(1)}(y), \varphi^{(2)}(y))$, being the solution of initial 2×2 matrix Dirac equation (2). Thus, if $\Psi_n(y)$ is eigenfunction of $\hat{H}_{\mathrm{CNT}}$ with eigenvalue E_n:

$$\hat{H}_{\mathrm{CNT}}\Psi_n(y) = E_n\Psi_n(y), \tag{6}$$

sought normalized $\varphi^{(1)}_n(y)$ and $\varphi^{(2)}_n(y)$ solutions must belong to the one and the same intertwined eigenvalue E^2_n:

$$\mathcal{H}^{(1)}_{\mathrm{CNT}}\varphi^{(1)}_n(y) = E^2_n\varphi^{(1)}_n(y) \tag{7}$$

$$\mathcal{H}^{(2)}_{\mathrm{CNT}}\varphi^{(2)}_n(y) = E^2_n\varphi^{(2)}_n(y). \tag{8}$$

By this strategy we obtain two solutions for two possible values of energy $|E_n|$ and $-|E_n|$. For positive energy states

$$\Psi^{(+)T}_n(y) = \left(\varphi^{(1)}_n(y), \varphi^{(2)}_n(y)\right)/\sqrt{2}, \tag{9}$$

and for negative energy states

$$\Psi^{(-)T}_n(y) = \left(\varphi^{(1)}_n(y), -\varphi^{(2)}_n(y)\right)/\sqrt{2}. \tag{10}$$

This symmetry between electron/hole states is violated by the presence of unpaired electron zero energy state in metallic CNT. It must be noted that this symmetry is restored (as it must be!) if we take into account the presence of solitary hole zero energy state at K' point of the Brillouin zone. In our work we consider within proposed approach the special case of the solutions for twisted CNT satisfying zero boundary conditions (rather unexpected result for linear Dirac-like equations). The possible form of the pseudo-scalar potential leading to transparent "twisting" of CNT is also discussed.

2. Foldy–Wouthuysen transformation in CNT

Using relations

$$[\mathcal{H}_{\mathrm{CNT}}, Q] = [\mathcal{H}_{\mathrm{CNT}}, Q^+] = [\mathcal{H}_{\mathrm{CNT}}, \sigma_3] = 0, \tag{11}$$

$$\{\sigma_3, Q\} = \{\sigma_3, Q^+\} = 0, \tag{12}$$

the following Hermitian generators of SU(2) algebra $[J_i, J_j] = i\varepsilon_{ijk}J_k$ can be defined [7]

$$J_1 = \frac{Q + Q^+}{2\sqrt{\mathcal{H}_{\mathrm{CNT}}}}, \tag{13}$$

$$J_2 = \frac{-i\sigma_3(Q+Q^+)}{2\sqrt{\mathcal{H}_{\rm CNT}}}, \tag{14}$$

$$J_3 = \frac{1}{2}\sigma_3. \tag{15}$$

Using these operators, we can rewrite $\hat{H}_{\rm CNT}$ as

$$\hat{H}_{\rm CNT} = 2\sqrt{\mathcal{H}_{\rm CNT}}J_1. \tag{16}$$

Using unitary operator $\exp(iJ_2\pi/2)$ we can bring $\hat{H}_{\rm CNT}$ to quasi-diagonal FW form by rotation about Y axis

$$\hat{H}_{\rm CNT} = 2\sqrt{\mathcal{H}_{\rm CNT}}J_3. \tag{17}$$

The same result can be achieved by application of Erikson [8] or FW unitary transformations, which we proved to be identical to considered SU(2) rotation. The existence of exact transformation separating electron and hole states means, that the definition of the ground state of the system (filled valence band) is maintained regardless of the intensity of pseudo-scalar perturbation. This effect has been named in [7] "stability of Dirac sea". In the new representation the electron/hole sectors of the system are described by scalar equations

$$i\partial_t\varphi_e^{\rm FW}(y,t) = \sqrt{A^+A}\varphi_e^{\rm FW}(y,t) \tag{18}$$

and

$$i\partial_t\varphi_h^{\rm FW}(y,t) = -\sqrt{AA^+}\varphi_h^{\rm FW}(y,t) \tag{19}$$

respectively. There are some problems to be overcome while describing the CNT carrier dynamics by these equations. First of all we are to define the action of pseudo-differential operators $\sqrt{A^+A}$ and $\sqrt{AA^+}$. It is shown that these formal expressions lead to non-local description. More serious problem is the violation of interpretation of $|\varphi_e^{\rm FW}(y,t)|^2$ and $|\varphi_h^{\rm FW}(y,t)|^2$ as probability density.

3. Position operator in FW representation

It is shown that the SU(2) rotation zeros one of the components of the two-component pseudo-spinor wave function $\Psi_n(y)$, violating interpretation of the square of the FW functions as spatial probability density because $|\Psi_n^{(\pm)}(y)|^2 \neq |\varphi_{n(e,h)}^{\rm FW}(y)|^2$. This points to the necessity of defining in our two band problem the probability density $P(Y)$ as the average of some operator $\hat{P}(y,Y)$ over corresponding wave function in accord with the definition of the value of an observable quantity in quantum mechanics. The natural choice of such operator in the original representation, where position operator is Dirac c-number, is delta function

$$P_n^{(\pm)}(Y) = \int \Psi_n^{(\pm)\dagger}(y)\delta(y-Y)\Psi_n^{(\pm)}(y)dy = |\Psi_n^{(\pm)}(Y)|^2. \tag{20}$$

It is convenient to consider Fourier transform of $P_n^{(\pm)}(Y)$ [9]

$$P_n^{(\pm)}(Y) = \int \Psi_n^{(\pm)\dagger}(y)e^{iky}\Psi_n^{(\pm)}(y)dy. \tag{21}$$

Under FW transformation the position operator becomes ($y \to \hat{y}_{\rm FW}$)

$$\hat{y}_{\rm FW} = \exp(iJ_2\pi/2)\,y\exp(-iJ_2\pi/2) = y + 2[\hat{\Gamma}, y]\hat{\Gamma}, \tag{22}$$

where

$$\hat{\Gamma} = (\hat{\lambda} - \sigma_3)/2, \tag{23}$$

$$\hat{\lambda} = (Q+Q^+)/\sqrt{\mathcal{H}_{\rm CNT}}. \tag{24}$$

$\hat{\Gamma}$ is some kind of projection operator whose action upon eigenfunctions of $\hat{H}_{\rm CNT}$ is defined as

$$\hat{\Gamma}\Psi_n^{(+)}(y) = -\varphi_{n(h)}^{\rm FW}(y), \tag{25}$$

$$\hat{\Gamma}\Psi_n^{(-)}(y) = -\varphi_{n(e)}^{\rm FW}(y). \tag{26}$$

It is straightforward to show that e.g.:

$$P_n^{(+)}(k) = \int \Psi_n^{(+)\dagger}(y)e^{iky}\Psi_n^{(+)}(y)dy \tag{27}$$

$$= \int \varphi_{n(e)}^{\rm FW}(y)e^{ik\hat{y}_{\rm FW}}\varphi_{n(e)}^{\rm FW}(y)dy. \tag{28}$$

The above discussion must be accounted for in relativistic Dirac theory, while analyzing spatial and temporal behavior of wave packets evolving according to one-component Salpeter Hamiltonian.

References

[1] G. Basar, G.V. Dunne, *Phys. Rev. D* **78**, 065022 (2008).
[2] V. Jakubski, M. Plyushchay, *Phys. Rev. D* **85**, 045035 (2012).
[3] H. Ajiki, T. Ando, *J. Phys. Soc. Jpn* **62**, 1255 (1993).
[4] C.L. Kane, E.J. Mele, *Phys. Rev. Lett.* **78**, 1932 (1997).
[5] M. Moshinski, A. Szczepaniak, *J. Phys A: Math. Gen.* **22**, L817 (1989).
[6] F. Cooper *et al*, *Supersymmetry in Quantum Mechanics*, (World Scientific, Singapore, 2001).
[7] R.P. Martinez y Romero *et al*, *Phys. Rev. D* **43**, 2036 (1991).
[8] E. de Vries, *Forstschr. Physik* **18**, 149 (1970).
[9] E.L. Rumyantsev *et al*, *Semiconductors* **53**, 2147 (2019).

28th Int. Symp. “Nanostructures: Physics and Technology”
Minsk, Belarus, September 2020

On the origin of photocurrents in pristine graphene

Yu.B. Vasilyev
Ioffe Institute, Polytechnicheskaya 26, 194021, St Petersburg, Russia

Atomically thin materials with Dirac electron dispersion are prospective platform for new generation of high-performance photodetectors. The photoelectric effects in thin-film Dirac materials are in the focus of intense studies.

Recently Ma *et al*. reported an intrinsic photocurrent in graphene [1], which occurs as the authors believe “in a different parameter regime from all the previously observed photothermoelectric or photovoltaic photocurrents in graphene”. This statement is supported by the observation that the photocurrent arises exclusively at the charge neutrality point and near the edges/corners. The phenomenon was attributed to the predicted specific effect of the electron–electron scattering at the Dirac point. The effect is based on the suppression of the photocurrent relaxation due to collinear alignment of the momenta of photoexcited carriers [2]. The photocurrents were observed in patterned graphene devices comprising a few rectangular regions of various widths. The authors neglected all types of scattering in graphene except electron-electron scattering. This needs justification, since the experiments were done on ordinary graphene samples on a SiO_2 substrate at temperatures up to 300 K. The question arises why these samples are so unusual that scattering can be ignored in them?

Obviously, the answer is that the reported results cannot be explained by the model used without such an assumption. Furthermore, the manifestation of the effect at 300 K is very surprising because it is not consistent with the mechanism based on the electron–electron scattering kinematics at the Dirac point, for which zero temperature is required. It is clear that as the temperature increases, the charge carriers are thermally excited into both the conduction and the valence bands, so the conditions for the momentum collinearity are violated.

Here we present an alternative — obvious and transparent explanation based on a photo effect in the *p*-*n* junctions formed at the boundary of two regions with different widths and different particle concentrations. The dependence of carrier concentration in a graphene ribbon on the ribbon width has been reported previously [3]. Applying the gate voltage, one can select the voltage at which the type of conductivity will be different in the neighboring parts of the sample, which leads to the formation of a *p*–*n* junction as shown schemattically in Fig. 1, where the *p*-type and *n*- type regions are indicated by blue and red colors respectively. The *p*–*n* junctions are formed when the chemical potential is near the global charge neutrality point, namely when it is in between the charge neutrality points of the parts. This explains why the photocurrent is observed near the global charge neutrality point.

Now we address the difference in carrier concentrations in the two parts of the sheet. It is related to edge doping, which, in contrast to the bulk oping, dependens on the sheet width.The edge doping is typically attributed to the dangling bonds formed at the graphene boundary [4]. The other possibility of the edge doping comes from the charged impurities on the surface of the dielectric substrate outside the sample perimeter. Only the

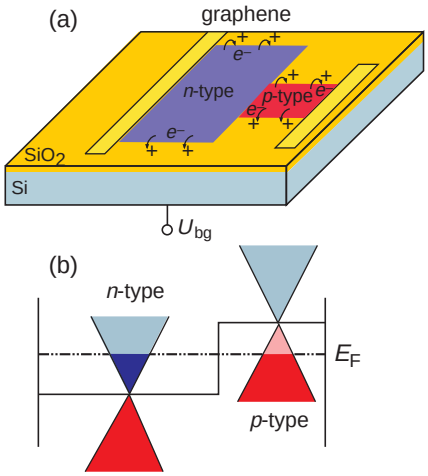

Fig. 1. *p*−*n* junction formation in graphene. (a) Schematic structure of graphene FET patterned with two parts of different widths and electron transfer from graphene to charged traps into SiO_2 substrate. (b) Schematic band diagram for the graphene when the bias voltage is shifted between the Dirac points of this parts.

impurities which are close enough to the sample perimeter contribute to carrier density in graphene. These inpurities can be formed by paramagnetic defects or dangling bonds in the substrate or on the substrate surface [5]. Such positively charged traps have a high probability of the electron capture and, hence, resulting in *p*-doping of graphene [6]. As far as the number of the transferred electrons is equal to the number of the traps, the concentration of such electrons decreases with increasing sheet width. The narrow sheet part becomes slightly more *p*-type compared to the broad part. Consequently, a natural *p*-*n* junction [7] is formed between the narrow and the broad parts of the device under a backgate voltage V_{bg} when $V_n > V_{bg} > V_b$. Here V_n and V_b are charge neutrality points for the narrow and the broad parts of the sheet (Fig. 1b). This method of *p*–*n* junction creation is universal and is applicable to any atomically flat structures located on insulating substrates.

To conclude, the photocurrent in graphene regions of various widths is related to photo effect in *p*–*n* junctions formed at the boundary of two regions with different particle concentrations.

References

[1] Ma Q. *et al*, *Nature Nanotech.*, **14**, 145 (2019).
[2] Junck,A., Refael G., von Oppen F. *Phys. Rev. B*, **90**, 245110 (2014).
[3] Nakada K. *et al*, *Phys. Rev. B*, **54**, 17954–17961 (1996).
[4] Brenner K., Yang Y., Murali R. *Carbon*, **50**, 637–645 (2012).
[5] DiMaria D.J., Weinberg Z.A., Aitken J.M. *J. Appl. Phys.*, **48**, 898–906 (1977).
[6] Nagashio K. *et al*, *J. Appl. Phys.*, **110**, 024513 (2011).
[7] Vasileva G.Y. *et al*, *Semiconductors*, **53**, 1672 (2019).

28th Int. Symp. "Nanostructures: Physics and Technology"
Minsk, Belarus, September 2020

Luminescence spectra of mesa-cavity

A.V. Belonovskii[1,2], K.M. Morozov[1,2], M.A. Kaliteevski[1,2,3]

[1] St Petersburg Academic University, St Petersburg, Russia
[2] ITMO University, St Petersburg, Russia
[3] Ioffe Institute, Politekhnicheskaya 26, 194021, St Petersburg, Russia

Abstract. We show a new method for studying the emission spectra from structures whose characteristic dimensions correspond to several wavelengths of exciton radiation in the material, and the frequency interval between the eigenmodes is comparable or less than the Rabi splitting between the exciton and photon modes. The distribution of eigenmodes in frequencies and Q factors for a square resonator GaN with a size of 2.3 μm is presented. The formal structure of the emission spectrum was modeled for square cavity GaN in the case of the implementation of strong and weak coupling between the exciton and cavity modes.

Introduction

The dynamics of an optical emitter changes dramatically when it is placed in a cavity. The cavity changes the density of states of the optical modes and, therefore, increases or suppresses the interaction with the emitter. To date, the interaction of photon modes in a cavity with an exciton located inside it is being actively studied [1–3]. In the study of the strong coupling between excitons and intrinsic photon modes in the cavity, an important parameter is the size of the microresonators. To ensure a large energy interval between the cavity modes, extremely small cavity sizes of the order of several nanometers are required. However, the manufacture of structures of such sizes is a complex technological task today. Meanwhile, resonators with dimensions that occupy an intermediate position between bulk materials and microcavities (mesa-cavity), where the exciton mode interacts with a limited number of optical modes of the system, remain poorly studied. Recently, in the works [4–6] the simplest types of such resonators were already studied. It has been shown that in mesa-cavity there are a small number of high-Q modes that can effectively interact with exciton resonance and lead to splitting of the luminescence peaks. In this paper, we show an effective method for calculating the luminescence spectra from such structures.

1. The formalism

To calculate the spectrum from the structure, we consider the complete state of the system, which is described by the density matrix $\hat{\rho}$, and its evolution is determined by the equation $\partial_t \hat{\rho} = \mathcal{L}[\hat{\rho}]$ with the Lindblad terms in the Liouvillian $\mathcal{L}$, accounting for damping [7], ($\hbar = 1$):

$$\begin{aligned}\mathcal{L}[\hat{\rho}] &= i[\hat{\rho}, \hat{H}] + \\ &+\frac{\gamma_0}{2}(2\hat{x}\hat{\rho}\hat{x}^+ - \hat{x}^+\hat{\rho}\hat{x} - \hat{\rho}\hat{x}^+\hat{x}) + \\ &+\sum_k \frac{\gamma_k}{2}(2\hat{a}_k\hat{\rho}\hat{a}_k^+ - \hat{a}_k^+\hat{\rho}\hat{a}_k - \hat{\rho}\hat{a}_k^+\hat{a}_k), \quad (1)\end{aligned}$$

where

$$\hat{H} = \omega_0\hat{x}^+\hat{x} + \sum_k \omega_k\hat{a}_k^+\hat{a}_k + \sum_k g_k(\hat{a}_k^+\hat{x} + \hat{a}_k\hat{x}^+), \quad (2)$$

w_0 is the exciton frequency, w_k are the frequencies of cavity modes, g_k are the constants, describing the exciton-photon interactions, and $\hat{x}$, $\hat{c}$ ($\hat{x}^+$, $\hat{c}^+$) are the operators of annihilation (creation) of exciton and photons, respectively. γ_0 and γ_k are rates of damping of the emitter and the cavity respectively.

Using the relations $\partial_t\langle O\rangle = Tr(O\partial_t\rho) = Tr(O\mathcal{L}\rho)$, we can obtain the mean values number of photons in cavity, the exciton occupation numbers and the mixed states:

$$\begin{aligned}\partial_t n_x &= i\sum_k g_k(n_{a_k x} - n_{x a_k}) - G_{xx}n_x \\ \partial_t n_{a_i a_j} &= i\Delta_{ij}n_{a_i a_j} - g_j n_{a_i x} + ig_i n_{x a_j} - G_{ij}n_{a_i a_j} \quad (3) \\ \partial_t n_{x a_i} &= i\Delta_{xj}n_{x a_i} + i\sum_k g_k n_{a_k a_j} - ig_i n_x - G_{xi}n_{x a_i},\end{aligned}$$

where $n_x = \langle x^+ x\rangle$ is the mean values of the exciton occupation numbers $n_{a_i a_i} = n_{a_i} = \langle a_i^+ a_i\rangle$ are the mean values number of photons in mode i. $n_{x a_i} = n^*_{a_i x}$ and $n_{a_i a_j} (i \neq j)$ the mixed states. And in this equations we using definitions: $G_{ij} = \frac{\gamma_i+\gamma_j}{2}$, $\Delta_{ij} = \omega_i - \omega_j$.

The mean number of photons in the system with frequency ω for mode i:

$$s_i(\omega) = \langle \hat{a_i}^+(w)\hat{a_i}(w)\rangle. \quad (4)$$

At the same time, we can obtain the function $s_i(\omega)$ through the first-order correlation function [7]:

$$s_i(\omega) = \frac{1}{\pi}\mathcal{R}\int_0^\infty\int_0^\infty G_i^{(1)}(t,\tau)e^{i\omega\tau}d\tau, \quad (5)$$

where $G_i^{(1)}$ the first-order correlation function:

$$G_i^{(1)} = \langle \hat{a_i}^+(t)\hat{a_i}(t+\tau)\rangle. \quad (6)$$

The general spectrum for the system, taking into account normalization, will look as follows:

$$S(\omega) = \sum_i s_i(\omega) / \sum_i \int_0^\infty n_i dt. \quad (7)$$

2. Results and discussion

As an example, we considered a square mesacavity of GaN with a side of $l = 2.3$ μm and a refractive index $n = 2.6267$. The exciton energy for GaN is $\omega = 3.46$ eV. Eigenmodes and Q for square meso-cavity have been studied using simulations in the COMSOL multiphysics software. Fig. 1 shows an example

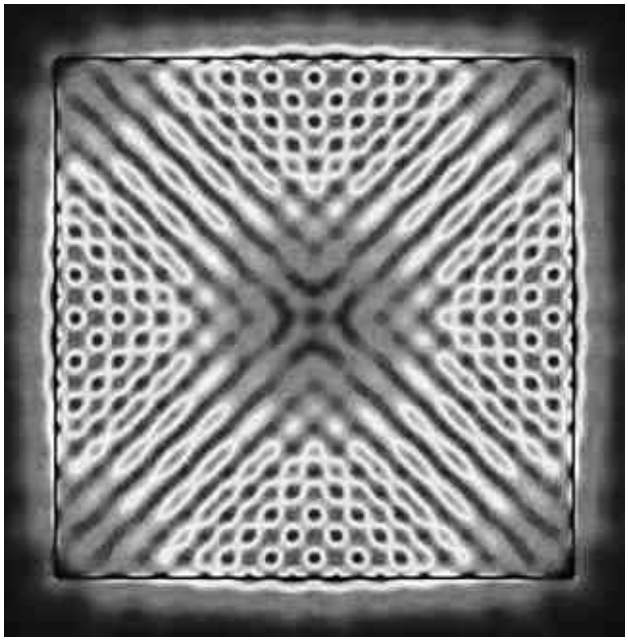

Fig. 1. Distribution of modes of the electromagnetic-field intensity inside the GaN square mesa-cavity ($\omega = 3.4622$ eV, $Q = 35 \cdot 10^3$).

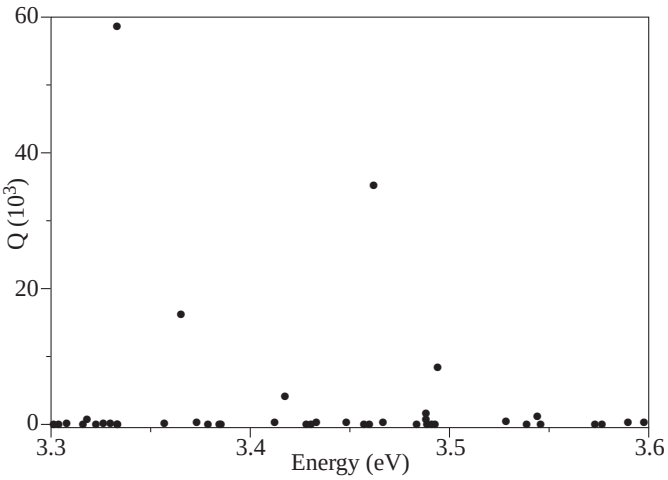

Fig. 2. Q factors and eigenmode energies of the GaN planar hexagonal microcavity.

of a photon mode localized in the structure with an energy of $\omega = 3.4622$ eV and $Q = 35 \cdot 10^3$. Fig. 2 shows the eigenmodes and their Q factors located near the exciton energy in GaN $\omega_{ex} = 3.46$ eV. The figure shows a low density of high-Q modes. And also one successful high-Q mode with an energy of $\omega = 3.4622$ eV which is very close to the exciton energy.

Using the found Q factors, we can find the photon dissipation for each mode, using the relation: $\gamma_i = \frac{\omega_i}{Q_i}$. We take the coupling constant proportional to the root of the frequency of the photon mode $g_i = k\sqrt{\omega}$.Where the proportionality factor k is simply a scale factor. Fig. 3 shows the spectrum $S(\omega)$ of a square GaN structure (for a better visualization, we took $k = 0.01$). As a result, we obtained a spectrum of a square cavity in which there are several high-Q modes and many low-Q ones. The picture also shows the realization of the strong coupling of the exciton and the nearby photon modes.

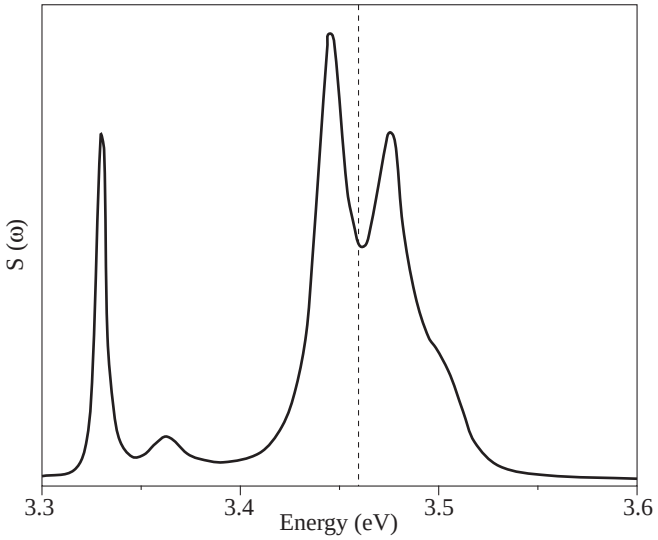

Fig. 3. The mean number of photons in the system with frequency ω.

References

[1] I. Abram and J.L. Oudar, *Phys. Rev. A* **51** (5), 4116 (1995).

[2] S. Pau, G. Bjrk, J. Jacobson, *et al*, *Phys. Rev. B* **51** (20), 14437 (1995).

[3] T.A. Fisher, A.M. Afshar , D.M. Whittaker, *et al*, *Phys. Rev. B* **51** (4), 2600 (1995).

[4] A.V. Belonovski, I.V. Levitskii, K.M. Morozov, *et al*, *Optics Express* **28** (9) 12688 (2020).

[5] G. Pozina, C. Hemmingsson, A.V. Belonovskii, *et al*, *Physica Status Solidi (b)* 00894 (2019).

[6] A.V. Belonovskii, G. Pozina, I.V. Levitskii, *et al*, *Semiconductors* **54**, 127 (2020).

[7] F.P. Laussy, E. Valle, C. Tejedor, *Phys. Rev. B* **79**, 235325 (2009).

28th Int. Symp. "Nanostructures: Physics and Technology"
Minsk, Belarus, September 2020

Spatio-temporal correlations in a gas of microcavity polaritons

M.V. Kochiev[1], V.V. Belykh[1], N.N. Sibeldin[1], C. Schneider[2] and S. Höfling[2,3]

[1] P.N. Lebedev Physical Institute of the Russian Academy of Sciences, Moscow, 119991 Russia
[2] Technische Physik, Physikalisches Institut and Wilhelm Conrad Röntgen Research Center for Complex Material Systems, Universität Würzburg, D-97074 Würzburg, Germany
[3] SUPA, School of Physics and Astronomy, University of St Andrews, St Andrews, KY16 9SS, United Kingdom

Abstract. We study a spatio-temporal correlations in a gas of microcavity polaritons by registering the dynamics of spatial distribution in single pulses of polariton photoluminescense. The second-order correlation function $g^{(2)}$ of registered numbers of photons reveals spatial anti-correlation at 20 μm shift under pump powers above the condensation threshold. At very high pump power we additionaly observed a temporal anti-correlation at 20 ps delay and increased correlation at both spatial shift and time delay.

Introduction

Recently several stochastic properties of the polariton Bose–Einstein condensate (BEC) were investigated: the jitter of BEC onset time [1] and the dynamics of spontaneous polarization [1,2], the random spatial distribution of the BEC [3]. Some more effects of spatial instability were predicted under both resonant [4] and non-resonant excitation [5].

1. Experimental details

In the present work, we have studied a spatio-temporal behavior of the polariton Bose condensate measuring the second-order correlation function. The sample under study is a $3/2\lambda$ microcavity (MC) with 12 GaAs/AlAs quantum wells of width 7 nm and top and bottom Bragg reflectors made of 32 and 36 AlAs/$Al_{0.13}Ga_{0.87}As$ pairs, respectively. It has a Q factor of about 7000 and a Rabi splitting of 5 meV. The experiments were performed at a temperature of $T = 10$ K and a photon–exciton detuning of $\Delta \sim -5$ meV. The sample was mounted in a cold-finger cryostat and excited by radiation from a mode-locked

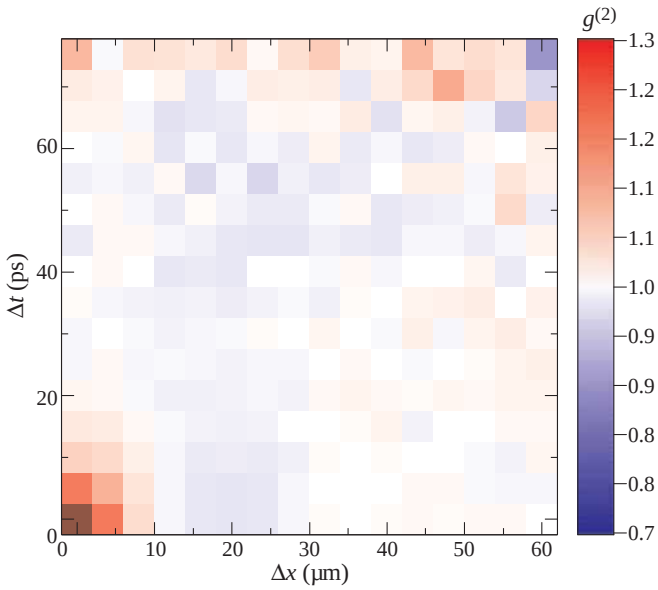

Fig. 1. Dependence of the $g^{(2)}$ function on time delay Δt and spatial shift Δx at pump power $P = 5P_{\text{thr}}$. The blue region around $\Delta t = 0$ and $\Delta x = 20$ μm corresponds to the anti-correlation related to fluctuations of the spatial distribution of polariton condensate.

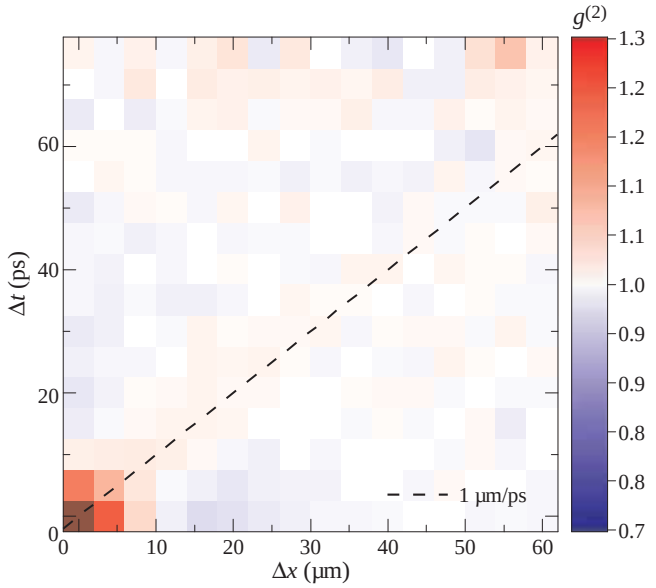

Fig. 2. Dependence of the $g^{(2)}$ function on time delay Δt and spatial shift Δx at pump power $P = 20P_{\text{thr}}$. The red region along the line $\Delta t = \Delta x$ corresponds to the correlation related to the formation and propagation of the spatial fluctuations.

Ti-sapphire laser generating a periodic ($f = 76$ MHz) train of 2.5-ps-long pulses at the wavelength corresponding to the minimum of the mirror reflectivity, 13–17 meV above the bare exciton energy. The laser beam was focused onto a 35 μm spot on the sample surface. The PL emitted within 15 deg around the sample normal was collected with a 0.25-NA microobjective and focused with two cylindrical lenses with orthogonal axes and different focal lengths. In this way, the PL spot at the sample surface was imaged onto a spot that was horizontally elongated along the slit of a Hamamatsu streak camera operating with 3 ps time resolution. The repetition rate of the laser pulses was lowered to 25 Hz by an acousto-optical pulse picker to match the frame rate of the streak-camera CCD, which is limited by the CCD readout time. Pulse picking was synchronized with the CCD to record a single emission pulse per frame.

2. Results

We splitted the spatio-temporal streak image into spatial and temporal bins of 4 μm and 5 ps and calculated the second-order correlation function $g^{(2)}(\Delta x, \Delta t)$ of the numbers of registered photons $n(x, t)$ and $n(x + \Delta x, t + \Delta t)$, where t is time and

x is horizontal coordinate. The values of $g^{(2)}$ function were averaged over x and t range with significant luminescence intencity with weights equal to $n(x,t)$. At $2.5P_{\text{thr}} < P < 20P_{\text{thr}}$ the values of the second-order correlation function at near-zero delay and spatial shift of 20 μm are less than 1 which means the presence of anti-correlation between different spatial points (Fig. 1). It corresponds to the formation of different spatial distributions of condensate from pulse to pulse [3]. At $P = 20P_{\text{thr}}$ we observed two regions of anti-correlation ($g^{(2)}(\Delta x, \Delta t) < 1$) — the first at the temporal shift of $\sim$20 ps and the second at the spatial shift of 20 μm — separated with the region of raised correlation (Fig. 2). The same behavior of the $g^{(2)}(\Delta x, \Delta t)$ function was predicted as evidence of the formation of tree-like spatio-temporal patterns due to the spatial instability of the condensate [5]. The region of increased correlation at both non-zero time delay and spatial shift corresponds to the propagation speed of the fluctuations of 1 μm/ps, which is of the order of the propagation speed of the spatial coherence in this sample [6].

This work was supported by the Russian foundation for basic research (grant No. 18-02-01143).

References

[1] M.V. Kochiev, V.V. Belykh, N.N. Sibeldin *et al*, *Phys. Rev. B* **99**, 035310 (2019).
[2] V.G. Sala, F. Marsault, M. Wouters *et al*, *Phys. Rev. B* **93**, 115313 (2016).
[3] E. Estrecho, T. Gao, N. Bobrovska *et al*, *Nature Commun.* **9**, 2944 (2018).
[4] S.S. Gavrilov, *Phys. Rev. Lett.* **120**, 033901 (2018).
[5] N. Bobrovska, A. Opala, P. Mię tki *et al*, *Phys. Rev. B* **99**, 205301 (2019).
[6] D.A. Mylnikov, V.V. Belykh, N.N. Sibeldin *et al*, *JETP Letters* **101**, 513 (2015).

28th Int. Symp. “Nanostructures: Physics and Technology”
Minsk, Belarus, September 2020

Polariton emission and polarization splitting in the ultrastrongly coupled Tamm plasmon-organic exciton system

K.M. Morozov[1,2], P. Pander[3], L.G. Franç[3], N. Selenin[4], S. Mikhrin[4], A.P. Monkman[3] and M.A. Kaliteevski[1,2,5]

[1] Alferov University, St Petersburg, Russia
[2] ITMO University, St Petersburg, Russia
[3] Physics Department, Durham University, Durham, United Kingdom
[4] Innolume GmbH, Dortmund, Germany
[5] Ioffe Institute, Politekhnicheskaya 26, 194021, St Petersburg, Russia

Abstract. We study a spatio-temporal correlations in a gas of microcavity polaritons by registering the dynamics of spatial distribution in single pulses of polariton photoluminescense. The second-order correlation function $g^{(2)}$ of registered numbers of photons reveals spatial anti-correlation at 20 μm shift under pump powers above the condensation threshold. At very high pump power we additionaly observed a temporal anti-correlation at 20 ps delay and increased correlation at both spatial shift and time delay.

Strong coupling between the cavity mode and exciton give rise to the new hybrid polariton states, split into value Rabi energy. Further increase of the light-matter interaction strength follows to new interaction regime [1,2] with peculiar properties [3] — ultrastrong coupling regime (USC). In the ultrastrong coupling regime the Rabi splitting between cavity mode and exciton is comparable to bare exciton energy (ratio between the Rabi splitting and the bare exciton energy ≈ 20%).

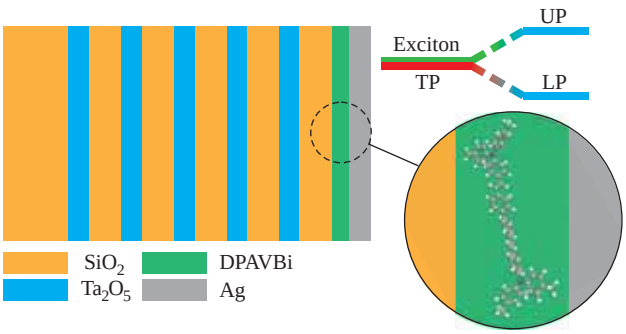

Fig. 1. Scheme of the Tamm plasmon cavity filled with the DPAVBi material.

Organic materials usually have high oscillator strength that makes them suited to study the room temperature USC regime. This work was aimed at the theoretical and experimental study of the Tamm plasmon [4] cavity structure filled with organic semiconductor material DPAVBi (4,4’-Bis[4-(di-p-tolylamino) styryl]biphenyl). The Tamm plasmon cavity structure under study is demonstrated in Fig. 1. The structure consists of the 5-pair SiO_2 (75 nm)/ Ta_2O_5 (49 nm) distributed Bragg reflector (DBR) layer of the DPAVBi material and the 50nm silver layer. The cavity was made using various fabrication techniques: magnetron sputtering was used for DBR fabrication, then, using thermal deposition method layers of the DPAVBi and silver were made ob the top of the DBR. The cavity structure was designed to support the Tamm plasmon (TP) mode near the exciton energy of DPAVBi (3.05 eV). A set of structures were fabricated with the various difference between TP mode and DPAVBi exciton. Results of the angle-resolved reflectivity spectra measurements for TE and TM polarizations for TP structure with 40nm DPAVBi layer thickness are presented in figure 2. Two narrow areas with low reflectivity divided by exciton energy (dashed black curve) corresponded to the lower (LP) and upper (UP) polariton branches. Value of the Rabi splitting (Ω_{Rabi}) for the case of TE polarization is ≈610 meV ($\Omega_{\text{Rabi}}/E_{\text{exc}} \approx 20\%$). Thus, the system is under the ultrastrong coupling regime.

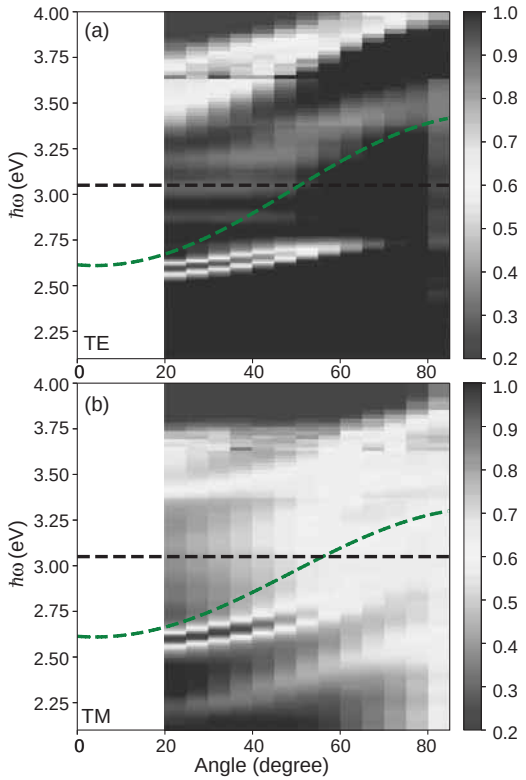

Fig. 2. Angle-dependent reflectivity spectra of the TP structure for the TE-polarization (a) and TM-polarization (b) case. Dashed black line shows the energy of the bare exciton. Dashed green line shows dispersion of the Tamm plasmon mode for the TE(a) and TM(b) polarization cases.

Another important property is the energy difference between TP mode dispersion in TE and TM called TE-TM splitting [5]. For the higher angles area, where TE-TM splitting

usually has a maximum value, large splitting between UP energy in TE and TM polarizations occurs (splitting value is up to 100 meV).

Acknowledgement

This work has been supported by the Russian Science Foundation, project No. 16-12-10503.

References

[1] A. Frisk Kockum *et al*, *Nat. Rev. Phys.* **1**, 19-40 (2019).
[2] P. Forn-Daz *et al*, *Rev. Mod. Phys.* **91**, 025005 (2019).
[3] C. Ciuti *et al*, *J. Phys. Rev. B* **72**, 115303 (2005).
[4] A.R. Gubaydullin *et al*, *Sci. Rep.* **7**, 9014 (2017).
[5] R. Brückner, *et al*, *Appl. Phys. Lett.* **100**, 062101 (2012).

28th Int. Symp. "Nanostructures: Physics and Technology"
Minsk, Belarus, September 2020

Resonant activation of resistive switching in $ZrO_2(Y)$ based memristors

V.N. Baranova, D.O. Filatov, D.A. Antonov, I.N. Antonov and O.N. Gorshkov
Lobachevskii State University of Nizhnii Novgorod, 603950 Nizhnii Novgorod, Russia

Abstract. We report on a comparative study of resistive switching in the memristors based on $ZrO_2(Y)$ films and on $ZrO_2(Y)/Ta_2O_5$ bilayer stacks by triangle voltage pulses with superimposed high-frequency sinusoidal signal. The dependencies of the current difference in the low resistance state and in the high resistance one on the sinusoidal signal frequency for the $ZrO_2(Y)$-based memristor and for the $ZrO_2(Y)/Ta_2O_5$-stack based one manifested one and two maxima, respectively attributed to the resonant activation of the migration of the oxygen ions via the oxygen vacancies by the alternating external electric field in $ZrO_2(Y)$ and in Ta_2O_5.

Introduction

Recently, resistive switching (RS) attracted much attention [1]. The effect consists in bistable (multistable) switching of the resistance of a dielectric film between two conductive electrodes under a voltage applied to the ones. Respective devices are called *memristors* [2]. The RS mechanism in metal oxides consists in forming of conductive filaments (composed of oxygen vacancies, V_Os) in an electric field between the electrodes [3]. The switching from a low resistance state (LRS) to a high resistance state (HRS) (RESET process) is achieved by the rapture of the filament by a voltage pulse of certain polarity. The filament is restored by another voltage pulse of the opposite polarity that results in the switching from the HRS to LRS (SET process).

The memristors are promising for applications in the non-volatile computer memory [4], the neuromorphic computing [5], etc. However, their application is limited by instability of the RS parameters, which is an intrinsic property of the memristors originating from the stochastic nature of the RS since a limited number of V_Os near the filament tip participate in the switching process [6]. Several approaches to improving the RS stability were proposed, e.g. a choice of suitable dielectric and electrode materials, the multilayered dielectrics, etc. [7]. Another approach is based on noise-enhanced stability effect [8], which is inherent to the multistable stochastic systems [15]. Earlier, we foud the high-frequency (HF) sinusoidal signal added to the switching pulses to improve the RS performance of $ZrO_2(Y)$-based memristors [11,12]. The effect was attributed to the resonant activation of the O^{2-} ion motion via the V_Os in the alternating electric field, which promotes the rapture and restoring of the filaments. Resonant activation of the transitions between the metastable states is another phenomenon manifesting the beneficiary role of noise [9].

In the present work, we studied effect of the frequency of the HF sinusoidal signal added to the switching pulses on the RS parameters of the memristors based on $ZrO_2(Y)$ films and on $ZrO_2(Y)/Ta_2O_5$ stacks. The Ta_2O_5 sublayers were found to improve the RS because of self-forming of the Ta-enriched nanoinclusions in the Ta_2O_5 layers, which play the role of the electric field concentrators promoting the filament growth [10]. The goal of the present study was to confirm resonant activation of the O^{2-} ion motion to be the origin of the RS improvement.

1. Experiment

The functional dielectric films were deposited by HF magnetron sputtering at the stubstrate temperature $T_s = 300$ °C onto the industrial Si(001) substrates with pre-deposited SiO_2 film ($\approx$ 500 nm thick), Ti adhesion layer, and TiN conductive one (each $\approx$ 25 nm in thickness) using Torr International ®2G1-1G2-EB4-TH1 setup. The thickness of the $ZrO_2(Y)$ ($\approx$ 12% mol. of Y_2O_3) films was $\approx$ 40 nm, the one of the Ta_2O_5 sublayers was $\approx$ 10 nm. The top Au($\approx$ 40 nm)/Zr($\approx$ 7 nm) contacts were deposited by direct current magnetron sputtering at $T_s = 200$ °C. The cross-point memristors with the active area of 20×20 μm^2 were fabricated by standard optical lithography.

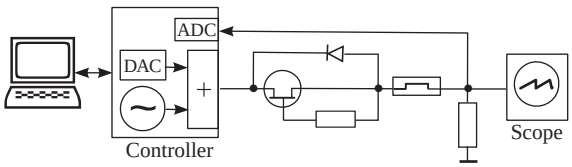

Fig. 1. Schematic representation of the experimental setup.

The RS was studied using a setup shown schematically in Fig. 1. The voltage $V(t)$ (t is the time) applied to the memristor was generated by a digital-to-analog converter (DAC) of NT-MDT ®Solver™atomic force microscope (AFM) controller used as a programmable voltage source. Current compliance during the SET process was provided by a field-effect transistor.

RS parameters were measured by multiple write/erase cycling according to protocol shown qualitatively in Fig. 2. The switching of the memristor was performed by triangular switching pulses with the amplitudes $V_{\rm SET} = 3.5$ to 4.5 V and $V_{\rm RESET} = -3.5$ to -2.5 V and the durations $T_{\rm SET}$, $T_{\rm RESET} =$ 1 s. Here $V_{\rm SET}$ and $V_{\rm RESET}$ are the switching voltages from HRS to LRS and back from LRS to HRS, respectively. The values of the current through the memristor in the LRS and HRS $I_{\rm ON}$ and $I_{\rm OFF}$, respectively were recorded at the read voltage $V_{\rm READ} = 2$ V and averaged over $N_{\rm READ} = 20$ samplings. The HF sinusoidal signal pulses generated by the built-in oscillator of NT-MDT ®SolverPro™AFM controller with amplitude $A = 0.2$ V, duration $T_{\rm m} = 0.1$ s, and frequency f varied from 100 Hz to 25 kHz were superimposed onto the tops of the triangle switching pulses. The measured values of $I_{\rm ON}$ and $I_{\rm OFF}$ were averaged over 100 write/erase switching cycles.

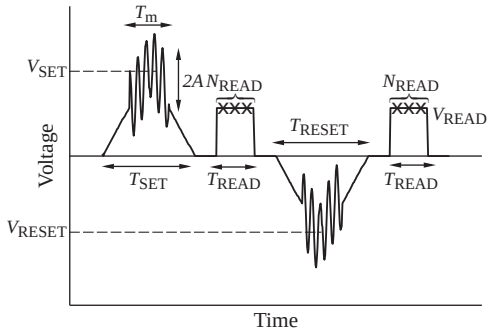

Fig. 2. Protocol ($V(t)$ waveform) for studying the effect of the HF signal on the RS parameters.

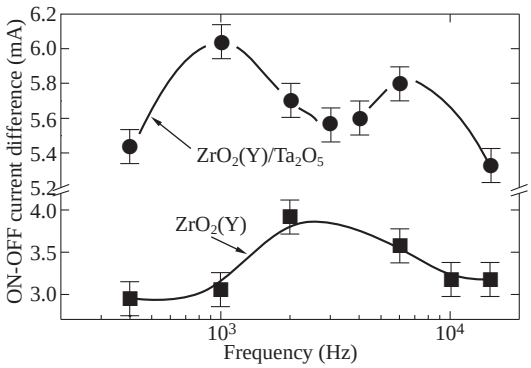

Fig. 3. Frequency dependencies of the difference $I_{ON} - I_{OFF}$ for the memristors based on the $ZrO_2(Y)$ film and on the $ZrO_2(Y)/Ta_2O_5$ stack.

2. Results and discussion

The frequency dependence of the difference $I_{ON} - I_{OFF}$ for the $ZrO_2(Y)$-based memristor (Fig. 3) manifested a maximum at $f \approx 2.5$ kHz that corresponds to the frequency of the O^{2-} ion jumps to the nearest neighboring V_Os in $ZrO_2(Y)$ at 300 K ranging from 0.4 to 8 kHz [14]. This observation confirmed the resonant activation of the O^{2-} ion migration to be the origin of the improvement of the RS performance when adding the HF signal to the switching pulses observed earlier [11,12].

The frequency dependence of the difference $I_{ON} - I_{OFF}$ for the memristor based on the $ZrO_2(Y)/Ta_2O_5$ bilayered stack (Fig. 3) manifested two maxima: one at higher frequency $f \approx 6.5$ kHz and another one at lower frequency $f \approx 400$ Hz. The maximum at higher frequency can be attributed to the resonant activation of the O^{2-} ion migration in the $ZrO_2(Y)$ layer whereas the low- frequency maximum can be ascribed to the resonant activation effect in the Ta_2O_5 sublayer. One can estimate the activation energy for the thermally activated jumps of the O^{2-} ions onto the adjacent V_Os in the Ta_2O_5 sublayer E_a from the corresponding maximum frequency f_i according to the formula

$$f_i \sim f_0 \exp\left(-\frac{E_a}{kT}\right), \qquad (1)$$

where $f_0 \sim 10^{13}$ Hz is typical lattice vibration frequency, k is Boltzmann constant, and T is the temperature. For $f_i = 1$ kHz one obtains $E_a \approx 0.6$ eV at $T = 300$ K. This value is approximately two times smaller than the activation energy of the oxygen diffusion in polycrystalline Ta_2O_5 at elevated temperatures (≈ 1.2 eV at $T > 700$ K) [16]. On the other hand, this value is ≈ 3 times greater than the one extracted from the $I - V$ curves for the Ta_2O_5 based memristors (≈ 0.2 V) [17]. This discrepancy can be attributed to the formation of the non-stoichiometric Ta-enriched nanoinclusions at the Ta_2O_5/TiN interface [10]. Also, one should take into account the possibility of the formation of other oxide phases (e.g. TaO, etc.) in the Ta_2O_5 sublayer.

It is worth noting that the estimate of E_a for $ZrO_2(Y)$ according to (1) gives $E_a \approx 0.57$ eV for $f_i = 2.5$ kHz and $E_a \approx 0.55$ eV for $f_i = 6.5$ kHz. These values coincide with the values of E_a for $ZrO_2(Y)$ extracted from the ion migration polarization measurements at moderate temperatures (0.53 to 0.55 eV within the range of $T = 300 - 500$ K) [13].

3. Conclusion

The results of present study confirm the resonant activation of the O^{2-} ion migration via the V_Os in the alternating electric field to be the origin of the beneficiary impact of adding the HF sinusoidal signal to the triangle switching voltage pulses on the performance and stability of the RS in the memristor based on the $ZrO_2(Y)$ films and on the $ZrO_2(Y)/Ta_2O_5$ stacks. These results manifest the fundamental properties of memristor as a stochastic multistable nonlinear system. From the practical point of view, the results of the present study indicate the prospects for the development of the innovative switching protocols applicable to the next-generation non-volatile memory devices to improve the performance and durability of these ones.

Acknowledgement

The present study was supported by Russian Foundation ror Basic Research (18-42-520059).

References

[1] D. Ielmini and R. Waser, *Resistive Switching: From Fundamentals of Nanoionic Redox Processes to Memristive Device Applications*, Wiley-VCH, 2016.
[2] D.B. Strukov *et al*, *Nature* **453**, 80 (2008).
[3] I. Riess, *Electroceram.* **39**, 61 (2017).
[4] J. Ouyang, *Emerging Resistive Switching Memories*, Springer, 2016.
[5] A. Huang *et al*, *in: Memristor and Memristive Neural Networks*, Intech, 2018. p. 249.
[6] W. Yi *et al*, *Nature Commun.* **7**, 11142 (2016).
[7] F. Alibart *et al*, *Nanotechnology* **23**, 075201 (2012).
[8] G.A. Patterson *et al*, *Appl. Phys. Lett.* **103**, 74102 (2013).
[9] W. Horsthemke and R. Lefever, *Noise-Induced Transitions: Theory and Applications in Physics, Chemistry, and Biology*, Springer, 1984.
[10] A. Mikhaylov *et al*, *Adv. Mater. Technol.* 1900607 (2019).
[11] D.O. Filatov *et al*, *Tech. Phys.* **89**, 1669 (2019).
[12] D.O. Filatov *et al*, *Phys. Solid State* **62**, 556 (2020).
[13] D.O. Filatov *et al*, *Adv. Cond. Mat. Phys.* 2028491 (2018).
[14] A.V. Yakimov *et al*, *Appl. Phys. Lett.* **114**, 253506 (2019).
[15] L. Gammaitoni *et al*, *Rev. Mod. Phys.*, **70**, 223 (1998).
[16] U.N. Gries *et al*, *Phys. Chem. Chem. Phys.* **20**, 992 (2018).
[17] J.-H. Hur, *Sci. Rep.* **9**, 17019 (2019).

28th Int. Symp. “Nanostructures: Physics and Technology”
Minsk, Belarus, September 2020

Graphite-based blade-type field emission cathodes

I.A. Kashko, V.V. Filippov, *V.A. Labunov* and Yu.M. Kukuts
Belarusian State University of Informatics and Radioelectronics, 220013 Minsk, Belarus

Abstract. In this work, the blade-type field emission cathodes (BFECs) of original construction have been developed and produced. As the basis of the cathodes the (110)-cut Silicon wafers were used. On the upper surface of Si substrate the parallel grooves of the 20 um width and 50 um depth of 1.7 mm in length were etched in a concentrated aqueous 44% KOH solution. As a result the parallel Si walls of the rectangular shape were created, which after imparting them a conic form were used as a pedestals for supporting of emitting graphite blades, obtained by the electron beam evaporation of graphite. The blades were sharpened to the thickness not exceeding 10 nm. It was shown that our BFECs can operate at field emission current up to 6 mA, depending on the sharpness of a blade.

Introduction

One of the new and rapidly developing areas in modern electronics is vacuum micro- and nanoelectronics. In connection with the rapid development of communication and information technologies electronics faces the task of creating active devices capable to operate at super-high frequencies. Unfortunately, the solution of these issues is difficult and in some cases nearly impossible because of a number of restricting physical effects in semiconductors. The development of field emission devices opens the prospects for the creation of devices that can be widely used in various fields of electronics. The key component of field emission vacuum devices is field-emission cathode (FECs).

The prospects of using allotropic forms of carbon [1] for these applications is due to their exclusive electrical, chemical, thermal and mechanical properties. Regardless of the field of FECs application, a number of requirements to their characteristics must be satisfied such as high emission efficiency, low threshold and operating voltages, high homogeneity, density and stability of electron emission, compatibility with the technology of microelectronics.

In previous our investigations [2-4] we studied application of carbon nanotubes (CNTs) for these purposes. Despite of the attractiveness of FECs based on CNTs the fabrication processes of controlled CNT arrays remain relatively complex and expensive. Furthermore, the problem of their fast degradation under operational conditions has not yet been solved. This drawback of the CNT-based technologies stimulates investigations of alternative forms of nanocarbon, such as nanodiamond, nanographitic, amorphous and composite films. This paper presents the results of development and investigation of FECs on the basis of graphite blades sharpened to nanographite - nanoscale blade-type FECs with a high-quality graphite structure.

Formation of Si pedestals and graphite blade.

The construction of the developed graphite-based blade-type field emission cathodes (BFEC) is presented in Fig.1.

As the basis of the cathodes, the (110) Silicon wafers were used. In general there might be produced multi blade BFECs. In this case on the upper surface of Si substrate the parallel grooves of the certain width (W) and depth (L) are formed by the anisotropic chemical etching of highly doped (110) Silicon (Fig.1a) in a concentrated aqueous 44% KOH solution heated to 73°C. As a result the strictly vertical Si walls of the grooves are obtained. The created rectangular shape Si islands separated by the grooves are considered as the pedestals for supporting of the e-emitting graphite blades. It has been established that in the multi blade structures, under creation of pedestals, etching rate of Si strongly depends on the ratio of the length L to the width W of the grooves. The optimum etching rate, with the pedestals height of 50 um or more, is achieved when L/W ratio is close to unit.

The initial etching profile on the Si wafer was created using the photoresist method. For photolithography, a special protective mask of high-temperature SiO_2 coated with a photoresist was formed on the Si wafer surface.

In the present work the one blade FEC is investigated, what gives possibilities to easier interpret the mechanism and peculiarities of the emission process of the BFECs. In this case from the multi pedestal Si substrate one pedestal section was cutting.

As the next step, by using additional isotropic etching method, the obtained silicon pedestal was sharpened. Under the realization of this process the conic shape is imparted to this pedestal (Fig.1b). The best etchant in this case was the aqueous solution of hydrofluoric and nitric acids with the addition of glacial acetic acidand ammonium fluoride. By changing the ratio of the components of the etching solution, a composition was found that provided the best etching mode from the point

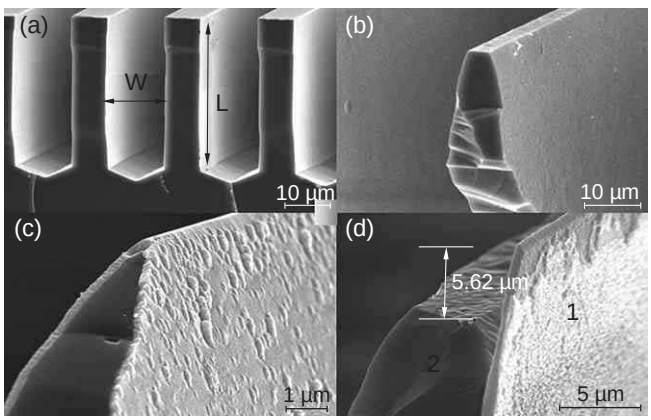

Fig. 1. (SEM) Graphite-based blade-type field emission cath-ode (BFEC): a) Si pedestals of multi blade FEC, b) Si pedestal of one blade FEC with imparted conic shape, c) conic shape Si pedestal covered by the layer of graphite, d) graphite blade (1) supported by Si pedestal (2).

of view of obtaining a theoretically grounded cathode profile that meets the requirements of the formed structure.

After, the layer of graphite is deposited on the surface of Si pedestal by the electron beam evaporation of bulk graphite (Fig.1c). The deposited films were subsequently subjected to high-temperature annealing in an inert atmosphere of (Ar, N_2, vacuum) at different temperatures up to 1000°C. With increasing temperature and annealing time, the solidity of graphite films increased and electrical properties improved. In particular, electrical conductivity increased by more than three orders of magnitude.

The most responsible operation in the production of efficient BFEC is creation the graphite blade on the basis of the obtained graphite film. A special technique was developed for this reason. Argon ion beam in vacuum chamber is used, which is directed at certain angle to the structure of Fig.1c creating the shadow effect. As a result of the etching process, the structure presented in Fig.1d consisting of Si pedestal (1) and graphite blade (2), was obtained. Because of the different rate of Si and graphite etching the graphite blade automatically juts out of the surface of Si pedestal. In the structure of Fig.1d, Si plays role not only a pedestal but as efficient heat sink.

The efficiency of the current emission of blade depends on its sharpness. A special operation of sharpening the blade was used by the ion beam etching. In our experiment we reached the smallest thickness of the blade-edge did not exceed 10 nm.

To achieve high emission currents, it is necessary to increase the thickness of the base of the graphite knife-edge, which in turn worsens the aspect ratio and increases the electric field strength at which the emission takes place. It was established experimentally that the optimum ratio of the height of the graphite proceed above the Si pedestal to its thickness is 20:1. During the operation of the cathode, the tip of the sharpened graphite proceed heats up rather strongly, but a graphite film about 500nm thick allows heat to be quite effectively removed from the emitting zone to the Si substrate. The knife-edge length of the obtained emission cathodes was 1.7 mm. In this case, an emission current of up to 5–6mA was achieved, depending on the thickness of the base of the knife edge. Current–voltage characteristics shown in Fig.2 were measured in sinusoidal signal mode at frequency of 50Hz for two different basis thickness graphite knife-edges. The thicker the base of the graphite knife-edges, the greater the current density they can work.

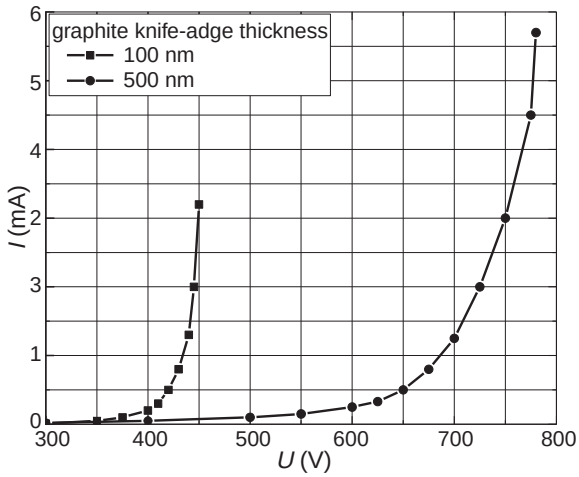

Fig. 2. Emission I–V characteristics of a graphite FECs blade-type with thickness of 100 and 500 nm; anode-cathode distance is 10 μm.

Thus, by means of isotropic and anisotropic etching heat-removing silicon pedestals are formed on which graphite blades are obtained. The undoubted advantage of a blade-type cathode based on a combination of nanographite structures and wedge-shaped silicon pedestals is the minimum dispersion of emitters in height and distance over a large surface area (technology on a silicon wafer is of 14 class of surface cleanliness and topological size of operations is up to 1 um). In addition, this technology enables the formation the required wedge-shaped profile along the height of the cathode, with high electrical and thermal conductivity, good mechanical, electrical and thermal contact with the substrate. According to their characteristics, the obtained field emission cathodes correspond to analogues fabricated by other methods on amorphous [1,5] or nano-crystalline graphite [6–8].

References

[1] N. Egorov, E. Sheshin, *Field Emission Electronics*. Springer Series in Advanced Microelectronics, vol 60. Springer, Cham. (2017).
[2] Z. Cheng *et al*, *World J. Res. and Rev.* **4**, 8 (2017).
[3] Z. Cheng *et al*, *IOP Conf. Ser.: Mater. Sci. Eng.* **475**, 012017 (2019).
[4] L. Sun *et al*, *IOP Conf. Ser.: Mater. Sci. Eng.* **475**, 012018 (2019).
[5] W.G. Xie, *et al*, *J. Appl. Phys.* **101**, 084315 (2007).
[6] Y. Neo *et al*, *Appl. Phys. Lett.* **88**, 073511 (2006).
[7] H.H. Busta *et al*, *Solid-State Electron.* **45**, 1039 (2001).
[8] V.A. Krivchenko *et al*, *J. Appl. Phys.* **107**, 014315 (2010).

28th Int. Symp. "Nanostructures: Physics and Technology"
Minsk, Belarus, September 2020

Photostability of fiber-optic photoacoustic transducer based on silver nanoparticle monolayer

A.P. Mikitchuk, K.V. Kozadaev
Belarussian State University, Minsk, 4, Nezavisimosti avenue, Republic of Belarus

Abstract. The work is devoted to the experimental study of the microstructural properties of nanostructures before and after of one hour optical irradiation within the photoacoustic transducer prototype. High photostability of nanostructure is shown, degradation of two-dimensional surface nanostructures has not been observed.

Introduction

There are a number of methods of non-destructive testing suitable for breakdown diagnostics of technical equipment [1,2], industrial machines and mechanisms, as well as eliminate defects in products manufactured [3,4]. One of the main approaches is the use of ultrasound signals as a diagnostic tool [4, 5]. Methods of ultrasound diagnostics are often used, when it is necessary to obtain high-resolution images in technical quality control [2], medical and biological testing [4]. But, such diagnostics is very complicated due to conventional bulky non-destructive testing ultrasound setups. Conventional piezoelectric electro-acoustic transducers are characterized by high supply voltages, large size and high weight, high electromagnetic interference susceptibility, relatively narrow operation bandwidth [5].

Photoacoustic transducer is very attractive alternative to electro-acoustic one. In photoacoustic transducers, absorber is heated and cooled, leading to mechanical deformations, which cause cycles of pressure, or, in the other words, acoustic waves in ambient surrounding [6,7]. However, the performance of such photoacoustic transducers is significantly limited by the bandwidth and large size. In order to minimize the thickness of the absorbing layer in ultrasound transducers, surface nanostructures based on monolayers of noble metal nanoparticles (NPs) can be used [8,9]. Typically, the noble NPs monolayer deposited on the optical fiber edge has intense maxima in the absorbtion spectrum. This maximum is associated with the localized surface plasmon resonance phenomenon [6]. The prototype of photoacoustic transducer has been created in order to confirm the theoretical investigations previously obtained by the authors [7,10]. To solve the main problem that arises when creating photoacoustic transducers, namely reducing the thickness of the absorbing layer, we used a nanostructure based on a monolayer of silver nanoparticles, which allows the reliable generation of ultrasound at frequencies of 10–18 MHz with a prototype of photoacoustic transducer [8,10].

The work is devoted to the experimental study of the microstructural properties of nanostructures before and after of one hour optical irradiation within the photoacoustic transducer prototype. High photostability of nanostructure is shown, degradation of two-dimensional surface nanostructures has not been observed. This allows such type of photoacoustic transducer to be used as part of a new generation of technical diagnostics systems.

1. Microstructural properties and photostability of nanostructures

The transducer prototype has been created to confirm the theoretical investigations previously obtained by the authors during the study the conditions of the most effective photoacoustic generation. In accordance with the previously developed theory, monolayer of silver nanoparticles with size gamma-distribution, the average diameter of 35 nm with RMS-size of 12 nm has been deposited on the surface of the optical fiber edge in order to provide the photoacoustic transducer frequency range exceeding 10 MHz [10]. Silver NPs monolayer has been deposited on the optical fiber edge using pulsed laser deposition method. The pulsed YAG:Nd^3 pulse-laser LOTIS-TII with a wavelength of 1064 nm and beam intensity of within the diameter of 1 mm has been used for experiments. Laser pulse has been focused on a silver 99.99% target (it was constantly moved to provide initial surface for ablation), which is mounted at angle of 45° with respect to the laser beam propagation. Preparation of the surface nanostructure for photoacoustic transducer prototype has been carried out at room temperature with the typical exposure time for of 2–3 min (approximately 600–900 laser 20 ns pulses). Fig. 1 shows the microphoto of photoacoustic transducer surface with monolayer of silver nanoparticles before measurement of acoustic signal (obtained with scanning electron microscope Hitachi S-4800). One can see that shape of NPs is approximately spherical. The analysis of binarized photos allows to conclude that NPs are characterized by gamma-distribution with average size of 35 nm, RMS size variation of 12 nm and surface occupation density of 3.8%.

Figure 2 shows the microphoto of photoacoustic transducer surface with monolayer of silver nanoparticles after the 1 hour measurement of acoustic signal. One can that there is no observable effect of 1 hour operation on the surface nanostructure microscopic parameters. Acoustic signal has been generated using optical 50 mW pulses with a period of 10 ms, a duration of 50 ns, fronts less than 12 ns. It is necessary to note that effective exposition of approximately 800 J/cm^2. During one hour irradiation, degradation of two-dimensional surface nanostructures has not been observed.

To study the photostability of the photoacoustic transducer prototype, a whole complex of long-term tests is required. In this paper, only initial experiments are conducted. It is seen that contamination and mechanical damage appeared on the surface outside the core of the optical fiber. However, no degradation of the power spectral density of the output ultrasonic signal is observed. It can be seen that the monolayer of nanoparticles deposited on the edge of the optical fiber has good adhesion —

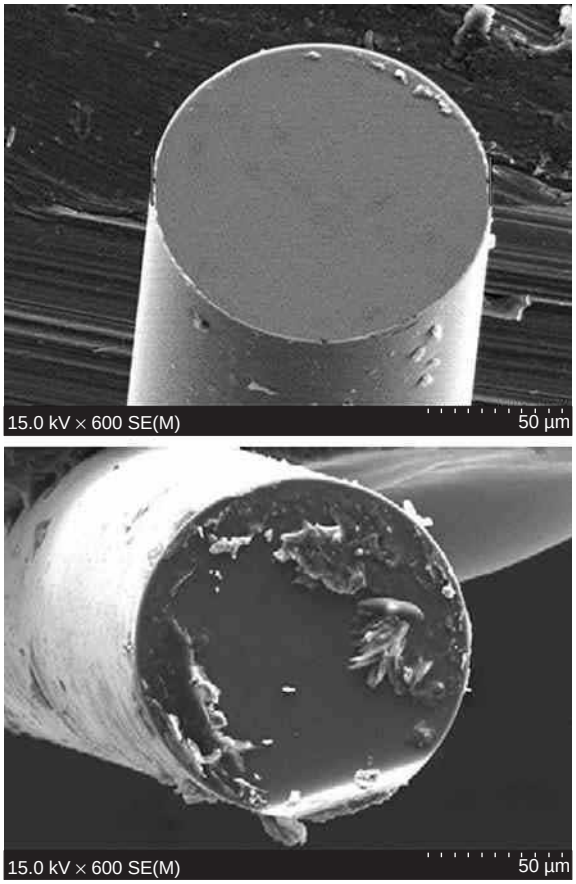

Fig. 1. Microphoto of photoacoustic transducer surface with monolayer of silver nanoparticles before measurement of acoustic signal (obtained with scanning electron microscope Hitachi S-4800).

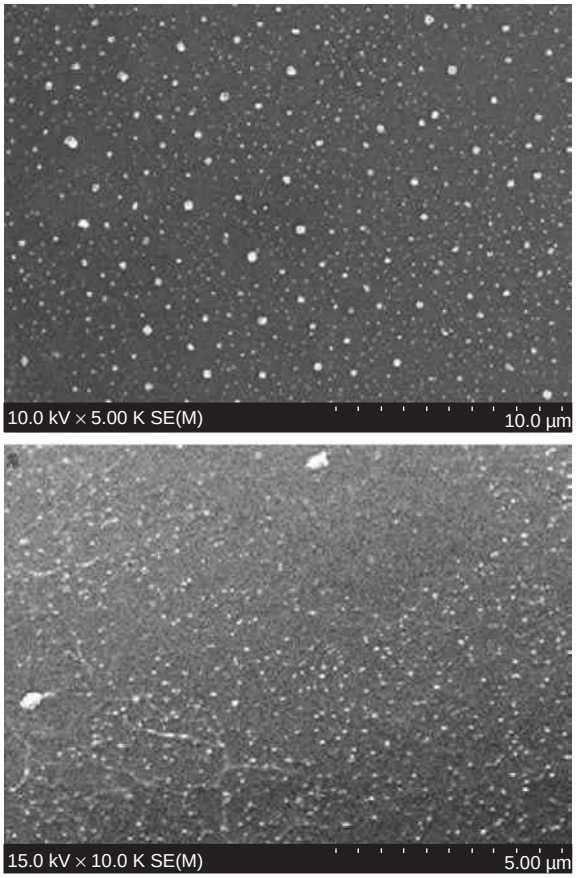

Fig. 2. Microphoto of photoacoustic transducer surface with monolayer of silver nanoparticles after measurement of acoustic signal (effective exposition of approximately 800 J/cm^2, obtained with scanning electron microscope Hitachi S-4800).

the size of the nanoparticles and the surface occupation density of the substrate do not change. Note, some samples have "grooves" associated with surface contamination. The presence of fine grain in microphotos is associated with the features of the study using scanning electron microscopy, when a technological layer of Pt was applied to the sample before the study.

2. Conclusion

In the paper, the photostability of the photoacoustic transducer prototype is studied. It is shown that effective exposition of approximately 800 J/cm^2 does not affect the nanostructure based on a monolayer of silver nanoparticles with size gamma-distribution, the average diameter of 35 nm with RMS-size of 12 nm, which is synthesized with atmospheric laser deposition.

The work is supported by grant "BRFFR-RFBR M-2019â" No. F19RM-006 "Study of 2D plasmonic nanostructures for photoacoustic transducers".

References

[1] R. Smith, A. Arca, X. Chen *et al*, *J. of Phys.: Conf. Ser.* **278**, 012035 (2011).
[2] Nan Wu, Ye Tian, Xiaotian Zou *et al*, *Proc. SPIE* **8694**, 86940 (2013).
[3] Tian Ye, Wu Nan, Zou Xiaontian *et al*, *J. Opt. Eng.* **52(6)**, 065005 (2013).
[4] Hou Yang, Kim Jin-Sung, Ashkenazi Shai *et al*, *Appl. Phys. Lett.* **91**, 073507 (2007).
[5] Zou Xiaotian, Wu Nan, Tian Ye *et al*, *J. Acoust. Soc. Am.* **137(1)**, 219 (2015).
[6] A.P. Mikitchuk, K.V. Kozadaev, *Semicond.* **52(14)**, 1839 (2018).
[7] A.P. Mikitchuk, K.V. Kozadaev, *Quantum Electronics.* **48(7)**, 630 (2018).
[8] A.P. Mikitchuk, K.V. Kozadaev, *Przeglad Elektrotechniczny.* **3**, 129 (2020).
[9] V.K. Goncharov, K.V. Kozadaev, A.P. Mikitchuk *et al*, *Semicond.* **53(14)**, 1950 (2019).
[10] A.P. Mikitchuk, K.V. Kozadaev, *J. of the Belarusian State University. Physics.* **1**, 4 (2020).

28th Int. Symp. “Nanostructures: Physics and Technology”
Minsk, Belarus, September 2020

Influence of hydrogen on the impedance of Pd/oxide/InP structures

V.A. Shutaev[1], E.A. Grebenshchikova[1], V.G. Sidorov[2], M.E. Kompan[1] and Yu.P. Yakovlev[1]

[1] Ioffe Institute, St Petersburg, Russia [2] IBSG Co., Ltd, St Petersburg, Russia

Abstract. The impedance, I–V and C–V properties of Pd/oxide/InP structures within the frequency range 10^{-1}–10^{5} Hz in air and in gaseous hydrogen–nitrogen mixture have been studied. The characteristics of the investigated structures are to be described by parallel RC circuit model with the connected serial resistance. In hydrogen medium the active resistance of the structures decreases by 3 orders of magnitude. The capacitance of the structures in hydrogen medium increases by 1–3 orders of magnitude depending on AC voltage frequency. In hydrogen medium the hysteresis has been found on CV-characteristics of the structures that is to be explained by ion polarization of the formed centers.

Introduction

Hydrogen is known to be an ecologically pure and high-efficiency energy carrier. Unlike hydrocarbon fuel, that pollute environment with harmful contaminants, the hydrogen combustion by-product is only harmless water. The efficiency of hydrogen fuel is twice higher than hydrocarbon one. Nevertheless, despite usefulness of hydrogen, its use for industry purposes is dangerous due to its high explosivity. That is why it is necessary to monitor hydrogen leakage during its storage and exploitation. For that reason, the hydrogen sensors are of great demand, nowadays.

To date, different scientific groups are investigate sensors based on the Pd/InP structures and electrical properties changing in that structures under hydrogen exposure [1–4]. Despite the numerous investigation and application of such devices it's still not clear what exact current conduction mechanism is revealed at the interface under hydrogen exposure. Currently the following mechanisms are considered: 1. Pd work function decreasing; 2. Ionization of hydrogen atoms to form a dipole layer at the Pd/InP interface; 3. Semiconductor surface states density changing.

Aim of this work is to study electrophysical properties of the Pd/oxide/InP structures in air and in hydrogen-nitrogen mixture in order to find out the mechanism of barrier height changing.

1. Experimental

Pd/oxide/InP Metal/Oxide/Semiconductor (MOS) structure is schematically shown in Fig. 1. The InP (100) $n \approx 10$ 16 served as substrate of the structure. An oxide layer was grown on substrate surface by the anodic oxidation method. Then, palladium layer was deposited with thermal vacuum evaporation method. Palladium was chosen due to its absorption ability to dissolve high volumes of hydrogen. The oxide layer was bounded on the perimeter with isolating layer (Si3N4) to decrease the current leakage over the surface.

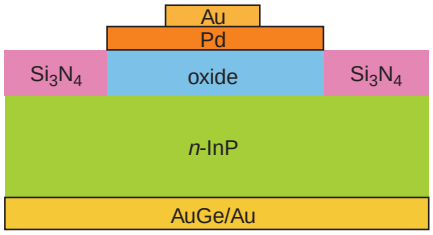

Fig. 1. Scheme of the structure Pd/Oxide/InP

2. Results and discussion

Recently, we've investigated the electrical properties of the Pd/Oxide/InP structures and Pd/InP Schottky diodes at a temperature range of 90–300‘K in air and in hydrogen-nitrogen mixture of 0.1–4 vol.% [5]. It has been shown that the barrier height changing depending on hydrogen concentration for both investigated structures is analogous to the Pd work function changing (Fig. 2).

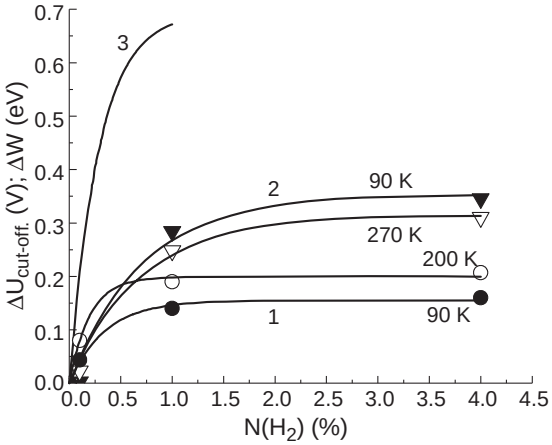

Fig. 2. The changing in ΔU cut-off for the I–V characteristic of the structures Pd/InP (1) and Pd/oxide/InP (2) and a change in the work function of palladium ΔW_{Pd} (3) [6] depending on the concentration of hydrogen in the gas medium

As one can see from the Fig. 2 there are a differences between the barrier heights changing curves of the structures and palladium work function changing curve under hydrogen exposure of different concentration. To find out if there was an additional charge at the interface influencing on barrier height changing of the Pd/oxide/InP structures or Pd/InP Schottky diodes the impedance of the structures has been investigated.

A Nyquist plot for the Pd/oxide/InP structure is presented in Fig. 3. It is well known that a semicircle with its center laying on the real axis of the imaginary-real curve corresponds to the parallel RC circuit [7]. A deviation in characteristics of the structure from the ideal RC circuit can be observed in Fig. 3. One can distinguish the center of semicircle arc laying below the real axis. This is due probably to the inhomogeneity of interfacial oxide layer. Also, it can be pointed out that the semicircle begins not from the zero point on the real axis. This corresponds to the presence of serial resistance of the interfacial layer. In air atmosphere this resistance has a value of 200 Ohm. The same value for the interfacial layer resistance has been

determined from I–V characteristics of Pd/oxide/InP structures in our previous work [5].

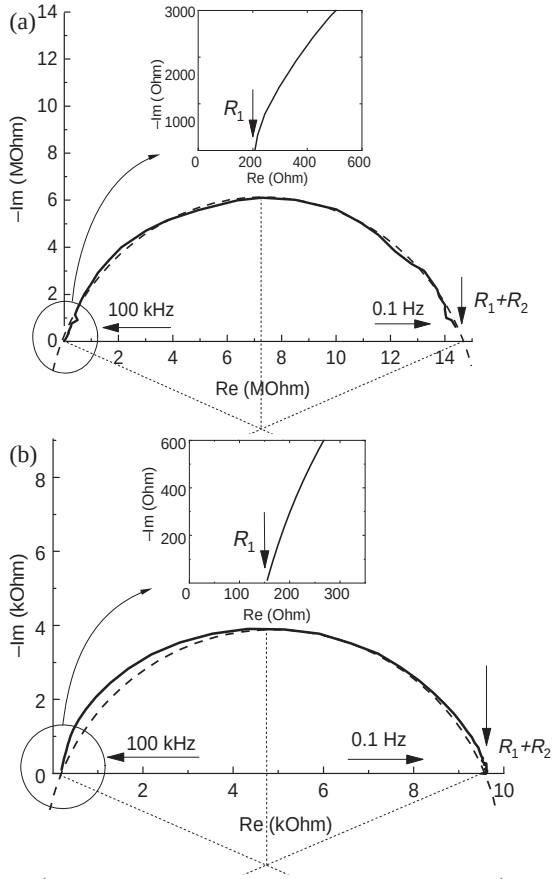

Fig. 3. The impedance of Pd/oxide/InP structure in air (a) and under hydrogen exposure of 4 vol.% (b)

In hydrogen-nitrogen medium the imaginary and real dependence on frequency also has the semicircle view but the active resistance is decreased by 3 orders of magnitude (Fig. 3b).

Thus, the equivalent scheme of Pd/oxide/InP structure is presented on Fig. 4, where R_1 is the serial resistance of the oxide layer, R_2 and C_2 are the resistance and capacitance of space charge in the InP, respectively.

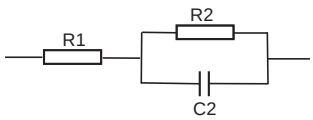

Fig. 4. The equivalent scheme of Pd/oxide/InP structure

The active resistance R_1 is constant and doesn't depend on frequency. In hydrogen medium R_1 insufficiently decreases from 200 to 170 Ohm. The reactive resistance of the Pd/oxide/InP structure is frequency dependent. The resistance of space charge in InP R_2 decreases by factor 3 of magnitude in hydrogen medium.

The capacitance of the Pd/oxide/InP structure in hydrogen atmosphere increases by 3–4 orders of magnitude (fig. 5). Such behavior cannot be explained by decreasing only barrier height.

For such a large changing in capacitance to occur an additional charge should be formed. This means that the increasing of capacitance of the Pd/oxide/InP structure is due to the bounded charge forming at Pd/oxide interface or in oxide layer. In hydrogen atmosphere the curves are shifted towards negative bias. This means that the increasing of capacitance of the structures is due to the presence of positive charges. In hydrogen atmosphere a hysteresis can be seen at the frequency of 33 Hz. This hysteresis decreases with increasing a frequency and disappearing at 30 kHz. The frequency range of the hysteresis existence corresponds to the ion polarization of the centers in a solid state.

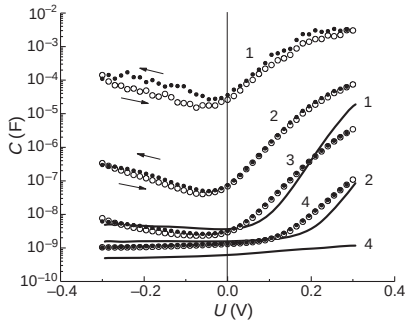

Fig. 5. C–V characteristics of the Pd/oxide/InP structure at a frequency: (1) 33 Hz, (2) 1 kHz, (3) kHz, (4) kHz; solid line — air medium, symbol — hydrogen 4% vol.

The quantity of charged particles can be derived from the C–V characteristics. On Fig. 6 the number of charged particles depending on frequency at different negative bias is presented.

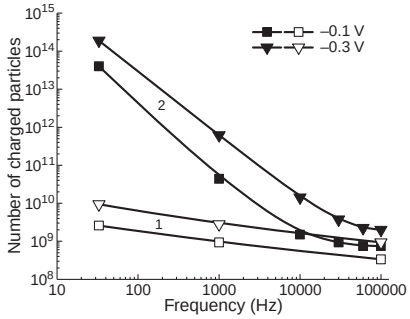

Fig. 6. Number of charged particles depending on frequency

From the plot on Fig. 6 one can see that at the frequency of 30 kHz the curves are saturated. This means that the charged particles stop their contribution in capacitance changing of the structures. At the same frequency the hysteresis disappears.

It is known that one Pd volume capable to dissolve 700–900 volumes of hydrogen [8]. The similar quantity of charges has been counted from the C–V characteristics. Thus, the suggesting that the additional charge in the structures Pd/oxide/InP is due to the presence of hydrogen in the structure is well approved.

References

[1] H.I. Chen, Y.I. Chou, and C.Y. Chu, *Sens. Actuators B*, **85**, 10 (2002).
[2] J. Grym, O. Procházková, R. Yatskiv, K. Piksová, *Nanoscale Research Letters*, **6** (392), 4 (2011).
[3] Kh.M. Salikhov, S.V. Slobodchikov, B.V. Russu. em SPIE, 3122, 494 (1997).
[4] K. Zdansky, *Nanoscale Research Letters*, **6** (490), (2011).
[5] V.A. Shutaev, V.G. Sidorov, E.A. Grebenshchikova, *et al*, *Semiconductors*, bf53 (10), 1389 (2019).
[6] N. Yamamoto, S. Tonomura, T. Matsuoka, H. Tsubomura, *J. Appl. Phys.*, **52** (10), 6227 (1981).
[7] E. Barsoukov, J. Ross Macdonald, *Impedance spectroscopy: theory, experiment, and applications*. (Hoboken, NJ : Wiley, 2018), p. 11.
[8] F.D. Manchester, A. San-Martin, J.M. Pitre, *J. of Phase Eguilibria*, **15**, 62 (1994).

28th Int. Symp. “Nanostructures: Physics and Technology”
Minsk, Belarus, September 2020

Optical spectroscopy of Schottky nanostructures Au/GaAs: plasmon resonances and anisotropy

V.L. Berkovits[1], V.A. Kosobukin[1], V.P. Ulin[1], F.Yu. Soldatenkov[1], P.A. Alekseev[1], V.S. Levitskii[2]

[1] Ioffe Institute, Politekhnicheskaya 26, 194021, St Petersburg, Russia
[2] R&D Center TFTE, Politekhnicheskaya 28, 194064, St Petersburg, Russia

Abstract. The Schottky nanostructures Au/GaAs(001) chemically prepared with atomic interlayer of nitride GaN are diagnosed and investigated by optical reflection anisotropy spectroscopy. Two types of Au nanoclusters located under and over GaAs surface are found with local plasmons detected at energies of 1.6 eV and 2.15 eV, respectively. The former plasmon possessing in-surface anisotropy is studied comprehensively.

Introduction

The Schottky junctions metal-semiconductor are known to be basic elements in various devices and nanostructures. As to Au/GaAs structures, getting those with abrupt defectless interfaces by the conventional annealing of deposited thin Au films remains an issue of challenge. It is because gold atoms diffuse into GaAs crystal and react chemically with GaAs at temperatures as low as 200 °C [1].

Recently it was found [2,3] that thermal stability of the Schottky diodes Au/GaAs is improved, and formation of on-surface Au nanoclusters becomes controllable when a monolayer of nitride GaN is prepared on GaAs surface prior the deposition of gold. In such Au/GaAs structures, annealed at 350 °C, Au clusters of two types appear which are, respectively, the oblate-shaped Au nanoislands located just on GaAs surface and the nanowires of Au buried into the crystal bulk [3].

This work is aimed at comprehensive investigating the local-plasmon spectra of on-surface Au nanocluster arrays in nitridized Au/GaAs structures with a special emphasis on understanding their anisotropy. The determined Au clusters are identified and monitored by their local plasmons during the annealing process .

1. Preparation and characterization of samples

The Au/GaAs structures are prepared on *n*-doped GaAs (001) substrates nitridized in low alkaline hydrazine-sulfide solution during 10 minutes [3]. A gold film of 10 nm thickness is thermally deposited onto the nitridized GaAs(001) surface in vacuum of 10^{-7} Torr, and the prepared Au/GaAs structure undergoes annealing at 300 °C. The annealing of as-deposited Au film at such the temperature activates the enlargement of its Au grains. Each annealing stage lasts 60 minutes, four stages being done.

The surface morphology of obtained Au/GaAs nanostructures is characterized by scanning probe microscope NtegrA AURA (NT-MDT). As the diagnostics shows, before annealing Au film consists of grains whose lateral sizes are 15–20 nm, the on-surface distribution of grains being uniform on the average. As well, the surface topography image, Fig. 1(a), measured after final annealing reveals an array of Au nanoclusters which are randomly distributed over the surface. The lateral sizes of Au clusters estimated from the Fig. 1(b) are in the range 35–50 nm, and their heights are about 1.5–2 nm.

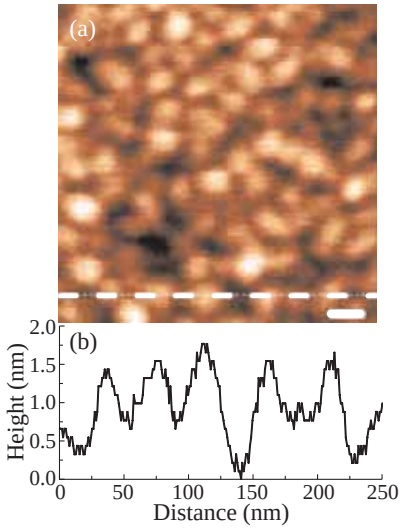

Fig. 1. (a) Atomic-force-microscopy image of (250×250) nm surface area of Au/GaAs(001) sample annealed at 300 °C during 4 hours, the bar scale is 25 nm. (b) The profile of the sample surface along the dashed line drawn in Fig. 1(a).

2. Detection of plasmons and surface anisotropy

In order to observe the plasmon resonances we use the optical reflection spectroscopy at room temperature. Reflectivity spectra are measured by spectrometer Cary 5000 at normal incidence of light with photon energies 1.5–5.5 eV.

The measured spectra of as-prepared Au/GaAs structures reveal the well-known peaks due to optical transitions E_1 and

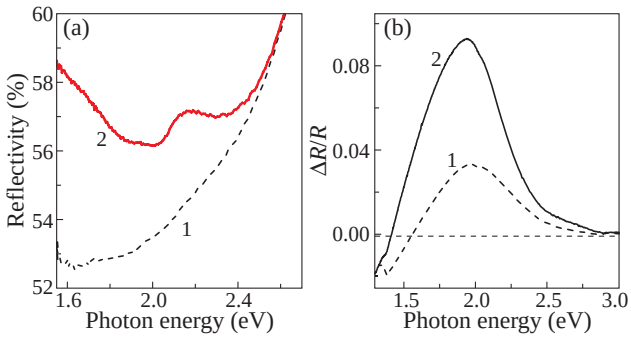

Fig. 2. (a) Reflectivity spectrum before (1) and after four-hour annealing of Au/GaAs(001) structure at 300 °C (2). (b) Reflectance anisotropy spectra after annealing of Au/GaAs structure for two (1) and four (2) hours.

$E_1 + \Delta_1$ (2.9–3.2 eV) and to $E_0^{'}$ (4.9 eV) in GaAs crystal. Besides, the reflectivity increases significantly at photon energies below 2.5 eV because of the plasma effect caused by Au electrons. Since both cubic GaAs crystal and structureless Au film are optically isotropic, the measured reflectivity spectra are insensitive to the polarization of light.

Postheating of Au/GaAs structures changes their spectra drastically in the range below 2.5 eV. As is seen from Fig. 2(a), the initial spectrum 1 transforms into spectrum 2 with a resonant feature that appears near 2.2 eV. This fact agrees with our earlier observation of a spectral peak at 2.15 eV assigned to localized plasmons of Au nanoclusters formed on GaAs surface [3].

To argue for the plasmon anisotropy, we use the reflectance anisotropy (RA) spectroscopy [3,4] dealing with the spectral dependence of the anisotropy signal

$$\frac{\Delta R}{R} = 2\,\frac{R_\alpha - R_\beta}{R_\alpha + R_\beta}, \qquad (1)$$

Here, R_α and R_β stand for the normal-incidence reflectivities of light waves polarized linearly along the orthogonal axes α and β, taken usually along [110] and $[1\bar{1}0]$ directions on the (001) surface for a cubic crystal. Since the anisotropy signal (1) from the bulk of cubic crystal is zero, no bulk contribution appears in its RA spectrum, and, therefore, the signal (1) is originated completely from the anisotropy of the surface Au/GaAs structure.

Experimental plasmonic RA spectra are shown in Fig. 2(b). Before annealing the structure, the anisotropy signal $\Delta R/R$ measured in the spectral region below 2.5 eV is nearly zero. Annealing of the structure gives rise to appearance of a peculiar RA spectral feature, whose magnitude increases with annealing duration. To illustrate, after two-hour annealing the broad peak *1* near 2 eV, Fig. 2(b), is observed. After four-hour annealing the magnitude of increases additionally (peak *2*), which fact is a sign of further increase of Au nanocluster anisotropy. It is worth noting that the scale of the plasmonic spectral feature ($\Delta R/R \approx 0.08$) is larger by an order of magnitude than that of features measured usually from reconstructed GaAs(001) surfaces. The plasmon anisotropy proved above by RA spectroscopy is related with the anisotropy of nanocluster arrays in the directions [110] and $[1\bar{1}0]$ of GaAs crystal[3]. Physically, the latter fact could point to the related anisotropy of gold adatoms diffusion over the nitridized GaAs(001) surface providing recrystallization of Au film.

3. Theoretical interpretation

The above experimental data (Fig. 2) are explained following the theory [4]. Considered is a model of the three-layer "air/Au film/GaAs" with on-film monolayer of Au nanoclusters in air. The total reflectivity for a normally incident wave with the in-surface α-polarization is

$$R_\alpha = \left| r^{(0)} + \Delta r_\alpha \right|^2, \qquad (2)$$

where $r^{(0)}$ corresponds to the cluster-free case. The resonant contribution $\Delta r_\alpha \neq \Delta r_\beta$ due to the plasmons of Au clusters imply the presence of anisotropy to provide $\Delta R/R \neq 0$ in Eq. (1). The optical anisotropy is introduced through the polarizability of model Au nanoellipsoids which are prolate in the surface plane and become the disks in the isotropic case [3,4].

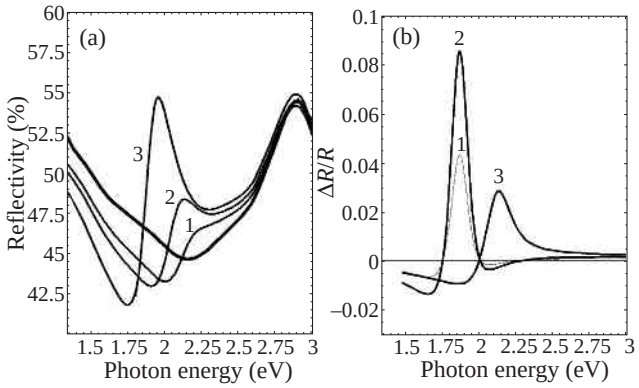

Fig. 3. (a) Reflectivity spectra R_α calculated for structures "air/Au film/GaAs" with Au disks whose height-to-diameter ratios η are 0.2 (1), 0.15 (2) and 0.1 (3), thick line shows the reflectivity of a reference three-layer with a residual Au film and without Au clusters. (b) The related reflectance anisotropy spectra $\Delta R/R$ for $\eta = 0.1$ (1,2) and 0.2 (3).

Figure 3 presents the spectra simulated in connection with the experimental data of Fig. 2. In Fig. 3(a), the reflectivity spectra R_α of Au spheroids (disks) reveal a feature which depends essentially on the height-to-diameter ratio $\eta = c/a$ of the disks. The feature is weak at $\eta \leq 1$ (nearly spheres) and becomes well-pronounced at $\eta = 0.1 - 0.3$ (very oblate spheroids). When the in-plane circular disks are deformed into ellipsoids with the in-plane semi-axes $a \neq b$, the in-plane optical anisotropy $\Delta r_\alpha \neq \Delta r_\beta$ occurs to result in non-zero RA spectra $\Delta R/R$, Fig. 3(b), obtained from Eqs. (1,2). The identical spectra presented in Figs. 2 and 3, are concluded to verify a general agreement between experiment and theory. Since the theoretical spectra in Fig. 3(b) are apparently narrower than their experimental counterparts in Fig. 2(b), the latter spectra $\Delta R/R$ are supposed to be inhomogeneously broadened due to a statistical distribution of Au clusters over η.

4. Summary

It has been found that at temperatures about 300 °C annealing of a thin Au film deposited on GaAs(001) substrate with GaN/GaAs interlayer leads to formation of surface array of Au nanoclusters. The clusters of Au possess local plasmons which are observed in optical reflectivity spectra below 2.5 eV. In turn, the above-reported observation of reflectance anisotropy spectra of Au/GaAs structures with a broad plasmonic feature near 2 eV is unambiguous evidence of anisotropy of both local plasmons and the shapes of Au nanoclusters supporting them.

Acknowledgement

The study was supported by RFBR grant 20-02-00257.

References

[1] R.M. Charatan, R. S. Williams, *J. Appl. Phys.* **72**, 5226 (1992).
[2] V.L. Berkovits, T.V. L'vova, V.P. Ulin, *Semiconductors* **45**, 1575 (2011).
[3] V.L. Berkovits, V.A. Kosobukin, V.P. Ulin, *et al*, *Appl. Surf. Sci.* **507**, 144982 (2020).
[4] V.A. Kosobukin, Phys. Solid State **54**, 2471 (2012).

28th Int. Symp. "Nanostructures: Physics and Technology"
Minsk, Belarus, September 2020

Plasmonic field enhancement by metallic sub-wavelength gratings on Silicon in the near-infrared range

A.A. Bloshkin[1,2], A.I. Yakimov[1] and A.V.Dvurechenskii[1,2]

[1] A.V. Rzhanov Institute of Semiconductor Physics, Siberian Branch of the Russian Academy of Science, 630090 Novosibirsk, Russia
[2] Novosibirsk State University, 630090 Novosibirsk, Russia

Abstract. We perform numerical simulations of electric field spatial distribution in plasmonic nanostructures on Si substrate in near-infrared range. Two-dimensional square arrays of circular holes of various diameters in a gold film serve as metasurfaces allowing the conversion of the external electromagnetic radiation into surface plasmon modes at the Au–Si interface. The plasmonic field enhancement, as a function of the diameter of holes of the array, shows the maximum at which the Bloch plasmon polaritons propagating along the Au–Si interface are transformed to localized surface plasmon modes. Two types of localized plasmons are detected. The short-wavelength plasmon is excited along the array diagonals and exists at any angles of incidence of light on the structure. The long-wavelength plasmon occurs only at nonzero angles of incidence and is located along orthogonal directions parallel to the sides of the square array. These results are directly related to the problem of fabricating effective silicon photodetectors with quantum dots.

Introduction

Detection in near infrared (NIR) wavelength range has become a very stringent technology requirement for development of efficient methods for transmitting information in television and telephone networks, the Internet, and optical computers. In a market largely dominated by III-V semiconductor compounds, Si compatible heterostructures have the advantage of low cost and inerrability by using the mature Si technology. Silicon has a high absorption in the range of ultraviolet and near infrared, but from a wavelength of 1.1 μm Si becomes transparent. In recent years, several optoelectronic components have been integrated on silicon platform, opening perspectives in silicon fotonics [1]. Among them, self-assembled Ge quantum dots epitaxially grown on Si are of particular interest as they are fully compatible with Si-CMOS and can be applied for 1.3–1.55 μm optical communication applications. Despite the recent progress in fabrication of NIR Ge/Si quantum dot (QD) photodetectors (QDPs), their quantum efficiency still remains a major challenge and different approaches to improve the QD photoresponse are under investigation.

Surface plasmon polaritons (SPPs) have demonstrated their capability in imroving the light detection in the mid-IR spectral range due to their light confinement in subwavelength scale. Several groups have reported multiple photocurrent enhancement of mid-IR InAs/(In)GaAs [2] and Ge/Si [3] QDPs using SPP wave coupling structures and demonstrated that the plasmonic enhancement scheme represents an efficient route to achieve the high responsivity in compact photodetectors with the optically thin active regions. Metallic films perforated with two-dimensional subwavelength hole arrays (2DHAs) on detector top were used to convert the incident electromagnetic IR radiation into the surface plasmons. The plasmonic enhancement of optical near-field components within an absorption layer was originally proposed to explain the photocurrent enhancement.

In this paper we perform simulations to examine the behavior of the near-field enhancement properties in the NIR spectral range of a structure which consists of 2DHAs in a gold film deposited on a Si substrate. Array periodicity was adjusted to excite the surface plasmon modes at the telecom wavelengths (between 1.3 and 1.55 μm). The calculations were made in a wide range of hole diameters and allow us to develop a more complete understanding of how the actual electric fields near the plasmon surfaces change with varying the parameters of plasmonic grating. Among the issues we address are the roles of propogating and localized plasmon modes.

1. Computational details

We considered a 50 nm thick gold film on a Si crystal. The film is perforated with an infinite, square array of circular holes of diameter d and periodicity a. The array pitch size was chosen to be $a = 300$, 350, and 400 nm and the hole diameter was varied from $d = 50$ nm to 350 nm depending on a. The near-field components distribution were calculated with the 3D finite-element frequency-domain method based commercial software Comsol Multiphysics by numerically solving the Maxwell equations. Floquet periodic boundary conditions were used along the planar x and y-directions to simulate an infinite array of unit cells. Perfectly matched layers were used along the vertical direction (z-direction) to prevent the reflection of the waves from the top and bottom domain boundaries. The plane wave radiation with a linear or circular polarization is incident from the substrate side of the QDP at various angles of incidence θ. The air and Si regions are modeled using rectangular parallelepiped geometry with correspondent refractive indices. We used frequency-dependent dielectric function of the gold from the study by Rakić *et al* [4], and refractive index of Si was taken to be 3.39.

2. Results

Figure 1(a) presents the near-field intensity (NFI) enhancement spectra for the 2DHA-Si structures with the hole diameter $d = 150$ nm and different lattice periods a. The spectra consist of a smoothly varying background superimposed on a set of peaks in the NIR region whose spectral positions shifts towards longer wavelengths as the 2DHA periodicity a is increased. The most pronounced peaks at 1.23 μm, 1.38 μm, 1.53 μm arise due to excitation of a zero-order surface plasmon resonance on

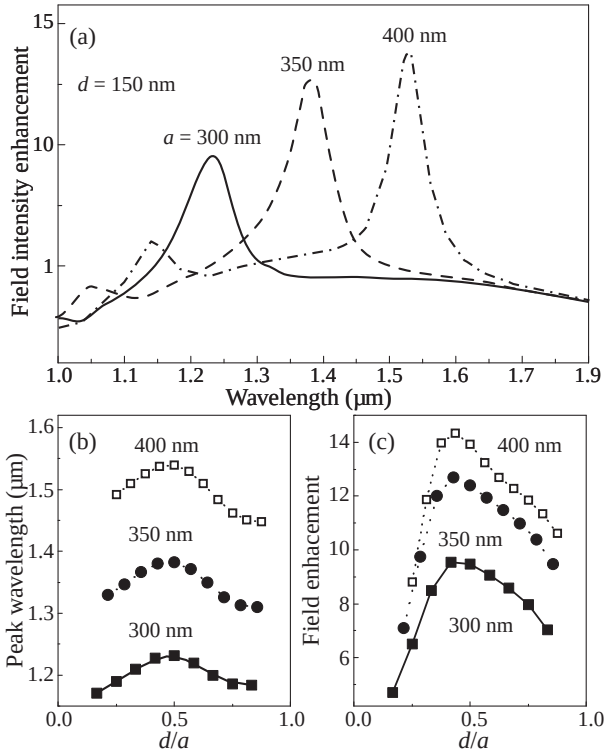

Fig. 1. (a) Near-field intensity enhancement spectra for 2DHA with the hole diameter $d = 150$ nm and various array periods $a = 300$, 350 and 400 nm at normal incident radiation with a circular polarization. The wavelength of the dominant field enhancement peaks (b) and the maximum value of the field intensity enhancement factor (c) as a function of the hole diameter for $a = 300$, 350 and 400 nm. In panels (b) and (c) the x-axis indicates the ratio between the hole diameter and the array period.

the Au/Si interface. The higher order plasmon modes with a smaller amplitude are also seen at shorter wavelengths. The magnitude and spectral positions of the field maxima depend strongly on the array parameters (figures 1(b) and (c)). For small holes, the enhancement increases with a hole diameter and its spectral position shifts towards the longer wavelength. The resonance redshift is usually attributed to the interference of the SPPs Bragg scattered by the holes in an array. The maximum peak wavelength and field intensity enhancement are reached at $d/a = 0.5$. An over 14 times field enhancement is obtained at $\lambda = 1.54\,\mu$m for $a = 400$ nm and $d = 200$ nm. For larger holes ($d/a > 0.5$),the mechanism of the NFI enhancement changes and both the field magnitude and the resonance peak position are found to decrease with increasing hole size. This behavior is associated with the localization of plasmon modes.

In order to clarify the character of plasmon excitations at various hole sizes, we analyzed the dispersion characteristics of surface plasmon modes. The procedure for such an analysis involves plotting the dependences of the plasmon energy $E = hc/\lambda_{SP}$ on the wave vector component of the incident wave in the array plane $k_x = k_0 \sin\theta$ where $k_0 = 2\pi/\lambda$, θ is angle of incidence of light on the sample plane. The wavelength of plasmon resonance λ_{SP} was the peak position of the near-field enhancement factor. In this work, we consider only the TM polarization. Figure 2 shows the dependence of the plasmon energy on the wave vector k_x for $a = 300$ nm and $d = 75$

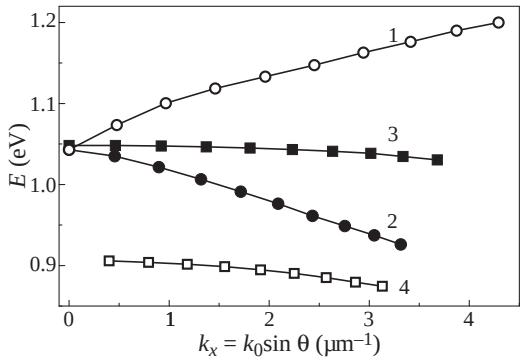

Fig. 2. Energy of plasmon excitations in the region of fundamental surface plasmon resonance versus the photon wave vector component in the array plane for a = 350 nm and d = (lines 1 and 2) 75 and (lines 3 and 4) 250 nm

and 250 nm. Two plasmon branches arrize in TM polarization in all samples at $k_x \neq 0$. In the case of small diameter holes ($d = 75$ nm), a typical dispersion behavior is observed corresponding to the excitation of Bloch plasmon polaritons with wave vectors $k_{SP} = 2\pi/a + k_x$ (line 1) and $k_{SP} = 2\pi/a - k_x$ (line 2) propagating in opposite direction. Similar dispersion characteristics were observed for all samples with $d \leq a/2$. At $d > a/2$ the dispersion curves are flattened and two dispersion modes appear for the largest hole, and long-wavelength mode exist only when $k_x \neq 0$ (line 4). The absence of dependence or a weak dependence of the SP energy on the wave vector of the radiation incident on the array is characteristic of the localized plasmon excitation. Typically, localized SPs are formed by isolated subwavelength metal nanoparticles. At the decrease in the size of such particles, plasmon resonance is blueshifted. Apparently, in our case, an array of almost isolated metal islands is formed by Au regions between large-diameter holes.

Acknowledgement

The work was funded by Russian Scientific Foundation (grant 19-12-00070)

References

[1] F. Priolo, T. Gregorkiewicz *et al*, *Nat. Photonics* **9**, 19 (2014).
[2] J. Vaillancourt, N. Mojaverian *et al*, *IEEE Photon. Technol. Lett.* **26**, 745 (2014).
[3] J. Vaillancourt, N. Mojaverian *et al*, *IEEE Photon. Technol. Lett.* **26**, 745 (2014).
[4] A.D. Rakić, A.B. Djurišić *et al*, *Appl. Opt.* **37** (22), 5271 (1998).

28th Int. Symp. “Nanostructures: Physics and Technology”
Minsk, Belarus, September 2020

Prospects for the use of structures with the Tamm plasmon in optoacoustic transducers

E.I. Girshova[1,2], A.P. Mikitchuk[3], K.A. Ivanov[1,2], K.M. Morozov[1,2], A.V. Belonovskii[1,2]

[1] ITMO University, St Petersburg, Russia
[2] St Petersburg Academic University, St Petersburg, Russia
[3] Department of Radiophysics and Computer Technology, Belorusian State University, Belarus

Abstract. Ultrasound technology is widely used in biology objects and construction materials diagnostic, in therapy of some deseases, in novel technology processes. In order to increase photoacoustic converters field of application, it is necessary to ensure the emitted wave front parameters according to given values and to minimize the device. This is to be achieved by using surface plasmonic nanostructures as an active medium of photoacoustic converter. We proposed a design of plasmonic structure with light wave electric field profile localized in small areas of space, thus increasing material deformation, ultrasound generation efficiency and contributing to wave front homogeneity.

Introduction

The increase in the intensity of research in the field of ultrasonic generation is due to a wide range of possible applications of broadband ultrasonic signal generators in biology, medicine and non-destructive testing of part defects. Currently, the most common source of ultrasound is piezoelectric electro-acoustic transducers. Such converters require a large supply voltage; they have large dimensions and weight. High sensitivity to electromagnetic interference and narrow band of operating frequencies limits the scope of their application [1]. An alternative to electroacoustic transducers can be photoacoustic transducers in which the absorption of modulated optical radiation causes deformation cycles of the photoacoustic material that generate acoustic waves [2–3]. The possibility of creating converters based on nanoparticles has been experimentally demonstrated [4]. The use of structures based on Tamm plasmon would ensure the absorption of modulated optical radiation in a specific given region [5]. It has been shown theoretically and experimentally that structures based on Tamm plasmons can be used both for controlled absorption enhancement in a given region of a nanostructure and for its suppression, and, therefore, potentially such structures are applicable for photoacoustic converters [6,7].

1. Structure design

A device capable of converting an optical signal into an ultrasonic one consists of a laser emitting a modulated signal and an irradiated plasmon structure [Fig. 1(a)]. The parameters of the plasmon structure must be selected so that absorption occurs at a given wavelength.

Absorption entails heating and deformation, and cyclic deformation gives rise to ultrasound. For the implementation of effective (from the point of view of the high power of optical radiation absorbed in the nanostructure) photoacoustic conversion, several conditions must simultaneously be met [8]:

1. The availability of the laser generating modulated optical radiation in the required wavelength range.
2. A sufficiently wide SPR peak (width of more than 25 nm at a level of 0.9) to provide the possibility of multiplexing the radiation of various lasers at wavelengths.
3. High absorption coefficient at the peak of SPR (50% or more).

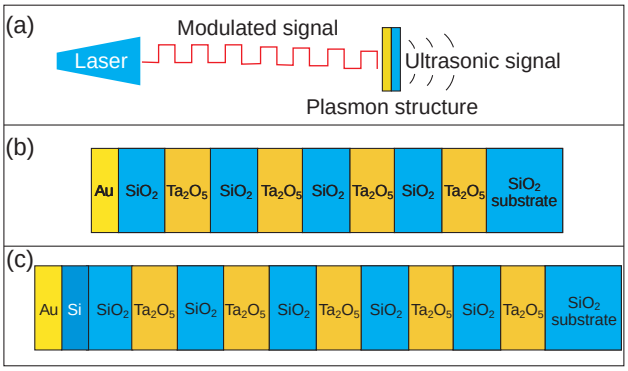

Fig. 1. Schematic diagram of a plasmonic photoacoustic transducer (a). The most promising structures: (b) the thickness of the metal layer is 31 nanometers, the ones for silicon oxide and tantalum oxide are 76.53 and 52.08 nanometers respectively, (c) the thickness of the metal layer is 28 nanometers, the thickness of the silicon layer is 8 nm, the ones for silicon oxide and tantalum oxide are 76.53 and 52.08 nanometers respectively.

We managed to choose the materials and thicknesses of the metal and Bragg reflector layers in structures with a Tamm plasmon, so that their absorption spectrums (theoretically calculated by transfer matrix method) satisfy all these requirements. The two suitable structures are shown in figure 1(b,c). They both consist of one layer of gold and five pairs of alternating layers of silicon oxide and tantalum oxide on a silicon oxide substrate, but the second one has one silicon extra-layer between metal and Bragg reflector. The thickness of the metal layer is 31 nanometers; the ones for silicon oxide and tantalum oxide are 76.53 and 52.08 nanometers respectively. The obtained absorption pattern for the indicated structure shows that it completely satisfies all the criteria presented [Fig. 2]:

1. There are simultaneously affordable and sufficiently powerful lasers with such a wavelength (for example LDI-450-FP-30).
2. Width at a level of 0.9 is 65 nm (from 423 to 488 nm) for the first structure and 25 nm (489–514 nm) for the second one.
3. Absorption coefficient at the peak of SPR equals 84% and 86% respectively.

It can be seen that the absorption spectra of both structures satisfy all three basic conditions for the implementation

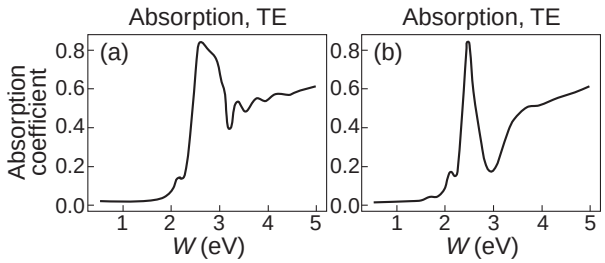

Fig. 2. Frequency dependence of the absorption coefficient for a structure without a silicon layer between the metal and the Bragg reflector (a) and with silicon layer.

of an effective optoacoustic conversion. However, there are significant differences between them. For a structure with an additional silicon layer between the metal and the Bragg reflector, the absolute value of the absorption coefficient is higher, but for the second structure, the absorption peak is much wider. A wider absorption peak provides a wider range of operating frequencies, which makes a structure without a silicon layer more promising for industrial applications.

To conclude, developed structures exhibit peaks in absorption spectra, high and wide enough for effective photoacoustic conversion. Thus, these structures with the Tamm plasmon can be used as the basis for a new-design photoacoustic transducer. The use of such structures can be a breakthrough in photoacoustics, since the parameters of structure with the Tamm plasmon can be selected in a special way in order to influence the distribution of the electric field of the mode and its overlap with the metal layer.

Acknowledgement

The reported study was funded by RFBR according to the research project No. 19-52-04005.

References

[1] E. Biagi *et al*, *Acoustical Imaging* **29**, 273–284(2008).
[2] A. Prost *et al*, *Phys. Rev. B.* **92**, (2015).
[3] G.A. Pang *et al*, *J. Phys. Chem. C.*,**120**, (2015).
[4] S.-L. Chen *et al*, *Appl. Sci.* **7**, 25 (2017).
[5] M.A. Kaliteevski *et al*, *Phys.Rev. B* **76**,(2007).
[6] M.A. Kaliteevski *et al*, *Plasmonics.* **10**, 281–284 (2015).
[7] R. Bruckner *et al*, *Nature Photonics.* **6**, 322–326(2012).
[8] A.P. Mikitchuk *et al*, *Quantum Electronics.* **48**, 630–636 (2018).

28th Int. Symp. “Nanostructures: Physics and Technology”
Minsk, Belarus, September 2020

Control of the surface plasmon dispersion and Purcell effect at the metamaterial-dielectric interface

K.A. Ivanov[1], K.M. Morozov[1,2], G. Pozina[3], E.I. Girshova[1,2], and M.A. Kaliteevski[1,2,4]

[1] ITMO University, 197101 St Petersburg, Russia
[2] Aferov University, 194021 St Petersburg, Russia
[3] Department of Physics, Chemistry and Biology (IFM), Linköping University, SE-58183 Linköping, Sweden
[4] Ioffe Institute, Politekhnicheskaya 26, 194021, St Petersburg, Russia

Abstract. The use of layered metal-dielectric metamaterial for control of the Purcell effect is investigated. The dispersion of the surface plasmon and the position of the peak in the local density of states are studied for various configurations of the periodic structure. The calculated frequency dependence of the Purcell factor demonstrates an increase in peak value compared to the conventional plasmonic structure.

Introduction

One-dimensional plasmonic structures are important for sensing applications, for surface-enhanced Raman scattering imaging [1] and for devices where light emission needs to be amplified. Previously, it was assumed that an enormous enhancement of light emission (giant Purcell factor) occurs at frequencies near the peak of plasmonic density of states [2]. However, in reality, this effect is largely cancelled by a high absorption in metal at the same frequency [3,4].

Different structures have been proposed that are described by the so-called effective plasma frequency [5], such as metallic wire structures and other 2D and 3D-metamaterials; this materials, however, are hard to fabricate and control. One-dimensional metal-dielectric structures, however, are easy to manufacture, and surface plasmon dispersion in them can be controlled to shift the peak of the plasmonic local density of states (LDOS) to the region where metal‘s absorption is weaker, as was shown previously [6].

1. Plasmon dispersion

The proposed metamaterial is a one-dimensional structure consisting of alternating layers of metal and dielectric parallel to the xy plane (see Fig. 1(a)). The dielectric functions are labeled by ε_{Me} and ε_D, and the corresponding layer thicknesses by a and b, respectively. It is known that in the long-wavelength limit, which is satisfied for the low-frequency range, such a structure can be considered as a uniform anisotropic medium with a dielectric tensor:

$$\begin{pmatrix} \varepsilon_x & 0 & 0 \\ 0 & \varepsilon_x & 0 \\ 0 & 0 & \varepsilon_z \end{pmatrix}. \tag{1}$$

The two different non-zero components are defined as

$$\varepsilon_x = \alpha\varepsilon_{\text{Me}} + (1-\alpha)\varepsilon_D, \quad \varepsilon_z^{-1} = \alpha\varepsilon_{\text{Me}}^{-1} + (1-\alpha)\varepsilon_D^{-1}, \tag{2}$$

where $\alpha = \frac{a}{a+b}$ is the filling factor of metal in the metamaterial.

If this metamaterial is stacked with a cladding whose dielectric constant equals to ε_1 (see Fig. 1), a surface plasmon state will appear. The dispersion relation for it has two branches corresponding to the ordinary and the extraordinary waves (Fig. 2):

$$k_{x(\text{ord})} = \frac{\omega}{c}\sqrt{\frac{\varepsilon_1\varepsilon_x}{\varepsilon_1+\varepsilon_x}}, \tag{3}$$

$$k_{x(\text{ext})} = \frac{\omega}{c}\sqrt{\frac{\varepsilon_1^2\varepsilon_z - \varepsilon_1\varepsilon_x\varepsilon_z}{\varepsilon_1^2 - \varepsilon_x\varepsilon_z}} \tag{4}$$

Using a metamaterial can shift the LDOS peak to the low-frequency range. In this range the metal dielectric constant can be modelled by the Drude theory: $\varepsilon_{\text{Me}}(\omega) = \varepsilon_0 - \frac{\omega_p^2}{\omega(\omega+i\gamma)}$. A straightforward derivation from the dispersion relation gives for the peak frequencies (that is, the frequencies of maximal k_x)

$$\omega_{\text{peak}}^{(\text{ord})} = \frac{\omega_p}{\sqrt{\varepsilon_0+\varepsilon_1+\frac{1-\alpha}{\alpha}(\varepsilon_D+\varepsilon_1)}}, \tag{5}$$

$$\omega_{\text{peak}}^{(\text{ext})} = \frac{\omega_p}{\sqrt{\varepsilon_0+\xi\pm\sqrt{\varepsilon_1^2+xi^2}}}, \tag{6}$$

where

$$\xi = \frac{(1-\alpha)(\varepsilon_D^2-\varepsilon_1^2)}{2\alpha\varepsilon_D}. \tag{7}$$

For an ordinary-wave plasmon decreasing α leads to a decrease in the peak frequency; for an extraordinary one it is necessary

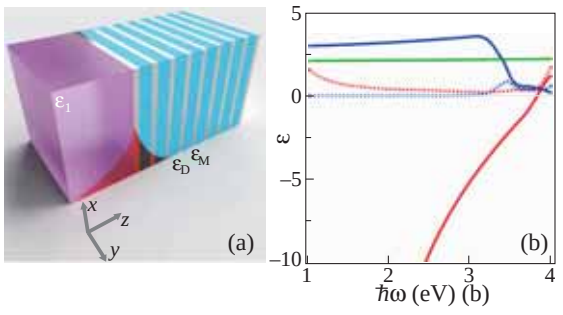

Fig. 1. (a) Geometry and composition of the structure. Silver and blue: metallic and dielectric layers; purple: dielectric cladding. The red curve represents the electric field of the surface plasmon. (b) Dielectric constant dispersion in materials used in calculations (solid — real part, dashed — imaginary part): red — silver, blue — CBP, green — silica.

to select "+" in "±" and satisfy $\xi > 0$, or $\varepsilon_D > \varepsilon_1$. It follows from this that

$$\lim_{\alpha \to 0} \omega_{\text{peak}}^{(\text{ord,ext})} = 0. \quad (8)$$

For an ordinary-wave plasmon decreasing α leads to a decrease in the peak frequency; for an extraordinary one it is necessary to select "+" in "±" and satisfy $\xi > 0$, or $\varepsilon_D > \varepsilon_1$. It follows from this that

$$\lim_{\alpha \to 0} \omega_{\text{peak}}^{(\text{ord,ext})} = 0. \quad (9)$$

For the extraordinary plasmon, this is valid only when $\varepsilon_D > \varepsilon_1$. In other words, by reducing the fraction of metal, we can achieve an arbitrarily small peak frequency with the same materials.

Fig. 2 presents the results of plasmon dispersion calculation. Silver was used for a metal, the organic light-emitting compound 4,4-Bis(N-carbazolyl)-1,1-biphenyl (CBP) was used for a filling material and silica ($\varepsilon_D = 1.45^2$) for a cladding material (see Fig. 1(b) for dielectric constant dispersion). For comparison, the dispersion of a simple surface plasmon at the interface between silver and both CBP and silica is also shown. Importantly, the plasmon associated with an ordinary wave is proved to be more effective in reducing the peak frequency of LDOS. It is obvious that by varying the filling factor α one can tune the peak frequency to any wavelength.

2. Purcell factor calculations

The values of the Purcell factor for a metamaterial-dielectric and metal-dielectric interfaces have been calculated as described in [4]. The results are shown in Fig. 3. We demonstrated that lowering the LDOS peak frequency towards the low-absorption range increases the value of the Purcell factor. For very small values of α the maximum Purcell factor is approaching zero as there can be no surface plasmon on

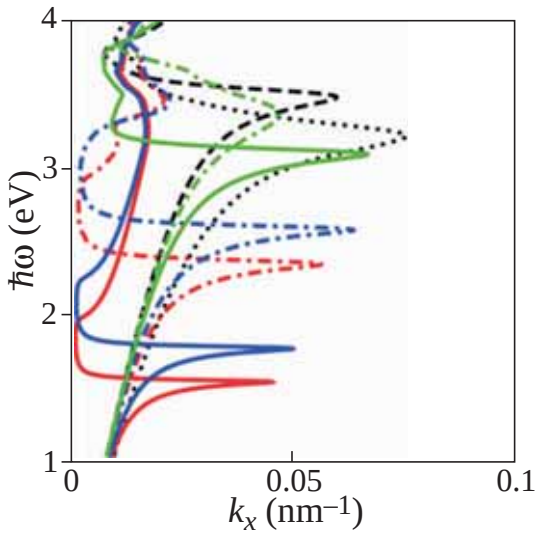

Fig. 2. Dispersion of the surface plasmon at the interface between silver/CBP metamaterial and silica: ordinary surface plasmon (solid), extraordinary surface plasmon (dash-dotted). Red: $\alpha = 0.15$, blue: $\alpha = 0.2$, green: $\alpha = 0.7$. Black lines denote dispersion of a simple plasmon at the interface between silver and CBP (dotted line) and silica (dashed line).

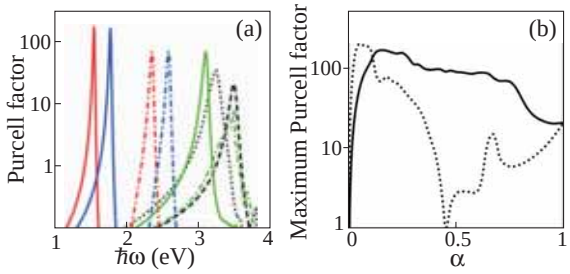

Fig. 3. (a) Dependence of the Purcell factor on frequency for an interface between silver/CBP metamaterial and silica. Ordinary plasmon (solid), extraordinary plasmon (dash-dotted). Red: $\alpha = 0.15$, blue: $\alpha = 0.2$, green: $\alpha = 0.7$. Black lines denote Purcell factor of a simple plasmon for an interface between silver and CBP (dotted line) and silica (dashed line). (b) Dependence of the peak Purcell factor on the value of $\hat{I}\pm$ for the same structure.

a dielectric-dielectric boundary. When α is increasing in the middle of its range, the value of the Purcell factor tends to decrease due to higher absorption and penetration of the electric field into the metamaterial half of the structure. Finally, at $\alpha = 1$ the maximum value of the Purcell factor is equal to the value for the conventional metal-dielectric interface plasmon as expected. Between the ordinary-and extraordinary-wave plasmons, the former is more effective in enhancing the Purcell effect.

Conclusion

To conclude, we have modelled the Purcell effect in a structure where layered metal-dielectric metamaterial is cladded by a bulk dielectric. We have shown that the peak of surface plasmon LDOS and the associated peak of the Purcell coefficient can be shifted towards lower energy, where the absorption of metal decreases, with simultaneous increase in Purcell factor.

Acknowledgement

The work has been supported by Russian Science Foundation grant No. 16-12-10503.

References

[1] B. Sharma *et al*, *Materials Today* **15**, 16 (2012).
[2] I. Iorsh *et al*, *Phys. Lett. A* **376**, 185 (2012).
[3] J. Khurgin *et al*, *Nat. Nanotechnol.* **10**, 2 (2015).
[4] K.M. Morozov *et al*, *Sci. Rep.* **9**, 9604 (2019).
[5] J.B. Pendry *et al*, *Phys. Rev. Lett.* **76**, 4773 (1996).
[6] T. Gric *et al*, *Appl. Sci.* **8**, 1222 (2018).

28th Int. Symp. “Nanostructures: Physics and Technology”
Minsk, Belarus, September 2020

Electro-optical properties of TiO_2 doped with gold nanoparticles

A. Kondrateva[1,2], Ya. Enns[1,2], A. Kazakin[1,2], R. Kleimanov[1], I. Morozov[2], P. Karaseov[1,2] and M. Mishin[2]

[1] Peter the Great St Petersburg Polytechnic University, St Petersburg 195251, Russia
[2] Alferov St Petersburg National Research Academic University, St Petersburg 194021, Russia

Abstract. In this work, a versatile method to increase the optical response of oxide nanostructures is described. Thin TiO_2 films with buried gold nanoparticles (TiO_2-AuNP) were synthesized on a crystalline Si surface. The localized surface plasmon resonance reflection maximum is formed around 720–750 nm. Current-voltage characteristics of planar structures formed by use of different contact materials were measured. Spectral features of an optical response of TiO_2-AuNP is discussed. The results obtained indicate a broad prospect of using the formed structures in the field of integrated optoelectronic devices.

Introduction

During last decades, a great interest in research of thin functional layers has been steadily observed. This is due to a wide range of extremely attractive properties of such layers, which the more, can be engineered by deposition parameters control. For example, one can tune optical density, resistivity, catalytic and photovoltaic characteristics of a functional coating. Thin semiconductor layers have found application in many modern devices such as solar energy converters, optoelectronics devices, MEMS, MOEMS etc. [1]. In particular, wide band gap semiconductors like transition metal oxides (TiO_2, ZnO, MnO, NiO) can be applied for UV optoelectronics [2]. Embedding of plasmon activators, for example, gold nanoparticles (AuNP), into a wide-bandgap material shifts fundamental absorption edge [3] thus shifting working wavelength of the composite material to visible region. Such an activated composite can serve as active media of photoconductors, field effect transistor sensors, transducers, optical coatings and so on [4]. In this work we present results of investigation of opto-electric properties of titanium dioxide activated with gold nanoparticles.

1. Sample preparation

The samples under study were grown on single crystal silicon substrate ((100) n-Si, 4.5 ohm/sq) by reactive magnetron sputtering of Ti target. RF Power density was kept at 300 W; working pressure was 1.5×10^{-3} mbar; flow rate of Ar and O_2 was kept at 9 sccm and 2 sccm respectively. Thickness of titanium dioxide coating was 190nm. Gold nanoparticles (10 nm in diameter) were embedded ∼150 nm deep into the dioxide matrix. Different metallic contacts (Ti, V, Cr, Al, Zr, Ti70-V30 alloy) (1×8 mm^2) in size were deposited onto sample surface by magnetron sputtering 6 mm from each other. Ohmic aluminum contact (8×8 mm^2) was applied onto the back side of each sample. Sample structure is presented in the Fig. 1.

2. Electrical characterization

The influence of contact metal was experimentally studied by current-voltage (CV) measurements in the dark and under white light illumination. Investigation was carried out using PM 8 probe station (SUSS MicroTec) and Agilent B1500A semiconductor analyzer. CV characteristics were taken in two modes. Bias was applied either in plane of the nanocomposite layer or across coating and silicon substrate (Fig. 1). Typical I-V dependencies are presented in the Fig. 2 and Fig. 3.

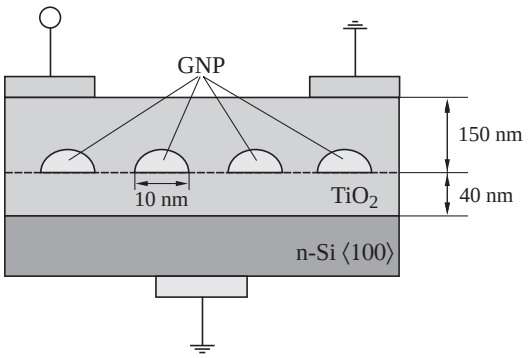

Fig. 1. Schematic of planar TiO_2-AuNP structures.

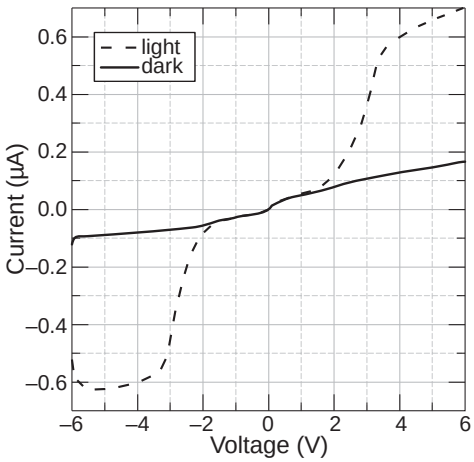

Fig. 2. Typical in-plane current-voltage characteristics of TiO_2-AuNP sample under illumination and in the dark.

In both cases, illumination with visible light causes significant effect on the CV characteristics. As it is seen from Fig. 2, the CV characteristics correspond to a system consisting of two p-n junctions with pronounced asymmetric characteristics connected towards each other. This behavior was typical for all types of contact materials (Ti, V, Cr, Al, Zr, Ti70-V30 alloy). We ascribe it to partial oxidation of metal contacts [5]. In the case (b) dependence was similar to a simple p-n junction. In both cases, light illumination significantly increases current of the reverse branch of the CV characteristics at voltages above 1 V. At zero bias the presence of irradiation did not lead to the current increase.

The ratio between dark and light current was different for

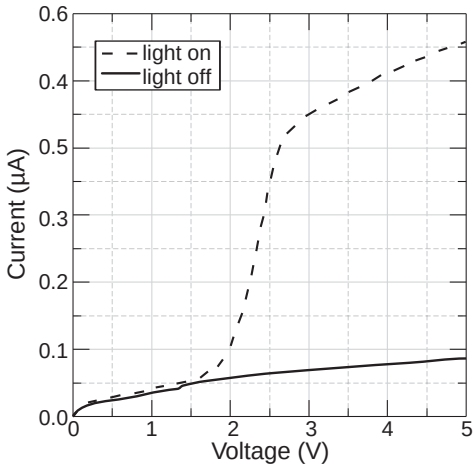

Fig. 3. Typical current-voltage characteristics taken under illumination and in the dark across the sample.

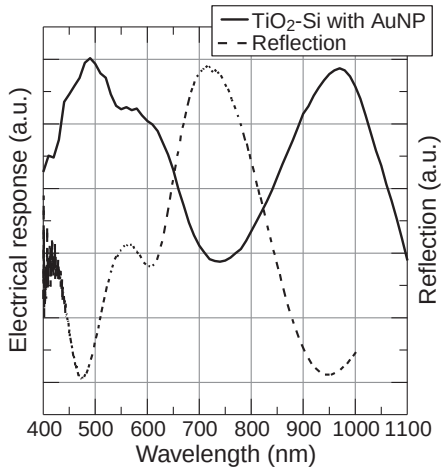

Fig. 4. Electric response and reflection of the samples as a function of wavelength of illuminating light.

Table 1. The contact material influence.

Contact material	Work function, eV [5, 7, 8]	I_l/I_d, a.u.
V	3.77	4.7±0.3
Zr	3.96	4.4±0.2
Ti70-V30 alloy	4.09	1.7±0.1
Ti	4.17	2.1±0.3
Al	4.3	2.5±0.1
Cr	4.5	5.2±0.1

various contact materials (see Table 1). If the work function of the metal is less than the energy of the bottom of conduction band of titanium dioxide (3.9 ÷ 4.1 eV, [3, 6]), the effect of the work function on the photoconductivity was not detected. For metals whose work function exceeded this value, an intense increase in the effect of illumination was observed. This corresponds to a transition from an Ohmic contact to Schottky contact.

3. Electro-optical properties

External quantum effieciency determination technique [9] with external bias 2.1 V was used to investigate the optical properties of nanocomposite. The electric response of samples illuminated with light of a specific wavelength (Fig. 3) was determined. The electrical parameters were measured using an SR810 Lock-In Amplifier (SRS). An irradiation wavelength was controlled by a monochromator. Spectral width was 10 nm.

Plasmonic activation of TiO_2 causes strong modification of the spectral reflection characteristics of the oxide [3]. Resonant absorption and reflection bands appear in the spectra as it is clearly seen in the Fig. 4. The maxima of the electric response correspond to the absorption of the TiO_2-AuNP plasmonic structures due to localized surface plasmon resonance.

4. Conclusions

Method to form active nanocomposite structures consisting of TiO_2 matrix with embedded AuNPs was demonstrated. Electro-optical characteristics of TiO_2-AuNP nanocomposites under visible light irradiation were investigated. Nanostructures have exhibited a good electric conductivity both along the sample surface and across the coating and Si substrate. Illumination with visible light strongly affects electric properties of nanocomposite. The ratio of light and dark current is found as much as 5/1. Spectral positions of maxima of the electric response correspond to the absorption of the TiO_2-AuNP plasmonic structures formed due to localized surface plasmon resonance of embedded gold nanoparticles.

Acknowledgements

This work is supported by the Ministry of Education (Project No. FSRM-2020-009).

References

[1] G. Silva-Oelke *et al*, *J. Quant. Spec. Radiative Transfer* **231**, 61 (2019).
[2] A.S. Kondrateva *et al*, *Key Eng. Mat.* **822**, 781 (2019).
[3] M.V. Mishin *et al*, *Sem. Sci. Tech.* **33**, 075014 (2018).
[4] Y. Garbovskiy, *Nanomaterials* **10**, 403 (2020).
[5] C.B. Lee *et al*, *Appl. Phys. Lett.* **93**, 042115 (2008).
[6] X. Zhang *et al*, *Rep. Prog. Phys.* **76**, 046401 (2013).
[7] G.F. Amelio *et al*, *Bell Sys. Tech. J.* **49**, 593 (1970).
[8] S. Seo *et al*, *Appl. Phys. Lett.* **87**, 263507 (2005).
[9] A.I. Baranov *et al*, *IOP Conf. Ser.* **1124**, 041034 (2018).

28th Int. Symp. "Nanostructures: Physics and Technology"
Minsk, Belarus, September 2020

InP quantum dots photostability enhancement by gold nanoparticles

O.S. Kulakovich[1], L.I. Gurinovich[1], Hui Li[2], A.A. Ramanenka[1], L.L. Trotsiuk[1], A.Muravitskaya[1], Jing Wei[2], Hongbo Li[2], N. Matveevskaya[3] and S.V. Gaponenko[1]

[1] B.I. Stepanov Institute of Physics, National Academy of Sciences of Belarus, 220072 Minsk, Belarus
[2] Beijing Institute of Technology, 100081 Beijing, China
[3] Institute for Single Crystals, National Academy of Sciences of Ukraine, 61178 Kharkiv, Ukraine

Abstract. We have studied the effect of gold plasmonic films on the photoluminescence and photostability of InP/ZnSe/ZnSeS/ZnS core/shell quantum dots. Colloidal gold films improve InP/ZnSe/ZnSeS/ZnS photostability at blue light-emitting diode (LED) excitation through reducing photoluminescence decay time. Via adjusting the excitation wavelength closer to the plasmon band of gold nanoparticles we were able to obtain a 1.8-fold enhancement of luminescence using a spacer between the metal nanoparticles and InP/ZnSe/ZnSeS/ZnS.

Introduction

Luminescent semiconductor nanocrystals or quantum dots (QDs) are widely used in optoelectronic devices as highly efficient luminophores [1]. Due to the spreading ban on the use of heavy metals in consumer products, the great challenge today is to find the composition without toxic chemical elements as well as provide high optical characteristics of nanocrystals. Initially, the leading companies produced commercial liquid-crystal displays (LCD) by the QLED technology using CdSe quantum dots in backlight scattering panel [2]. The alternative decision is nanostructures based on colloidal Cd-free quantum dots [3–6]. Compared to A2B6, InP QDs exhibit high luminescence lifetime and poor photostability [3], but they are environmentally friendly due to consisting of non-toxic metal. Significant attention has been given to improving these aspects when use InP-based QDs for LED production [7]. A possible approach to improve the properties of the fluorescent species is to place them nearby the plasmonic nanoparticles. In this work, we report gold plasmonic nanostructures effects on InP/ZnSe/ZnSeS/ZnS core/shell quantum dots photoluminescence and show that favorable interplay of several plasmonic effects can be useful both in photoluminescence intensity enhancement and quantum dot photostability enhancement.

1. Sample preparation and characterization

The InP/ZnSe/ZnSeS/ZnS core/multiple shell QDs studied in this work were synthesized according to the protocol reported by Tessier et al with modifications [8]. Two types of gold colloidal films were prepared: the first one by electrostatic deposition of gold nanoparticles on pre-treated with polycation glass substrate (Au type 1) and, second, by reduction of Au^{3+} ions directly on a glass surface (Au type 2). The average gold nanoparticle size determined by electron microscopy was estimated as 20 nm for both types of films.

Normalized optical density spectra gold films are shown in Fig. 1. Optical density maximum for "Au type 2" film is 550 nm while "Au type 1" film, consisted from nanoparticles with the same size as "Au type 2" has the broad absorbance maxima about 590 nm. This indicates the difference in the organization of particles on the surface. Photoluminescence (PL) band of quantum dots is centered at 627 nm (Fig. 1). The quantum yield was measured to be 20%.

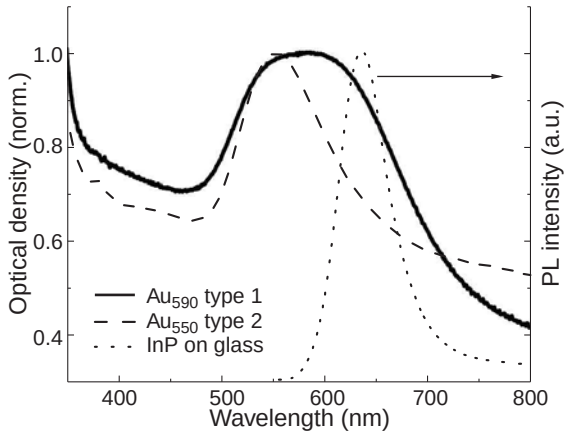

Fig. 1. Normalized optical density spectra Au_{590} "type 1", Au_{550} "type 2" films and photoluminescence spectrum of InP/ZnSe/ZnSeS/ZnS nanoparticles.

2. Plasmonic effects on photoluminescence

To diminish the role of non-radiative processes, the plasmon films were pre-coated with polyelectrolyte (PE) layers as in our previous work [9]. Quantum dots on glass in the absence of metal nanoparticles were used as a reference sample.

Fig. 2 shows the dependences of PL intensity of the experimental samples on exposure time during 10 hours. The PL of InP/ZnSe/ZnSeS/ZnS QDs on Au substrates is more stable in comparison with glass substrate.

QDs average PL lifetime on a substrate with gold nanoparticles was nearly 37.7 ns and decreased by 17% relative to the control glass sample value. Experimental data for gold nanostructures clearly shows decreasing both for each lifetime components and for average lifetime, which indicates the probable plasmon effect of gold nanoparticles on radiative decay rate of InP/ZnSe/ZnSeS/ZnS QDs. It is possible due to overlapping of QDs emission spectra with plasmon band of gold films (Fig. 1). Increasing of radiative and nonradiative rates results in enhanced photostability because the emitter spends less time in the excited state and thus have fewer possibilities for photophysical and photochemical processes.

Important to note, InP/ZnSe/ZnSeS/ZnS photostability enhancement accompanied by PL decay time decreasing was observed for both types of Au films. The differences appeared in InP/ZnSe/ZnSeS/ZnS PL intensity: quenching for the Au_{590}

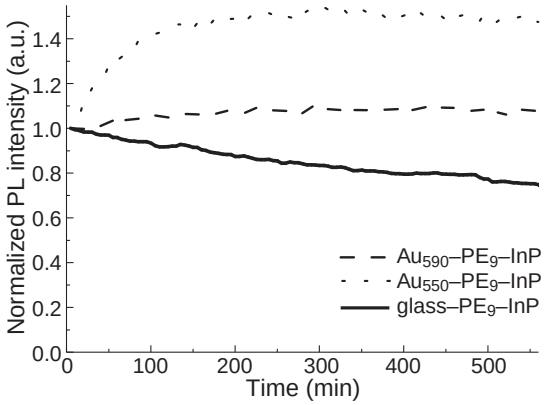

Fig. 2. The dependence of normalized PL intensity on exposure time for InP/ZnSe/ZnSeS/ZnS nanocrystals deposited on gold films and glass slide pre-coated with 9 polyelectrolyte layers as a spacer. The wavelength of PL measurement is 630 nm. The source of incident light is a blue LED with $\lambda_{em} = 460$ nm and optical output power $P_{\text{out}} = 1.0$ mW. Optical power density of incident light on the samples is 0.3 mW/mm^2 and total acquired dose is 10.1 J / mm^2.

but enhancement for the Au_{550} with the spacer of 11 polyelectrolyte layers (Fig. 3). It is probably due to the difference in the absorbance spectra (Fig. 1) and morphology of the gold films manifested in a greater nonradiative decay rates for Au_{590}-PE-InP system.

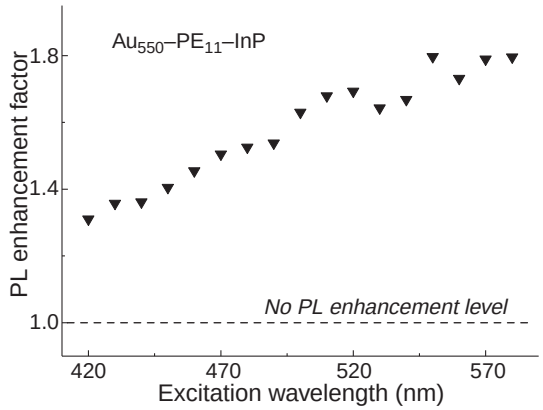

Fig. 3. Photoluminescence enhancement factor dependence on excitation wavelength for Au_{550}-PE_{11} — QDs sample.

Fig 3 shows the dependence of PL enhancement factor (EF) on excitation wavelength for Au550-PE11-QDs system: from EF=1.3 at 420 nm excitation to EF=1.8 at 580 nm excitation. Since QDs in dielectric environment are excited more efficient at shorter wavelength the inverse dependence on the gold substrate is associated with a more efficient excitation of the InP/ZnSe/ZnSeS/ZnS PL when approaching the plasmon band.

3. Conclusions

Gold plasmonic films increase the photostability of red InP/ZnSe/ZnSeS/ZnS quantum dots under 460 nm excitation.

At the same time gold nanoparticle gives rise to faster decay of the quantum dot excited states. The tuning of excitation wavelength closer to the plasmon band provides almost 2-fold photoluminescence enhancement when placing quantum dots at a distance of the order of 10 nm from gold surface. The results obtained can be useful for improving the reliability and stability of optical characteristics of light-emitting devices.

Acknowledgement

This work has been supported by the Belarusian Basic Research Foundation F20PTI-004.

References

[1] S.V. Gaponenko, H.V. Demir, *Applied Nanophotonics*, (Cambridge: Cambridge University Press) 2018.
[2] C.-Y. Han *et al*, *J. Korean Ceramic Society* **54**, 449 (2017).
[3] H. Li *et al*, *Front Chem* **6**, 652 (2018).
[4] J. Ziegler *et al*, *Adv. Mat.* **20**, 4068 (2008).
[5] X. Yang *et al*, *Adv. Mat.* **20**, 4180 (2012).
[6] Lanlan. Yang *et al*, *Nanotechnology* **30**, 395603 (2019).
[7] Y.-H. Won *et al*, *Nature* **575**, 634 (2019).
[8] M.D. Tessier *et al*, *Chemistry of Materials* **27**, 4893 (2015).
[9] O. Kulakovich *et al*, *Nano Lett.* **2**, 1449 (2002).

28th Int. Symp. "Nanostructures: Physics and Technology"
Minsk, Belarus, September 2020

Plasmonic-related light absorption in periodic multilayer silicon structures: The effect of inter-island distance

A.I. Mukhammad[1], M.V. Lobanok[1], K.V. Chizh[2], V.G. Plotnichenko[2], V.A. Yuryev[2], P.I. Gaiduk[1]

[1] Department of Physical electronics and nanotechnology, Belarusian State University, Belarus
[2] A.M. Prokhorov General Physics Institute of the Russian Academy of Sciences, Moscow, Russia

Abstract. Absorption spectra of $Si/SiO_2/Si$ structure with highly doped silicon layers are simulated with FDTD as a function of periodicity of surface islands. The effect of multiple resonance is studied for different inter-island distances. A wide band (> 12 μm) of high light absorption ($> 70\%$) is registered for a structure with period of 8 μm and an inter-island distance of 3 μm. It is revealed for the spectral range of 10–20 μm that the reduction of the inter-islands distance shifts the absorption peak position to the region of longer waves and results in the growth of absorption level.

Introduction

Infrared (IR) photodetectors and other opto-electronical devices are very important for technical, biological and medical applications [1]. Development of new generation of IR photodetectors is connected to their sensitization in the IR optical range, e.g. through increase of light absorption. A promising rote is to use excitation of plasmon resonances which may increase light absorption in both wide and selected spectral regions. However, the problem is related to the search for suitable material for effective plasmonic excitations in the IR optical range. Traditional metals (silver, gold, cupper etc.) are not suitable because the plasmon resonance is located in the visible region of the spectrum. Recently, it has been suggested that highly doped semiconductors can be a reasonable alternative to metals for exciting plasmon resonances in the infrared region [2–4]. In particular, it has been established that highly degenerate silicon exhibits a higher intensity of plasmon modes in the infrared range compared to metals. In this paper, the effect of plasmon absorption in multi-layer silicon structures with a periodically structured upper layer was studied using FDTD modeling, and the dependence of the position and intensity of the absorption peaks on the inter-island distance was revealed.

1. Experimental

In this work, a modeling of the structure shown in figure 1 is proceeded. The structure consists of three layers: the layer of islands of different topology on the surface, the intermediate layer of silicon dioxide and the layer of polycrystalline silicon as a substrate. Square-shaped silicon islands are assembled on the surface periodically with equal period of 8 μm for all structures. Inter-island distance (d_{inter}) and the size of the islands (d_{isl}) are varied within 3–7 μm. The thickness of islands in the surface layer is 1.2 μm, intermediate SiO_2 layer is 0.8 μm thick and the thickness of substrate is 2.5 μm. To attain the plasmon effect, both surface silicon islands (n-type) and polycrystalline silicon substrate (p-type) are supposed to be highly doped up to concentration of 3×10^{19} cm^{-3}. Optical constants for doped silicon are taken from [5]. The simulation was performed by the FDTD (Finite Difference Time Domain) Solutions program [6] using the FDTD simulation code. Periodic boundary conditions are used for modeling. To reduce the calculation time, we use a non-uniform grid with a minimum step of 30 nm in the area of the surface layer. Transmission and reflection spectra of the samples were explored using a IFS-113v spectrometer (Bruker) with a microscope "IR Scope" attached to it. This made possible to measure spectra with a lateral spatial resolution from 400 to 500 μm. An opaque golden mirror was used as reference sample during recording of reflectance spectra. The absorption is determined by the ratio $A(\lambda) = 1 - R(\lambda) - T(\lambda)$, where $R(\lambda)$ — reflected and $T(\lambda)$ — transmitted radiation.

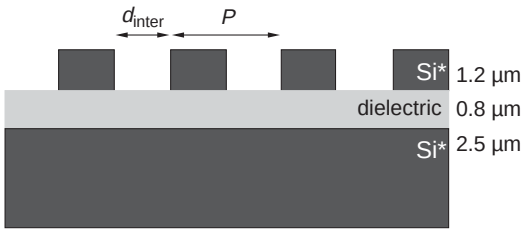

Fig. 1. Model of the structure.

2. Result and discussion

Figure 2 shows the absorption spectra of structures with an inter-island distance of 3–7 μm. The simulation is carried out in the wavelength range of 7–20 μm. To make analysis more simple, the range is divided into three regions: 7–9 μm, 9–12 μm and 12–20 μm, which are different significantly in the manifestation of the plasmon-related absorption effect.

The absorption peak at a wavelength of about 8 μm of the region I (Fig. 2) is of special interest. This peak takes place at all spectra presented but with very different intensity. It is most intensive in a spectrum, obtained from the structure with $d_{\text{inter}} = 3$ μm (Fig. 2, curve 3), in which it is located at a

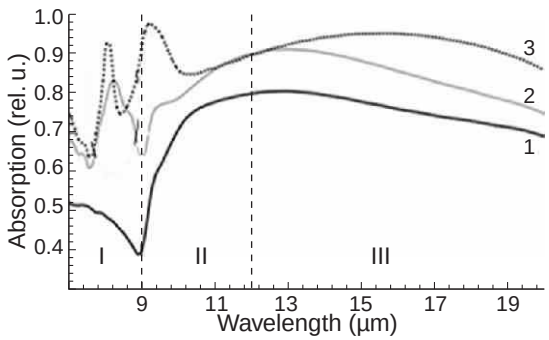

Fig. 2. Absorption spectra obtained from the structures of Si-SiO_2-Si with different inter-island distances: (1) $d_{\text{inter}} = 7\mu$m, (2) $d_{\text{inter}} = 5$ μm, (3) $d_{\text{inter}} = 3$ μm.

wavelength of 8.2 μm and has an intensity of more than 90%. An increase of the inter-island distance to 7 μm (curve 1) leads to a sharp change in the 8 micrometers absorption peak: in this case, there is a barely discernible peak with a one-percent increase in intensity against the background of a 50% absorption level. In addition, there is an acute dip of up to 40% at a wavelength of about 9 μm. Perhaps because of the small size of the islands compared to the distance between them, most of the incident radiation is reflected, and, consequently, there is interference between the incident radiation and the reflected one [7]. Similar tendency to decrease the intensity of the 8-micron peak is also observed when the inter-island distance is increased from 3 to 5 micrometers (curve 2). In addition, there is a sharp broadening of the peak at a wavelength of 8.7 μm at the curve 2. We assume that absorption peaks at wavelengths of about 8 μm occur due to the appearance of surface plasmons, which are excited due to the periodicity of the structure [2]. According to the literature data, absorption by free carriers in the range from 6 to 9 μm prevails in heavily doped silicon layers [2]. The comparison of the curves in Fig. 2 shows a tendency toward an increase in the intensity of the absorption peak at a wavelength of about 8 micrometers and a decrease in the width of the peak with a decrease in inter-island distances. In region II, the maximum absorption of unstructured heavily doped silicon is observed at a wavelength of about 9.5 μm, which corresponds to its plasma wavelength at 9.42 μm. Similarly, the molecular resonance of silicon dioxide occurs in the range of 9–10 μm [2]. We assume that the absorption in this range is most likely due to valence antisymmetric oscillations of Si-O-Si bridge groups [8]. This absorption band is also typical for the absorption spectrum of an undoped silicon structure [3]. There is an increase in the absorption intensity for all curves (Fig. 2) in the range of 9–10 μm, and absorption intensity for curve 3 is about 98–99%. It is in the second region that the behavior of all three curves is most similar (especially in the range of 10–12 μm), although the absorption intensity of the three curves is not the same. Since the absorption in this region is primarily due to constant parameters, such as the thickness of a layer of silicon dioxide and a heavily doped unstructured silicon substrate, the absorption level in the range of 9–12 μm should not depend on the inter-islands distance. However, as our recent experimental studies have shown, changes in the level and type of doping of silicon layers or changes in the period with a constant size of islands affect the behavior of absorption curves in region II [4]. The nature of this influence will have to be determined in future studies. In Fig. 2, in the range of 10–14 μm, it can be noted that the absorption curve 1 forms a gentle peak of low intensity. And in the range of 14–20 μm, it decreases slowly, almost linearly. The same dependence is typical for a structure with an inter-island distance of 5 μm (curve 2, Fig. 2). However, the position of the flat peak is shifted to the range of 11–15 μm, and its intensity increases by 5–10% (compared to curve 1). When the inter-island distance is reduced to 3 microns (curve 3, Fig. 2) we can observe a significant (more than 85%) increase in absorption in the region of 12–20 μm. In addition, the absorption peak in region III becomes less flat compared to previous structures, and the region of slow linear decline shifts to a longer wavelength range. From the foregoing, it can be noted that when the distance between the islands decreases, the absorption level in the range of 10–20 μm increases, and the position of the peak in this range shifts to the region of a longer wavelength. A set of structures with patterned surface layer of highly doped Si was manufactured and optical spectra were measured. The results of experimental measurements correlate well with simulation data. In conclusion, absorption spectra of $Si/SiO_2/Si$ structure with highly doped silicon layers are simulated with FDTD method as a function of periodicity of surface islands. It is shown that such structures are characterized by the effect of multiple resonance. In particular, for a structure with a period $P = 8$ μm and an inter-island distance $d_{\text{inter}} = 3$ μm, the bandwidth at which the average absorption capacity exceeds 70% is about 12 μm. The theoretical absorption spectra of structures with different inter-island distances are compared. It is shown that the position of the first absorption peak in the spectrum does not depend on the inter-island distance, in contrast to the intensity of this peak. It is also shown that when the distance between the islands decreases, the absorption level in the range of 10–20 μm increases, and the peak position in this range shifts to a longer wavelength region. The results obtained showed the possibility of using this structures in microbolometers without the direct use of metals.

Acknowledgements

The research was conducted with the financial support of the BRFFR project No. T18P-190, and the project of state scientific research program (No. G/R 20162098). The research was funded by the Russian Foundation for Basic Research [grant number 18-52-00033].

References

[1] Kaikai Du *et al*, *IEEE Photonics Journal* **7**, 3 (2015).
[2] K. Gorgulu *et al*, *Scientific reports* **6**, 38589 (2016).
[3] A. Mukhammad *et al*, *VIII international scientific conference: Materials and structures of modern electronics* Minsk 10–12 October 2018, 318–322.
[4] A.I. Mukhammad *et al*, *Collection of articles 1 of the international scientific and technical conference "Opto Micro and microwave Electronics-2018"* Minsk, October 22–26, 320–323 (2018).
[5] E.D. Palik *et al*, *Handbook of optical constants of solids vol. 2* London: Academic Press 1091 (1985).
[6] Lumerical FDTD Solutions [Electronic resource], Lumerical Solutions, Inc, 2003–2020, Mode of access: http://www.lumerical.com/ - Date of access : 14.02.2020.
[7] A. Moreau *et al*, *Nature* **492**, 86–89 (2012).
[8] A.G. Vlasov *et al*, *Infrared spectra of inorganic glasses and crystals,*, Leningrad: Chemistry, 304 (1972).

28th Int. Symp. "Nanostructures: Physics and Technology"
Minsk, Belarus, September 2020

Fourier-imaging spectroscopy of two-dimensional gold nanodisk array on photoluminescent layer

S.I. Pavlov[1], S.A. Dyakov[2], A.I. Solomonov[1,3], A.V. Nashchekin[1], N.A. Feoktistov[1], N.A. Gippius[2], S.G. Tikhodeev[4,5], I.M. Fradkin[2] and A.B. Pevtsov[1]

[1] Ioffe Institute, St Petersburg, Russia
[2] Skolkovo Institute of Science and Technology, Nobel Street 3, Moscow, Russia
[3] ITMO University, St Petersburg, Russia
[4] Lomonosov Moscow State University, Moscow, Russia
[5] A.M. Prokhorov General Phyics Institute, Moscow, Russia

Abstract. In this paper we theoretically and experimentally study the angular dependencies of reflection and photoluminescence spectra of two-dimensional gold nanodisk array on top of thin luminescent layer. Hydrogenated amorphous silicon-carbon alloy was used as a luminescent material with high refractive index in the visible spectral range. Optical spectra with angular resolution have been measured by a Fourier imaging spectroscopy in p- and s- polarizations. Both TE and TM quasiguide modes are clearly seen in the reflection and photoluminescence spectra in both polarizations simultaneously.

Introduction

Two-dimensional arrays of metallic nanoparticles are promising structures for tailoring light-matter interaction at the nanoscale [1,2]. Under light illumination of single nanoparticle localized surface plasmon resonance (LSPR) can be excited which can modify spontaneous emission rate due to strong field enhancement and subwavelength character of LSPRs [3,4]. Placed on top of a thin dielectric layer with high refractive index periodic array couples part of the incoming light into the waveguide due to periodicity [5]. Two-dimensional nanoparticle array has an advantage, that is lower absorption in metal compared to one-dimensional stripe array of similar size-to-period ratio. Coupling of localized plasmon mode to a guide mode of a planar waveguide forms waveguide plasmon-polariton mode [5]. In order to examine effect of such hybrid mode to photolumenescent properties we created two-dimensional array of gold nanodisks on hydrogenated amorphous silicon-carbon alloy (α-Si_{1-x}:C_x:H) layer which exhibits a wide emission band in visible spectral range. We measured reflection and photoluminescence (PL) spectra angular dispersion by the Fourier-imaging spectroscopic setup.

1. Methods

1.1. Sample preparation

The sketch of the sample is shown in Fig. 1. The α-Si_{1-x}:C_x:H layer with thickness of 200 nm was deposited on fused silica substrate by the plasma enhanced chemical vapor deposition (PECVD) technique in a capacitive reactor at various relative flows of silane (SiH_4) and methane (CH_4) [6]. The optical thickness of the layers was monitored in-situ by the laser beam interference pattern. Carbon content in the film is $x = 0.58$, which corresponds to PL peak at 1.7 eV and refractive index $n = 2.2$ [7].

Square lattice array of gold disks with period $P = 500$ nm and diameter $a = 200$ nm was created by lift-off electron beam lithography (EBL) as follows. At first 300 nm thick positive e-beam resist PMMA 950K (Allresist, Gmbh) was spin-coated on the substrate and then EBL was carried out using SEM JSM 7001f (JEOL, Japan) equipped with EBL-system 'Nanomaker' (Interface Ltd, Russia). Gold disks were formed in developed e-beam pattern, after depositing of 20 nm gold by thermal evaporation and subsequent lift-off process. Before EBL processes 5 nm optically transparent conductive ITO layer was deposited which is also known to be a good adhesive layer for gold.

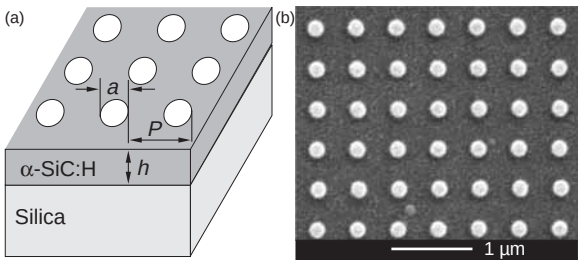

Fig. 1. (a) Sketch of sample structure, (b) SEM image of prepared structure.

1.2. Measurements

Angle-resolved optical spectra have been measured using a Fourier imaging spectroscopy setup. Unpolarized white light from a halogen source was focused on the sample by microscope objective Olympus PlanFL with numerical aperture N.A.=0.95. Reflected light was collected by the same objective and projected to a spectrometer slit, after being passing through a Glan-Thompson polarizer. For PL measurements the sample was illuminated by the 405 nm laser diod from the backside. Spectral resolution of the setup was 0.17 nm by wavelengths and not less than 0.4° by angles. Measurements of reflection and PL spectra with an azimuthal angle rotation were also carried out.

1.3. Calculation

The reflection and PL spectra of the spatially-periodic structures with gold nanoparticles were calculated using the Fourier modal method in the scattering matrix form [8]. The contribution of gold nanoparticles to the total scattering matrix was

calculated in dipole approximation [11]. In this method, the solutions of Maxwell's equations for each layer are found by expansion of the electric and magnetic fields into Floquet–Fourier modes (plane waves). The exact solution can be presented as an infinite series over these modes.

2. Results and discussions

2.1. Reflection

Experimental reflection spectra in two different polarizations are presented in Fig. 2. Minima and maxima in spectra form tracks which positions depend on the incidence light angle. These tracks can be attributed to dispersion curves of the structure eigenmodes, and their spectral position can be approximated by the waveguide mode dispersion equation for a planar waveguide:

$$\frac{2\pi}{\lambda}h = \frac{1}{\sqrt{n_1^2 - n_m^2}}\left[\pi m + \operatorname{arctg}\left(\frac{n_2}{n_3}\right)^{\chi}\sqrt{\frac{n_m^2 - n_3^2}{n_2^2 - n_m^2}} + \operatorname{arctg}\left(\frac{n_2}{n_1}\right)^{\chi}\sqrt{\frac{n_m^2 - n_1^2}{n_2^2 - n_m^2}}\right] \quad (1)$$

Here λ — incident light wavelength, n_1, n_2 and n_3 — refractive indexes of air, waveguide and substrate respectively, $n_m = n_2 \sin\theta$ — effective refractive index, h — waveguide thickness, $\chi = 0$, 2 for TE and TM modes and m — mode number.

Solutions for TM_0, TE_0 and TE_1 modes are marked on Fig. 2. It should be noted that due to two-dimensional periodicity TE modes are seen in p-polarized spectra and vice versa [9].

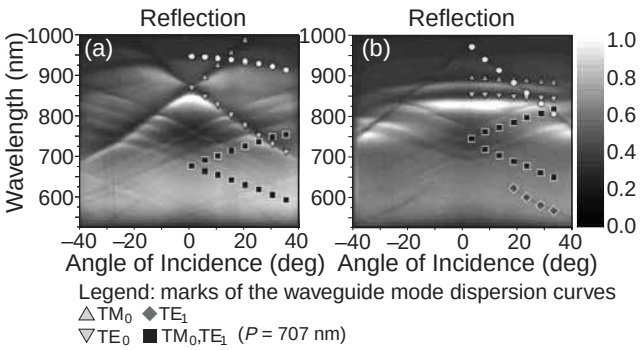

Fig. 2. Angle-resolved reflection spectra in (a) p- and (b) s-polarization.

Group of tracks observed in range 600–850 nm can result due to off-axis lattice diffraction waveguide mode coupling with period $P = 500 \cdot \sqrt{2} = 707$ nm because of polarizers setup inaccuracy. Confirmation of this explanation is that these tracks transform from X-shape to almost straight at 45° azimuthal angle rotation, like TM_0 mode at s-polarization and TM_0 mode at p-polarization (i.e. 90° azimuthal angle).

2.2. Luminescence

PL spectra are presented in Fig. 3. Due to a wide PL band in range of 700–1000 nm all the quasiguided modes are effectively coupled to emission. Also one can see that upper branch of the TM_0 mode is not seen in the PL spectrum at normal incidence. Such behavior is characteristic for an optically inactive symmetric plasmon-polariton mode [10].

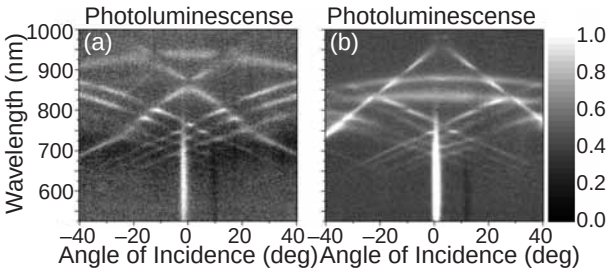

Fig. 3. Angle-resolved photoluminescence spectra in (a) p- and (b) s-polarization

3. Conclusions

In this work the angle-resolved reflection spectra of the two-dimensional square periodic array of gold nanodisks on top of the thin luminescent α-$Si_{0.42}$:$C_{0.58}$:H film were studied. Both TM and TE quasiguided modes are seen in both polarizations with different polar angle dependences. Photoluminescence spectral features follow the reflection ones which is attributed to quasiguided modes of the structure. Theoretical calculations are in agreement with the measured reflection and PL spectra.

Acknowledgements

This work was partially supported by the Presidium of RAS (Program I.7 "Modern problems of photonics, the probing of inhomogeneous media and materials").

EBL has been carried out in the Joint Research Center "Materials science and characterization in advanced technology".

Theoretical part of this work was supported by Russian Foundation for Basic Research (Project No. 18-29-20032)

References

[1] A. Vaskina, R. Kolkowskia, A.F. Koenderinka *et al*, *Nanophotonics* **8(7)**, 1151 (2019).
[2] V.G. Kravets, A.V. Kabashin, W.L. Barnes *et alChemical Reviews* **118**, 5912 (2018).
[3] J.S. Biteen, N.S. Lewis, H.A. Atwater *et al*, *Applied Physics Letters* **88**, 131109 (2006).
[4] J. Henson, E. Dimakis, J. DiMaria *et al*, *Optics Express* **18**, 21322 (2010).
[5] S. Linden, J. Kuhl and H. Giessen, *Physical Review Letters* **86**, 4688 (2001).
[6] M.V. Rybin, A.V. Zherzdev, N.A. Feoktistov *et al*, *Physical Review B* **95**, 165118 (2017).
[7] W. Siebert, R. Carius, W. Fuhs *et al*, *Physica Status Solidi (b)* **140**, 311 (1987).
[8] S.G. Tikhodeev, A.L. Yablonskii, E.A. Muljarov *et al*, *Physical Review B* **66**, 045102 (2002).
[9] R. Guo, T.K. Hakala and P. Törmä, *Physical Review B* **95**, 155423 (2017).
[10] S.A. Dyakov *et al*, *Scientific Reports* **8**, 4911 (2018).
[11] I.M. Fradkin, S.A. Dyakov, and N.A. Gippius, *Physical Review B* **99**, 075310 (2019).

28th Int. Symp. "Nanostructures: Physics and Technology"
Minsk, Belarus, September 2020

How electron collisions activate the two-dimensional plasmons

D. Svintsov

Laboratory of 2d Materials for Optoelectronics, 9 Institutsky lane, Dolgoprudny, Russia

The main challenge in the field of plasmonics lies in increasing the plasmon propagation length that is severely limited by Ohmic losses A mainstream approach to achieve this goal was the fabrication of ultra-pure plasmonic materials with reduced electron scattering by impurities, phonons, boundaries, and other carriers. In this paper, we show that the effect of electron-electron collisions on the propagation length of 2d plasmons is highly non-trivial [1–4]. Counter-intuitively, increased strength of electron–electron (e–e) collisions can increase plasmon free path in equilibrium electron systems [1], and lead to novel current-driven plasmon instabilities in non-equilibrium ones [2,4].

To reveal the effect of e–e collisions on the properties of 2d plasmons, we have developed an exactly solvable kinetic model for 2d electrons that takes into account these collisions explicitly in the generalized relaxation-time approximation [1]. It is applicable at arbitrary frequencies across the hydrodynamic-to-ballistic crossover. In the high-frequency ballistic regime, e–e collisions result in plasmon damping, while the plasmon velocity always exceeds Fermi velocity This preserves graphene plasmons from Landau damping In the low-frequency hydrodynamic regime, strong collisions lead to weakening of plasmon damping while the lower bound of plasmon velocity is $V_F/\sqrt{2}$.

Dissipationless reduction of plasmon velocity below Fermi velocity in the deep hydrodynamic regime has a strong effect on plasmons in the presence of direct current As the drift velocity of electrons exceeds the plasmon phase velocity the Cerenkov-type emission of plasmons becomes possible [2]. We have theoretically shown the presence of hydrodynamic Cerenkov-type plasmon instabilities in two experimentally relevant setups: parallel graphene layers and graphene layer covered by a sub-wavelength grating The Cerenkov emission of plasmons can serve as a hallmark of ac hydrodynamic transport as the effect is fully prohibited in the ballistic regime due to high velocity of plasmons [3].

The Cerenkov-type plasmon generation requires large currents; yet low-current plasmon instabilities are feasible for special types of non-equilibrium carrier distributions. Namely, a collimated bunch of electrons can become unstable with respect to generation of plasmons. We have revealed a new type of beam instabilities associated with viscous transfer of beam momentum to 2d plasmons [4]. This instability develops favourably at moderate frequency of e–e collisions order of plasmon frequency All these results let us conclude that ballistic motion of electrons is not a necessary condition for low-loss plasmonics, and e–e collisions can activate the 2d plasmons.

References

[1] D. Svintsov *Phys. Rev. B*, **97**, (2018) 121405(R).
[2] D. Svintsov *Phys. Rev. B*, **10**, (2019) 195428.
[3] D. Svintsov, V. Ryzhii *Phys. Rev. Lett.123*, (2019) 219401.
[4] [4] D. Svintsov arXiv:1910.01190 (2019).

28th Int. Symp. “Nanostructures: Physics and Technology”
Minsk, Belarus, September 2020

Epitaxial phosphide nanowires as perspective platform for future optoelectronics

A.D. Bolshakov[1], V.V. Fedorov[1] and I.S. Mukhin[1,2]

[1] Alferov University, Khlopina 8/3, 194021, St Petersburg, Russia
[2] ITMO University, Kronverkskij 49, 197101, St Petersburg, Russia

Abstract. Today information technology is going through an era of transition from electronic to integrated photonic circuits. The latter are a promising platform for computing systems of the future that go beyond Moores law. The development of such systems requires the advancement of new technologies and component base. III-V semiconductors are promising materials in the field of optoelectronics. Due to the geometry, nanostructures provide new opportunities to control electromagnetic radiation. The effects of reduced dimensionality in nanostructures can significantly expand their functionality for optoelectronics and nanophotonics compared to conventional thin-film heterostructures. Over the past few decades, nanowires (NWs) have shown great potential in photonics because of their unique quasi-one-dimensional morphology, which allows one to create both passive (waveguides) and active (emitters) elements of photonic schemes. The resonant geometry contributes to the efficient generation of stimulated radiation in such structures, and the high refractive index of semiconductor materials makes it possible to couple the optical signal in structures having deimension on the order of hundreds of nanometers, which determines the prospects for using these structures in close-packed integrated circuits. Among the semiconductor materials suitable for nanowires synthesis, phosphide alloys are of particular interest from the point of view of photonics. Firstly gallium phosphide is a material with a relatively high refractive index, while it has low optical losses in a wide range, including the visible region and IR, which is especially important for data transmission systems. Despite the fact that GaP itself is an indirect-gap material, its dilution with isovalent elements of group 5 (N,As) leads to a direct-gap structure. Thus, on the basis of phosphide NWs, it is possible to create both passive and active elements of photonic circuits, including hybrid elements — the active medium in the waveguide. Modern epitaxial growth technologies make it possible to synthesize NWs on cheap silicon substrates with a given morphology (including the ability to synthesize ordered arrays by selective epitaxy methods), high crystalline perfection and good faceting, as well as obtain heterostructured nanowires with axial and radial geometry which determines the prospects of this approach for the implementation of various submicron in the cross section elements of integrated photonic circuits. In this paper we demonstrate the latest results on synthesis and applications of phosphide nanowires grown via self-catalysed growth method using molecular beam epitaxy technique.

28th Int. Symp. “Nanostructures: Physics and Technology”
Minsk, Belarus, September 2020

Peculiarities of nanolithography for transport devices on sensitive substrates containing HgTe epilayers

T. Borzenko, P. Shekhar, K. Martin, J. Baumann, J. Kleinlein, C. Gould, and L.W. Molenkamp
Physikalisches Institut der Universität Würzburg, Am Hubland 9774 Würzburg, Germany

Since the experimental demonstration of the quantum spin Hall effect in HgTe quantum wells in 2007 [1], HgTe/(Hg,Cd)Te/CdTe based heterostructures have become the prototypical material system for transport studies in topological insulators and other topological states of matter. While the growth of high structural quality and high mobility heterostructures of these materials is now relatively well established in our group the establishment of a reliable and universal lithographic process line remains a work in development.

The special lithographic challenges posed by this material stem from the high volatility and diffusiveness of Hg as well as the materials extreme sensitivity to heat or other form of radiations. On this last point, experience has shown that any process requiring temperatures in access of 8˚C, or even long exposure at slightly lower temperatures, significantly degrades the material properties. The material is similarly negatively impacted by exposure to high energy electron or ion beams that used in many standard lithography processes.

Here we outline a newly established process set, appropriate for both basic microstructures (Fig. 1) or sophisticated nanostructures (Fig. 2,3), optimized to minimize any adverse effects of the lithography on the material properties of the sample.

Our processes incorporate:

- developing non-standard resist bake recipes and etching procedures to minimize thermal and energetic invasion to preserve transport properties as verified by Hall measurements (Figure 1);
- development of wet etching technique for CdHgTe/HgTe structures suitable for relatively uniform;
- etching of both small and big elements (Fig. 2);
- applying mainly low voltage (25–3 kV) electron beam lithography (EBL) with specific adjustments for precise focusing and alignment as well as the elimination of charging effects;
- further development of our metallic air-bridge technique [2] to smaller structure dimensions;
- a study of ohmic contact formation to CdHgTe/HgTe surface.

As an example we present in detail a complex structure (Fig. 3), used in studies of current induced magnetization switching in a CoFe/Cu/NiFe pillar located on top of CdHgTe/HgTe/ CdHgTe/CdTe mesa.

We will also discuss ongoing refinements to our processes as we explore the potential benefits of inductively coupled plasma etching (ICP), maskless 385 nm laser exposure and helium focused ion beam etching (FIB) to further decreases of mechanical and energetic loads on the sensitive samples.

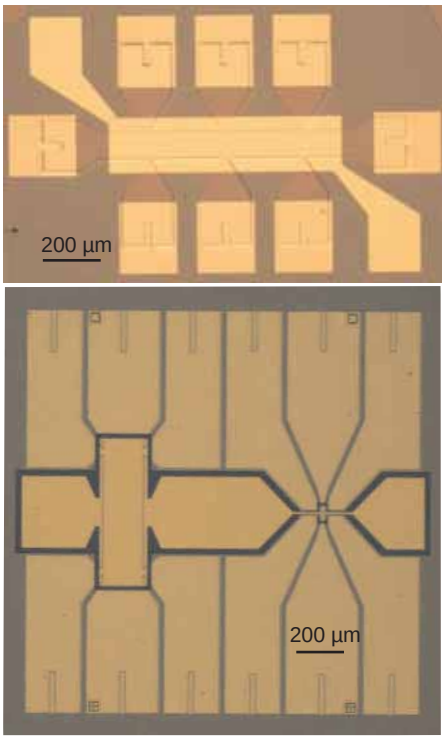

Fig. 1. Hall bar structures with various dimensions for transport properties verification and comparison of processing steps. Profles of dry (left) and wet (right) etching.

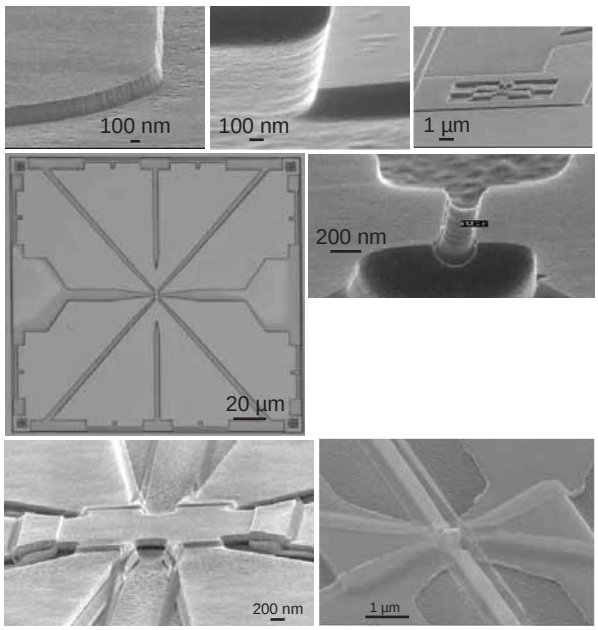

Fig. 2. Structures obtained with wet etching: after mesa etch and final devices.

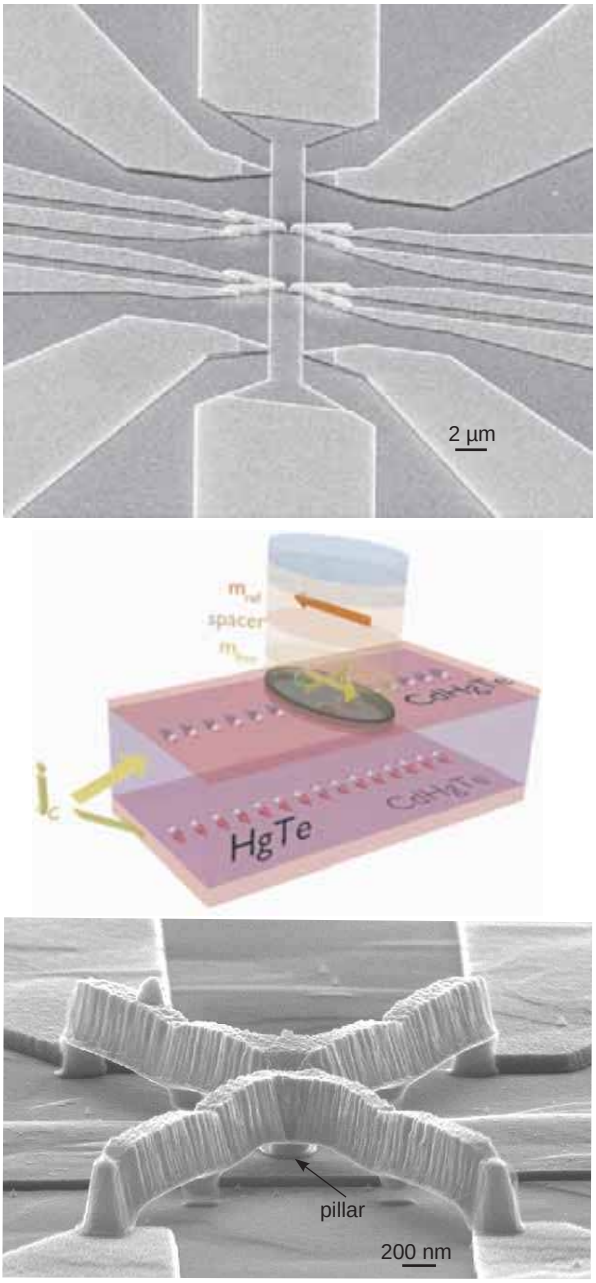

Fig. 3. A complex device for current induced magnetization switching in a CoFe/Cu/NiFe pillar on top of a TI (CdHgTe/HgTe/ CdHgTe/CdTe): fabrication consists of six steps including air-bridges of ∼100 nm resolution.

References

[1] M.König, S. Wiedmann C. Brüne, *et al*, *Science*. **518**, 76677 (2007).

[2] T. Borzenko, C. Gould, G. Schmidt, L.W. Molenkamp *Microelectronic Engineering* **75** (2) 210215 (2004).

28th Int. Symp. "Nanostructures: Physics and Technology"
Minsk, Belarus, September 2020

Formation and phase transformations of platinum silicide films at the interface of platinum and polycrystalline silicon at low temperatures

K.V. Chizh[1], V.M. Senkov[2], I.V. Pirshin[2], A.S. Orekhov[3], V.P. Dubkov[2], L.V. Arapkina[2], S.A. Mironov[2] and V.A. Yuryev[2]

[1] A.M. Prokhorov General Physics Institute of the Russian Academy of Sciences, Moscow, Russia
[2] P.N. Lebedev Physical Institute of the Russian Academy of Sciences, Moscow, Russia
[3] A.V. Shubnikov Institute of Crystallography of Federal Research Center "Crystallography and Photonics" of the Russian Academy of Sciences, Moscow, Russia

Abstract. Phase formation and transitions in platinum silicide films on polycrystalline Si in the process of Pt magnetron sputtering and heat treatments at different temperatures are studied using X-ray photoelectron spectroscopy, high-resolution transmission electron microscopy and X-ray diffractometry. Phases of amorphous and polycrystalline Pt_3Si and Pt_2Si are shown to form during the room-temperature Pt deposition on poly-Si beneath the Pt layer. The relaxation of the interfacial film and partial transformation of Pt_3Si into Pt_2Si result from the annealing at the temperatures up to 300 °C. The Pt_3Si and Pt_2Si phases crystallize to PtSi due to annealing at the temperatures up to 480 °C.

Introduction

Platinum silicides are widely applied in microelectronic industry due to their compatibility with the CMOS technology. The metallic nature of the conductivity, low electrical resistance and thermal stability make them an optimal material in the production of Schottky diodes [1], IR detectors [2], field-effect transistor gates, MEMS technology and the metallic conjunctions in microchips [1]. In the last decade, platinum silicides applications in the quantum wires [3], quantum dots and nanostructures based on them were reported. In this paper, the phase composition and the structure of an interfacial layer, originating between a magnetron sputtered platinum film and a poly-Si layer formed on a Si_3N_4/SiO_2/c-Si dielectric substrate, which is widely used in MEMS technology [4], during the room-temperature magnetron sputtering of Pt followed by the annealing at the temperatures ranging from 100 °C to 500 °C for 30 min, are studied using X-ray photoelectron spectroscopy (XPS), high-resolution transmission electron microscopy (HR TEM) and X-ray diffractometry (XRD).

1. Experimental

Structures with Pt silicide/poly-Si films were formed on Si wafers ($\rho = 12\Omega$·cm, (100)-oriented, p-type) coated by a 527 nm thick layer of SiO_2 formed by the thermal oxidation and a 180 nm thick layer of pyrolytic Si_3N_4. A film of poly-Si with the thicknesses of 120 nm was deposited using CVD; then it was doped by the implantation of P^+ ions ($E_{P+} = 60$ keV) to the dose of 1.25×10^{14} cm^{-2} and annealing at 850 °C for 30 min. A (20–22) nm thick layer of Pt was deposited on the poly-Si layer by the magnetron sputtering at room temperature. Platinum silicides were formed by annealing of the formed structure at different temperatures ranging from 125 °C to 480 °C for 30 min in the atmosphere of Ar. Unreacted platinum was removed by chemical etching in a warm aqueous solution of aqua regia $H_2O : HCl : HNO_3$ [4 : 3 : 1] for about 15 min. The XPS study was carried out in the analytical chamber of the Riber SSC2 UHV surface science center, equipped with cylindrical mirror type (CMA) electron energy analyzer (Riber EA 150). Non-monochromatic Al $K_{\alpha1,2}$ X-ray radiation ($h\nu = 1486.6$ eV) generated at the source power of 180 W was used for the photoexcitation. HR TEM analysis was performed using FEI TITAN 80–300 microscope equipped with a Cs probe corrector and operated at the accelerating voltage of 300 kV. X-ray phase analysis was carried out with a D2 PHASER diffractometer (Bruker). The measurements were carried out in the ranges of diffraction angles (2θ) from 15 ° to 60 ° and from 71 ° to 115 °,

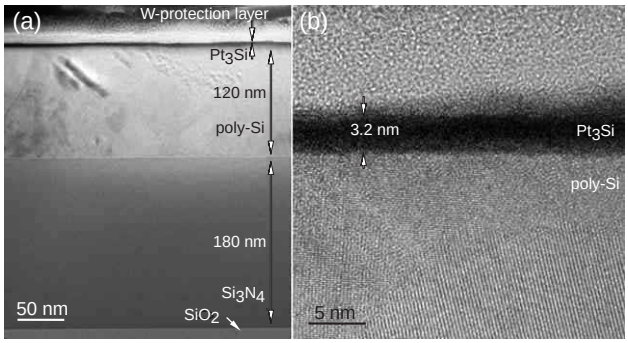

Fig. 1. A TEM image of a c-Si/SiO_2/Si_3N_4/poly-Si/Pt_3Si sample cross-section after magnetron sputtering of Pt followed by Pt wet etching (a) and a HR TEM image of the Pt_3Si/poly-Si interface (b).

2. Result and discussion

In the STEM micrograph of the cross section of the initial structure (Fig. 1), a uniform layer of 3 to 5 nm thick with the atomically sharp borders is shown. The formed film prevents further migration of atoms to the bulk, which explains the presence of unreacted platinum on the surface. Chemical removing of pure metal Pt enabled the determination of chemical composition of the interfacial layers using XPS. It has been obtained that the layer formed after Pt deposition without annealing consists mainly of the Pt_3Si compound and in lesser degree of Pt_2Si. This is consistent with our previous data [5]. The data obtained by the X-ray diffraction have shown that

a part of the Pt_3Si silicide forms a crystalline phase in this sample.

Heat treatment of samples at $T = 125$ °C leads to the relaxation of the compressive strain in the interfacial film that results in the equalization of the Pt_3Si and Pt_2Si signals in the Pt 4*f* photoemission peak indicating an increase in the Pt_2Si content in the interfacial layer, while Pt_3Si phase content goes down. This is proofed with X-ray diffraction data, which show that Pt_3Si signal ($2\theta = 39.80$ °) decreases. When the contents of Pt_3Si and Pt_2Si become approximately equal, the phase composition of the interfacial film remains stable until the annealing temperature exceeds 214 °C [6].

An increase of the annealing temperature to $T = 250$ °C causes a decrease in the Pt_3Si signal, which can be explained by the gradual transformation of this phase to the Pt_2Si compound and by the diffusion of Pt atoms into the silicon bulk activated at this temperature [6].

The XPS spectrum of the Pt 4*f* core line of the sample annealed at $T = 350$ °C reveals the presence of the PtSi phase, while Pt_3Si content sufficiently decreases [6].

Heat treatment of samples at $T = 400$ °C causes a sharp increase in the PtSi signal, which begins dominating the spectrum. Finally, Pt 4*f* spectrum of the sample annealed at $T = 480$ °C almost entirely consists of the PtSi signal, which indicates the completion of the Pt/poly-Si interface [6]. These data are in good agreement with the results of the X-ray diffractometry, according to which the diffraction patterns obtained from the heat-treated samples at the temperatures from 320 °C to 480 °C present intense peaks of PtSi, while the signals from Pt_3Si and Pt_2Si are not detected (Fig. 2).

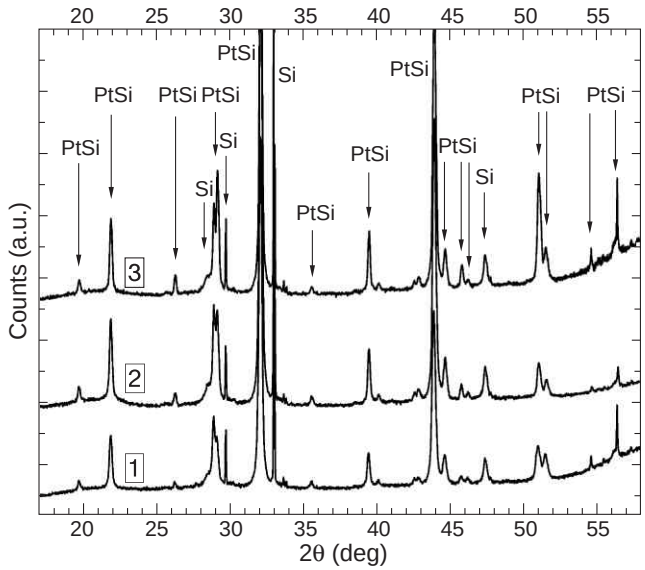

Fig. 2. Diffraction patterns (mixed CuK_α and CuK_β) of the samples heat-treated at 320 °C (curve 1), 400 °C (curve 2) and 480 °C (curve 3), respectively, recorded within the angle range $2\theta = 17°$ to 58°; for clarity, the curves are offset vertically.

This study shows that the kinetics of PtSi film formation at the platinum–silicon interface under appropriate thermal treatment are very similar, if polycrystalline or monocrystalline silicon substrates are used, but there are significant differences as well. The first one is the presence of unreacted platinum on each poly-Si sample after annealing in this study, while on monocrystalline silicon, all platinum deposited under ultra-high vacuum conditions is consumed during heat treatment. The next distinction is that the diffusion is activated at the temperature about 250 °C on the poly-Si surface, while this takes place at 190 °C to 200 °C for the monocrystalline Si substrates. Finally, the diffusion in the layers studied in this work is slower compared to that occurring in the films formed on the monocrystalline Si substrates.

3. Conclusion

In summary, it is shown that the metal-enriched interfacial film formed on the surface of poly-Si beneath a layer of the magnetron sputtered platinum consists of Pt_3Si and Pt_2Si silicides being in amorphous and crystalline states.

Sample heating in the temperature range from 125 °C to 214 °C for 30 minutes causes the interfacial film relaxation via the partial transition of Pt_3Si to Pt_2Si. Further increase in the annealing temperature leads to the further reduction of the Pt_3Si phase content in the layer; this phase is detected up to annealing temperature of 350 °C. At annealing temperatures from 320 °C to 480 °C, the transition of Pt_3Si and Pt_2Si phases into the PtSi phase occurs.

Acknowledgements

The research was conducted under the financial support of the BRFFR project number T18P-190 and the RFBR grant number 18-52-00033.

The Center for Collective Use of Scientific Equipment of GPI RAS supported this research via presenting admittance to its equipment.

TEM measurements were performed with financial support of the Ministry of Science and Higher Education of the Russian Federation within the state assignment for the Federal Scientific Research Centre “Crystallography and Photonics” of the Russian Academy of Sciences.

References

[1] S.P. Murarka, *Silicides for VLSI Applications*, (New York: Academic Press), p. 200, 1983.

[2] V.A. Yuryev, K.V. Chizh, V.A. Chapnin *et al*, *Proc. SPIE Microtechnologies (Barcelona, Spain, 2015)*, SPIE, 95190K, 2015.

[3] Y.C. Lin, K.C. Lu, W.W. Wu *et al*, *Nano Lett.* **8**, 913–918 (2008).

[4] F. Komarov, O. Milchanin, T. Kovalyova *et al*, *9th Int. Conf. “Interaction of Radiation with Solids” (Belarus, Minsk, 2011)*, p. 367, 2011.

[5] M.S. Storozhevykh, V.P. Dubkov, L.V. Arapkina *et al*, *Proc. SPIE Microtechnologies (Barcelona, Spain, 2017)*, SPIE, 102480O, 2017.

[6] K.V. Chizh, V.P. Dubkov, V.M. Senkov *et al*, *arXiv:2002.11189*, (2020).

28th Int. Symp. "Nanostructures: Physics and Technology"
Minsk, Belarus, September 2020

Structure and magnetic properties of the FeCo films reduced by carbohydrates

C. Denisova[1,2], L.A. Chekanova[1], S.V. Komogortsev[1,2], I.V. Nemtsev[3], Yu.L. Mihlin[4] and R.S. Iskhakov[1]

[1] Kirensky Institute of Physics, Federal Research Center KSC SB RAS, 660036, Krasnoyarsk, Russia
[2] Siberian Federal University, 660041, Krasnoyarsk, Russia
[3] Krasnoyarsk Scientific Center, Federal Research Center KSC SB RAS,660036, Krasnoyarsk, Russia
[4] Institute of Chemistry and Chemical Technology SB Russian Academy of Sciences, 660036, Krasnoyarsk, Russia

Abstract. The structural and magnetic properties of FeCo films produced by electroless plating with different carbohydrates as reducing agents have been investigated. The surface morphology and coercivities of FeCo films are dependent on the iron content and type of reducing agent. The local magnetic anisotropy field value increases with a decrease in Fe content. For all systems, deposits with good soft magnetic properties were obtained, with coercivities less than 15 Oe and saturation magnetizations close to 220 emu/g for the $Fe_{70}Co_{30}$ film. The best soft magnetic properties corresponded to the deposits with bcc structure and grain sizes less than 20 nm.

Introduction

Soft magnetic films have been widely used in the fields of magnetic recordings, magnetic sensors [1–2]. As a kind of typical soft magnetic materials, CoFe alloy films exhibit superior magnetic properties such as high Curie temperature, low coercivity, low magneto-crystalline anisotropy, high permeability and high saturation magnetization (can reach up to 245 emu/g). The magnetic properties of CoFe films depend on their morphology, crystal structure and composition. Although there are many methods available for the preparation of CoFe films, such as sputtering, molecular beam epitaxy, ion beam deposition, electrodeposition and so on [3–5]. Electroless plating shows low cost and no size or shape limit for the preparation of nano-scale films. On one hand, electroless deposition represents a simple, cost-effective way of fabricating FeCo film [6]. However, use of conventional reducing agents (sodium hypophosphite or borohydride, hydrazine) leads to significant contaminations with phosphorus and boron in deposited films damaging the magnetic performance. On the other hand, researchers found that polysaccharides (e.g. chitosan, cellulose) could be an efficient, low-cost, and environmental alternative to conventional reducing agents [7]. Herein, we report a facile and highly efficient method for fabricating nanostructured FeCo films. The FeCo alloy was directly synthesized on copper supports via electroless deposition with different carbohydrates as reducing agents (arabinogalactan, starch, sucrose), the composition of which can be easily controlled by changing the concentration of metal salt in the solution. Magnetic studies of these films which exhibit high saturation magnetization are also reported in this work.

1. Experimental

The FeCo films were prepared by electroless reduction of metals from aqueous solutions of the corresponding salts at 80 °C. We used several types of reducing agents: arabinogalactan, starch and sucrose. The morphology of the deposited films was analyzed with scanning electron microscopy (SEM: Hitachi S-5500). Compositional analyses were performed via energy dispersive X-ray spectroscopy (EDS) associated with SEM. X-ray photoelectron spectroscopy (XPS) studies were performed using a SPECS spectrometer equipped with a PHOIBOS 150 MCD-9 analyzer employing monochromatic Al Kα radiation (1486.6 eV) of an X-ray tube. Measurements performed on equipment of the Krasnoyarsk Regional Center of Research Equipment of Federal Research Center "Krasnoyarsk Science Center SB RAS". Structural analysis of the studied systems was carried out using X-ray diffraction (Cu-Kα). The magnetic properties were investigated using a vibrating sample magnetometer. Information on local anisotropy field H_α is obtained from investigation of approach magnetization to saturation law.

2. Results and discussion

The surface morphologies of the obtained samples are shown in Fig. 1. The morphology of the samples can be varied by changing the Fe/Co molar ratio. With increase of Fe content in the film for all types of reducing agents, the surface morphology of the samples changed greatly, as shown in Fig. 1a and b.

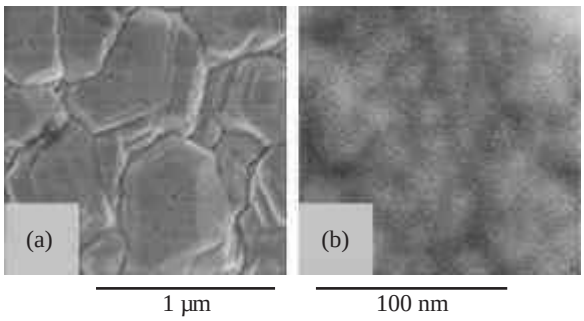

Fig. 1. SEM imagines of the FeCo films, produced with sucrose as reducing agent (a) $Fe_{94}Co_6$; (b) $Fe_{14}Co_{86}$.

The metallized surfaces consist of agglomerates of spheroidal particles for FeCo films with Fe/Co< 0.4. Replacing the arabinogalactan with a sucrose produced surfaces comprised of larger, more faceted metal particles in case Fe/Co> 0.5. The glycosidic bonds forming the carbohydrates molecules are stable at a low temperature. However, synthesis of FeCo films carried out at bath temperature 80 °C at in an alkaline medium. The carbohydrates degradation occurs at the ends

of the molecules under such conditions. Aldehyde groups at the ends of molecules have reduction properties. Thus, the monosaccharide unit is separated and then oxidized to a carboxylic acid. Therefore, it can be assumed that the formation of a metal film is due to decomposition of the carbohydrates. This assumption is confirmed by the presence of carboxyl group lines in the X-ray photoelectron spectra. According to the results of X-ray photoelectron spectroscopy studies, carbon concentration in FeCo(C) alloy does not exceed $\sim$ 1.4 at % for all film series. The XRD patterns of FeCo-C films revealed peaks that perfectly matched with those of the bcc phase of CoFe or fcc-Cu substrate and no oxides phases were observed within the detection limits of the X-ray diffractometer. The average crystallite size calculated using the Scherrer formula for the all types of reducing agents was in rage 10–27 nm. The bcc structure is found to be stable even for films with very high concentration of Co ($\sim$ 0.85) beyond the thermodynamically stable bcc regime for bulk $Fe_{1-x}Co_x$ alloys ($0 < x < 0.25$ [8].

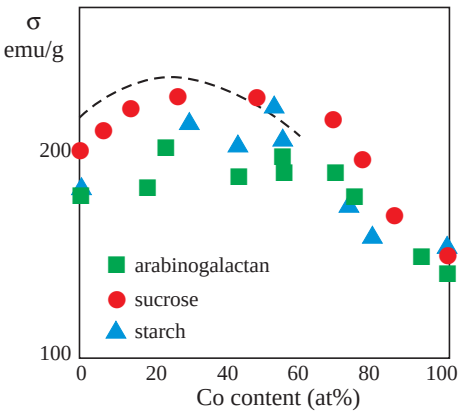

Fig. 2. The saturation magnetization of FeCo films produced with different types of reducing agent as a function of cobalt content. Data [2] is shown by the dashed line.

Magnetic parameters such as the saturation magnetization, the coercivity of the films were studied as a function of Fe content. The data show a strong dependence of the magnetic parameters on the iron content. The saturation magnetization dependences of the FeCo films as expected were nonlinear (see Fig.2). The magnetization values of the samples are relatively higher than those of the usual FeCo-C alloy. It is mainly due to carbon is not included in the FeCo lattice. For all systems, deposits with good soft magnetic properties were obtained, with coercivities less than 15 Oe and saturation magnetizations close to 220 emu/g for the $Fe_{70}Co_{30}$ film. The best soft magnetic properties corresponded to the deposits with bcc structure and grain sizes less than 20 nm. Approach magnetization to saturation in the log-log plot follows $M(H) \sim H^{-2}$ dependence for H from 3 to 12 kOe for all film series. Magnetization approaches to saturation as $M \sim H^{-a}$ with $0.75 < a < 1.1$ in the field range from 1 to 3–6 kOe. Such behavior indicates that the FeCo alloy is nanocrystalline [9]. It was found that the local anisotropy field for all series of FeCo alloys depends on Fe content. The H_α value increases with a decrease in Fe content.

Conclusions

In summary, the FeCo films were synthesized by electroless plating with arabinogalactan (natural polysaccharides), starch and sucrose as nontoxic reducing agents. It was found that Fe concentration and type of reducing agent affect the surface morphology. Maximum of saturation magnetization magnitude is 220 emu/g for $Fe_{70}Co_{30}$ films. The local anisotropy field value increases with a decrease in Fe content for all series of FeCo alloys.

Acknowledgement

This work was supported by the Russian Foundation for Basic Research, the Government of the Krasnoyarsk Territory, the Krasnoyarsk Regional Fund for the Support of Scientific and Technical Activities (project No. 18-42-240006. Nanomaterials with magnetic properties determined by the topological features of the nanostructure).

References

[1] M. Alper, H. Kockar, T. Sahin *et al*, *IEEE Transaction on magnetics* **46**, 390 (2010).
[2] C. Rizal, J. Kolthammer, R.K. Pokharel *et al*, Choi, *Journal of Applied Physics* **113**, 113905 (2013).
[3] P.Wetzel, P.Bertoncini, D.Berling *et al*, *Surface Science* **499**, 210 (2002).
[4] S. Amsarajan, B.R. Jagirdar, *Journal of Alloys and Compounds* **816**, 152632 (2020).
[5] T. Yanai, K. Shiraishi, Y. Watanabe *et al*, *Journal of Applied Physics* **117**, 17A925 (2015).
[6] K. Sun, K. Wang, T.Yu *et al*, *International journal of hydrogen energy* **44**, 1328 (2019).
[7] S. Machado, S.L. Pinto, J.P. Grosso *et al*, *Sci. Total Environ.* **445–446**, 1 (2013).
[8] H.P.J. Wijn (Ed.), *Magnetic Properties of Metals d-elements, Alloys and Compounds (Data in Science and Technology)*, Springer, 1991.
[9] R.S. Iskhakov, S.V. Komogortsev, *Bulletin of the RAS: Physics* **71**, 1620 (2007).

28th Int. Symp. "Nanostructures: Physics and Technology"
Minsk, Belarus, September 2020

Angular divergence decreasing of X-ray fluxes

V.K. Egorov[1], E.V. Egorov[1,2]

[1] IMT RAS, 142432 Chernogolovka, Russia
[2] Financial University under the goverment of Russian Federation, Moscow, Russia

Abstract. Work presents short description the waveguide-resonance phenomenon of X-ray quasimonochromatic radiation fluxes featured for nanosize planar extended slit clearances. There are discussed advantages and shortages of the device functioned in frame of the phenomenon — the planar X-ray waveguide-resonator (PXWR). The composite planar X-ray waveguide-resonator (CPXWR) use allowed to decrease the angular divergence of its emergent beam. Simplified model of this device functioning is formulated.

It is well known that the X-ray beam diagnostics of materials is the most widespread and universal means of its properties investigation. In result time, specific devices for the nanosize objects analysis by X-ray methods were elaborated. There are planar X-ray waveguide-resonance structures. Planar X-ray waveguide-resonator (PXWR) is the simplest device from the structures set. Main feature of these devices is the functioning in frame of the waveguide-resonance radiation propagation phenomenon. The phenomenon discovery was result of the creative rethinking of literature data and our systematic experimental investigations. Our systematic investigations of X-ray quasimonochromatic flux propagation through the extended slit clearance in conditions showed that the nanosize slit clearance transports X-ray radiation fluxes by the specific mechanism, which did not mention early. We called the mechanism as the waveguide-resonance radiation propagation one and understood that it is the fundamental phenomenon. Devices functioned in frame of the phenomenon we called planar X-ray waveguide-resonators.

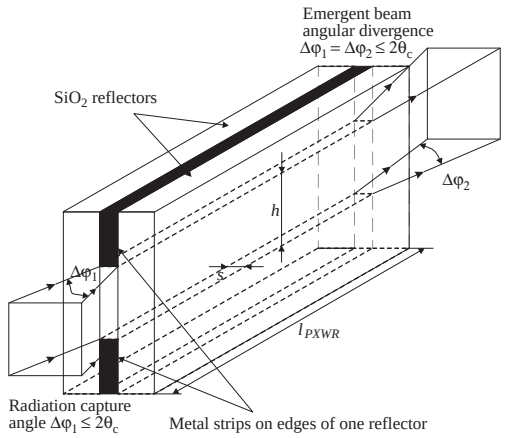

Fig. 1. Scheme of X-ray initial flux capture by entrance cut of PXWR simplest design and emergent beam formation by this device.

Construction of the planar X-ray waveguide-resonator is shown on Figure 1. It device captured of X-ray quasimonochromatic flux by its entrance cut in the angular range, which can not exceed the double critical angle of the radiation total reflection for reflectors material, transports the flux almost without attenuation and forms X-ray emergent beam. It is significant that the emergent divergence angle is equal to the radiation capture angle. The conception allowed to build the model of X-ray flux waveguide-resonance propagation which was based on the revolutionary hypothesis about the uniform interference field of X-ray standing wave arising in all space of the planar extended slit clearance. This situation is characterized by the principle difference from the multiple flux total reflection in the planar extended slit clearance. The difference is readily illustrated by the Figure 2. X-ray flux of the quasimonochromatic radiation in the wide slit clearance undergoes the multiple external total reflection with set appearing of the local interference fields of X-ray standing wave (Fig. 2a). The longitudinal size of local interference areas is defined by the radiation coherent length parameter value L and the traverse size is equal to half of it in line with the expression [7]:

$$c = L/2 = \lambda_0^2/2\Delta\lambda_0 \quad (1)$$

where λ_0 is the main wavelength of the radiation, $\Delta\lambda_0$ is the radiation monochromatization degree. Because of the interference field is excited not only in the space under material interface but in the reflector material volumes the minimum flux attenuation can be achieved in conditions of the phase-conjugation consecutive reflections, only. In the conjugation violation case, X-ray flux attenuation increases owing to reexcitation the interference field in reflectors volumes. X-ray flux transportation conditions will change when the distance between reflectors is smaller as half of the radiation coherence length magnitude. This case is characterized by the local interference field areas confluence and the uniform interference field of X-ray standing wave arising in all space of the planar extended slit clearance (Fig. 2b). The arising of uniform interference field is the necessary and sufficiency condition for the realization of X-ray flux waveguide-resonance propagation mechanism through the planar extended slit clearance. The mechanism allows to propagate X-ray flux captured under any angles, which are smaller as the total external reflection critical angle almost without attenuation realizing the radiation superfluidity effect.

PXWR of simplest construction demonstrates other specific peculiarities. It is well known that coherence lengthes of the characteristic radiation generated by laboratory X-ray sources are characterized by nanosize magnitudes. For example, the coherence length of CuKα radiation is equal to 430 nm. Our systematic investigations of emergent beam propagation through extended slit clearances with distances between reflectors, which were smaller as half of the transported radiation flux coherence length showed that beams had nanosize width and heightened radiation density exceeding its parameter in beams formed by slit-cut systems on 3–4 orders. These facts were very useful for the element material diagnostics improving by TXRF method.

In spite of PXWR evident merits this device is characterized by essential shortage. Its emergent beam demonstrates the angular divergence near 0.1 degree. This magnitude is not great but owing it existence the emergent beam losses its main advantage on distance of some centimeters from PXWR outlet. So, the fundamental task of PXWR modification is the search of approaches for the angular divergence decreasing.

Experimental search of waveguide-resonance constructions allowed to decrease its emergent beam angular divergence in comparison with the radiation capture angle without reduction of its integral intensity offered to elaboration of modified PXWR designs. Simplest solution of the task was connected with the waveguide-

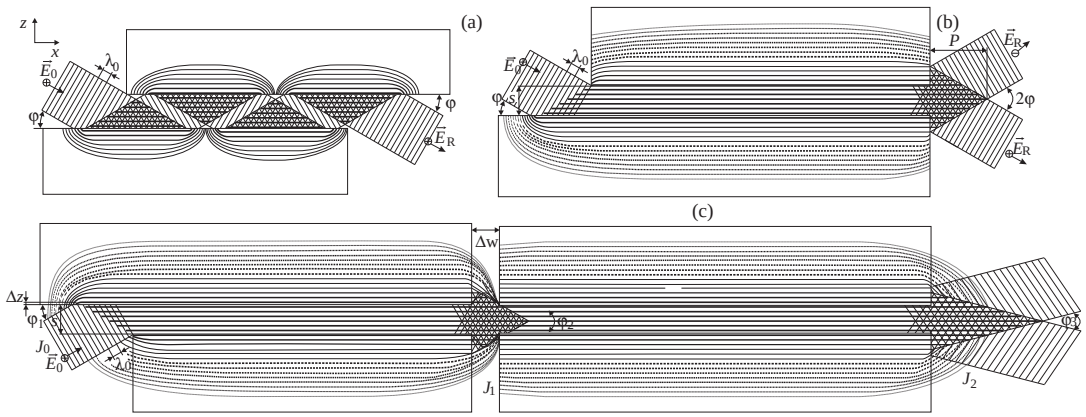

Fig. 2. Schemes of X-ray quasimonochromatic flux transportation visualization by the planar extended slit clearence in case of great distance S between reflectors (a) and small magnitude of the distance (b). P is the protrusion parameter of the uniform interference field. The model of X-ray flux partial angular tunneling in the CPXWR (c).

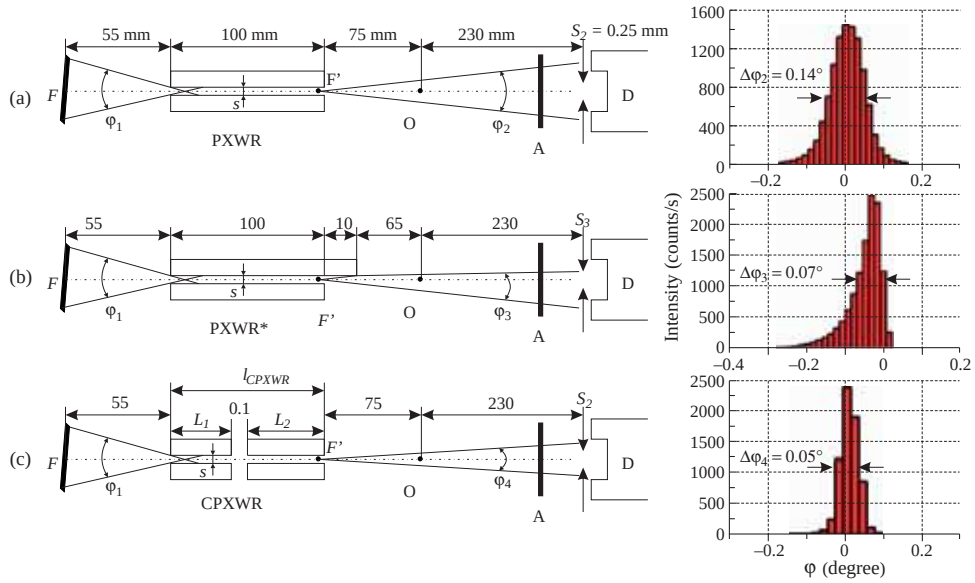

Fig. 3. Schemes of X-ray quasimonochromatic beams formation by simplest PXWR, waveguide-resonator built on base (a) of nonequivalent length reflectors (b) and composite waveguide-resonator and intensity spatial distributions in emergent beams of its devices.

resonance device arrangement by nonequivalent length reflectors. But the cardinal solution of the emergent beam divergence decresing can be executed by use the composite planar X-ray waveguide-resonator in result of the beam partials tunneling effect (Fig. 2c). Specific approach allowed to built the original construction completed by two PXWR of simplest design, which were installed one after another on some distance with execution of its mutual alignment. Comparative experimental data reflected spatial intensity distributions characteristics for emergent beams formed by PXWR with simplest design, PXWR with nonequivalent length reflectors and composite PXWR are presented on Fig. 3. The waveguide-resonance device built on base of nonequivalent length reflectors decreases the divergence angle by 50 per cents, at the integral intensity conservation. But the device application distorts form of the intensity spatial distribution. At the same time, CPXWR use for the X-beam formation reduces the intensity spatial distribution divergence at conservation of the integral intensity and form of the distribution.

Experimental investigations showed that the composite wave guide-resonator demonstrates its unique properties at the specific conditions realization. Conservation of X-ray flux integral intensity is possible if the distance (gap) between PXWRs compiling CPXWR is not exceed the protrusion parameter P (Fig. 2b) defined by the expression:

$$P = \lambda_0^3 / 8\Delta\lambda_0^2 \tag{2}$$

The composite waveguide-resonator function is result of the X-ray flux partial angular tunneling in the gap between PXWR. Moreover, experimental investigations showed that the angular divergence value of its emergent beam is depended on value of the gap. The function connection determination remains in perspective. At the same time, the precision diffraction measurements showed that the emergent beam angular divergence reduction is accompanied by the radiation monochromatization worsening. In the result, the model of CPXWR functioning, which took into account the Liouville theorem demands was elaborated. Accordingly to this model the connection between the monochromatization worsening $\delta\lambda$ and the angular divergence decreasing $(\varphi_1 - \varphi_2)$ is defined by the expression:

$$\delta\lambda = \varphi_1\lambda_0(\varphi_1 - \varphi_2) \tag{3}$$

where φ_1 is the angle of the initial flux radiation capture, φ_2 is the angular divergence of emergent beam. In the result, the monochromatization degree of the emergent beam will be described by the expression:

$$\Delta\lambda_2 = \Delta\lambda_0 + \varphi_1\lambda_0(\varphi_1 - \varphi_2) \tag{4}$$

CPXWR is very useful for TXRF measurements but it application for diffractometry has limited perspectives.

28th Int. Symp. "Nanostructures: Physics and Technology"
Minsk, Belarus, September 2020

Laser assisted fabrication of surface oxide nanostructures for photovoltaic applications

E.A. Shustova, N.N. Tarasenka, A.A. Nevar, V.G. Kornev, A.V. Butsen and N.V. Tarasenko
B.I. Stepanov Institute of Physics of National Academy of Sciences of Belarus

Abstract. The paper discusses the application of laser-assisted processes for synthesis of oxides nanoparticles (NPs) and their assembling into the nanostructured thin films. The study of the laser parameters influence on the NPs formation and thin film deposition conditions allowed to find optimal conditions for the formation of ZnO, CuO colloidal NPs as well as ZnO/CuO nanostructured thin films suitable for practical applications. The morphology, structure, as well as electronic and optical characteristics of the formed oxide nanostructures were studied and their potential optoelectronic and photovoltaic applications are discussed.

Introduction

Fabrication of nanostructured thin film layers with well-defined morphology and chemical composition of structural elements is crucial for achieving their unique properties attractive for practical applications in microelectronics and photonics as light sources, thermoelectric elements, detectors, memory elements, solar batteries, etc. As the functional properties of the nanostructured layers are largely determined by composition, size, morphology and surface properties of the nanoparticles (NPs) forming the layers, fabrication of novel nanostructured devices implies development of the effective methods for generation of NPs with desired parameters and for assembling them into ordered structures as specific building blocks. Laser-assisted methods, that recently have been shown to have a large potential for preparation of NPs of different composition with well tailored size and surface properties can be considered as a relatively simple and powerful technique for nanostructured devices fabrication. Namely, laser ablation in liquids technique can produce spherical colloidal NPs of different materials [1–3]. Afterwards, colloidal NPs prepared by this technique can be incorporated into polymer and glass matrices and can also be deposited as thin films. Several techniques have been reported in literature, describing the assembly of colloidal NPs into organized structures, including gravity sedimentation, electrophoretic assembly, spin- or dip-coating, self-assembly and directed self-organization. These deposition methods are quite simple and cheap, but they do not ensure a good control of the deposited film thickness and uniform coverage of the substrate. That is why the development of novel and more effective deposition approaches, like laser assisted technique can be considered as a very attractive alternative. However, the most common methods of laser deposition of NPs, such as the LDMS-laser deposition of metals from solutions, LIFT-laser-induced forward transfer, LCVD-laser chemical vacuum deposition, and others allow fabricating mainly the films of metallic particles.

In this paper laser assisted techniques based on pulsed laser ablation (LA) in liquid were developed for fabrication of oxide (ZnO, CuO) NPs and the prepared colloidal NPs were used for assembling into nanostructured layers aiming to fabricate ZnO/CuO heterojunctions for their potential applications in photovoltaics and optoelectronics.

1. Experimental

Laser ablation experiments were carried out by focusing the radiation of a Nd:YAG laser (LOTIS TII, LS2134D), operating in a double-pulse mode at 1064 nm (energy 80 mJ/pulse, repetition rate 10 Hz, pulse duration 8 ns), on the surface of a relevant target placed in the cell filled with a liquid (water or acetone). The temporal delay between two collinear laser pulses could be varied in the range 0–120 μs. In order to provide control over the NPs formation process the plasma parameters were investigated using optical emission spectroscopy. For laser-induced modification of the formed colloids the unfocused beam of the second harmonic (wavelength 532 nm) of the same Nd:YAG laser was used. After the preparation, the obtained NPs were studied using optical absorption and Raman spectroscopy, transmission and scanning electron microscopy, electron and X-Ray diffraction.

To clarify the possibility of using the prepared NPs in a range of energy-relevant applications we have investigated the properties of the nanostructured thin films deposited from the synthesized colloids. For this, ZnO and CuO colloidal solutions were spray-coated on the indium tin oxide (ITO) coated glass substrates and annealed at 270 °C.

2. Results and discussion

The developed LA technique was shown to be suitable for preparation of particles with desired compositions and morphologies and with sizes in the nanometric range (of 5–30 nm in diameters). The ability of manipulating and controlling the fabrication of oxide NPs together with the capabilities of laser-induced modification of their morphology and structure was demonstrated. The main factors that determine the final composition and morphology of the NPs produced by LA in liquid have been analyzed. The control of stability, size, stoichiometry, crystallinity and chemical composition of the formed particles has been achieved by a proper selection of several experimental parameters such as laser fluence, interpulse delay, a sort of liquid used and post ablation irradiation conditions.

The influence of the interpulse delay on the optical properties and size of the prepared ZnO NPs are demonstrated in Fig. 1. As can be seen, for all interpulse delays the exciton band was observed at around 350 nm that is lower than the wavelength corresponding to the bandgap of bulk ZnO (388 nm) that implies the formation of the NPs of zinc oxide in the solution. The intensity of the exciton bands that is related to

the production efficiency is also dependent on the interpulse delay and is maximal for the interpulse delay of 10 μs. The bandgap *(Eg)* values can be estimated from absorption coefficient (α) dependence on the incident photon energy *($h\nu$)* using the Tauc relation $\alpha h\nu = A(h\nu - Eg)^n$ where A is a constant that depends on the transition probability, and n is an index that characterizes the optical absorption process and is 2 for indirect semiconductors and 1/2 for direct ones. As ZnO is the direct bandgap semiconductor material the intersection of linear fits of $(\alpha h\nu)^{1/n}$ versus $h\nu$ plots to the $h\nu$-axis allows to estimate the bandgap. The results of bandgap calculation are presented in Fig. 1. The dependence of the bandgap values may correlate with the bubble dynamics that has an impact on the NPs formation and growth process [3].

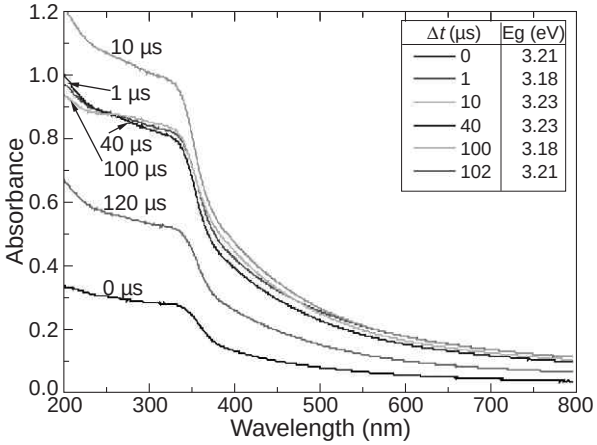

Fig. 1. UV-Vis spectra of the colloids prepared by double pulse LA of Zn target in distilled water using different interpulse delays.

Apart from the laser parameters, the result of the laser synthesis depends on the composition of the target to be ablated and the liquid used. To find the optimal conditions for CuO nanostructures formation and to study the influence of these parameters, laser ablation of Cu as well as CuO targets was performed in both water and acetone. It was found that laser ablation of both targets in water results in the oxides NPs formation and no characteristic plasmon band around 580 nm typical to metal Cu NPs was observed. This may be related to high reactivity of the initially formed copper clusters that leads to their interaction with the surrounding water and formation of copper oxide NPs or core-shell Cu@CuO nanostructures. The situation is different if acetone is used as a solvent. In the latter case ablation of both Cu as well as CuO targets results in the formation of metallic Cu NPs proved by the observation of the plasmonic band in the spectra of both samples. These results may indicate that the copper oxide NPs most likely are formed not through direct ejection from the target surface but CuO formation process includes the production of Cu atoms and small clusters which are then oxidized in a liquid.

However, after additional laser irradiation of the prepared colloids with the unfocused beam of the second harmonic (wavelength 532 nm) of the Nd:YAG laser all the colloids demonstrated complete disappearance of the surface plasmon band, implying that metallic particles were oxidized and the product was eventually transformed to CuO NPs. This proves that additional laser treatment may serve as a tool to control not only NPs morphology but also composition and inner structure.

Scanning electron microscopy was used to study the morphology of the fabricated films. As can be seen from the SEM images of the ZnO and ZnO/CuO structures deposited on glass substrate and annealed at 270 °C (Fig. 2), the resulting structures are fairly uniform and consist of densely packed round-shaped nanosized particles with diameters in the range 70–130 nm. The deposited films are practically free of pinholes and cracks. In order to measure the thickness of deposited layer, the samples were cut and SEM images of the cross sections were taken, which are shown in the insets to Fig. 2. The deposited layers on the substrate are clearly seen. The thickness of the deposited ZnO layer (Fig. 2a) was estimated to be approximately 135 nm while the thickness of the bi-layer ZnO/CuO structure was estimated to be around 950 nm.

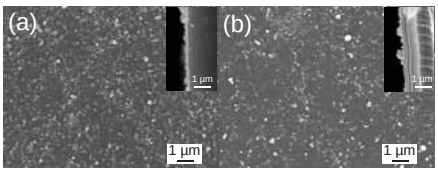

Fig. 2. Surface SEM microphotographs of the ZnO and bilayer ZnO/CuO films deposited on a glass substrate with cross-sectional SEM images of these samples in the insets.

To confirm a concept of the potential photovoltaic applications of the formed NPs, a bilayer solar cell comprised of p-CuO and n-ZnO heterojunction interface was fabricated on the ITO substrate. It is expected that the low dimensional bilayer structure of NPs could provide a large surface area for more efficient light absorption and better carrier collection compared to the bulk materials due to the reduced collection length of charge carriers responsible for increasing power conversion efficiency.

hus, the method of laser ablation in liquids can be an effective tool for preparation of metal oxide colloidal (ZnO, CuO) NPs and assembling them into nanostructured layers for photovoltaic, photodetector and sensing applications.

Acknowledgement

The work was supported by the National Academy of Sciences of Belarus under project Convergence 2.4.06.

References

[1] D. Zhang, B. Gökce and S. Barcikowski, *Chem. Rev.* **117**, 3990 (2017).

[2] N. Tarasenka, V. Pankov and N. Tarasenko, *Nano-Structures & Nano-Objects* **12**, 210 (2017).

[3] M. Dell'Aglio, R. Gaudiuso, R. ElRashedy *et al*, *Phys.Chem.Chem.Phys* **15**, 20868 (2013).

28th Int. Symp. "Nanostructures: Physics and Technology"
Minsk, Belarus, September 2020

Research of supercapacitors based on carbon allotropes and aqueous electrolytes

L.V. Tabulina[1], *V.A. Labunov*[1], D.V. Grapov[1], Yu.M. Kukuts[1], P.A. Rozel[2] and A.A Shustikov[3]

[1] Belarusian State University of Informatics and Radioelectronics, 220013 Minsk, Belarus
[2] IZOVAC Technologies, 220040 Minsk, Belarus
[3] Institute of Physical and Organic Chemistry, National Academy of Sciences, 220072 Minsk, Belarus

Abstract. The complex electrochemical effect of carbon electrodes and aqueous electrolytes on the capacitive characteristics of supercapacitors was studied. In the supercapacitor electrode structures were tested amorphous carbon, carbon nanotubes, reduced graphene oxide and vertical graphene nanowalls (VGN) coatings formed on copper and aluminum substrates. The electrolytic components were aqueous solutions of KOH and H_2SO_4, while using VGN coatings, an aqueous solution of H_3PO_4. The results obtained allowed us to identify the optimal conditions for supercapacitor structures with a capacity of ≈ 100 F/g simple fabrication from different crystalline allotropic forms of carbon and aqueous electrolytes.

Introduction

In recent years the rapid development of digital technology has necessitated improvement of the rechargeable power sources technology. These include supercapacitors (SC), which occupy intermediate position in capacitance and charge-discharge rate between batteries and dielectric capacitors. SC functioning is based on the electrical double layer (EDL) formation at the electrode/electrolyte interface. The capacity and power properties of these devices are determined by the porous electrode specific surface area and electroconductive properties of the electrodes and electrolyte. Scientific publications devoted to study of SC formation features often ambiguous due to differences in electrode fabrication methods and various types of electrolytes used [1].

Nevertheless, a general approach to the design of these devices based on the need to use accessible and effective electroconductive charge storage materials and cheap, and most importantly environmentally friendly electrolytes, has been highlighted.

This research is devoted to the complex study of SC components influence on the effectiveness of SC functioning.

1. Experimental

Multiwalled carbon nanotubes (CNTs) (Fibermax), reduced graphene oxide [2], and graphene-based submicron vertical graphene nanowalls (VGN) coatings [3], were used as electrode materials for SC formation.

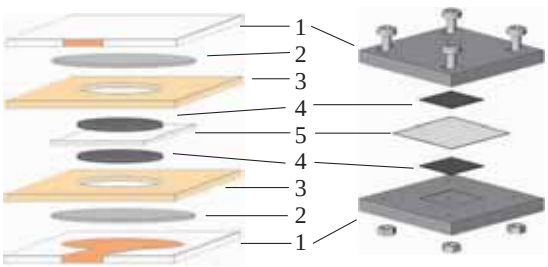

Fig. 1. SC test cell designs: (a) for powdery materials; (b) for VGN coatings. 1 — housing cover with contact pad, 2 — graphite paper current collector, 3 — dielectric spacer, 4 — electrode material, 5 — separator membrane

Of these materials, VGN coatings are of particular interest because of their unique physico-chemical properties inherent to graphene and thermodynamic stability preserved in the SC structure.

VGN were obtained by the inductively coupled plasma chemical vapor deposition (ICP CVD) method, which provides large-scale synthesis of the material in a single technological cycle.

VGN-coatings were formed on copper and aluminum substrates by the ICP CVD at a temperature of 400 °C. The thickness and packing density of VGN on substrates were varied by the synthesis process duration and pressure of a precursor gas propane.

The most of research for VGN coatings was performed using an aluminum substrate, since when measuring the capacitive characteristics of SC, the copper substrate is corroded in aqueous electrolytes with the formation of porous surface oxide layer. This to a greater extent than on an aluminum substrate reduces the adhesion of the synthesized VGN coatings, which leads to the irreproducibility of the capacitive characteristics of tested SC samples. In addition, when choosing electrodes with VGN coatings optimal for designing SC electrodes, it was taken into account that aluminum foil substrates are much cheaper than copper ones.

To protect the metal substrate from interaction with aqueous electrolytes, a VGN coating was formed on a dense carbon barrier sublayer. The formation of the sublayer was carried out in the mode without heating the substrate. The barrier sublayer was deposited for 20 minutes at a temperature of 30 °C. VGN coating was deposited for 10 minutes at a temperature 400 °C. Propane consumption was 100 sccm/min.

To use powdered substances and VGN coatings as SC electrode structure, two types of SC designs were developed (Fig. 1). The design for the use of powdered carbon materials was tested using amorphous carbon, which is the main electrode material for industrially produced SCs.

For powdered carbon materials electrodes, KOH and H_2SO_4 aqueous electrolytes solutions with concentrations of 1–6 M were used. For SCs electrodes based on VGN coatings, phosphoric acid aqueous electrolytes (1–3 M) were used, which provided chemical passivation of the metal substrate. To improve the wettability of carbon electrode materials exhibiting hydrophobic properties in aqueous electrolytes, two

options for activating SC electrodes were used: 1 — treatment in isopropyl alcohol vapor before assembly of SC structures; 2 — the use of aqueous electrolytes with the addition of isopropyl alcohol in the volume ratio 9:1 described as optimal in [4]. Polysulfone membranes used as a separator in SC were produced by the IPOC NAS.

The structural characteristics of crystalline carbon materials used in the SC structures were studied by scanning electron microscopy (SEM), Raman spectroscopy data, and the elemental composition of the materials was studied using X-ray energy dispersive spectroscopy.

SEM images of VGN coatings with graphite barrier layers are shown in Fig. 2.

The characteristics of SCs were studied by cyclic voltammetry (potential window 1 V, potential sweep rate 0.05–0.50 V/s), and galvanostatic charge–discharge methodes.

The complex of physico-chemical studies made it possible to establish that all test samples of SCs have characteristics similar to SC based on EDL, their capacitance values are in the range of 40–100 F/g for crystalline carbon materials, and 4–20 F/g for activated carbon. These characteristics substantially depend on the electrode materials surface activation methods and the concentration of electrolytic components of SC. Activation of electrode materials in isopropyl alcohol vapors provides an increase in electric capacity at identical potential sweep rates and electrolyte concentrations. Sulfuric acid electrolytes provided the highest capacitive characteristics of SC. An increase in electrolyte concentration contributes to an increase in the SC capacitance due to a decrease in the thickness of the diffuse layer of the EDL.

It was found that the use of VGN coatings in SCs greatly facilitates and simplifies the assembly of SC structures. The capacitive characteristics of SCs with VGN coatings are almost independent of the thickness of the carbon barrier layers. Their application is associated with the need to use aqueous and aqueous-organic electrolytes with the ability to passivate the substrates on which VGN coatings are formed. An aqueous solution of phosphoric acid meet this requirement, and its optimal concentration was found 3M.

Acknowledgement

This research was funded by the Belarusian Republican Foundation for Fundamental Research under grant agreement T18ARMG-001.

References

[1] A. Borenstein *et al*, *J. Mat. Chem. A.* **5**, 12653-12672 (2017).
[2] V.A. Labunov *et al*, *Russian Journal of Physical Chemistry A.* **91**, 1088-1092 (2017).
[3] P. Rozel *et al*, *Coatings* **9**, 60 (2019).
[4] G. Gromadskyi *et al*, *Appl. Energy.* **159**, 39-50 (2015).

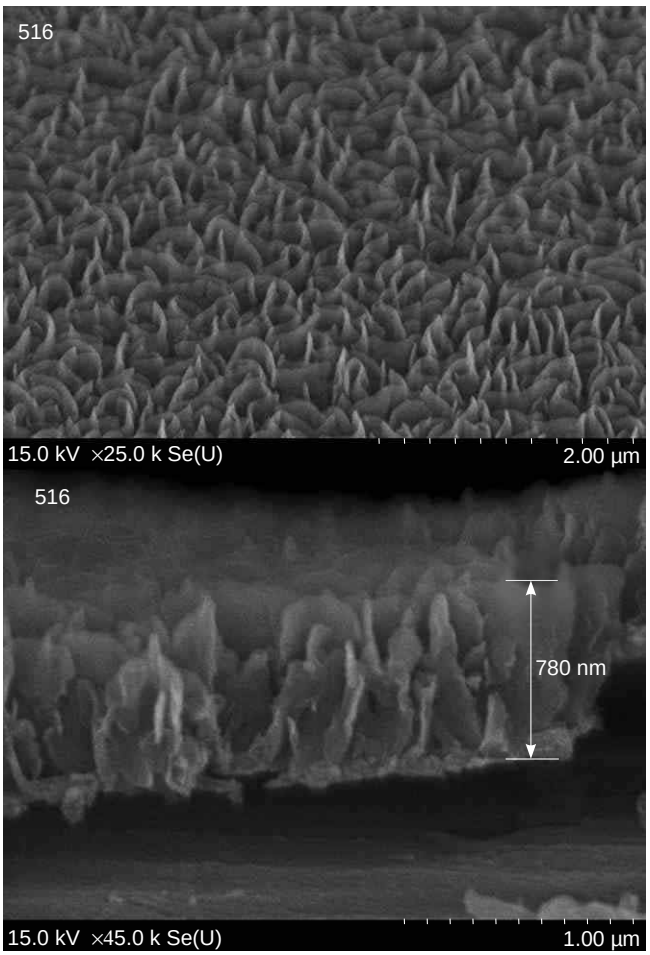

Fig. 2. SEM images of a VGN coating with a carbon barrier sublayer

28th Int. Symp. "Nanostructures: Physics and Technology"
Minsk, Belarus, September 2020

Sulfide passivation of InP(100) surface

M.V. Lebedev[1], Yu.M. Serov[1], T.V. Lvova[1], I.V. Sedova[1], R. Endo[2], T. Masuda[2]

[1] Ioffe Institute, Politekhnicheskaya 26, 194021, St Petersburg, Russia
[2] National Institute for Materials Science (NIMS), Tsukuba, Ibaraki 305-0044, Japan

Abstract. Passivation of the n-InP(100) surface with sodium sulfide (Na_2S) aqueous solution is analyzed by photoluminescence (PL) and x-ray photoemission spectroscopy (XPS). It is shown that even the short treatment with sulfide solution for 1 min results in essential enhancement of the PL intensity. This improvement of the PL intensity occurs just after transformation of the native oxide layer to the passivating layer consisting of indium sulfides and oxides. The surface bands in n-InP(100) remain almost flat after sulfide treatment.

Introduction

Indium phosphide (InP) is a very important III–V semiconductor material used in various applications as high-speed electronics, optoelectronics, and photo-electrochemical solar cells. Novel generation of semiconductor devices is based on nanostructures for which InP is especially promising due to its direct band gap, high electron mobility and rather low surface recombination velocity [1]. A number of InP-based nanostructured electronic and optoelectronic devices has been demonstrated [2,3].

The continuous scaling of semiconductor devices is accompanied by an increasing impact of surface and interface properties on the device performance. One of the most widely used methods for III–V surface passivation is the treatment with sulfide-containing solutions. Sulfide solutions cause removal of the native oxide layer and the formation of the passivating layer consisting of the sulfides and residual oxides. In the case of InP-based structures, sulfur passivation was used for modification of nanowires [4]. The passivating layer on indium phosphide involves In–S bonds, in addition to residual indium and phosphorous oxides.

Usually, for the InP surface passivation the aqueous ammonium sulfide solutions are used since such solutions can remove effectively the native oxides from the surfaces of III–V semiconductors. On the other hand, the aqueous solutions of sodium sulfide (Na_2S), which were the first solutions used for III–V surface passivation, have not been used so far for InP surface modification; though such solutions demonstrated the higher efficiency of GaAs(100) surface passivation than the aqueous $(NH_4)_2S$ solutions [5]. In this study the modification of the InP(100) surface with aqueous Na_2S solution is analyzed by photoluminescence (PL) and x-ray photoemission spectroscopy (XPS).

1. Experimental

The InP(100) samples were cut from a Te-doped n-type wafers with the doping density of about $2 \cdot 10^{17}$ cm^{-3}. Prior to chemical treatment the wafers were cleaned by boiling in toluene and twice in acetone for 5–7 min each and then rinsed with stream of Milli-Q water for 5 min. The sulfur treatment was performed with a 1M aqueous solution of sodium sulfide ($Na_2S{:}9H_2O$, Aldrich) at a temperature of about 40 °C for different time. After termination of the sulfur treatment the samples were rinsed with Milli-Q water and dried in air.

The PL spectra were measured at room temperature (300 K). The PL was excited with a diode laser with the wavelength of 377 nm in continuous mode. The laser beam was focused on the sample surface into the spot of about 50 μm in diameter by the lens with the focal length of 79 mm. The PL signal was collected with the apochromatic triplet and focused on the spectrometer entrance slit. PL spectra were obtained with a Princeton Instruments SP-2500 spectrometer ($L = 0.5$ m, grating of 300 lines/mm) and detected with a CCD-camera.

The XPS studies were performed on an AXIS NOVA (Shimadsu Kratos) setup equipped with a monochromatic Al-Kα source ($h\nu = 1486.6$ eV). All spectra were obtained at normal emission. The binding energies of the core levels were calculated with respect to the Fermi level calibrated with the Au $4f_{7/2}$ line (84.0 eV) of the reference gold sample. Core-level spectra were fitted after Shirley background subtraction with Voigt functions using IGOR Pro software (WaveMetrics, Inc.).

2. Results

Typical PL spectra of the n-InP(100) ($n = 2 \cdot 10^{17}$ cm^{-3}) measured at room temperature are shown in Fig. 1. Spectra contain one asymmetrical peak with the maximum at about 1.35 eV corresponding to the band edge emission. Even after short treatment with aqueous sodium sulfide solution the PL intensity essentially increased more than by a factor of six (Fig. 1). Longer sulfide treatment for 3–15 min resulted in smaller enhancement of the PL intensity relative to the native-oxide-covered surface (by a factor of five).

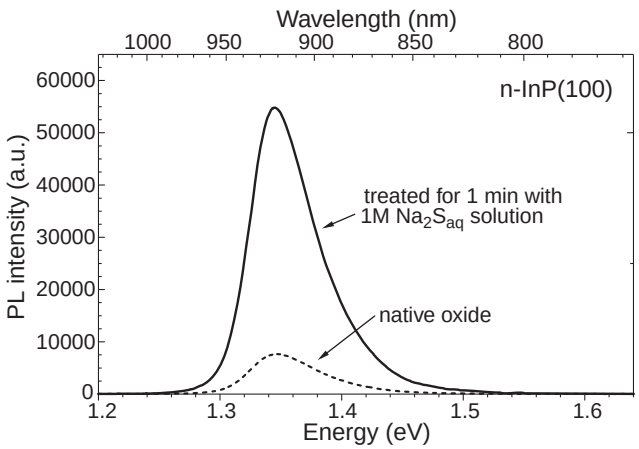

Fig. 1. PL spectra of the native-oxide-covered n-InP(100) ($n = 2 \cdot 10^{17}$ cm^{-3}) measured before and after treatment with 1M aqueous Na_2S solution for 1 min.

To understand the effect of treatment with 1M aqueous Na_2S solution on chemical composition and electronic properties of n-InP(100) surface, the XPS analysis was performed before and after sulfide treatment. Prior to sulfide treatment, the n-InP(100) surface is covered with the native oxide layer consisting of different indium oxides and phosphates (Fig. 2). The P 2p core level spectrum of the native-oxide covered n-InP(100) surface can be fitted with three different components (Fig. 2). Besides the P–In bulk photoemission component with the binding energy of about 129.1 eV, there are components shifted from the bulk one to higher binding energies by 1.0 and 4.7 eV, which can be assigned to elemental phosphorous P^0, and phophates (e.g. $InPO_4$), respectively. As the binding energy of the P–In($2p_{3/2}$) bulk component relative to the valence band maximum (E_{VBM}) of InP is 127.74 ± 0.03 eV [6], the position of the surface Fermi level in the native-oxide-covered n-InP(100) is $E_{\mathrm{F}} = E_{\mathrm{VBM}} + 1.36$ eV, i.e. the surface Fermi level lies at or slightly above (up to 50 meV) the conduction band minimum and thus the conduction and valence bands are almost flat at the n-InP(100) surface.

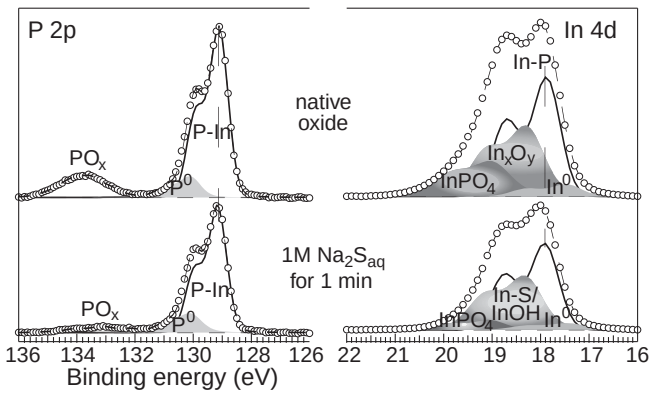

Fig. 2. P 2p and In 4d core level spectra of the native-oxide-covered n-InP(100) surface measured before and after treatment with the 1M aqueous sodium sulfide solution for 1 min.

The In 4d core level spectrum of the native oxide covered surface can be fitted with four components. In addition to the In–P bulk photoemission component, the component shifted from the bulk one to the lower binding energy by –0.4 eV, as well as shifted to higher binding energies by 0.4 and 1.1 eV can be found. These components can be assigned to the metallic indium In^0, indium oxide In_xO_y and indium phosphate $InPO_4$, respectively. It should be noted that the component with the chemical shift of 0.4 eV can be assigned both to In_2O_3 and In_2O, while the component with the chemical shift of 1.1 eV can contain the contribution from In_2O_3 as well.

Even short treatment of the native oxide covered n-InP (100) surface with the 1M aqueous Na_2S solution for 1 min causes essential modification of the P 2p and In 4d core level spectra (Fig. 2), as well as the appearance of sulfur photoemission lines S 2p and S 2s. In particular, the amount of phosphorous oxides decreases essentially (Fig. 2) and the corresponding high binding energy component of the In 4d core level spectrum is reduced as well (Fig. 2b). At the same time, the surface band bending remained intact since the binding energy of bulk P–In and In–P components did not change after treatment with the 1M aqueous Na_2S solution (Fig. 2). It should be noted that it is very difficult to distinguish In–O and In–S bonds in the fitting of the indium core level spectra since the corresponding components have similar chemical shifts from In–P bulk photoemission. Therefore, after treatment with sodium sulfide solution the component of the In 4d core level spectrum with the chemical shift of 0.4 eV should contain essential contribution from the In–S chemical bonds (Fig. 2) since sulfur photoemission appears at this stage of surface treatment.

Thus, the enhancement of the PL intensity of n-InP(100) after surface treatment with 1M aqueous Na_2S (Fig. 1) occurs just after transformation of the native-oxide layer to the passivating layer consisting of indium sulfides and oxides (Fig. 2). For this process, even short treatment for only 1 min is enough. Longer treatment neither appreciably improved the passivation efficiency, nor modified essentially the composition of the passivating layer. The bands at the native-oxide-covered n-InP(100) surface under study were almost flat and the surface band bending remained unaffected by treatment with aqueous sodium sulfide solution.

3. Summary

Passivation of the n-InP(100) surface with sodium sulfide (Na_2S) aqueous solution has been analyzed by photoluminescence (PL) and x-ray photoemission spectroscopy (XPS). It has been shown that even the short treatment with sulfide solution for 1 min causes essential enhancement of the PL intensity. This improvement of the PL intensity occurs just after transformation of the native oxide layer to the passivating layer consisting of indium sulfides and oxides. The surface bands in the native-oxide-covered n-InP(100) are almost flat and after sulfide treatment no essential band bending appeared.

Acknowledgement

The reported study was funded by RFBR, project number 20-03-00523.

References

[1] H.J. Joyce, J. Wong-Leung, C.-K. Yong *et al*, *Nano Lett.* **12**, 5325 (2012).
[2] F. Zafar, A. Iqbal, *Proc. R. Soc. A* **472**, 20150804 (2016).
[3] D. Li, B. Kristal, Y. Wang *et al*, *ACS Appl. Mater. Interfaces* **11**, 34067 (2019).
[4] N. Tajik, C.M. Haapamaki, R.R. LaPierre, *Nanotechnology* **23**, 315703 (2012).
[5] V.N. Bessolov, E.V. Konenkova, M.V. Lebedev, *Mater. Sci. Engineering B* **44**, 376 (1997).
[6] Y. Ishikawa, T. Fukui, H. Hasegawa, *J. Vac. Sci. Technol. B* **15**, 1163 (1997).

28th Int. Symp. "Nanostructures: Physics and Technology"
Minsk, Belarus, September 2020

Catalytic activity of palladium-ultradispersed diamonds nanocomposite in a Suzuki cross-coupling reaction

A.A. Lugovski[1,2], G.A. Gusakov[3], M.P. Samtsov[3], A.P. Lugovski[3] and V.A. Parhomenko[2]

[1] Physics Department, Belarusian State University, Minsk, 220030 Belarus
[2] Republican Center of Human Issues, Belarusian State University, Minsk, 220050 Belarus
[3] A.N. Sevchenko Research Institute for Applied Physical Problems, Belarusian State University, Minsk, 220050 Belarus

Abstract. Pd - ultradispersed diamonds (UDD) nanocomposite were synthesized by reduction palladium nitrate with hydrogen or hydrazine in aqueous suspention UDD. Structural studies of Pd-UDD nanocomposites by set of techniques IR spectroscopy, scanning electron microscopy/electron microprobe and X-ray diffraction analysis showed that palladium deposition takes place on predominantly primary aggregates of UDD. Size of Pd-UDD are weakly depending on the reduction conditions and vary from 14 to 23 nm. All synthesized samples showed high catalytic activity in Suzuki cross-coupling reaction.

Introduction

The cross-coupling reaction of Suzuki (Suzuki–Miyaura) of an organohalide with an organoborane is widespread in organic synthesis [1–3]. It is used primarily for the preparing of polyolefins, biphenyls which applied as intermediates for pharmaceuticals, liquid crystals or fine chemicals. Soluble palladium complexes such as palladium acetate, N-heterocyclic carbene complexes, $Pd(PPh_3)_4$ (tetrakis (triphenylphosphine) palladium), 9-fluorenyl-(dialkyl) phosphines and another complexes with phosphine ligand are typically used for Suzuki-coupling as a catalysist. In additional to these compounds hetegeneous catalysts (Pd(C)) are still used. Modern single atoms palladium catalyst such as Pd atoms anchored on exfoliated graphitic carbon nitride or palladium nanoparticles immobilized on polymer were proposed due to avoid the problem of using conventional cross-coupling reaction catalysts [4,5]. Based on this data we are assumed that detonation synthesis ultradispersed diamonds (UDD) will be a suitable carrier for nanoparticle palladium. The large active surface of UDD particles and the possibility of control its functional composition and suspension stability make this material very attractive for heterogeneous catalysis [6].

In the present research methods of synthesis of palladium -ultradispersed diamonds nanocomposite and their catalytic activity in Suzuki cross-coupling reaction were investigated.

1. Experimental

Nanodiamond powder "UDA-S" produced by "Sinta" (Minsk) [http://sinta.biz/nanoalmazy] were used in the present work. Prepurification of the UDD from non-diamond impurities was carried out by the treatment of the diamond blend with nitric acid at elevated temperature and pressure and then by acid-alkaline treatment of the powder, washing with distilled water and drying was carried out in two stages. In the second stage UDD samples were annealed for 1 hour at temperature 430°C in air and were purified of metal impurities by ultrasonic treatment in hydrochloric acid. Palladium deposition was carried out by treatment an aqueous suspention UDD with $Pd(NO_3)_2$ with hydrogen or hydrazine. The Pd-UDD composites were isolated by centrifugation after the reaction. Both two samples of nanocomposide were used in the Suzuki reaction to study catalytic activity.

The starting material after annealing and the samples of palladium-ultradispersed diamonds nanocomposite were characterized using a set of techniques IR spectroscopy, scanning electron microscopy/electron microprobe, X-ray diffractionlbf analysis.

2. Results and discusion

The amount of precipitated palladium after depotision procedure was determined by spectrophotometric study of a fugate. Spectrophotometric determination of the metal complex with Arsenazo III showed that the concentration of palladium on the diamond surface reaches 6 mass percent.

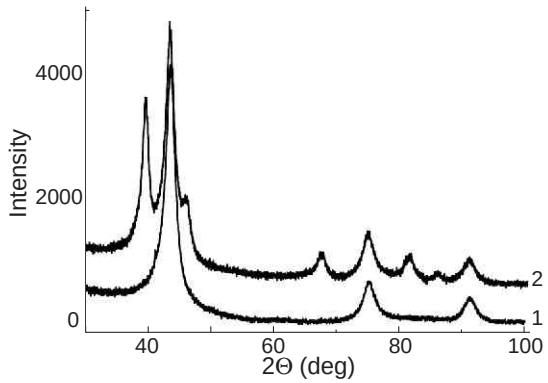

Fig. 1. Diffractograms of the initial UDD sample annealed in air at temperatures 450 °C (1) and Pd-UDD composite (2) reduced by hydrazine.

X-Ray diffraction spectra of source UDD samples contain wide, symmetrical diffraction maxima at $2\theta = 43.9$, 75.3 and 91.5 degrees, which can be adequately described by Lorentz profiles and correspond to the (111), (220) and (311)- reflections of the diamond-like lattice with a parameter $a_0 = 3.568 \pm 0.008$ Å. Diffraction spectra of Pd-UDD is additionally observed diffraction maxima at $2\theta = 39.9$, 46.3, 67,8 and 81.8 degrees that correspond respectively (111), (200), (220) and (311)- palladium reflections Figure 1 shows the diffraction patterns of the initial sample of annealed UDD and Pd-UDD

(hydrazine reduction). The average size of Pd particles determined by using the Selyakov-Scherrer relationship from the half-widths of these lines for all diffraction maxima is equal to $L = 7 \pm 2$ Å.

There was also no significant difference between the samples Pd-UDD nanocomposide obtained by different reduction methods.

The study of nanocomposites by scanning electron microscopy showed that size of Pd-UDD nanocomposites are weakly depending on the reduction conditions (treatment with hydrogen or hydrazine as a Pd^{2+} reducing agent). Pd-UDD composides as shown on Fig. 2 on average vary from 14 to 23 nm. Comparing with the data obtained on the X-Ray diffraction, we can conclude that palladium deposition takes place on predominantly primary aggregates.

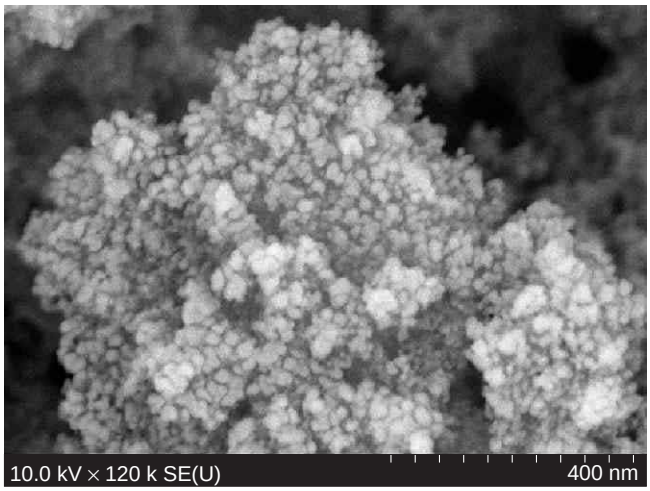

Fig. 2. SEM microphotograph of Pd-UDD nanocomposite formed by hydrazine reduction.

In the IR absorption spectrum of the initial annealed UDD powder (Fig. 3) in the range 1000–1900 cm^{-1}, an intense band with maxima of 1785 cm-1 and two broad bands with maxima of 1150 and 1280 cm^{-1} are observed. which can be attributed to vibrations of the functional groups –C=O and ≥COC≤ in acid anhydrides and lactones. The band with a maximum of 1630 cm -1 corresponds to vibrations of –OH groups in water molecules (adsorbed moisture). As a result of the deposition of palladium, a "red" shift of the –C=O vibration band from 1785 to 1770 cm^{-1} occurs, which is obviously a consequence of the interaction of these functional groups with metal nanoparticles. In addition, there is a slight increase in the absorption intensity in the 1384 cm^{-1} band due to the use of $Pd(NO_3)_2$ as a reduction precursor.

Both synthesized samples of Pd-UDD nanocomposite were tested as catalysts in the reaction Suzuki. The cross-coupling reaction used traditional reagents para-methoxyphenioboric acid and bromobenzene in toluene with potassium phosphate. Both samples of the catalyst turned out to be effective and allow the Suzuki reaction to be carried out in 75–82 yield for a 30–40 min. It should be noted that catalytic activity strictly depends on the temperature conditions of the reactions. The most effective reaction was at a temperature of 70–80 $^{\circ}C$. Based on the experimental results described above, the following conclusions can be drawn. Pd-UDD nanocomposites were

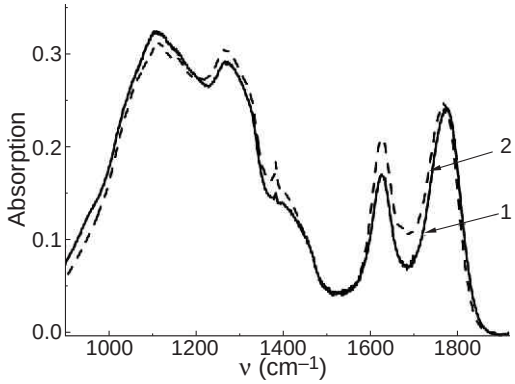

Fig. 3. FTIR spectra of the initial UDD sample (1) and Pd-UDD composite (2).

synthesized. A study of their structure showed that palladium nanoparticles on average 7 nm size deposides on predominantly primary aggregates of UDD. The synthesized samples showed high catalytic activity in Suzuki cross-coupling reaction.

References

[1] N. Miyaura and A. Suzuki, *Chem. Rev.* **95**, 2457 (1995).
[2] D. Roy and Y. Uozumi, *Advanced Synthesis and Catalysis* **360**, 602 (2017).
[3] J. J. Lennox and G. C. Lloyd-Jones, *Chem. Soc. Rev.* **43**, 412 (2014).
[4] Z. Chen *et al*, *Nature Nanotech.* **13**, 702 (2018).
[5] Saeideh Ghazali-Esfahani *et al*., *Science China Chemistry* **59**, 482 (2016).
[6] G. Gusakov *et al*, *J. of Appl. Spect.* **87**, 33 (2020).

28th Int. Symp. “Nanostructures: Physics and Technology”
Minsk, Belarus, September 2020

Calculation of the Ga+ FIB ion dose distribution by SEM image

M.I. Mitrofanov[1], G.V. Voznyuk[1], S.N. Rodin[1], W.V. Lundin[1], V.P. Evtikhiev[1] and A.F. Tsatsulnikov[2]

[1] Ioffe Institute, St Petersburg, Russia
[2] SHM R&E Center, RAS, St Petersburg, Russia

Abstract. A new approach for calculating the ion dose spatial distribution of focused ion beam is proposed. The approach is based on the analysis of the secondary electron microscopy image of the area irradiated by focused ion beam.

Introduction

Ion dose is one of the key parameters of focused ion beam (FIB) nanolithography. Ion dose is the quantity of ions absorbed by a medium. It is commonly used for estimation of etching rate or material removal rate [1]. Ion dose has units of ions/cm^2 and includes several technological parameters: ion beam current, time of exposure and step size or pixel distance. Generally, for investigation of FIB etching parameters, ion dose is estimated for area is much larger than the ion beam diameter (typically submicron). However, during FIB lithography of nanostructures the real diameter of ion beam and ion dose distribution should be taken into account because a size of structures is comparable to the ion beam diameter.

Ion beam diameter is estimated as a full width at half maximum of Gaussian ion intensity distribution [2]. Experimentally the profile of ion beam distribution is estimated by atomic force microscopy (AFM) topography of etched hole or trench, or by rise distance method on the “knife-edge” of the sample [2,3]. Nevertheless, rise distance method has several sources of error, which should be kept in mind. Method also can be used only for low current ion beams due to destruction of the “knife-edge” of the sample. AFM topography estimates only etched area and does not includes “tails” of implanted ions.

Figure 1 shows secondary electron microscopy (SEM) image of the Si_3N_4/GaN sample surface exposed by a Ga^+ FIB. From the figure one can see that oval “d” and “D” confines etched area and highly exposed area correspondingly. In this case both above mentioned methods are inapplicable due to large errors. We suggest approach for calculation of ion dose distribution within focused ion beam in the sample surface plane. The approach is based on a gradual increase in the exposure time and analysis of the exposed areas using secondary electron microscopy. SEM images show an increase in exposed area, which allows us to calculate a histogram of the spatial distribution of the ion dose.

1. Experiment

Si_3N_4/GaN sample was exposed in different points by custom designed ultra high vacuum Ga^+ FIB equipped with Orsay Physics Cobra FIB column. Ion beam energy and current was 30 keV and 490 pA correspondingly. FIB with 5 pA probe current was used for obtaining SEM images of the exposed areas (see fig. 1). From SEM images we obtain dimensions of exposed and etched areas. One can see from figure 1, that areas have an oval shape due to imperfection of ion beam focusing. Ideal beam has axial symmetry, therefore, the diameters of circles equal in area to the exposed areas were calculated. Exposure times and diameters (outside and inside for exposed and etched area accordingly) of equivalent circles are listed in the table 1.

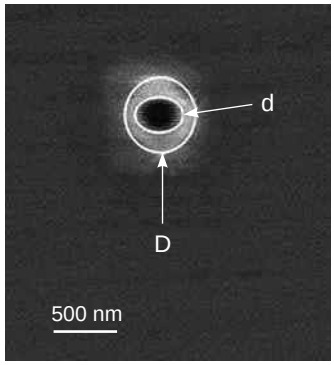

Fig. 1. SEM image of Si_3N_4/GaN sample surface exposed by a Ga^+ FIB. Ion energy 30 keV, ion beam current 490 pA, time of exposure 100 ms. Image was achieved by 5 pA FIB microscopy. D — highly exposed region and d — etched region.

Table 1.

Exposure time (ms)	Outside diameter (μm)	Inside diameter (μm)
50	0.371	0.202
100	0.422	0.267
500	0.621	0.397
1000	0.706	0.527
5000	0.894	0.695

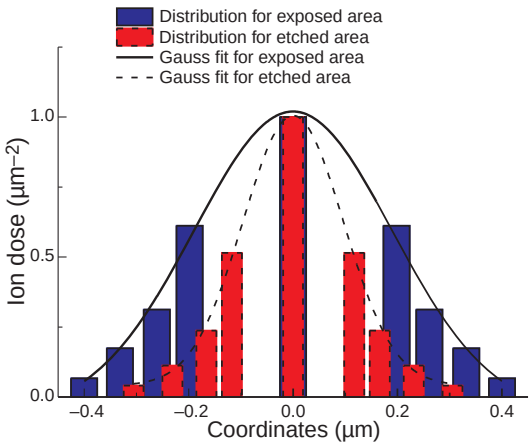

Fig. 2. Normalized ion dose distribution for exposure and etched areas for the 5 second exposure. Maximum is equal to $7{\cdot}10^{18}$ ions/cm^2.

2. Results and discussions

Based on data from table 1, it is possible to plot a histogram of the ion dose spatial distribution. The ion dose for each point is calculated as the sum of the ion dose for areas corresponding to the exposure time. Figure 2 shows histogram and fitting of Gaussian curve of the spatial distribution of ion dose for etched and exposed areas.

From the graphs one can see a significant part of the implanted ions that do not include into the etching region. That fact should be kept in mind during design and fabrication of the nanostructures by FIB lithography technique. Details of the ion dose calculation and possible errors will be discussed.

References

[1] C.-S. Kim *et al*, *Vacuum* **86**, 1014 (2012).
[2] M.Y. Ali *et al*, *Int. J. Precis. Eng. Manuf.* **11**, 157 (2010).
[3] J. Orloff, *Proc. of SPIE 7729 (Monterey, California, United States, 2010)*, SPIE, 77290C, 2010.

28th Int. Symp. "Nanostructures: Physics and Technology"
Minsk, Belarus, September 2020

Reasons of crystallite formation during the GaAs nanowire self-catalyzed growth

A.G. Nastovjak[1], N.L. Shwartz[1,2], E.A. Emelyanov[1], M.O. Petrushkov[1], A.V. Vasev[1], M.A. Putyato[1] and V.V. Preobrazenskii[1]

[1] Rzhanov Institute of Semiconductor Physics, SB RAS, 13 Lavrentiev aven., 630090, Novosibirsk, Russia
[2] Novosibirsk State Technical University, 20 K. Marx aven., 630073, Novosibirsk, Russia

Abstract. During the self-catalyzed GaAs nanowire growth the formation of parasitic GaAs crystallites is observed. The reasons of crystallites formation are explained on the base of Monte Carlo simulation results. The appearance of liquid gallium droplets results in a sharp decrease of gallium adatom concentration. It is shown that too high arsenic and gallium deposition rates lead to the crystallites formation at the initial growth stage. The appeared GaAs crystal clusters collect part of deposited gallium and arsenic decreasing their surface concentration, thereby, adjusting the growth condition for the NW growth. Therefore, during the self-catalyzed GaAs NW growth the self-regulation of growth conditions takes place.

Introduction

III–V nanowires (NWs) are perspective low-dimensional objects for novel optoelectronic devices. The most appropriate technique for the III–V NW fabrication is the self-catalyzed growth according to the vapor-liquid-solid (VLS) mechanism [1]. A self-catalyzed NW growth is possible only in a certain range of growth conditions. There is a strong correlation between the nanostructure morphology and growth conditions [1]. It was demonstrated that, even at optimal temperatures and the As flux, along with NWs, GaAs crystallites were formed [1,2]. In this work we proposed a model of massive GaAs crystallite formation on a defect-free oxide layer. This model is verified by the atomistic Monte Carlo (MC) simulation.

1. Methods

The GaAs NW growth was carried out using the MBE equipment 'Stat' at T= 620 °C and at As_4/Ga flux ratio $\sim$ 20. The gallium deposition rate was equivalent to the growth rate of 0.25 ML/s on GaAs(100). A thin silicon dioxide layer was previously grown on the GaAs(111)B substrate. The details of SiO_2 layer formation can be found elsewhere [2]. The morphology of the surface with NWs was investigated using scanning electron microscopy.

The MC simulation of self-catalyzed GaAs NW growth was carried out using the software SilSim3D on the base of 3D lattice crystal model [3]. The 5-component system was considered in the model: Ga(s), Ga(l), As, As_2, M_f–gallium in solid and liquid state, atomic and molecular arsenic and mask film material, correspondingly. The initial model substrate was the zinc blend crystal of 120×100 nm covered with a thin mask film. The following processes were taken into account for the self-catalyzed growth simulation: deposition of Ga atoms and arsenic molecules As_2, reversible decomposition of arsenic molecules $As_2 \leftrightarrow As + As$, diffusion of all types of particles, mask film etching by liquid gallium droplets, arsenic dissolution and diffusion through the liquid Ga drop, GaAs dissolution in the liquid gallium and liquid gallium crystallization in GaAs form at the liquid-crystal interface.

2. Results

The morphology of the grown GaAs NWs is demonstrated in Fig. 1. One can see that, along with vertical NWs, a lot of large GaAs crystallites are formed. The most of vertical NWs grow between the massive crystallites. Several tilted NWs are also present on the surface. The crystallites and NWs have a noticeable variation in size.

The MC simulation of self-catalyzed GaAs NW growth was fulfilled at T = 620 °C and Ga and As_2 fluxes 5 and 25 ML/s, correspondingly. The model temperature is in agreement with the experimental temperature. We use gallium flux larger than that in the experiment to provide a sufficient diffusion collection of Ga atoms for the drop on a small model substrate. Due to calculation limits, the model substrate size is lower than that in the experiment. Since in calculations we consider As_2 molecules, instead of As_4 molecules in the experiment, the model and experimental arsenic fluxes do not match. The model substrate evolution during the Ga and As_2 deposition is demonstrated in Fig. 2. At the initial deposition stage, two Ga drops are formed on the mask layer surface (Fig. 2a). Due to the high volatility of arsenic molecules, a greater part of deposited arsenic molecules is desorbed; the rest of As_2 molecules reach Ga droplets, decay on its surface with a following arsenic atom dissolution in liquid gallium creating a Ga–As alloy. The Ga droplets enlarge in size during

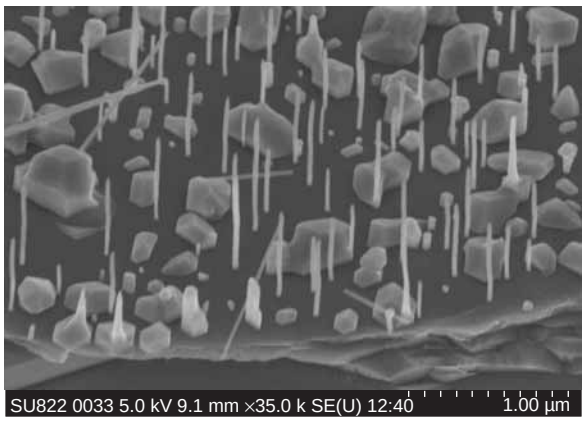

Fig. 1. SEM image of GaAs(111)B substrate after the 60 min NW growth.

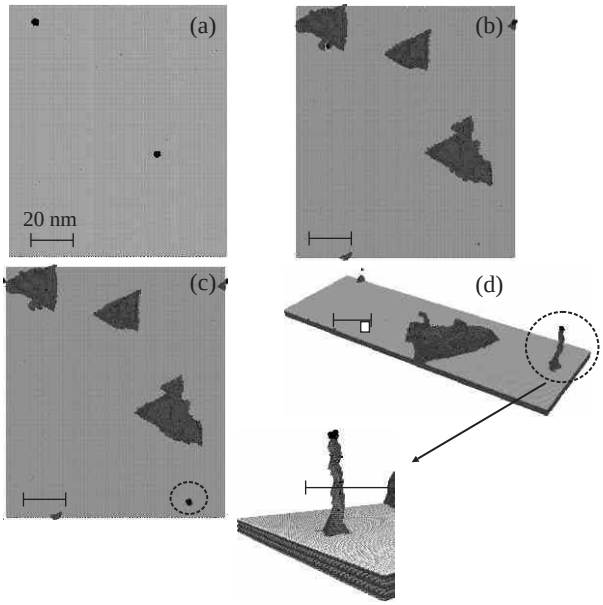

Fig. 2. The model substrate images at various growth moments: (a-c) top views of the model substrate and (d) 3D image of the substrate fragment; deposition time increases from (a) to (d). Dotted circles indicate the Ga droplet in (c) and GaAs NW in (d). The insert to Fig. (d) corresponds to the enlarged image of GaAs NW. GaAs is marked in dark-gray, Ga drop — in black and the mask-film material — in gray color.

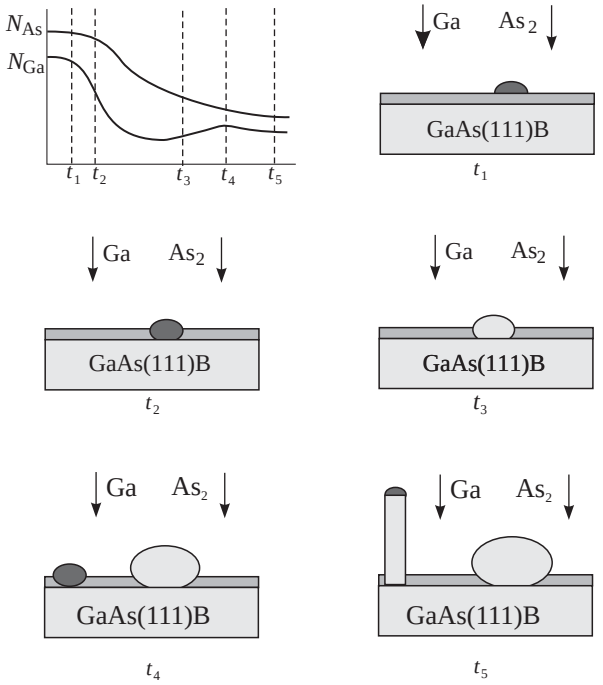

Fig. 3. The schematic view of the arsenic and gallium surface concentration dependence on the growth time and the substrate images at time moments t_1–t_5. GaAs is marked in light-gray, Ga drop — in dark-gray and the mask-film material — in gray color.

the deposition and, at the same time, they gradually etch the underlying mask film. After liquid droplets reach the crystal substrate, the GaAs crystallization starts under the drops. At high Ga and As_2 fluxes, instead of wires, GaAs crystallites start to grow on the surface (Fig. 2b). During the time interval between a) and b) snapshots in Fig. 2, the third Ga droplet was formed on the model surface that was transformed into the third GaAs crystallite. These crystallites are the sinks for gallium adatoms and arsenic molecules. Thus, the gallium and arsenic concentration decreases on the surface. Since crystallites are randomly distributed over the surface, the Ga adatom concentration changes along the surface. In some parts of the surface, the gallium concentration is sufficient for the formation of new Ga droplets between the crystallites (Fig. 2c). Since the gallium and arsenic concentration now is lower than that at the initial deposition stage, this droplet originates the NW growth (Fig. 2d).

The examination of simulation results made it possible to explain the simultaneous presence of large GaAs crystallites and NWs on the substrate surface. The scheme of both GaAs structures growth is presented in Fig. 3. The changes of gallium and arsenic surface concentrations with time and the time evolution of the surface morphology corresponding to the key points of the growth process are illustrated in Fig. 3. Initially, the arsenic and gallium concentrations are high enough and a gallium droplet appears (time moment t_1), After the droplet nucleation the Ga surface concentration decreases, while the arsenic surface concentration remains high. When the Ga drop etches through silicon oxide (moment t_2), the liquid gallium crystallization at the drop-crystal interface starts leading to the GaAs cluster growth. Arsenic is required for the GaAs formation. That is why the arsenic concentration decreases too at $t > t_2$. At time moment t_3 the Ga droplet is completely consumed. The further arsenic and gallium deposition leads to the crystallite enlargement. The presence of large GaAs crystallite provides the gallium and arsenic concentration lower than that at the initial deposition stage. At some moment (t_4) a new droplet is formed. Later, this droplet initiates the NW growth (time moment t_5). It is evident that the appearance of crystallites and NWs is not simultaneous. The self-catalyzed GaAs NW growth is the self-regulated process in which not only external fluxes determine arsenic and gallium flows to a catalyst drop, but these flows are also adjusted by the surface morphology.

Acknowledgement

This work was supported by the RFBR (grant 18-02-00764).

References

[1] F. Bastiman, *et al*, *Nanotechnology* **27**, 095601 (2016).

[2] E.A. Emelyanov, *et al*, *Tech. Phys. Lett.* **46**(2), 162 (2020).

[3] A.N. Karpov, *et al*, *Vychisl. Metody Programm.* **15**, 388 (2014).

28th Int. Symp. "Nanostructures: Physics and Technology"
Minsk, Belarus, September 2020

Tunable photoluminescence of silver molecular clusters in silicate glass for spectral converters and solid-state lighting applications

E.M. Sgibnev[1,2], N.V. Nikonorov[2]

[1] Dukhov Automatics Research Institute,Moscow, Russia
[2] ITMO University, St Petersburg, Russia

Abstract. Influence of sodium-silver ion exchange and subsequent heat treatment durations on photoluminescent properties of silver molecular clusters formed in silicate glass matrix was studied. Increase in the ion exchange duration was shown to result in substantial shift of photoluminescence spectrum. The latter allows effective tuning emission color of silver clusters from cool and warm white to yellow and orange. The studied glass samples doped with silver molecular clusters was characterized by photoluminescence quantum yield up to 60%. The results of the study can find applications in solid-state light-emitting devices and spectral converters with tunable emission spectrum.

Introduction

Subnanometer silver molecular clusters (SMCs) stabilized in a glass matrix is known to possess intense and broadband emission in the visible and NIR ranges under UV excitation. This makes such materials attractive for developing phosphors for white LEDs, spectral converters for solar cells, and optical data storage devices [1–4]. Among wide family of inorganic glass materials silicate glass is the most widely used one owing to excellent transparency in a wide spectral range, high mechanical strength and chemical durability. However, silver oxide concentration in silicate glasses does not exceed 0.1 mol% due to a low solubility of silver. The limitation can be overcome by ion exchange (IE) method allowing to get high concentration of silver ions in surface layers of glass. The IE technology is based on substituting one kind of alkali cations (usually Na^+) in glass substrate for another one (Li^+, K^+, Rb^+, Cs^+) or transition metal ions (Ag^+, Cu^+, Tl^+) from a salt melt [4]. In this work influence of the Na^+-Ag^+ IE and subsequent heat treatment time on photoluminescent properties of SMCs grown in a silicate glass matrix was studied.

1. Experimental

Glass based on the Na_2O-Al_2O_3-ZnO-SiO_2-F system doped with 0.002 mol% Sb_2O_3 as reducing agent for silver ions was synthesized in an electric furnace at 1500 °C in air atmosphere using the platinum crucibles and mechanical stirrer. The glass transition temperature of the glasses measured with STA 449 F1 Jupiter (Netzsch) differential scanning calorimeter was found to be 464±3 °C. Planarpolished samples 1 mm thick were prepared for further investigation. Na^+-Ag^+ IE was performed by immersion of the samples into a bath with a melt of the nitrate mixture $5AgNO_3/95NaNO_3$ (mol%) at 320 °C for 15 min – 21 h. For growth of SMCs the ion-exchanged samples were then heat-treated at 450 °C for up to 24 h. Absorbance spectra of the samples were recorded with double-beam spectrophotometer Lambda 650 (Perkin Elmer). The registration of emission spectra excited by UV light at 365 nm and photoluminescent quantum yield (PLQY) measurements were carried out inside integrated sphere with Photonic Multichannel Analyzer (PMA-12, Hamamatsu) at room temperature.

2. Results

Na^+-Ag^+ IE had significant effect on the absorbance spectra of silicate glass shifting the UV edge of strong absorption to long-wavelength side. The shift is explained by absorption of the embedded silver ions that are characterized by strong absorption band around 225 nm in silicate glass matrix [6, 7].That is why the shift magnitude depends on the IE duration. Heat treatment of the ion-exchanged glass samples induced several processes: migration of silver ions deeper into the glass due to concentration gradient, reduction of silver ions, and aggregation of silver atoms and/or ions into molecular clusters. In the studied glasses reduction of silver ions occurs through interaction with trivalent antimony ions:

$$2Ag^+ + Sb^{3+} \leftrightarrow 2Ag^0 + Sb^{5+} \quad (1)$$

Chemical equilibrium of the redox reaction shifts to the right side due to a high concentration of silver ions exceeding that of the trivalent antimony ions by several orders. Further interaction of silver atoms and ions resulted in growth of various SMCs:

$$Ag^0 + Ag^+ \rightarrow Ag_2^+ \quad (2)$$

$$Ag^0 + Ag^0 \rightarrow Ag_2^0 \quad (3)$$

$$Ag^0 + Ag_2^0 \rightarrow Ag_3^0 \quad (4)$$

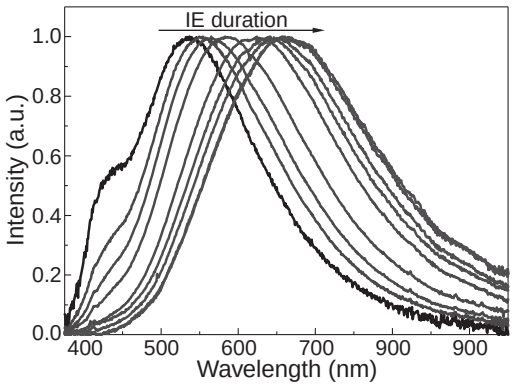

Fig. 1. Normalized emission spectra of the glass samples after the IE for different time period and heat treatment at 450 °C for 24 h.

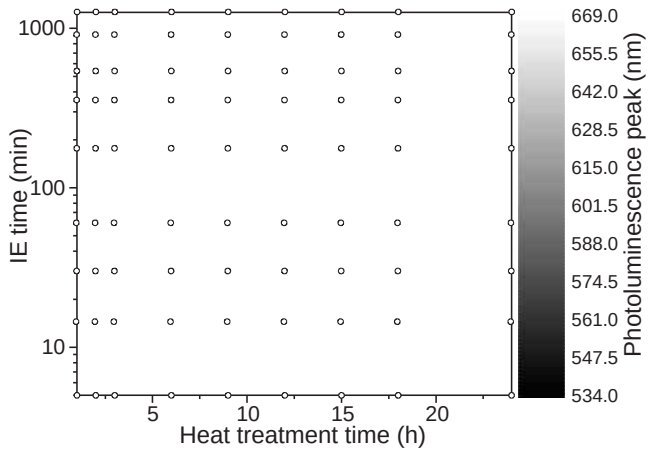

Fig. 2. Dependence of SMCs photoluminescence peak on the IE and heat treatment time.

Presence of SMCs in the ion-exchanged and heat-treated samples manifested as a broad absorption in the UV and visible ranges. The amplitude of clusters-related absorption rises with increase in the IE time. In Na^+-Ag^+ ion-exchanged glass SMCs grow in a layer with gradient of silver concentration, which results in formation of clusters with various number of atoms (2, 3, 4, ldots) [8]. Thus, the observed broad absorption in the spectra is the envelope of absorption bands assigned to various SMCs. All samples after the IE and heat treatment were characterized by bright emission in the range of 400–950 nm under UV excitation at 350 nm. As an example emission spectra of the samples heat-treated for 15h are shown in Fig. 1. Photoluminescence peak shifts from 535 to 660 nm with extension of the IE process from 15 min to 21 h. It should be noted that the shift occurs in the spectral region, where absorbance of the studied samples differs insignificantly, and reabsorption can be excluded from possible reasons of the emission peak shift. Thus, the shift was resulted from changes in relative concentration of various emitting SMCs. Dependence of the emission peak on the IE and heat treatment time is shown in Fig. 2. A short-wavelength shift of the photoluminescence peak was observed with extension of the heat treatment process at a fixed IE time. It was related to continuing growth of silver clusters and redistribution of emission bands assigned to various SMCs in emission spectrum. Thus, emission of SMCs formed in the Na^+-Ag^+ ion-exchanged silicate glass can be easily tuned in a wide range by varying the IE and subsequent heat treatment parameters. For example, color temperature of the SMCs emission in the samples varies between 2300 and 6250 K. The latter allows to tune emission color from cool and warm white to yellow and orange. PLQY magnitude above 40% was observed for the samples ion-exchanged for 5–60 minutes with maximum reaching 60%. The samples ion-exchanged for longer durations were characterized by PLQY below 30%. Moreover, for these samples increase in the IE time caused lowering PLQY value due to absorption of silver ions at the excitation wavelength. PLQY values as well as photoluminescence peak location changed insignificantly after the heat treatment for 6 hours. It is explained by lowering a rate of silver reduction and, as a consequence, growth of SMCs. Further treatment did not lead to fall of the PLQY values that proves thermal stability of SMCs in the prepared glass at temperature as high as 450 °C.

3. Conclusions

In this work the influence of the low temperature Na^+-Ag^+ IE and subsequent heat treatment time on the formation and spectral-luminescent properties of SMCs stabilized in silicate glasses was studied. The IE duration was shown to have significant effect on absorbance and photoluminescence spectra of silicate glasses with SMCs. The latter allows one to tune emission of SMCs in a wide range from cool and warm white to yellow and orange. The studied glasses doped with SMCs can find applications as phosphors for white LEDs with high thermal stability (up to 450°C) and chemical durability typical for silicate glasses. The results might also pave the way to a new class of spectral converters to overcome poor spectral response most of the solar cells in the UV and blue ranges.

References

[1] A.S. Kuznetsov *et al*, *Nanoscale* **21**, 10065 (2013).
[2] Y. Sgibnev *et al*, *Part. Part. Syst. Char.* **35**, 1800141 (2018).
[3] E. Cattaruzza *et al*, *Ceram. Int.* **41**, 7221 (2015).
[4] D. Klyukin *et al*, *Opt. Express* **25**, 12944 (2017).
[5] A. Tervonen *et al*, *Opt. Eng.* **50**, 071107 (2011).
[6] A.M. Efimov *et al*, *Glass. Technol.-Part A* **54**, 155 (2013).
[7] E.M. Sgibnev *et al*, *J. Non-Cryst. Solids* **278**, 213 (2013).
[8] A. Simo *et al*, *J. Am. Chem. Soc* **134**, 18824 (2012).

28th Int. Symp. "Nanostructures: Physics and Technology"
Minsk, Belarus, September 2020

Resist employing ion beam lithography: features and advantages

Ya.L. Shabelnikova, S.I. Zaitsev

Institute of microelectronic technology problem and high purity materials RAS, 142432 Chernogolovka, Moscow distr., Russia

Abstract. In this paper the undoubted advantages of resist employing ion beam lithography are listed. All of them, from sub-ten-nanometer lateral resolution achievable to thousand times higher energy efficiency than in electron lithography, are caused by that ions are massive particles and they transfer the tangible part of its energy to resist atom at each interaction. The important feature of ion beam lithography, namely, strongly inhomogeneous in depth deposited energy of ions, is described. Taking it into account, the procedure for resist contract determination is derived.

Introduction

One of the approaches to employ a focused ion beam for high resolution nanofabrication is a lithographic patterning of resist [1–5]. This method is very similar to electron beam lithography (EBL). But in EBL high resolution achieved due to that only a small part (upper and narrow) of beam with target interaction volume locates in the resist. Ions are much higher particles than electrons and have much shorter ranges so that nearly all energy of ion beam deposits in thin resist layer. As a consequence ion beam lithography has about 10^3 times higher energy efficiency [6] and performance than EBL with sub-ten-nanometer range lateral resolution achievable [2,5,7] and no proximity effect (parasitic resist illumination by backscattered and secondary particles from substrate [8]).

But in the case of ion beam the procedure of resist contrast determination developed for electron beam lithography cannot be applied anymore because deposited energy is not homogenous in the resist depth as in EBL. So to determine the resist contrast γ more accurate model should be used.

1. The procedure of resist contrast determination

The model in that the etching velocity of exposed resist V was proportional to spatial density of deposited energy ϵ in the power of γ was applied.

$$\frac{V}{V_0} = \left(\frac{\epsilon}{\epsilon_0}\right)^{\gamma} \tag{1}$$

In the case of uniform exposure of large resist area, the deposited energy density depends only on depth z and related to exposure doze D as

$$\epsilon(z) = \frac{D}{Z} E_b \epsilon_{zp}(z), \tag{2}$$

where Z is ion — charge, E_b is beam energy and $\epsilon_{zp}(z)$ is the part of energy absorbed in the layer at the depth z. The empirical description of ion beam deposited energy evaluated in [9] can be used to describe $\epsilon_{zp}(z)$.

Model (1)–(2) allows to obtain the dependence of the resist etching depth h on exposure doze

$$h = F^{-1}\left[\left(\frac{D}{D^*}\right)^{\gamma} F(h_0)\right] \tag{3}$$

as the solution of differential equation

$$\int_0^T dt = \int_0^h \frac{dz}{V} = \frac{1}{V_0}\int_0^h \left(\frac{\epsilon_0}{\epsilon}\right)^{\gamma} dz \tag{4}$$

with boundary condition

$$h(D = D^*) = h_0. \tag{5}$$

This boundary condition reflects the definition of resist sensitivity. Namely, the etching depth at doze equal to the sensitivity D^* is equal to the thickness of resist layer h_0. Here T is the development time and

$$F(h) = \int_0^h \frac{dz}{\epsilon_{zp}^{\gamma}}. \tag{6}$$

So the contrast γ can be assessed as a value at that the approximation of measured etching depth dependence by calculated with (3) one is the best. It is sensible to use depth profile etched in thick resist layer that was not dissolved till the substrate in used range of dozes and where the sensitivity cannot be determined. In this case the coordinates of any point of measured profile $h(D)$ can be used as D^* and h_0. The results of depth profiles fitting for PMMA resist and Ga^+ 30 keV ion beam are shown at Fig. 1. Beside the contrast, ions' energy length and the point (D^*, h_0) was fitting parameters. The value of contrast determined was 2.1 and it is close to values typical for electron beam lithography. Energy length of ions determined was 42 μm. This value is approximately 20 percents less than the energy length obtained by modeling with TRIM (53 nm). This difference can be due to the imperfection of the formulas (interaction cross sections of TRIM) embedded in the modeling

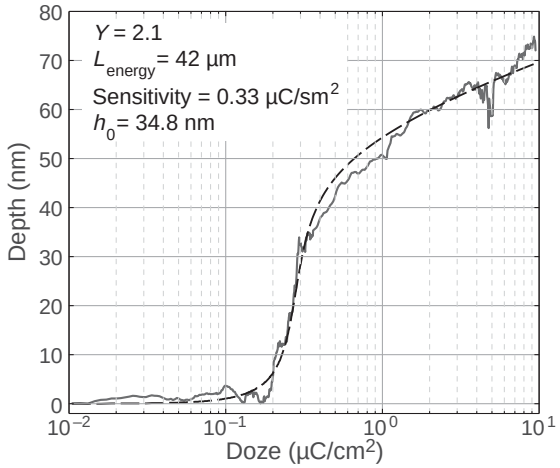

Fig. 1. Depth-dependence of deposited energy density (top) and resist etching velocity (bottom) for electron (1) and ion (2) beam exposure.

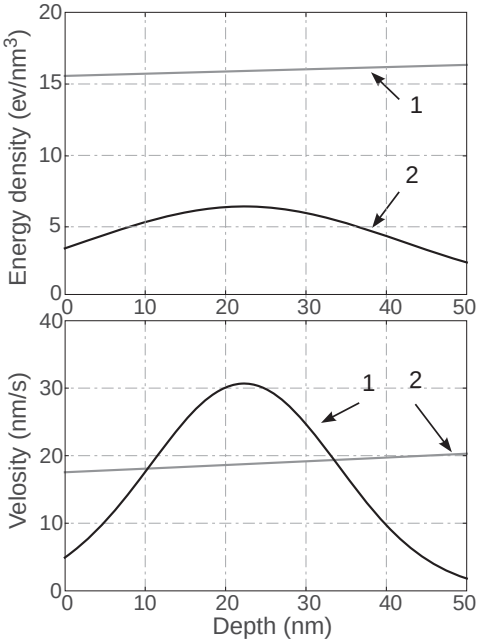

Fig. 2. Measured etching depth profile (black curve) and fitted one (gray curve).

algorithm as well as due to the simplicity of the development model.

By using the boundary condition (5) etching velocity (1) depending on deposited energy density ϵ can be written as

$$V(z) = \frac{F(h_0)}{T}\left(\frac{Z}{D^* E_b}\right)^{\gamma} \epsilon^{\gamma}(z). \qquad (7)$$

Equations (2) and (7) were used to compare the typical values of deposited energy density and the resist etching velocity for ion and electron beam lithography. The results of the comparison of these values for the case when exposure dose is equal to sensitivity are shown at Fig. 2.

The values of sensitivity used was determined in our early experiment [6], in that PMMA resist ($h_0 \sim 50$ nm, $T \sim 5$ s) was exposed by Ga+ ions and electrons with 30 keV energy. Certain sensitivity values were 150 μC/cm^2 for electrons and 0.15 μC/cm^2 for ions. To describe the depth distribution of deposited energy an empirical expression [9] was used for ions and a program described in [10] for electrons.

Fig. 2 shows that the deposited energy density values for ions and electrons have the same order of magnitude and the resist etching velocities are of the same order of magnitude as well. This implies that the etching rate of the resist is defined (through the number of broken chemical bonds and residual molecular mass) by the quantity of deposited energy density. So that the mechanism of energy loss, which is utterly different for electrons (the ionization of atoms in resist) and ions (the knocking out of atoms from polymeric chains), does not play a crucial role.

Acknowledgement

This work was supported by RFBR, grant No. 18-07-01402-a.

References

[1] M. Komuro, N. Atoda and H. Kawakatsu, *J. Electrochem. Soc.* **126**, 483 (1979).

[2] R.L. Kubena, J.W. Ward, F.P. Stratton *et al*, *J. Vac. Sci. Technol. B Microelectron. Nanom. Struct.*, **9**, 3079 (1991).

[3] K. Arshak, M. Mihov, S. Nakahara *et al*, *Superlattices Microstruct.* **36**, 335 (2004).

[4] D. Winston, J. Ferrera, L. Battistella *et al*, *Scanning* **34**, 121 (2012).

[5] J. Cai, Z. Zhu, P.F.A. Alkemade *et al*, *Adv. Mater. Interfaces* **5(12)**, 1800203 (2018).

[6] S.I. Zaitsev, N. Gusseinov, M. Gabdullin *et al*, *26th Int. Symp. Nanostructures: Physics and Technology*, Minsk, Belarus, 130 (2018).

[7] S.I. Zaitsev and Ya.L. Shabelnikova, *Int. Conf. Modern Problems in Physics of Surfaces and Nanostructures*, Yaroslavl,Russia, 41 (2019).

[8] T.H.P. Chang, *J. Vac. Sci. Technol.* **12**, 1271 (1975).

[9] S.I. Zaitsev, Ya.L. Shabelnikova, N. Gusseinov *et al*, *Workshop X-ray optics*, Chernogolovka, Russia, 178 (2018).

[10] V.N. Pavlov, V.Ya. Panchenko and M.A. Polikarpov, *Surface. X-ray, synchrotron and neutron investigations.* **9**, 46 (2013).

28th Int. Symp. "Nanostructures: Physics and Technology"
Minsk, Belarus, September 2020

Study of wurtzite crystal phase stabilization in heterostructured Ga(As,P) nanowires

N.V. Sibirev[1,2], V.V. Fedorov[3], D.A. Kirilenko[1,4], E.V. Ubiyvovk[2,3], Y.S. Berdnikov[1,2], A.D. Bolshakov[1,3], and I.S. Mukhin[1,3]

[1] ITMO University, St Petersburg, Russia
[2] St Petersburg State University, St Petersburg, Russia
[3] St Petersburg Academic University, St Petersburg, Russia
[4] Ioffe Institute, Politekhnicheskaya 26, 194021, St Petersburg, Russia

Abstract. GaP as well as GaAs have face centered cubic crystal phase at standard conditions. Despite it GaP and GaAs nanowires frequently grow in a metastable hexagonal crystal phase called wurtzite. In this work stable growth of nanowire in metastable phase is explained by accounting the elastic strain in the nucleus of a new layer. Crystal phase switch in heterostructured Ga(As,P) nanowire caused by heterointerface studied theoretically and experimentally. Wurtzite segment after crystal phase switch linearly increase with nanowire diameter. Such dependence can't be explained by only kinetically driven effects. We consider such dependency as evidence of elastic strain stabilization of metastable phase in nanowires.

The crystal structure is one of the basic characteristics of the material which strongly influences its physical properties. Most of III-V in the bulk phase form a face-centered cubic lattice, so called zinc blende crystal structure. In contradiction to it, III-V nanowires (NWs) frequently have hexagonal crystal structure, named wurtzite. GaP in stable zinc blende phase is indirect bandgap semiconductor, while wurtzite GaP has direct band gap. This attracts additional interest for crystal switching in GaP nanowire. Usually such growth in metastable phase is explained by crystallization at the triple-phase line. The explanation requires, that NW growth proceeds in monocentric layer-by-layer growth, sidewalls surface energy is less for metastable wurtzite phase and nucleation at the triple line is more favorable than in the center [1]. This explanation has a certain critical value of NW radius above which NW always should grow in stable crystal phase. Yet there are a lot of papers where experimentally observed thick GaP NWs with wurtzite crystal phase [2].

Here we would like to consider another opportunity to explain crystal growth of GaP nanowire in hexagonal phase — the elastic strain. NW growth proceeds in layer-by-layer mode, when growth of each layer starts when the formation of a previous layer is completed [2,1]. In this case nuclei of new layer are strongly influenced by previous layers[2,3]. Let us assume that GaP NW start grow in metastable phase. In this case elastic barrier for the formation of nucleus of new layer in stable phase could reach the value 5–12 meV depends on position of nucleus and quality of crystal structure. This barrier could be greater than the energy difference of GaP formation in wurtzite and zinc blende crystal phase 6–9 meV. Similar consideration for GaAs gives following estimation, elastic barrier is less than 25 meV, energy difference of formation zinc blende and wurtzite 8–12 meV. Thus, it is energetically favorable if nucleus adopt crystal structure of previous layer. So, growth of GaP nanowire in wurtzite crystal phase could be stabilized via elastic stress. It should be noted that for fast NW growth rate size of nucleus is very small several atoms, so nucleation barrier for formation zinc blende and wurtzite nucleus is less than kT. Therefore, thermal fluctuations could switch growth of NW from metastable phase to stable phase.

Let us now consider the formation of narrow bandgap $GaAs_xP_{1-x}$ insertion in broad bandgap $GaAs_yP_{1-y}$ NW, $x > y$. Lattice constant of GaAs is greater than GaP. So broad band gap stem compress insertion. Lattice constant of wurtzite is less than zinc blende. So, one of the opportunities to reduce elastic barrier is formation of narrow band gap insertion in wurtzite phase. Figure 1 represents the energy difference of the new layer formation in wurtzite and zinc blende phase with accounting of the elastic stress from previous layer. Black region corresponds to stable growth in zinc blende phase, white region stable growth in wurtzite phase, blue growth in zinc blende phase with twins, red growth in wurtzite phase with stacking faults. So, if composition of Ga(As,P) insertion is strongly differs from the rest of NW it should have metastable phase. To verify our theoretical model, two samples were grown.

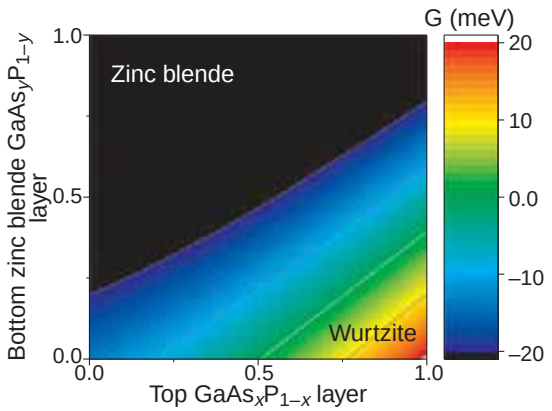

Fig. 1. The dependence of difference of formation energy of wurtzite and zinc blende nucleus on zinc blende stem.

First, the GaP NWs with several Ga(As,P) insertion with different As composition were grown. Growth of the GaP/Ga(As,P) axial NW heterostructures was initiated with a pure GaP stem synthesis. The fabricated heterostructures represent GaP NW with 8 embedded $GaP_{1-x}As_x$ nanodisks with a thickness of about 30–40 nm, separated by GaP segments with a length of ∼850 nm. GaP NW stem formed at the initial growth stage as well as GaP segments were synthesized at V/III BEP ratio of ∼8 and mean axial growth rate of 0.45 nm/s.

Detailed of the NW structure were obtained with HAADF-STEM and HRTEM. GaP NW segments showing lamellar twinned zinc blende structure. All $GaAs_{1-x}P_x$ nanodiscs demonstrates wurtzite crystal structure independently on the As composition, typical image is represented in Fig. 2.

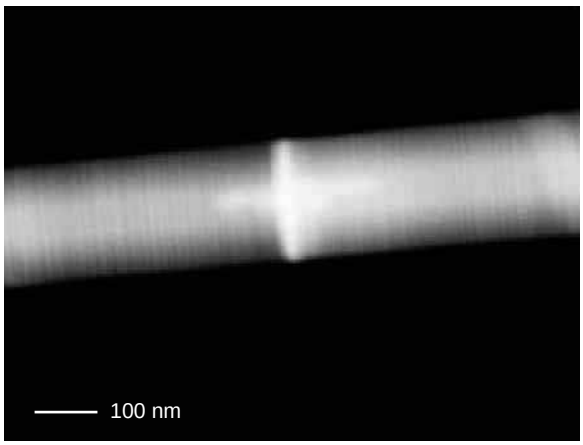

Fig. 2. HAADF-STEM images of the Ga(As,P) nanodisk in GaP NW.

Such behavior could be explained if we take into account that elastic stress expels initial nucleus to the edge of the NW, where energy gain of wurtzite phase increase via surface energy.

Second, inside pure GaP NWs long Ga(As,P) segments was formed. The length of Ga(As,P) segment has been selected much greater the NW diameters, which allows to relax all elastic strain from heterointerface. Typical HAADF-STEM is shown in Fig. 3.

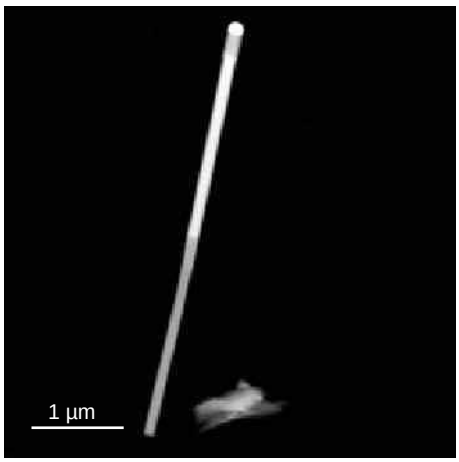

Fig. 3. HAADF-STEM images of the $GaP/GaAs_{0.64}P_{0.36}/GaP$ NW.

Both GaP segments of these NW have demonstrated zinc blende crystal phase with twins similar to previous experiment. Ga(As,P) segment just after the heterointerface has pure wurtzite crystal phase. After several ten nanometers some stacking faults appears. Density of stacking faults increases with increasing distance from heterointerface. Finally, Ga(As,P) segment adopt zinc blende crystal structure.

The dependence of length of wurtzite segment on NW diameter should allow us to distinguish which mechanism are responsible for polytypism in Ga(As,P) NWs. Triple line nucleation model didn't affect by NW diameter, yet elastic stress relaxed exponentially with the ratio of distance from heterointerface and NW diameter. So elastic strain model predicts that wurtzite segment thickness directly proportional for NW diameter, while triple line nucleation mechanism predicts the wurtzite segment length is independent from NW diameter. Experimentally measured dependence is represented in Fig 4.

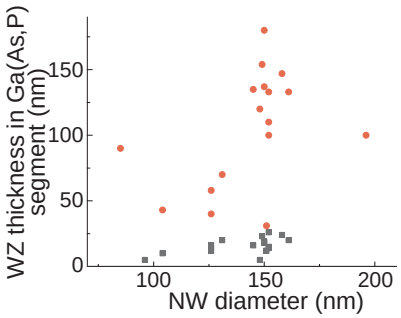

Fig. 4. The dependence of length of wurtzite segment on NW diameter: red wurtzite with stacking fauts, black pure wurtzite.

Experimental data didn't allow us to determine which mechanism is more effective in our case. But it clearly demonstrates necessity to taking into account the influence of elastic stress on NW crystal phase.

Authors thank the Ministry of Education and Science of the Russian Federation for financial support under grant 05.617.21.0058 (project ID RFMEFI61719X0058).

References

[1] F. Glas, J. Harmand and G. Patriarche, *Phys. Rev. Lett.*, **99**, 3, (2007).

[2] N. Sibirev, Y. Berdnikov, V. Sibirev, *et al*. *Phys. Sol. Stat.*, **61**, 2313, (2019).

[3] A. Bolshakov, V. Fedorov, N. Sibirev, *et al*. *Phys. Stat. Sol. (RRL)*, **13**, 1900350, (2019).

28th Int. Symp. "Nanostructures: Physics and Technology"
Minsk, Belarus, September 2020

Microsphere lithography for Fe_3Si-Au magnetoplasmonic nanostructures

T.E. Smolyarova[2,3], I.A. Tarasov[1], I.A. Yakovlev[1], I.V. Nemtsev[2], S.N. Varnakov[1], S.G. Ovchinnikov[1,3]

[1] Kirensky Institute of Physics, Federal Research Center KSC SB RAS, Krasnoyarsk, Russia
[2] Federal Research Center KSC SB RAS, Krasnoyarsk, Russia
[3] Siberian Federal University, Krasnoyarsk, Russia

Abstract. Magnetoplasmonic nanostructures combine ferromagnetic and plasmonic materials to exploit field enhancement in order to create active optical devices, which are tunable by an external magnetic field. Here we show the investigation of magnetoplasmonic activity of iron silicide thin films coupled with gold layers.

Introduction

Nowadays, hybrid noble metal/ferromagnetic metal nanostructures being investigated are FM-Au bi- and trilayers (FM–Co, Fe, Ni, YiG), and patterned thin films with a dot and antidot structures [1,2]. The further investigations spread on other plasmonic materials as Ag, Cu or Al. In this work, we aim to examine the MO activity of ferromagnetic iron silicide thin films coupled with gold layers. The patterned dot and antidot nanostructures are also under investigation (Fig. 1). The utilization of Fe_3Si instead of pure ferromagnetic metals gives us an opportunity to alter intrinsic optical and MO properties of ferromagnetic metal through the chemical composition and chemical order [3].

1. Experimental

The substrates were cleaned of organic contaminants in a solution of distilled and deionized water, hydrogen peroxide and aqueous ammonia in a ratio of 1:1:1 at a temperature of 80 °C for 2–3 minutes. Then a solution of ethanol and surfactant Triton X-100 was prepared and added to the suspension with microspheres in a ratio of 1:1.

Then followed the step of centrifuging the solution on the surface of the substrates. A prepared solution with microspheres was applied to a substrate untwisted at a speed of 1000 r/sec and distributed over the substrate into a disordered monolayer due to gravitational forces for 60 s. Then, the spin speed was increased to 2500 r/sec for 20 s to reduce the volume of solvent. Further, the speed increased to 5000 r/s to start the self-assembly process in a hexagonal tight package. And the final stage was the drying of a tightly packed monolayer at 8000 r/s.

This was followed by a stage of reactive ion etching in an oxygen atmosphere to reduce the size of the microspheres.

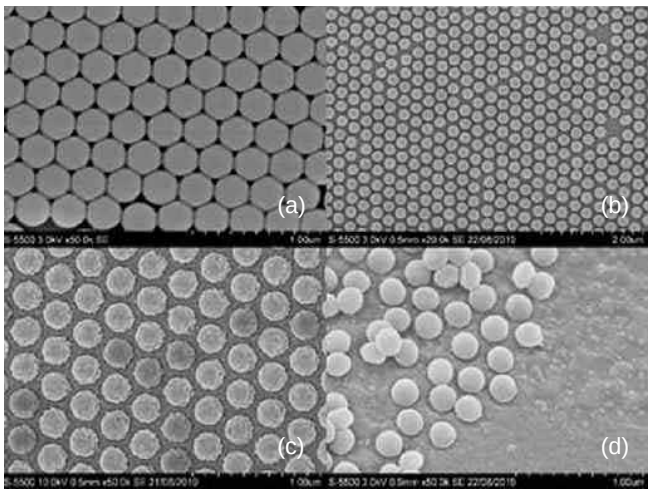

Fig. 1. Scanning electron microscopy image of polystyrene nanospheres used for preparation of dot and antidote Fe_3Si-Au nanostructures (a) 320 nm and (b) 272 nm in diameter, (c) covered with gold layer, (d) on Fe_3Si surface treated in HNO_3 acid.

2. Results

The utilization of Fe_3Si instead of pure ferromagnetic metals gives us an opportunity to alter intrinsic optical and MO properties of ferromagnetic metal through the chemical composition and chemical order [3]. The optical and magneto-optical properties of highly textured hybrid nanostructures of four types with different layer thicknesses were studied: I — Fe_3Si, II — Fe_3Si/Au, III — Au/Fe_3Si/Au, IV — Au/Fe_3Si. Some samples were used to create a monolayer of polystyrene microspheres on their surface with the help of microsphere lithography.

A positive result was achieved using a weakly concentrated solution of ethyl alcohol and a surfactant (1: 200), with an aqueous suspension of microspheres 300 nm in size. A significant increase in the magneto-optical response was shown on structures with a surface modified by a monolayer of polystyrene nanospheres. The maximum position of the magneto-optical effect can vary in the wavelength range from 270 to 413 nm for samples with an initial nominal size of 320 nm by changing their size to 276 nm (Fig. 2). As a result of the studies, a wide variability of changes in the magneto-optical properties of nanostructures based on thin epitaxial films of ferromagnetic

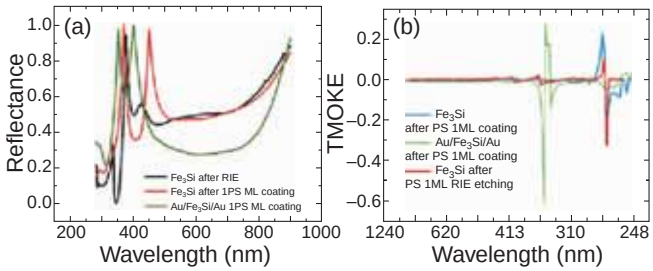

Fig. 2. (a) Measured spectral reflectivity and (b) transversal Kerr effect spectra for the heterostructure samples with the nanosphere monolayer on the surface.

iron silicide by modifying the surface through the creating of a monolayer of polystyrene microspheres, changing their size, and also applying a plasmon metal to their surface was demonstrated.

Acknowledgement

The work is carried out with the assistance of Krasnoyarsk Regional Center of Research Equipment of Federal Research Center “Krasnoyarsk Science Center SB RAS”.

References

[1] A.V. Kimel *et al*, *ACS Photonics* **3**, 1385âŁ“1400 (2016).
[2] M.U. GonzÃ¡lez *et al*, *Adv. Opt. Mater.***1**, 10âŁ“35 (2013).
[3] I. Tarasov *et al*, *EPJ Web Conf.* **185**, 03014 (2018).

28th Int. Symp. "Nanostructures: Physics and Technology"
Minsk, Belarus, September 2020

Tuning of GaAs nanowires photovoltaic properties via Ga droplet size control

A.S. Sokolovskii[1], D.P. Wilson[2], N.I. Goktas[2], V.G. Dubrovskii[1,3], R.R. LaPierre[2]

[1] ITMO University 197101 St Petersburg, Russia
[2] Department of Engineering Physics, McMaster University L8S4L7, Hamilton, ON, Canada
[3] St Petersburg State University 199034, St Petersburg, Russia

Abstract. GaAs nanowire (NW) arrays were grown on Si substrates by selective-area molecular beam epitaxy (MBE) using the self-assisted vapor-liquid-solid (VLS) method. In the self-assisted VLS method, the GaAs NW diameter is determined by the size of a Ga droplet at the top of the NW. An analytical model was developed to describe the evolution of the inverse-tapered NW morphology.

Introduction

III–V nanowires (NWs) with heterostructures are of great interest for device manufacturing due to their exceptional optoelectrical properties. The diameter of vertically standing III–V NWs determines the optical absorption spectrum due to resonant radial modes HE_{11}. This means that NWs with continuously varying diameters are able to absorb light in a larger wavelength range compared to NWs with a constant radius. The main properties of the growth of self-catalyzed GaAs NWs grown by the "vapor-liquid-crystal" (VLS) mechanism is the ability to control the diameter of the NWs by changing the flow ratio of the 3rd and 5th groups elements.

In this work, conditions were selected and a series of experiments on the growth of GaAs NW with a linearly increasing radius depending on the length of the NW was performed. Numerical simulations of conical and straight NWs were also performed to compare light absorption and photocurrent density for different vertex diameters.

1. Modeling and experimental

An attempt was made for theoretical description of the GaAs NW growth process leading to the unusual inverse-tapered NW shape. Ga-catalyzed III–V NWs were grown by gas source molecular beam epitaxy (MBE) on patterned Si(111) substrate with SiO_2 mask. Firstly GaP NWs stems were grown during 25 min, V/III flux ratio (F_{53}) was equal to 2. The gallium flux was kept as constant value 0.125 m/h throughout the growth experiment, the growth temperature was 700 °C. After that, "ramp" stage was implemented, when phosphide flux was switched off and arsenic flux was switched on under the same value of $F_{53} = 2$ for 5 min.

GaAs NWs growth after "ramp" stage can be divided into 2 phases. In the first phase, NWs radius R increases very rapidly until some stationary radius value R_0 is achieved. In the second phase, NWs diameter increases linearly until the stopping of growth process. Let us express NWs top radius extension in terms of gallium droplet radius. According to Ref. [1,2], excessive Ga influx leads to increasing of NW top diameter. Hence, III/V flux imbalance is positive.

We observed radial self-focusing growth regime before and during "ramp" stage. It is obvious that switching F_{53} to value 1 means the influx rate of group III atoms becomes greater than influx of group V atoms. Alteration of occurs instantly therefore III/V flux imbalance changes sign and takes a new fixed value. Decreasing of As flux leads to reducing of arsenic concentration in liquid phase until certain stationary concentration will be reached. According to Ref. [3], we know that weak difference in As concentration relates to strong variation of chemical potential. Furthermore, the result of As concentration declining is increasing of Ga concentration until certain value. We assume that after "ramp" stage extra-rapid diameter extension correlates with the process of steady-state conditions achievement. In other words, when steady-state condition is achieved the difference reverse diffusion from droplet equalizes Ga adatom surface diffusion from sidewall facets to the droplet.

The expected photocurrent density was calculated by integrating the volume of the NW under the assumption that each absorbed photon generates one electron–hole pair. The straight NW only slightly surpassed the conical NW in photocurrent density (25.6 and 24.7 mA/cm^2 respectively). At the same time, a conical NW is able to support a photocurrent with 96% of the volume, and a straight NW with only 64% of the volume. Thus, the resulting conical NWs are of particular interest for integration with silicon solar cells in multi-pass photovoltaic devices.

2. Summary

We have shown that the most effective way of obtaining wide diameter NWs is to controllably inverse-taper the structures to create NWs with thin bases and wide tops. The thinner base is advantageous because the diameter lies below the critical diameter for misfit dislocations. Controlling diameter through the droplet presents the possibility of adjusting the diameter throughout the growth process, allowing for more complex NW structures. A comparison of inverse-tapered NWs with straight NWs indicated that they are capable of giving comparable optical absorptance.

References

[1] V.G. Dubrovskii *et al*, *Nano Lett.*, **15** 5580 (2015).
[2] G.A. Priante *et al*, *Cryst. Growth Des*, **13** 3976 (2013).
[3] F. Glas *et al*, *Phys. Rev. B*, **88** 195304 (2013).

28th Int. Symp. "Nanostructures: Physics and Technology"
Minsk, Belarus, September 2020

Laser assisted fabrication of nanostructured ZnO thin films doped with cobalt

N.N. Tarasenka, A.A. Nevar, E.A. Shustova, V.G. Kornev and N.V. Tarasenko
B.I. Stepanov Institute of Physics National Academy of Sciences of Belarus

Abstract. In the present work a laser assisted method has been developed for the formation of Co-doped ZnO nanostructured layers based on laser processing of the films pre-deposited on a substrate. Structural and optical properties of the obtained samples have been studied. The formation of Co-doped ZnO nanostructures on the glass substrates has been proved by X-ray diffraction, Raman and optical absorption measurements.

Introduction

Zinc oxide, a direct and wide band gap (3.37 eV) II–VI semiconductor has attracted much attention as a promising material for optoelectronic devices owing to its optical and electronic properties such as high exciton binding energy (nearly 60 meV at room temperature), good transparency and long term stability, excellent sensing and piezoelectric properties. ZnO found technological applications in fabrication of various microelectronic devices like light emitting diodes, lasers, solar cells, sensors, and recently in spintronics. Recent studies showed that optical, magnetic, and electrical properties of ZnO nanostructures can be controlled by incorporation of dopants in the ZnO lattice [1, 2]. Among the different doped ZnO structures, Co-doped ZnO can be one of the most promising materials for applications in spintronic devices due to room-temperature ferromagnetic properties.

As a dopant, cobalt is a promising material for the ZnO doping as it is able to modulate both optical, electronic and magnetic behavior of ZnO due to its abundant electron states. Its similar ionic radius as well as its divalent state ensures high solubility in ZnO. In addition, remarkable optical and magnetic behavior is observed even at small concentration of cobalt substitution in the ZnO structure due to which it has been widely used for tuning the properties of ZnO for the potential applications in magneto-electrical and magneto-optical devices, spintronics, and as passive Q-switchers (saturable absorbers) for near- and mid-infrared lasers [2–4].

In the present work a laser assisted method has been developed for the formation of Co-doped ZnO nanostructured layers based on laser processing of the pre-deposited thin films. The purpose was to achieve substitutional incorporation of Co^{2+} ions on the Zn site inside ZnO nanoclusters through the fast laser induced heating, subsequent melting, and re-solidification processes at high cooling rates. The process time is rather short — tens of ns =– and process occurs under thermal non-equilibrium. Therefore, higher concentrations of dopant can be expected compared to the conventional doping methods operating under thermal equilibrium.

1. Experimental

Initially, ZnO and Co colloidal NPs were prepared by laser ablation of Zn and Co targets in distilled water and acetone, respectively. Laser ablation experiments were carried out by focusing the radiation of a Nd:YAG laser (LOTIS TII, LS2134D), operating in a double-pulse mode at 1064 nm (energy 80 mJ/pulse, repetition rate 10 Hz, pulse duration 8 ns), on the surface of a relevant target placed in the cell filled with a liquid (water or acetone). The temporal delay between two collinear laser pulses could be varied in the range 0–120 μs. In order to provide control over the NPs formation process the plasma parameters were investigated using optical emission spectroscopy.

After the preparation, the prepared NPs were studied using optical absorption and Raman spectroscopy, transmission and scanning electron microscopy, X-ray photoelectron spectroscopy, electron and X-Ray diffraction.

To clarify the possibility of using the prepared NPs in a range of applications we have investigated the properties of the nanostructured thin films deposited from the synthesized colloids. For this, two techniques were used. The first approach used in this work consisted in laser processing of pre-deposited ZnO and Co films for fabrication of cobalt-doped zinc oxide nanostructured films. For this, Co colloidal nanoparticles (NPs) were deposited by spin-coating over the 100 nm ZnO layer preliminarily formed on a glass substrate followed by laser processing of the obtained bi-layer structure (Fig. 1). The second technique was based on sequential laser ablation of Zn and Co targets in distilled water followed by spray-coating of the prepared colloid on the glass substrate and annealing at 270 °C during 1 hour.

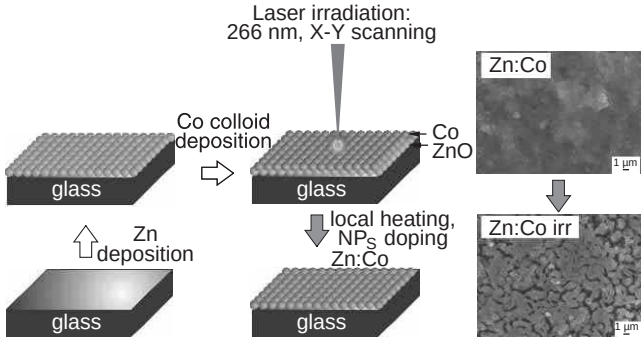

Fig. 1. Scheme of the ZnO:Co fabrication procedure (left) and the SEM images (right) of the prepared films before (top) and after 266 nm laser irradiation.

After the formation, the thin films were exposed to laser-induced modification. As an annealing laser source, the fourth harmonic of Nd:YAG laser (266 nm, pulse duration of 10 ns, energy 0.5–5.5 mJ/pulse, laser beam diameter 2 mm) was used. For the determination of optimal conditions, the dependence of Co incorporation on the laser wavelength (second and fourth harmonic) and laser fluence was studied. Adjusting the laser fluence it is possible to provide very rapid melting/solidification cycles for the deposited samples. Different methods of inves-

tigation of the optical and structural properties (XPS, XRD, Raman and optical absorption measurements) were applied to prove the doping achievement in the prepared nanostructures.

2. Results and discussion

We demonstrated that successful preparation of the Co-doped ZnO nanocrystalline layers on the glass substrates can be achieved under the optimized laser parameters (wavelength, laser fluence, irradiation duration). The changes induced by laser irradiation of the prepared nanostructures were first elucidated from the morphology analysis using scanning and transmission electron microscopy. The SEM images in Fig. 1 evidence NPs elongation due to their possible co-melting. The influence of the laser fluence on the optical properties of the nanostructured films are presented in Fig. 2. The UV-Vis absorption spectroscopy was used to find out the changes in the energy band structure of ZnO due to Co doping.

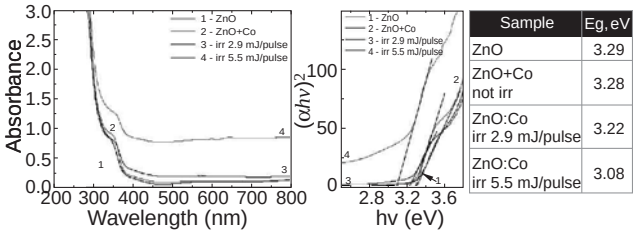

Sample	Eg, eV
ZnO	3.29
ZnO+Co not irr	3.28
ZnO:Co irr 2.9 mJ/pulse	3.22
ZnO:Co irr 5.5 mJ/pulse	3.08

Fig. 2. UV-visible absorption spectra of ZnO and Co-doped ZnO samples prepared by laser irradiation of the pre-deposited ZnO and Co thin films.

he UV-Vis spectra of ZnO and Co-doped ZnO samples exhibited a strong absorption around 370–395 nm, and the absorption edge was red-shifted upon cobalt doping in ZnO. The bandgap *(Eg)* values can be estimated from absorption coefficient (α) dependence on the incident photon energy *($h\nu$)* using the Tauc relation $\alpha h\nu = A(h\nu - Eg)^n$ where A is a constant that depends on the transition probability, and n is an index that characterizes the optical absorption process and is 2 for indirect semiconductors and 1/2 for direct ones. As ZnO is the direct bandgap semiconductor material the intersection of linear fits of $(\alpha h\nu)^{1/n}$ versus $h\nu$ plots on the x-axis allows to estimate the bandgap, the results of bandgap calculation are presented in Fig. 2b. From the results presented in the table it is clear that the optical band gap decreases from 3.29 eV in the undoped sample upto 3.08 eV in the irradiated sample that may also serve as an evidence of Co doping after laser treatment and increase of the Co content in ZnO thin film after laser treatment with higher laser fluence. The narrowing of the bandgap is usually observed upon transition metals doping of the II–IV semiconductors and are typically attributed to the sp–d spin exchange interactions between the conduction band electrons and the localized d electrons of transition metals ions [3]. The shift of the absorption edge to lower wavelengths and decrease of the bandgap was also observed in UV-Vis spectra of samples prepared by sequential laser ablation of zinc and cobalt in distilled water.

To quantify the Co content incorporated into the doped samples after laser treatment, LIBS analysis of the synthesized samples composition was performed. The results showed the formation of films constituted of nanocrystallites having rather homogenous distribution of cobalt ions inside the ZnO matrix. The percentage of cobalt incorporated into the doped samples was measured to be at a level of 6% under our experimental conditions.

The results of XRD studies showed that the ZnO:Co sample prepared by laser irradiation of ZnO-Co layers had wurtzite structure without the appearance of any secondary phase, suggesting Co^{2+} incorporation to the Zn^{2+} sites in the crystal. After laser irradiation the reflections were weakened and broadened indicative of lattice distortion. In addition, variation of ZnO XRD peaks relative intensity was observed that can be attributed to Co^{2+} substitution of Zn^{2+} in the ZnO lattice forming Co-doped ZnO.

The disorder was also observed in the results of the Raman spectra analysis of the deposited nanostructured films that can be induced both by Co incorporation in the ZnO lattice and presence of defects. The disorder was proved by the broadening and intensity decrease of the $E_2^{(high)}$ mode at 437 cm^{-1}. At the same time the intensity of the defect-related bands like LO band at 580 cm^{-1} increased. In addition, $B_1^{(high)}$ mode shifted upto 530 cm^{-1} giving a remarkable feature assigned to local vibration mode related to Co that is bound with donor defects like doubly ionized oxygen vacancies and zinc interstitials [2]. From XRD and Raman spectra it can be deduced that incorporation of Co into ZnO leads to a decrease in crystal quality, but there is no change in wurtzite crystal structure.

In summary, we report the successful preparation of the Co-doped ZnO nanocrystalline layers on glass substrate. Two techniques were developed for Co incorporation: sequential laser ablation of Zn and Co targets as well as laser irradiation of Co layer deposited on ZnO layer. The doping was proved by XPS, XRD, Raman and optical absorption measurements. Laser irradiation of the NPs after their deposition results in co-melting of NPs with doped nanostructures formation. XRD studies confirmed the formation of ZnO having wurtzite crystal structure and its distortion after laser irradiation. Shifting and broadening of the Raman bands at 437 cm^{-1} and 580 cm^{-1} as well as decreasing of the bandgap in the Co-doped ZnO samples indicated the incorporation of Co in ZnO. For the control of the composition and size of the prepared particles further tuning of the experimental parameters is required.

Acknowledgement

The work was supported by the National Academy of Sciences of Belarus under project Convergence 2.4.06.

References

[1] N. Tarasenka, V. Pankov and N. Tarasenko, *Nano-Structures & Nano-Objects* **12**, 210 (2017).
[2] A. Chanda, S. Gupta, M. Vasundhara, S.R. Joshi, G.R. Mutta and J. Singh *RSC Adv.* **7**, 50527 (2017).
[3] R. Mimouni, K. Boubaker and M. Amlouk *J. Alloys Compd.* **624**, 189 (2015).
[4] A. Kaphle, T. Reed, A. Apblett and P. Hari *J. Nanomater.*, 7034620 (2019).

28th Int. Symp. "Nanostructures: Physics and Technology"
Minsk, Belarus, September 2020

Photoluminescence study of AlGaAs/GaAs after focused ion beam milling

G.V. Voznyuk[1], I.N. Grigorenko[1,2], M.I. Mitrofanov[1] D.N. Nikolaev[1], M.N. Mizerov[3] and V.P. Evtikhiev[1]

[1] Ioffe Institute, St Petersburg, Russia
[2] Saint Petersburg Electrotechnical University 'LETI', Russia
[3] RAS, SHM R&E Ctr, Saint Petersburg, Russia

Abstract. Light-emitting devices of modern photonics are based on the semiconductor structures containing layers with various physical parameters. To preserve initial parameters during focused ion beam (FIB) lithography, it is necessary to take into account the processes of radiation defect formation. Radiation-induced defects in target play role of nonradiative recombination centers leading to photoluminescence (PL) quenching. In our work, the FIB impact on the photoluminescence were examined using PL spectroscopy of milled $Al_{0.18}Ga_{0.82}As$/GaAs double heterostructure. In order to exclude photoexcited carriers losses in emitter layer, an experiment with subbarrier photoexcitation was organized. Finally, we compare our experimental findings with theoretical data proposed by stopping and range of ions in matter (SRIM) calculation.

Introduction

Development of methods for three-dimensional micro/nanoscale devices fabrication is one of the most important tasks of modern semiconductors technology. At the stage of prototypes development conventional photolithography methods is impractical due to high economic and time costs. In this case, the most relevant method is maskless fabrication by FIB direct-write lithography. The FIB lithography method allows to solve a wide range of tasks from preparing samples for transmission electron microscopy [1] to prototyping elements of integrated photonic circuits [2] and modifying the characteristics of ready-made devices [3]. The main obstacle for the development of this method is the radiation defects formation during the interaction of a high-energy ion beam with the material [4]. This circumstance is especially important when processing light-emitting semiconductor heterostructures. The occurrence of defects in such structures leads to quenching of luminescence and reduction of quantum yield. In this regard, the development of active (emitting) devices is impossible. The formation of radiation defects is well studied for the ion implantation process in ion energy range from 100 to 300 keV [5]. However, the formation of radiation defects in practically important A3B5 semiconductor heterostructures during FIB lithography at 10–30 keV is not sufficiently studied.

1. Photoluminescence study of FIB milled regions

For this study we have grown double heterostructure with $Al_{0.18}Ga_{0.82}As$ emitters each 1 μm thick and 1 μm thick GaAs active region by metalorganic chemical vapour deposition (MOCVD). FIB milling was carried out in an ultra-high vacuum working chamber of FIB/FEB dual beam system with Ga ion source at 30 keV accelerated voltage and 2 nA working current. The milling pattern in the form of 100x100 μm square blind holes with different depths were formed (see table 1). FIB milling was accompanied by XeF_2 gas-assisted etching to improve milled surfaces by reducing redeposition effects and enhance the milling speed.

Examination of the milled structure properties was performed by PL measurement at 77 and 300 K. To get rid of photoexcited carriers losses in the emitter layer, an experiment with subbarrier photoexcitation was organized. PL spectra were obtained by exciting the sample with a 808 nm laser.

Table 1. Milling depth

Number of square	Milling depth (nm)
1	139
2	276
3	428
4	600
5	663
6	747

After FIB processing PL measurements at 300 K were carried out. PL signal from milled areas was below the noise floor of the recording equipment. In our opinion, such PL quenching is associated with formation of radiation defects that play role of Shockley-Read-Hall non-radiative recombination centers (traps). It's well known that carriers at RT can have enough energy to get on traps and non-radiative recombination occurs . With decreasing temperature, the carriers become effectively frozen, thus traps effectiveness can be decreased and it becomes easier to analyze the intrinsic properties of the material. In with regard we perform low temperature PL measurement in liquid nitrogen at 77 K. Low-temperature measurements (figure 1) allow to detect a signal from milled regions.

To restore initial properties of milled structure we have performed annealing at 630 K in As atmosphere during 20 minutes, which was close to incongruent melting temperature of $Al_{0.18}Ga_{0.82}As$/GaAs. The PL signal evolution after annealing, measured at 77 and 300 K, presented in the figure 1. The deviation of the signal between measurements at 77 and 300 K does not exceed 10%, which indicates a high internal quantum yield of processed structure. A signal drop was observed from area of 3rd square (milling depth 428 nm). To explain this phenomenon, we analyzed the luminescent region in milled squares using a images from CCD camera. To prevent the contribution of 808 nm radiation laser pumping in total PL signal, an edge longpass filter with a cut-off wavelength of 825 nm was used. The optical imagine of luminescence area demonstrated on figure 2. Dark (non-luminous) line that cross luminescent region are clearly visible. The ratio of the non-luminous area

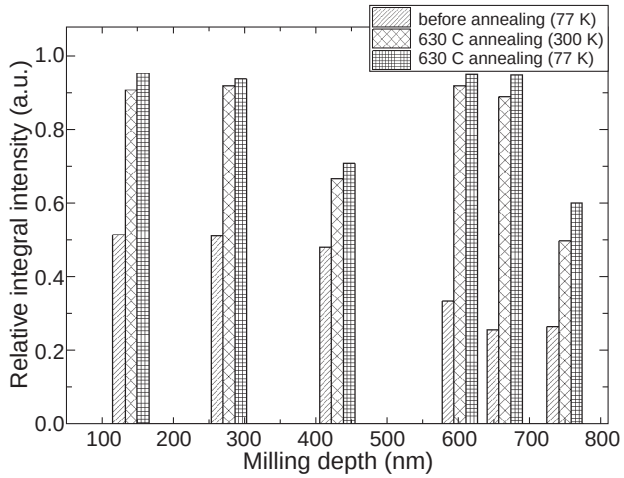

Fig. 1. The comparison of the relative integral PL intensity from milled regions before and after annealing mesured at 77 and 300 K.

to the whole photoluminescence region is about 25%, which correlates with drop in the integral intensity. PL intensity distribution in 3rd square demonstrated on figure 3. In our opinion, this phenomenon can be caused by a crystal defect such as a linear defect appeared after annealing.

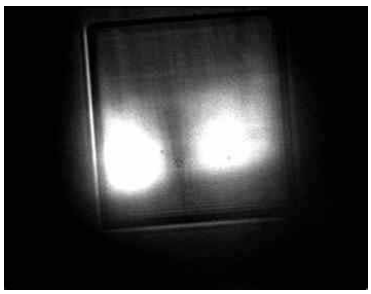

Fig. 2. Optical image of luminescence area inside 3rd milled square with 428 milled depth.

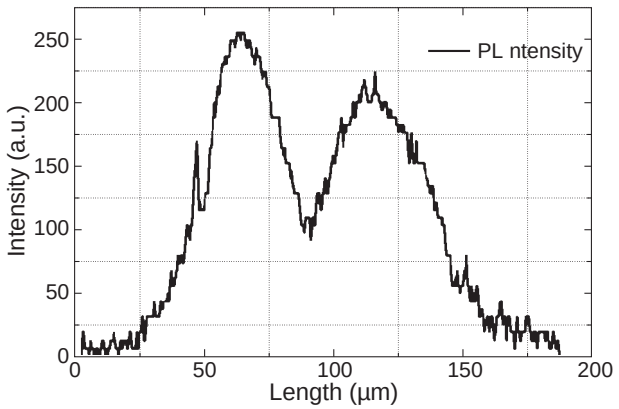

Fig. 3. Distribution of PL intensity inside milled region of 3rd square.

2. Discussion

The FIB impact on $Al_{0.18}Ga_{0.82}As$/GaAs double hetero-structure leads to strong quenching of luminescence. In our opinion quenching of PL is associated with the formation nonradiative recombination centers due to FIB induced radiation defects. In our previous work, calculations in a popular software SRIM showed that the depth of radiation defects in the $Al_{0.18}Ga_{0.82}As$ layer does not exceed 70 nm [6]. PL measurements showed that the influence of radiation damage on the active region in the $Al_{0.18}Ga_{0.82}As$/GaAs heterostructure occurs at small etching depths from 150 nm and deeper that correspond the distance to the heterointerface was about 850 nm. Thus, experimental results more then 10 times exceed the calculated data by SRIM. Such deviations could be explained by limitations of the software model. The model of ion-atom interactions in SRIM is based on linear collision cascades (LCC). LCC means that the primary knocked-on atom receives enough energy to create a cascade of knocked-on atoms. LCC is characterized the low spatial density of the moving atoms. Each new charged ion with a solid interaction considered as a separate event. Such approach does not allow to take into account the possibility of overlapping cascades of atomic collisions from a large number of simultaneously incident ions. In real conditions, collision cascades may overlap and a distribution density of atoms is so high that most of the atoms inside a certain volume are in motion. This mode is called the heat spikes mode. When heat spikes occurs, the irradiated region is heated, which leads to enhance of radiation defects diffusion in material. Another significant drawback of SRIM is the use of only the universal Ziegler, Biersack and Littmark (ZBL) potential, although other types of potential can be used to model ion sputtering process [7].

3. Conclusion

The FIB impact on $Al_{0.18}Ga_{0.82}As$/GaAs leads to quenching of luminescence. Quenching of luminescence is associated with the formation of nonradiative recombination centers. During PL studies we find linear structural defect in the area of milled square that formed after annealing. It was shown that annealing at 630 K allows to achieve 90% recovery of initial luminescence signal from FIB milled areas. The PL signal difference in milled region at 77 and 300 K after annealing did not exceed 10% which indicates high quantum yield of milled structures. It was shown that real penetration depth of radiation defects in $Al_{0.18}Ga_{0.82}As$ layer exceeds the SRIM calculated data more than 10 times. Thus, modern theoretical models cannot always give adequate value of the radiation defects penetration depth. Our findings expand ion beam lithography application area making it a convenient method for prototyping devices based on light-emitting semiconductor heterostructures.

References

[1] L.J. Tang, Y.J. Zhang, M. Bosman, Jasmine Woo, *17th IEEE International Symposium on the Physical and Failure Analysis of Integrated Circuits (Singapore*, 2017*)*, IEEE, 24, 2017.
[2] JePPIX roadmap 2018.
[3] C.R. Musil, B. D.Patterson, H. Auderset *Nuclear Instruments and Methods in Physics Research Section B: Beam Interactions with Materials and Atoms* **127–128**, page 428–432 (1997).
[4] C.A. Volkert, A.M. Minor *MRS Bulletin* **32**, page 389–399 (2007).
[5] A.J. Steckl, P. Chen, A.G. Choo, *et al*. *MRS Proceedings* **281**, page 319 (1992).
[6] G.V. Voznyuk, I.V. Levitskii, M.I. Mitrofanov, *et al*, *Journal of Physics: Conference Series (Saint Petersburg, Russian Federation,* 2018*)*, **1038**, (2018).
[7] S.V. Dovnar, V.V. Grigoriev, A.V. Leontiev, Some aspects of the modernization of the TRIM algorithm for the Monte Carlo method. *The 4th International Conference on the Interaction of Radiation with Solids (Minsk,* 2001*).*

28th Int. Symp. "Nanostructures: Physics and Technology"
Minsk, Belarus, September 2020

CoC films synthesized with arabinogalactan

S.V. Stolyar[1,2,3], *R.N. Yaroslavtsev*[1,2], L.A. Chekanova[1], S.V. Komogortsev[1], E.V. Cheremiskina[3], D.S. Neznakhin[4] and R.S. Iskhakov[1]

[1] Kirensky Institute of Physics, SB Russian Academy of Sciences, 660036, Krasnoyarsk, Russia
[2] Krasnoyarsk Scientific Center, Federal Research Center KSC SB RAS, 660036, Krasnoyarsk, Russia
[3] Siberian Federal University, 660041, Krasnoyarsk, Russia
[4] Ural Federal University, Ekaterinburg, Russia

Abstract. Cobalt coatings containing carbon were obtained by chemical deposition using arabinogalactan as a reducing agent. The crystal structure and chemical composition of the coatings are determined. We found that carbon in coatings is present in the form of graphite inclusions. The saturation magnetization, the local anisotropy field, the size of the correlation radius, and the anisotropy field of the synthesized coatings were determined by magnetometry.

Introduction

Electroless deposition is the easiest and most economical way to apply metal coatings. The method is based on the reaction of metal ions with a dissolved reducing agent, which results in the formation of a metal layer on a catalytically active surface. Formaldehyde, hydrazine, sodium hypophosphite, hydrazinborane are used as reducing agents in the production of magnetic metal coatings. The most common reducing agent in the production of Co and Ni coatings is sodium hypophosphite NaH_2PO_2. Currently, a new approach to metal recovery is rapidly developing, known as green synthesis [1]. Extracts of natural plant products are used in green synthesis. This approach is developing as promising environmentally friendly methods that will overcome existing barriers in chemical production methods. Such extracts are generally non-toxic, and function as a dispersing and coating agent, minimizing oxidation and agglomeration processes. This work aims to synthesize Co-based coatings using green chemistry methods and study their properties.

1. Experimental

In this work, the natural polysaccharide arabinogalactan was first used to obtain Co coating. Coating samples were studied using a Hitachi HT7700 transmission electron microscope, a scanning electron microscope of the collective use center of the Krasnoyarsk Scientific Center of the SB RAS, and vibration magnetometry method.

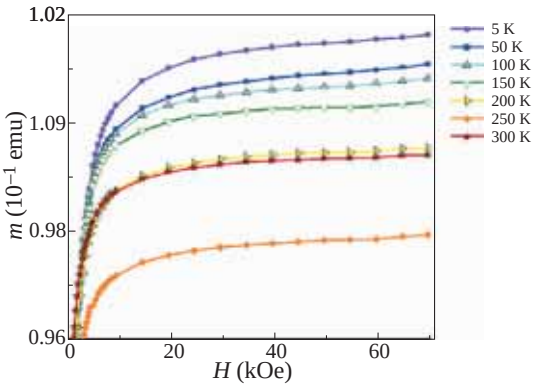

Fig. 1. Magnetization curves at various temperatures

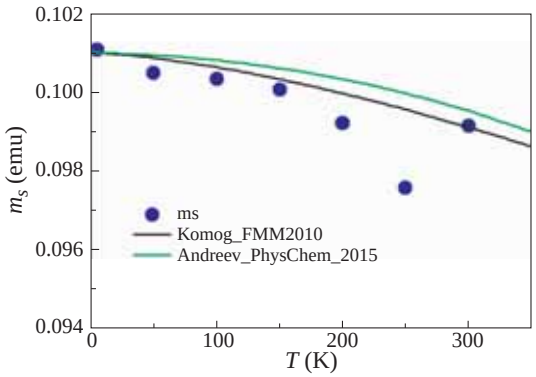

Fig. 2. Temperature dependence of saturation magnetization

2. Results and discussion

According to the results of electron microscopic and diffraction studies, the coatings are characterized by the presence of carbon 20%. The coercive force, remanence magnetization, and saturation magnetization decrease with increasing temperature (Fig. 1,2). A comprehensive analysis of structural and magnetic data indicates that the cobalt lattice does not contain carbon impurities. This indicates that the carbon in the coatings is contained in separate phases, for example, in the form of graphite inclusions.

The formation of the metal coating is probably due to the catalytic decomposition of the polysaccharide on metal substrates. The glycosidic bonds forming the polysaccharide molecule are stable in an alkaline medium at a low temperature. However, degradation occurs at the ends of the polysaccharide molecules under such conditions. Aldehyde groups at the ends of molecules have reduction properties. Thus, the monosaccharide unit is separated and then oxidized to a carboxylic acid. The catalytic decomposition of the polysaccharide on the substrate is not limited to the proposed reaction. The final decomposition product of the polysaccharide is graphite, which we detected by the XRD method. Carbon, which is a product of reactions occurring on a metal surface, forms exclusively the graphite phase and is not included in the crystal lattice of the magnetic coating.

Acknowledgements

This work was supported by the Russian Foundation for Basic Research, the Government of the Krasnoyarsk Territory, the Krasnoyarsk Regional Fund for the Support of Scientific and Technical Activities (project No. 18-42-240006 Nanomaterials

with magnetic properties determined by the topological features of the nanostructure). This work was supported by a grant from the President of the Russian Federation for state support of young Russian scientists-candidates of sciences No. MK-1263.2020.3.

References

[1] S. Machado, S.L. Pinto, J.P. Grosso *et al*, *Total Environ* **1**, 445 (2013).

28th Int. Symp. "Nanostructures: Physics and Technology"
Minsk, Belarus, September 2020

Diffusion of H-atoms in Si and Ge films grown by MBE method on Si_3N_4 and SiO_2 substrates

K.V. Chizh[1], *L.V. Arapkina*[1], D.B. Stavrovsky[1], V.P. Dubkov[1], P.I. Gaiduk[2] and V.A. Yuryev[1]

[1] Prokhorov General Physics Institute of the Russian Academy of Sciences, Moscow, Russia
[2] Department of Physical Electronics and Nanotechnology, Belarusian State University, Minsk, Belarus

Abstract. The growth of a silicon or germanium films on a Si_3N_4 layer deposited using CVD or on a SiO_2 layer formed using thermal oxidation of a silicon substrate is accompanied by the diffusion of hydrogen atoms from the dielectric layer into the growing film. The difference in chemical potentials of hydrogen atoms in the dielectric layer and the silicon film explains the transfer of hydrogen atoms from the Si_3N_4 or SiO_2 layer into the growing silicon film. In the opposite direction atoms Si and Ge could diffuse into Si_3N_4 layer. These processes could be defined by FTIR, XPS and Raman spectroscopy methods.

Introduction

Presently, MEMS technology is a rapidly developing branch of science, one of the promising areas of which is the production of IR sensors based on amorphous (a-Si) or polycrystalline silicon films formed on Si_3N_4/SiO_2 dielectric layers.The properties of a-Si and poly-Si films are determined both by the technological modes of deposition and by the properties of the substrate, primarily, the upper layer of silicon nitride of a complex Si_3N_4/SiO_2/c-Si substrate. The most commonly used methods of depositing Si_3N_4 are LPCVD with thermal and PECVD with plasma-chemical decomposition of nitrogen-containing components. Application of any of these methods leads to the production of films saturated with hydrogen atoms.The concentration of hydrogen atoms in PECVD films can reach 25%, and in LPCVD films 8% [1–4]. Such hydrogen concentrations can significantly affect the properties of a-Si (a-Ge) and poly-Si (poly-Ge) films grown on the surface of a complex Si_3N_4/SiO_2/c-Si substrate due to desorption of hydrogen from the Si_3N_4 film during and after the deposition of silicon layers. In this paper, the processes occurring during low-temperature growth from molecular beams under conditions of ultrahigh vacuum (UHV) of non-hydrogenated a-Si (a-Ge) and poly-Si (poly-Ge) films on a multilayer Si_3N_4/SiO_2/c-Si or SiO_2/c-Si substrate are studied in detail. Ther Si_3N_4 and SiO_2 layers are the source of hydrogen atoms in our experiment. A diffusion process of H-atoms in the thin epitaxial Si or Ge layers has been researched using FTIR, XPS and Raman spectroscopy.

1. Experimental

Experimental samples were prepared by depositing Si or Ge layers on Si_3N_4/SiO_2/c-Si or SiO_2/c-Si substrates [5]. Si(Ge) films were deposited on the substrates from molecular beams in the ultra-high vacuum EVA 32 (Riber) molecular beam epitaxy (MBE) chamber. The MBE chamber was evacuated down to about $\sim 10^{-11}$ Torr before the processes. The pressure did not exceed $\sim 5\times10^{-9}$ Torr during growth. Si and Ge deposition rate were ∼0.3 Å/s and ∼0.25 Å/s, respectively; the film growth temperature was varied from 30–650 °C. Before moving into the MBE chamber, the substrates were annealed at 600 °C at the residual gas pressure of less than ∼5x10^{-9} Torr in the preliminary annealing chamber for 6 h. RHEED study was carried out during growth process. The XPS study was held in the analytical chamber of the Riber SSC2 UHV surface science center. Photoexcitation was performed by means of the non-monochromatic Al Ka1,2 X-ray radiation (1486.6 eV) generated at the source power of 180 W. The Fourier transform IR (FTIR) transmission and reflection spectra of the samples were explored using a vacuum IFS-66v/S spectrometer (Bruker).

2. Results and discussion

By Raman spectroscopy and RHEED it is found with the temperature increase layer structure changed from amorphous to polycrystalline. For Si layers transition was about 420–500 °C and for Ge layers one was about 300 °C. Raman spectroscopy did not revealed Si-Ge bounds. Fig. 1 and 2 show IR absorbance spectra in the range from 650 to 1350 cm^- for samples with Si and Ge layers. The spectra are characterized by the presence of two wide bands peaked at ∼825 and ∼1090 cm^{-1}.They are composed of eight spectral components peaked at about 735, 805, 860, 965, 1075, 1100, 1150 and 1190 cm^{-1}. Peaks are named according to works [6–10]. For all samples (Si and Ge) there are observed decreasing of intensity of N-H peak (∼1150 cm^{-1}) with growth temperature. For samples with Si layers intensity of the Si-N absorption band (∼860 $cm^{-1)}$ increases but for ones with Ge layers this peak decreases intensity. During Si growth at the temperatures under 160 °C the band assigned to the vibrations of the Si-H (∼2100 cm^{-1} bond appears. This band was absent into initial samples before the processes of Si layer growth. During deposition on the SiO_2 surface at 30 °C this band is observed too but it is absent in the samples grown on Si(001) substrate at all. The reduction of IR absorption at the bands related to the N–H bonds vibrations and the increase of IR absorption at the bands relating to the Si–N bonds vibrations in IR spectra demonstrate that hydrogen atoms leave Si_3N_4 layer during Si deposition. The absorption band assigned to the vibrations of the Si–H bond emerging in IR spectra obtained at samples deposited both on Si_3N_4 and SiO_2 layers indicates the accumulation of hydrogen atoms in silicon films if growth temperature is lower than one of H-desorption. During Ge growth regardless of temperature we did not observe appearance of Ge-H band (∼1850 cm^{-1}). It is known H-desorption temperature for Ge is lower than one for Si. Intensity of vibration of the N-H bond reduced and did not depend on growth temperature but one of Si-N bond reduced in process increasing growth temperature. We suppose that hydrogen atoms leave Si_3N_4 layer during Ge deposition as well as in case Si one. We propose that observed processes could be explained by model presented in [11,12]. The differ-

ence in chemical potentials of hydrogen atoms in the dielectric layer and the silicon (germanium) film explains the transfer of hydrogen atoms from the Si_3N_4 or SiO_2 layer into the growing silicon (germanium) film at low temperatures.

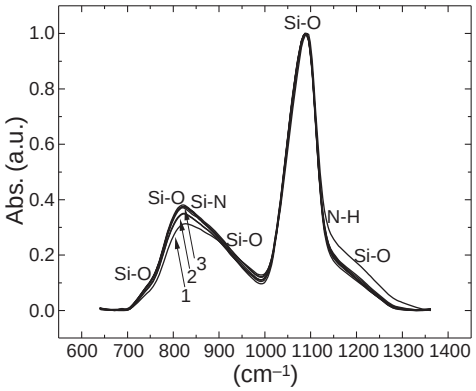

Fig. 1. FTIR absorbance spectra of samples Si grown at different temperatures:(1) substrate Si3N4; (2) 30 °C and 160 °C; (3) 300–650 °C growth temperatures.The absorbance spectra are normalized to the maximum of the peak at ∼1090 cm^{-1}.

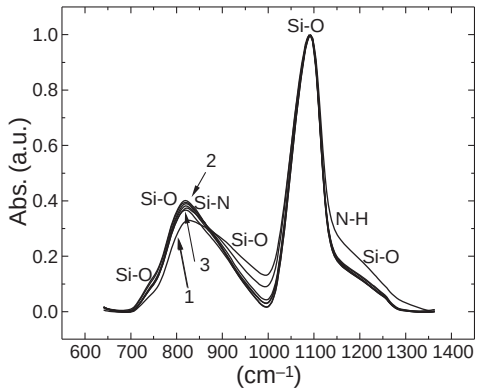

Fig. 2. FTIR absorbance spectra for the samples Ge grown at different temperatures:(1) substrate Si3N4; (2) 30 °C and 120 °C; (3) 450–650 °C growth temperatures. The absorbance spectra are normalized to the maximum of the peak at ∼1090 cm^{-1}.

Results of XPS study for initial sample and one with thin Ge layers (20Å) grown at 500 °C [13,14]. N1s peak of initial Si_3N_4/SiO_2/c-Si sample consists of two components: Si-N (398.6 eV) and, presumably, N-O or N-H (399.7 eV). Deposition of Ge layer leads to appearance adding peak. Now N1s peak could be decomposed on three components: Ge-N (397.8 eV), Si-N(398.6 eV) and N-O or N-H (399.6 V). Si2p spectrum of initial sample has Si-N(102.4eV) and Si-O (103.5 eV) parts. One with Ge layer could be decomposed on three components: Si^+ (101.4 eV), Si-N (102.6 eV) and Si-O (103.6 eV). Si-Si or Si-Ge bonds do not form. Ge3d spectrum has two components: Ge-Ge (29.6 eV) and Ge-N (30.4 eV). Ge-O bond are not. We propose Ge and Si atoms could diffuse into Si_3N_4 layer during growth and form Ge-N and Si-N bonds. In IR spectra these processes could be detected as decreasing and increasing intensity Si-N absorption band during Ge or Si deposition, respectively. According to XPS results surface of initial Si_3N_4/SiO_2/c-Si substrate has natural oxynitride layer (SiON). Si2p spectrum of etched by Ar^+ ions of sample lose component Si-O. In IR spectra Si-O-Si absorption band (∼970cm^{-1}) corresponds to natural oxynitride layer and its intensity changes at deposition of Ge and Si layers. Ge atoms penetrating into it introduces deformation resulting to reduction of IR activity of Si-O-Si absorption band but Si atoms do not make such impact.

Concluding the article, we emphasize its main inference: the growth of a silicon or germanium films on a Si_3N_4 layer deposited using CVD or on a SiO_2 layer formed using thermal oxidation of a silicon substrate is accompanied by the diffusion of hydrogen atoms from the dielectric layer into the growing film. In the opposite direction atoms Si and Ge could diffusion into Si_3N_4 layer. These processes could be defined by FTIR, XPS and Raman spectroscopy methods.

Acknowledgements

The research was funded by the Russian Foundation for Basic Research through the grant No. 18-52-00033 and the Belorusian Republican Foundation for Fundamental Research through the grant No. T18P-190. The Center for Collective Use of Scientific Equipment of GPI RAS supported this research via presenting admittance to its equipment.

References

[1] P. Paduschek, P. Eichinger, *Appl.Phys.Lett.* **36**, 62 (1980).
[2] I.P. Chernov, V.N. Shadrin, J.P. Cherdantsev, V.N. Sulema, L.V. Chramova,T.P. Smirnova, V.I. Belyi *Thin Solid Films* **83**, 49 (1982).
[3] P.S. Peercy, H.J. Stein, B.L. Doyle, S.T. Picraux *J. Electron. Mater.* **8**, 11 (1979).
[4] H.J. Stein *J. Electron. Mater.* **5**, 161 (1976).
[5] K.V. Chizh, L.V. Arapkina, D.B. Stavrovsky, P.I. Gaiduk, V.A. Yuryev *Mat. Sci. Semicon. Proc.* **99**, 78 (2019).
[6] D. Davazoglou, V.E. Vamvakas *J. Electrochem. Soc.* **150**,F90 (2003).
[7] E.A. Taft *J. Electrochem. Soc.* **118**,1341 (1971).
[8] C. Moore, T.S. Perova, B. Kennedy, K. Berwickc, I.I. Shaganovd, R.A. Moore*Proc. SPIE* **4876**,1247 (2003).
[9] S. Rath, D. Kabiraj, D.K. Avasthi, A. Tripathi, K.P. Jain, M. Kumar, H.S. Mavi, A.K. Shukla*Nucl. Instr. Meth. Phys. Res. B* **263**,419 (2007).
[10] W.A. Lanford, M.J. Rand*J.Appl.Phys.* **49**,2473 (1978).
[11] R.A. Street *Phys. Rev B* **43**,2454 (1991).
[12] W. Beyer *Phys. Stat. Sol. (a)* **213**,1661 (2016).
[13] G.-R. Yanga, Y.-P. Zhao, Y.Z. Hu, T.P. Chow, R.J. Gutmann *Thin Solid Films* **333**,219 (1998).
[14] S.J. Wang, J.W. Chai, J.S. Pan, A.C.H. Huan *Appl. Phys. Lett.* **89**,022105 (2006).

28th Int. Symp. "Nanostructures: Physics and Technology"
Minsk, Belarus, September 2020

Resistive switching in memristors based on Ge/Si(001) epitaxial layers

D.O. Filatov, M.E. Shenina, V.G. Shengurov, S.A. Denisov, V.Yu. Chalkov, A.V. Kruglov, V.A. Vorontsov, D.A. Pavlov and O.N. Gorshkov

Lobachevskii State University of Nizhnii Novgorod, 603950 Nizhnii Novgorod, Russia

Abstract. The Ag/Ge/Si(001) stacks with threading dislocations growing through the Ge epitaxial layers (ELs) manifested bipolar resistive switching (RS) between two metastable resistance states. Scanning transmission electron microscopy (STEM) provided a direct evidenced the RS mechanism to consist in the electrodiffusion of Ag^+ ions along the dislocations in the Ge ELs. Also, STEM revealed multiple RS cycling to result in the metallization of the Ge matrix around the dislocations and in the accumulation of Ag in the misfit dislocation layer near Ge/Si interface. Both above phenomena may lead potentially to degradation of the RS performance.

Introduction

In recent years, the physical and chemical processes underlying the resistive switching (RS) in thin dielectric films have been studied extensively [1]. The RS effect consists in a reversible change in the resistance of a thin dielectric layer enclosed between two conducting electrodes under a voltage applied to these ones. The electronic devices, the functioning of which is based on the RS effect are called *memristors*. RS has been observed in a variety of materials, such as oxides (NiO_x, TiO_x, HfO_x, TaO_x, SiO_x, etc.), perovskites ($SrTiO_3$, etc.), as well as in chalcogenides, polymers, etc. The RS mechanism is based on forming and rapture of conductive filaments in the dielectric layer in the electric field between the electrodes. In the oxides, the filaments consist of the oxygen vacancies [2]. In so-called conducting bridge (CB) memristors, the functional dielectrics are doped with metal atoms (Ag, Cu, etc.), which the filaments consist of [4,5]. Despite good characteristics of the memristors achieved to date, these ones suffer from a scatter of the RS parameters from one switching cycle to another (C2C scatter) and from one device to another (D2D scatter) owing to an uncontrolled filament dynamics [3]. Thus, in CB memristors, uncontrolled ion transport through defects in the dielectric leads to the formation of three-dimensional filaments that, in turn, leads to increased C2C scatter of the RS parameters [6].

Several approaches were proposed to solve the memristor instability problem. Although considerable success was achieved, this problem still remain vital. Recently, a new type of CB memristors based on relaxed $Si_{0.9}Ge_{0.1}$/Si(001) epitaxial layers (ELs) — so called epitaxial resistive random access memory (EpiRRAM) was proposed [7]. The authors aimed at preventing lateral spreading of the Ag filaments by confinement in the cores of the dislocations growing through the SiGe ELs. Earlier, the dislocations in $SrTiO_3$ were proposed for the same purpose [8]. An increased long-time scale stability of the RS parameters, a small D2D scatter, and a sufficiently long storing time were achieved in SiGe-based EpiRRAM [7]. However, despite the promising preliminary results, the details of RS mechanisms in EpiRRAM remain unexplored [9].

The present work aimed at direct observation of the Ag^+ ion dynamics in the Ag/Ge/Si EpiRRAM by cross-sectional scanning transmission electron microscopy (X-STEM).

1. Experimental

The single crystal Ge/n^+-Si(001) ELs of ∼100 nm in thickness were grown by hot wire chemical vapor deposition (HW CVD) at low temperature (325°C). This method admits controlling the threading dislocation density in the Ge ELs within 10^5-10^{10} cm^{-2} by varying growth conditions [10].

Prior to depositing top Ag electrodes of ≈250 μm in size and ≈40 nm in thickness by magnetron sputtering through a shadow mask, etch pits decorating the dislocations growing through the Ge ELs were formed by selective wet etching. The Ag-filled etch pits were to stimulate the electrodiffusion of Ag^+ into the dislocation cores acting as the electric field concentrators. According to atomic force microscopy data, the etch pit depth was 10−20 nm, the lateral sizes were 100−200 nm, and the surface density was $\sim 10^8$ cm^{-2}.

Current-voltage (I-V) curves of the EpiRAAM devices were measured by Agilent®B1500A semiconductor device analyzer. The X-STEM studies were performed in the bright field mode with Jeol®JEM 2100/F instrument using energy-dispersive spectroscopy (EDS).

2. Results and Discussion

Bipolar RS in the EpiRRAM devices was observed when sweeping the voltage from −2 to 2 V (Fig. 1). The ratio of currents in the low resistance state (LRS) and in the high resistance one (IHRS) was ≈ 1.5 at the read voltage 0.8 V.

The X-STEM results confirmed the filaments in the EpiRRAM devices to consist of Ag atoms filling the dislocations growing through the Ge ELs (Fig. 2) [7]. EDS profiling (Fig. 4)

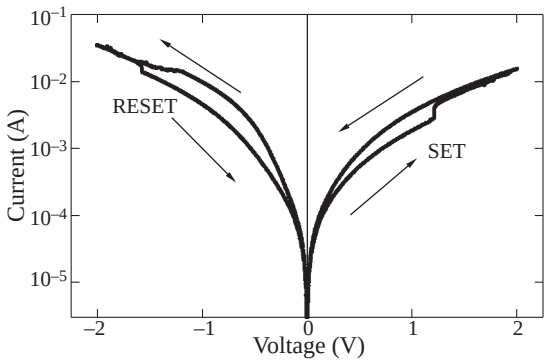

Fig. 1. Cyclic I-V curves of Ag/Ge/Si EpiRRAM device.

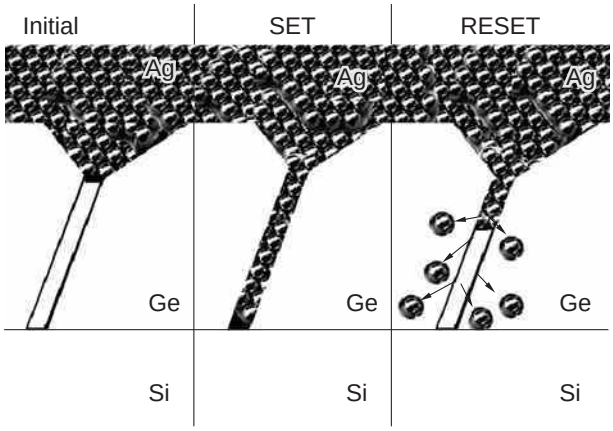

Fig. 2. Scheme of the RS in Ag/Ge/Si EpiRRAM device.

revealed no Ag in the Ge ELs prior to forming except some traces at the detection threshold ($\approx$ 2% at.), see also X-STEM image in Fig. 3a. During forming and switching from HRS to LRS (SET process) by applying a positive voltage to the top Ag electrode (relative to the n^+-Si substrate), the Ag^+ ions moved along the dislocation thus forming the filament (Fig. 2, middle panel). Filling the dislocation cores by Ag is manifested as increased contrast in Fig. 3b. While applying a negative voltage, the memristor switched back from LRS to HRS (RESET process). The authors of [7] claimed the mechanism of the RESET process in the SiGe-based EpiRRAM to be related to the electrodiffusion of the Ag^+ ions back into the Ag-filled etch pit along the dislocation cores. The results of EDS profiling (Fig. 4) revealed $\approx 2-3$ % at. of Ag in the Ge matrix around the dislocations after 50 switching cycles. Probably,

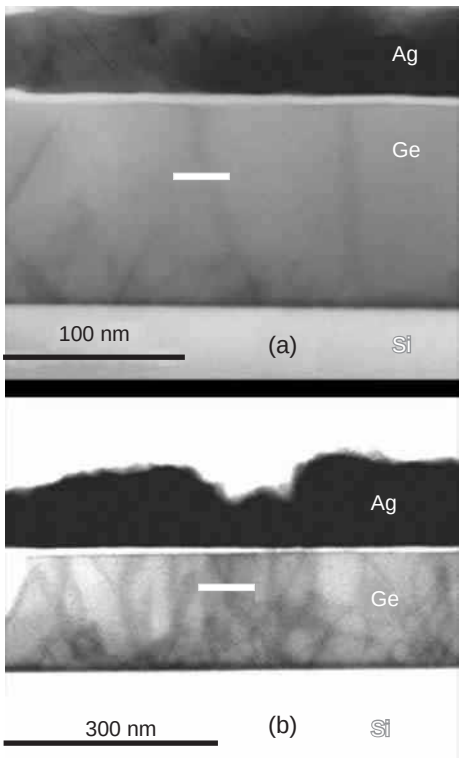

Fig. 3. X-STEM images of Ag/Ge/Si EpiRRAM devices before forming (a) and after 50 switching cycles (b). White bars indicate the lines of EDS profiles shown in Fig. 4.

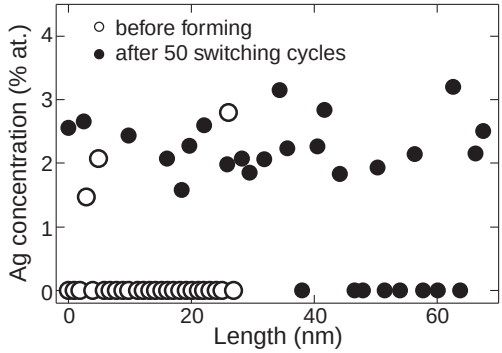

Fig. 4. EDS profiles of Ag concentration (along the lines shown in Fig. 3) in the Ge layer inside the Ag/Ge/Si EpiRRAM devices before forming and after 50 switching cycles.

the accumulation of Ag in the Ge matrix originates from its diffusion from the dislocations enhanced by Joule heating of the filaments (Fig. 2, right panel).

Also, the accumulation of the Ag atoms in the misfit dislocations concentrated at the Ge/Si interface is manifested as an increased dark contrast in Fig. 3b.

3. Conclusion

In the present study, a direct evidence of the RS in the Ag/Ge/Si EpiRRAM devices to originate from the filling of the dislocations growing through the Ge ELs was obtained by X-STEM with EDS profiling. Also, the accumulation of Ag in the Ge ELs as well as in the misfit dislocations at the Ge/Si interface after multiple switchings were observed. Both phenomena may result in degradation of the RS parameters thus limiting the EpiRRAM durability.

Acknowledgement

The present study was supported by RF BR (19-29-03026).

References

[1] D. Ielmini and R. Waser, *Resistive Switching: From Fundamentals of Nanoionic Redox Processes to Memristive Device Applications*, Wiley-VCH, 2016.
[2] I. Riess, *Electroceram.* **39**, 61 (2017).
[3] S. Goswami *et al*, *Nature Materials* **16**, 1216 (2017).
[4] J.J. Yang *et al*, *Nature Nanotech.* **8**, 13 (2013).
[5] A.L. Mehonic *et al*, *Adv. Mater.* **30** 1801187 (2018).
[6] I. Valov *et al*, *Nanotechnology* **22**, 254003 (2011).
[7] S. Choi *et al*, *Nature Materials* **17**, 335 (2018).
[8] K. Szot *et al*, *Natre Materials* **5**, 312 (2006).
[9] D.B. Strukov, *Nature Materials* **17**, 293 (2018).
[10] V.G. Shengurov *et al*, *Semicond.* **49**, 1365 (2015).

28th Int. Symp. "Nanostructures: Physics and Technology"
Minsk, Belarus, September 2020

Strain-induced formation of nano-voids and self-assembling of dots inside

P.I. Gaiduk
Department of Physical electronics and nanotechnology, Belarusian State University, Belarus

Abstract. Self-assembling of voids in strained Si/SiGe(Sn)/Si heterostructures, and formation of nano-shells and nano-particles of gold, germanium and tin through a gettering process is demonstrated. A very well defined layer of voids was formed in the strained SiGe layer at a depth of 500 nm as a result of helium implantation and thermal annealing. Due to strain enhanced vacancy accumulation, the voids nucleate and grow exclusively in the SiGe layer. The voids then getter large amount of Au, Ge or Sn which cover the inner walls of voids at low temperature or precipitates into void-located nano-crystals at a temperature of 700–850 °C. Effects connected to structural transformations in the Si/SiGe layers during self-assembling of nano-voids and metallic dots, the optical properties of the layers, and the resulting effects of nanostructures on the photoluminescence and spectral dependence of the photocurrent in the Si/SiGe(Sn)/Si structures are reported.

Introduction

The formation of new Si-based materials with enhanced light absorption and emission is of great importance for the development of high efficient photovoltaic and LED devices. A possible approach for improved light absorption is connected to excitation of localized surface plasmons, which are then transferred to the semiconductor to generate additional electron-hole pairs. The concept of this study is based on self-assembling of plasmonically active nano-voids and dots in strained Si/SiGe(Sn)/Si hetero-structures. To produce 2D array of plasmonic nanoparticles, we used an original approach, including sequential self-assembling of nanovoids in strained SiGe or SiSn layers [1–3] followed by gettering of dopant atoms into the voids [4]. Epitaxial SiGe or SiSn layers of under-critical thickness are compressively strained after the growth, and these layers effectively collect vacancies and small-size dopants (H, He) which are then transformed into voids as it is demonstrated in Refs. [1-3]. It was established [1-4] that in such layers the voids are of nanometer size and strictly assembled within the strained SiGe layers buried in the Si matrix.

It has been frequently shown that voids are very efficient gettering sites for metallic atoms. Due to their long stretched strain fields, voids attract and accumulate metallic contaminants and, under certain conditions, nano-particles might be created by filling the empty volume of the voids. Thus, voids offer great possibilities for formation of buried nano-particles. The purpose of the present study is to demonstrate that 2D layers of nano-voids might be effectively implemented as a template for gettering of Au, Sn and Ge atoms to obtain nanoparticles and nanoshells incorporated in the Si matrix for possible optoelectronic applications. We employ He+ ion implantation for the generation of vacancies and voids, and high temperature thermal treatment for gettering of metallic atoms from the surface layer.

1. Experimental

Strained structures of Si/SiGe(Sn)/Si are grown in a solid-source VG Semicon V80 MBE machine on n-type (001) Si substrates. Thin SiGe(Sn) film of about 7–15 nm is cupped with 500 nm Si surface layer. To suppress relaxation during the growth, the thickness of the SiGe or SiSn layers is chosen below the critical thickness for relaxation of strained SiGe(Sn) alloy layers. No dislocations, voids or any other type of extended defects is registered in as-grown Si/SiGe(Sn)/Si multilayered structure by TEM (Fig. 1a). The samples were then implanted with 60-keV He+ ions to a total fluence of 6×10^{14} or 6×10^{15} cm^{-2}. During implantation, the sample holder was kept at 250 °C. Furnace-thermal annealing in a dry N2 ambient was finally performed at temperatures of 700–850 °C for 30 min for a set of samples. The layers were investigated by transmission electron microscopy (TEM) using a Philips CM20 instrument operating at 200 kV. The TEM specimens were thinned down to electron transparency using a procedure consisting of successive mechanical polishing and ion-beam milling at room temperature. Photoluminescence (PL) was excited at 4.2 K by a 488.8-nm line of Ar+ laser with the excitation power density of about 1 W/cm^2. The PL intensity was measured using a liquid nitrogen cooled Ge photoresistor with an MDR-2 fast monochromator and a conventional lock-in technique. Optical spectra were measured using a Perkin Elmer Lambda 1050 double beam spectrophotometer in the spectral range of 200–2000 nm.

2. Result and discussion

It is registered by TEM that the Si/SiGe(Sn)/Si layered system is strained after both MBE growth and following high temperature annealing. Ion implantation of He+ results in formation of a 2D array of near-spherically shaped voids at a depth of 500 nm. The voids are of 10–25 nm in size, and they are exclusively adjusted with the original SiGe strained layer (Fig. 1b). Such well-defined depth and size distribution of voids are different from the well-known literature examples of He+ implanted Si wafer with no incorporated SiGe layer. Most of the voids are of facetted tetrakaidecahedron shape which is close to the equilibrium for Si.

Thermal annealing of ion implanted Si/SiGe/Si structure with on-surface-deposited thin layer of Au results in the accumulation of Au in the voided SiGe layer. Depending on annealing temperature, segregated Au atoms cover the walls of the voids (Fig. 1b) or create particles of Au in the voids (Fig. 1c). High temperature (850 °C) annealing results in bulk Au-Si eutectic phase formation. Other examples of segregation and core-shell formation inside the voids are presented for the

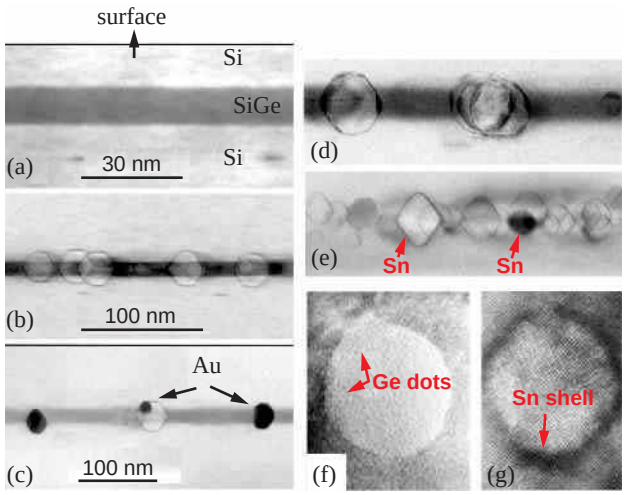

Fig. 1. TEM images of MBE grown Si/SiGe/Si (a-d,f) and Si/SiSn/Si (e,g) structures after He+implantation and annealing at 700 °C (b), 800 °C (d,f), or 850 °C (e,g). (a) — as grown and not implanted. Au thin film was deposited on the samples b and c before implantation. Panels f and g are HRTEM images of Ge (Sn) dots and shells.

case of germanium (Fig. 1d,f) and tin (Fig. 1e,g) dopants.

Optical measurements of the Si/SiGe/Si samples with in-void-incorporated Au show a successive increase of the reflectivity in the yellow-red and infrared (IR) spectral range of 800–1800 nm after Au deposition, He+ implantation and high temperature annealing (Fig. 2). A comparison with the TEM pictures of the Au-coated surface evidences that the major reflectivity changes are due to plasmonic-related light scattering on the Au nanoparticles

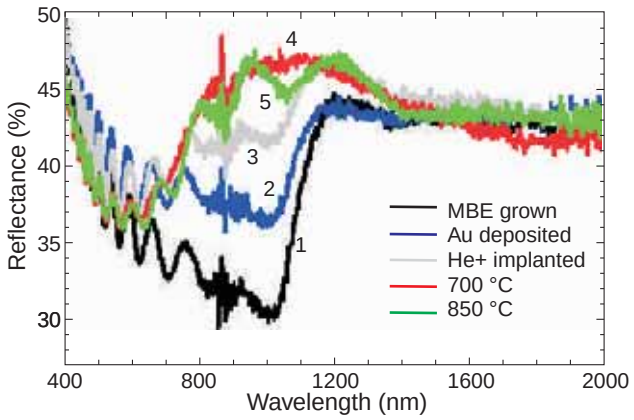

Fig. 2. Reflection spectra for the MBE grown Si/SiGe/Si structure (1), and after deposition of 2.5 nm Au (2), implantation of He+ (3) and annealing at 700 °C (4), or 850 °C (5).

Figure 3 shows PL spectra, taken from the samples with in-void-incorporated Ge dots (as illustrated at fig. 1d) in comparison with the Stranski-Krastanow Ge dots. In addition to the bound exciton transverse-optical (TO) emission from the substrate region, the spectra consist of a broad line located at about 0.8–0.9 eV. The intensity of this PL is much stronger in the case of Ge dots, incorporated inside the voids. Similar behavior is dicscussed for in-void incorporated Sn dots and shells.

It has been demonstrated in many studies that nano-shells possess unique, geometrically tuneable optical resonances. In

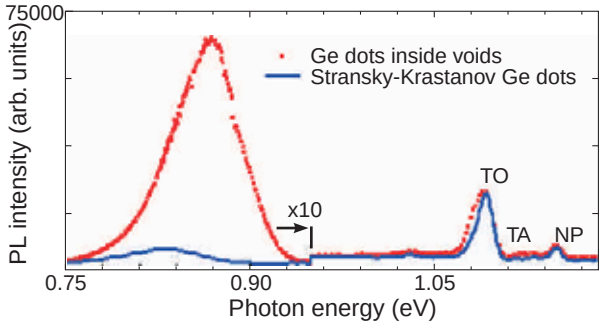

Fig. 3. PL spectra obtained from the samples with different Ge dots

contrast to the resonant properties of solid metallic nanostructures, which exhibit only a weak tunability with size or aspect ratio, the optical resonance of the nano-shells is very sensitive to the inner and outer dimensions of the metallic shell layer. In particular, by varying the relative core and shell thicknesses, the absorption and scattering properties of metallic nano-shells can be varied in a broad range of the optical spectrum.

In conclusion, MBE grown compressively strained SiGe layer is demonstrated to be attractive for vacancies and He atoms which are accumulated and transformed to voids after He implantation and thermal treatment. The voids are 10–25 nm in size and are located exclusively within the SiGe layer. The voids have equilibrium tetrakaidecahedron shape dominated by 111 and 100 planes. High temperature thermal treatment results in gettering of Au, Ge or Sn atoms to the voids, located at a depth of 500 nm in the SiGe(Sn) layer. Au covers the inner walls of the voids at lower temperature (formation of Au nano-shells) and turns into Au–Si eutectic precipitates at a temperature of 850 °C. A favorable difference of metallic nano-shells as compared to nanoparticles is their potentially higher resistivity that might be useful to overcome the problem of the Ohmic dissipation channel for plasmonic excitations. Metallic nano-shells can be made to either preferentially absorb or scatter light by varying the size of the particle relative to the wavelength of the light at their optical resonance with a possibility to tune the plasmon resonance of nano-shells into the near-infrared region of the spectrum.

Acknowledgements

This work is supported by GPNI “Photonics, opto- and microelectronics” (Registration number 20190644). Special thanks to Arne Nylandsted Larsen and John Lundsgaard Hansen for MBE growth and discussions.

References

[1] P.I. Gaiduk *et al*, *Phys. Rev. B.* **67**, 235310 and 235311 (2003).
[2] P.I. Gaiduk *et al*, . *Nucl.Instr. and Meth.in Phys. Res.***267**, 1239 (2009).
[3] P.I. Gaiduk *et al*, *Appl. Phys. Lett.*, 153107 (6) (2014).
[4] P.I. Gaiduk *et al*, *Phys.Stat.Sol.(b)*, 1700635(5); DOI: 10.1002/pssb.201700635 (2018).

28th Int. Symp. "Nanostructures: Physics and Technology"
Minsk, Belarus, September 2020

Self-organization of Ge(Si) nanoisland groups on pit-patterned Si(001) substrates

Zh.V. Smagina[1], V.A. Zinovyev[1], S.A. Rudin[1], E.E. Rodyakina[1,2], P.L. Novikov[1,2], A.V. Nenashev[1,2], V.A. Armbrister[1], A.V. Dvurechenskii[1,2]

[1] Rzhanov Institute of Semiconductor Physics, 630090 Novosibirsk, Russia
[2] Novosibirsk State University, 630090 Novosibirsk, Russia

Abstract. Self-organization of Ge(Si) nanoisland groups grown on Si substrates with the square or hexagonal lattice of pits is studied. In the case of small spacing between pits (0.5–0.6 μm) the pit lattice type is found to be significant for the nucleation process. Nanoislands are nucleated outside the pits when grown on hexagonally arranged pits, while no nucleation is observed on the square pit lattice.

Introduction

Heterostructures with quantum dots (QDs) attract significant interest due to their unique physical properties. QDs are promising as the key elements in many electronic and optoelectronic device applications, such as a single-photon emitters and detectors or quantum computer [1–3]. Their practical realization requires the precise space arrangement of QDs with the predetermined interaction between the charge carriers localized in the neighbor QDs. An additional advantage of space-arranged QDs is their size and chemical composition homogeneity, which lead to significant decreasing of energy level dispersion in QD array [4]. The most effective way of positioning QDs is by heteroepitaxial growth on a pit-patterned substrate, where pits serve as the centers of nucleation. By variation of pit geometry (diameter, depth, sidewall inclination angle, bottom shape) and of their period in an array it becomes available to obtain arrays with variable shapes of QDS, density and arrangements [3]. In the present work, we present experimental and simulation results on the self-organization of Ge(Si) QD groups by the heteroepitaxial growth on the pit-patterned SOI (silicon-on-insulator) substrates.

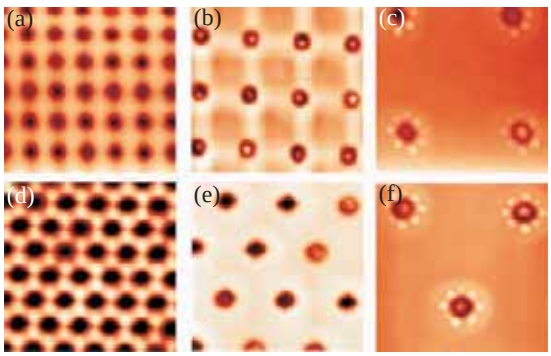

Fig. 1. AFM-images (3.0×3.0 μm) of arrays of laterally ordered Ge(Si) QDs on pit-patterned SOI substrates: (a)–(c) — pits arranged to the square lattice with a period of 0.5, 1.0, 2 μm, respectively; (d)–(f) — pits arranged to the hexagonal lattice with a period: 0.5, 1.0, 2 μm, respectively.

1. Experiment and discussion

SOI substrate was used as a template for creation of space-arranged arrays of QDs. Patterning was performed by electron lithography and plasma-chemical etching. Arrays of pits, ≈40 nm deep, restricted to square and hexagonal lattice, with a period from 0.5 to 4 μm were formed. Consequently, growth of multilayered Ge/Si structure with QDs was carried out. First, 4 monolayers (ML) of Ge were deposited on the pit-patterned substrate. This amount was chosen to provide the nucleation of QDs inside the pits or at their edges, rather than at the flat surface. Then a 15 nm-thick separation Si layer was deposited, followed by a 4 ML Ge deposition at 700 °C. By repeating this process 10 layers of laterally ordered Ge(Si) QDs on pit-patterned SOI substrates were formed. The detailed description of nucleation and growth of Ge(Si) nanoislands as depending on the pit depth and the shape is presented elsewhere [5,6]. The study carried out in the present work is focused on the influence of the pit lattice geometry (period and lattice type) on QDs nucleation. It was shown by scanning electron (SEM) and atomic force microscopy (AFM) that QDs grow only inside the pits arranged to the square lattice with a period of 0.7–1.2 μm (Fig. 1). The increase of the period up to 4 m results in QD formation both inside and at the edges of pits (Fig. 1). An average number of QDs nucleated around any pit becomes more with increasing period from 2 to 4 μm. For structures with hexagonally ordered pits with the periods larger than 0.7 μm the formation of nanoislands occurs in a similar way. The difference is observed for smaller periods (0.5–0.6 μm). In this case the islands are nucleated around pits (Fig. 1), while for the square lattice of pits no nucleation is observed. The narrowing of the period leads to the decrease of an average Ge amount per pit [6]. Therefore in the case of small periods the volume of Ge does not reach the critical value necessary for the three dimensional (3D) islands formation. In a dense array of the pits, when the spacing between pits is comparable to their diameter, the strain distribution in the growing Ge layer is different for hexagonal and square lattices, respectively. Probably, this is the reason for the favorable nucleation of Ge nanoislands around pits, in the case the hexagonal lattice with a small period (<0.7 μm). No difference in the nucleation of islands is observed for the larger periods, when the elastic interaction between pits can be neglected.

2. Simulation

Monte Carlo simulation of Ge heteroepitaxial growth on Si(001) substrates with pits is carried out. The underlying physical model was described elsewhere [7]. Growth of 3D-

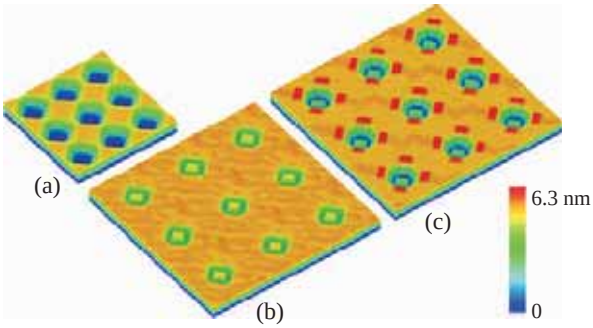

Fig. 2. Side view of the Si/Ge structure obtained by MC simulation of Ge deposition on the Si(001) pit-patterned substrate at 720 K. The amount of Ge deposited is (a)–(b) — 5 ML (7.0 Å); (c) — 5.4 ML (7.56 Å. The rate of Ge deposition is 0.14 Å/s. Spacing between pits is (a) — 140 Å; (b)–(c) — 280 Å.

islands in relation to the spacing between pits was studied. As the atomistic model is used, the calculations within a real size cell would require the huge calculation resources. For this reason the simulation cell sizes were scaled down by a factor of 10 approximately with its proportions conserved. Pit shape and relative sizes were adequate to those in experiment: pit diameter was 100 atomic units (a.u. = 1.36 Å), sidewall inclination angle was 54°, pit bottom had a V-like profile. In order to fit the characteristic length of atomic diffusion to the cell size, the simulation temperature was decreased in comparison with the experimental one and was equal to 720 K. The amount of Ge deposited (7.0–7.56 Å) and the rate of deposition (0.14 Å/s) were taken the same as in the experiments. Spacing between pits was varied from 140 to 280 Å. The simulation cell sizes were $280 \times 80 \times 140$ Å^3. The results of simulation are presented in Fig. 2. Like in experiment, the nucleation of 3D-islands depends on spacing between pits. For spacing equal to 140 Åno nucleation is observed at the flat surface, while for larger spacing (up to 280 Å) the nucleation takes place inside pits (Fig. 2,b). When structures are characterized with a larger spacing and Ge amount deposited is 5.4 ML (7.56 Å), the nucleation occurs both inside pits and at their periphery (Fig. 2,c). The results of simulation concerning the dependence of island nucleation on spacing between pits are in a good accordance with those from experiment.

Acknowledgements

This work was supported by RFBR (Grant 19-42-540002). The Government of Novosibirsk Region in part of preparation of structures with QDs embedded in photonic crystals, and by RFBR (Grant 18-29-20016-mk) in part of luminescence measurements. Authors thank the NSU Multiple-access Center "VTAN" for the provision of measurement equipment.

References

[1] M.V. Stepikhova *et al*, *Semicond. Sci. Technol.* **34**, 024003 (2019).
[2] V. Jovanovic' *et al*, *IEEE Electron Device Lett.* **31**, 1083 (2010).
[3] M. Grydlik, *et al*, *Nanotechnology* **24**, 105601 (2013).
[4] M. Brehm and M. Grydlik, *Nanotechnology* **28**, 392001 (2017).
[5] Zh.V. Smagina *et al*, *J. Appl. Phys.* **123**, 165302 (2018).
[6] Zh.V. Smagina *et al*, *Semiconductors* **52**, 1028 (2018).
[7] A. Rudin *et al*, *Optoelectron. Instrum. Data Proc.* **49**, 461 (2013).

28th Int. Symp. "Nanostructures: Physics and Technology"
Minsk, Belarus, September 2020

The study of crystal structure of intermediate layers in Ge/Si heterostructures with low-temperature quantum dots using high-resolution transmission electron microscopy and Raman spectroscopy

M.S. Storozhevykh[1], L.V. Arapkina[1], S.M. Novikov[2], V.S. Volkov[2], O.V. Uvarov[1] and V.A. Yuryev[1]

[1] A.M. Prokhorov General Physics Institute of the RAS, Moscow, Russia
[2] Center for Photonics and 2D Materials, Moscow Institute of Physics and Technology, 9 Institutskiy per., Dolgoprudny, Russia

Abstract. The method of software analysis of high-resolution TEM images using the "peak pairs" algorithm in combination with Raman scattering was employed to study lattice deformations in Ge/Si(001) structures with low-temperature Ge quantum dots. It was found that the stresses do not spread in a thick Si layer over quantum dots, but completely relax in a thin boundary layer of mixed composition. The critical thickness of Si coverage at which the intense strain-induced diffusion takes place is determined to lie in the range from 5 to 8 nm. The obtained results shed light on the growth process of chains of vertically correlated quantum dots.

Introduction

The combination of the analysis of direct images of the crystal internal structure obtained using high-resolution transmission electron microscopy (HRTEM) with Raman spectroscopy was found to be an effective approach in studies of strains and composition in complex multilayer heterostructures containing layers of variable composition.

In this work the above mentioned methods were employed to study Ge/Si structures containing layers of low- temperature self-assembled Ge quantum dots divided by Si layers of different thicknesses. The study of strains arising in multilayer Ge/Si heterostructures with QDs is important for any problems associated with the use of such structures in optoelectronics because the environment of QDs plays an important role in the formation of the band structure [1].

Experimental

The studied samples with layers of Ge QDs in the Si matrix were grown by MBE in ultra-high vacuum (UHV) using an EVA32 chamber of an SSC 2 surface-science centre (Riber) equipped with Ge and Si sources with the electron-beam evaporation. Czochralski-grown (100) oriented p-type silicon wafers of 50 mm in diameter ($\rho = 12\,\Omega{\cdot}$cm) were used in experiments. A Si buffer layer of ∼100 nm in thickness was grown on atomically clean Si(001) surface at the substrate temperature of 650 °C. Layers of Ge QDs were grown at the temperature of 360 °C; the Ge coverage was varied in different samples from 6 to 10 Å. Si spacers and cap were grown at the temperature of 530 °C in heterostructures with spacers of 50 nm and at 360 °C in the structures with spacers of 5 and 8 nm.

HRTEM images of the grown structures were obtained using a Libra-200 FE HR instrument (Carl Zeiss) after the ion treatment in argon plasma using a Model 1010 ion mill (E.A. Fischione Instruments) for obtaining thin defectless lamellae. Images with the highest contrast of separate atoms were selected among all the obtained ones; they were processed using the authors software that applied the "peak pairs" algorithm for analyzing lengths of separate inter-atomic bonds [2].

Raman spectra were obtained using a LabRAM HR Evolution confocal scanning Raman microscope (Horiba Scientific). Measurements were carried out using linearly polarized excitation at a wavelength of 632.8 nm. The spot size was ∼0.43. We used unpolarized light detection in order to have a significant signal-to-noise ratio. Gaussian or Voigt profiles were used for the deconvolution of Raman bands.

Result and discussion

For the structure having Ge layers of 10 Å, a narrow crystal region with lattice deformation, from ∼10 to 20 monolayers in thickness, is observed above the layer of QDs at HRTEM images processed by the software implementing the "peak pairs" algorithm (Fig. 1). The lattice parameter in this region is increased by 2 to 4% relative to the unstrained Si crystal in the growth direction ([001]). In the [110] direction, in the crystal growth plane, the lattice over QD layer corresponds to the unstrained Si crystal as well as in the whole presented domain. We assume that the observed part of a crystal with the increased lattice parameter in the growth direction [001] corresponds to the domain of a mixed composition Si_xGe_{1-x} the lattice parameter of which linearly depends on x [3]. According to the Vegard's law [4] an increase in the lattice parameter by 2 to 4% corresponds to the Ge content from 50 to 100%. Thus it might be supposed that the stresses over a layer of Ge QDs occurring due to the further growth of a thick Si layer are relieved by compressing the thin domain of a mixed composition in the [110] direction with preservation of the own lattice parameter of Si_xGe_{1-x} in the [001] direction.

For the structure having Ge layers of 6 Å, no lattice deformation is observed in both [001] and [110] directions. This may be due to the predominance of Ge diffusion into the Si matrix from the {105} facets of Ge huts, not from the Ge wetting layer, at low temperatures of the Ge/Si structure deposition. The same can explain the absence of intermixing below the Ge layer and the absence of the peak related to Si-Ge vibrational mode in the Raman spectra of uncapped Si/Ge structures with QDs studied before [5].

The above suggestions are proved by investigation of Ra-

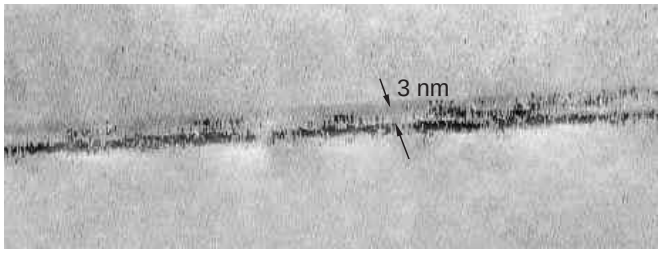

Fig. 1. A HRTEM image of a fragment of a multilayer structure with Ge/Si(001) QD arrays in Si matrix ($h_{Ge} = 10$ Å, $T_{Ge} = 360\,^{\circ}$C, the Si spacer thickness $h_{Si} \approx 500$ Å, $T_{Si} = 530\,^{\circ}$C) proceeded by "peak pairs' algorithm in [001] direction.

man scattering from the structures. Raman signal related to Ge–Ge vibrational mode grows up with the increasing of the thickness of deposited Ge (Fig. 2a) and undergoes red shift with the increasing of the thickness of Si spacers (Fig. 3a). At the same time Raman signal from Si–Ge vibrational mode grows up both with the increasing of the thickness of deposited Ge (Fig. 2b) and with the increasing of the thickness of Si spacers (Fig. 3b). It can be explained by stain-induced diffusion of Si atoms into Ge that takes place when the thickness of above Si layer is enough to provide sufficient stress. In this case, the stress of a heterostructure caused by the misfit between lattice parameters of Si and Ge relaxes via compressing of the mixed layer that leads to the blue shift of Si–Ge peak with the increasing of the thickness of Si spacers (Fig. 3b). The small Si–Ge peak always presents in Raman spectra of studied structures due to the effect of segregation of Ge during coverage by Si [6].

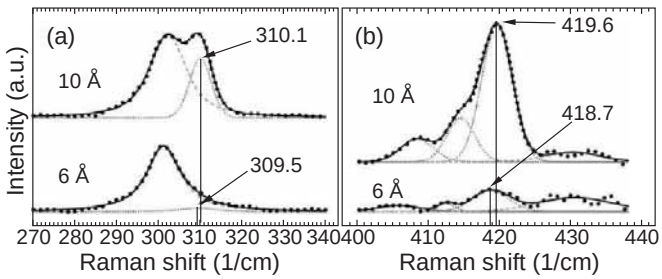

Fig. 2. Raman spectra of Ge–Ge (a) and Si–Ge (b) bands for Ge/Si heterostructures with Ge layers of different thickness ($h_{Ge} = 6$ and 10 Å).

Conclusion

In the studied Ge/Si(001) heterostructures, a thin domain of the crystal (1.5 to 3 nm thick) over a layer of Ge quantum dots with the lattice parameter in the [001] growth direction exceeding that of unstressed silicon was discovered by HRTEM images analysis using the "peak pairs' algorithm. This result is explained by the mixed composition of the Si_xGe_{1-x} crystal lattice in this region, which has the parameter greater than pure Si. The stress above the quantum dot relaxes by compressing the Si_xGe_{1-x} crystal in the [110] direction since the lattice parameter in this direction corresponds to pure Si. The transition region of mixed composition is present only above the QD layer and is absent below it. It is also absent in structures with thin Ge layers and small QDs which do not cover the wetting layer. We suppose that the formation of the transition region is based on strain-induced diffusion rather than on temperature-induced diffusion or segregation and the source of Ge atoms is the {105}

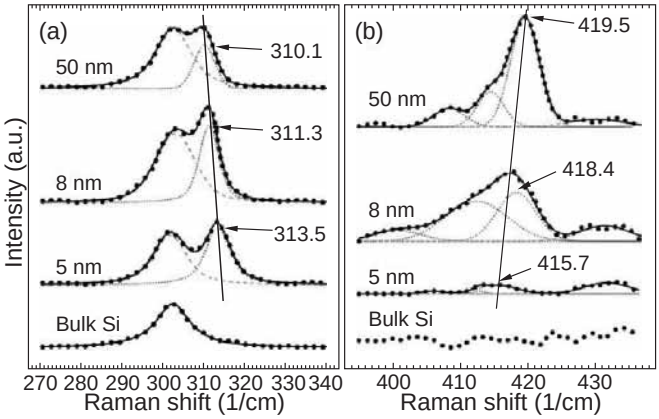

Fig. 3. Raman spectra of Ge–Ge (a) and Si–Ge (b) bands for Ge/Si heterostructures with Ge layers of 10 Åand Si spacers of different thickness ($h_{Si} = 5$, 8 and 50 nm).

QD steps. The analysis of Raman scattering spectra proves this result and shows that Ge diffuses into Si after reaching a critical thickness of the covering Si layer that reaches ∼5–8 nm.

Acknowledgement

The Center for Collective Use of Scientific Equipment of GPI RAS supported this research via presenting admittance to its equipment.

References

[1] T. Meyer, M. Klemenc and H. von Kanel, *Phys. Rev. B*, **60** (1999) R8493.
[2] P.L. Galindo, S. Kret, A.M. Sanchez, *et al*, *Ultramicroscopy* **107**, (2007) 1186–1193.
[3] R.A. Logan, J.M. Rowell and F.A. Trumbore, *Phys. Rev.* **136**, (1964) A1751.
[4] A.R. Denton and N.W. Ashcroft, *Phys. Rev. A*, **43**, (1991) 3161.
[5] I.V. Kucherenko, V.S. Vinogradov, N.N. Mel'nik, *et al*, *Phys. Solid State*, **50**, (2008) 1970–1977.
[6] P.C. Zalm, G.F.A. van de Walle, D.J. Gravesteijn *et al*, *Appl. Phys. Lett.*, **55**, (1989) 2520.

28th Int. Symp. "Nanostructures: Physics and Technology"
Minsk, Belarus, September 2020

Modeling of plasmonic enhancement of GeSi quantum dot emission in hybrid structures with silver nanopaticles

V.A. Zinovyev[1], A.F. Zinovieva[1], A.V. Nenashev[1,2], A.V. Dvurechenskii[1,2]

[1] Rzhanov Institute of Semiconductor Physics, 630090 Novosibirsk, Russia
[2] Novosibirsk State University, 630090 Novosibirsk, Russia

Abstract. We carried out a theoretical study of the effect of amplification of radiation from quantum dots upon resonance excitation of localized surface plasmons in three-dimensional silver nanoislands located on the surface of a Ge/Si heterostructure with quantum dots. It was found that the interaction of the emitters with silver nanoparticles can lead to a significant increase (by more than an order of magnitude) of the quantum dot emission.

Introduction

Currently, there is a problem of creating efficient emitters compatible with silicon technology [1–4]. These sources are one of the key elements of optical processing and data transmission schemes that are being developed for modern processors and computers. The difficulty lies in the fact that silicon is an indirect bandgap semiconductor material and the radiative transitions in it are strongly suppressed, since phonons are necessary for observing the law of conservation of momentum during interband recombination. One of the possible approaches to solving this problem is the creation of Si/Ge structures with quantum dots (QDs) [3,4]. In these structures, an increase in the probability of radiative recombination due to the spatial localization of charge carriers is observed. However, Si/Ge is a type II heterostructure where the electron and hole are localized on opposite sides of the interface: the electron is localized in Si, and the hole is located inside the Ge QD. In this regard, the overlap integral of the wave functions of charge carriers is rather small and the radiation intensity from such structures is not very high. One of the most promising approaches to increasing the efficiency of emitters is the inclusion of SiGe QDs in microcavities [3,4], where amplification of the electromagnetic field at resonant frequencies provides an increase in the probability of radiative recombination. Most of the work in this area is devoted to low-dimensional resonators based on photonic crystals, which are formed by introducing defects into a photonic crystal [4]. However, the technology of creating a microcavity is rather complicated and expensive. An alternative approach to creating efficient emitters based on structures with QDs is to use the principles of nanoplasmonics. The use of hybrid structures with QDs and metal nanoparticles allows one to increase the radiation intensity and also modify the radiation spectrum of QDs. In these structures, there is a local amplification of the electric field near the metal-semiconductor interface [5]. This allows one to multiply increase the intensity of the radiative recombination of electrons and holes localized in QDs. Recently, a multiple amplification of photoluminescence (PL) from GeSi quantum dots upon resonance excitation of plasmon waves in three-dimensional Ag nanoislands located on the surface of a Ge/Si heterostructure with QDs has been observed [6]. In the present work, to understand the main mechanism of this effect we carry out a theoretical study of optical properties of QDs coupled with metal nanoparticles.

1. Modeling results and discussion

The interaction of the light with the electronic subsystem occurs in the region where the wave functions of the electron, hole and the electric field of the emerging photon overlap. For QDs the size of this region is small, and the radiation source can be considered as a point dipole. The electric field distribution in the system "Ag island + point dipole" were determined by numerical solution of Maxwell equations. The calculated area represents a sphere surrounded by a perfect matched layer (PML). The upper hemisphere is filled by the air, the down hemisphere is filled by silicon. The Ag island is modeled as

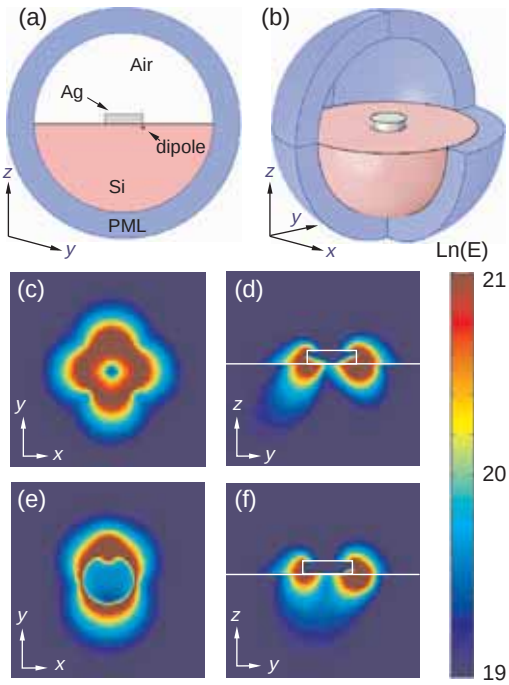

Fig. 1. (a) The yz-section of the model structure. (b) A three-dimensional view of the model structure. (c)–(f) The electric field distribution in the system "dipole + Ag island for quadrupole resonance mode (c,d) and dipole resonance mode, excited by dipole radiation at 1.06 μm and at 1.6 μm (e,f) respectively. The calculation was done for disk-shaped Ag island with $L = 200$ nm and $h = 50$ nm, positioned on Si substrate. xy-sections (c,e) are taken at the interface air/Si. yz-sections (d,f) cross the center of Ag island. The point dipole is placed under the edge of Ag disk and oriented along y-axis ([010] direction). The magnitude of electric current dipole moment is the same for all considered wavelengths.

a disk with the height h = 50 nm and lateral size L = 200 nm (the parameters are chosen on the basis of atomic force microscope measurements [6]). This island is placed on the Si substrate in the center of the calculated domain. The QD emitter is modeled as a point dipole placed under the bottom of Ag island at the depth $d_0 = 10$ nm. Two dipole orientations are considered: vertical (along the z-axis, [001] crystallographic direction) and horizontal (along y-axis, [010] crystallographic direction) ones. We model two cases of characteristic dipole positions, when the point dipole is placed under the edge and under the center of Ag disk. The dipole coordinates are ($L/2$, 0, $-d_0$) in the first case, and (0, 0, $-d_0$) -0 — in the second case. To study the coupling between the metal nanoparticle and the QD emitter we calculated the absorption by the Ag island (by the integration of energy flux through the island surface) and the emission through the surface of the upper hemisphere of the calculated area (up-emission).

The electric field distribution corresponding to quadrupole and dipole plasmonic resonances is shown in Fig. 4. According to calculation results the dipole resonance with $\lambda = 1.6$; μm is found closer to the GeSi QD emission band [6] (≈ 1.4 μm), in contrast to the quadrupole resonance with $\lambda = 1.06$ μm. Since we deal with PL measurements, we calculate the *up*-emission enhancement Y_{up}= I_{up}/I_0, where I_{up} (I_0) is the energy flux through the upper hemisphere calculated for the dipole placed under the Si surface with (without) the Ag island. It was found, that the emission from the dipole positioned under the center of Ag island is almost lost. Then one can conclude that, in the experiments, the more efficient increase occurs for the QDs positioned close to the edge of Ag islands. Further, we discuss the calculation results only for the dipoles positioned at the edge of Ag islands. The calculation results have shown that the vertical dipole does not practically irradiate through the upper hemisphere in the presence of air/Si interface. The interface suppresses the upward irradiation making it approximately 200 times smaller (for $\lambda = 1.4$ μm), as compared with the upward irradiation $I_{d(Si)}$ of a dipole embedded in a homogeneous Si matrix. This is a consequence of the effect of internal reflection and the dipole radiation pattern that is maximum perpendicular to the z-axis, falling to zero in the direction perpendicular to the interface. The Ag island placed at the interface above the vertical dipole significantly increases I_{up} (approximately 170 times), which practically returns it to a level of dipole irradiation in Si $\sim$0.85 $I_{d(Si)}$. The radiation of horizontally oriented dipole is also limited by the interface, but not so much as for the vertical dipole. In this case the dipole radiation pattern is more optimal for the up-irradiation, and the air/Si interface reduces I_{up} 17 times, as compared with the case of an infinite Si matrix. In the presence of Ag island, the increase of I_{up} for the horizontal dipole is not so large, as for vertical dipole, it is approximately 6 times. Therefore, the resulting I_{up} for horizontal dipole is $\sim$0.35 $I_{d(Si)}$. On the basis of this consideration one can conclude that the electromagnetic coupling between the vertical dipole and Ag island is more efficient. To find the maximum possible effect we calculate the wavelength dependence of the emission enhancement for the y-oriented dipole for different sizes of Ag islands (Fig. 2, the aspect ratio $h/L = 0.25$ in all cases). It is clearly seen that the position of plasmon resonance depends on the Ag island size. Thus, the resonance conditions can be tuned to the QD emission wavelength by changing the Ag nanoparticle parameters. It should

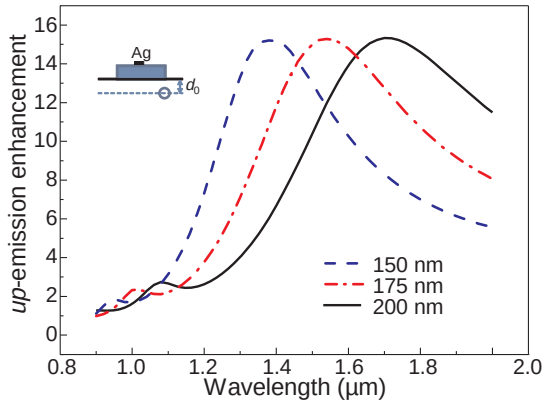

Fig. 2. The dependence of emission enhancement Y_{up} on the wavelength, calculated for disk-shaped Ag islands with different lateral sizes (aspect ratio is kept constant h/L=0.25). The point dipole is placed under the edge of Ag disk at the depth d_0=10 nm and oriented along y-axis ([010] direction).

be noted that for size $L = 200$ nm the amplification coefficient $Y_{up} \approx 6$ is very close to the experimental data in Ref. [6], that confirms the correctness of our theoretical consideration. The calculated emission enhancement is only due to an increase in the electromagnetic field in the vicinity of Ag island, because we do not take into account increase of the electron-hole pairs generation rate in Si. Even in this case we obtain a good correspondence between experimental data and modeling results, which gives us the right to conclude that the main mechanism of the observed effect is the increase of carriers recombination rate in QDs. Based on the calculation results presented in Fig. 2 one can conclude that the effect observed in our experiment is not maximal. A greater increase can be obtained if the plasmon resonance peak position coincides with the emission peak of GeSi QDs. It is possible to achieve the best result by selecting the optimal parameters of metallic nanostructures (for example, the size of metallic nanoparticles). It is clearly seen that the Ag island with $L = 150$ nm can give a more pronounced enhancement of the GeSi QD emission at λ = 1.4 μm, I_{up} is approximately 15 times larger than that in the case without the Ag island. Further decrease in the lateral size L shifts the plasmon resonance out of the GeSi QD emission range.

Acknowledgement

This work is funded by the Russian Science Foundation (19-12-00070).

References

[1] R.E. Camacho-Aguilera *et al*, *Opt. Express* **20**, 11316 (2012).
[2] S. Wirths *et al*, *Nature Photonics* **9**, 88 (2015).
[3] M. Grydlik *et al*, *nACS Photonics* **3**, 298 (2016).
[4] M.V. Stepikhova *et al*, *Semicond. Sci. Technol.* **34**, 024003 (2019).
[5] H. Mertens *et al*, *Nano Lett.* **6**, 2622 (2006).
[6] V.A. Zinovyev *et al*, *Semiconductors* **52**, 2149 (2018).

28th Int. Symp. "Nanostructures: Physics and Technology"
Minsk, Belarus, September 2020

Spectral and luminescent properties of an indotricarbocyanine dye upon complex formation with detonation nanodiamonds

N.V. Belko[1,2], *M.P. Samtsov*[2], G.A. Gusakov[2], A.P. Lugovski[2] and A.A. Lugovski[3]

[1] Belarusian State University, Minsk, Belarus
[2] A.N. Sevchenko Institute of Applied Physical Problems of the Belarusian State University Minsk, Belarus
[3] Belarusian State University Institution Republican Center for Human Problems, Minsk, Belarus

Abstract. Spectral and luminescent properties of an indotricarbocyanine dye were studied upon complex formation with detonation nanodiamonds in aqueous medium. The complex formation is accompanied by a loss of absorbance in the H*-aggregate band and a bathochromic shift of the monomeric absorption peak from 706 to 718 nm. The dye monomers that are not bound to the nanodiamond surface are responsible for the most of the fluorescence.

Introduction

Nanodiamonds (ND) possess biocompatibility, chemical stability, and low toxicity [1]. This nanomaterial has the potential for applications in delivery of organic molecules in a living organism and bioimaging *in vivo* [2].

A possible development of fluorescent labels for bioimaging is preparation of the complexes of ND with organic dyes. In such a system ND provide chemical stability as well as selectivity of accumulation, whereas, the dye molecules are responsible for the spectral and luminescent properties suitable for a specific application.

The aim of this work is to study the complex formation between an indotricarbocyanine dye and detonation ND in aqueous medium and the spectral and luminescent properties of the complexes obtained.

1. Experimental

Detonation ND from Sinta (Belarus) were used. Crude ND powder was vacuum annealed for 1 hour at 750 °C and 10^{-2} Pa. These annealing conditions resulted in effective removal of the surface functional groups. ND suspensions were prepared in deionized water upon ultrasonication. The suspensions were then centrifuged and the supernatant was separated to be used in the experiments.

The indotricarbocyanine dye studied is soluble in many organic solvents, but is hydrophobic. For this reason, aqueous solutions of the dye were prepared by injection of the ethanolic stock solution into water resulting in EtOH content of 5 vol.%. Stabilization of the absorption spectrum was typically reached ca. 100 min after preparation [3]. At this point the aqueous solution of the dye was mixed with the ND aqueous suspension with the volume ratio of 1:1.

2. Results

Aqueous solutions of the indotricarbocyanine dye with concentration below 0.002 mM contain monomers, dimers, and H*-aggregates [3] characterized by absorption maxima at 706, 660, and 514 nm, respectively (Fig. 1, curve 1). The H*-aggregates are rod-like nanostructured objects that can reach a length of several micrometers. The H*-aggregates are therefore composed of many dye molecules [3]. After mixing of the dye solution with a ND suspension a decrease in the H*-band is observed with a concomitant increase in absorbance at

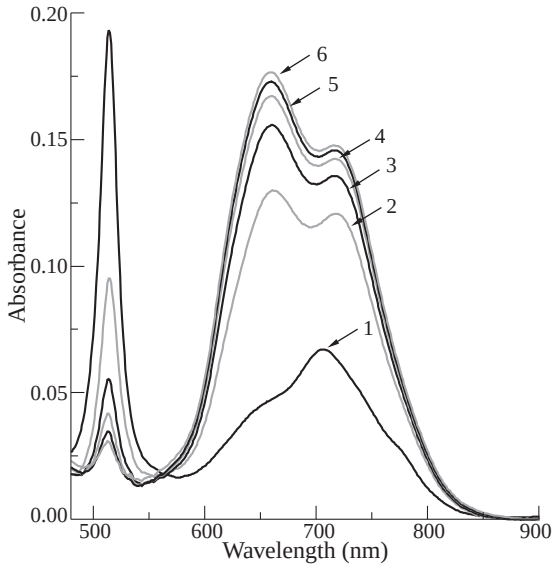

Fig. 1. Absorption spectrum of the dye aqueous solution before mixing with the ND suspension (1) and 1 min (2), 4 min (3), 10 min (4), 20 min (5), and 60 min (6) after mixing with the ND suspension with the volume ratio of 1:1; dye concentration 0.0025 mM, ND concentration 0.25 g/l, sample thickness 1 cm.

660 and 718 nm (Fig. 1, curves 2–6). The absorption band at 660 nm corresponds to the dye dimers. Thus, in the presence of the ND the concentration of the dimeric dye increases at the expense of the H*-aggregates. Moreover, a new species with the absorption peak at 718 nm is formed.

Additional information on the nature of this absorption peak can be obtained from the fluorescence excitation and emission spectra. Aqueous solution of the dye with low concentration (below 0.002 mM) is characterized by an absorption peak at 706 nm (Fig. 2, curve 1) and fluorescence emission peak at 738 nm (Fig. 2, curve 2). The corresponding fluorescence excitation spectrum is very similar to the absorption spectrum (Fig. 2, curve 3). As a consequence, the fluorescence in such solution is ascribed solely to the dye monomers. In the presence of the ND new absorption peaks at 660 and 718 nm arise (Fig. 1) and the peak at 706 nm is not observed. The peak of the excitation spectrum shifts concomitantly from 706 to 710 nm. The peak position of the emission spectrum is unchanged, however, the fluorescence intensity is slightly increased at the long-wave side of the spectrum.

The fluorescence lifetime of the dye monomers in aque-

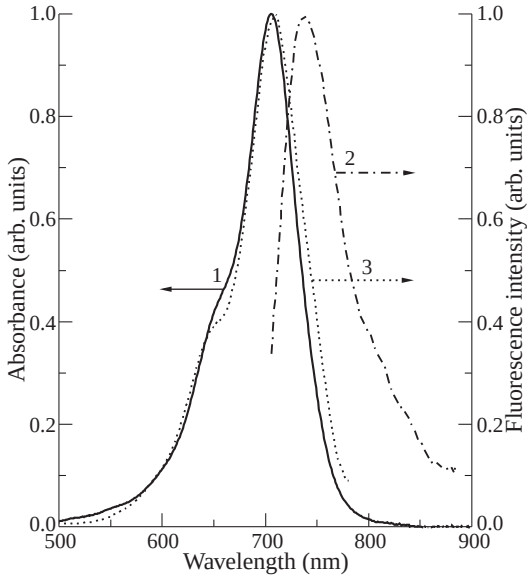

Fig. 2. Normalized absorption (1), fluorescence emission (2), and fluorescence excitation (3) spectra of an aqueous solution of the dye; dye concentration 0.0005 mM, sample thickness 1 cm.

ous solution is 0.5 ns, and the fluorescence anisotropy is 31%. Interestingly, in the presence of the ND the same values are obtained. Based on the presented experimental data, in the suspensions containing both the dye and the ND most of the fluorescence is attributed to the dye monomers that are not bound to the ND surface. The dye molecules bound to the ND are characterized by the absorption band peaked at 718 nm and are responsible for the low-intensity long-wave shoulder of the fluorescence spectrum.

The interaction between the dye and the ND was studied with the aid of infrared vibrational spectroscopy as well. It was established that the carboxyl groups within the dye molecules play an important role in the complex formation.

Conslusions

In aqueous medium the complexes of the indotricarbocyanine dye with the detonation ND are characterized by a red-shifted absorption band and faint fluorescence. Most of the fluorescence is contributed by admixture of the dye monomers that are not bound to the ND. The carboxyl groups within the dye molecules are responsible for the complex formation. Absorption band of the complexes are in the far-red to near-infrared spectral region, where biotissues are transparent and interference of the biotissue autofluorescence is negligible [4,5]. Therefore, these complexes can be useful for biological applications.

References

[1] V.N. Mochalin, A. Pentecost *et al*, *Molecular Pharmaceutics* **10**, 3728 (2013).
[2] J.M. Say, C. van Vreden *et al*, *Biophys. Rev.* **3**, 171 (2011).
[3] N.V. Belko, M.P. Samtsov *et al*, *J. Appl. Spectr.* **85**, 997 (2019).
[4] P. Agostinis, K. Berg *et al*, *CA: a cancer journal for clinicians* **61**, 250 (2011).
[5] M. Monici, *Biotech. Ann. Rev.* **11**, 227 (2005).

28th Int. Symp. "Nanostructures: Physics and Technology"
Minsk, Belarus, September 2020

A single-molecule label-free identification of single-nucleotide colorectal-cancer-DNA polymorphism using impedance spectroscopy of self-redox-active decorated carbon nanotubes

V.P. Egorova[1], *H.V. Grushevskaya*[2], A.S. Babenka[3], R.F. Chakukov[2], N.G. Krylova[2,4], I.V. Lipnevich[2] and E.V. Vaskovtsev[1]

[1] Chemistry Department, Belarusian State Pedagogical University, 220030 Minsk, Belarus
[2] Physics Faculty, Belarusian State University, 220030 Minsk, Belarus
[3] Bioorganics Department, Belarusian state medical university, 220116 Minsk, Belarus
[4] Department of Electrical Engineering, Belarusian State Agrarian Technical University, 220023 Minsk, Belarus

Abstract. A novel label-free impedance assay which is based on self-redox active carbon nanotube arrays decorated by nanocyclic organometallic complex monolayer is offered to discriminate single-nucleotide polymorphism of colorectal-tumor genome. The assay is based on the following effects. A mass transfer for the multiwalled carbon nanotubes (MWCNTs) is testified by a Cole–Cole plot with Warburg impedance in dielectric spectra. Charging $K(K')$-point of graphene Brillouin zone is associated with the mass transfer for MWCNTs that leads to arising of charged MWCNT-end states. Plasma oscillations of charge carriers shield electric field of charged electrodes. Complementary hybridization of target deoxyribonucleic acid (DNA) with probe DNA on the MWCNT surface facilitates the penetration of single-stranded target DNA in the nanopores. Dielectric-band appearance and shielding effects testify the duplex formation.

Introduction

Modern methods of molecular-genetic analysis, which are used in clinical practice, require an amplification of target single-stranded (ss) DNA sequences in polymerase chain reaction (PCR).

However, the extremely low concentrations of tumor DNA are out of detection limit of PCR-based methods because the losses of the target DNA in the isolation, purification and detection processes. Because of very small concentrations from 0.01 to 0.002% of mutated allele DNA in the cancer samples, only single double-stranded (ds) DNA molecules with single-nucleotide mismatch (gene point-mutation or single nucleotide polymorphism (SNP) of genome) are isolated from tumor tissue of patients at early-stage cancer. Single long DNA molecules in the plasma of patients with cancer are diagnostic marker and prognostic factor also. Because of these facts new methods of DNA-analysis should be developed [1,2],. The most promising method for sequencing of single DNA molecules in samples is nanosequencing based on surface plasmon resonance effects and surface-enhanced Raman scattering in quantum materials: nanoparticles, graphene, carbon nanotubes, graphene-like monomolecular layers (monolayers) and nanostructured composite materials [3,4]. In the present work we utilize long ds- and short ss-DNA-probes for label-free genotyping. The purpose of this study is to perform dielectric and Raman spectral analysis of DNA-hybridization on surface of decorated-MWCNT monolayer suspended on nanopores and to develop an label-free impedance assay utilizing self-redox activity of carboxylated MWCNTs decorated by nanocyclic organometallic complexes to discriminate single-nucleotide polymorphism of colorectal tumor genome.

1. Experimental

Materials. We utilize two types of DNA probes at single-base-mismatch discrimination: short primer ss-DNAs for perfect-matched (wild-type) and single-mismatched (mutant-type) hybridization with native ds-DNAs and long primer single-base mismatched ss-DNA/blocker composition system as ds-DNA probe for complementary hybridization with a mutant-type oligonucleotide sequence ss-DNA$_m$. The blocker oligonucleotide prevents a hairpin-structure formation and contains inosine (I) substitutions. All oligonucleotide label-free probes are presented in Table 1. The DNA probes were purchased in "Primetech ALC" (Minsk, Belarus). An oncogene KRAS, native ds-DNA$_T$ isolated from colon-cancer tumor, and placental ds-DNA$_p$ of healthy donors were utilized as a marker gene. The purity of the DNA samples was confirmed by a spectrophotometric method. All experiments were performed at root temperature. For experiment, the ds-DNA probe was prepared by annealing a 2:1 ratio of the blocker ss-DNA$_{W_m}$ to ss-DNA$_{lp}$ in TE buffer at $37 \pm 0.1^{\circ}$C. The hybridization reaction lasted 30 minutes. All chemical reagents of analytical grade were used without further purification.

Biosensitive nanostructured ultra-thin films which transduce hybridization signals was fabricated by the Langmuir–Blodgett (LB) technique and consisted of five monomolecular layers (monolayers) formed by nanocyclic complexes of high-spin octahedral iron with dithionylpyrrole (DTP) ligands and two monolayers from complexes of carboxylated hydrophilic MWCNTs with different DNA-probes.

Methods. Electro-physical studies have been performed using planar interdigital electrode structures on pyroceramic support. The dielectric coating of the electrodes represents itself a nanoporous anodic alumina layer (AOA) with a pore diameter of 10 nm. The synthesized LB-nanoheterostructures were suspended on the interdigital electrode system. Spectral studies in visible range were carried out using a confocal micro-Raman spectrometer Nanofinder HE ("LOTIS-TII", Tokyo, Japan-Belarus) by laser excitation at wavelengths 532, 785 nm at room temperature.

All results were confirmed by Sanger sequencing method. We have discriminated mutation and wild type in 100% of 20 samples.

Table 1. Oligonucleotide sequences used in experiments.

Oligonucleotide name	Sequence structure ($5' \rightarrow 3'$)
wild-type ss-DNA probe $KRAS_w$	GTTGGAGCTGGTGGCGTAG
mutant-type ss-DNA probe $KRAS_m$	AGTTGGAGCTG**A**TGGCGTAG
long primer single-base mismatched ss-DNA_{lp}	ÀATAAGGAGGCACTCTTGCCTACGCCATCAGCTCCAACTACCACAAG
blocker ss-DNA_{W_m}	ÑTTGTGITAGTTGGAGCTGATGICGTAGICAAIAGTICCT
target single-base mismatched ss-DNA_{lm}	CTTGTGGTAGTTGGAGCTG**A**TGGCGTAGGCAAGAGTGCCTCCTTATT

2. Hybridization effects on MWCNT enhancement of light scattering and mass transfer in MWCNT monolayers

MWCNT-enhanced light scattering and MWCNT-based quenching. MWCNT-enhanced long-distance energy transfer is excited in the DTP monolayers with a hybridized ds-DNA at the green laser excitation with 532 nm as fig. 1 a demonstrates. The charge transfer into high excited levels is originated by perfect match between $KRAS_m$ and the mutant ds-DNA_T of colorectal cancer tissue. Chiral massless charge carriers confined on MWCNT surface are in lower impurity levels and become free after excitation of the impurity charge carriers to the high energy levels. Therefore, destroying of electron-hole pairs in graphene plane leads to decreasing number of charged $K(K')$, Γ-points of graphene Brillouin zone for MWCNTs and, accordingly, the intensity of G band of the spectrum in fig. 1 a decreased.

Complementary hybridization between the single-stranded chain of target ds-DNA_T and the $KRAS_m$ DNA-probe leads to touching between MWCNTs and DTP surfaces the distortion of ON/MWCNT complexes by formed perfect duplexes. Then the target ss-DNA_T penetrates through nanocavities of nanocyclic compound into the nanopores. As result, Coulomb forces between the DNA and self-redox active DTP-monolayers push out the last from nanopore and, accordingly, the touching surface for DTP-molecules and MWCNTs grows with subsequent increment of $\pi-\pi$-stacking. Meanwhile, a decrement in the impurity energy levels makes them acceptable for MWCNT charge carriers. Since the chiral charge carriers occupy and are not destroyed on the impurity levels the transitions of impurity charges are suppressed in virtue of Pauli exclusion principle signifying that MWCNTs quench scattering light with wavelengths 532, 785 nm after the hybridization as comparison between pairs of spectra 1–2 and 3–4 in Fig. 1 a shows.

Impedance spectroscopy analysis. Figure 1b,c. Dielectric spectra of nanoporous alumina do not contain dielectric Cole–Cole plots (bands) with diffusion element or Warburg impedance W. Since the Warburg impedance is absent for AOA and, accordingly, the oxidation of aluminium electrodes does not occurs, the formed nanoheterostructures are stable. The Cole–Cole plot for the metal-containing dithionylpyrrole LB-films testifies both electric capacity of Helmholtz double layer and the Warburg impedance W of diffusion layer in which electrochemical reactions with mass transfer proceed (self-redox activity). The oxidation-reduction potential of dithionylpyrrole films emerges due to self-redox activity of pyrrole groups with transport of electric charge along conjugated double bonds. MWCNTs are also self-redox active ones according to a Cole–

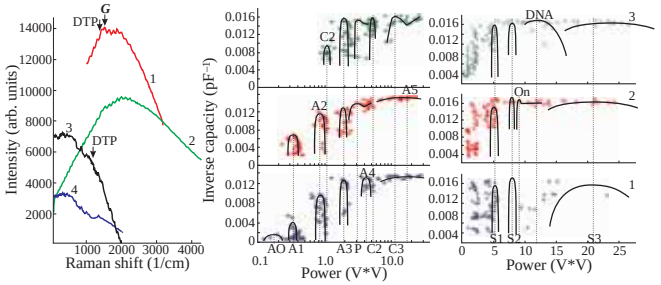

Fig. 1. (a)Raman spectra of decorated MWCNTs after hybridization of target DNA_T with $KRAS_w$ (spectra 1,3) and $KRAS_m$ (spectra 2,4) on MWCNT surface. Wavelengths of laser excitation were 532 (1,2), 785 mn (3,4).; (b) Dielectric spectra: "1" for nanoporous AOA, "2" for metal-containing DTP-LB-film deposited on AOA, "3" for decorated MWCNTs suspended on nanopores; (c) dielectric spectra: "1" and "2" for DNA-sensor with $KRAS_w$ and a probe system $KRAS_w$–ds-DNA-probe respectively, "3" after binding with target ss-DNA_{lm}. Cole-Cole plots in the spectra are marked as Ai, $i = 0, \ldots, 5$ for AOA; "P" for the DTP compound and Ci, $i = 0, \ldots, 3$ for MWCNTs; Si, $i = 0, \ldots, 3$ for DNA-sensor with $KRAS_w$ only; "On" for ds-DNA probe; "DNA" for duplex.

Cole plot with W labeled by P in spectrum 3, Fig. 1b,c. Mass transfer for the complex ds-DNA probe/ MWCNT is observed that a dielectric spectrum of EIS-transducer including the complexes ds-DNA probe/MWCNT is characterized by presence of Warburg impedance in a Cole–Cole plot labeled by "On" in Fig. 1c. It testifies redox activity of the ds-DNA probe on MWCNT-surface. Fig. 1c shows that a dielectric band of duplex (Cole–Cole plot labeled by "DNA" in dielectric spectrum 3) appears after specific hybridization.

So, dielectric and Raman spectral analysis of DNA hybridization on surface of decorated-MWCNT monolayer suspended on nanopores has been performed. It has been shown that self-redox activity of carboxylated MWCNTs decorated by nanocyclic organometallic complexes can be used to discriminate single-nucleotide polymorphism of colorectal tumor genome.

References

[1] E. Rasouli *et al*, *Analytical Biochemistry*, **556**, 136 (2018).
[2] H. Grushevskaya *et al*, *Semiconductors* **52**, 1836 (2018).
[3] P.A. Rasheed *et al*, *Biosensors and Bioelectronics*, **97**, 226 (2017).
[4] H. Grushevskaya *et al*, *Int. J. Mod. Phys. B*, **32**, 1840033 (2018).

28th Int. Symp. "Nanostructures: Physics and Technology"
Minsk, Belarus, September 2020

Effect of colchicine on the cytoskeleton of living fibroblasts revealed by atomic force and confocal laser scanning microscopy

A.V. Ankudinov[1], *M.M. Khalisov*[1,2], V.A. Penniyaynen[2], K.I. Timoshchuk[1,2], and B.V. Krylov[2]

[1] Ioffe Institute, St Petersburg, Russia
[2] Pavlov Institute of Physiology of the RAS, St Petersburg, Russia

Abstract. Using atomic force and confocal microscopy the effect of colchicine (1 μg/ml) on the primary culture of rat fibroblasts was studied. Nanoindentation of cells in an atomic force microscope showed that the substance increases the rigidity of fibroblasts. In the group of cells with stress fibers, an almost 60% increase in the average Young's modulus was recorded compared to the control fibroblasts. In a confocal microscope, under the action of colchicine, a 40% increase in the fluorescence intensity of F-actin relative to the control level was observed. Thus, colchicine, which inhibits the polymerization of tubulin microtubules, also caused a compensatory cell response that increases the rigidity of fibroblasts due to the activation of actin polymerization.

Introduction

Colchicine inhibits the polymerization of tubulin microtubules — one of the main components of the cell cytoskeleton. Using atomic force microscopy (AFM), it was found that, despite this, the substance can provoke an increase in the rigidity of the surface layer of the VERO and SMCC-7721 cell lines [1]. Such an unexpected result can be associated with an augmentation of the F-actin content and, in particular, with the formation of stress fibers, previously observed in 3T3 and Rat-2 fibroblasts [2]. The actin microfilament network is also a key component of the cytoskeleton. It is considered to be most responsible for the mechanical properties of cells [3]. In [1], there is no confocal microscopy data for an unambiguous correlation between cell hardening and increase in F-actin concentration. In contrast to the VERO and SMCC-7721 cells, it was found that colchicine doesn't significantly affect the mechanical properties of HL-7702 cells It testifies against the versatility of the substance effect on cells. In the current work, the effect of colchicine on the primary fibroblast culture of warm-blooded animals was studied by AFM and confocal microscopy

1. Experiment

The primary fibroblast culture was obtained from the heart of a newborn *Wistar* rats. Cells were cultured in 40 mm Petri dishes, pre-coated with collagen, for 5 days at 36.5°C and 5% CO_2 Colchicine at a concentration of 1 μg/ml was added to part of the Petri dishes. Control fibroblasts were cultured in standard culture medium.

The AFM study was carried out via a Bruker BioScope Catalyst setup under physiologically adequate conditions (at ≈37°C). Indentation of cells was performed using CSG10 probes (the average spring constant was 0.35 N/m) in the PeakForce QNM mode, and the apparent Young's modulus [4] was determined according to the Sneddon model, which assumes approximation of the probe shape by the cone.

A Carl Zeiss LSM 710 confocal laser scanning microscope was used for cytological analysis. Intravital staining of fibroblasts was carried out using phalloidin, conjugated with a fluorescent dye Texas Red (Life Technologies, USA). Phalloidin binds to F-actin highly specifically and allows to visualize and quantify actin cytoskeleton of cells. The nuclei of cells were counterstained with DAPI (Sigma, USA).

2. Results

According to the results of AFM studies, all fibroblasts were divided into two groups. The (I) group of the cells were characterized by the presence of very rigid fibrous structures and showed large values of Young's modulus, and the (II) group of fibroblasts did not have such structures and were considerably softer. In the (I) group, colchicine led to a significant increase in the average Young's modulus: from 48 ±18 kPa ($n = 28$) to 76 ±38 kPa ($n = 29$) for control and colchicine-treated cells, respectively In the (II) group, the Young's modulus after exposure to colchicine was 23 ±7 kPa ($n = 21$), and in control cells it was 18 ±4 kPa ($n = 21$). In both cases, the difference between the Young's modulus values was statistically significant (Mann–Whitney U-test, $p < 0.05$).

A confocal microscope recorded a significant increase in intracellular F-actin in fibroblasts after exposure to colchicine. Fibroblasts treated with the substance showed an enhancement of the fluorescence intensity of F-actin by an average of about 40% relative to the control level. 45 fibroblasts cultured with colchicine and 43 control cells were examined in a confocal microscope. The recorded difference in fluorescence intensities was statistically significant (Student t-test, $p < 0.05$).

Thus, the study of the effect of colchicine on primary fibroblasts of newborn rats using AFM and confocal laser scanning microscopy revealed the presence of a compensatory cell response activated by colchicine, which consists in the increased actin polymerization.

Experiments were carried out using the equipment of the Confocal Microscopy Collective Use Center (Pavlov Institute of Physiology of the Russian Academy of Sciences).

Acknowledgement

This work has been supported by the Russian Foundation for Basic Research (grant No. 18-015-00079).

References

[1] L. Liu *et al*. *J. Biomech.* **67** 84 (2018).
[2] H.I. Jung *et alMol. Cells.* **7** 431 (1997).
[3] C. Rotsch *et alBiophys J.* **78** 520 (2000).
[4] K.I. Timoshchuk *et al*, *Technical Physics Letters* **45** 947 (2019).

28th Int. Symp. "Nanostructures: Physics and Technology"
Minsk, Belarus, September 2020

Plasmonic gold nanostars characterization for theranostic applications

W.G. Pearl I[1], *E. Perevedentseva*[1,2], A.V. Karmenyan[1], N. Ali[3], V.A. Khanadeev[4], N.G. Khlebtsov[4,5], S. Vanio[3], M. Kinnunen[6], C.-L. Cheng[1]

[1] Physics Department, National Dong Hwa University, Hualien, Taiwan
[2] P.N. Lebedev Physics Institute of RAS, Moscow, Russia
[3] Biocenter Oulu University of Oulu, Oulu, Finland
[4] Institute of Biochemistry and Physiology of Plants and Microorganisms of RAS, Saratov, Russia
[5] Saratov State University, Saratov, Russia
[6] Faculty of Information Technology and Electrical Engineering University of Oulu, Oulu, Finland

Abstract. In present work Au nanostars (AuNSts) are considered in terms of their multifunctional applications in biomedical research and theranostics. Two types of AuNSt with plasmonic resonance at 590 and 730 nm are prepared by a seed-meditated method and characterized as agent for bio-imaging and phototherapy. To characterize cytotoxicity of AuNSts lung cancer cell line A549 was used. Photothermal effect of AuNSts was observed at irradiation with 730 nm LED light of A549 cell treated with AuNSts. To estimate the imaging ability, AuNSts were visualized at their interaction with murine skin in vitro u sing fluorescence lifetime imaging (FLIM) at two-photon excitation with femtosecond laser and detected in skin samples using optical coherent tomography (OCT).

Introduction

Properties of nanoparticles open possibilities for their applications for nanotheranostics. Nanotheranostics combines diagnostic and treatment abilities of one nanostructure and is expected to develop methods for excellent personalized therapy. Gold nanoparticles are shown very convenient for multifunctional bioapplications [1].They have been shown in general biocompatible, their surface can be functionalized with drugs (and other molecules) for drug delivery. Due to their plasmonic properties AuNP can be used like imaging agent and for biosensing. Also their applications for photothermal therapy and photodynamic therapy are demonstrated. Among other nanoparticles gold nanostars (AuNSts) have gained great attention in cancer therapy and bio-imaging due to enhanced local fields around multiple gold tips and tunable plasmon resonance across UV-Visible-Near Infrared (NIR) range. This makes them a prospective candidate for imaging and photothermal therapy (PTT).

In present work AuNSts were fabricated by seeded growth through a two-step surfactant-free approach [2] and characterized in terms of their applications for bio-imaging and phototherapy.

1. Characterization of AuNSts

Absorption spectra were measured for AuNSts water suspensions and shown plasmon resonance peak near 590 nm for one kind of particles (AuNSt-590) and 730 nm for other one (AuNSt-730). The size and shape of the particles were analyzed using a Scanning Electron Microscope. The size of particles AuNSt-590 was varied in range 40–100 nm, the average number of tips was accordingly from 1 to 8–10 with length up to 50 nm. The average size of AuNSt-730 was estimated about 85 nm, the average number of tips could be estimated 8–12 with length in range 40–60 nm. Both kinds of AuNSts reveal strong fluorescence at 2-photon excitation using tunable femtosecond Ti-sapphire laser with excitation wavelength 780 nm, pulse duration 140 fs, repetition rate 80 MHz, laser power 3.5 mW. The signal was detected in spectroscopic range 450–650 nm. Fluorescence lifetime was estimated and found in range 0.25–0.6 ns.

2. Interaction with cell culture

To estimate the AuNSt imaging ability, AuNSt penetration and localization in biological tissue was studied using murine skin *in-vitro*. Murine skin patch samples were prepared and treated with AuNSts suspensions as described in [3]. Mice experiments were done in accordance with Finnish national legislation on the use of laboratory animals, the European Convention for the protection of vertebrate animal used for experimental and other scientific purposes (ETS 123), and EU Directive 86/609/EEC. The animal experimentation was also authorized by the Finnish National Animal Experiment Board (ELLA) as compliant with the EU guidelines for animal research and welfare. Skin samples were subjected to OCT studies, than cut to thin slices for FLIM investigation at two-photon excitation with using tunable femtosecond Ti-sapphire laser with excitation wavelength 780 nm, pulse duration 140 fs, repetition rate 80 MHz, laser power 11 mW. Strong emission of AuNSts at two-photon excitation allowed their visualization in the skin using FLIM at two-photon excitation. Lifetime in range 0.25–0.6 ns allows confidently distinguishing AuNSts with cells and skin autofluorescence at FLIM. It is shown that AuNSts can be observed deep inside the tissue sample at relatively low (safe) laser power. With FLIM AuNSts are predominantly observed in hair follicles. Detection of AuNSts in skin using FLIM was compared with OCT 2D images and 1D in-depth scans analysis which also demonstrates the influence of AuNSts on the tissue scattering.

Our results demonstrate the ability of AuNSt penetration into animal skin and prospective to use these kinds of AuNSts for multimodal imaging in combination with photothermal therapy.

Acknowledgements

We appreciate the Ministry of Science and Technology (MOST) of Taiwan (MOST 106-2112-M-259-009-MY3), Russian Scientific Foundation (Project No. 19-72-00120), and thelb Academy of Finland (318103) for financial support of the research.

References

[1] N. Khlebtsov *et al*, *Theranostics*, **10** (5) 2067–2094 (2020).
[2] H. Yuan *et al*. *Nanotechnology*, **23** (7) 075102 (2012).
[3] E. Perevedentseva *et al*, *Materials* **12**(22) 3762 (2019).

28th Int. Symp. "Nanostructures: Physics and Technology"
Minsk, Belarus, September 2020

Precipitation of magnetically driven drug carriers in capillaries: theory and *in vitro* experiment

M.A. Pyataev, M.N. Zharkov, D.E. Yakobson and N.A. Pyataev
National Research Ogarev Mordovia State University, 430005, Saransk, Russia

Abstract. The work is devoted to the modeling of the magnetic drug carriers distribution in living organisms in the presence of a non-uniform magnetic field. A theory and experimental model are proposed to understand the mechanism of particle accumulation in tissues.

Introduction

The magnetically driven microcapsules are considered as a promising tool for targeted drug delivery. Investigation of the precipitation mechanism is necessary for correct choice of carrier parameters such as particle size, content of magnetic substance, magnetic field gradient and so on. At least roughly estimation of these parameters must be done to evaluate the ability of magnetic targeting. Many papers [1–4] are devoted to the study of magnetic particle motion based on the analysis of forces acting on them. In the present paper, we generalize this approach taking the diffusion process into account and obtain the partial differential equation for the concentration of capsules in the capillary. Based on our theory we have determined the parameters of carriers necessary for their precipitation. The results of calculation is compared to the *in vitro* experiment performed on a model of a blood vessel.

1. Experimental model

We consider a model of a blood capillary made of a polyethylene tube with inner diameter of 1 mm. The capillary was located near the boron-neodymium permanent magnet of cylindrical shape. The magnet has diameter of 45 mm and height of 35 mm. The magnetization vector is parallel to the axis of the cylinder and the field at the base is equal to 0.47 T. The schematic representation of capillary and magnet relative position is shown in Fig. 1.

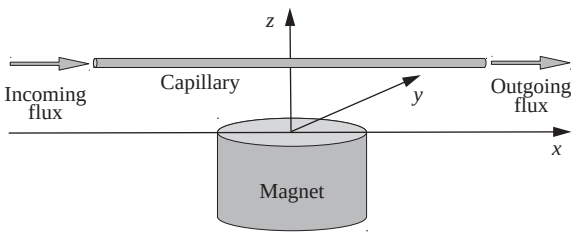

Fig. 1. Scheme of the device.

A suspension of polymer microcapsules containing iron oxide Fe_3O_4 nanoparticles was used for the experiment. The capsules were synthesized by the "layer by layer" method on the spherical $CaCO_3$ nuclei which was coated with polymeric layers alternating with the layers of magnetite nanoparticles stabilized by citrate ions. The average diameter of capsules measured by transmission electron microscopy was about 700 nm.

The suspension of microcapsules was pumped through the capillary by the syringe infuser allowing precise control of the flow rate. We have studied spatial distribution of precipitated capsules in the magnetic field. For this reason, the capillary was fixed at the distance z from one of the magnet bases and then 6 ml of suspension were pumped through it. After that the flow was stopped, the tube was frozen (together with the magnet) and then cut in pieces of 5 mm length. The content of iron in each piece was determined by the photocolorimetry. The results of measurements were compared with the theoretical investigation.

2. Theory

The theoretical model is based on the analysis of particle distribution in a liquid taking the diffusion into account. The vector of particle flux $\mathbf{j}$ in presence of the diffusion can be written as

$$\mathbf{j} = c\mathbf{v} - D\nabla c, \tag{1}$$

where c is the concentration of particles, $\mathbf{v}$ is the particle velocity obtained from mechanics and D is the diffusion coefficient.

The continuity equation in stationary regime ($\frac{\partial c}{\partial t} = 0$) gives

$$\nabla c \cdot \mathbf{v} + c\nabla\mathbf{v} - D\Delta c = 0. \tag{2}$$

To find the velocity $\mathbf{v}$ we consider the Newton's law of motion for the particle taking into account the Stockes drag force and the magnetic force. Our analysis shows that due to the very small volume of the particle we can neglect terms including mass m and volume V (that is inertia, gravity and buoyant force are neglected). So the equation of motion gets the form

$$\mathbf{F}_S + \mathbf{F}_m = 0. \tag{3}$$

The magnetic force acting on the particles can be found from equation

$$\mathbf{F}_m = (\mathbf{p}_m\nabla)\,\mathbf{B}, \tag{4}$$

where $\mathbf{p}_m$ is the average particle magnetic moment that is calculated based on experimentally measured magnetization of the suspension. The moment $\mathbf{p}_m$ is proportional to particle mass and directed parallel to $\mathbf{B}$.

The Stokes force $\mathbf{F}_S$ for spherical particles can be represented in terms of relative velocity $\mathbf{v}_r$ of the particle with respect to the liquid

$$\mathbf{F}_S = -6\pi r\eta\mathbf{v}_r, \tag{5}$$

where η is the liquid viscosity and r is the particle radius.

We assume that the particles does not disturb the motion of liquid due to their low concentration and consequently the liquid velocities in the capillary are distributed according to Poiseuille's theory

$$v_l(\rho) = v_0(1 - \rho^2/R^2), \tag{6}$$

where R is the capillary radius and v_0 is the speed of the liquid at the capillary axis. Total particle velocity $\mathbf{v} = \mathbf{v}_l + \mathbf{v}_r$ is found as a sum of liquid velocity $\mathbf{v}_l$ and relative velocity $\mathbf{v}_r$. Taking into account that $\nabla \mathbf{v}_l = 0$ we finally obtain from equations (3) and (5)

$$\nabla c \cdot \left(\mathbf{v}_l + \frac{1}{6\pi r \eta} \mathbf{F}_m \right) + \frac{c}{6\pi r \eta} \nabla \mathbf{F}_m - D \Delta c = 0. \qquad (7)$$

We have solved equation (7) numerically and found the stationary distribution of particles.

3. Results and discussion

The results of calculations and experimental measurements of magnetite concentration in different parts of of the capillary are shown in Fig. 2. The values are normalized so that the area

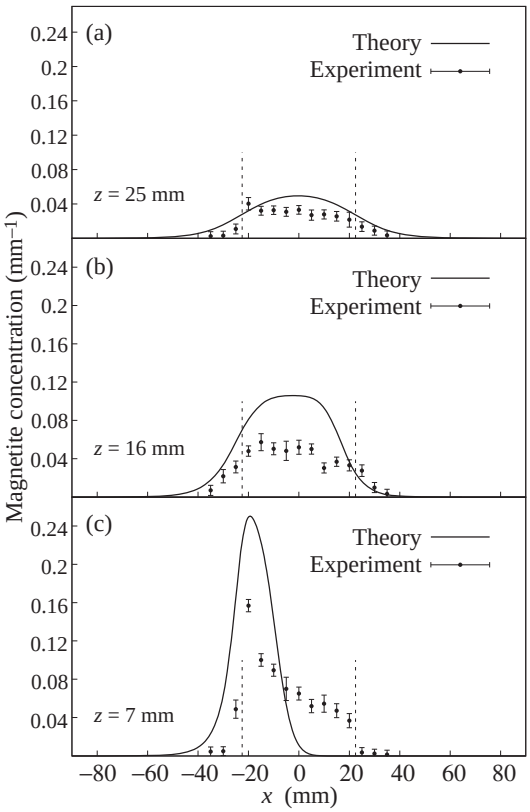

Fig. 2. Distribution of precipitated particles for different distances z from the magnet. Dashed lines show the x-position of the magnet edges.

under curve (AUC) defines the total percentage of precipitated capsules. One can see that experimentally measured concentrations are smaller then theoretically calculated and shifted towards the direction of flow. The difference between the theory and experiment is most pronounced in the area of high magnetite concentration.

For detailed investigation of the difference we have performed a real-time microscopic observation of the precipitation process. We have found that the precipitated capsules are forming the grass-like pillar structures (Fig. 3). The formation of such structures can be explained by concentration of magnetic field inside ferromagnetic column that leads to appearance of high magnetic field gradient near the apex of the pillar and consequently strong attractive force driving the particle to the apex.

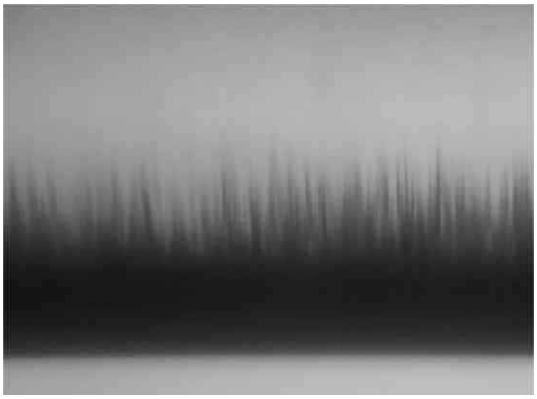

Fig. 3. Microphotograph of the pillar structures formed by precipitated capsules.

We have seen with the microscope that some highest pillars are breaking by the liquid flow and debris are carried away. This process can explain the difference between theoretical and observed distribution of magnetite.

Conclusion

The theory allows one to estimate the parameters of the magnetic field and particle characteristics necessary for obtaining required concentrations of particles in a given site of the body. In the framework of our model, the relative part of particles accumulated in the area of magnetic field depends on two dimensionless parameters $g\tau/v_0$ and l/R, where R is the capillary radius, l is the typical length passed by the particle under the action of the field, $\tau = m_0/(6\pi r\eta)$ is the relaxation time and $g = F_m/m_0$ is the effective "magnetic gravity" i.e. the magnetic force per unit of magnetite mass m_0. In our experiment, l was determined by the diameter of magnet (45mm), but in a living body, it is restricted by the geometry of capillary and the ratio l/R is of the order of 200. It is clear that the effective gravity g has to be at least an order of magnitude larger than the standard gravity. It leads to the following estimation for parameters of microcapsules: if the ratio m_0/r exceeds the value of $1\text{pg}/\mu\text{m}$ then the most of microcapsules will be precipitated in a magnetic field with $g = 10^2 \text{m/s}^2$.

Acknowledgement

The work has been supported by the RFBR (grant 18-415-130007).

References

[1] M.O. Avilés *et al*, *J. Magn. Magn. Mater.* **320**, 2704 (2008).
[2] A.E. David *et al*, *J. Controll. Release* **152**, 67 (2011).
[3] S. Sharma *et al*, *J. Magn. Magn. Mater.* **379**, 102 (2015)
[4] L. Agiotis *et al*, *J. Magn. Magn. Mater.* **401**, 956 (2016).

28th Int. Symp. "Nanostructures: Physics and Technology"
Minsk, Belarus, September 2020

Time-resolved photoluminescence of excitons and biexcitons in CdSe/CdS/CdZnS colloidal quantum dots

V.I. Pavlenko[1], *I.V. Beloussov*[1], I.I. Dobynde[1] and D.I. Ozol[2]

[1] Institute of Applied Physics, 5, Academy str., Kishinev, MD-2028, Republic of Moldova
[2] Moscow Institute of Physics and Technology, 9 Institutskiy per., Dolgoprudny, Moscow Region, 141700, Russian Federation

Abstract. The time evolution of a strongly nonequilibrium state of electrons and holes excited in quantum dots by a long laser pulse in the p-states are studied using the time-resolved photoluminescence. Three bands of the transient photoluminescence spectra were identified, and the ignition and decay of each of them were investigated. The complex picture of the time evolution of the bands is explained by the fast processes of cascade intraband relaxation and the Pauli exclusion principle. The durations of formation and decay for each of the photoluminescence bands are determined.

The time-resolved photoluminescence (PL) triggered by a ∼30 ps long exciting pulse centered at the time 154 ps was investigated. The use of long pulses allows one not only to trace the decay of multi-exciton complexes, but also to study the process of their formation and, thus, to give a more complete picture of the physical processes occurring in the system. In addition, in contrast to [1–3], in order to achieve a fast relaxation to the lowest state, we excite electron-hole pairs by a laser directly near the p-states. We obtained from the spectrogram with ∼50 ps resolution the temporal trace of PL in the main (low-energy) spectral range. The entire process of the PL decay can be conventionally divided into three consecutive stages (I,II, and III) characterized by the different rates of the intensity decrease. We will assume that this difference is associated with sequential processes; in each of them the decay of a spectral component is accompanied by the excitation of the other, lower-lying energy state. However, unlike these works, we will not assume a single- or multi-exponential character of the decay, expecting that while some states are depleted, the filling of others may increase, and their decay will begin later. Therefore, the total radiation from these states will not have a simple form of decreasing exponents in the entire studied PL region. The fitting function for the time-integrated PL spectrum can be decomposed into two Gaussian functions and a constant part that takes into account the noise background. The first of these functions, associated with the radiation from the s-states of electrons and holes, has a maximum at 1.98 eV and a full width at half maximum of the peak ∼100 meV. The second function, associated with radiation from the p-states, significantly overlaps the first one and has a maximum at 2.1 eV and a width of ∼340 meV. A strong overlap of the spectral bands occurs due to the inhomogeneous broadening associated with the size dispersion of the quantum dots. Since the radiation of biexcitons is a fast transient process, the time-integrated PL spectrum does not contain any information about their presence. However, they can be detected by studying transient spectra at different points in time. This would make it possible to determine such parameters of biexcitons as the binding energy, excitation and decay times.

We obtained a series of transient PL spectra extracted at different delays relative to the center of the exciting laser pulse using a 50 ps integration window. The asymmetric fitting function can be presented as a sum of three Gaussian components $F_i \exp\left(-(\epsilon-\epsilon_i)^2/\gamma_i^2\right)$ centered at $\epsilon=\epsilon_i$ $(i = X, B, P)$ and some background constant F. We associate the broad peak in each transient PL spectrum described by the Gaussian function with a maximum at ϵ_P=2.1 eV with the radiative recombination of e-h pairs in p-states. It quickly disappears, but since its width is large, it also appears in the time-integrated spectrum. The high peak at ϵ_X=1.98 eV makes a major contribution to the time-integrated spectrum. We associate it with the decay of single excitons. And, finally, we explain the peak at ϵ_B=1.92 eV, which first arises and then disappears, as the decay of biexcitons [2]. This peak is relatively low and is strongly overlapped by the other peaks; therefore, we can say that *biexcitons hide behind excitons*. The binding energy $2\epsilon_X - \epsilon_B$ of two excitons in the biexciton is 60 meV.

Comparing the spectral dependences we see that the parameters of the fitting function change with time. To find out how this occurs, let us study the temporal dependences of the amplitudes of Gaussian functions and their widths. The corresponding results are shown in Figs. 1 and 2.

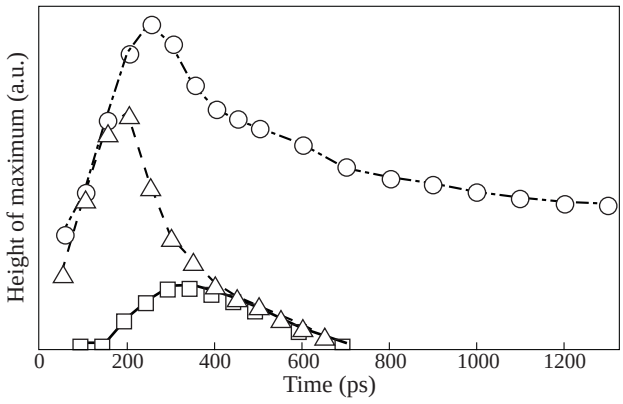

Fig. 1. The temporal dependence of the height of the maximum of the fitting function at ϵ_X (circles), ϵ_B (squares), and ϵ_P (triangles).

As can be seen from Figs. 1 and 2, the laser pulse excites radiation, mainly from the p-states of electrons and holes, that occurs in a wide energy range and reaches a maximum value at 200 ps. Simultaneously, radiation appears from the s-states. It has an almost unchanged spectral range and reaches a maximum at 250 ps. The emission of biexcitons appears with even greater delay and much slower. Its growth ceases at 350 ps when two previous PL bands are already significantly reduced.

The spectral range where this radiation occurs also does not almost change. Starting from 350 ps the radiative recombination of e-h pairs in $1P$-states is accompanied by the decay of biexcitons within ∼140 ps. The decrease of radiation from single excitons within this time interval slows down. After 700 ps only a very slowly decreasing emission of single excitons occurs that can be described by a simple exponential curve. Using the exponential function for fitting only at times greater than 700 ps we obtain a value of ∼10 ns for the decay time of a single exciton.

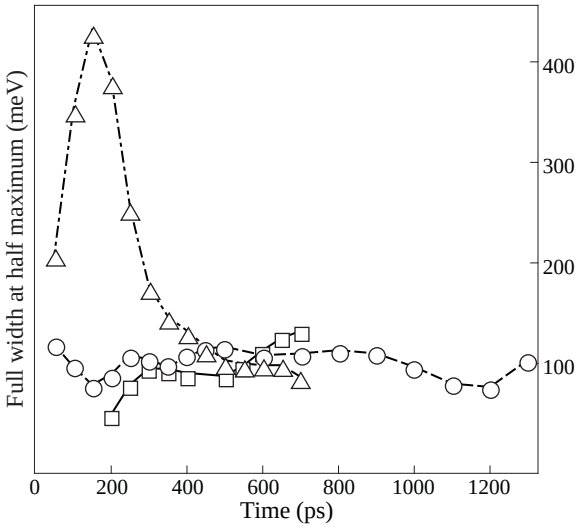

Fig. 2. The temporal dependence of the width of the maximum of the fitting function at ϵ_X (circles), ϵ_B (squares), and ϵ_P (triangles).

We assume that all microscopic processes occurring in the system can be divided into fast and slow ones. The accuracy of the measurements does not allow us to follow the fast processes, but we can take into account the results of their actions. These processes involve an Auger-like scattering of the electron by the hole and subsequent intraband relaxation of the scattered hole with emission of phonons. This sequence of processes leads to the fact that e-h pairs excited by a laser pulse near the $1P_e$–$1P_{3/2}$ state convert into e-h pairs in the lowest $1S_e$–$1S_{3/2}$ state. Moreover, due to the described mechanism of intraband relaxation the creation of pairs in the s-states may continue even after the end of the action of the laser pulse if this is allowed by the filling of the $1S_e$–$1S_{3/2}$ states of the e-h pairs in accordance with the Pauli exclusion principle. The number of pairs in p-states at this time decreases. This explains the behavior of the curves in Fig. 1 within the time interval from 100 to 200 ps.

If there is only one e-h pair in the s-states, then taking into account the Coulomb interaction, we can speak about the formation of an exciton. If the number of e-h pairs in this state reaches a maximum value equal to two, we can speak about the formation of a biexciton. In this terminology, the appearance of the second pair in the state where one pair is already present automatically means the disappearance of both pairs (or two excitons) and the formation of a biexciton. The second pair, like the first one, can quickly transit to the s-state from the p-state as a result of fast intraband relaxation. In this case, the appearance of a biexciton means the disappearance of one pair from the s-state and one pair from the p-state. The corresponding behavior of the curves in Fig. 1 manifests itself within the time interval from 200 to 350 ps where the ignition of the biexciton band of PL is accompanied by a rapid decrease in both the radiation from the single excitons and the emission from the e-h pairs in the p-states.

By the time of 350 ps, the generation of biexcitons seems to reach saturation, and their decay begins. We can consider the annihilation of any constituent e-h pair of the biexciton as a decay of the biexciton resulting in the creation of an exciton and a photon. The remaining pair can also annihilate; this means a radiative decay of the exciton. Another channel for the biexciton's decay is associated with an Auger-like interband process where the annihilating e-h pair transfers its energy to an electron or hole of the second e-h pair. We see that the biexciton and exciton decay processes are slower than those indicated for the formation of excitons and biexcitons. Note, that the decay of the biexciton PL band in the interval from 350 to 700 ps is accompanied by almost the same decay of other bands. In our opinion, this also indicates the saturation of biexciton states. Electrons and holes in the p-states do not hasten to radiatively recombine, but wait for the opportunity to stay in a lower energy state.

Thus, the stage I of the PL decay corresponding to the peak is the shortest and fastest; it has the widest spectrum and is associated with the recombination of electrons and holes from the p-states. The stage II located at the foot of the peak is characterized by complex processes associated with both the formation and decay of biexcitons, as well as the slowdown of the decay of single excitons and e-h pairs in the p-state. And, finally, the slowest stage III located in the tail of the dependence is associated with the radiative decay of single excitons.

We excited electrons and holes near the energy of the p-states expecting to get their fast relaxation in one step. However, the obtained results are very different from those previously presented in [1–3], where the excitation was high in the energy zone. We managed to trace not only the disintegration of the main PL bands, but also their ignition. This gives evidence that taking account of the Pauli exclusion principle plays a significant role in the description of the temporal evolution of the system. An external pulse can excite only six e-h pairs in the p-state, while the s-states are ready to accept only two. Therefore, the pair conversion from the p- to the s-state does not occur until the s-state is at least partially vacant. The results presented by us show that in our case the Poisson distribution cannot be used as an initial condition for the rate equations at any fixed point in time. And the rate equations themselves cannot be linear, since one should take into account such a phenomenon as the saturation of the state of Fermi particles.

References

[1] M. Achermann, *et al*, *Phys. Rev. B* **68**, 245302 (2003).
[2] J.-M. Caruge, *et al*, *Phys. Rev. B* **70**, 085316 (2004).
[3] C. Bonati, *et al*, *Proc. SPIE* **6892**, 68920H – 11 (2008).

28th Int. Symp. "Nanostructures: Physics and Technology"
Minsk, Belarus, September 2020

Structural and dynamic properties of short-period GaN/AlN superlattices: experiment and theory

I.A. Eliseyev[1], V.Yu. Davydov[1], E.M. Roginskii[1], Yu.E. Kitaev[1], A.N. Smirnov[1], M.A. Yagovkina[1], D.V. Nechaev[1], V.N. Jmerik[1] and M.B. Smirnov[2]

[1] Ioffe Institute, 194021, St Petersburg, Russia
[2] Saint Petersburg State University, 199034, St Petersburg, Russia

Abstract. The structural and dynamic properties of short-period GaN/AlN superlattices with the thicknesses of the constituent layers varying from two to several monolayers, which were grown by using the submonolayer digital molecular beam epitaxy technique, have been studied experimentally and theoretically. The results of complex studies can be successfully used to optimize the growth parameters in order to fabricate structurally perfect short-period GaN/AlN superlattices.

Introduction

The great scientific interest in low-dimensional epitaxial heterostructures based on wide-gap A3-nitride compounds (Al, Ga) N is due to the unique possibility of creating optoelectronic devices, operating both in the mid-ultraviolet and infrared-terahertz spectral ranges. Such devices are promising for applications in multi-range spectroscopy, for the development of photodiagnostics and phototherapy methods in medicine, for the implementation of indirect optical communication systems, etc. Among the most important elements of such devices are short-period superlattices (SLs), with the thicknesses of the constituent layers varying from one to several monolayers (ML), i.e. the $(GaN)_m/(AlN)_n$ SLs (where m and n are the numbers of GaN and AlN MLs, respectively). The most important requirements for such SLs are the presence of atomically smooth and homogeneous surfaces of the constituent layers, and the extremely sharp interfaces. The solution of these problems requires a detailed study of the fundamental physical properties of SLs, as well as the development of new methods for the quantitative diagnostics of their parameters with atomic resolution.

1. Results and discussion

Short-period $(GaN)_m/(AlN)_n$ SLs (m = 2,4,6; n =4,6) were grown using low-temperature plasma-activated molecular beam epitaxy technology at substrate temperatures of 690–740 °C in metal (Ga) — enriched conditions using the submonolayer digital epitaxy technique [1]. This technique was modified to obtain SLs with a total thickness of up to $\sim 1\ \mu m$ and the number of periods up to 600. The structural properties of SLs were studied using high-resolution X-ray diffractometry, small-angle X-ray scattering, and diffuse small-angle scattering [2–4]. An analysis of the X-ray data made it possible to determine the period of the grown SLs and the ratio between the thicknesses of their constituent layers, as well as to analyze the degree of interface replicativity. It was found that in the grown SLs there are two types of interfaces. One type is the interface between bilayers $(GaN)_m/(AlN)_n$, and the other type is formed under periodic stops during digital epitaxy to evaporate excess (Ga) metal. The dynamic properties of the SLs were studied experimentally using Raman spectroscopy. The interpretation of the Raman spectra was carried out using *ab initio* calculations of nonlinear optical properties in the framework of the density functional theory aimed at studying the phonon states of SLs. The calculations were performed for both equal and non-equal constituent-layer-thickness SLs. Figure 1 shows the experimental Raman spectra of the studied SLs in the $z(xx)\bar{z}$ polarization (where z is the direction of the C_3 optical axis) in comparison with those calculated theoretically in three frequency ranges. The good agreement between experiment and theory is found, which made it possible to establish unambiguously a relationship between the features observed in the Raman spectra and the displacement patterns of the acoustic and optical phonon modes.

In the low-frequency spectral range, the narrow lines were found whose position monotonically changed from ∼50 to 160 cm^{-1} with decreasing period of SLs. The nature of these lines was established using quantum mechanical calculations in order to study the dynamic properties of the SL structures. An analysis of the calculated eigenvectors of vibrational modes (Fig. 2) brings to conclusion that the most intense lowfrequency lines correspond to the phonons that are genetically connected with folded longitudinal acoustic (LA) phonons of a bulk crystal as a result of multiple folding of the Brillouin zone (BZ). The displacement patterns of these modes have the character of one period of a standing wave within the unit cell of the SL. With help of group-theoretical analysis, a relationship was established between mode eigenvectors in the center of the Brillouin zone and the vectors of the acoustic and optical phonon branches at the BZ boundary. It was shown that the symmetry-determined degeneracy of the two complex-conjugated $A_1 \oplus A_4$ modes at the BZ boundary of a bulk GaN (AlN) crystal with the space group C_{6v} is lifted in the C_{3v} space subgroup of the SL, which results in appearance of two different lines in the low-frequency range of the Raman spectra having similar eigenvector patterns.

It has been established that the line with the maximum intensity in the low-frequency region of the Raman spectrum corresponds to the mode in which atomic displacements reach their maximum in the interface region. It was shown that the position of these lines depends not only on the total SL period, but also on the ratio of the thicknesses of the constituent layers. To interpret the features of the Raman spectra in the low-frequency region, the elastic continuum model (ECM) was also applied [5]. As a result of theoretical analysis, it was established that the determination of the folded LA phonon frequencies from Raman spectra in the scattering geometry, for which

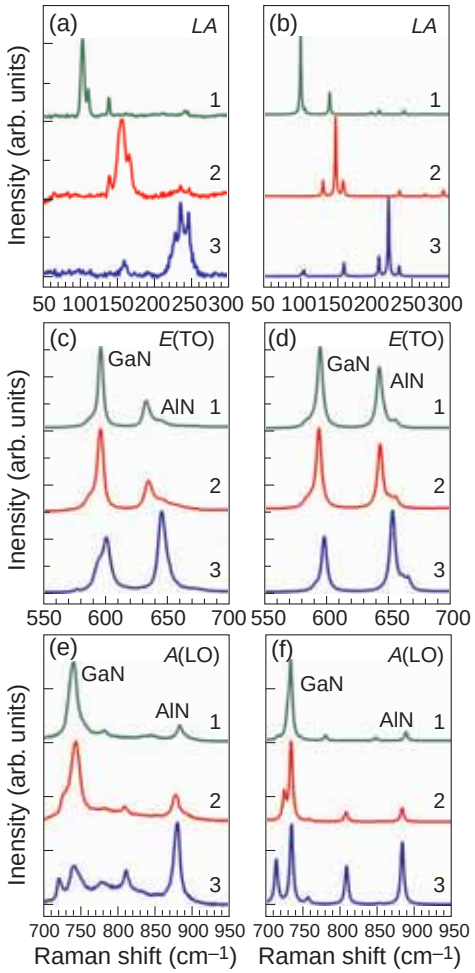

Fig. 1. Experimental (a,c,e) and calculated (b,d,f) Raman spectra of (GaN)/(AlN) SLs in $z(xx)\bar{z}$ polarization. Green (1), red (2) and blue (3) curves correspond to $(GaN)_6/(AlN)_6$, $(GaN)_4/(AlN)_4$, and $(GaN)_2/(AlN)_4$, respectively.

Raman-active phonons correspond to nonzero diagonal components of the Raman tensor, allows one to obtain quantitative estimates of the structural parameters of SLs. Note that the use of scattering geometry $x(zz)\bar{x}$ (excitation and registration of the Raman spectrum from the SLs cleavage) has a significant advantage compared to the traditionally used scattering geometry $z(xx)\bar{z}$ when performing experimental measurements of folded LA phonons. This is due to the fact that the intensity of Raman spectra, which is proportional to the thickness of the test sample, is not limited by the number of layers of the multilayer structure when using the scattering geometry $x(zz)\bar{x}$. As a result, use of such geometry makes it possible to obtain reliable information even in the case of SLs with a thickness much less than 1 μm.

The analysis of the displacement patterns of optical phonons in the ranges 500–700 cm^{-1} and 700–900 cm^{-1} made it possible to divide phonon modes into two types. The first type are delocalized modes, which are characterized by the displacements of all atoms of the SL unit cell. The second type are the modes localized either in the GaN or AlN constituent layers. In these modes, atomic displacements involve only atoms from one of the constituent layers. The dependence of the position and intensity of lines in the spectra on the period of the superlattice was determined, and a symmetry relationship was

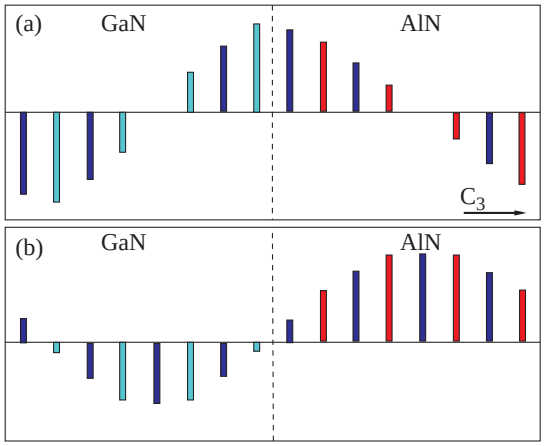

Fig. 2. Patterns of atomic displacements corresponding to folded from BZ boundary A_1 (a) and A_4 (b) phonons. Green, red and blue bars correspond to the values of Ga, Al, and N atomic displacements, respectively, along the C_3 axis. The dashed line denotes the layers boundary.

established between the vibrations of bulk GaN (AlN) crystals and the SL at the high-symmetry points of the BZ. The most striking features were found in the high-frequency region of the spectrum recorded in the polarization $z(xx)\bar{z}$, where the maximum response was obtained from the polar modes. The fine structure of the low-frequency shoulder of the intense E(TO) GaN line and the high-frequency shoulder of the intense E(TO) AlN line genetically related to the E_2^{high} modes of the bulk crystal were discovered and explained for the first time. It was also shown that the polar modes localized in the thin AlN layers are significantly more intense in the SLs with non-equal constituent-layer-thicknesses. In summary, the combination of X-ray and Raman spectroscopy methods, group theory analysis and *ab initio* calculations of normal mode frequencies and the corresponding displacement patterns proved to be a sensitive tool for characterization of crystal structure of short-period GaN/AlN SLs. The results of comprehensive studies can be successfully used to optimize the growth parameters in order to fabricate structurally perfect short-period GaN/AlN SLs.

Acknowledgement

The work was supported in part by the Russian Foundation for Basic Research (project RFBR-BRICS [1] 17-52-80089).

References

[1] V.N. Jmerik, D.V. Nechaev, S.V. Ivanov, *In Molecular Beam Epitaxy: From research to mass production*, Henini M., Eds.; 2nd Edition; Elsevier Inc., 135 (2018).
[2] V. Holy and T. Baumbach, *Phys. Rev. B*, **49**, 10669 (1994).
[3] S.A Stepanov, *Kristallografiya*, **39** 221 (1994).
[4] U. Pietsch, V. Holy, T. Baumbach, *High-Resolution X-Ray Scattering*, Springer (2004).
[5] S.M. Rytov, *Akust. Zh.*, **2**, 71 (1956).

28th Int. Symp. "Nanostructures: Physics and Technology"
Minsk, Belarus, September 2020

Surface morphology electrophysics, and photoluminescence of GaAs:Si epitaxial films on (110)-oriented substrates

G.B. Galiev[1], E.A. Klimov[1], S.S. Pushkarev[1], A.A. Zaitsev[2], and A.N. Klochkov[1]

[1] V.G. Mokerov Institute of Ultra High Frequency Semiconductor Electronics of RAS, 117105 Moscow, Russia
[2] National Research University of Electronic Technology MIET, 124498 Zelenograd, Moscow, Russia

Abstract. The electrophysical and photoluminescent characteristics and the surface morphology of GaAs epitaxial films grown by molecular beam epitaxy on GaAs (110) substrates are studied. Silicon-doped GaAs epitaxial layers were obtained in a wide range of beam equivalent pressure ratios of arsenic and gallium from 14 to 84. It is shown that at a fixed growth temperature the type of conductivity of GaAs:Si films depends on BEP ratio: it changes from p-type at low BEP ratio to n-type at high BEP-ratio through semiinsulating state. The occurrence of point defects Si_{Ga} and Si_{As} as well as the formation of arsenic and gallium vacancies $V_{As}$and V_{Ga} were interpreted by analyzing the photoluminescence spectra of the grown samples.

Introduction

In modern electronics, the most studied and widely used are A_3B_5 semiconductor compounds grown epitaxially on substrates with a crystallographic surface orientation of (100). The use of semiconductor structures on less common (110)- and (111)-oriented GaAs substrates is associated with difficulties of epitaxial growth of high-quality films with good surface morphology and necessary electrophysical parameters. This is associated with a narrower range of optimal technological parameters of epitaxial growth as well as a more complex behavior of silicon atoms as a dopant in GaAs (111)A (110) films compared to GaAs (100). In recent years there has been an interest increase in structures grown on substrates with orientations (110) and (111) due to fundamental properties of such structures, for example built-in piezoelectric field. That makes (110) GaAs structures promising for creating a new field-effect transistors, optoelectronic and spintronics devices.

In this work we study the properties of uniformly silicon-doped GaAs epitaxial films grown on GaAs (110) substrates at different temperatures.

1. Samples growth

Uniformly Si-doped GaAs films were grown by molecular-beam epitaxy on semi-insulating (100)-, (110)- and (111)A-oriented substrates. The samples on (100)- and (111)A-oriented substrates were used as reference. The samples on (100)- and (111)A oriented substrates were used as reference. The substrate pieces were glued down to the molybdenum holder using molten indium. The samples on three different substrates were grown simultaneously at identical conditions: the same substrate temperature of $T_g = 580$ °C, and under different BEP ratios γ in the range from 16 to 80. After substrate anneal an undoped GaAs buffer layer 135 nm thick was grown, then a silicon-doped GaAs:Si layer 675 nm thick was grown. The temperature of Si cell (1080°C) corresponds to the doping with electron concentration of 10×18 cm^{-3} for GaAs film grown on (100)-oriented substrate under standard growth conditions. Growth speed was 90 Å/min.

The electrophysical characteristics (charge carrier mobility and concentration) were determined by measuring the resistivity and the Hall effect using the four-probe method in Van der Pau geometry at temperatures of 300 K in the dark. Photoluminescence (PL) spectra were measured in a combined optical cryostat in nitrogen vapor at 77 K. To excite the PL, focused radiation from a solid-state laser with a wavelength of 409 and 532 nm and a power of 200–300 mW was used. The PL signal detector in the region of 1.2–2.0 eV was an FEU-62 photoelectron multiplier cooled by liquid nitrogen. The energy resolution of the setup was 5 meV. The surface roughness of the samples was measured using an atomic force microscope (AFM) in the NT-MDT Solver Pro setup in contact mode.

2. Type of conductivity

Table 1 presents the results of Hall effect measurements at room temperature: charge carrier type, mobility and volume concentration for the investigated samples. The electrophysical properties of GaAs:Si films strongly depend on γ. It is shown that Si dopant reveals amphoteric properties for GaAs:Si epitaxial films grown on GaAs (111)A and (110) substrates depending on γ. The type of conductivity changes with increasing γ: for samples on GaAs (111)A it is p → i, for samples on GaAs (110) it is p→i→n. Strong amphoteric properties of Si dopants for GaAs (110) and (111) A are associated with the dependence of As atoms incorporation into GaAs lattice on γ.

Table 1. Electrophysical parameters (mobility μ and concentration of charge carriers N) and RMS roughness R_q ("–" sign means high resistance). X axis coincide with [001] direction.

N	γ	Substr.	R_q (nm)	Type	N (cm^{-3})	μ (cm^2)/(V·s)
		(100)		n	10.8	2260
87	16	(110)	117	p	4.3	51
		(111)A		p	6.0	60
		(100)		–	–	–
75	25	(110)	12.3	–	–	–
		(111)A		–	–	–
		(100)		n	3.4	1000
73	58	(110)	15.1	n	2.7	950
		(111)A		–	–	–
		(100)		n	0.23	290
76	80	(110)	21.9	n	0.18	16
		(111)A		–	–	–

3. Surface morphology

Atomic force microscopy (AFM) scans were measured for (110)-type samples only and are presented in Fig. 1. At low $\gamma =$ 16 the sample surface contains large elliptical objects 1–2 μm in diameter and 0.3–0.5 μm in height with two-dimensional concentration of $1.5{\cdot}10^7$ cm^{-2}. These objects consist of non-stoichiometric GaAs with Ga excess. They formed in As-deficit conditions due to low incorporation coeffcient of As atoms for GaAs (110) growth. With an increase in γ. Faceted hills of various shapes are formed on the surface. The hills are mainly oriented along the [001] direction, separated by deep pits. The surface roughness with increasing γ from 25 to 80 increases from 12.3 to 22 nm. The surface of sample 75, as can be seen from Fig. 1, consists of overlapping triangular pyramids. One of the corners at the base looks in the direction [001], and the opposite edge of the base is parallel to [11$\bar{1}$]. Root mean square (RMS) surface roughness R_q of the GaAs:Si films is presented in table 1. R_q substantially depends on γ and lies in the range 12.3–117 nm.

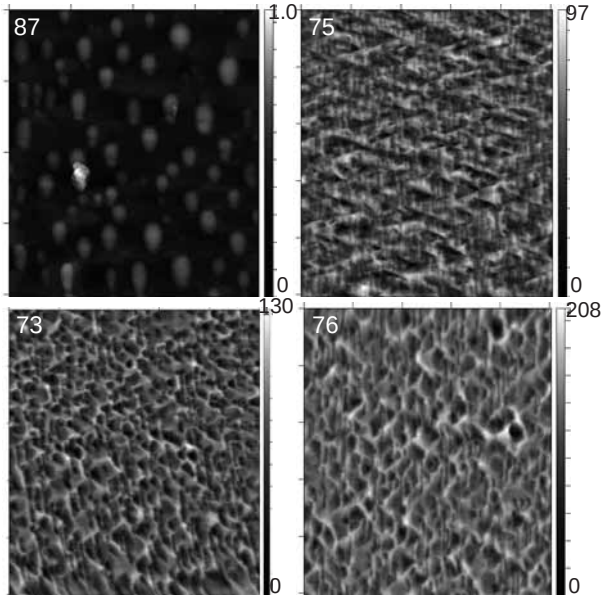

Fig. 1. AFM scans of the surface of GaAs:Si films on (110)- oriented GaAs substrates. Scan field 10×10 μm^2 (except 87 sample for which it is 20×20 μm^2).

4. Photoluminescence spectra

Figure 2 shows the comparison of PL spectra of investigated samples with different orientations (100), (111) A, and (110). The PL spectra differ not only in intensity but also in shape. In this case, the peak due to the edge PL of GaAs for all samples is at 1.50–1.52 eV. The position of other peaks is related to different point defects and defect complexes which originated in GaAs crystal structure due to different growth conditions and the dependence of As atom incorporation on crystal orientation.

All the features in the PL spectra observed in the photon energy range 1.20–1.55 eV are associated with point defects or their complexes. The band present in many cases at 1.36–1.40 eV is associated with V_{As} and Si_{As}. On the other hand, it is known that a change in the shape and intensity of the PL band at 1.4 eV is accompanied by a rearrangement of point defects. For p-GaAs, the V_{As} defect is considered responsible

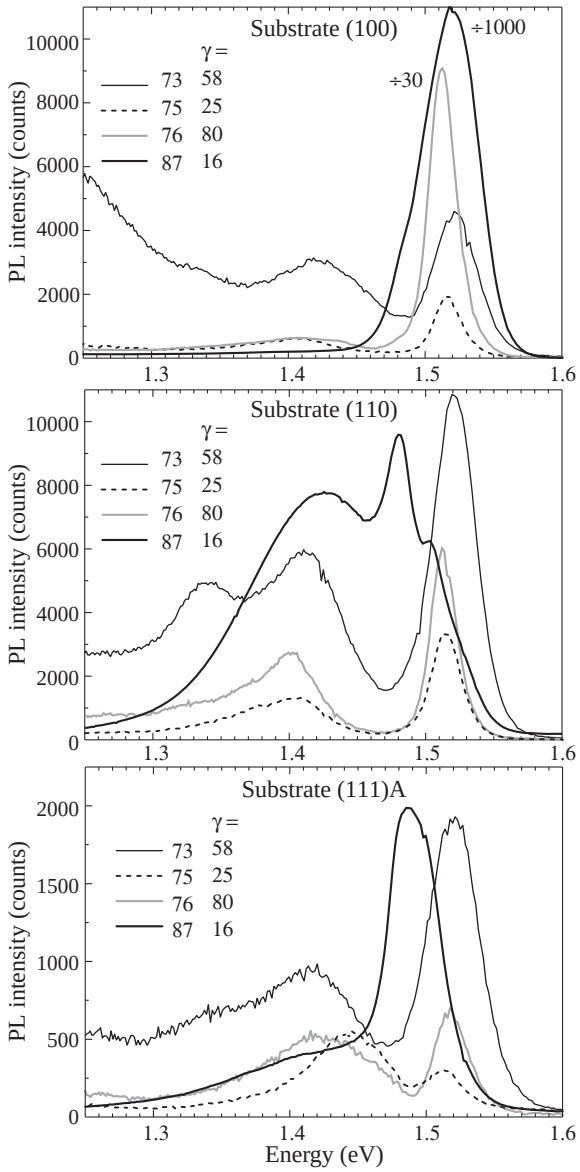

Fig. 2. Photoluminescence spectra of Si-doped GaAs films of different surface orientation at 77 K.

for the peak at 1.4 eV, and for n-GaAs–Ga_{As} or V_{Ga} defects. In addition, if V_{Ga} is formed during epitaxial growth, they give bands in the PL spectra at 1.32 eV and 1.2 eV.

Acknowledgement

This research was funded by RFBR (grant No. 18-32-20207).

28th Int. Symp. "Nanostructures: Physics and Technology"
Minsk, Belarus, September 2020

Features of reflection from the layer of hyperbolic metamaterial

S.N. Kurilkina[1], N.S. Petrov [2], V.N. Belyi[1] and A.B. Zimin[3]

[1] B.I. Stepanov Institute of Physics, National Academy of Sciences of Belarus, 220072 Minsk, Belarus
[2] Institute for Advanced Training and Retraining of Personnel on New Directions for the Development of Technics, Technology and Economics of the Belarusian National Technical University, 220107 Minsk, Belarus
[3] Belarusian State University of Informatics and Radioelectronics, 220013 Minsk, Belarus

Abstract. In this paper, we investigate the features of reflection of a plane elliptically polarized electromagnetic wave fallen from isotropic transparent dielectric on a layer of hyperbolic metamaterial with optical axis in an interface and main effective dielectric permittivities less than the permittivity of dielectric. The cases are analyzed when one (ordinary or extraordinary) wave or two waves, exited inside the layer, are inhomogeneous. It is shown that for certain sub-wavelength thickness of the layer one can choose the angles of incidence for which two inhomogeneous (evanescent) waves existing in this layer totally tunnel through it. It is established that, in contrary to ordinary uniaxial crystal, maximal value of reflection coefficient from the metamaterial layer approaches the unity when the thickness increases.

Introduction

Currently, the attention of many researchers is attracted to metamaterials — artificially synthesized media containing, as a rule, metal nanoinclusions, orderly embedded in a dielectric matrix [1]. This interest is associated with the prospects of using such materials to control the parameters of light beams, to obtain images with sub-wavelength resolution [2,3], in nanolithography, etc.

One type of metamaterials is hyperbolic metamaterials (HMM), described in the approximation of an effective medium by the uniaxial dielectric permittivity tensor, the main values of which differ by sign. Most practical applications of HMM are associated with the features of the electromagnetic waves generated in them, among which inhomogeneous waves occupy a special place. They arise, for example, in transparent media with less refractive index in condition of total reflection of light. In Ref. [4] it is shown the possibility of existence of special inhomogeneous waves near the boundary of hyperbolic metamamterial. For these waves vector amplitude decays non-exponentially moving from the boundary.

In this paper, we study the reflection of a plane elliptically polarized light wave incident from an isotropic transparent medium on a hyperbolic metamaterial layer (Fig. 1), the optical axis of which is parallel to the interface, and the principal permittivities are less than the permittivity of an isotropic medium. Thus, at least one of the waves arising in the layer is inhomogeneous.

1. Reflection of elliptically polarized light waves from the HMM layer

On the basis of solution of boundary problem we obtained analytical expressions for electric and magnetic vectors of the field inside and outside the HMM layer the optical axis of which is parallel to the interface, and the principal permittivities are less than the permittivity of an bordered isotropic transparent medium. Incident plane electromagnetic wave is elliptically polarized (Fig. 1). For these conditions at least one of the waves arising in the layer is inhomogeneous.

Using obtained relations we demonstrated for the case of HMM on the basis of ITO/Ag nanostructure sandwiched between sub-space of BK7 glass that, depending on the angle of incidence α and the angle ρ between the plane of incidence

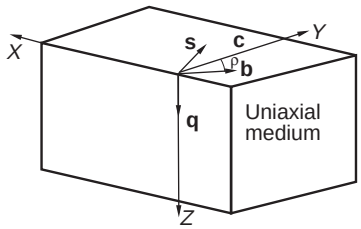

Fig. 1. Considered structure in approximation of effective medium. Here **c** is the unit vector along the optical axis, (**b**, **q**, **s**) is triplet of unit vectors where **q** is the vector orthogonal to interface, (**c**, **q**) is the main plane of anisotropic medium, (**b**, **q**) is the plane of incidence of the light wave.

and the optical axis of the hyperbolic metamaterial, various cases are possible (Fig. 2). As seen from Fig. 2, for the first of them (region I related to $\alpha < \alpha_0 = 51.3^\circ$) homogeneous ordinary and inhomogeneous extraordinary waves propagate inside the HMM layer independently on the angle between the plane of incidence and optical axis of metamaterial. For region II related to the case when $\alpha > \alpha_0$ and $\rho > \rho_1$ both ordinary and extraordinary waves inside the layer are inhomogeneous. For region III when $\alpha > \alpha_0$ and $\rho < \rho_1$ there are inhomogeneous ordinary and homogeneous extraordinary waves inside the layer. Meanwhile, at certain α and ρ the birefringence within the HMM is absent, and an inhomogeneous wave of a special type arises inside the hypebolic metamaterial, which non-exponentially decays with distance from the input boundary of the layer.

Amplitude reflection coefficient (ARC) is found as a matrix connecting incident and reflected fields. 2D energetic reflection coefficient (ERC) matrix is calculated as a product of ARC matrix by its Hermitian conjugate one.

For definite values of α and ρ the changes of incident wave polarization causes the variation of the energetic reflection coefficient from maximum $R_{\max}$ to minimum $R_{\min}$ which are determined as eigenvalues of the ERC matrix. Numerical modeling of the energy reflection coefficient from the layer of the periodic ITO/Ag nanostructure is performed for three cases indicated above. Fig. 3 shows the dependence of $R_{\max}$ and $R_{\min}$ on the thickness h of the HMM layer for the angles α and ρ corresponding to different reflection modes shown in Fig. 2.

As can be seen from Fig. 3, if only one of the forward

waves (ordinary or extraordinary) in the layer is inhomogeneous, the minimum value of the reflection coefficient periodically is changed with the layer thickness from zero to a certain value less than unity. The maximum value rapidly increases and for small h it turns out to be close to unity. The minima of the dependence of $R_{\min}(h)$ correspond to the conditions of interference transmission.

The case is interesting when the angles α and ρ are located in region II. As is seen from Fig. 3 (below), for a certain layer thickness $h < \lambda$, depending on the angles α and ρ, the reflection coefficient $R_{\min}$ becomes equal to zero. It should be noted that vanishing the reflection from the layer upon excitation of exponentially decaying waves in it is characteristic only of the hyperbolic metamaterial and does not occur in the case of total reflection from the usual uniaxial medium. Thus, at certain angles α and ρ, inhomogeneous (evanescent) waves completely tunnel through a layer of metamaterial with a subwavelength thickness. With a further increase of thickness h, the coefficient $R_{\min}$ increases too and approaches unity, in contrast to the interference behavior in regions I and III.

Unlike ordinary anisotropic media, in all cases the maximum value of the reflection coefficient tends to unity with increasing the layer thickness.

2. Conclusion

Thus, in this paper, we studied the features of light reflection from a layer of hyperbolic metamaterial in the case when it is possible existence as one inhomogeneous wave (ordinary or extraordinary), or both them. Analytical expressions are obtained that make it possible to calculate the reflection coefficients of radiation for an arbitrary elliptical polarization of the incident light.

Numerical calculations of the reflection coefficient from the layer of HMM on the basis of ITO/Ag nanostructure for various reflection modes are performed. It is shown that if there is only one (ordinary or extraordinary) inhomogeneous wave in the HMM layer, then the reflection coefficient $R_{\min}$ vanishes at certain layer thicknesses, which corresponds to the condition of interference transmission.

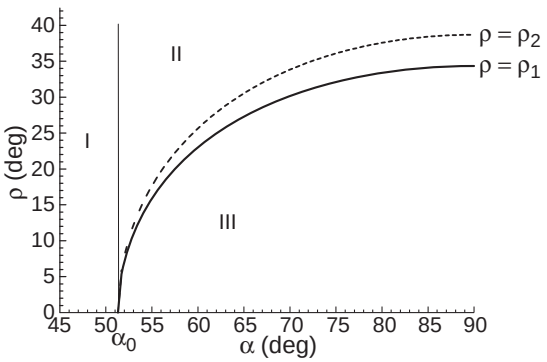

Fig. 2. Dependence of the limiting angles ρ_1 and ρ_2 on the angle of incidence of light α, where ρ_1 is the angle between the plane of incidence and the optical axis of the HMM, at which the total reflection condition for the extraordinary wave (solid curve) is satisfied, ρ_2 is the angle for which birefringence is absent inside the metamaterial layer (dashed curve). Here and below the HMM is formed on the basis of a layered periodic ITO/Ag structure with the thickness of the metal layer of 20 nm, and filling factor $f = 0.3$. The layer is sandwiched between sub-space of BK7 optical glass. $\lambda = 360$ nm.

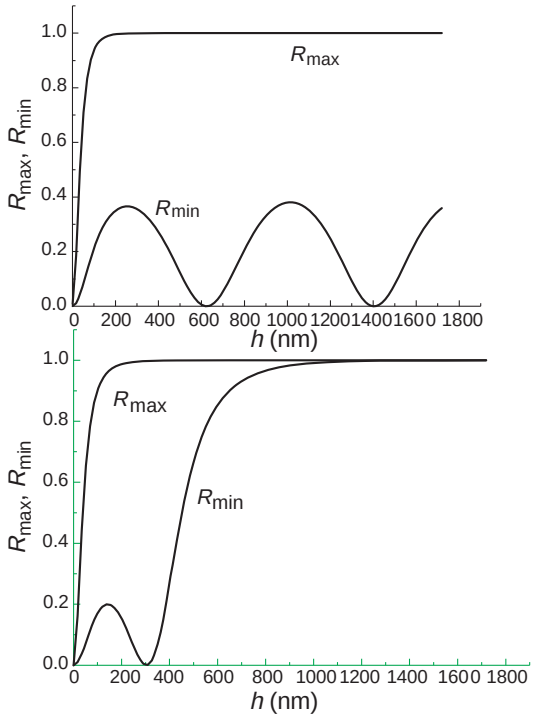

Fig. 3. Dependence of $R_{\max}$ and $R_{\min}$ for arbitrary linearly polarized light on HMM layer thickness. The metamaterial is created on the basis of ITO/Ag nanostructure. Above $\alpha = 50^\circ$, $\rho = 12^\circ$; below $\alpha = 53^\circ$, $\rho = 12^\circ$.

When both exponentially decaying forward waves or special inhomogeneous wave characterized by non-exponential amplitude decrease with the distance from the layer boundary occur in the layer, the minimum reflection coefficient $R_{\min}$ calculated for all possible values of the incident light polarization approaches zero that corresponds to full transmission of light.

The obtained results are promising for microscopy and development of new methods of testing of near-surface defects of different materials.

References

[1] *Metamaterials. Handbook. Theory and Phenomena of Metamaterials* Ed. by F. Capolino, Boca Ration, CRC Press (2009).
[2] J.B. Pendry, *Phys. Rev. Lett.* **85**, 3966 (2000).
[3] P. Shekhar, J. Atkinson, Z. Jacob, *Nano Convergence* **1**, 14 (2014).
[4] N. Petrov *et al*, *J.Optics* **19**, 125102 (2017).

28th Int. Symp. "Nanostructures: Physics and Technology"
Minsk, Belarus, September 2020

Electronic structure of molybdenum oxide oxidized at different pressures

P.A. Dementev[1], E.V. Ivanova[1], *M.N. Lapushkin*[1], D.A. Smirnov[2], and S.N. Timoshnev[3]

[1] Ioffe Institute, St Petersburg, 194021 Russia
[2] Institut fuŕ Festkörper- und Materialphysik, Technische Universität Dresden, 01062 Dresden, Germany
[3] Alferov University St Petersburg, 194021 Russia

Abstract. Electronic structure of molybdenum oxides obtained by the oxidation of molybdenum at a pressure of 1 Torr (thin film) and 1 atm (thick film) was studied. It is shown that the thickness of thin film is less than 3.5 nm. The surface states in the band gap are observed for both layers.

Introduction

Molybdenum oxides, in particular, MoO_3 are widely used in electronics, in designing various sensors and detectors, in energy storages, in electro- and photochrom systems, solar cells, catalysts in oxidation reduction reactions, etc. Molybdenum oxides are widely used as emitters at the thermal ionization of metals and organic molecules [1], and also in detectors of organic nitrogen-containing molecules operating in air at normal pressure. There are various methods of obtaining molybdenum oxide films: the evaporation of molybdenum oxides in vacuum by various methods, the liquid phase methods, including the electrochemical synthesis, and others [2]. A simple and low-cost method of preparing molybdenum oxide thin films is a heating of molybdenum in an oxygen atmosphere at various pressures.

1. Experiments

The purpose of this work was to study the electronic structure of a molybdenum oxide films obtained during heating at the temperature $T = 1000$ K and two pressures: in 1 air atmosphere and the oxygen pressure 1 Torr. Oxygen was made by thermal decomposition of K_2MnO_4. The thick oxide film obtained at $P = 1$ atm is used in a detector of organic molecules operating in air, the thin oxide film obtained at $P = 1$ Torr is used as an emitter of surface ionization of organic molecules in mass spectrometers. The obtained data will allow us to clarify the processes occurring during the surface ionization of atoms and molecules.

The photoemission studies were carried out in the Russian–Germany laboratory on the HBZ BESSY II synchrotron (Berlin, Germany) using the photoelectron spectroscopy with excitation in the photon energy range 80–600 eV. Photoelectrons were registered along a normal to the surface; the exciting beam was incident on the sample surface at an angle of 45°. The studies of the oxidized molybdenum film (MoO_3) were performed *in situ* in a vacuum of $P < 5 \cdot 10^{-10}$ Torr at room temperature. The photoelectron spectra in the region of the valence band and the O 1*s* O 2*s* and Mo 4*s* core level spectra were measured. The total energy resolution was 50 meV. The background was subtracted for all spectra presented below using the Shirley method. Before the photoemission studies, the samples were subjected to annealing in a high vacuum at a temperature of ∼900 K.

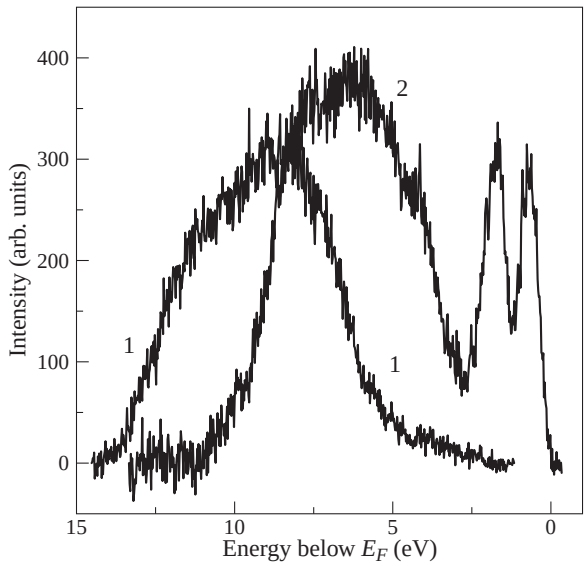

Fig. 1. Normalized photoemission spectra in the valence band region for thick (1) and thin (2) molybdenum oxide flms at excitation energies $h\nu = 600$ eV.

2. Results

Figure 1 and 2 shows the normalized photoemission spectra in the region of the valence band of molybdenum oxides obtained for diferent pressures at the excitation energies 600 and 100 eV, respectively The spectra are reduced to the Fermi level. The position of the Fermi level was determined by the position of the Fermi level of stainless steel in ohmic contact with the oxide molybdenum samples.

Figure 1 shows the valence band spectra for both films at an excitation energy of 600 eV. Photoemission spectra at the excitation energy $h\nu = 600$ eV corresponds to volume photoemission. It is known that the oxidation of molybdenum in one atmosphere leads to the formation of a thick oxide films up to several microns. For a thick film, the valence band spectrum coincides with the known spectra for molybdenum oxide [3] and has no features in the band gap region. However, the valence band maximum is 5 eV below the Fermi level, which indicates a downward band bending. At low oxidation pressure ($P = 1$ Torr), the oxide layer thickness is several nanometers. Therefore, the spectrum for a thin film correlates with the spectrum of pure molybdenum [4], so that the valence band maximum coincides with the Fermi level (E_F). The spectrum shows two distinct peaks with binding energies relative to the

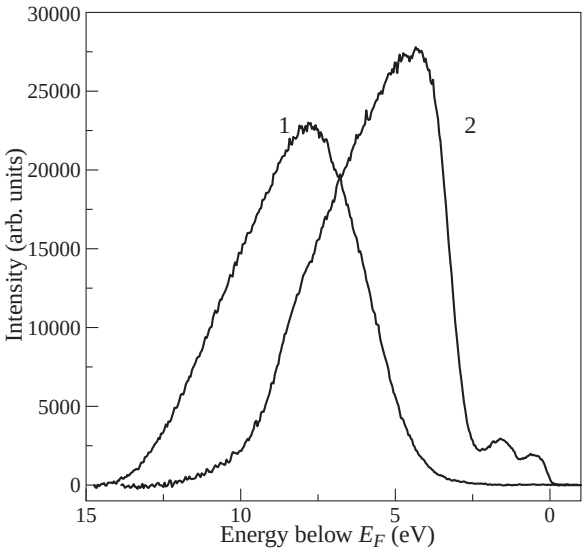

Fig. 2. Normalized photoemission spectra in the valence band region for thick (1) and thin (2) molybdenum oxide films at excitation energies $h\nu = 100$ eV.

Fermi level at 0.7 and 1.7 eV which correlates with the results of [5].

Figure 2 shows the valence band spectra for both films at an excitation energy of 100 eV. The photoemission spectrum at the excitation energy $h\nu = 100$ eV from the valence band corresponds to the surface photoemission, since the kinetic energy of photoelectrons is close to the escape minimum in the universal curve of the dependence of the photoelectron escape on the kinetic energy. The spectra of the valence band for a thick and thin oxide flms are not coincide. In comparison with the spectrum of the valence band at excitation energy $h\nu = 600$ eV for the thick and thin film the position of the of the maximum of valence band relative to the Fermi level shifts in opposite direction by 0.5 eV and -2.0 eV to low binding energy respectively. However, for a thin film in the band gap region, two states are observed with binding energies at 0.4 and 1.6 eV relative to the Fermi level, which can obviously be associated with molybdenum states. A decrease in the intensity of these peaks relative to the intensity of the maximum of valence band can be associated with a decrease in the concentration of molybdenum due to the formation of oxide on the surface and the spectral dependence of the excitation of these states. The presence of these states indicates that the surface oxide has a semiconductor nature, but it contains metallic-like surface states in the band gap. The ratio of the peak intensities of core leves O 1s and O 2s for a thin oxide layer at an excitation energy of $h\nu = 600$ eV indicates the fact that the thickness (d) of the oxide layer is less than 3 photoelectron inelastic mean free path (λ). Since the λ values for Mo and MoO_3 calculated in the TTP2M model [6] are close, then $d < 3.5$ nm. The valence band width is the same for both oxides. It should be noted that the spectra of oxygen core levels for a thick film contain a component that is associated with hydroxyl. This is due to the fact that water vapor is present in the atmosphere of the air used to oxidize molybdenum.

3. Conclusion

Thus, the electronic structure of molybdenum oxidized at various pressures has been studied. It is shown that a downward valence state band bending is observed for a thick layer of molybdenum oxide, while it is not observed for a thin layer. The photoemission measurements were used to estimate the thickness of a thin film of molybdenum oxide.

Acknowledgements

This research study has been supported by the Russian–German Laboratory at BESSY II and funded by RFBR according to the research project No. 20-02-00370.

References

[1] E.Ya. Zandberg, *Tech. Phys.*, **40,** 865 (1995).
[2] I.A. de Castro, R.S. Datta, J.Z. Ou, *et al*, *Adv. Mater.*, **29**, 1701610 (2017).
[3] Y.Zh. Wang, M. Yang, D.C. Qi, *et al*, *Tech. Phys.*, **134**, 034706 (2011).
[4] P. Mikugik, R. Nyholm and N. Mfirtensson *Czech. J. Phys. B*, **31**, 1165 (1981).
[5] P. Soukiassiant, P. Roubin, J. Cousty, *et al*, *J. Phys. C: Solid State Phys.*, **18**, 4785 (1985).
[6] S. Tanuma, C.J. Powell and D.R. Penn, *Surf. Interf. Anal.*, **21**, 165 (1994).

28th Int. Symp. "Nanostructures: Physics and Technology"
Minsk, Belarus, September 2020

Au@Ag nanorods for multiplex analysis of molecules by SERS spectroscopy

A.S. Matsukovich[1], L.L. Trotsiuk[1], O.S. Kulakovich[1], E.V. Shabunya-Klyachkovskaya[1], I.A. Mamedova[2]

[1] B.I. Stepanov Institute of Physics of NASB, 220072 Minsk, Belarus
[2] Institute of Physics, NAS of Azerbaijan, Baku AZ1143, Azerbaijan

Abstract. This work reports on surface-enhanced Raman scattering (SERS) activity of bimetallic core-shell Au@Ag nanorods. These nanostructures feature four plasmon maxima in the UV-visible range. Their application for SERS analysis enables matching individual optical properties of organic analytes by using the optimal excitation wavelength resonant both for plasmon nanostructures and analytes. It promotes higher sensitivity of surface enhanced resonance Raman scattering (SERRS) of specific analytes. The intensity of SERRS spectrum is higher up to 2 orders of magnitude for alizarin and up to 4 times for malachite green as compared to the corresponding SERS spectra. Thus, Au@Ag nanorods can be successfully used for sensitive multiplex SERRS analysis of organic molecules, i.e., a single SERS substrate can be used simultaneously for a number of molecules.

Introduction

Nowadays, there are a number of experimental studies of surface-enhanced Raman spectroscopy (SERS) analysis using Au and Ag nanorods (NRs) [1,2]. Nanorods have a great advantage over nanospheres due to the presence of a tunable in wide spectral region longitudinal plasmon resonance. Moreover, it is well known that silver is much more active in SERS than gold. However synthesis of Ag NRs is difficult because of their high reactivity and fast oxidation in water and in air. To avoid this problem we synthesized bimetallic Au NRs-core Ag-shell structures and investigated their efficiency as SERS-active substrates.Because of their Au-core, they are more stable than Ag NRs, and due to the Ag-shell, they should probably be more effective than Au NRs. It was proposed the synthesis of bimetallic systems Au@Ag (core-shell) NRs and use it as SERS-active substrates [3]. Thus, the aim of this work was to show the possibility of using Au@Ag NRs for multiplex SERS analysis including SERRS.

1. Sample preparation and characterization

Au@Ag and Au nanorods (NRs) were synthesized via the modified [4] method. Au@Ag and Au NRs sols (5×10^{-6} l) were dropped on glass substrate and dried. Aqueous solutions of malachite green (MG, $C = 0.8\times10^{-5}$ M), methylene blue (MB, $C = 0.6\times10^{-5}$ M), and ethanol solution of alizarin ($C = 7.9\times10^{-5}$ M) were deposited on Au@Ag and Au NRs layers and dried. Absorption spectra of analytes are presented in Fig. 1a. Malachite green has absorption maximum at 617 nm (green line), methylene blue — at 617 and 663 nm (blue line), and alizarin has a broad absorption band with two maxima at 497 and 528 nm (violet line). Absorption spectra of Au@Ag and Au NRs are presented in Fig. 1b. Au@Ag NRs have wide absorption maxima at 372, 403, 489 and 628 nm, that allows to simultaneously obtain SERRS for analytes with different absorption maxima. To compare the SERS efficacy of Au nanorods with and without silver shell we choose gold nanorods (Au NRs) with the same position of the long-wave plasmon band as for Au@Ag NRs (Fig. 1b).

Two Raman spectrometers were used for SERS measurements. The first one is lab-designed Raman spectrometer based on S-3801 grating spectrometer (Solar TII, Belarus) and LN-

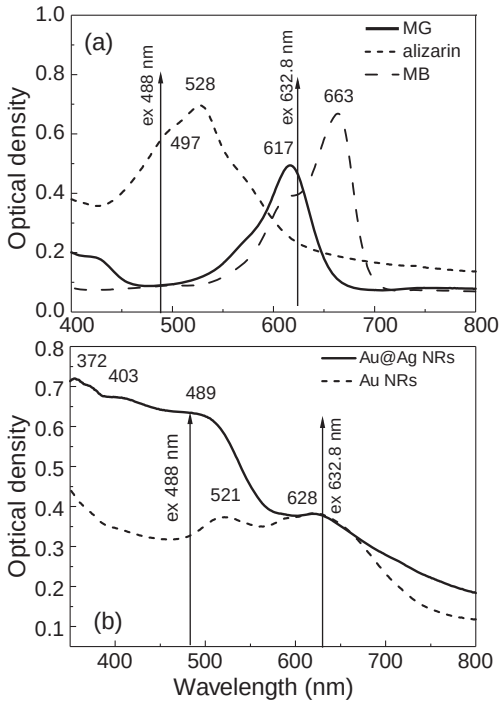

Fig. 1. Absorption spectra of (a) malachite green (MG), methylene blue (MB), alizarin; (b) Au@Ag NRs and Au NRs.

CCD-1152-E PROD FG LN-cooled silicon CCD detector (Princeton Instruments, USA) with a He-Ne (632.8 nm) excitation laser. The second one is NanoFlex (Solar LS, Belarus) Raman spectrometer equipped with the argon laser (488 nm), optical microscope "Olympus" 100x and a diffraction grating (1200 lines/mm). Exposure time was 60 s.

2. Results

The SERS and SERRS spectra of alizarin and MG are shown in Fig.2. It should be noted that Raman spectra of analytes on the glass were not registered at these concentrations. The intensity of SERRS spectrum of MG ($\lambda_{ex} = 632.8$ nm) is 4 times of magnitude higher than the intensity of SERS at $\lambda_{ex} = 488$ nm (Fig. 2a). SERRS spectrum of MG has intensive peaks at 1173, 1219, 1295, 1367, 1394, 1440, 1489, 1592 and 1616 cm^{-1}, but SERS spectrum is characterised just 2 low peaks

1592, 1616 cm^{-1}. The excitation at 488 allows obtaining SERRS of alizarin. The intensity of SERRS spectrum is up to 2 orders of magnitude higher than the intensity of SERS at $\lambda_{ex} = 632.8$ nm (Fig. 2b). In addition, SERRS spectrum has peaks at 1575 and 1595 cm^{-1} not pronounced in SERS. Our experiments show compliance with early results concerning SERS activity of other types of metal nanostructures, viz. the excitation at long-wave part of localized surface plasmon resonances (LSPR) is less effective than excitation at LSPR maximum or short-wave part of LSPR [5].

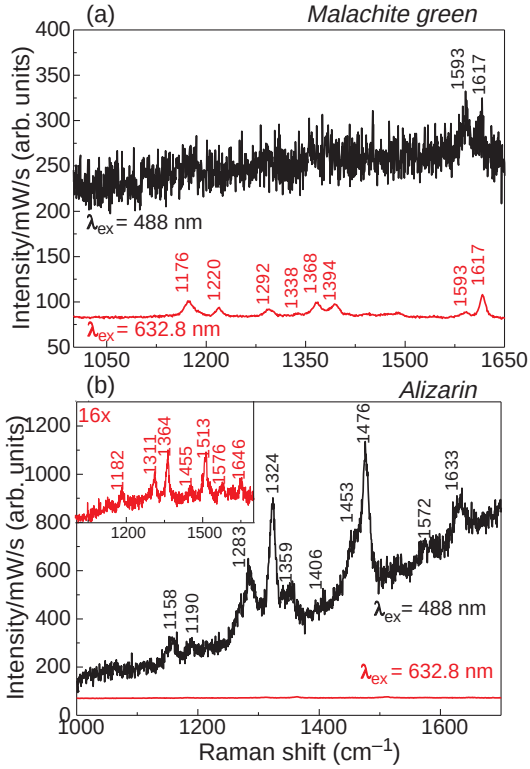

Fig. 2. SERS and SERRS spectra of (a) malachite green and (b) alizarin on Au@Ag NRs. In the case of malachite green, the resonant excitation was 632.8 nm; while for alizarin, it was 488 nm.

We compared SERRS spectra of methylene blue and alizarin obtained using Au NRs and Au@Ag NRs (Fig. 3).

The intensity of SERRS spectra of methylene blue obtained using Au NRs and Au@Ag NRs are the same (Fig. 3a). This result is explained by the same intensity of absorption for both types of plasmonic nanoparticles at the 632.8 nm (Fig. 2b). The intensity of SERRS spectrum ($\lambda_{ex} = 488$ nm) of alizarin obtained using Au@Ag NRs is up 2 times higher than the intensity of SERS spectrum (Fig. 3b) probably due to greater intensity of plasmon band at the excitation wavelength (Fig. 2b) leading to greater electromagnetic field enhancement.

Acknowledgement

This work has been supported by the Belarusian Basic Research Foundation, project No. T20R-140.

References

[1] L. Smitha *et al.*, *Nanotechnology* **22**, 265705 (2011).
[2] C.R. Rekha *et al.*, *J. of Sci.: Adv. Mat. and Dev.* **3(2)**, 196 (2018).
[3] D. Philip *et al.*, *Spectrochimica Acta Part A* **70**, 780 (2008).
[4] M. Liu *et al.*, *J. of Phys. Chem. B* **108(19)**, 5882 (2004).
[5] J. Grand *et al.*, *Phys. Rev. B* **72(3)**, 033407 (2005).

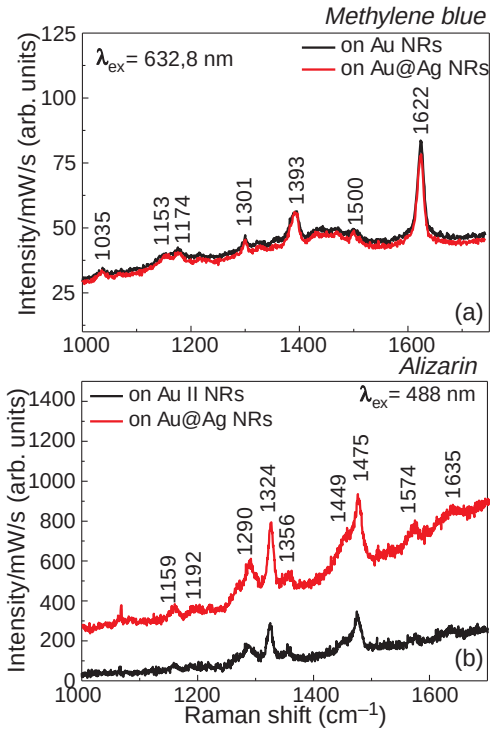

Fig. 3. SERRS spectra ($\lambda_{ex} = 632.8$ nm) of methylene blue (Fig. 3a) are characterized with peaks at 1035, 1153, 1174, 1301, 1393, 1500 and 1622 cm^{-1}.

28th Int. Symp. "Nanostructures: Physics and Technology"
Minsk, Belarus, September 2020

Optical characteristics of partially ordered planar structures from spherical nanoparticles at oblique illumination

A.A. Miskevich, N.A. Loiko and V.A. Loiko
Institute of Physics, National Academy of Sciences of Belarus, 220072 Minsk, Belarus

Abstract. The method is proposed to describe optical characteristics of a monolayer of spherical particles at oblique illumination by the plane wave with arbitrary polarization. It is based on the quasicrystalline approximation (QCA) of the theory of multiple scattering of waves, the average field approximation, and the expansion of fields and the tensor Green's function in terms of vector spherical wave functions. The method is applied to analyze the optical characteristics of monolayers of silver nanoparticles at different filling factors.

Introduction

Description of the optical properties of particulate layers with taking into account the multiple scattering of waves at oblique illumination is complex problem. It can be solved by numerical methods [1-3]. Mainly, they are used for the ensembles of inhomogeneous, anisotropic, or arbitrary shape particles. For the systems of spheres, spheroids, and cylinders the analytical and semi-analytical solutions are preferable. At present the methods based on the low-energy electron diffraction (LEED) theory and the Korringa–Kohn–Rostoker (KKR) method [4–5] are known. They are used, for example, to describe near field distribution in the photonic bands of the monolayer of periodically located spheres [4] and light absorption by the monolayer of silver nanospheres at different illumination angles [5]. These methods are suitable to simulate the structures with perfect (ideal) lattices.

To describe scattering and absorption of light in random and partially ordered layers the statistical theory of multiple scattering of waves (TMSW) is used [6]. Recently we obtained the solution of the problem to describe the incoherent part of light scattered by a particulate monolayer normally illuminated by the plane wave [7–9]. In the present work the methods, which we developed to solve the scattering problem for the normally illuminated monolayer [7–11], are generalized for the case of arbitrary angle of incidence of arbitrarily polarized wave. Our solution is based on the quasicrystalline approximation [12] of the TMSW and multipole expansion of fields and tensor Green's function in terms of vector spherical wave functions. The significant distinction from the case of normal illumination consists in existence of phase shift of averaged (effective) fields inside the different particles, which occurs at oblique illumination. It determined by the phase of plane wave incident on the particle. At the normal incidence the phases of the fields are identical for all particles, and equations derived in the present work pass to equations obtained in our previous works [7–9]. Here we apply the developed method to analyze the optical properties-of a monolayer of spherical metallic nanoparticles.

1. Main equations

Based on the QCA, the average field approximation and multipole expansion of fields and the tensor Green's function, we obtained the equations for coherent transmission T_c, reflection R_c, incoherent scattering F_{inc} coefficients of a monolayer and the angular distribution of intensity I_{inc}^{rd} of light scattered by a monolayer at arbitrary illumination angle θ_0:

$$T_c = \left|\varepsilon_\theta - \frac{8\pi\eta}{x^2\cos\theta_0}\sum_{l=1}^{\infty}\sum_{m=0}^{l}\alpha_{ml}\left[m\,\pi_l^{(m)}(\mu_0)d_{mlM}^{(o)} + \tau_l^{(m)}(\mu_0)d_{mlE}^{(e)}\right]\right|^2 +$$
$$+\left|\varepsilon_\varphi - \frac{8\pi\eta}{x^2\cos\theta_0}\sum_{l=1}^{\infty}\sum_{m=0}^{l}\alpha_{ml}\left[m\,\pi_l^{(m)}(\mu_0)d_{mlE}^{(o)} + \tau_l^{(m)}(\mu_0)d_{mlM}^{(e)}\right]\right|^2,$$

$$R_c = \left|\frac{8\pi\eta}{x^2\cos\theta_0}\sum_{l=1}^{\infty}\sum_{m=0}^{l}(-1)^{l-m}\alpha_{ml}\left[m\,\pi_l^{(m)}(\mu_0)d_{mlM}^{(o)} - \tau_l^{(m)}(\mu_0)d_{mlE}^{(e)}\right]\right|^2 +$$
$$+\left|\frac{8\pi\eta}{x^2\cos\theta_0}\sum_{l=1}^{\infty}\sum_{m=0}^{l}(-1)^{l-m}\alpha_{ml}\left[m\,\pi_l^{(m)}(\mu_0)d_{mlE}^{(o)} - \tau_l^{(m)}(\mu_0)d_{mlM}^{(e)}\right]\right|^2,$$

$$\alpha_{ml} = \frac{(2-\delta_{0m})(l-m)!}{2\pi(l+1)(l+m)!(1+\delta_{0m})}, \quad \delta_{0m} = \begin{cases}1, m=0\\ 0, m\neq 0\end{cases},$$

$$F_{inc} = \int_0^{2\pi} d\varphi \int_0^{\pi} I_{inc}^{rd}(\theta,\varphi)\sin\theta\, d\theta,$$

$$I_{inc}^{rd}(\theta,\varphi) = \frac{16\pi\eta S_2}{x^2\cos\theta_0}\left\{\left|\sum_{l=1}^{\infty}\sum_{m=0}^{l}\alpha_{ml}\left[\begin{array}{l} m\,\pi_l^m(\mu)\left(\cos(m\varphi)d_{mlM}^{(o)} + i\sin(m\varphi)d_{mlM}^{(e)}\right)+\\ +\tau_l^m(\mu)\left(\cos(m\varphi)d_{mlE}^{(e)} + i\sin(m\varphi)d_{mlE}^{(o)}\right)\end{array}\right]\right|^2 +\right.$$
$$\left.+\left|\sum_{l=1}^{\infty}\sum_{m=0}^{l}\alpha_{ml}\left[\begin{array}{l}\tau_l^m(\mu)\left(\cos(m\varphi)d_{mlM}^{(e)} + i\sin(m\varphi)d_{mlM}^{(o)}\right)+\\ +m\,\pi_l^m(\mu)\left(\cos(m\varphi)d_{mlE}^{(o)} + i\sin(m\varphi)d_{mlE}^{(e)}\right)\end{array}\right]\right|^2\right\}.$$

Here ε_θ and ε_φ are components of polarization vector $\hat{\varepsilon}_0 = \varepsilon_\theta\,\hat{\boldsymbol{\theta}}_0 + i\varepsilon\,\hat{\boldsymbol{\varphi}}_0$ of incident wave, η is monolayer filling factor (it characterizes the part of surface area occupied by particles), $\mu_0 = \cos\theta_0$, $\mu = \cos\theta$, $\pi_l^{(m)} = P_l^m/\sin\theta_0$, $\tau_l^{(m)} = dP_l^m/d\theta_0$, P_l^m are the associated Legendre functions, θ_0, φ_0 and θ, φ are polar, azimuthal angles of incidence and scattering, $d_{mlM,E}^{(o,e)}$ are expansion coefficients taking into account the multiple scattering of waves and depending in complex manner on the structure parameters of a monolayer and geometry of illumination.

2. Optical properties of monolayer of metal nanoparticles

It is well known that nanoparticles of noble metals possess plasmonic resonance in visible spectrum [5]. Spectral dependences of extinction Q_{ext}, scattering Q_{sc}, and absorption Q_{abs} efficiency factors of a single spherical silver (Ag) nanoparticle with diameter $D = 100$ nm are shown in the inset of Fig. 1. The calculations are performed using the Mie theory. The plasma resonance peaks are formed in the wavelength range from ~0.35 to ~0.45 μm. The results for a partially ordered monolayer of such particles are shown in other graphs of Fig. 1. The influence of illumination angle and polarization of incident wave on the T_c, R_c, F_{inc}, and absorption $A = 1 - T_c - R_c - F_{inc}$ coefficients is illustrated. It is seen that at high monolayer filling factor the sharp dips can occur in the T_c and R_c spectra of a monolayer.

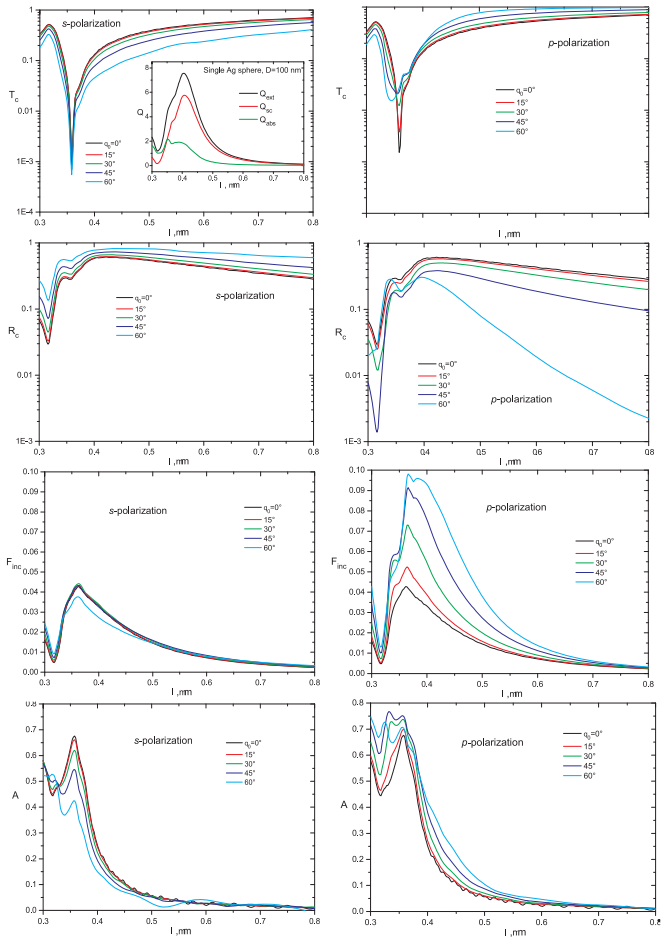

Fig. 1. Spectra of T_c, R_c, F_{inc}, and A coefficients of partially ordered monolayer of Ag particles with $D = 100$ nm illuminated by the s-polarized ($\epsilon_\theta 0 + 0i$, $\epsilon_\varphi = 0 + 1i$) and p-polarized ($\epsilon_\theta = 1 + 0i$, $\epsilon_\varphi = 0 + 0i$) plane wave at different angles of incidence ϵ_0, $\eta = 0.5$. Inset: spectral dependences of extinction Q_{ext}, scattering Q_{sc}, and absorption Q_{abs} efficiency factors of single spherical Ag nanoparticle with diameter $D = 100$ nm.

The depth and spectral position of dips depend on the angle of incidence θ_0. At that the more pronounced influence of θ_0 take place for p-polarized incident wave. In the wavelength region of Q_{abs}-peak (see λ-range of 0.33–0.4 μm in the inset) there are peaks in the spectra of absorption coefficient A of a monolayer. The θ_0-increase results in significant increase or decrease of A in this region dependently on polarization of incident wave.

In Fig. 2 we show the influence of monolayer filling factor on the absorption spectra of partially ordered monolayer of Ag particles at different polarizations (p- and s-) and angles of illumination ($\theta_0 = 30^\circ$, 60° of incident wave. It is seen that at low η the spectra strongly correlate with the Q_{abs} of individual Ag particle. With η-increasing the significant differences in the spectra occur in the region of Q_{abs} peak for different angles of incidence and polarization states of incident wave.

3. Conclusions

The method to describe optical characteristics of monolayer of spherical particles at oblique illumination by the plane wave with arbitrary polarization is proposed. It is shown the influence of the polarization state of incident wave, angle of illumination, and monolayer filling factor on the optical properties of partially ordered monolayers of silver nanoparticles. The results can be used to develop the thin-film solar cells, detectors, light emitting diodes and other optical and electro-optical devices based on the particulate layers.

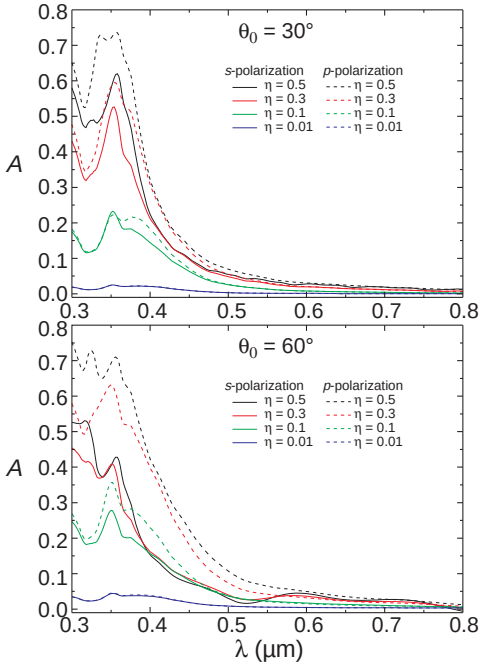

Fig. 2. Spectra of A coefficient of partially ordered monolayer of Ag particles with $D = 100$ nm illuminated by the s- and p-polarized plane wave at different angles of incidence θ_0 and filling factors η.

Acknowledgement

This work was supported by the Belarusian Republican Foundation for Fundamental Research, project F20KI-004.

References

[1] J.B. Pendry, A. MacKinnon, *Phys. Rev. Lett.* **69**, 2772 (1992).
[2] B.T. Draine, *Astrophys. J.* **333**, 848 (1988).
[3] A. Andueza *et al*, *J. App. Phys.* **111**, 104902 (2012).
[4] H. Miyazaki, K. Ohtaka, *Phys. Rev. B* **58**, 6920 (1998).
[5] N. Stefanou, A. Modinos, *J. Phys: Condens. Matter*. **3**, 8135, and 8149 (1991).
[6] V.A. Loiko, A.A. Miskevich, *Multiple Scattering of Light in Ordered Particulate Media*", chapter in book: *Multiple Light Scattering, Radiative Transfer and Remote Sensing*, ed. by A.A. Kokhanovsky (Springer) p. 101–230, 2018.
[7] N.A. Loiko *et al. JOSA A* **35**, 108 (2018).
[8] N.A. Loiko *et al. JETP* **126**, 159 (2018).
[9] N.A. Loiko *et al. Opt. spectrosc.* **125**, 655 (2018).
[10] A.A. Miskevich, V.A. Loiko, *JETP* **113**, 1 (2011).
[11] A.A. Miskevich, V.A. Loiko, *JQSRT* **112**, 1082 (2011).
[12] M. Lax, *Phys. Rev.* **85**, 621 (1952).

28th Int. Symp. "Nanostructures: Physics and Technology"
Minsk, Belarus, September 2020

Spatial and hyperfine characteristics of SiV^- and SiV^0 color centers in diamond: DFT simulation

A.P. Nizovtsev[1,2], S.Ya. Kilin[1], A.L. Pushkarchuk[3,4], S.A. Kuten[4], N.A. Poklonski[5], D. Michels[6], D. Lyakhov[6] and F. Jelezko[7]

[1] Institute of Physics, Nat. Acad. Sci. of Belarus, 220072 Minsk, Belarus
[2] National Research Nuclear University "MEPhY", 115409 Moscow, Russia
[3] Institute of Physical-Organic Chemistry, Nat. Acad. Sci. of Belarus, 220072 Minsk, Belarus
[4] Institute for Nuclear Problems, Belarusian State University, 220006 Minsk, Belarus
[5] Physics Department, Belarusian State University, 220030 Minsk, Belarus
[6] Computer, Electrical and Mathematical Science and Engineering Division, 4700 King Abdullah University of Science and Technology, Thuwal 23955-6900, Saudi Arabia
[7] Institute for Quantum Optics, Ulm University, 89069 Ulm, Germany

Abstract. One of the most promising platforms to implement quantum technologies are coupled electron-nuclear spins in diamond in which the electrons of paramagnetic color centers play a role of "fast" qubits, while nuclear spins of nearby ^{13}C atoms can store quantum information for a very long time. Essential prerequisite for a high-fidelity spin manipulation in these systems is a complete knowledge of hyperfine interactions. Here we are resenting recent results of computer simulation of spatial, electronic and hyperfine characteristics of the negatively charged "silicon-vacancy" (SiV^-) and neutral (SiV^0) color centers in H-terminated cluster $C_{128}[SiV]H_{98}$ along with their comparison with available experimental data.

Introduction

Single negatively charged and neutral silicon-vacancy (SiV^- and SiV^0) color centers in diamond exhibiting narrow zero-phonon lines at $\sim$ 738 and $\sim$ 947 nm with high Debye–Waller factor ($\sim$ 0.7) and having doublet ($S = 1/24$) and triplet ($S = 1$) ground electronic states are currently of great interest because they allow for effective optical interfacing their spin state to photons (see, e.g. [1]). By analogy with the well-known nitrogen-vacancy (NV) color center the nuclear spins ^{29}Si belonging to the SiV centers as well as nearby ^{13}C nuclear spins in a hosting diamond lattice can be used in numerous applications as additional resource for quantum memory. Recent experiments [2–4] done at low temperatures ($\sim$ 4 K) demonstrated simultaneous microwave control and optical readout of the SiV^- center spin, a key prerequisite for further quantum information processing tasks. However, at these temperatures the SiV^-center exhibits very short spin coherence time of 38 ns [2]. Therefore, further progress with SiV^- centers was expected at temperatures reduced to mK [5], which will provide a significant (up to 10 ms) increase in the coherence time of the electron spin of single SiV^- centers. Very recently the quantum register [6,7] and quantum repeater [8] were demonstrated for a first time using *hfi*-coupled electron-nuclear spin systems $SiV^- - ^{13}C$ at mK temperatures. In turn, the neutral color SiV^0 center [9] has much longer spin coherence time [10] at liquid-helium temperatures but can be optically bright and stable only in special boron-doped diamond samples. The SiV^0 center is associated with the KUL1 electron paramagnetic resonance center [9,11] with zero-field splitting $D = 942$ MHz. Hyperfine interaction data for the center are known only for ^{29}Si and ^{13}C atoms being nearest to Si [12]. Essential point for high-fidelity spin manipulation in the above systems with tailored control pulse sequences is a complete knowledge of hyperfine interactions (*hfi*) in them. It is the aim of this report to present our recent results concerning simulation of *hfi* characteristics for different hybrid electron-nuclear spin systems SiV-^{13}C in diamond and their comparison with available experimental data [4].

Methods and basic results

Here we are presenting the analysis of hyperfine interactions (*hfi*) of the SiV^0 and SiV^- centers with the ^{13}C nuclear spins differently located in the diamond lattice with respect to the electronic spins of these centers. The center properties were studied by simulating (using ORCA software package) the H-terminated carbon cluster $C_{128}[SiV]H_{98}$ hosting the SiV center in their central parts. Calculations were performed for neutral and negatively charged clusters having the triplet and doublet ground states, respectively. The structures were optimized carefully using DFT theory of DFT/UKS/PW91/RI/def2-SVP level. Then, using different levels of the theory (UKS/PW91/RI/def2-SVP, UKS/B3LYP/G/3-21G, ROKS/PW91/RI/def2-SVP), we found the total spin density distribution over the clusters and calculated the matrices AKL (K,L=X,Y,Z) describing *hfi* of the electronic spin of the SiV centers with the nuclear spins I=1/2 of ^{13}C atoms located in all possible positions within the clusters as well as for the nuclear spin I=1/2 of isotopic ^{29}Si nucleus of the center.

For the neutral cluster (i.e. the cluster containing the SiV^0 center) relaxed geometry exhibited usual D_{3d} symmetry where the Si atom located in the interstitial position between two lattice vacancies is the center of inversion. There are six equivalent nearest-neighbor (NN) carbon atoms at near-equal distances of $\sim$2.025 Å from Si atom. Spin density was localized near-equally at these 6 carbon atoms (see Fig. 1a). *Hfi* matrices A_{KL}, calculated in the coordinate system with the Z axis directed along the (111) crystallographic direction of the diamond lattice, were nearly coinciding for couples of ^{13}C nuclear spins inversion-symmetrically located with respect to the Si atom. In turn, the matrices A_{KL} calculated for the three such equivalent pairs of NN ^{13}C were interconnected by 120° rotation matrices about the Z axis. We found [13] at UKS/B3LYP/G/3-21G theory level the values $A_{\|} \approx 7.5$ MHz

and $A_\perp \approx 44.5$ MHz for these six C atoms (experimental values are $A_\parallel \approx 66.2$ MHz and $A_\perp \approx 30.2$ MHz [12]). For the ^{29}Si nucleus we got $A_\parallel \approx A_\perp = 81$ MHz (experimental values are 76.3 and 78.9 MHz, respectively [12]). We also calculated the *hfi* matrices A_{KL} for all other possible systems SiV^0–^{13}C in the cluster $C_{128}[SiV^0]H_{98}$.

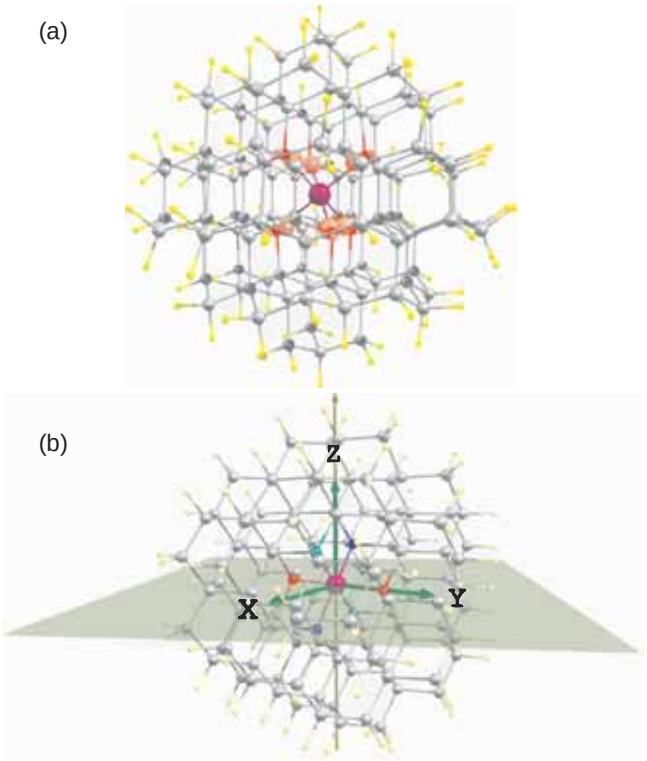

Fig. 1. Illustrations of the simulated clusters $C_{128}[SiV^0]H_{98}$ (a) and $C_{128}[SiV^-]H_{98}$ (b) with the spin density distributions shown. Si atom is shown in violet, passivating H atoms — in yellow, and closer C atoms in the Fig. 1b are shown in red and blue. Additionally, the $C_2^{(Z)}$ symmetry axis and the $\sigma_h^{(XY)}$ symmetry plane (C_{2h} symmetry elements) are shown in the Fig. 1b.

For the negatively charged clusters (SiV^- centers) inversion symmetry with respect to the Si atom also took place but nearest six C neighbors were no longer equivalent with two of them (shown in red in the Fig. 1b) being located at ∼0.03 Å further from Si atom then the other four (shown in blue in the Fig. 1b), for which the C-Si distance was ∼2.00 Å. Resulting C_{2h} symmetry of the cluster was different from usually considered D_{3d} symmetry which took into account the dynamical Jahn–Teller effect being essential for the center even at liquid-helium temperatures (∼4 K) but which can reduce to the static Jahn-Teller effect at mK temperatures. The $\sigma_h^{(XY)}$ symmetry plane was passing through the two more distant C neighbors of silicon and through the (111) diamond crystallographic direction and the $C_2^{(Z)}$ symmetry axis was perpendicular to the $\sigma_h^{(XY)}$ plane (see Fig. 1b). Spin density in this case was localized basically on the two more distant nearest C atoms resulting in $A_\parallel = 175$ MHz and $A_\perp = 105$ MHz, while for the other two NN ^{13}C pairs, located a little closer to the Si atom the spin density was essentially lower and respective *hfi* data were $A_\parallel = 37$ MHz, $A_\perp$=21 MHz. For the ^{29}Si nucleus we got $A_\parallel \approx 66$ MHz and $A_\perp \approx 78$ MHz. We also got the full *hfi* matrices for all other possible coupled SiV^-–^{13}C spin systems in the $C_{128}[SiV^-]H_{98}$ cluster and were able to identify the position (with respect to the SiV^- center) of the ^{13}C nuclear spin which was experimentally studied in [4].

Acknowledgements

This work has been supported in part by BRFFI, grants ΦMC-036 and by MEPhY.

References

[1] J.N. Becker, C. Becher, *Phys. Status Solidi A.* **214**, 170058 (2017).
[2] L.J. Rogers *et al*, *Phys. Rev. Lett.*, **113**, 263602 (2014).
[3] B. Pingault *et al*, *Nat. Communs.*, **8**, 15579 (2107).
[4] M.H. Metsch *et al*, *Phys. Rev. Lett.*, **122**, 190503 (2019).
[5] D.D. Sukachev *et al*, *Phys. Rev. Lett.*, **119**, 223602 (2017).
[6] S.T. Nguyen *et al*, *Phys. Rev. Lett.*, **123**, 183602 (2019).
[7] S.T. Nguyen *et al*, *Phys. Rev. B.*, **100**, 165428 (2019).
[8] M.K. Bhaskar *et al*, *Nature*, **580**, 60 (2020)
[9] U.F.S. D'Haenens-Johansson *et al*, *Phys. Rev. B* **84**, 245208 (2011)
[10] B.C. Rose *et al*, *Science*, **361**, 60 (2018)
[11] A. Gali, J. Maze, *Phys. Rev. B.*, **88**, 235205 (2008)
[12] A.M. Edmonds *et al*, *Phys. Rev. B.*, **77**, 245205 (2008)
[13] A.L. Pushkarchuk *et al*, *Int. J. of Nanoscience*, **18**, 1940010 (2019)

28th Int. Symp. "Nanostructures: Physics and Technology"
Minsk, Belarus, September 2020

Hyperfine characteristics of quantum registers NV-^{13}C in diamond nanocrystals formed by seeding approach from isotopic aza-adamantane and methyl-aza-adamanthane

A.P. Nizovtsev[1,2], S.Ya. Kilin[1], A.L. Pushkarchuk[3,4], S.A. Kuten[4], A.S. Gusev[2] and F. Jelezko[5]

[1] Institute of Physics, Nat. Acad. Sci. of Belarus, 220072 Minsk, Belarus
[2] National Research Nuclear University "MEPhY", 115409, Moscow, Russia
[3] Institute of Physical-Organic Chemistry, Nat. Acad. Sci. of Belarus, 220072 Minsk, Belarus
[4] Institute for Nuclear Problems, Belarusian State University, 220006 Minsk, Belarus
[5] Institute for Quantum Optics, Ulm University, 89069 Ulm, Germany

Abstract. We predict the characteristics of hyperfine interactions (*hfi*) for a number of electron-nuclear spin systems NV-^{13}C in diamonds grown by seeding approach from the specific isotopic aza-adamantane or methyl-aza-adamantane molecules differing in ^{13}C position in the precursor as well as in the orientation of the NV center in the post-obtained diamond. For the purpose we have used the spatial and *hfi* data simulated previously for the cluster $C_{510}[NV]^{-}H_{252}$. The data obtained can be used to identify (and correlate with the precursor used) the specific NV-^{13}C spin system by measuring the *hfi*-induced splitting in optically detected magnetic resonance spectra being characteristic for the NV-^{13}C system.

Introduction

Nanostructured diamonds hosting optically active paramagnetic color centers (NV, SiV, GeV etc.) and hyperfine-coupled with them quantum memory ^{13}C nuclear spins situated in some sites of a diamond lattice are currently of great interest to implement emerging second-generation quantum technologies (quantum information processing, quantum sensing and metrology). Current methods (high pressure high temperature (HPHT), chemical vapor deposition (CVD), fast ion beam implantation with subsequent annealing etc.) of creation such electronic-nuclear spin systems are inherently probabilistic with respect to mutual location of the color center electronic spin and the ^{13}C nuclear spins.

Recently new bottom-up approach to fabricate such systems was suggested (see, e.g. [1–4]) based on the idea to synthesize first chemically appropriate diamond-like organic molecules containing desired constituents in definite positions and then use them as precursors/seeds for CVD or HPHT growth to produce macroscopic diamonds. In particular, diamonds incorporating coupled NV-^{13}C spin systems (quantum registers) with definite mutual arrangements of NV and ^{13}C can thus be obtained from isotopically substituted aza-adamantane or methyl-aza-adamantane. Very recently first successful experiments [5–7] have been done to implement this idea and macroscopic diamonds were grown from series of lower diamondoids using laser-heated diamond anvil cell.

Basic results

Here we are presenting the simulated data which can be used to correlate the finally obtained NV-^{13}C spin system with the precursor used. For the purpose one can measure the hyperfine-induced splitting of the $m_S = \pm 1$ sublevels ($S = 1$ is the NV ground-state electronic spin) of the NV-^{13}C system using optically detected magnetic resonance (ODMR). As is well-known (see, e.g. [8]) this splitting is characteristic for NV-^{13}C systems having different location of the ^{13}C nuclear spin with respect to the NV center. Therefore, here we are predicting the characteristics of hyperfine interactions (*hfi*) for a number of NV-^{13}C systems in the diamonds grown from specific isotopic aza-adamantane (Fig. 1a,b) and methyl-aza-adamantane (Fig. 1c,d) molecules differing in ^{13}C position in the precursor as well as in the orientation of the NV center in the post-obtained diamond.

For the purpose we have used the spatial and *hfi* data simulated previously in our work [9] for the H-terminated cluster $C_{510}[NV]$-H_{252} were we got full *hfi* matrices for all possible positions $j = 1$–510 of the ^{13}C atom in the cluster hosting specifically oriented NV center in its central part (Fig. 2). Rotating this cluster so as to obtain the desired configuration of one of the considered isotopic precursors (from which this cluster can be grown), we were able to identify the ^{13}C nuclear spins in this precursor. Then using the table in the supplement to the article [9], we found the *hfi* characteristics for the NV-^{13}C system obtained from the specific precursor as a result of diamond growth and creation a vacancy in one of the lattice site near the existing nitrogen atom. The results obtained clearly demonstrate essentially different *hfi* characteristics (and, respectively, different *hfi*-induced splitting of the zero-field ODMR lines) for different NV-^{13}C systems thus providing the way to iden-

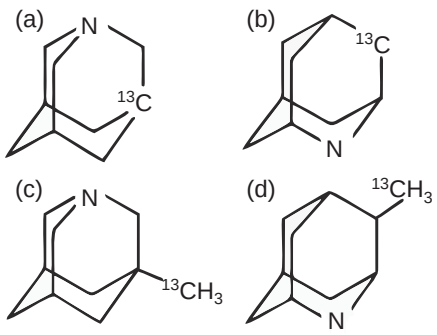

Fig. 1. Examples of a) 1-aza-adamantane (N is in the tertiary position) and b) 2-aza-adamantane (N is in the secondary position) with isotopic ^{13}C atom in one possible position in adamantane molecule and c),d) respective methyl-aza-adamantanes having ^{13}C atom in the methyl group.

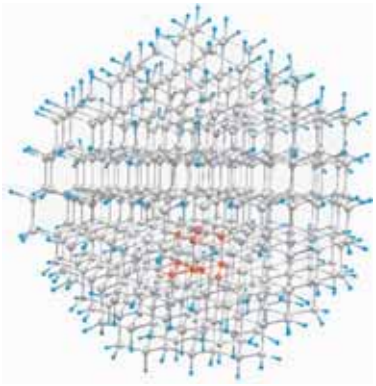

Fig. 2. Illustration of one possible arrangement of NV center in the cluster $C_{510}[NV]H_{252}$ obtained from the seeding adamantine molecule (highlighted in red with N atom shown by violet).

tify precursor and to determine position of the vacancy with respect to the N atom in the precursor.

Acknowledgements

This work has been supported in part by BRFFI, grants]LB No. ΦMC-036, the Belarus state program of scientific investigations “Convergence-2020”, as well as by MEPhY.

References

[1] W.A. Clay *et al*, *Rep. Prog. Phys.* **78**, 016501 (2014).
[2] T. Zapata *et al*, *arXiv:* 1702.06854.
[3] M.H. Alkahtani *et al*, *Nanophotonics* **7**, 1423 (2018).
[4] E.A. Ekimov *et al*, *Chem Nano Mat.* **4**, 269 (2017).
[5] T. Zapata *et al*, *Advanced Materials: TechConnect Briefs* TechConnect.org, p.72 (1995).
[6] E.A. Ekimov *et al*, *Inorganic Materials* **55**, 437 (2019).
[7] S. Park *et al*, *Sci. Adv.* **6**, eaay9405 (2020).
[8] A.P. Nizovtsev *et al*, *New. J. Phys.* **16**, 083014 (2014).
[9] A.P. Nizovtsev *et al*, *New J. Phys.* **20**, 023022 (2018).

28th Int. Symp. "Nanostructures: Physics and Technology"
Minsk, Belarus, September 2020

The motion of a magnetic vortex in the field of magnetic inhomogeneity

V.A. Orlov[1,2], G.S. Patrin[1,2] and I.N. Orlova[3]

[1] Siberian Federal University, 660041 Krasnoyarsk, Russia
[2] L.V. Kirenskiy Institute of Physics, Federal Research Center, Regional Scientific Center of Siberian Branch of the RAS, 660036 Krasnoyarsk, Russia
[3] Krasnoyarsk State Pedagogical University named after V.P. Astafyev, 660049 Krasnoyarsk, Russia

Abstract. The problem of the motion of a magnetic vortex near a defect in the form of a crystallite with uniaxial anisotropy is theoretically solved. Variants of bidirectional and unidirectional defect anisotropy are considered. The possibilities of capture and reflection of a vortex core from a defect are investigated. The existence of two modes of motion of the core with different frequencies.

The keen interest in vortex-type magnets is due to the prospects of their application in various spintronic devices. The magnetic state of the vortex (skyrmion) is given by the parameters: polarity of the core p and chirality q. The core of the vortex is its central region of rather small size $r_0 \sim 10$ nm.

In this work, we carry out a theoretical analysis of the effect on the behavior of a magnetic vortex of a defect in the form of an embedded crystallite with magnetic anisotropy different from the main matrix. Let us consider a model of a thin film in which there is interspersed in the form of a crystallite of small volume V. The parameters of the crystalline magnetic anisotropy are characterized by the constant K and the unit vector of the local anisotropy axis $\mathbf{l}$. In a cylindrical system, the position of the center of the vortex is determined by the length of the radius vector ρ and the azimuthal angle φ. The evolution of magnetization is reduced to solving the equation for the quasiparticle [1]:

$$\mathbf{G} \times \mathbf{v} + \vec{D}\mathbf{v} + \nabla W = 0. \qquad (1)$$

Here $\mathbf{G} = 2\pi \mathbf{e}_z pq M_S b/\gamma_g$ is the gyrovector [2,3], M_S is the saturation magnetization, b is the thickness of the magnetic film, γ_g is the gyromagnetic ratio, $\mathbf{e}_z$ is the unit vector of the z axis, $\mathbf{v}$ is the core velocity, W is the potential energy of the magnetic vortex, which contains crystalline magnetic anisotropy energy, $\hat{D}$ is the tensor of effective friction force coefficients, for the core as a quasiparticle in the presence of attenuation [4,5]. The vector equation (1) can be converted to:

$$\begin{aligned} \frac{d\rho}{dt} &= \frac{-1}{G^2+D^2}\left(D(\nabla W)_\rho + G(\nabla W)_\varphi\right), \\ \rho\frac{d\varphi}{dt} &= \frac{1}{G^2+D^2}\left(G(\nabla W)_\rho - D(\nabla W)_\varphi\right). \end{aligned} \qquad (2)$$

We write the magnetic energy as follows: $W = \frac{\kappa\rho^2}{2} - KV\,(\mathrm{ml})^2$ Here, the second term is the magnetic anisotropy energy the first term is the quasielastic energy with a stiffness coefficient κ, which ensures the existence of a force with axial symmetry acting on the vortex core towards the origin. Solving the system of equations (2) in general is difficult. The following are some special cases.

First of all, we considered the case when the axis of the anisotropy of the defect is oriented perpendicular to the surface of the magnet. The characteristic dependences of $\rho(t)$ and $\varphi(t)$ are shown in the Fig. 1. From the figures it follows that at $\rho \approx r_0$ the functional dependence of the azimuthal angle and the radius vector. A numerical solution of the equation (1) confirms this result. Estimating the distance from the kernel to the defect at which the mode changes gives: $\rho_c \approx r_0\sqrt{\ln(\sqrt{\Lambda})}$.

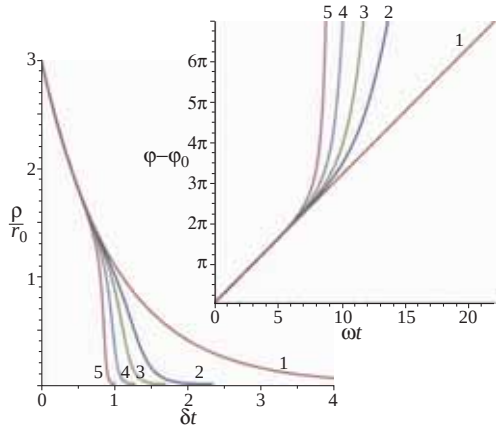

Fig. 1. A graphical representation of the solutions $\rho(t)$ and $\varrho(t)$. The curve numbers correspond to different values of the parameter $\Lambda = 4KV/(\kappa r_0^2)$: $\Lambda_1 = 0$, $\Lambda_2 = 5$, $\Lambda_3 = 10$, $\Lambda_4 = 20$, $\Lambda_5 = 40$. All curves are plotted for the initial dimensionless length of the radius vector: $\rho_0/r_0 = 3$ and for $\eta = 0.1$.

It is of interest to study the nature of the motion of a magnetic vortex in the presence of a defect with unidirectional anisotropy. In particular, such an option is possible when an antiferromagnetic inclusion is introduced into the ferromagnetic matrix. It is important to note here that, unlike a defect with bidirectional anisotropy in the present case, the right-hand sides in the equations of the system (2) have the ability to vanish and even change sign. This is possible with the opposite orientation of the axis of unidirectional c rystalline anisotropy and the vortex core polarity. The solution to this system is shown in the Fig. 2. In the presence of a defect with the axis of unidirectional anisotropy perpendicular to the film surface, the capture of a core by a defect can be realized so that the center of the core appears at a certain distance from the crystallite, but not at the defect itself, as in the case of bidirectional anisotropy.

The following is a scenario of the motion of a magnetic vortex in a defect field, whose anisotropy axis lies in the plane of the magnet. In this case, the potential is not cen trally sym-

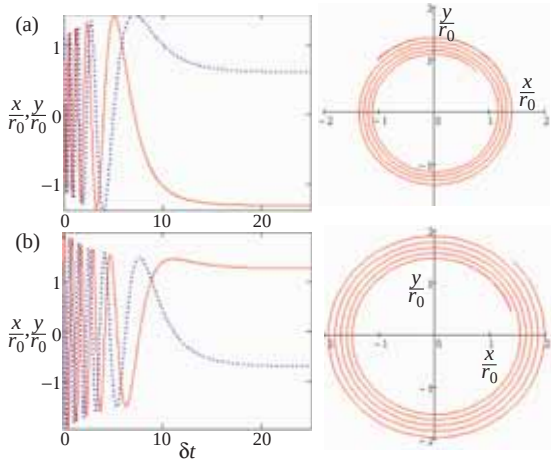

Fig. 2. Time dependence of the Cartesian coordinates of the vortex core in the model of unidirectional crystallite anisotropy. The solid line is the dependence $x(t)$, the dotted line is $y(t)$. The graphs are plotted for the case: $\Lambda = 1$, $p = -1$, $\eta = 0.01$. (a) is constructed for $\rho_0/r_0 = 1.1$, (b) for $\rho_0/r_0 = 2$.

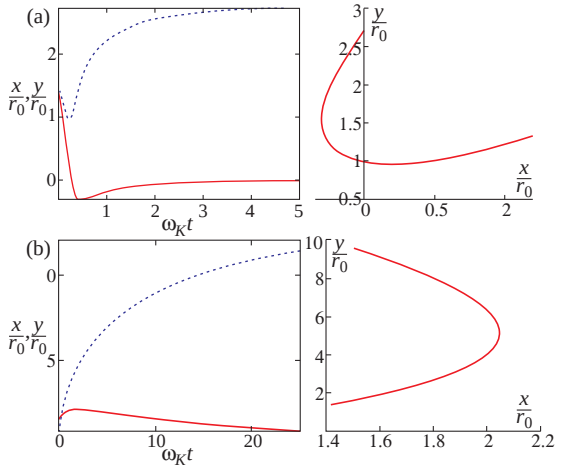

Fig. 3. The characteristic form of the trajectories for the case $\rho_0/r_0 = 2$, $\varphi_0 = \pi/4$, $\kappa = 0$ according to the results numerical solution of the system of equations (1). The axis of anisotropy of the crystallite lies in the plane of the film. Figure a) is built for $G < 0$, figure (b) is for $G > 0$. The solid line shows the dependence $x(t)$, and the dashed curve shows the dependence $y(t)$.

metric and depends on the azimuthal angle of the core of the vortex φ. In the absence of a centrally symmetric term and damping ($\kappa = 0$, $D = 0$) in the total energy, the trajectory equation is the function: $m_z(\rho) = 1-\left(1 - m_z^2(\rho_0)\right)\left(\frac{\sin(\varphi_0)}{\sin(\varphi)}\right)^2$. This state corresponds to the maximum distance of the core from the crystallite ($\rho \to \infty$), i.e. the vortex is repelled by a defect. The direction of motion of the vortex core is determined — the azimuthal angle φ_∞. As a result, we have: $\sin(\varphi_\infty) = \pm\sin(\varphi_0)\sqrt{1 - m_z^2(\rho_0)}$ At a sufficient distance from the crystallite $m_z(\rho) \ll 1$ the azimuthal angle does not change and the vortex moves pro gressively in the direction from the crystallite like a particle repelling from a defect. Despite the absence of axial symmetry in the field created by the defect, the motion of the core occurs along the radius vector. Obviously, this phenomenon is a consequence of the complex influence of the asymmetric potential and the gyrotropic effect associated with the precession of magnetization during the movement of the vortex. The dependence $\rho(t)$ is described by the function: $\rho(t) = \left[\rho_0^2 + \frac{2}{G}KV\sin(2\varphi_\infty)t\right]^{1/2}$. The dependence the distance from the center of the vortex to the repulsive center according to the law $\rho^2 \sim t$ means that at a sufficiently large distance the core, as a quasiparticle, is in the effective defect potential, changing according to the law $W_{\text{eff}} \sim 1/\rho^2$.

In the presence of attenuation, the trajectories of the motion of the vortex core are shown in the Fig. 3. Note that the attenuation leads to a fast orientation of the radius vector of the core in the direction perpendicular to the local axis of the crystalline anisotropy axis.

To summarize, the following can be noted. In the case when the axis of magnetic anisotropy of the defect crystallite does not lie in the plane of the magnet, the vortex is "captured" by the defect field. If the defect has bidirectional anisotropy the core of the vortex, as a quasiparticle, seeks to settle directly on the defect. Moreover, if the potential in which the core moves is created not only by the defect field, but also by a field with axial symmetry of a diffwrent nature, an interesting clearly pronounced effect of a change in the vortex motion modes with a difference in the frequency of rotation of the core around the crystallite is observed. This circumstance can be extremely important in the design of control devices for the motion of magnetic vortices and skyrmions. If a crystallite defect possesses unidirectional magnetic anisotropy, the vortex core can undergo both attraction and repulsion depending on the mutual direction of the crystalline anisotropy axis and the vortex polarity.

In the case when the crystallite axis lies in the plane of the magnet, the core of the vortex is reflected from the defect. In the presence of noticeable attenuation, the trajectory of the core is curved, and the equilibrium position corresponds to the direction of the radius vector perpendicular to the direction of the axis of anisotropy of the crystallite.

Acknowledgement

The reported study was funded by RFBR, project No. 18-02-00161.

References

[1] A. Thiele, *Phys. Rev. Lett.*, **30**, 230 (1973).
[2] J. Kim, S.-B. Choe, *J. Magn.*, **12(3)**, 113 (2007).
[3] K.Yu. Guslienko, B.A. Ivanov, V. Novosad, *et al*, *J. of Appl. Phys.*, **91**, 8037 (2002).
[4] P.D. Kim, V.A. Orlov, V.S.Prokopenko, *et al*, *Physics of the Solid State*, **57**, 30 (2015).
[5] [5] D. Reitz, A. Ghosh, O. Tchernyshyov, *Phys. Rev. B*, **97**, 054424 (2018).

28th Int. Symp. "Nanostructures: Physics and Technology"
Minsk, Belarus, September 2020

Photoluminescence of extended defects in metamorphic heterostructures with InAlAs/InGaAs/InAlAs quantum well at different excitation wavelengths

S.S. Pushkarev, G.B. Galiev, E.A. Klimov, V.B. Kopylov
V.G. Mokerov Institute of Ultra High Frequency Semiconductor Electronics of RAS, 117105 Moscow, Russia

Abstract. The photoluminescence (PL) of energy levels within the bandgap associated with extended defects in metamorphic buffer $In_xAl_{1-x}As$ ($x = 0.05 \rightarrow 0.65$) is observed. While the interband photoexcitation wavelength increases ($409 \rightarrow 450 \rightarrow 532$ nm), the ratio of luminescence intensities for defect levels and quantum well $In_{0.65}Al_{0.35}As/In_{0.65}Ga_{0.35}As/In_{0.65}Al_{0.35}As$ increases, since radiation with a longer wavelength penetrates deeper into the heterostructure and generates a greater photocarrier concentration on the defect levels. Subband infrared excitation with 1064 nm wavelength (with photons energy less than bandgap of metamorphic buffer) also results in appearance of "defect" PL. The using of infrared excitation with the same power density instead of visible one leads to an increasing of "defect" PL in samples with high density of twins by an order of magnitude, whereas in more perfect samples with stacking faults and threading dislocations it causes an increasing of "defect-to-QW" PL intensities ratio. The study of PL intensity as a function of the pump power in the range of power density 10–4000 W/cm^2 reveals that the non-radiative recombination plays an important role during the recombination of photoexcited charge carriers from "defect" levels because the "defect" PL intensity dependence on the pump power density is mainly sublinear while for the QW PL the power law with exponent 1.2–1.4 is observed.

To reveal the role of defects in the photoluminescence of semiconductor MHEMT heterostructures the defective samples with an $In_{0.65}Al_{0.35}As/In_{0.65}Ga_{0.35}$ quantum well (QW) and an $In_xAl_{1-x}As$ metamorphic buffer ($x = 0.05 \rightarrow 0.65$) on GaAs substrates (100) were studied. The heterostructures were grown by the molecular-beam epitaxy and contain extended defects of various types and densities, as was earlier ascertained using transmission electron microscopy [1–3]. Furthermore, defects of a certain type dominate in each of the heterostructures (Table 1). The different defectiveness of these heterostructures is resulting from the different design of the metamorphic buffer (while the design of the active region is kept), as well as different technological growth conditions. Hereinafter the studied samples are designated as "low defective" (A), "medium defective" (B), and "highly defective" (C). The mobility of conduction electrons measured using the Hall effect by the van der Pauw method and shown in Table 1 confirms the different degree of the samples defectiveness.

Table 1. Characteristics of defects and electrophysical parameters measured at room temperature for the samples under investigation.

Sample	Threading dislocations (cm^{-2})	Stacking faults (cm^{-2})	Twins (cm^{-2})	μ (cm^2/(V·s))	n_S (cm^{-2})
A	$5{\cdot}10^5$	0	0	11600	1.53
B	$5{\cdot}10^7$	$2{\cdot}10^7$	0	8700	1.84
C	probably masked	probably masked	~10^8	300	0.98

The studies were carried out on a PL spectroscopy unit, which includes: the solid-state lasers with a wavelength (intensity) of 409 nm (100 mW), 450 nm (100 mW), 532 nm (300 mW), 1064 nm (600 mW); optic cryostat cooled by liquid nitrogen; uncooled InGaAs pin-photodiode with a sensitivity range of 1.0–2.0 μm (0.6–1.2 eV) and a photoelectron multiplier FEU-62 cooled by liquid nitrogen with a sensitivity range of 0.4–1.0 μm (1.2–3.1 eV). The laser radiation was focused in sample surface with the spot size of about 150 μm, it's power varied using a set of neutral filters from 0.3 to 100% (power density varied from 10 to 3600 W/cm^2).

The PL spectra of samples exhibit the radiation from the QW with photon energy of 0.6–0.8 eV and a number of peaks at 0.8–1.2 eV (three peaks for sample A and two peaks for samples B, C), and also a weak peak at 1.55 eV only for sample B.

Radiation from the QW appears as a result of recombination of two-dimensional photoelectrons from $e1$ and $e2$ subbands and two-dimensional photoholes from hh1 subband. The QW spectrum consists of peak e1–hh1 fused with the much more intense peak $e2-hh1$. However, the reliable separation of these peaks by approximating the PL spectrum by two Gaussian components is possible only for a low defective sample A.

Peaks at 0.8–1.2 eV cannot originate from near-band-edge recombination in any of the heterostructure layers (otherwise, only peaks with energies above 1.1 eV would appear). These peaks are assumed to be concerned with transitions of electrons from the energy levels of defects inside the band gap to the valence band. No PL of "defect" levels is observed at room temperature, it begins to play a noticeable role when the samples are cooled below 180 K, and at 77 K the intensity of "defect" PL in samples with medium and high defectiveness (samples B and C) exceeds the intensity of QW PL. The PL of "defect" levels cannot be confused with the near-band-edge PL of separate sublayers of a metamorphic buffer, because the latter is observed relatively weakly and in other energy range: the near-band-edge PL from the $In_{0.65}Al_{0.35}As$ barrier is observed for sample A at $\sim$ 1.17 eV; for sample B, this peak is not observed since it is possibly masked by a bright "defect" PL; for sample C this peak is absent, likely due to the high imperfection of the $In_{0.65}Al_{0.35}As$ barrier and the predominance of non-radiative recombination.

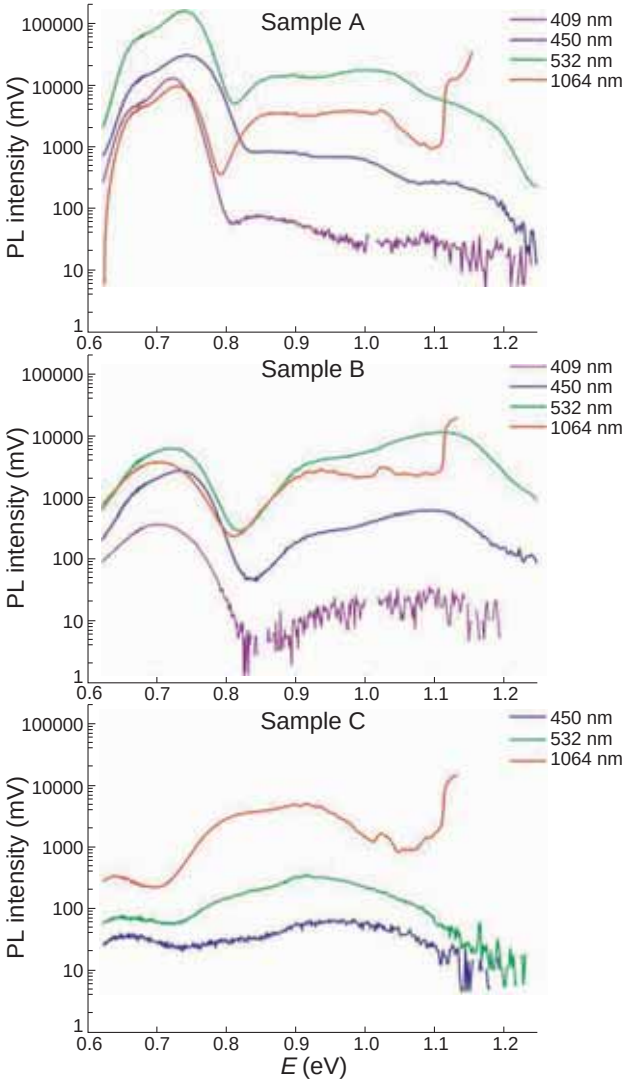

Fig. 1. PL spectra of samples measured at 77 K under laser pumping with different wavelength

As the defectiveness of heterostructures increases (samples A→B→C), the PL intensity of the QW decreases and the relative intensity of "defect" peaks at 0.8–1.2 eV increases under pumping by the same laser (Table 2). The PL of QW with high density of twins (sample C) is extremely weak, and corresponding peak in the spectrum is 70 meV shifted to lower energy in comparison with the QW peak for the more perfect samples A and B.

As the pump wavelength increases from 409 to 532 nm, a monotonic increase in the PL relative intensity of defect levels with respect to PL of QW is observed for all samples, since radiation with a longer wavelength is absorbed in a thicker surface layer of the sample and penetrates more into the metamorphic buffer containing the main portion of defects. When replacing a green laser with an infrared laser with 1064 nm wavelength, it is found that the response of the heterostructure depends on its defectiveness degree, as one can see in Fig. 1 and in Table 2 in the form of quantitative ratios.

PL intensity depends on the photoexcitation power as $I_{\mathrm{PL}} = \eta \cdot I_{\mathrm{pump}}^{\alpha}$, where the exponent α allows one to estimate the contribution of different mechanisms to radiative recombination: $\alpha = 1$ correspond to pure exciton recombination and $\alpha = 2$ correspond to pure free carriers recombination [4].

Table 2. Integrated intensity of QW PL and "defect" PL (in the arb. units), and their ratio under pump by green laser ($\lambda = 532$ nm, intensity 300 mW) and infrared laser ($\lambda = 1064$ nm, intensity 600 mW).

Sample	Green laser			Infrared laser		
	S_{QW}	S_{def}	$S_{\mathrm{def}}/S_{\mathrm{QW}}$	S_{QW}	S_{def}	$S_{\mathrm{def}}/S_{\mathrm{QW}}$
A	1206	466	0.39	788	1033	1.31
B	595	1765	2.97	350	605	1.73
C	8.7	73.6	8.5	23.5	910	39

The dominant role gradually passes from the recombination of free charge carriers to exciton recombination with decreasing temperature. However, in heavily doped QWs even at low temperatures the exciton formation is prevented due to screening by free carriers (in the investigated samples $n_0 \sim 10^{12}$ cm^{-2}), and the rate of radiative recombination are proportional to the product of electron and hole concentrations: $I_{\mathrm{PL}} \propto (n_0 + \Delta n) \cdot (p_0 + \Delta p) \approx n_0 \cdot \Delta p \propto \Delta p \propto I_{\mathrm{pump}}$.

Table 3. Experimentally determined values of α.

Sample	Λ (nm)	α			
		QW		Defects	
		*e*1–*hh*1	*e*2–*hh*1	Peak 1	Peak 2
A	532	1.23	1.20	0.93	1.09
B	532	1.39		1.00	1.04
C	1064	—		0.93	1.21

The calculated values of α are shown in Table 3. The values of α for "defect" PL confirm that non-radiative recombination plays an important role in the recombination of electrons from energy levels associated with defects in a metamorphic buffer, and its contribution increases with increasing of photoexcitation intensity. This leads to a sublinear dependence of the PL intensity on the pump power when $\alpha < 1$. For the QW PL the power law with exponent 1.2–1.4 is observed. The less exponent value of ∼1.2 is found for a sufficiently perfect QW whereas the larger exponent value of ∼1.4 is found for a QW with increased threading dislocation density and penetrating stacking faults.

Acknowledgement

This work was supported by the Russian Foundation for Basic Research (project 18-32-00157 mol_a).

References

[1] G.B. Galiev, S.S. Pushkarev, I.S. Vasil"evskii, *et al*, *Semiconductors*, **47**, (4), 532 (2013).
[2] G.B. Galiev, I.S. Vasil'evskii, S.S. Pushkarev, *et al*, *J. of Crystal Growth*, **366**, 55 (2013).
[3] G.B. Galiev, S.S. Pushkarev, A.S. Orekhov, *et al*, *Crystallography Reports*, **59**, (3) 425 (2014).
[4] S. Martini, A.A. Quivy, A. Tabata, *et al*, *J. Appl. Phys.*, **90**, (5) 2280 (2001).

28th Int. Symp. “Nanostructures: Physics and Technology”
Minsk, Belarus, September 2020

The diagram of *p-n* junction formed on the *n*-GaAs surface by 1.25 keV Ar^+ ion beam

V.M. Mikoushkin[1], E.A. Makarevskaya[1], *A.P. Solonitsyna*[1] and M. Brzhezinskaya[2]

[1] Ioffe Institute, 194021 Saint Petersburg, Russia
[2] Helmholtz-Zentrum Berlin für Materialien und Energie, 12489 Berlin, Germany

Abstract. The core-level and valence band electronic structure of *n*-GaAs (100) was studied by synchrotron-based high-resolution photoelectron spectroscopy after irradiation by an Ar^+ ion beam with energy $E_i = 1250$ eV and fluence $Q = 1\times10^{15}$ ions/cm^2. Conversion of the conductivity type and formation of a *p-n* structure have been observed. The *p*-layer thickness was experimentally determined from the Ga3d photoelectron spectrum by separation and analysis of the contribution from the *n*-type bulk layer ($d \sim 5.5$ nm). A band diagram of the *p-n* junction formed on the *n*-GaAs surface by Ar^+ ion bombardment was reconstructed.

Introduction

GaAs and GaAs-based semiconductors are ones of the most important materials for modern high-frequency electronics [1]. Therefore, development of new approaches to fabrication of GaAs-based devices is a topical problem. Recently, the process of the *p*-nanolayer creation on the GaAs surface under Ar^+ ion bombardment has been revealed [2]. The *p*-layer creation effect was shown to be related to formation of the Ga-antisite *p*-type centers due to mechanical action of ions. In addition, the effect of a *p-n* structure formation on the *n*-GaAs surface by low energy Ar^+ ions was observed. $J-V$ characteristics of the created *p-n* structure revealed the diode effect [3]. The attractiveness of the studied approach for possible applications is that the *p-n* junction can be formed in high vacuum locally with the lateral resolution determined by the ion beam diameter without using wet lithography. Despite obtaining some information on the ion-beam-made *p-n* structure, such important characteristics as *p*-layer thickness and band diagram of the *p-n* junction have been estimated only roughly. By using synchrotron-based *X*-ray photoelectron spectroscopy, we directly determined in this paper the *p*-layer thickness and deduced the band diagram of the *p-n* junction formed on the *n*-GaAs surface under low energy Ar^+ ion irradiation.

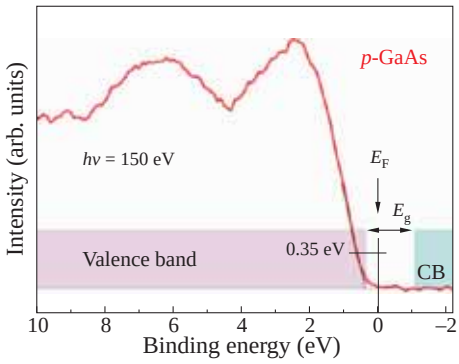

Fig. 1. Valence band (VB) photoelectron spectrum of the *p*-GaAs nanolayer formed on the *n*-GaAs(100) surface by Ar^+ ion irradiation (*p*-GaAs).

1. Experiment

The experiment was carried out in ultrahigh vacuum at the Russian-German synchrotron radiation beamline of the BESSY-II electron storage ring of Helmholtz-Zentrum Berlin [4] by using a photoelectron spectrometer with hemispherical analyzer CLAM-4 (VG). The high–resolution ($\Delta E = 150$ meV) spectra were measured at photon energies $h\nu = 150$ and 350 eV providing different information depths. A commercial GaAs (100) *n*-type ($n \sim 1.25{-}2.5\times10^{18}$ cm^{-3}) wafer was irradiated by Ar^+ ions with energy $E_i = 1250$ eV in the preparation chamber of the spectrometer. The dose density (fluence) $Q = 1\times10^{15}$ ions/cm^2 was sufficient to remove the layer of native oxide and a part of the bulk layer. The survey spectrum measured at the photon energy ($h\nu = 600$ eV) sufficient for observation of the O1s line exhibited virtual absence of oxygen and carbon as well as of possible impurities, which evidenced removal of the native oxide layer and purity of the ion beam.

2. Results and Discussion

The *p*-type conductivity of the irradiated layer is confirmed by the valence band (VB) photoelectron spectrum measured at photon energy $h\nu = 150$ eV and represented in Fig. 1. The spectrum characterizes the density of occupied VB states just of the surface layer whose thickness is determined by the photoelectron mean free path $\lambda = 1$ nm [5]. The electron binding energy scale is counted relative to the Fermi level. The VB, conduction band (CB) and bandgap width ($E_g = 1.42$ eV) are schematically indicated in the figure. Extrapolation of the spectrum top enables determination of the valence band edge position which, as the figure shows, is 0.35 eV below the Fermi level. This value proved to be a bit larger compared to that (0.25 eV) observed for the higher Ar^+ ion energy $E_i = 2500$ eV [2]. Closeness of the VB top to the Fermi level evidences for conversion of the conductivity type of the near-surface layer under ion bombardment. The conductivity type transformation was accounted for by the preferable sputtering of arsenic atoms and enrichment of the irradiated layer with gallium, followed by creation of the Ga-antisite *p*-type centers [2]. Since the initial sample is *n*-type, a *p-n* structure is formed.

The *p*-layer thickness was obtained experimentally from the Ga3d photoelectron spectrum presented in Fig. 2 by separation and analysis of the *n*-type bulk contribution. This contribution was searched in the high-energy part of the Ga3d spectrum: ~ 1 eV above the peak, which corresponds to the Fermi level shift from CB to VB. Figure 2 shows the Ga3d photoemission spectra in the electron binding energy scale at two

photon energies $h\nu = 150$ (dotted line) and 350 eV (solid line) which characterize thin and thicker material layers. The peaks for both photon energies coincided in energy ($E_B = 19.35$ eV) and proved to be very close to our former data for GaAs irradiated by Ar^+ ions [2] and to the data known from literature. This energy is a characteristic of the irradiated near-surface p-layer. As mentioned above, the contribution of the unirradiated n-type bulk should be expected at the higher binding energy $E_B \sim 20.35$ eV where the difference between the compared spectra is observed (Fig. 2). This difference reveals a small but statistically reliable contribution at binding energy $E_B = 20.15$ eV which was identified as belonging to the top of the n-GaAs bulk underneath the modified p-GaAs layer. The bulk signal occurred to be rather weak due to attenuation in the upper layer. Figure 2 also shows the presence of interstitial Ga (Ga-*int*) at binding energy $E_B = 18.55$ eV discussed elsewhere [2,3]. A kink at binding energy $E_B = 20.2$ eV was revealed also in the doubly differentiated spectrum, thus confirming the presence of the $n-$GaAs bulk contribution.

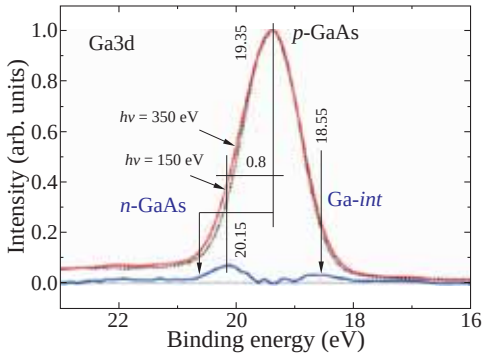

Fig. 2. Ga3d photoelectron spectra of the n-GaAs sample irradiated by the 1250-eV Ar^+ ion beam. The spectra were measured with photon energies $h\nu = 150$ eV (dotted line) and $h\nu = 350$ eV (solid line).

The binding energy ($E_B = 20.2$ eV) of the Ga3d n-GaAs contribution proved to be a bit less than the estimated one ($E_B = 20.35$ eV). The reason for this is that the probing depth ($l \sim 2\lambda = 3.8$ nm) is sufficient to observe only the upper part of the p-GaAs/n-GaAs interface. The band diagram with theschematic abrupt interface (dotted lines) and more realistic extended one (solid curves) is shown in Fig. 3 in the scale of the distance from the surface. The effective thickness of the p-GaAs layer can be estimated by comparing intensities (I_p and I_n) of the p and n contributions to the Ga3d line intensity: $d = \lambda ln(I_p/I_n + 1)$. The estimation gives value $d = 5.5$ nm which proved to be equal to the width at the half maximum of the depth profile of implanted ions calculated by TRIM 2006 [7]: $\langle x \rangle = 2\mathrm{Rp} = 5.4$ nm, where Rp is the projected range. The estimated Fermi level position relative to the CB top ($\sim$ 0.8 eV) is rather far yet at this depth from the value in the bulk ($\sim$ 1.0 eV). The interface length should be determined by the region of the space charge which is equal to $\Delta L = 41-28$ nm at the condition when the acceptor concentration essentially exceeds that of donors for typical commercial wafers ($n \sim 1.25-2.5\times10^{18}$ cm^{-3}).

3. Conclusions

Imparting p-type conductivity to the GaAs layer and formation of a p-n structure on the n-GaAs surface has been observed

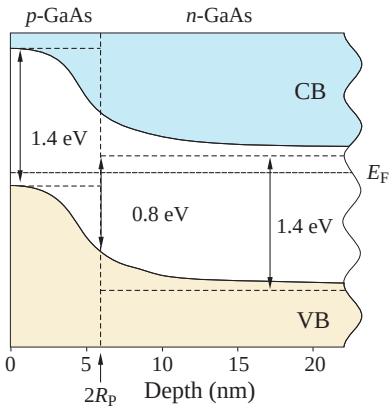

Fig. 3. Band diagram of the p-GaAs nanolayer formed on the n-GaAs (100) surface by Ar^+ ion irradiation.

under irradiation by Ar^+ ions with energy $E_i = 1250$ eV and fluence $Q = 1\times10^{15}$ ions/cm^2. The conductivity type conversion occurs due to purely mechanical action of chemically neutral argon diffusing away after implantation. The effect manifests itself in shifting the valence band edge to the Fermi-level and fixing it 0.35 eV below the Fermi-level. The p-layer thickness and Fermi level position were obtained experimentally from the Ga3d photoelectron spectrum by separation and analysis of the n-type bulk contribution. Finally, a band diagram of the p-n junction formed on the n-GaAs-surface under the 1250-eV Ar^+ ion bombardment was reconstructed.

Acknowledgements

This work was supported by the Russian Science Foundation (Project No. 17-19-01200). The authors thank Helmholtz-Zentrum Berlin (Germany) for the allocation of synchrotron radiation beamtime. This research project was supported by the Russian-German Laboratory at BESSY II.

References

[1] *Fabrication of GaAs devices*, ed. A.G. Baca and C.I.H. Ashby, London: IET, 2005.
[2] V.M. Mikoushkin, V.V. Bryzgalov *et al*, *EPL* **122**, 27002 (2018).
[3] V.M. Mikoushkin, V.S. Kalinovskii *et al*, *Semiconductors* **53**, 52 (2019).
[4] S.L. Molodtsov, S.I. Fedoseenko *et al*, *App. Phys. A* **94**, 501 (2009).
[5] S. Tanuma, C.J. Powel, and D.R. Penn, *Surf. Interface Anal.* **17**, 927 (1991).
[6] V.M. Mikoushkin, V.V. Bryzgalov *et al*, *Semiconductors* **52**, 2057 (2018).
[7] *The Stopping and Range of Ions in Solids*, ed. J.F. Ziegler, J.P. Biersack, and U. Littmark, New York: Pergamon Press, 1985.

28th Int. Symp. "Nanostructures: Physics and Technology"
Minsk, Belarus, September 2020

Approach for prediction of orientation relationships and interface structures and its application to α-, β-, γ-$FeSi_2$ and Si

M.A. Visotin[1,2], I.A. Tarasov[1]

[1] Kirensky Institute of Physics, Federal Research Center KSC SB RAS, Krasnoyarsk, 660036, Russia
[2] Siberian Federal University, 660041, Krasnoyarsk, Russia

Abstract. Pure crystallogeometrical approach is proposed for predicting orientation relationships, habit planes and atomic structures of the interfaces between phases, which is applicable to systems of low-symmetry phases and epitaxial thin film growth. The suggested models are verified on the example of epitaxial growth of α-, β-, γ-$FeSi_2$ silicide thin films on silicon substrates. The density of Near-Coincidence Sites is shown to have a decisive role in the determination of epitaxial thin film orientation and explains the superior quality of β-$FeSi_2$ thin grown on Si(111) over Si(001) substrates despite larger lattice misfits. Ideal conjunctions for interfaces between the silicide phases are predicted and this allows for utilisation of thin buffer α-$FeSi_2$ layer for oriented growth of β-$FeSi_2$ nanostructures on Si(001).

Introduction

The physics of surfaces and interfaces contribute greatly to the properties of the materials in real applications, especially when miniaturisation and low-dimensional and nanostructures are considered. This includes a wide variety of effects, from Schottky barriers and electron scattering to topological materials [1]. Unlike the bulk properties, which are studied nowadays with a set of robust theoretical and experimental methods, investigation of structure and properties of the interfaces is yet a great challenge for materials science. Even the mechanisms defining possible orientation relationships (ORs) and habit planes (HPs) between two phases are not fully known [2]. It is still desirable to adapt crystallogeometrical methods for predicting ORs and HPs between more complex phases with the capability of taking into account the internal chemical bonding properties. In that, prediction of possible coherent interfaces with regular atomic structure is of great importance due to the stability of their electronic and transport properties on the one hand, and the compatibility of such substrate and film phases for epitaxial growth on the other hand. Feasibility of high-quality thin film synthesis is of particular interest in lattice strain band engineering [3] and for most of the applications in spintronics and optoelectronics. A vivid example of such case is an epitaxial synthesis of β-$FeSi_2$ on silicon substrates. Semiconducting β-$FeSi_2$ phase can be utilised as active material in photon crystals, photovoltaics, thermoelectrics and also for electric charge storage, while being of particular interest for light emission diodes (LED) [4]. However, many possible application opportunities are hindered by the poor quality of monocrystalline thin films, along with insufficient tunability and band control.

1. Interface prediction approach

Herein we focus on a purely geometrical approach to finding possible interfaces between α-, β-, γ-$FeSi_2$ and Si phases, which is simple enough to search through numerous variants and yet have already shown its efficiency. We use a systematic combination of edge-to-edge matching method [5] to find possible ORs and subsequent near-coincidence sites (NCS) [6] density maximisation for prediction of the relative position of phases at the interface and for comparison of different interfaces between each other. In that, a concept of atomic row density is reformulated to take into account small atomic displacements, which lies in the basement of the NCS matching, and thus both methods are used in a unified manner. Finally, the information about the coincidence sites is used to construct a simple atomistic model for the interface structure, which can be used as input for more advanced atomic structure prediction methods, e.g. Monte-Carlo, evolutionary or other heuristic algorithms [7] or directly in molecular dynamics or quantum-chemical studies. The proposed approach gives a framework to construct possible interface structures basing only on the equilibrium crystal structures of the phases. The general scheme of the approach is the following: 1. Find pairs of close-packed rows with low misfits; 2. Find ORs and HPs (relative orientation); 3. Stretch phases in accordance with the misfits; 4. Find highest NCS density (relative position); 5. Resolve the atomic structure of the interface. An illustration of the NCS model is given in Fig. 1c. Two phases are intersecting in some interface region, the borders of which are shown with black solid lines. The near-coincidence sites between two phases, which are marked with arrows, are searched for within the interface region. The atomic sites, which do not coincide with other or coincide with atoms of different chemical elements, are considered not-matched sites and marked with "$times$" symbols. Here, we use the following value to assess the goodness of the atomic site match:

$$R = \frac{1}{2}\left(\frac{m_1}{N_1} + \frac{m_2}{N_2}\right) \quad (1)$$

where N1 and N2 are the numbers of phase #1 and #2 atoms in the interface; m1 and m2 are the counts of near coincidence sites from the corresponding phases.

2. Interfaces in β-$FeSi_2$ and Si system: an example

Among the predicted interfaces for β-$FeSi_2$ with Si, the highest R values correspond to Si(111) and Si(001) habit planes. The first couple of best-matching ORs, i.1 $\beta(101)||\mathrm{Si}(111)$ and i.2 $\beta(110)||\mathrm{Si}(111)$, have R values of 0.75, ahead of the $\beta(100)||\mathrm{Si}(100)$ interface with $R = 0.7$. Another technologically important silicon substrate plane Si(110) is presented utmost at the 10th position in the ranking by $\beta(001)) \parallel \mathrm{Si}(110)$ ORs, having $R = 0.48$, which makes it less favourable for thin film growth. Although these interfaces contain the same pair of matching close-packed atomic rows $\mathrm{Si}< 110 > ||\beta < 010 >$

with 1.54% misfit, the second pairs of crystallographic vectors determining the HPs have different misfits and, as a result, the interface strain is rather different. $\beta(100)\|$ Si(100) has the lowest strain of $\tilde{\varepsilon} = 1.52$ %, while the strain for $\beta(101)||$Si(111) is significantly higher, $\tilde{\varepsilon} = 2.47$ %. Both values, R and $\tilde{\varepsilon}$, affect the possibility of interface formation; nevertheless, the experimental synthesis reports state the β-$FeSi_2$ thin films grown on silicon (111), despite higher lattice misfits, exhibit better quality and higher structural stability whereas the films grown on Si(100) tend to agglomerate in course of thermal treatment[11]. Therefore, it can be supposed the NCS density is more important than the interface strain and plays a decisive role in the determination of the orientation relationship of growing phases. Moreover, possible interfaces of β-$FeSi_2$ with Si(110) substrate have much lower values of NCS density ($R < 0.48$) and there are also several high-index habit planes with higher values of R, which indicates the possibility of formation of such facets instead of interface with Si(110).

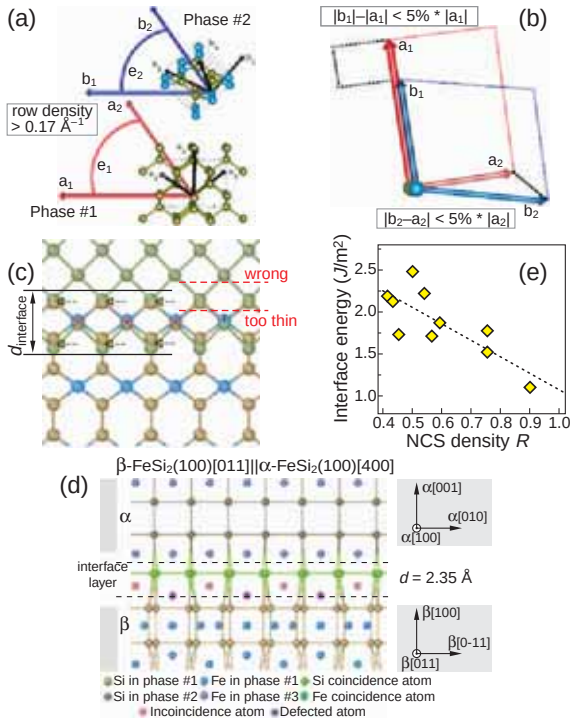

Fig. 1. Illustration of the method for finding possible favourable ORs and interface atomic structures. (a) Search of vectors to form good matching surface unit cells of two crystals. (b) Calculation of misfit between two surface unit cell considered. (c) Schematic illustration of NCS atomic matching on an interface. (d) An example of automatically created atomic structure model for an interface between two crystals. (e) NCS density plotted VS interface energies calculated within DFT for some α || Si coherent interfaces.

These facts agree well with the experimental observations of mainly endotaxial islands formation on Si(110) with other types of $\beta||$Si interface planes [12]. Also, the intrinsic presence of $\beta(100)$ [011]/2 stacking faults at the interfaces of $\beta(001)$ or $\beta(010)$ facets parallel to substrate's inward Si(110) planes observed in β-$FeSi_2$ island formation [13] are explained with high interface strain value of 4.65%.

$$R = \frac{1}{2}\left(\frac{m_1}{N_1} + \frac{m_2}{N_2}\right) \quad (1)$$

Thus, the predictions for the β-$FeSi_2||$Si reproduce well the experimentally observed ORs with the same order of formation favourability, which argues for the applicability of the current approach to the silicide family compounds. The stability of i.1 $\beta(101)||$Si(111) interface may be also assessed by predicted atomic structure. Within the same orientation relationship, two distinct types of atomic configuration corresponding to different relative displacements of the phases were found, both having $R = 0.75$.

Overall, the proposed approach appears to be a powerful tool for prediction of ORs and the interface structures between arbitrary phases, which may be obtained by epitaxial growth techniques. While it demands only bulk crystal structure knowledge and, optionally, some prior knowledge on the bonging nature in the phases accessible by basic DFT calculations, the approach is suitable for the rapidly developing field of high-throughput computational material science investigations.

Acknowledgement

This work was supported by the Russian Science Foundation, project No. 16-13-00060-П.

References

[1] K. Song *et al*, *Nat. Nanotechnol.* **13,** 198 (2018).
[2] J. M. Howe *et al*, *Phys. Metall.*, Fifth Edit (Elsevier, 2014), pp. 1317–1451.
[3] O. Seo *et al*, *Sci. Rep.* **9**, 4304 (2019).
[4] H. Tokushige *et al*, *Jpn. J. Appl. Phys.* **79**, 3125 (2001).
[5] M. X. Zhang *et al*, *Acta Mater.* **53**, 1073 (2005).
[6] Q. Liang *et al*, *Metall. Mater. Trans. A* **29**, 2059 (1998).
[7] B. Gao *et al*, *Sci. Bull.* **64**, 301 (2019).
[8] H. Yamane *et al*, *J. Alloys Compd.* **476, 282** (2009).
[9] W. Miiller *et al*, *J. Phys. Condens. Matter* **27**, 175601 (2015).
[10] S. Liang *et al*, *J. Cryst. Growth* **295**, 166 (2006).
[11] T. Suemasu *et al*, *Thin Solid Films* **461**, 209 (2004).
[12] Z.Q. Zou *et al*, *Appl. Surf. Sci.* **399**, 200 (2017).
[13] N. Jedrecy *et al*, *Phys. Rev. B* **48**, 8801 (1993).

28th Int. Symp. "Nanostructures: Physics and Technology"
Minsk, Belarus, September 2020

About the features of electric conductivity models for polymer composite nanomaterials based on Cu(Cu_2O)-LDPE

N.M. Ushakov[1,2], I.D. Kosobudskii[1,3]

[1] V.A. Kotel'nikov Institute of RadioEng.&Electr. of RAS, Saratov Branch, Saratov, Russia
[2] National Research University, Saratov, Russia
[3] Yu. Gagarin Technical State University, Saratov, Russia

Abstract. Polymer nanocomposites based on Cu(Cu_2O)-LDPE with a volume fraction of 0.1–0.4 copper filler in the form of spherical nanoparticles with sizes from 10 to 25 nm were synthesized. The electrical conductivity of such composite nanomaterials was measured, which is 5 times higher than the electrical conductivity of a polyethylene matrix. To predict the electrical conductivity of such materials, an analysis of well-known mathematical models is carried out and models for predicting the electrical conductivity of such materials are selected that are adequate to the experimental data.

Introduction

Randomly arranged composites of nanoscale metal and dielectric elements, sometimes known as metal-dielectric composites (MDCs) are useful in a wide variety of electromagnetic and optical processes [1]. However, accurate simulations of random metal-dielectric systems are still challenging for several reasons, not the least of which is the complexity of the problem. As a rule, statistical, thermodynamic, structure-oriented, geometric, etc. models rely on percolation theory. To predict the electrical conductivity of polymer composites, many mathematical and empirical models have been proposed [2]. At the same time, models should include the matrix and filler parameters, on which the final properties of materials depend [3]. To date, several models have been developed and proposed, each of which uses different design parameters [4]. Therefore, it is necessary to analyze known models in order to determine the model that is most appropriate for the experiment.

Unlike conjugated polymers, which can have a conductivity higher than 1 S/m, MDCs based on linear polymers such as polyethylene can only increase their conductivity by incorporating a highly conductive nanoscale filler such as copper, silver, etc. In this work, the samples were prepared in the form of a powder of a polymer nanocomposite based on Cu(Cu_2O)-LDPE with various mass concentrations of nanoparticles in a polymer matrix, the electrical conductivity of the samples was measured, and various mathematical models were analyzed to best fit the calculated and experimental data.

1. Experimental

Samples of composite nanomaterial were obtained by a known method [5]. Copper diacetate ($(CH_3COO)_2Cu$) was used as the starting compound, the thermal decomposition of which was carried out at 255 °C in a polymer medium. Samples were obtained in the form of powders with various copper concentrations from 10 to 40 mass %. Thick films of the size $10\times10\times0.4$ mm^3 were made from powders by thermopressing. The phase composition of the powder samples was determined by x-ray diffractometry. Particle sizes were determined from the Debye–Scherrer equation by the broadening of the diffraction peak, which, in turn, was determined by the Warren formula [6,7]. The electrical conductivity of the film samples was measured under normal conditions at alternating current at a frequency of 1 MHz using an E7-12 meter (Russia).

2. Results and discussion

Figure 1 shows the X-ray spectrum for 4 wt.% Cu(Cu_2O-LDPE) MDC. It follows from the presented spectrum that responses from the copper oxide phase dominate in such composite nanomaterials.

This is explained by the fact that the surface of the copper nanoparticle is coated with an oxide film with the formation of a 'peatch] structure, which should substantially affect the electrical conductivity of the metal–polymer composite. The average nanoparticle size D in MDCs, calculated from X-ray diffraction patterns from the characteristic peak broadening, was for 10 mass.% — $D = 11 \pm 2$ nm, äëÿ 40 mass.% — $D = 24 \pm 2$ nm.

Several models were analyzed, such as the Maxwell Equation, Maxwell–Wagnar Equation, Pal Model, and Sigmoidal Function [2]. Among the analyzed models, the smallest discrepancy with the experimental data was shown by the Maxwell–Wagnar Equation and Sigmoidal Function.

The Maxwell–Wagner equation takes into account a high concentration of fillers [2]. Wagner performed a functional extension of the Maxwell equation. The Maxwell–Wagner equation shows that conductivity is directly proportional to the volume fraction of fillers. If the ratio of the electrical conductivities of the composite (σ_c) and the matrix is (σ_m) large, then in the limit the specific conductivity of MDCs is determined as: $\sigma_c/\sigma_m = (1 + 2\theta)/(1 - \theta)$

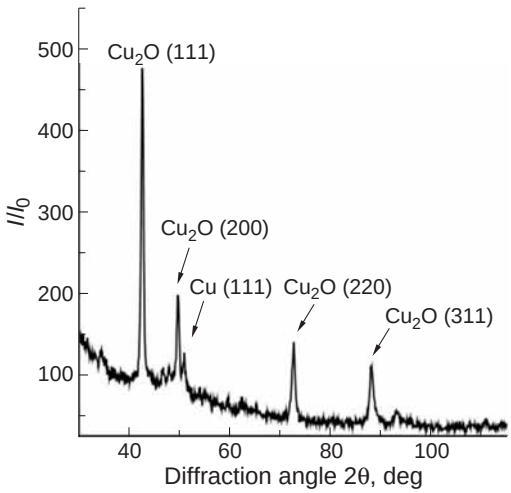

Fig. 1. X-ray spectrum for 40 wt.% Cu(Cu_2O-LDPE) MDCs.

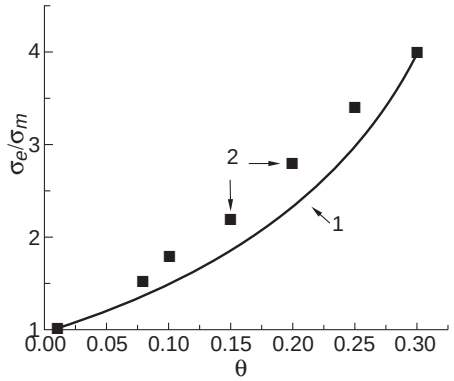

Fig. 2. Dependences of the relative conductivity of Cu(Cu2O)-LDP MDCs on the volume fraction of nano-filler. Solid curve (1) calculated data for Maxwell—Wagnar Equation. Symbol curve (2) experimental data.

Figure 2 shows the dependences of the experimental relative conductivity of MDCs (curve 2) based on Cu(Cu_2O)-LDPE and calculated for the Maxwell–Wagnar Equation (curve 1) on the volume fraction of the nano filler.

Figure 3 shows the dependences of the experimental relative conductivity of MDCs (curve 2) based on Cu (Cu_2O)-LDPE and calculated for the Sigmoidal Function (curve 1) on the volume fraction of nano-filler. There are several sigmoidal functions presented in [8], which include a logistic function, a Gompertz model, an extremal value function, a Hill function, etc.

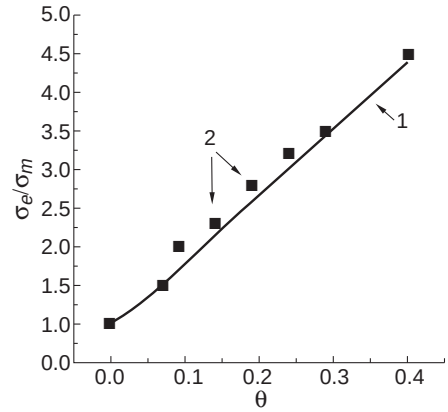

Fig. 3. Dependences of the relative conductivity of Cu(Cu2O)-LDPE MDCs on the volume fraction of nano-filler. Solid curve (1) calculated data for the Sigmoidal Function. Symbol curve (2) experimental data.

In our work, a logistic function of the type

$$y(x) = y_0 + \frac{ax}{1 + exp(-bx)}$$

where y_0, a, b are constants. σ_c -electrical conductivity of the composite.

This feature has been adapted to predict the conductivity of nanocomposites. The following constant values $y(x) = \sigma_c(\theta)$ were used in the calculations:

$$y_0 = \sigma_m = 10^{-12}\ S/m,\ a = 18\sigma_m,\ b = 20$$

The analysis showed that not all known models have sufficient parametric ability to accurately determine the electrical conductivity of polymer nanocomposites. Thus, polymer nanocomposites based on Cu(Cu2O)-LDPE with different volume fractions of the filler were synthesized in the work, their electrical conductivity was measured, and models for predicting the electrical conductivity of such materials that were adequate to the experimental data were selected.

Acknowledgement

The authors are grateful to Dr. Dzumaliev A.S. for assistance in the experimental studies.

References

[1] C. Sella *et al*, *Solid Films* **517**, 5848 (2009).
[2] R. Taherian, *Experiments, Modelling and Applications; ResearchGate* , Berlin, Germany, 297 (2019).
[3] Q. Zhang *et al*, *J. Polymers* **9**, 404 (2017).
[4] N. A. M. Radzuan *et al*, *J. of Hydrogen Energy* **42**, 9262 (2017).
[5] I.D. Kosobudskii, *J. High-Molecular Compounds* **27(A)**, 689 (1985).
[6] U. Holzwarth *et al*, *Nature Nanotechnology* **6**, 534 (2011).
[7] A. L. Patterson, *Phys. Rev. B* **56**, 978 (1939).
[8] M. Rahaman *et al*, *Polymers* **9**, 527 (2017).

28th Int. Symp. “Nanostructures: Physics and Technology”
Minsk, Belarus, September 2020

Exciton dynamics in MOCVD-grown monolayer MoS_2

M.A. Akmaev[1], M.V. Kochiev[1], P.V. Vinokurov[2], S.A. Smagulova[2], P.V. Fedotov[3], E.D. Obraztsova[3] and V.V. Belykh[1]

[1] P.N. Lebedev Physical Institute of the RAS, Moscow, Russia
[2] M.K. Ammosov North-Eastern Federal University, Yakutsk, Russia
[3] A.M. Prokhorov General Physics Institute RAS, Moscow, Russia

Abstract. We study photoluminescence (PL) spectra and time dynamics of MoS_2 monolayers grown by the MOCVD method. In addition to the usual direct A-exciton, low-temperature PL spectra reveal low-energy line which becomes suppressed with increase in temperature. We find extremely long PL lifetime for this line of 100 ns and attribute it to the indirect exciton transition. For the direct A-exciton transition we measure the rate of exciton diffusion and show that it increases with excitation power and becomes suppressed at low temperature.

Introduction

The interest in studies of transition metal dichalcogenide monolayers is due to the fact that they exhibit a direct optical transition [1], in contrast to multilayer materials. Furthermore the high exciton binding energy of about 500 meV [2], makes observation of the intense PL at room temperature possible.

1. Measurement technique

The sample under study was grown by metal-organic vapor deposition (MOCVD) on a Si/SiO_2 substrate. The sample is placed in a helium flow cryostat to reach the temperatures 10–300 K. The stationary PL spectra are recorded using a spectrometer coupled to a CCD matrix, while the sample was excited using a CW semiconductor laser with a wavelength of 457 nm. The PL dynamics was measured with a Hamamatsu streak camera coupled to a spectrograph. The temporal resolution up to 3 ps was achieved. Here the excitation was performed using the second harmonic (400 nm) of a pulsed (2 ps) Ti-sapphire laser.

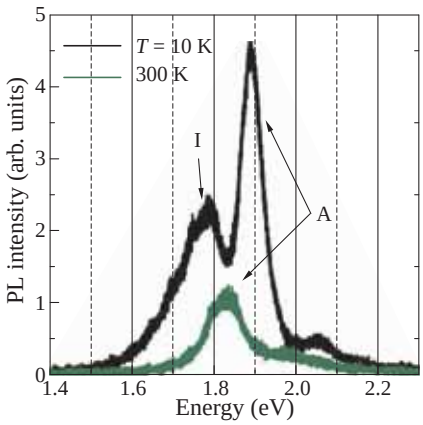

Fig. 1. PL spectra of monolayer MoS_2 at 10 and 300 K. A is the direct exciton, I is the indirect exciton.

2. Results

At room temperature the PL spectrum of MoS_2 monolayer is dominated by the so-called A-exciton line [Fig. 1] in agreement with the literature data [1,3]. At helium temperatures, an additional low-energy line is observed in the PL spectra. It was previously attributed in the literature to the lines of bound excitons [3–5]. When the temperature is increased from 10 to 100 K, the intensity of the additional line decreases more than 5 times, while the intensity of the A-exciton line changes insignificantly. Also, the energy position of the additional line shifts much faster than the position of the exciton line. PL temporal dynamics of the additional line at 10 K revel long nonexponential decay with the lifetime ranging from few ns for the initial region to about 100 ns [Fig. 2]. The long dynamics suggests indirect transition nature of this line.

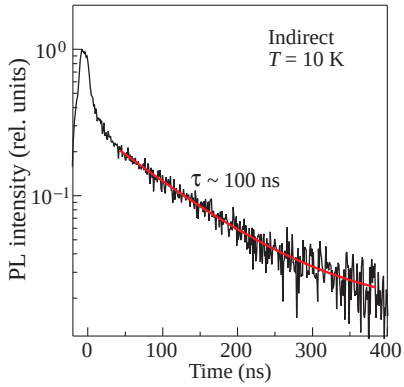

Fig. 2. PL dynamics of the indirect transition. Note the timescale.

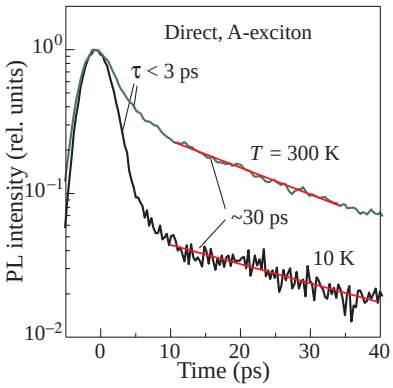

Fig. 3. PL dynamics of the direct exciton at 10 and 300 K.

The measured lifetime of the A exciton is expectedly short, less than 3 ps [Fig. 3], which is consistent with the literature data [3]. Interesting, we also observe the long decay component with characteristic time about 30 ps. This component corresponds to decay of the reservoir of excitons with k-vector lying outside the light cone. With increase of the temperature this component becomes much more pronounced.

We also study the transport of excitons in monolayer MoS_2

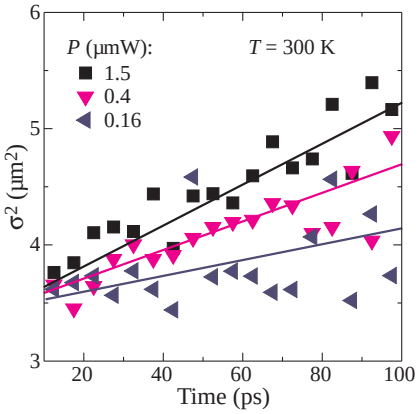

Fig. 4. Dynamics of the spatial distribution width squared, σ^2, for different excitation powers. Linear increase of σ^2 with time indicates diffusive exciton transport.

by monitoring the dynamics of PL spatial distribution. The squared width of this distribution as a function of time is shown in Fig. 4. It shows a linear increase indicating diffusive character of the exciton transport with diffusion coefficient increasing with excitation density in agreement with results obtained on WS_2 monolayers [6]. At low temperatures the exciton diffusion is strongly suppressed.

Acknowledgement

The work is supported by the Russian foundation for basic research through the grant No. 18-32-20202.

References

[1] K.F. Mak *et al*, *Phys. Rev. Lett.* **105**, 136805 (2010).
[2] T. Cheiwchanchamnangij and W. R. L. Lambrecht, *Phys. Rev. B.* **85**, 205302 (2012).
[3] T. Korn *et al*, *Appl. Phys. Lett.* **99**, 102109 (2011).
[4] S. Tongay *et al*, *Sci. Rep.* **3**, 2657 (2013).
[5] N. Saigal and S. Ghosh, *Appl. Phys. Lett.* **109**, 122105 (2016).
[6] M. Kulig *et al*, *Phys. Rev. Lett.* **120**, 207401 (2018).

28th Int. Symp. “Nanostructures: Physics and Technology”
Minsk, Belarus, September 2020

Precision diagnostics of high-quality InGaAs/GaAs quantum-wells heterostructures by exciton spectroscopy

N.R. Grigorieva[1], A.V. Mikhailov[2], I.V. Ignatiev[2], Yu.P. Efimov[3] S.A. Eliseev[3], V.A. Lovtcius[3], and P.Yu. Shapochkin[3]

[1] Saint-Petersburg State University, 194034, St Petersburg, Russia
[2] Spin Optics Laboratory, St Petersburg State University, Ulyanovskaya 1, Petrodvorets, St Petersburg 198504, Russia
[3] Recourse Center “Nanohotonics”, St Petersburg State University, Ulyanovskaya 1, Petrodvorets, 198504, St Petersburg, Russia

Abstract. Low-temperature reflection spectra of the high-quality InGaAs/GaAs MBE-grown heterostructures are studied. Parameters of the ground state for excitons with the light and heavy holes are determined using a model analysis.

Introduction

The progress in molecular beam epitaxy (MBE) technology allows one to grow semiconductor heterostructures of exceptional quality widely used in various applications, e.g., light-emitting diodes and semiconductor lasers [1–3]. The high quality of MBE structures requires precise methods of their characterization. The study of the dielectric response of structures in the spectral region of exciton resonances allows for quantitative control of the electronic properties of the heterostructure. In particular, the analysis of the amplitude, profile and half-width of exciton lines in the reflection spectra provides information about the magnitude of radiative and non-radiative broadenings. This information is important for further development of the growth technology for such structures.

1. Experiment

We study two types high-qualityInGaAs/GaAs heterostructures with narrow InGaAs quantum wells (QW) grown by MBE.

Structure P552 contains the narrow ($L = 2$ nm) and wide ($L = 100$ nm) QWs. Parameters of all layers in the structure are: substrate GaAs:Si, buffer layer GaAs–1100 nm, QW $In_xGa_{1-x}As$ ($x = 0.02-0.025$) — 2 nm, barrier layer GaAs — 130 nm, QW $In_xGa_{1-x}As$ ($x = 0.02-0.025$) — 100 nm, cap layer GaAs — 70 nm.

Structure P562 is the Bragg grating that is contained 10 thin QWs separated by thick barrier layers so than the QWs are in the antinodes of the light wave. The layer parameter are: substrate GaAs:Si, buffer layer GaAs — 900 nm, ten QWs $In_xGa_{1-x}As$ ($x = 0.02-0.025$) — 3 nm, barrier layers GaAs between the QWs — 116 nm, cap layer GaAs — 116 nm.

Reflection spectra were measured using a standard optical scheme at the Brewster angle and the sample temperature $T = 8$ K [4]. The spectral region in the vicinity of the lowest exciton states in the narrow QWs was detected. Examples of the spectra are shown in Figs. 1 and 2.

2. Modeling and results

A standard model of resonant optical response of excitons in QWs is used [5]. The reflection coefficient is given by expression:

$$R_m(\omega) = \left| \frac{r_s(\theta_{\text{ext}}, \omega) + \sum_j^m r_{xj}(\omega) e^{2i\phi_{\theta j}}}{1 + r_s(\theta_{\text{ext}}, \omega) \sum_j^m r_{xj}(\omega) e^{2i\phi_{\theta j}}} \right|^2 . \quad (1)$$

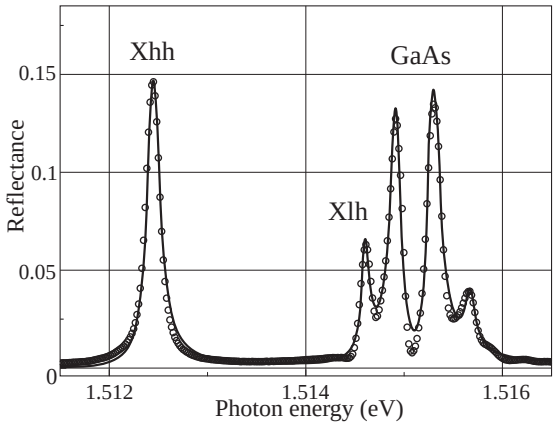

Fig. 1. Reflectance spectrum of structure P552 with the 100-nm and 2-nm (In,Ga)As/GaAs QWs measured at the Brewster angle, $\theta_{\text{ext}} = 75\ ^\circ$. The solid line shows the fit by Eqs. (1) and (2).

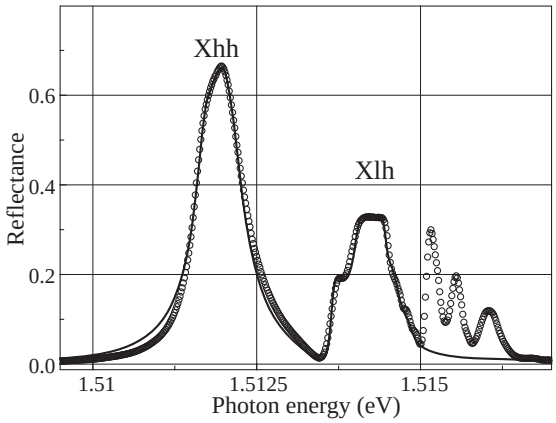

Fig. 2. Reflectance spectrum of structure P562 with ten (In,Ga)As/GaAs QWs of width 3 nm measured at the Brewster angle, $\theta_{rmext} = 75\ ^\circ$. The solid line shows the fit by Eqs. (1) and (2).

with an amplitude reflection coefficiente

$$r_x(\omega) = \frac{i\Gamma_0 \cos(\theta)}{(\omega_0 - \omega) - i(\Gamma_0 \cos(\theta) + \Gamma)}. \qquad (2)$$

where ω_0 is the exciton frequency, Γ_0 and Γ are the radiative and nonradiative decay rates of the excitons. Respective values of the radiative broadenings, $\hbar\Gamma_0$, are taken close to that obtained in the microscopic modeling in Ref. [6], $\hbar\Gamma_0 = 30$ μeV, for such QW. For the Bragg structure P562 with ten QWs, it was taken into account that the total value of radiative broadening for the heavy and light hole exciton resonances should be $10, \hbar\Gamma_0$.

Figure 1 compares the experimental and theoretical light reflection spectra for the sample P552. We should note that the modeling almost perfectly reproduces main features of the experimental spectrum. There are small deviations of the theoretical spectrum at the wings of the lowest resonance and between the GaAs resonances at energy $E \approx 1.515$ eV. The faster decay of the wings of exciton resonances observed experimentally indicates some contribution of the inhomogeneous broadening, which cannot be described by the Lorentz-like theoretical contours. The obtained fit parameters corresponding to the theoretical reflectance are given in Table 1.

Table 1. Exciton parametrs for structure P552.

exciton	E_x(eV)	$\hbar\Gamma_0(\mu$eV)	$\hbar\Gamma(\mu$eV)
Xhh	1.51244	30.4	51.4
Xlh	1.51460	8.6	41.1
GaAs	1.51492	21.9	47.9
barrier	1.51529	25.2	51.4
cap	1.51567	5.81	55.3

Figure 2 compares the experimental and theoretical reflectance spectra for sample P562 with the Bragg set of the QWs. Only the heavy-hole and light-hole exciton bands are modeled. The spectral width the bands is considerably larger than those for sample P552. The large width indicates that the QWs in the Bragg structure are slightly different. This is caused by some instability of the technological parameters during the long MBE growth process of thick structures. The light-hole excitons are particularly sensitive to this instability because their energies are very close to the energy of barrier excitons. The best fit parameters corresponding to the theoretical reflectance are given in Table 2.

In conclusion, exciton spectra of two high-quality heterostructures with InGaAs/GaAs quantum wells are experimentally studied and modeled. Valuable parameters of the exciton resonances, such as the energies and the radiative broadenings are obtained. The small values of $\hbar\Gamma < 100$ μeV confirm the high quality of studied samples.

Acknowledgements

This work is supported by the Russian Foundation For Basic Research, grants No. 19-02-00576a. The authors acknowledge Saint Petersburg State University for a research Grant No. 51125686. The authors thank Recourse Center "Nanophotonics" for the heterostructure studied in the present work.

Table 2. Exciton parametrs for structure P562.

exciton	E_x(eV)	$\hbar\Gamma_0(\mu$eV)	$\hbar\Gamma(\mu$eV)
Xhh	1.51177	29	136
Xhh	1.51197	271	72
Xlh	1.51365	36	80
Xlh	1.51409	24	96
Xlh	1.51419	12	90
Xlh	1.51428	12	86
Xlh	1.51437	12	90
Xlh	1.51443	12	84
Xlh	1.51462	11.9	87

References

[1] *Molecular Beam Epitaxy: From Research to Mass Production*, Ed. by Mohamed Henini (Elsevier Inc., Amsterdam, 744 p., 2013).

[2] J. Faist, *Quantum Cascade Lasers* (Oxford University, 307 p., 2005).

[3] Q. Lu and M. Razeghi, *Photonics* **3**, 42 (2016).

[4] S.V. Poltavtsev, Yu.P. Efimov, Yu.K. Dolgikh, *et al*, *Sol. St. Commun.* **199**, 47–51 (2014).

[5] E.L. Ivchenko, *Optical Spectroscopy of Semiconductor Nanostructures* (Alpha Science, Harrow) 427, 2005.

[6] E.S. Khramtsov, P.A. Belov *et al*, *J. Appl. Phys.* **119**, 184301 (2016).

28th Int. Symp. "Nanostructures: Physics and Technology"
Minsk, Belarus, September 2020

Modeling of exciton exchange interaction in GaAs/AlGaAs quantum wells

E.S. Khramtsov, *B.F. Gribakin*, A.V. Trifonov, and I.V. Ignatiev

Spin Optics Laboratory, St Petersburg State University, Ulyanovskaya 1, Petrodvorets, 198504, St Petersburg, Russia

Abstract. In this work, we study the exchange interactions between two excitons in the GaAs/AlGaAs quantum wells of various widths. We numerically solved the Schrödinger equation for an exciton in a quantum well to build the two-exciton wave functions and to calculate the exchange integral. The results suggest that the strongest interactions between excitons occur in the quantum wells of widths of about 40–50 nm, with the exchange energy being of about of 9 μeV for an exciton density of 1 μm^2.

Introduction

Optical nonlinearities in semiconductor structures give rise to various phenomena such as photon blockade and photon crystallization [1]. These nonlinearities allow the photons to interact, thus making the concept of optical computations possible. The nonlinearity can arise at sufficiently high exciton densities due to the exciton-exciton interactions. However, the magnitude of the interactions must be known with reasonable precision in order to estimate the required exciton densities.

Two main exciton-exciton interactions exist in a two-exciton system: the Coulomb interaction and different variants of the exchange interaction. In quantum wells (QWs), the exchange interaction is expected to be considerably stronger than the Coulomb one [2]. In present work, we study the exchange interaction between two excitons in the GaAs QWs of various widths. For simplicity, we assume the interacting excitons to be in the same spin states. This is a typically realized in experiments when the excitons are resonantly created by the circularly polarized light. We compare our QW data to the results obtained by Ciuti *et al.* [2] for the 2D excitons and to the case of excitons in the bulk GaAs. The results suggest that the strongest interactions between excitons occur in QWs of widths of about 40 nm.

1. Basic equations

The quantities under study are the energy contributions to the exchange interaction, $J^{xx}_{e-e}n$ and $J^{xx}_{h-h}n$, caused by the electron-electron (*e*-*e*) or hole-hole (*h*-*h*) exchange between two excitons in a QW. Here n is the exciton concentration. The simultaneous exchange by electrons and holes results in a much smaller contribution [2], therefore it is not considered here. As shown by Ciuti *et al.* [2], the exchange by electrons and by holes gives rise to the same exchange energy, so the total energy of the exchange interaction is $J^{xx}n = 2J^{xx}_{e-e}n$, where the exchange constant J^{xx} is determined by expression:

$$\begin{aligned} J^{xx} &= -2S_n \int\cdots\int \Psi^*(\mathbf{r}_e,\mathbf{r}_h)\Psi^*(\mathbf{r}_{e'},\mathbf{r}_{h'}) \\ &\times V_I(\mathbf{r}_{e'},\mathbf{r}_h,\mathbf{r}_e,\mathbf{r}_{h'})\Psi^*(\mathbf{r}_{e'},\mathbf{r}_h) \\ &\times \Psi^*(\mathbf{r}_e,\mathbf{r}_{h'})\, d^3\mathbf{r_e} d^3\mathbf{r_h} d^3\mathbf{r}'_\mathbf{e} d^3\mathbf{r}'_\mathbf{h}. \end{aligned}$$

Here $S_n = 1/n$ is the area occupied by a single exciton, $\Psi^*(\mathbf{r}_e,\mathbf{r}_h)$ is the wave function of the exciton in the QW, and V_I is the interaction potential given by

$$\begin{aligned} V_I(\mathbf{r}_{e'},\mathbf{r}_h,\mathbf{r}_e,\mathbf{r}_{h'}) &= V(|\mathbf{r}_e-\mathbf{r}'_e|)+V(|\mathbf{r}_h-\mathbf{r}'_h|) \\ &-V(|\mathbf{r}_e-\mathbf{r}'_h|)-V(|\mathbf{r}_h-\mathbf{r}'_e|). \end{aligned}$$

Here $V(r) = e^2/(\varepsilon r)$, vectors $\mathbf{r}_e$, $\mathbf{r}_h$ determine coordinates of the electron and the hole in the exciton, and ε is the dielectric constant of the medium.

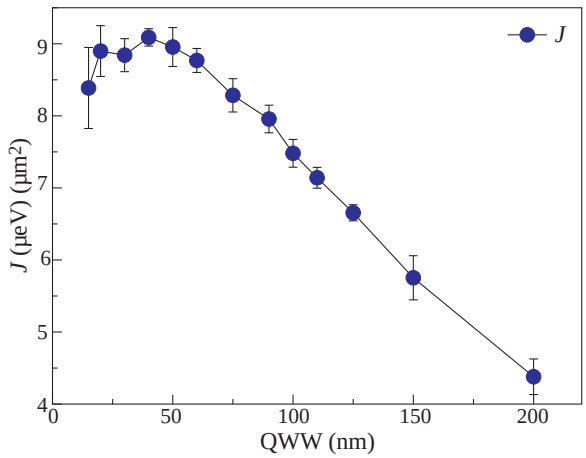

Fig. 1. Dependence of the exchange constant on the QW width.

The method of the numerical solution of the Schrödinger equation for a heavy-hole exciton in a GaAs QW is described in Refs. [3,4]. The cylindrical symmetry of the problem is considered and the degeneration of the valence band in the GaAs crystal is neglected. These approximations are well justified for relatively narrow QWs in which the degeneracy is removed because of different quantum confinement energies for the heavy-hole and light-hole excitons. In the wide QWs, the degeneracy can be removed by a build-in or external stress of the structure. Material parameters of GaAs and $Al_xGa_{1-x}As$ is taken from Ref. [3]. The aluminum concentration in the barrier layers, $x = 0.3$, is chosen as it is frequently used in experimental studies.

The 12-dimensional exchange integral (1) is calculated using a simple Monte Carlo method. A pseudorandom number generator was used to generate coordinates of electrons and holes in a large enough three-dimensional region where the exciton wave functions are noticeably nonzero. Then the expression under the integral is calculated and accumulated. Typically 10^{10} random coordinates have been used to obtain the integral with reasonable accuracy for each QW width.

Figure 1 shows the QW width dependence of the exchange

constant obtained in the calculations. As seen the exchange constant has a maximum for the QW width range 20–60 nm, and then it slowly decreases with the QW width increase. The decrease can be qualitatively explained by the fact that the average distance between the interacting excitons increases when the QW width becomes larger than the effective diameter ($\approx 2a_B$ with $a_B = 14$ nm for GaAs) of the excitons. More quantitative approximation of the dependence as well as the value of the exchange constant for the limiting case of the bulk GaAs will be reported in the conference presentation. The comparison with results obtained in Ref. [2] will be also done.

Acknowledgement

This work is supported by the Russian Science Foundation, grant No. 19-72-20039. The calculations were carried out using the facilities of the SPbU Resource Center Computational Center of SPbU.

References

[1] I. Carusotto and C. Ciuti, Quantum fluids of light, *Rev. Mod. Phys.* **85**, 299 (2013).
[2] C. Ciuti, V. Savona, C. Piermarocchi, A. Quattropani, and P. Schwendimann, *Phys. Rev. B* **58**, 7926 (1998).
[3] E.S. Khramtsov, P.A. Belov, P.S. Grigoryev, *et al*, *J. Appl. Phys.* **119**, 184301 (2016).
[4] P.A. Belov, *Phys. E* **112**, 96-108 (2019).

28th Int. Symp. "Nanostructures: Physics and Technology"
Minsk, Belarus, September 2020

Coupling of quantum well excitons to plasmons in one-dimensional metal nanocylinder gratings

A.V. Korotchenkov
Ioffe Institute, 194021, Saint Petersburg, Russia

Abstract. Theory of plasmon-exciton coupling is developed for a metal nanocylinder grating located in the vicinity of a semiconductor quantum well. In dipole approximation, the effective polarizability of cylinders is derived, taking into account generation of quantum-well excitons in the near field of surface plasmons. Given the polarizability, the spectra of reflection and absorption are calculated for metal-semiconductor systems to study the effect of plasmon-exciton interaction. The excitonic response is shown to be enhanced by high-quality plasmons of Ag cylinders, although strong coupling is not attained for realistic nanostructure parameters.

Introduction

Plasmons in metal nanostructures have proved useful in numerous optical applications due to localization of electromagnetic field on nanometer scale. Recently, considerable attention has been drawn to the coupling between excitons in organic molecules and surface plasmons in metal nanoparticles. In such systems hybrid excitations called plasmon-excitons can occur, manifesting themselves in anticrossing in resonant scattering and luminescence spectra, as discussed in the review [1]. Interaction of excitons in solids with plasmons has been studied as well, both in theory [2] and by experiment. An evidence for plasmon-exciton coupling has been obtained for a few metal-semiconductor structures including semiconductor quantum wells (see references in [2]). While numeric simulations were employed to explore the plasmon resonances and match them to the exciton frequencies in particular structures, an elementary model is yet required to estimate the magnitude of coupling effects.

This theoretic paper studies the coupling of quantum-well (QW) excitons and plasmons in metal nanocylinder (NC) grating. Based on electrodynamic model of [2], we consider the near-field interaction between NC plasmons and low-dimensional excitons. As a result, the cylinders are characterized by the resonant effective polarizability, from which the plasmon-exciton coupling strength is obtained. Then, we calculate the reflection and absorption spectra and demonstrate the excitonic features to be enhanced when in resonance with plasmons.

1. Model

A grating of metal NCs is considered, embedded in semiconductor material with background permittivity ε_b in the vicinity of a QW (Fig. 1). The size of NC cross-section, the grating period and the distance between cylinders and QW are assumed to be sub-wavelength. In absense of NCs, two-dimensional excitons cause resonances in the QW reflection coefficient, which for TM-polarized waves with transverse wavenumber $\boldsymbol{\kappa} = \kappa \mathbf{e}_x$ and frequency ω reads

$$r^p_{\mathrm{QW}}(\kappa) = \frac{i\Gamma_{0x}(\kappa)}{\omega_x - \omega - i\Gamma - i\Gamma_{0x}(\kappa)} \qquad (1)$$

Here ω_x is the frequency of the exciton with polarization parallel to $\boldsymbol{\kappa}$, Γ and Γ_{0x} are its non-radiative and radiative damping rates. The latter $\Gamma_{0x} = \omega_{\mathrm{LT}} k_b L$ is expressed in terms of the bulk exciton LT-splitting ω_{LT}, wavenumber $k_b(\kappa) = \sqrt{\varepsilon_b \frac{\omega^2}{c^2} - \kappa^2}$ and a "length" parameter $L = \frac{1}{2}\pi a_B^3 \times \left(\int dz \times \Phi(z) \cos k_b z\right)^2$, where $\Phi(z)$ is the envelope of the exciton ground-state in QW, and a_B is the bulk exciton radius. For "dark" excitons with $\kappa > \sqrt{\varepsilon_b}\frac{\omega}{c}$ that interact with evanescent waves, the parameter Γ_{0x} in Eq. (1) becomes imaginary and provides the shift of the exciton frequency.

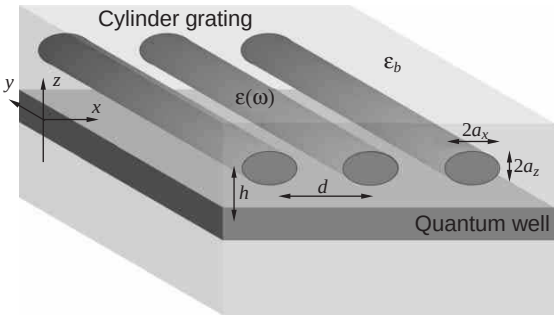

Fig. 1. Schematic of the structure consisting of a metal NC grating and a semiconductor QW. The cross-sections of cylinders are ellipses, their centers positioned in $z = h$ plane at $x_n = n\ d$ with integer n. The QW midplane is $z = 0$.

NCs are treated in dipole approximation and characterized by the quasi-static polarizability $\hat{\chi}^0$. Assuming the cross-section of each NC to be an ellipse with semi-axes a_x and a_z, we obtain the diagonal components

$$\chi^0_{\alpha\alpha} = \frac{a_x a_z}{4} \frac{\varepsilon - \varepsilon_b}{\varepsilon_b + n_\alpha(\varepsilon - \varepsilon_b)} \approx \frac{a_x a_z}{4} \frac{U^2_{0\alpha}}{u^2_{0\alpha} - \omega^2 - i\omega\gamma} \qquad (2)$$

with $\alpha = x, z$. Here $\varepsilon(\omega)$ is the frequency-dependent permittivity of NC material, $n_x = a_z/(a_x + a_z)$ and $n_z = 1 - n_x$ are the depolarization factors. Dipole plasmon resonances in (2) are determined by $\mathrm{Re}\{\varepsilon_b + n_\alpha(\varepsilon - \varepsilon_b)\} = 0$. Given the metal permittivity $\varepsilon(\omega) = \varepsilon_\infty - \omega_p^2/(\omega^2 + i\omega\gamma)$, we derive the plasmon frequencies $u^2_{0\alpha} = \omega_p^2 n_\alpha/(\varepsilon_b + n_\alpha(\varepsilon_\infty - \varepsilon_b))$, whereas γ corresponds to the non-radiative damping of plasmons.

For NC grating near QW an effective polarizability is introduced, taking into account interaction of cylinders both with each other and with their images caused by QW

$$\hat{\chi}(\kappa) = \left[(\hat{\chi}^0)^{-1} - \hat{\Sigma}^0(\kappa) - \hat{\Sigma}^{QW}(\kappa, h)\right]^{-1} \qquad (3)$$

It determines the dipole moments $\mathbf{p}_n = e^{i\kappa x_n}\hat{\chi}(\kappa)\mathrm{E}^0(\kappa; h)$ induced in NCs by the field $\mathrm{E}^0(\kappa; z)e^{i\kappa x}$ that consists of the incident radiation and waves reemitted by QW. The interaction

of NCs with each other in homogeneous medium is considered by the grating sum $\hat{\Sigma}^0$. Its components are readily evaluated for short-period gratings ($\sqrt{\varepsilon_b}\frac{\omega}{c}d \ll 1$) in quasi-static approximation $\Sigma^0_{xx} = -\Sigma^0_{zz} = q^2/6 - \kappa q + \kappa^2$, where $q = \frac{2\pi}{d}$. However, in case of resonant scatterers the retardation must be taken into account, and the sum is evaluated using Ewald method [3], to obtain the radiative damping of grating plasmon $g_{0\alpha}(\kappa)$. This adds to the total damping rate $g_\alpha = \gamma/2 + g_{0\alpha}$, while the real part $\mathrm{Re}\,\Sigma^0_{\alpha\alpha}$ shifts the frequencies $u_\alpha(\kappa)$ of plasmons in absence of QW.

The interaction of NC grating with the QW is consistently taken into account by $\hat{\Sigma}^{QW}$, which is the sum of reflected waves, and its components with $\alpha, \beta = x, z$ are

$$\Sigma^{QW}_{\alpha\beta} = \sum_{m=-\infty}^{+\infty} iqr^p_{\mathrm{QW}}(\kappa_m)e^{2ik_b(\kappa_m)h}\begin{pmatrix} k_b(\kappa_m) & \kappa_m \\ -\kappa_m & \frac{-\kappa_m^2}{k_b(\kappa_m)} \end{pmatrix}, \tag{4}$$

with $\kappa_m = \kappa + mq$. Thus, the radiating plasmon modes with wavenumber $\kappa < \sqrt{\varepsilon_b}\frac{\omega}{c}$ are coupled to the excitons with various κ_m due to the diffraction. For short-period grating the terms with $m \neq 0$ in Eq. (4) correspond to evanescent waves that decay exponentially with the distance h, whereas only the term with $m = 0$ represents the radiated wave.

Given the effective polarizability (3), we have derived the observable quantities affected by plasmon-exciton coupling, such as reflectance or absorption. For example, if the structure is illuminated from the grating side with normally incident light having polarization orthogonal to NC, the power reflection and transmission coefficients are

$$R = \left|r_{\mathrm{QW}} + iqk_b\chi_{xx}\left(e^{-ik_bh} + r_{\mathrm{QW}}e^{ik_bh}\right)^2\right|^2, \tag{5}$$

$$T = \left|t_{\mathrm{QW}} + iqk_b\chi_{xx}t_{\mathrm{QW}}\left(e^{-ik_bh} + r_{\mathrm{QW}}e^{ik_bh}\right)\right|^2, \tag{6}$$

and the absorption is $A = 1 - R - T$. Here $t_{\mathrm{QW}} = 1 + r_{\mathrm{QW}}$ is the QW transmission coefficient, and the wavenumber k_b, reflection r_{QW} and polarizability χ_{xx} are taken at $\kappa = 0$.

2. Results and discussion

We have considered different metal-semiconductor systems and demonstrate the results for silver NC and GaAs QW which provide the lowest non-radiative damping of plasmon and exciton. The reflection $R(\omega)$ and absorption spectra $A(\omega)$ calculated from Eqs. (5-6) are plotted in Fig. 2. When the ratio $\eta = a_z/a_x$ is adjusted so that plasmon frequency u_x coincides with the frequency of exciton ω_x, the reflection exhibits a narrow dip within a broad plasmon-related peak (spectrum 2 in Fig. 2a). Then, as the shape of NC is varied and plasmon resonance is detuned from the exciton, lesser exciton-related peak begins to split off (spectra 1,3) and eventually (for $u_x \gg \omega_x$) is defined by QW reflection $\left|r_{\mathrm{QW}}\right|^2$ (spectrum 4). This picture is quite typical of coupled resonances. At the same time in absorption (Fig. 2b), the less pronounced dip appears in the resonant spectrum 2 for $u_x = \omega_x$, and the magnitude of the exciton peak is the same for spectra 1,3 and 4, of which the latter is essentially the QW absorption $1 - \left|r_{\mathrm{QW}}\right|^2 - \left|t_{\mathrm{QW}}\right|^2$.

To interpret the spectra, we highlight the plasmon and exciton resonances in χ_{xx} (3) and reduce Eqs. (5-6) to

$$R = \left|r_{\mathrm{PE}}e^{-2ik_bh} + \frac{r_{\mathrm{QW}}t^2_{\mathrm{PE}}}{1 - r_{\mathrm{PE}}r_{\mathrm{QW}}e^{2ik_bh}}\right|^2 \tag{7}$$

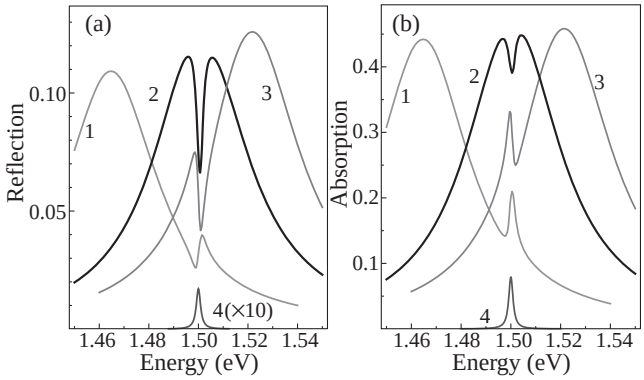

Fig. 2. (a) reflectance spectra $R(\omega)$ and (b) — absorption spectra $A(\omega)$ of silver NC grating near the GaAs/AlGaAs QW. Calculated from Eqs. (5-6) with the exciton energy $\hbar\omega_x = 1.50$eV, damping $\hbar\Gamma = 1$ meV, and different plasmon energies $\hbar u_x$ for $\eta = 0.345$ (1), 0.365 (2, $u_x = \omega_x$) and 0.375 (3) with structure parameters $a_x = 3$nm, $d = 60$ nm and $h = 6$ nm. Spectra 4 show the reflection and absorption of the QW in absence of NCs.

$$T = \left|\frac{t_{\mathrm{QW}}t_{\mathrm{PE}}}{1 - r_{\mathrm{PE}}r_{\mathrm{QW}}e^{2ik_bh}}\right|^2 \tag{8}$$

These are the reflection and transmission of a bilayer, where

$$r_{\mathrm{PE}}(\omega) \approx \frac{ig_{0x}(\omega_x - \omega - i\Gamma)}{(u_x - \omega - ig_x)(\omega_x - \omega - i\Gamma) - \Delta^2/4} \tag{9}$$

and $t_{\mathrm{PE}} = 1 + r_{\mathrm{PE}}$ are attributed to the NC plasmons coupled to "dark" excitons of the QW. If the contribution of excitons with $\kappa = 0$ is weak, $\left|r_{\mathrm{QW}}\right| \approx \Gamma_{0x}/\Gamma \ll 1$, the reflection spectra are governed by "plasmon-exciton" reflection $r_{\mathrm{PE}}(\omega)$, and essentially by the coupling strength Δ relative to the damping rates g_x and Γ. For the structure discussed above, the estimated value $\hbar\Delta \approx 6.5$ meV exceeds the damping of exciton $\hbar\Gamma = 1$ meV, but is smaller than plasmon damping $\hbar g_x \approx 23$ meV. Then, the dip and the split peak in reflection spectra 1–3 in Fig. 2a result from the resonant feedback of "dark" excitons on externally-driven plasmon in NC grating. Similar features in absorption spectra Fig. 2b are partially obscured by the exciton absorption in QW.

To summarize, this work provides a theory of resonant optical effects in metal-semiconductor nanostructures that consist of a QW and a grating of metal NCs. Plasmon resonances in short-period NC grating are affected by "dark" excitons generated in QW in presence of diffracted evanescent waves. The plasmon-exciton coupling is shown to result in the peak-splitting feature that appears in reflection spectra if the coupling strength exceeds the damping of exciton.

Acknowledgement

This work was supported by the Russian Foundation for Basic Research, project No. 18-02-00668.

References

[1] M. Pelton, S.D. Strom and H. Leng, *Nanoscale* **11**, 14540 (2019).
[2] V.A. Kosobukin, *Solid State Communications* **228**, 43 (2016).
[3] C.M. Linton, *SIAM Rev.* **52**, 630 (2010).

28th Int. Symp. "Nanostructures: Physics and Technology"
Minsk, Belarus, September 2020

Polarization conversion in MoS_2 flakes

L.V. Kotova, A.V. Platonov, A.V. Poshakinskiy, and T.V. Shubina
Ioffe Institute, St Petersburg 194021, Russia

Abstract. We have studied experimentally a series of samples of layered MoS_2 flakes with thicknesses varying from 1 to 10 μm and observed their strong optical anisotropy, which we attribute to the effects on in-plane strain or C-axes fluctuations. This optical anisotropy allows the conversion of the transmitted light polarization from linear to circular with the degree up to 15%.

Introduction

In recent years, researchers have been particularly interested in two-dimensional semiconductor atomically thin materials. In particular, the prospects of creating van der Waals heterostructures are associated with such systems [1]. The most striking representative of two-dimensional semiconductors is graphene, a monolayer of carbon atoms located at the sites of the hexagonal lattice. The electrical, transport, and optical properties of graphene have been actively studied for over a decade. Another well-known example of a two-dimensional material is a hexagonal boron nitride monolayer. In recent years, the family of two-dimensional semiconductors has been replenished with monomolecular layers of transition metal dichalcogenides: MoS_2, $MoSe_2$, WS_2, and WSe_2, as well as some tellurium-based compounds.

Monolayers of transition metal dichalcogenides occupy a special place in the series of two-dimensional semiconductors. Unlike graphene, MoS_2 has a pronounced band gap; the uniqueness of its band structure is manifested in the fact that with increasing thickness the band gap decreases from $\sim$1.8 eV in a monolayer (direct gap transition) to $\sim$1.3 eV in a bulk sample (indirect transitions). This allows the use of thin MoS_2 films in light emitting diodes [2], phototransistors [3] and solar cells [4]. This makes compounds like MoS_2 particularly attractive for studying optical effects. The optical properties of atomically thin semiconductors based on monolayers of transition metal dichalcogenides are mainly due to excitons, the binding energy of which reaches hundreds of meV, and the radiation attenuation time is less than picoseconds [5]. The optical properties of these materials are controlled by excitons, electron-hole pairs bound by the Coulomb interaction [6].

Our work is aimed at the experimental study of the polarization properties of transition metal dichalcogenides, specifically polarization properties of MoS_2 flakes.

Content part

To quantify the optical properties of the films, we have studied how the polarization of the transmitted light depends on the polarization of the incident light. We measured polarization of the light transmitted trough different samples of MoS_2 multilayer films with a thickness of 1 to 10 μm. Flakes were made by exfoliation from bulk high quality MoS_2 cristall. The measurements were performed at room temperature.

The incident light from a halogen lamp was linearly polarized. We studied the dependencies of the transmitted light polarization state on the orientation of the incidence plane relative to the crystallographic axes. Spectral dependencies of the transmitted light intensity $I(\omega)$ were registered by a CCD detector conjugated to a monochromator. The sample orientation dependencies have been measured to obtain full set of the Stokes parameters given in the following form:

$$P_{\rm circ} = \frac{I_{\sigma_+} - I_{\sigma_-}}{I_{\sigma_+} + I_{\sigma_-}}, \quad \tilde{P}_{\rm lin} = \frac{\tilde{I}_1 - \tilde{I}_2}{\tilde{I}_1 + \tilde{I}_2}, \quad P_{\rm lin} = \frac{I_\perp - I_\parallel}{I_\perp + I_\parallel}. \quad (1)$$

In this way three Stokes parameters $P_{\rm lin}$, $\tilde{P}_{\rm lin}$ and $P_{\rm circ}$ have been considered for analysis. This approach has been used recently to study the optical activity of QWs [7].

It was found that the intensity of transmitted light that is component cross polarized to the incident light reaches maximum when the incident light is polarized along a certain axis. The circular polarization degree of the transmitted light $P_{\rm circ}$ is also nonzero. It can reach 15% and changes sign when the incident light polarization is rotated by 90°, see Fig. 1. The Stokes parameter $\tilde{P}_{\rm lin}$ corresponding to the linear polarization degree in the axes rotated by $\pm$45° relative to the incidence plane is small (less 2%). The above effects are present in a wide spectral range and we attribute them to the presence of some in-plane stress or shear deformation that lead to linear birefringence.

On top of this background anisotropy, we observed a smaller effect that is present only in the range from 1.8 to 2.1 eV, which corresponds to A and B excitons. The corresponding conversion degree does not exceed 1.5%. The effect is characterized by the different symmetry and we attribute it to a anisotropy arising due to the particular stacking of the layers inside the film.

X-ray studies of the samples were carried out. It was confirmed that the structure of the samples has the corresponding

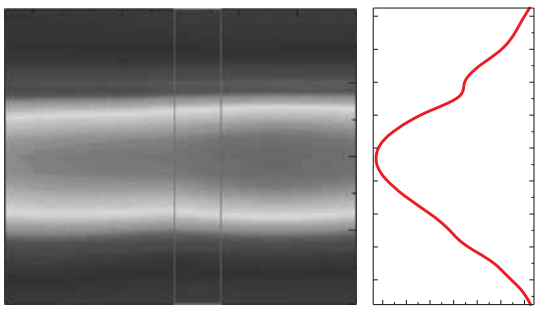

Fig. 1. Sample orientation dependencies of polarization degrees of transmitted light: spectral dependency image of the P_{circ} parameter (a) and polarization amplitude P_{circ} profile (b). Sample was rotated 180 degrees, the second half had similar character as it should be.

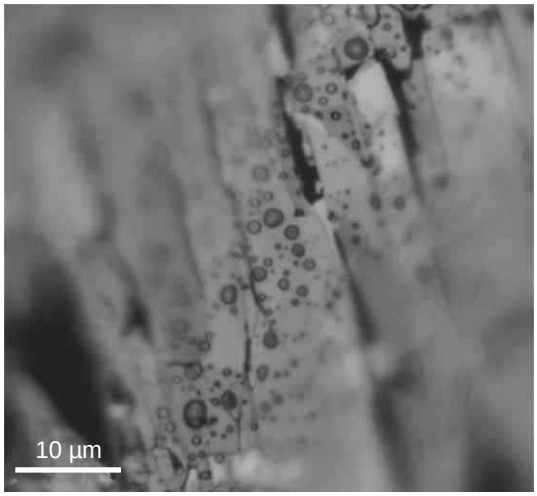

Fig. 2. MoS_2 flake's image with bright-field microscopy made by Nikon industrial microscope ECLIPSE LV150.

crystal structure of MoS_2. The presence of slight C-axis deviations in the samples was established. C-axes fluctuations could lead to stress and strain in the layered MoS_2 flakes.

We studied our different samples of MoS_2 multilayer films with a thickness of 1 to 10 μm by polarization microscopy for characterization. Measurements were performed on Nikon industrial microscope ECLIPSE LV150. Image magnification was 5000 times. For thin samples the presence of distinguished directions was discovered with a decrease in thickness by the exfoliation method. For example, Fig. 2 1μm thick MoS_2 flake. In the test sample noticeable distinguished directions are observed. Carrying out the analysis of the obtained data and sample orientation dependences, it was found that the maximum signal in the region of exciton resonances corresponds to these distinguished directions. Thus, the preparation of samples by exfoliating can lead to a certain laying of layers, which contributes to the appearance of anisotropy.

Conclusion

In an experimental study using a polarization spectroscopy method for a series of samples of MoS_2 multilayer films with a thickness of 1 to 10 μm, strong optical anisotropy was detected, which leads to the conversion of transmitted light polarization from linear to circular with a degree of up to 15%. These effects are present in a wide spectral range, and are associated with the presence of a certain strain in the plane, which leads to linear birefringence. In addition to this background anisotropy, a smaller effect is observed, which is present only in the range from 1.8 to 2.1 eV, which corresponds to A and B excitons. The corresponding degree of conversion does not exceed 1.5%. The effect is characterized by different symmetries and arises due to the special laying of layers inside the film.

Acknowledgements

The support from the Russian Science Foundation (project 19-12-00273) is gratefully acknowledged. Optical measurements was supported by program no. 5 "Photonic technologies in sensing inhomogeneous media and biological objects" of the Presidium of RAS. We thank M.A. Yagovkina for X-ray measurements. The sample characterizations were performed using equipment owned by the Joint Research Center "Material science and characterization in advanced technology" (Ioffe Institute, St Petersburg, Russia).

References

[1] A.K. Geim and I.V. Grigorieva, *Nature* **499**, 419–425 (2013).
[2] R.S. Sundaram, M. Engel, A. Lombardo *et al*, *Nano Lett.* **13**, 1416–1421 (2013).
[3] W. Zhang, J.K. Huang, C.H. Chen *et al*, *Adv. Mater.* **25**, 3456–3461 (2013).
[4] S. Mariyappan, C.A. Durcan, Y. Bin, *Nanoscale* **4**, 7399–7405 (2012).
[5] M.V. Durnev, M.M. Glazov, *UFN* **188**, 913 (2018).
[6] G. Wang, A. Chernikov, M.M. Glazov *et al*, *Rev. Mod. Phys.* **90**, 021001 (2018).
[7] L.V. Kotova, A.V. Platonov, V.N. Kats *et al*, *Phys. Rev. B* **94**, 165309 (2016).

28th Int. Symp. "Nanostructures: Physics and Technology"
Minsk, Belarus, September 2020

Band offsets in a shallow quantum well probed by exciton spectroscopy

A.S. Kurdyubov[1], B.F. Gribakin[1], A.V. Trifonov[1], Yu.P. Efimov[2], S.A. Eliseev[2], V.A. Lovtcius[2], P.Yu. Shapochkin[2], and I.V. Ignatiev[1]

[1] Spin Optics Laboratory, St Petersburg State University, 1 Ul'anovskaya str., Peterhof, St Petersburg 198504, Russia

[2] Recourse Center for Nanofabrication of Photoactive Materials, St Petersburg State University, 1 Ul'anovskaya str., Peterhof, St Petersburg 198504, Russia

Abstract. The conduction and valence band offsets in the shallow GaAs quantum well are experimentally studied by the exciton spectroscopy and dynamics.

Introduction

The high quality of GaA-based heterostructures currently achieved requires precise methods for their experimental and theoretical study. In several recent papers, we reported on the precise experimental study of exciton states in quantum wells (QWs) by reflectance spectroscopy and in the pump-probe experiments with the spectral resolution [1–3]. The theoretical analysis of these results has been performed in the framework of microscopic models of exciton states developed in the number of works [2,4,5]. Excellent agreement between the experiment and the theory has been achieved by appropriate choice of the model parameters.

Some of the parameters, e.g., the electron effective mass, are well known now with good accuracy. Other parameters, such as the hole effective masses and the band offsets, need further clarification. For deep QWs, when the quantization energy of carriers and excitons is much smaller than the discontinuities of the valence and conduction bands (the band offsets) of the QW and barrier layers, the precise values of the offsets are not so important for theoretical modeling. The situation is different for the shallow QWs. In the present work, we demonstrate how the band offsets in the shallow GaAs/$Al_{0.03}Ga_{0.97}As$ QW can be determined from the study of exciton states in the QW.

1. CW experiments

We study a high quality heterostructure with the 14-nm GaAs QW grown by the molecular beam epitaxy. The structure quality is verified by the reflectance spectra (see Fig. 1), in which no noticeable inhomogeneous broadening of exciton resonances is observed. The resonances are well fitted by the standard expressions [1,4,6]. The amplitude reflection from the QW layer is described by expression:

$$r_{\mathrm{QW}} = \frac{i\Gamma_0}{\omega_0 - \omega - i(\Gamma_0 + \Gamma)}, \qquad (1)$$

where ω_0 is the exciton frequency, $\hbar\Gamma_0$ and $\hbar\Gamma$ are the radiative and nonradiative broadenings of the resonance. Taking into account the amplitude reflection from sample surface, r_{01}, the reflection from the sample is:

$$R(\omega) = \left| \frac{r_{01} + r_{\mathrm{QW}} e^{2i\phi}}{1 + r_{01} r_{\mathrm{QW}} e^{2i\phi}} \right|^2. \qquad (2)$$

Here 2ϕ is the phase shift between the light waves reflected from the QW and the sample surface.

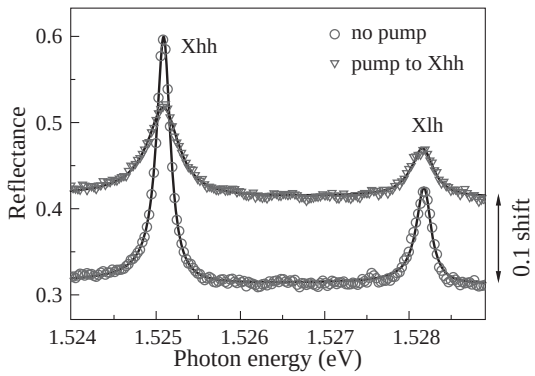

Fig. 1. Reflectance spectra measured with no CW excitation (circles) and in the presence of additional CW illumination into the Xhh resonance (triangles). The second spectrum is shifted by 0.1 for the clarity of presentation. Solid curves are the fits by Eqs. 1,2.

The excellent correspondence of the fit curve to the experiment allows us to reliably determine all fitting parameters. The magnitude of the nonradiative broadening $\hbar\Gamma$ is of particular interest for the present study. It is governed by various scattering processes like the exciton-phonon, exciton-exciton, and exciton-carrier scattering. All these processes can be controlled by the experimental conditions.

Figure 1 shows the reflectance spectrum measured in the presence of a monochromatic continuous wave (CW) excitation into the heavy-hole exciton transition. As seen this excitation gives rise to considerable broadening of the exciton resonances. This is a clear demonstration of the exciton-exciton scattering, which is increased due to resonant light absorption and generation of excitons by the CW excitation. So, the nonradiative broadening is a good test for the absorption.

Fig. 2 shows the spectral dependence of the broadening when the CW excitation is continuously tuned in a broad spectral range, while keeping its intensity constant. We refer to this dependence as to the nonradiative broadening excitation (NBE) spectrum. As seen the spectrum displays several resonances superimposed onto a slowly varying background. The main resonances can be easily attributed to the heavy-hole (Xhh) and light-hole (Xlh) excitons in the QW and to the exciton in the barrier layer (Xb).

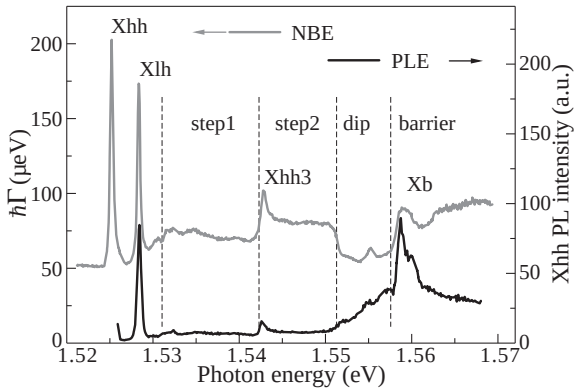

Fig. 2. NBE (gray curve) and PLE (black curve) spectra. The vertical dashed lines separate spectral regions discussed in the text.

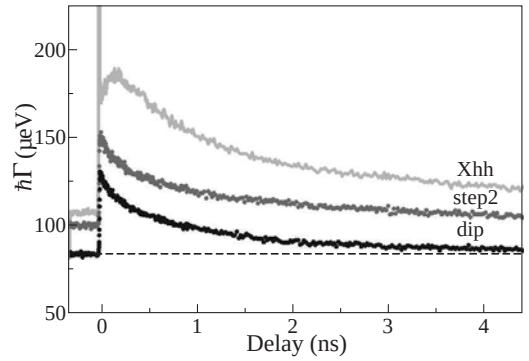

Fig. 3. Delay dependence of the nonradiative broadening of the Xhh resonance under excitation by the pump pulses into the Xhh exciton transition (light-gray curve), the region "step2" (gray points), and the "dip" (black points). The dashed line shows the broadening with no pump.

To identify other features in the NBE spectrum, we, first, measured the photoluminescence excitation (PLE) spectrum with the detection of PL intensity of the Xhh exciton (see black curve in Fig 2). As seen, the main features, namely Xlh, Xhh3, Xb, as well as step1 and step2, are reproduced in the PLE spectrum. Their identification can be done by means of the theoretical modeling of exciton states in the QW. The region "step1" can be attributed to the 2D density of states of free electrons and holes. The low boundary of this region is above the Xhh exciton energy by the exciton Rydberg, $R_X \approx 7$ meV in this QW. The feature "Xhh3" is presumably the third quantum-confined state of the heavy-hole exciton. We should note that the second Xhh state is almost invisible (its expected energy is of 1.5325 eV), probably, because of odd symmetry of its envelope function. The "step2" region is the 2D density of state of free carriers coupled to the second quantum-confined heavy-hole state.

2. Exciton dynamics

There is a drastic difference in the NBE and PLE spectra in the region marked "dip" in Fig. 2. To understand this difference, we have studied the exciton dynamics in the pump-probe experiments. In these experiments, the spectrally narrow pump pulses, $\delta E_{\text{pump}} \approx 2$ meV, excited the sample at a selected spectral point. The spectrally broad probe pulses, $\delta E_{\text{probe}} \approx 17$ meV, delayed in time by τ relative to the pump pulses, were used to detect the total reflection from the sample. The whole set of the spectra measured at different delays was normalized to the probe pulse spectral profile and processed using Eqs. (1,2).

The delay dependencies of the nonradiative broadening of the Xhh resonance thus obtained are shown in Fig. 3 for three spectral points. The dependence $\overline{\hbar}\Gamma(\tau)$ measured at the Xhh excitation reveals a very sharp peak of $\overline{\hbar}\Gamma$ at zero delay, a small increase during the first 300 ps, and a slow decay visible up to the next pump pulse as a pedestal at the negative delay. All these features of the dependence can be understood in terms of scattering of the excitons created by the pump and probe pulses [1]. In particular the long-lived signal is caused by the excitons with large in-plane wave vector forming a nonradiative reservoir.

he delay dependence of $\overline{\hbar}\Gamma$ measured at excitation into the "step2" region reveals similar behavior except that at the small delays. The free electrons and holes created by the pump pulses in the QW at excitation in this spectral region are coupled into excitons populating the nonradiative reservoir.

n contrast to the first two dependencies, the curve measured at the "dip" region has no long-lived component and, correspondingly, no pedestal at the negative delays. This fact as well as the data presented in Fig. 2 allow us to conclude that the "dip" region corresponds to the excitation of electrons or holes into the barrier layers. In other words, the low-energy edge of the "dip", $E_l \approx 1.552$ eV, corresponds to the delocalization of one type of the carriers in the barrier layers. The high-energy edge, $E_h \approx 1.558$ eV, corresponds to the delocalization of both types of the carriers. These values allow us to evaluate the offsets for the conduction and valence bands, $\Delta E_c = 22$ meV and $\Delta E_v = 16$ meV. Their ratio strongly deviates from the ratio 2:1 commonly accepted in literature for the GaAs/AlGaAs heterostructures 6.

n conclusion, we experimentally studied NBE and PLE spectra as well as the exciton dynamics of a heterostructure with the shallow GaAs/AlGaAs 14 nm QW. The obtained results allowed us to determine band offsets of the conduction and valence bands to be 22 meV and 16 meV.

Acknowledgements

This work is supported by the Russian Foundation For Basic Research, grants No. 19-02-00576a, 18-32-00516, and 20-32-70131. The authors thank Recourse Center "Nanophotonics" for the heterostructure studied in the present work.

References

[1] A.V. Trifonov, S.N. Korotan, A.S. Kurdyubov *et al., Phys. Rev. B* **91**, 115307 (2015).

[2] P. Yu. Shapochkin, S. A. Eliseev, V. A. Lovtcius *et al., Phys. Rev. Applied* 12, 034034 (2019).

[3] A.V. Trifonov, E. S. Khramtsov, K. V. Kavokin *et al., Phys. Rev. Lett.* 122, 147401 (2019).

[4] P.S. Grigoryev, A.S. Kurdyubov, M.S. Kuznetsova *et al., Superlatt. Microstr.* **97**, 452–462 (2016).

[5] P. A. Belov, *Phys. E* **112**, 96–108 (2019).

[6] E. L. Ivchenko, *Optical Spectroscopy of Semiconductor Nanostructures* (Alpha Science, Harrow, 2005).

28th Int. Symp. “Nanostructures: Physics and Technology”
Minsk, Belarus, September 2020

Spin-valley dynamics of interlayer excitons in heterobilayers Mo $_x$W$_{1-\ x}$Se$_2$/WSe$_2$

A.D. Liubomirov[1], V.Kravtsov[2] and R.V. Cherbunin[1]

[1] St Petersburg State University, St Petersburg 198504, Russia
[2] ITMO University, Saint Petersburg 197101, Russia

Abstract. We study spin-valley relaxation dynamics in two-dimensional $Mo_xW_{1-x}Se_2/WSe_2$ heterobilayers with different relative Mo/W concentration x in the monolayer alloy. Three types of heterobilayers with $x = 1.00$, 0.50, 0.33 are studied in time-resolved Kerr rotation experiments for different wavelengths and temperatures. The spin-valley relaxation times are found to decrease from ~ 10 nanoseconds for $x = 1.00$ to ~ 50 picoseconds for $x = 0.33$. The observed relaxation times are limited by the recombination of indirect excitons formed in the heterobilayers. Our results demonstrate that spin-valley relaxation in alloy-based van der Waals heterostructures can be controlled via their chemical composition.

Famous two-dimensional crystals of layered transition metal dichalcogenides (TMDC) are very promising materials for valleytronics – a novel approach to information processing based on the valley degree of freedom. Importantly, monolayer TMDC host direct excitons and exhibit valley polarization (at the K/K′ points of the hexagonal Brillouin zone) at room temperature. However, the spin-valley dynamics of excitons in TMDC monolayers is generally too fast for practical applications [1], with typical times on the order of picoseconds. In heterostructures consisting of two different monolayers, the dynamics can be extended up to microseconds [2]. In such heterobilayers interlayer excitons (ILE) are formed and spatial separation of charge carriers (electron and hole are located in different layers) is achieved owing to the specific conduction and valence band alignment between the two monolayers. Therefore, band structure engineering in such systems can provide a means to control the associated spin-valley dynamics [2].

The idea of this investigation is to study the spin-valley dynamics in heterostructures consisting of TMDC monolayers (ML) with different chemical composition. We measure and compare spin-valley relaxation times in heterobilayers (HBL) of $Mo_xW_{1-x}Se_2/WSe_2$ with different relative Mo/W concentrations x of the ML alloy [3,4], for three types of HBLs with $x = 1.00$ 0.50, 0.33.

The dependences of the spin-valley dynamics on the excitation wavelength and temperature for different x are measured via microscopic time-resolved Kerr rotation (TRKR) spectroscopy. We use a degenerate pump-probe technique with Ti:Sapphire laser femtosecond pulses. An angular separation is introduced between the pump and probe pulses for sensitive detection of the weak probe signal focused to a ~ 5 μm size spot on the sample.

The experimental TRKR data were fitted by triexponential decay functions. Examples of fitting curves for 725–730 and 760–765 nm excitation wavelength are shown in Fig. 1. Spin-valley relaxation times were obtained as exponential time decay constants $\tau_{1,2,3}$ used as parameters of the fitting, where τ_3 is the most long-lived time. Relaxation times decrease from several nanoseconds to tens of picoseconds with decreasing x. The temperature dependences of relaxation times $\tau_{1,2,3}$ obtained by fitting the TRKR data show an acceleration of dynamics with increasing temperature from 10 to 100 K (for the sample with $x = 1$ and 720 nm excitation on Fig. 2a). Fig. 2b shows how amplitudes $a_{2,3}$ of the two long-lived components of the signal

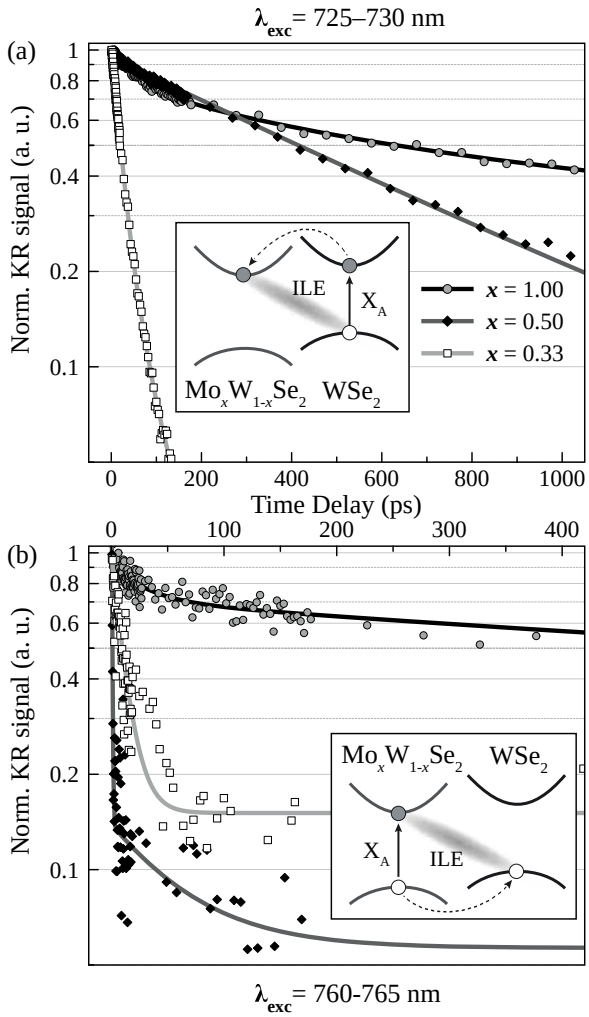

Fig. 1. Normalized Kerr Rotation signal as a function of time delay between pump and probe pulses measured on heterostructure samples with different relative Mo/W concentrations x at 12 K. (a) Excitation and detection wavelength correspond to the monolayer exciton transition in WSe_2 (725–730 nm). (b) Dynamics for the excitation/detection wavelength corresponding to the exciton transition in $MoSe_2$ (760–765 nm). Points are experimental data, lines are fitting curves, insets are schematics of interlayer exciton formation.

depend on the excitation/detection wavelength (for the sample with $x = 1.00$ at 12 K). The maxima of the signal correspond to the exciton/trion resonances in individual $Mo_xW_{1-x}Se_2$ and WSe_2 MLs.

The studied heterobilayers have a type II band alignment, that is the minimum of the conduction band is located in $Mo_xW_{1-x}Se_2$ layer, and the minimum of the valence band is located in WSe_2 layer for studied HBLs. Following photoexcitation, one of the charge carriers very quickly (100 fs) tunnels to the neighbour layer with the minimum (electron to $Mo_xW_{1-x}Se_2$ layer and hole to WSe_2 layer, on Fig. 1). Therefore, the dynamics associated with holes within the interlayer exciton is observed when probing the 720–725nm spectral region in WSe_2, while the dynamics associated with electrons is probed at 760–765nm in $Mo_xW_{1-x}Se_2$.

All the studied samples exhibit a strong TRKR signal on the WSe_2 excitonic resonance at 720–735nm, which means high spin-valley polarization of holes in the ILE (Fig.2b). The signal probed on the $Mo_xW_{1-x}Se_2$ resonance at 760–765nm, which corresponds to the dynamics of electrons, shows an initial fast decay and therefore smaller overall TRKR signal in comparison with the hole spin-valley dynamics (Fig. 2b). In samples with $x = 1.00$, we observe relatively long-lived polarization holes ($\tau_3 \sim 5$ ns) and electrons ($\tau_3 \sim 1$ ns). For HBLs with $x = 0.33$ in the alloy, we observe fast dynamics for both holes and electrons ($\tau_3 \sim 50$ ps) and a similar strength of the initial TRKR signal. However, for samples with $x = 0.50$ we see "medium-lived" spin-valley polarization associated with holes ($\tau_3 \sim 600$ ps) and very fast initial relaxation of the spin-valley polarization associated with electrons (several picoseconds; ten times less than for $x = 0.33$). We note that the measured dynamics may be further influenced by different twisted angles of crystal lattice orientation between two MLs in different samples.

In addition, we do not observe any TRKR signal in the wavelength range corresponding to the ILE photoluminescence (800–900 nm).

In summary, we observe that spin-valley polarization dynamics in $Mo_xW_{1-x}Se_2/WSe_2$ heterobilayers changes with increasing the relative Mo/W concentration x from tens of picosecond for $x = 0.33$ to 10 nanoseconds for $x = 1.00$. The observed dynamics is complex and depends on the tunnelling between the two layers, electron/hole spin-valley depolarization, and interlayer exciton recombination times. Further experiments should consider different twisted angles of the crystal lattice orientation between two MLs in the heterostructure and are currently under way. However, the obtained results already demonstrate the possibility of the control on the polarization dynamics via band engineering in a van der Waals heterostructure using monolayer alloys with different Mo/W concentration ratios.

Acknowledgement

The authors acknowledge Saint Petersburg State University for a research Grant No. 51125686.

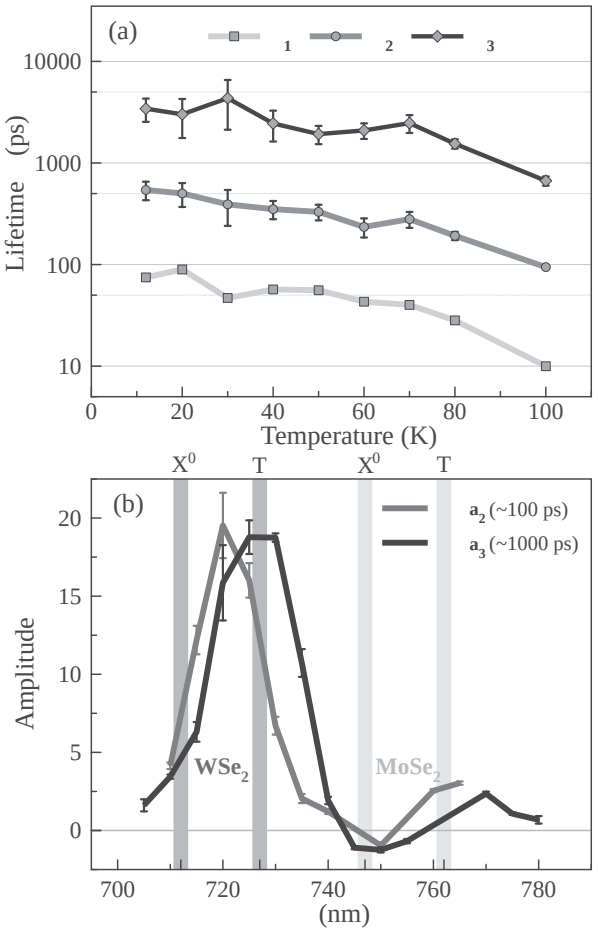

Fig. 2. Dependencies of the fitting parameters τ and a of the tri-exponential function on temperature and wavelength for the sample with $x = 1.00$ ($MoSe_2/WSe_2$). (a) Lifetimes $\tau_{1,2,3}$ for the 720 nm excitation/detection wavelength. (b) Amplitudes of the long-lived signal components $a_{2,3}$ as functions of wavelength at 12 K. X^0, T are exciton, trion resonance positions respectively.

References

[1] C.R. Zhu, K. Zhang, M. Glazov, B. Urbaszek, T. Amand, Z.W. Ji, B.L. Liu, X. Marie, *Phys. Rev. B* **90**, 161302 (2014).

[2] C. Jin, E. Ma, O. Karni, E. Regan, F. Wang and T .Heinz, *Nature Nanotechnology* **13**, 994–1003 (2018).

[3] G. Wang, C. Robert, A. Suslu, *et al*, *Nat Commun* **6**, 10110 (2015).

[4] M. Zhang, *et al*, *Phys.: Condens. Matter* **31**, 505302 (2019).

28th Int. Symp. "Nanostructures: Physics and Technology"
Minsk, Belarus, September 2020

Theoretical modeling of polariton interference in electric field

D.K. Loginov, P.A Belov, I.Ya. Gerlovin, and I.V. Ignatiev

Spin Optics Laboratory, St Petersburg State University, Ulyanovskaya 1, Petrodvorets, 198504, St Petersburg, Russia

Abstract. A theoretical modeling of the interference of polaritonic waves propagating across a quantum well in the presence of a tilted electric field is performed. Constructive and destructive interference patterns are observed at different strengths of the electric field. The role of the in-plane component of the electric field and the linear in wave vector term in the exciton Hamiltonian is discussed.

Introduction

The effect of an electric field on excitons in heterostructures has attracted particular attention for several decades [1–3]. Most of the recent works are mainly devoted to the study of relatively narrow QWs, in which a modification of the relative electron-hole motion in the exciton occurs thus causing the Stark shift of exciton states and inducing a static dipole moment of excitons 4,5.

The electric-field-induced effects in wide QWs are less studied so far. The wide QWs, however, are of a particular interest because they offer an opportunity to study the effect of an electric field on the motion of the exciton as a whole particle. The excitons with large wave vectors, $K \gg q$, where q is the wave vector of light, can be experimentally observed due to their quantum confinement in the wide QWs. In high-quality heterostructures, one can observe many quantum-confined exciton states as resonant features (oscillations) in the reflectance spectra [6,7].

In recent experiments [8], the electroreflectance spectra of a heterostructure with the 120-nm GaAs QW in an external electric field have been measured. Multiple resonant peculiarities (spectral oscillations) related to the quantum-confined exciton states are observed in the spectra. The application of an electric field F tilted at an angle θ to the structure growth axis reduces the oscillation amplitude down to zero at some critical value F_c. However the oscillations appear again when the field increases further. The phase of these oscillations becomes inverted with respect to that for $F < F_c$.

Basic idea of a theoretical model of the observed effect has been proposed in Ref. [8]. The inversion of the phase of spectral oscillations is governed by the linear in exciton wave vector K term of the exciton Hamiltonian induced by the in-plane electric field component. Here, we theoretically show that multiple phase inversion of polariton resonances is possible at the large enough electric field.

1. Model

The model considers the exciton-like and photon-like polaritonic waves. Their dispersions are determined by equation [3, 9]:

$$\varepsilon(\omega, K) = \frac{c^2 K^2}{\omega^2}, \tag{1}$$

where c is the speed of light and ω is the frequency of light creating the polaritons. The dielectric function is described by expression [9]:

$$\varepsilon(\omega, K) = \varepsilon_0 + \frac{\varepsilon_0 \overline{h}\omega_{\mathrm{LT}}(F)}{H(F, K) - \overline{h}\omega + i\overline{h}\Gamma}. \tag{2}$$

Here ε_0 is the background dielectric constant, $\overline{h}\omega_{\mathrm{LT}}$ is the longitudinal-transverse exciton splitting, and $\overline{h}\Gamma$ is the exciton damping rate. Exciton energy $H(F, K)$ obtained from the exciton Hamiltonian is:

$$H(F, K) = E_g - R + \frac{\overline{h}^2 K^2}{2M} + \lambda(F)\zeta K, \tag{3}$$

where R is the interaction energy of electron and hole in the exciton and M is the exciton mass. Factor ζ is determined in Ref. [8].

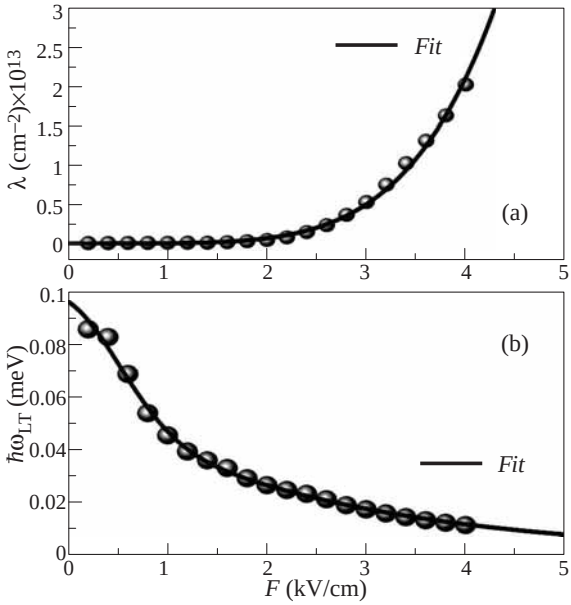

Fig. 1. (a) Electric field dependence of factor $\lambda(F)$ (symbols) calculated by means of Eq. (4). The solid curve is the fit by function $\lambda(F) = cF^5$ with $c = 2.1 \times 10^{10}$ (kV/cm)$^{-5}$ cm^{-2}. (b) Constant $\overline{h}\omega_{\mathrm{LT}}(F)$ as a function of the electric field (symbols). The solid curve is the fit by function $f = 0.036\exp(-1.64F^2) + 0.06\exp(-F/2.4)$.

The dependence of exciton energy on the electric field is controlled by factor $\lambda(F)$,

$$\lambda(F) = \frac{1}{\overline{h}^2}\langle\phi(F, r)|\hat{p}_x^2 - \hat{p}_y^2|\phi(F, r)\rangle = \frac{1}{\overline{h}^2}\left(p_x^2 - p_y^2\right). \tag{4}$$

Here, matrix elements of the momenta of relative electron-hole motion squared, $\hat{p}_x^2$ and $\hat{p}_y^2$, are calculated with the exciton wave function, $\phi(F, r)$. The method of calculation of this function is described in Ref. [8]. Note that $\lambda(F) \neq 0$ only if the electric field has a nonzero in-plane component. Indeed, if

$F_x = 0$, the cylindrical symmetry of the problem is preserved, therefore $p_x^2 = p_y^2$ and $\lambda(F) = 0$ at any F. The constant $\hbar\omega_{\rm LT}(F)$ entering Eq. (2) is calculated in a standard way [9]:

$$\hbar\omega_{\rm LT}(F) = \left(\frac{2eP_1}{E_g}\right)^2 \frac{\pi}{\varepsilon_0} |\phi(F,0)|^2. \qquad (5)$$

Here $\phi(F,0)$ is the wave function taken at the coinciding coordinates of the electron and the hole in the exciton; $P_1 = 10.3 \times 10^{-5}$ meV$\cdot$ cm for the GaAs crystal [10]. The electric field dependencies of $\lambda(F)$ and $\hbar\omega_{\rm LT}(F)$ are shown in Fig. 1. We used angle $\theta = 20^\circ$ in these calculations.

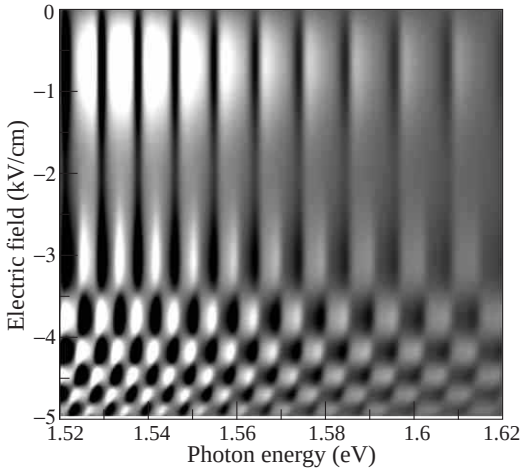

Fig. 2. Two-dimensional plot of the differential reflectance as a function of the photon energy and the applied electric field demonstrating the phase inversion effect for the spectral oscillations.

2. Reflectance spectra

Equations (1,2) as well as the standard Maxwell's boundary conditions (MBC) and the Pekar's additional boundary conditions (ABC) [3,9] at the QW interfaces allow one to obtain the amplitudes of the polaritonic waves propagating in the QW. The MBC and ABC also couple the amplitudes of the incident ($E_{\rm i}$), transmitted ($E_{\rm t}$), and reflected ($E_{\rm r}$) light waves with those of polaritonic waves in the QW. This allows one to calculate the light reflection from a heterostructure with polaritonic resonances, $R(\omega, F) = |E_{\rm r}/E_{\rm i}|^2$.

Figure 2 shows an example of the numerically obtained spectra. The electroreflectance spectra, $dR(\omega, F)/dF$, are calculated to compare them with the experimental results presented in Ref. [8]. As it can be seen from the figure at small electric fields, the spectra show many spectral oscillations related to the quantization of exciton motion across the QW. When the strength of the electric field increases, the oscillation amplitude decreases so that they disappear at some critical field $F_c \approx 3.5$ kV/cm.

This effect is caused by the destructive interference of polaritonic wave propagating across the QW in the forward and backward directions. The exciton-like components of these waves propagate with different wave vectors, $K_\pm = K \pm \Delta K(F)$, because the electric field shifts the excitonic dispersion curve by value: $\Delta K(F) = -\lambda(F)\zeta M/\hbar^2$, as it is seen from Eq. (3). Correspondingly, the phases acquired by the polaritons propagating in the forward and backward directions are: $\varphi_\pm = [K \pm \Delta K(F)]\, L$, where L is the QW width. The photon-like modes are not affected by the electric field and, therefore, they do not contribute to the phase shift difference. When the difference of phases, $\Delta\varphi = \varphi_+ - \varphi_- = \Delta K(F_c)L = \pi$, the interference becomes destructive.

Further increase of the electric field is followed by the constructive or destructive interference of the polaritonic waves at the phase shifts $\Delta\varphi = (n+1)\pi$, where n is integer. Correspondingly, the multiple phase inversion of the resonances can be observed, see Fig. 2. The critical values of the electric field for these phase inversions become closer because of rapid increase of factor $\lambda(F)$ with the field, see Fig. 1(a).

Acknowledgements

This work is supported by the Russian Science Foundation, grant No. 19-72-20039. The calculations were carried out using the facilities of the SPbU Resource Center "Computational Center of SPbU".

References

[1] D.F. Blossey, *Phys. Rev. B* **2**, 3976 (1970).
[2] B.S. Monozon and P. Schmelcher, *Phys. Rev. B* **82**, 205313 (2010).
[3] A.V. Kavokin, J.J. Baumberg, G. Malpuech *et al*, Microcavities (Oxford University, New York, 2017).
[4] L.V. Butov, *Superlattices Microstruct.* **108**, 2 (2017).
[5] S.I. Tsintzos, A. Tzimis, G. Stavrinidis *et al*, *Phys. Rev. Lett.* **121**, 037401 (2018).
[6] V.A. Kiselev, B.S. Razbirin, and I. N.Uraltsev, *Phys. Status Solidi B* **72**, 161 (1975).
[7] E.S. Khramtsov, P.S. Grigoryev, D.K. Loginov *et al*, *Phys. Rev. B* **99**, 035431 (2019).
[8] D.K. Loginov, P.A. Belov, V.G. Davydov *et al*, *Phys. Rev. Res.* (submitted).
[9] E.L. Ivchenko, Optical Spectroscopy of Semiconductor Nanotstructures (Alpha Science, Harrow, 2005).
[10] G. Pikus, V. Maruschak, and A. Titkov, *Fiz. Tekh. Poluprovodn.* **22**, 185 (1988); [*Sov. Phys. Semicond.* **22**, 115 (1988)].

28th Int. Symp. "Nanostructures: Physics and Technology"
Minsk, Belarus, September 2020

Symmetric and asymmetric two-dimensional magnetoexciton superposition states in the conditions of strong perpendicular magnetic field

S.A. Moskalenko[1], I.V. Podlesny[1], I.A. Zubac[1], B.V. Novikov[2]

[1] Institute of Applied Physics, Academiei str. 5, Chisinau, MD-2028 Republic of Moldova
[2] Department of Solid State Physics, Institute of Physics, St Petersburg State University, 1, Ulyanovskaya str., Petrodvorets, 198504 St Petersburg, Russia

Abstract. The properties of the two-dimensional (2D) magnetoexcitons in the GaAs-type quantum wells subjected to the action of a strong perpendicular magnetic field with the binding energy determined by the direct Coulomb electron–hole e–h interaction and with the summary e–h spin projections $F\pm1$ are discussed. Under the influence of the Coulomb exchange electron-hole interaction the new superposition states formed by the magnetoexcitons appear. The symmetric (asymmetric) state is allowed in the case of linear polarization with positive (negative) parity and is forbidden in the case of linear polarization with negative (positive) parity. These two symmetric and asymmetric superposition states revealed the quantum interference effects. The obtained optical results open the possibility to investigate the thermodynamic properties of the 2D Bose gas with Dirac cone dispersion law.

Introduction

The electrons have a simple spin structure with $s_z^e = \pm 1/2$ and the heavy holes are characterized by the full angular momentum projections $j_z^h = \pm 3/2$ or by the effective spin projections $s_z^h = \pm 1/2$. The magnetoexciton states discussed below are characterized by the e–h angular projections $F = s_z^e + j_z^h$ with the four possible values ±1 and ±2. Two of them with $F = \pm1$ are spin allowed in optical quantum transitions giving rise to dipole-active, bright excitons in GaAs quantum wells (QWs), whereas the another two are spin forbidden, forming the dark states. The two dipole-active bright magnetoexciton states with $F = \pm1$ under the influence of the direct Coulomb e–h interaction have the coincident energy levels. Their degeneracy will be removed by the influence of the exchange e–h Coulomb interaction. The description in which way it will take place and the new physical properties arising in these conditions are the main contents of our paper. First of all we will remember the influence of the exchange e–h Coulomb interaction in the case of the Wannier–Mott excitons. So the 1*s* exciton states of the yellow series in Cu_2O crystal with electron and hole band structures characterized by the Γ_6^+ and Γ_7^+ irreducible representations correspondingly of the crystallographic group O_h are forming two energy levels. One of them is a non-degenerate para-exciton level described by the irreducible representation Γ_2^+ and another one is the three-fold degenerate ortho-exciton energy level, the states of which are forming the irreducible representation Γ_5^+ following the product of two band representations $\Gamma_6^+ \times \Gamma_7^+ = \Gamma_2^+ \times \Gamma_5^+$.

In difference on the 3D Cu_2O crystal the 2D GaAs-type quantum wells (QWs) has the 2D crystallographic symmetry group, the irreducible representations of which have maximum only the two-fold degeneracy. The four spin states of the e–h pair are forming one twice degenerate energy level $F = \pm1$ of the dipole-active bright excitons and another one energy level with $F = \pm2$ of the dark excitons, spin forbidden in optical band-to-band transitions. The states with $F = \pm1$ are forming the para- and of the ortho-exciton states with $S_z = 0$ in Cu_2O crystal.

1. The influence of the exchange electron-hole Coulomb interaction in the physics of the two-dimensional magnetoexcitons

The Hamiltonian describing the electron–electron Coulomb interaction is deduced, taking into account the direct and the exchange terms. To this end electron density operator in coordinate representation $\hat{\rho}(\vec{r})$ was generalized. As usual it contained only the square moduli of the periodic parts of the electron Bloch wave functions in the conduction band $|U_c(\vec{r})|^2$ and in the valence band $|U_v(\vec{r})|^2$. They describe the densities of the electron and of the hole electric charges localized inside the lattice unit cells, and give rise to the direct charge–charge Coulomb interaction. Side by side with them we have included also the mixt terms such as $U_c^*(\vec{r})U_v(\vec{r})$ and $U_v^*(\vec{r})U_c(\vec{r})$ with different from zero interband dipole moments $\rho_{c-v} \neq 0$. It happens only in the case of the dipole-active, bright excitons investigated below. The e–h exchange Coulomb interaction looks as the interaction of two dipoles. A new property of the 2D magnetoexciton is the interdependence between the center-of-mass and the relative e–h motions induced by the action of the Lorentz force. This interdependence happens to play an important role promoting to the formation of the Dirac cone dispersion law under the influence of the exchange e–h Coulomb interaction.

The main new results are related with the appearance of the non-parabolic Dirac cone-type dependence of the energy spectrum on the wave vector $|\vec{k}_\parallel|$, as well as with the new type selection rules describing the optical quantum transition from the ground state of the crystal in the bright magnetoexciton states.

2. Results and discussions

The symmetric magnetoexciton state due to the exchange e–h Coulomb interaction acquires a Dirac cone dispersion law in the range of small in-plane wave vectors with the group velocity V_g proportional to the magnetic field strength B, with equal probabilities of the quantum transitions from the ground state of the crystal in both light circular polarizations but with maximum

probability in the Faraday geometry of the light propagation and vanishing probability in the Voigt one. In difference on it, the asymmetric superposition state remains with the usual dispersion law inherited from the bare magnetoexciton states and has a dipole-active quantum transitions in both circular polarizations, indifferent on the direction of the light propagation. When the light is arbitrary propagating in 3D space, the symmetric superposition state is dipole active in the case of the linear polarization vector $\vec{S}_{\vec{k}}$ with the longitudinal projection on the 2D exciton inplane wave vector $\vec{k}_{\parallel}$ and is forbidden in the linear light polarization with the vector $\vec{t}_{\vec{k}}$, which has a transverse projection on $\vec{k}_{\parallel}$.

In the case of the circular polarizations the probability of quantum transition is proportional to $k_z^2/|\vec{k}|^2$, and the probability is different from zero when the incident light has perpendicular projection to the layer. The asymmetric superposition state is dipole active in the linear polarization vector $\vec{t}_{\vec{k}}$ with transverse projection as regards the in-plane exciton wave vector, is forbidden in the $\vec{S}_{\vec{k}}$ polarization vector and does not depend on the light orientation. The case of 2D magnetoexcitons [1] is similar with the quantum transitions in the excitons states of the transition metal dichalcogenides monolayers [2]. This marvelous property was firstly discussed and underlined by the authors of theoretical and experimental investigations published in the Ref. [2].

The both symmetric and asymmetric superposition states with the interference effects in the case of the light with two linear polarizations, which have different parities as regards the inversion of the light wave vector $\vec{k}$ were revealed. The result was obtained by applying the perturbation theory of a degenerate energy level [3]. In such a way the symmetric (asymmetric) state is allowed in the case of linear polarization with positive (negative) parity and is forbidden in the case of linear polarization with negative (positive) parity. The obtained optical results open the possibility to investigate the thermodynamic properties of the 2D Bose gas with Dirac cone dispersion law.

References

[1] S.A. Moskalenko, I.V. Podlesny, I.A. Zubac, and B.V. Novikov, *Solid State Commun.*, **308**, 113714 (2020).

[2] Y. Hongyi, L. Gui-Bin, G. Pu, X. Xiaodong and Y. Wang, *Nature Commun.*, **5** 3876 (2014).

[3] L.D. Landau and E.M. Lifshitz, *Quantum Mechanics Non-Relativistic Theory. Volume 3 of Course of Theoretical Physics*, (Oxford: Pergamon Press) 616 p., 1965.

28th Int. Symp. “Nanostructures: Physics and Technology”
Minsk, Belarus, September 2020

Longitudinal spin dynamics of high-mobility two-dimensional electron gas

V.V. Belykh[1,2], M.V. Kochiev[2], D.N. Sob'yanin[2], D.R. Yakovlev[1,3], M. Bayer[1,3]

[1] Experimentelle Physik 2, Technische Universität Dortmund, D-44221 Dortmund, Germany
[2] P.N. Lebedev Physical Institute of the Russian Academy of Sciences, 119991 Moscow, Russia
[3] Ioffe Institute, Russian Academy of Sciences, 194021 St Petersburg, Russia

Abstract. We study the spin dynamics in a high-mobility two-dimensional electron gas confined in a GaAs/AlGaAs quantum well in high magnetic field using pump-probe Kerr rotation technique. We find an unusual behavior of the longitudinal spin relaxation time T_1 with increasing magnetic field. Initially quadratic dependence becomes linear, with a slope inversely proportional to the temperature. At higher field, when entering the Quantum Hall regime, the magnetic field dependence of T_1 eventually takes on an oscillatory character with peaks corresponding to even filling factors. We show that the transition from quadratic to linear dependence can be related to a transition from classical to Bohm diffusion and reflects an anomalous behavior of the two-dimensional electron gas, while the oscillations correspond to oscillations of the density of states appearing at low temperatures and high magnetic fields.

Introduction

Two-dimensional electron gas (2DEG) is a uniqueX system which motional properties can be drastically modified by the magnetic field, which, in particular, leads to the Quantum Hall (QH) effect. This fact can be used to control spin relaxation rate with magnetic field in 2DEG systems with spin-orbit interaction such as GaAs-based quantum wells (QWs). In QWs signatures of QH regime were found in the transverse spin dynamics (spin precession about the magnetic field) in works [1,2] where a sharp increase in transverse inhomogeneous relaxation time T_2^* was observed for the magnetic field corresponding to the odd filling factors ν.

In this work [4], we report on the longitudinal spin dynamics in a high-mobility 2DEG measured using the Extended pump-probe Kerr rotation spectroscopy [3]. For not too high magnetic fields and moderate temperatures we find an unusual crossover from quadratic to linear magnetic field dependence of the longitudinal spin relaxation time T_1. In the QH regime T_1 shows maxima at even filling factors contrary to the case of transverse spin relaxation.

1. Experimental details

The results are obtained on a structure with a single modulation doped GaAs QW containing a 2DEG concentration n_e around 1×10^{11} cm^{-2} and the Hall mobility $\mu_e > 2\times10^6$ cm^2/Vs at $T = 2$ K.

For optical measurements the sample is placed in the variable temperature insert of a split-coil magnetocryostat ($T = 2-300$ K). The magnetic fields up to 6 T are applied parallel to the light propagation direction that is parallel to the sample growth axis (Faraday geometry). The extended pump-probe Kerr rotation(ellipticity) technique is used to study the electron spin dynamics in the microsecond time range with picosecond resolution [3].

2. Results and discussion

Spin polarization along the magnetic field created by a pump pulse decays in time allowing to determine T_1 (inset in Fig. 1. The dependence of T_1 on the magnetic field is shown in Fig. 1 for 3 different temperatures. At low B $T_1 \propto B^2$, while $T_1 \propto B$ at higher B. The slope of linear dependence is roughly inversely proportional to the temperature T. For even higher B and the lowest $T = 2$ K distinct peaks in the dependence $T_1(B)$ appear. Positions of the peaks correspond to the even filling factors ν, i.e. when $\nu/2$ Landau levels are completely filled by electrons with both spin states parallel and antiparallel to the magnetic field.

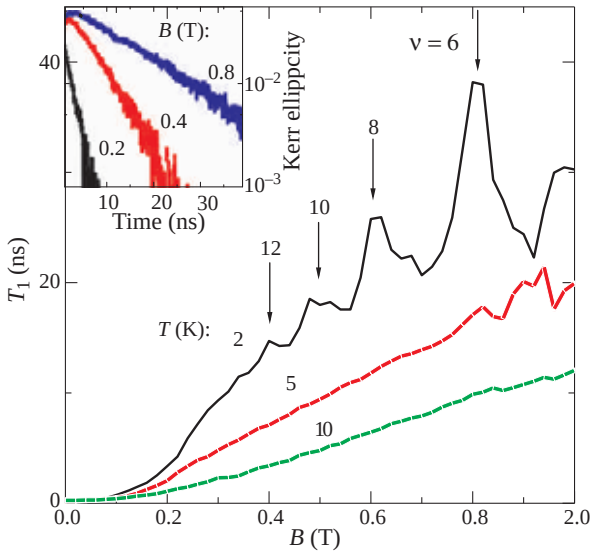

Fig. 1. Magnetic field dependence of the longitudinal spin relaxation time of 2DEG T_1 at different temperatures. Inset shows dynamics of Kerr ellipticity at different magnetic fields.

We theoretically show that the observed strong suppression of spin relaxation with magnetic field is related to connfined spin nutation appearing because of electron gyration in a magnetic field that causes rotation of the spin-orbit field. Spin relaxation appears closely related to electron spatial diffusion, and the longitudinal spin relaxation time is inversely proportional to the spatial diffusion coefficient D:

$$T_1 \sim \frac{l_S^2}{D}, \qquad (1)$$

where l_S reflects the length traveled by the electrons' orbit center during time T_1 and depends on the parameters of the struc-

ture only. The transition from quadratic to linear magnetic-field dependence of T_1 can be related to a transition from classical to Bohm diffusion of the electron and reflects an anomalous behavior of 2DEG in a magnetic field analogous to that observed in magnetized plasmas. The oscillations of T_1 with magnetic field are related to the oscillations of the density of states at the Fermi level and correspond to a transition at high fields and low temperatures to the quantum Hall regime.

Acknowledgements

The work was supported by the Deutsche Forschungsgemeinschaft in the frame of the ICRC TRR 160 (project A1). V.V.B, M.V.K. and D.N.S. acknowledge the financial support of the Russian Science Foundation through the grant No. 18-72-10073.

References

[1] D. Fukuoka *et al*, *Phys. Rev. B* **78**, 041304 (2008).
[2] A.V. Larionov *et al*, *Phys. Rev. B* **92**, 165417 (2015).
[3] V.V. Belykh *et al*, *Phys. Rev. B* **94**, 241202(R) (2016).
[4] V.V. Belykh *et al*, *Phys. Rev. B*, accepted (2020).

28th Int. Symp. “Nanostructures: Physics and Technology”
Minsk, Belarus, September 2020

Electron spin relaxation time in Mn-doped GaAs structures with different level of compensation

A.E. Evdokimov[1], M.S. Kuznetsova[1], A.V. Mikhailov[1], K.V. Kavokin[1] and R.I. Dzhioev[2]

[1] Spin Optics Laboratory, Saint Petersburg State University, St Petersburg, Russia
[2] Ioffe Physico-Technical Institute, Russian Academy of Sciences, St Petersburg, Russia

Abstract. The electron spin relaxation time in Mn-doped GaAs samples have been studied by measuring the photoluminescence depolarization in the transverse magnetic field and polarization recovery in the longitudinal magnetic field. The spin relaxation time increases with the optical pumping from 14 ns for low pumping power to about 100 ns for threshold pumping powers and then decreases to the initial value. Such unusual behavior is related to the different spin relaxation rates of electron precessing in the fluctuating fields of ionized or neutral Mn acceptors.

Introduction

The disappearance of initial non-equilibrium spin polarization — spin relaxation has been intensively studied for over half a century as a major aspect out of all spin phenomena. An improved understanding of spin relaxation processes is the main task on the way to the development of spintronics. It has been shown in earlier experiments that electrons in n-GaAs can have a long spin relaxation time around 300 ns [1,2], which could solve some problems for quantum information processing. On the contrary p-GaAs even at low temperatures has quite a short spin relaxation time and was not considered for these purposes.

In this paper, we study the electron spin dynamics by measuring the degree of polarization of photoluminescence (PL) in the transverse magnetic field (the Hanle effect) and recovery of electron spin polarization in the longitudinal magnetic field (PRC). We determine electron spin relaxation time τ_s and electron lifetime τ. We find that in Mn-doped GaAs structures with different compensation levels the behavior of the spin relaxation time has a complex nature and may consist of several processes.

1. Experimental details

The experiments are performed on two GaAs:Mn structures grown by liquid-phase epitaxy (LPE) on a (001)-oriented GaAs substrate and have different densities of dopants: for Sample A $N_{\rm Mn} = 7.8{\times}10^{17}$ cm^{-3}, $N_d - N_a = 14.9 \times 10^{15}$ cm^{-3}, where $N_{\rm Mn}$, N_d, N_a — concentrations of Mn acceptors, shallow donors and acceptors, respectively. For Sample B the following values are implemented: $N_{\rm Mn} = 2.8{\times}10^{17}$ cm^{-3}, $N_d - N_a = 3.4{\times}10^{15}$ cm^{-3}.

The samples are placed in a closed-cycle cryostat and cooled to the temperature of liquid helium ($T = 4.2$ K). For the creation of magnetic fields either perpendicular to or in the sample plane (Faraday and Voigt geometry, respectively) an electromagnet installed outside the cryostat is used.

We experimentally study electron spin dynamics using optical orientation under continuous wave excitation provided by a Ti:sapphire laser system. In the experiment, we use modulation of polarization of optical excitation that allows us to avoid the build-up of the dynamic nuclear polarization. In these experiments, the excitation light is modulated between σ^+ and σ^- polarization, while PL is detected only in one selected circular polarization (either σ^+ or σ^-). The degree of circular polarization of photoluminescence is expressed as

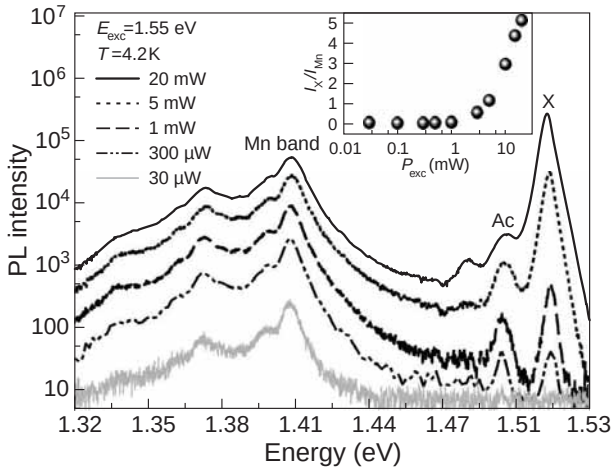

Fig. 1. PL spectra of Sample A for different excitation powers. Inset shows peak intensity ratios $I_X/I_{\rm Mn}$ of the excitonic X and Mn lines vs excitation power.

$\rho_c = (I^{++} - I^{-+})/(I^{++} + I^{-+})$, where $I^{++}(I^{-+})$ is the intensity of $\sigma^+(\sigma^-)$-polarized PL with σ^+ polarized excitation. The PL is detected using an avalanche photodiode. The PL spectra of the GaAs:Mn sample detected at different pumping powers are shown in Fig. 1. The PL peak at the energy 1.51 eV is labeled as ‘X’ and represents the emission of the free and donor-bound excitons. The peak at the energy 1.49 eV is labeled as ‘Ac’ and results from the conduction-band-acceptor and shallow-donor-acceptor transitions. At lower PL energies a Mn-related band is observed with a peak at 1.41 eV. It is significantly spectrally broadened by phonon coupling. This part of the spectra can be interpreted as transitions from the conduction band and shallow donors to the Mn acceptor levels and their phonon replicas. One can see that the Mn band appears for all pumping powers used in the experiments. Whereas there is a threshold value $P_{\rm th} = 1 - 3$ mW for the appearance of the X and Ac lines in the PL spectra for both samples. It can be also observed from the insets in the Fig. 1, where the ratio $I_X/I_{\rm Mn}$ of the PL magnitudes is plotted vs pumping power, taken at 1.51 (I_X) and 1.41 eV ($I_{\rm Mn}$).

2. Experimental results

To extract electron spin relaxation time τ_s and electron lifetime τ we measure the series of the Hanle curves and PRC at different pumping powers. As hole spins relax much faster, the

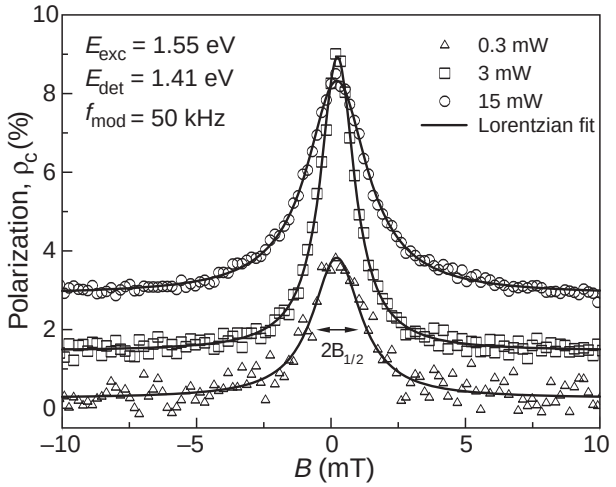

Fig. 2. The Hanle curves measured at the modulation frequency $f_{\rm mod} = 50$ kHz as a function of pumping power for Sample A.

PL polarization ρ_c indicates average spin polarization of the electrons. The degree of circular polarization can be described as follows:

$$\rho_c = \frac{\rho_{c0}}{1+\frac{\tau}{\tau_s}} \frac{1}{1+(\frac{B_x}{B_{1/2}})^2}, \qquad (1)$$

here ρ_{c0} is the initial electronic polarization, $B_{1/2}$ is the half width at half maximum (HWHM) of the Hanle curve $B_{1/2} = \overline{h}/(g_e \mu_B T_s)$, μ_B is the Bohr magneton, g_e is the electronic g factor (for GaAs $g_e = -0.44$), $T_s^{-1} = \tau_s^{-1} + \tau^{-1}$ is the inverse spin lifetime. Fig. 2 shows the set of Hanle curves measured at fixed modulation frequency of polarization of optical excitation $f_{\rm mod} = 50$ kHz for the Sample A as a function of pumping power. At high modulation frequencies of pumping helicity, the Hanle curves, shown in Fig. 2 can be assumed with good accuracy to have Lorentzian shape. To determine electron spin relaxation time τ_s and electron lifetime τ, we analyze the Hanle curves and PRC. For the analysis of the Hanle curves, the initial polarization ρ_{c0} was estimated from the fitting of the PRC. Fig. 3 shows the set of experimentally measured PRC at different pumping powers with modulation frequency $f_{\rm mod} = 50$ kHz. Analysis of these curves can be

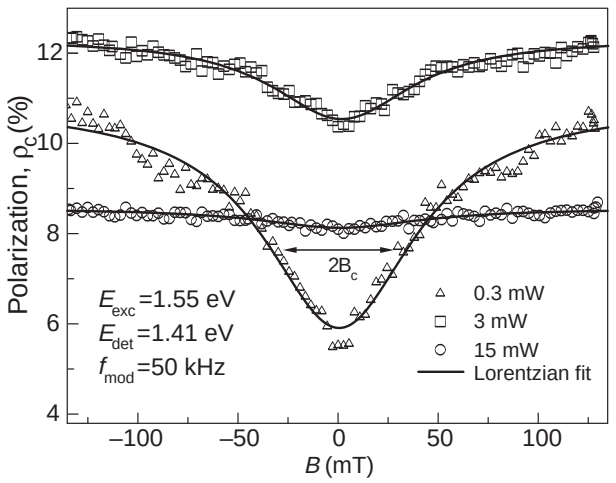

Fig. 3. Polarization recovery curves measured as a function of pumping power for the Sample A at fixed frequency of modulation.

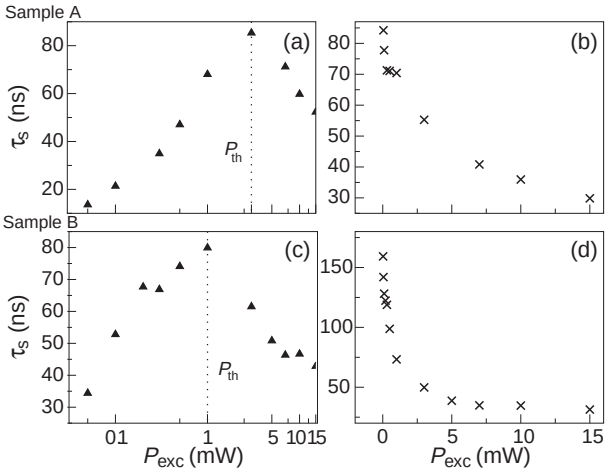

Fig. 4. The dependencies of spin relaxation time τ_s and lifetime τ on the pumping power for Samples A (a,b) and for Sample B (c,d).

done with the following equation:

$$\rho_c = \frac{\rho_{c0}}{1+\tau/\tau_s^*}, \tau_s^* = \tau_s[1+(B/B_c)^2] \qquad (2)$$

where the correlation field $B_c = \overline{h}/[(g_A - g_e)\mu B]\tau_c^{-1}$, g_A is the g factor of Mn [3].

From the fitting of the Hanle curves and PRC with equations (1) and (2) we obtain the power dependencies of τ_s and τ for both samples under study, see Fig. 4. From Fig. 4 it is seen that the dependencies of τ_s and τ as a function pumping power for both samples display similar behavior. In Mn-doped GaAs ionized acceptor centers create fluctuating fields, in which electron spin precession occurs. At low pumping powers charged Mn acceptor traps photogenerated holes which leads to compensation of this fluctuating field which affects the electron spin. It results in the increase of the electron spin relaxation time at the pumping powers lower than the $P_{\rm th}$. At the pumping power $P_{\rm exc} = P_{\rm th}$ all Mn impurities are converted to the neutral configuration and τ_s has its maximum value. At high excitation powers fast electron spin relaxation is observed due to the exchange interaction of the holes bound to the acceptors. The electron lifetime is very long for such type of structure and decreases with increasing pumping power.

Acknowledgements

We acknowledge the financial support of the Deutsche Forschungsgemeinschaft in the frame of the International Collaborative Research Center TRR 160 (Project No. A6), the Russian Foundation for Basic Research (Grant No. 19-52-12043), and Saint Petersburg State University Research Grant No. ID 40847559.

References

[1] R.I. Dzhioev *et al*, *JETP Lett.* **74**, 182 (2001).
[2] R.I. Dzhioev *et al*, *Phys. Rev. Lett.* **88**, 256801 (2002).
[3] G.V. Astakhov *et al*, *Phys. Rev. Lett.* **101**, 076602 (2008).

28th Int. Symp. “Nanostructures: Physics and Technology”
Minsk, Belarus, September 2020

Weak magnetic field effects on the photoluminescence of an ensemble of NV centers in diamond: experiment and modelling

D.S. Filimonenko[1], V.M. Yasinskii[1], A.P. Nizovtsev[1], S.Ya. Kilin[1], and F. Jelezko[2]

[1] B.I. Stepanov Institute of Physics, National Academy of Sciences of Belarus, Minsk, 220072 Minsk, Belarus
[2] Institute for Quantum Optics, Ulm University, Ulm, D-89081, Ulm, Germany

Abstract. The relationship between the photoluminescence intensity of the ensemble of NV centers in diamond and external magnetic field was studied. The magnetic spectra exhibit two resonances. The broader one has a width of 20 G and its amplitude is independent of the polarization of the incident radiation. The narrow resonance with a width of 4 G is found to be polarization dependent and is only visible if the direction of magnetic field is more or less perpendicular to the laser light polarization. To describe the appearance of these resonances we have modified the 8-level model of the NV center by taking into account the cross-relaxation between the ground-state spin of the center and other surrounding electronic spins (those of differently aligned NV centers, substitutional N spins etc.).

Introduction

NV centers in diamond have attracted enormous attention in connection with the prospects of their use in various fields of science and technology. One of the promising applications is the use of NV centers for magnetometry. Among numerous papers [1] on this subject there are only a few which focus on the behavior of the NV centers fluorescence in the presence of a weak magnetic field [2,3]. Here we are presenting the experimental and theoretical results which relate to this issue.

1. Experimental

The schematic of the experimental setup used in this study is similar to the one in our previous work [3]. The experiments were performed using 1 mm diamonds produced by HPHT method. NV centers were created by high-energy particles irradiation and subsequent thermal annealing. A continuous-wave linearly polarized Nd:YAG laser operating at a 532 nm wavelength was used to excite fluorescence. The radiation power was 30 mW. The radiation was focused on a spot of 0.3 mm diameter. A quarter-wave plate converts linearly polarized light into circularly polarized, and the direction of polarization was controlled using linear polarizers. This way, we were also able to investigate the eï¬Łect of the laser light polarization on the fluorescence of NV centers in weak magnetic fields.

To measure the magnetic field dependence on the fluorescence, we applied a slowly varying voltage from the generator at a frequency of 0.01 Hz to the coil of the electromagnet. At the same time, an alternating voltage of about 1200 Hz was applied to the same coil, which led to a slight modulation of the magnetic FIWeld and is also used as the reference signal for the lock-in amplifier.

The signal from the photomultiplier was fed to the lock-in amplifier.

2. Results and discussion

The signal from the lock-in amplifier, which is proportional to the derivative of the sample fluorescence intensity as a function of the magnetic field, is shown on Figure 1.

As can be seen in Figure 1 the magnetic spectra exhibit two resonances. The broader one has a width of 20 G and its amplitude is independent of the polarization of the incident radiation. The narrow resonance with a width of 4 G is found to be polarization dependent. This resonance is only visible if the direction of magnetic field B is more or less perpendicular to the laser light polarization E.

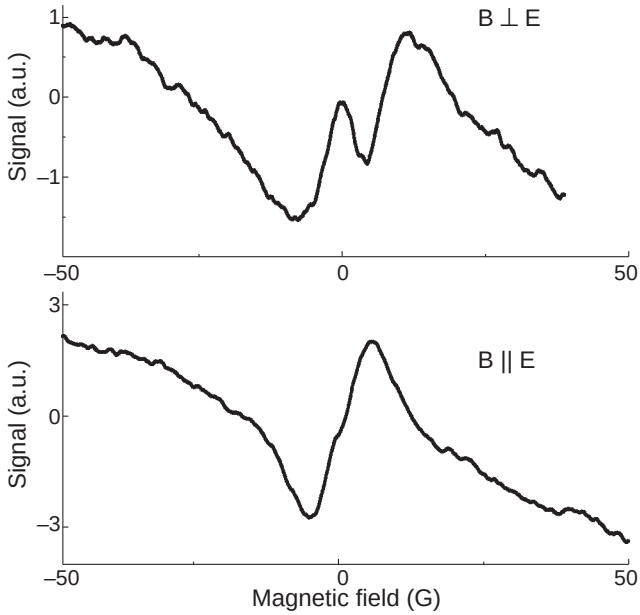

Fig. 1. Lock-in amplifier signal as a function of the applied magnetic field for perpendicular (top) and parallel (bottom) orientations of laser light polarization with respect to the magnetic field.

As mentioned above, the signal from the lock-in amplifier is proportional to the derivative of the sample fluorescence as a function of the magnetic field and its absolute magnitude cannot be obtained from such a measurement but needs to be reconstructed. For a better understanding of the mechanisms underlying the resonance effects we experimentally registered the direct relationship between sample fluorescence intensity and external magnetic field.

As one can see from the Fig. 2, for perpendicular directions of E and B there is a local maximum in the middle of the

dip in fluorescence intensity. This maximum corresponds to the narrow resonance, while the dip corresponds to the broad resonance from Fig. 1.

To increase the generalizability of the results we have also repeated the experiment using ultra-pure (99,999% carbon-12) CVD diamonds with different concentrations of NV centers obtained from Ulm, Germany. The weak-field resonance effect was observed in all the samples.

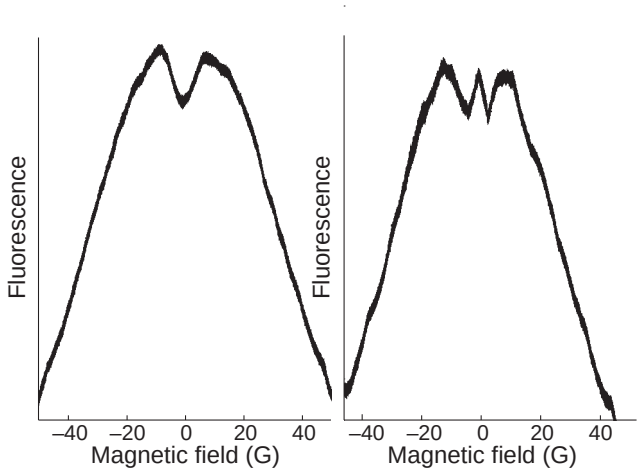

Fig. 2. The relationships between sample fluorescence intensity and external magnetic field for parallel directions of E and B (left) and perpendicular directions of E and B (right).

Existing theoretical models did not accurately predict the appearance of these resonances [4,5]. The usual 7/8-level photophysical models of the NV center [5] describe well only a smooth decrease (see Fig. 3) in the fluorescence intensity of the NV center with increasing the transverse magnetic field which mixes spin sublevels $m_S = 0, \pm 1$ both in ground and excited states of the center.

To capture the fine structure of this decrease (the dip and peak in fluorescence intensity at weak magnetic field) we have modified the 8-level model of the NV center by taking into account the cross-relaxation between the ground-state spin of the center and other surrounding electronic spins (those of differently aligned NV centers, substitutional N spins etc.).

With due consideration to the experimental observations [6, 7], the magnetic-field-dependent spin-lattice relaxation rate $\Gamma = 1/T_1$ of the ground-state electronic spin of the NV center was entered into the balance equations of the 8-level model. Next, using the known photophysical parameters, we calculated the total fluorescence emitted by ensemble of variously oriented NV centers in the presence of differently directed magnetic field. A simple Lorentzian model $\Gamma = \Gamma_0 + \Gamma_{CR}$ $(\Gamma_{CR}{}^2 + B^2)$ allows us to describe the appearance of the dip in the region of low magnetic field B (see Fig. 3).

Figure 3 presents some results along with previously obtained [3] experimental data. Apparently, a more complicated model of the $\Gamma(B)$ dependence is needed to describe both observed resonances.

Acknowledgement

This work has been supported by Belarusian Republican Fund of Fundamental Research (grant F18P-118).

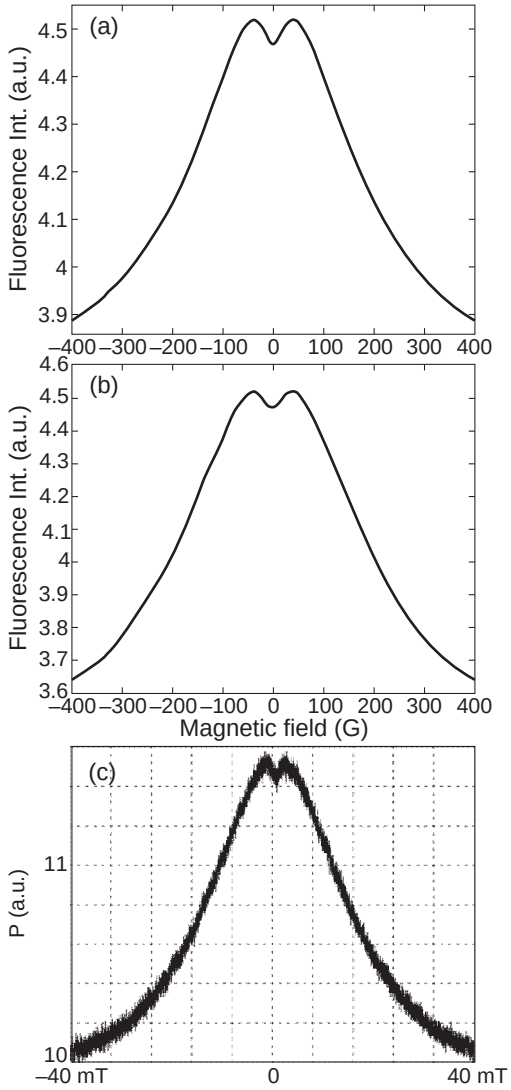

Fig. 3. Calculated magnetic field dependencies of fluorescence emitted by ensemble of NV centers. The [1 1 1] axis of one of the groups of NV centers coincides with the magnetic field direction (a); the field is aligned along the [1 0 0] axis (all NV-axes form an angle of 54.7° with the field) (b); experimental findings of [3] (c).

References

[1] A. Grosz *et al*, *High Sensitivity Magnetometers*, Switzerland, Springer International Publishing, 553–576, 2017.
[2] S.V. Anishchik *et al*, *New J. Phys.* **17**, 023040 (2015).
[3] D.S. Filimonenko *et al*, *Semiconductors* **52**, 1865 (2018).
[4] L.J. Rogers *et al*, *New J. Phys.* **11**, 063007 (2009).
[5] P. Tetienne *et al*, *New J. Phys.* **14**, 103033 (2012).
[6] A. Jarmola *et al*, *Phys. Rev. Lett.* **108**, 197601 (2012).
[7] M. Mryzek *et al*, *EPJ Quantum Technol.* **2**, 22 (2015).

28th Int. Symp. "Nanostructures: Physics and Technology"
Minsk, Belarus, September 2020

Spin waves interference under excitations by focusing transducers

M. Madami[1], G. Gubbiotti[1,2], Y.V. Khivintsev[3,4], G.M. Dudko[3], V.K. Sakharov[3], A.V. Kozhevnikov [3], *Y.A. Filimonov*[3,4], and A.G. Khitun[5]

[1] Dipartimento di Fisica e Geologia, University di Perugia, via A. Pascoli, I-06123 Perugia, Italy
[2] Istituto Officina dei Materiali del CNR (CNR-IOM), sede secondaria di Perugia, c/o Dipartimento di Fisica e Geologia, University di Perugia, I-06123 Perugia, Italy
[3] Kotelnikov IRE RAS, Saratov Branch, 410019 Saratov, Russia
[4] Saratov State University, 410012 Saratov, Russia
[5] University of California-Riverside, Riverside, California, USA 92521a

Abstract. Magnetostatic backward volume spin-waves (MSBVW) interference in yttrium iron garnet film under excitation by a pair of curvilinear focusing transducers placed at distance l oppositely to each other was studied by means of micro-focused Brillouin-Mandelstam light scattering technique and micromagnetic simulations. We found that the positions of local interference maxima and minima in the measured two-dimensional spin-waves intensity maps are characterized by strong frequency dependence as well as by the absence of mirror symmetry with respect to magnetic field direction. These effects are the consequence of MSBVW anisotropic and nonreciprocal propagation at an angle to the bias field direction, that, in turns, leads to chromatic aberration of the transducer and variation of the spin-waves interference pattern from that typical for short focus distance F ($F \ll l$) to one typical for long focus distance ($F \sim l$) transducers. The obtained results demonstrate an intrigue possibility of using spin wave interference for addressing magnetic bits. Potentially, spin wave focusing transducers can be utilized for magnetic memory readout.

Introduction

Spin waves (SW) interference phenomena in magnetic microstructures are being actively studied in connection with the prospect of building energy-efficient logic devices based on the principles of magnonics [1]. The Mach–Zehnder-type SW interferometers were studied typically to demonstrate the possibility to perform basic logic functions [2]. Additionally, computing algorithms which exploit interference pattern formation between coherent wavefronts were proposed to implement non-Boolean computation, [3] for special data processing such as pattern recognition [4], spectrum analysis [5] and to perform spin-wave Fourier optics [6].

Such ideas stimulated efforts to integrate optic-like components (prisms, lenses, mirrors, splitters) into magnetic films to perform SW based signal processing directly on-chip [7,8]. Besides that, it is necessary to solve the problem to integrate a number of SW sources into magnetic films, capable to generate directional SW beams in the absence of geometrical confinement. For that purpose, both point-like SW sources and specially designed antennas [7,9] can be used.

Note that both the design of the SW optic elements and the features of the SW interference pattern strongly depend on the character of the SW dispersion. The focusing elements for SWs with an isotropic dispersion, like the forward volume SWs in a normally magnetized film, have a concave form with respect to the focus [7] that is quite similar to that of traditional optics. In contrast, for waves with anisotropic dispersion, like magnetostatic surface waves (MSSWs) or magnetostatic backward volume waves (MSBVWs) in tangentially magnetized films, the shape of the focusing elements is convex [7]. The diffraction pattern for MSBVWs excited by a focusing transducer is characterized by caustics formation and by a strong asymmetry after focus position [9].

In this work, we explore such effect for counter propagating MSBVWs using micro-focused Brillouin-Mandelstam light scattering (μ-BLS) and micromagnetic simulations. In particular, we study the interference of MSBVWs excited by a pair of curvilinear coplanar waveguides (CPW) placed oppositely to each other atop of a micrometer-thick yttrium iron garnet (YIG) film.

1. Results

The investigated sample consists of an epitaxial YIG film grown on gadolinium gallium garnet (GGG) substrate with (111) crystallographic orientation. YIG films have lateral dimensions $L_z \approx L_y \approx 15$ mm, thickness $d \approx 3.9$ μm, saturation magnetization $4\pi M \approx 1750$ G, FMR linewidth $\Delta H \approx 0.5$ Oe. Several pairs of 500 nm-thick copper CPW transducers (see

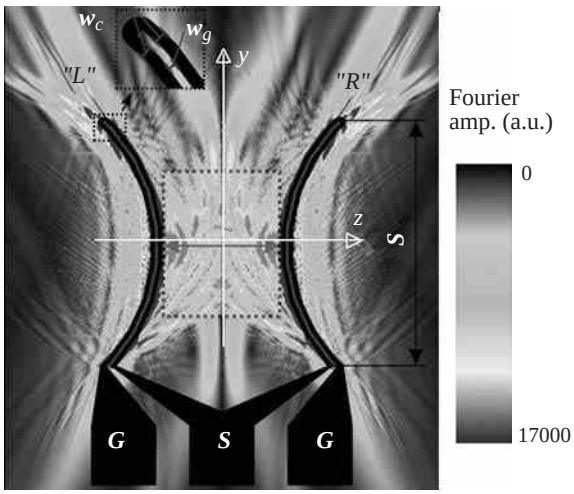

Fig. 1. Studied structure with the curvilinear transducer parameters' notations. Intensity map represent the simulated distribution of MSBVW normal component of the dynamic magnetization m_x excited by curved transducers in YIG film. Rectangle between left ("L") and right ("R") transducers indicates BLS scanned area, see Fig. 2.1(a) and 2.2(a).

Fig .1) were fabricated using DC-magnetron sputtering, photolithography and ion etching. The arc shape CPW has the curvature radius $r \approx 300$ μm, span S between antenna's edges $S \approx 430$ μm. Both signal and ground conductors of antennas had width $w_c \approx 7$ μm with the gap between wires $w_g \approx 4$ μm. At the end of antennas, ground and signal conductors had gradual transition to 100 μm 100 μm contact pads with 150 μm pitch for access with microwave probes. The distance l between centres of "left" (transducer center at $z = -l/2$) and "right" ($z = l/2$) antennas along main optical axis ($y = 0$) was equal to $l \approx 200\mu m$ for CPW with convex form with respect to point $z = 0$ and $l \approx 250$ μm for transducers with concave form with respect to $z = 0$.

The interference intensity maps $P(z, y)$ correspondent to MSBVW excitation by transducers with focus distance $F \approx 20$ μm$\ll l$ ("short" focus transducers) and $F \approx 100$ μm$\approx l/2$ are shown in Fig. 2.1 and 2.2. Results shown in Fig. 2.1 correspond to excitation frequency $f = 1.4$ GHz and bias field $H = 200$ Oe while ones in Fig. 2.2 — for frequency $f \approx 5.8$ GHz and $H \approx 1500$ Oe.

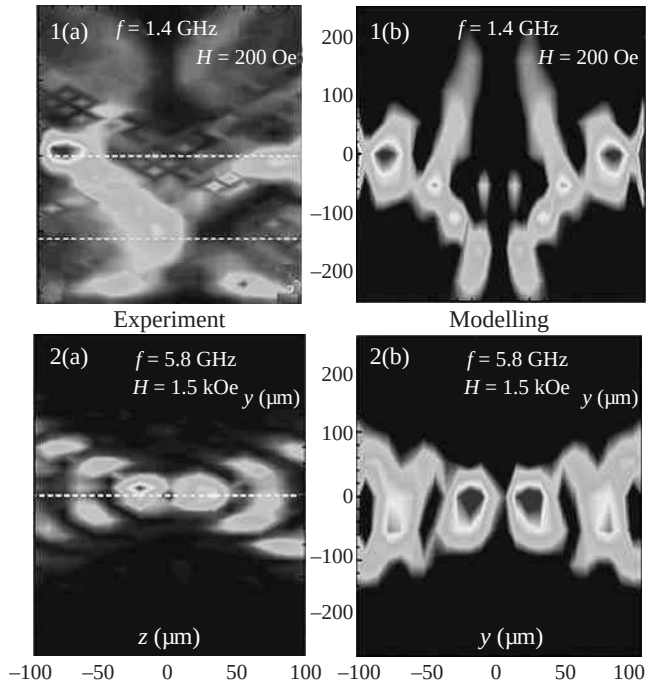

Fig. 2. Measured (a) and simulated (b) MSBVW intensity maps $P(z, y)$. Maps 2.1(a),(b), correspond to MSBVW interference under excitation by "short" ($F \approx 2$ μm $\ll l \approx 200$ μm) focus distance transducer at frequency $f = 1.4$ GHz and $H = 200$ Oe. Maps 2.2(a),(b)correspond to SW interference under parameters $F \approx 10$ μm$\approx l/2$, $f = 5.8$ GHz, $H = 1500$ Oe.

Fig. 2 shows a qualitative agreement between measured (Fig. 2(a)) and calculated (Fig. 2(b)) 2D interference maps. As used trunsducers have common signal line the intereference takes destructive character-intensity drops to zero at z=0 cross-section.

Fig. 3 illustrates the potential ability to use the focused SW beams interference for magnetic memory readout. In Fig. 3a the simulated 2D-map intensity map $P(z, y)$ of MSBVW interference pattern under parameters correspondent to Fig. 3.2(b) after introducing in YIG film the magnetic nonuniformity in the form of hole ($\approx$ 20 μm in diameter) at focus position of the "left" (see "L" jn Fig. 1) transducer is shown. One can see, that "hole" can strongly change the character of SWs interference along cross-section $z = 0$. Fig. 3b illustrates the sensitivity of the intensity $P(0, y)$ distribution in patterned YIG film with frequency variation. Such dependencies is a result of the chromatic aberration of the BVMSW focusing transducer.

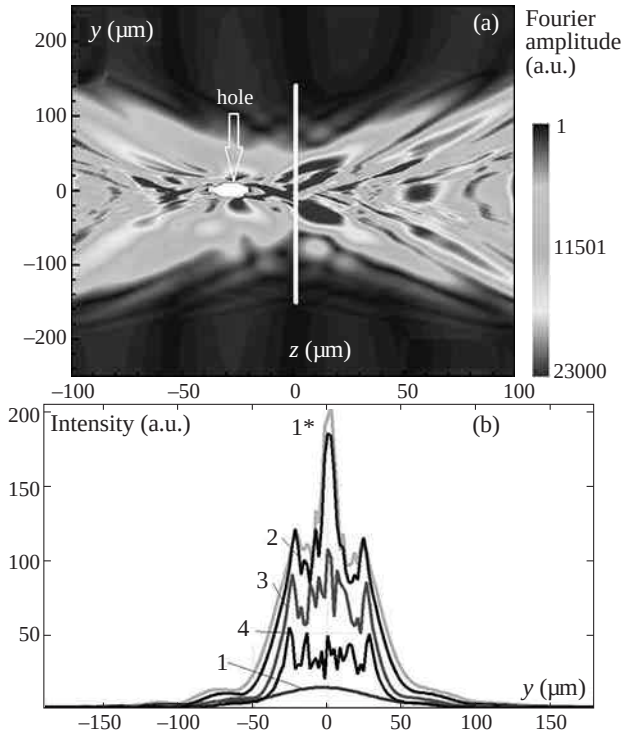

Fig. 3. (a) Simulated MSBVW interference pattern under parameters correspondent to Fig. 3(b) after introducing the hole at focus position of the "left" (see "L" jn Fig. 1) transducer. (b) cross-sections of the calculated intensity of the interference pattern along axis $z = 0$ as a function of frequency. Curves 1*,2,3,4 correspond to frequencies 5.85, 5.8, 5.7 and 5.6 GHz. Curve 1 corresponds to interference pattern in unpatterned structure — see Fig. 2.2(b).

Acknowledgement

The work of Y. Khivintsev, G. Dudko, A. Kozhevnikov, V. Sakharov and Y. Filimonov was supported by Russian Science Foundation grant No. 17-19-01673.

References

[1] A. Khitun *et al*, *J. Phys. D Appl. Phys.*, **43**, 264005 (2010).
[2] M.P. Kostylev *et al*, *Appl. Phys. Lett.*, **87**, 153501 (2005).
[3] A. Khitun *J. Appl. Phys*, **113**, 164503 (2013).
[4] F. Gertz *et al*, *IEEE Trans. Magn.*, **51(4)**, 1-5 (2015).
[5] A. Papp *et al*, *Sci. Rep.*, **7**, 9245 (2017).
[6] G. Csaba *et al*, *J.Appl. Phys.*, **115**, 17C741 (2014).
[7] A. Vashkovskii *et al*, *Sov. Phys. Journ.*, **31**, 908 (1988).
[8] C.S. Devies *et al*, *Low Temp.Phys.*, **41**, 760 (2015).
[9] M. Madami *et al*, *Appl. Phys. Lett.*, **113**, 152403 (2018).

28th Int. Symp. "Nanostructures: Physics and Technology"
Minsk, Belarus, September 2020

Floquet engineering of structures based on gapless semiconductors

O.V. Kibis[1], M.V. Boev[1,2], V.M. Kovalev[1,2], R.E. Sinitskiy[1] and I.A. Shelykh[3,4]

[1] Department of Applied and Theoretical Physics, Novosibirsk State Technical University, 630073 Novosibirsk, Russia
[2] Institute of Semiconductor Physics, Siberian Branch of Russian Academy of Sciences, 630070 Novosibirsk, Russia
[3] Science Institute, University of Iceland, Dunhagi 3, IS-107, Reykjavik, Iceland
[4] ITMO University, 197101 Saint Petersburg, Russia

Abstract. Applying the conventional Floquet theory of periodically driven quantum systems, we developed the theory of optical control of structures based on gapless semiconductors. It is demonstrated that electronic properties of the structures crucially depends on irradiation. Particularly, irradiation by a circularly polarized electromagnetic wave lifts spin degeneracy of electronic bands and induce surface electronic states. Thus, a high-frequency off-resonant electromagnetic field can serve as an effective tool to control electronic characteristics of the structures and be potentially exploited in optoelectronic applications of them.

Introduction

During last years, the control of electronic parameters of condensed-matter structures by a high-frequency electromagnetic field (so-called "Floquet engineering" based on the Floquet theory of periodically driven quantum systems) became the important and established research area which resulted in the discovery of many fundamental effects (see, e.g., Refs. [1,2]. Particularly, many works dedicated to the Floquet engineering of various nanostructures — including quantum wells [3,4], graphene and related 2D materials [5,6], quantum rings [7,8], topological insulators [9] — were published. Among various nanostructures important to both fundamental science and device applications, it should be noted those of them which are based on gapless semiconductors (HgTe and related materials). Since electronic structure of the gapless semiconductors near the band edge (the electronic term Γ_8 in the center of the Brillouin zone) is described by the Luttinger Hamiltonian [10,11], it is necessary to develop the Floquet theory for the Luttinger Hamiltonian in order to control electronic properties of the corresponding semiconductor nanostructures by a high-frequency electromagnetic field. The present work is dedicated to solving this theoretical problem.

1. Model

Let us consider a structure with the electron energy spectrum described by the Luttinger Hamiltonian (the electronic term Γ_8), which is irradiated by a plane electromagnetic wave with the frequency ω and the electric field amplitude E_0. Assuming size of the irradiated structure along the direction of the wave propagation to be much less than the wave length, $\lambda = 2\pi c/\omega$, we can consider the wave field inside the structure as uniform. Then electronic states of the irradiated structure within the conventional minimal coupling approach can be described by the time-dependent Hamiltonian,

$$\hat{\mathcal{H}}(\mathbf{k}, t) = \hat{\mathcal{H}}_L(\mathbf{k} - e\mathbf{A}(t)/\hbar) + \hat{\mathcal{H}}_{\rm BIA}(\mathbf{k} - e\mathbf{A}(t)/\hbar), \quad (1)$$

where $\mathbf{k} = (k_x, k_y, k_z)$ is the electron wave vector, $\mathbf{A}(t) = (A_x, A_y, A_z)$ is the vector potential of the field inside the structure, which periodically depends on the time, t,

$$\hat{\mathcal{H}}_{\rm L}(\mathbf{k}) = (\gamma_1 + 5\gamma/2)\,\mathbf{k}^2 - 2\gamma(\mathbf{kJ})^2, \quad (2)$$

is the Luttinger Hamiltonian written in the isotropic approximation,

$$\begin{aligned}\hat{\mathcal{H}}_{\rm BIA} &= \alpha[k_x\{J_x, (J_y^2 - J_z^2)\} + k_y\{J_y, (J_z^2 - J_x^2)\} \\ &+ k_z\{J_z, (J_x^2 - J_y^2)\} \quad (3)\end{aligned}$$

is the term coming from the bulk inversion asymmetry (BIA) of the crystal structure, $\gamma = (2\gamma_2 + 3\gamma_3)/5$ and $\gamma_{1,2,3}$ are the Luttinger parameters, α is the BIA parameter, and $\mathbf{J} = (J_x, J_y, J_z)$ is the 4×4 vector matrix corresponding to the electron angular momentum $J = 3/2$ [11].

In the most general form, the nonstationary Schrödinger equation with the periodically time-dependent Hamiltonian (1) can be written as $i\hbar\partial_t\psi(\mathbf{k}, t) = \hat{\mathcal{H}}(\mathbf{k}, t)\psi(\mathbf{k}, t)$, where $\hat{\mathcal{H}}(\mathbf{k}, t + T) = \hat{\mathcal{H}}(\mathbf{k}, t)$ and $T = 2\pi/\omega$ is the field period. It follows from the Floquet theorem that solution of the Schrödinger equation is the Floquet function, $\psi(\mathbf{k}, t) = e^{-i\varepsilon(\mathbf{k})t/\hbar}\varphi(\mathbf{k}, t)$, where $\varphi(\mathbf{k}, t+T) = \varphi(\mathbf{k}, t)$ is the periodically time-dependent function and $\varepsilon(\mathbf{k})$ is the electron (quasi) energy describing behavior of the electron in the periodical field. The Floquet problem is aimed to find the electron energy spectrum, $\varepsilon(\mathbf{k})$, which is modified by the periodical field. In the present research, we solved the problem for the Hamiltonian (1) within the conventional Floquet approach [1,2] for different field polarizations. The results of the numerical solution are presented in Fig. 1 and discussed below.

2. Results and discussion

To analyze bulk electronic states, let us neglect the relativistically small BIA term (3). Then the bulk electronic term Γ_8 is described by the Luttinger Hamiltonian (2) and consists of the two branches which correspond to the conduction and valence bands of HgTe (see the dashed lines in Figs. 1a and 1b). These branches are degenerated at $\mathbf{k} = 0$ and, in addition, their electron states are doubly degenerated in spin at any electron wave vector $\mathbf{k}$. It follows from the plots that the irradiation lifts the degeneracy but the lifting strongly depends on the light polarization. Namely, a linearly polarized wave splits the electron bands at $\mathbf{k} = 0$ but does not lift the spin degeneracy of the bands (see the two solid lines in Fig. 1b), whereas a circularly polarized wave lifts also the spin degeneracy at any electron wave

vector (see the four solid lines in Fig. 1a). To clarify physical nature of the light-induced band splitting, it should be noted that a circularly polarized electromagnetic wave breaks the time-reversal symmetry (since the time-reversal turns left-polarized photons into right-polarized ones and vice versa). Therefore, a circularly polarized electromagnetic wave acts similarly to a magnetic field which lifts the spin degeneracy of electronic states. As to a linearly polarized electromagnetic wave, it acts similarly to an uniaxial mechanical stress along the direction of polarization vector, which splits the degeneracy of electron states at $\mathbf{k} = 0$ [11].

To analyze light-induced surface electronic states, we have to take into account the BIA term (3) which is responsible for their existence. Solving the Floquet problem with the total Hamiltonian (1) and the zero boundary conditions at the (001) surface of HgTe for the Floquet wave function, $\psi(\mathbf{k}, t)\big|_{z=0} = \psi(\mathbf{k}, t)\big|_{z=\infty} = 0$, we arrive at the optically-induced surface electronic states with the energy spectrum, $\varepsilon(\mathbf{k})$, which are localized near the (001) surface and plotted by the solid lines in Fig. 1c, where $k = \sqrt{k_x^2 + k_y^2}$ is the electron wave vector in the (001) plane.

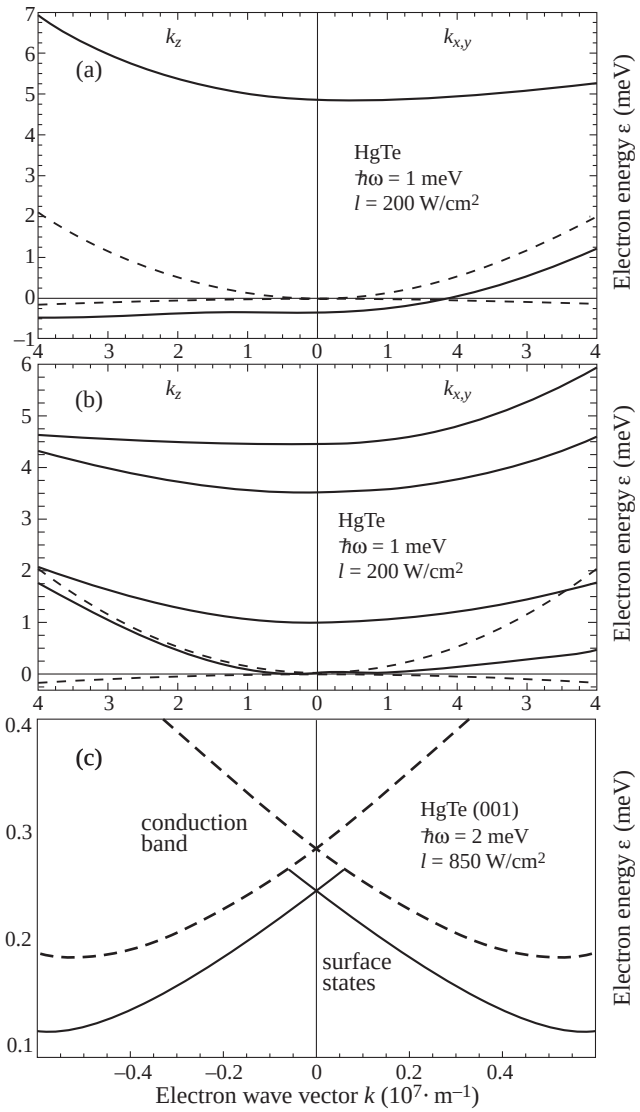

Fig. 1. Electron energy spectrum of HgTe, $\varepsilon(\mathbf{k})$, without irradiation (dashed lines) and in the presence of an electromagnetic wave with the intensity I, photon energy $\hbar\omega$ and different polarizations (solid lines): (a) bulk electronic states if the wave is circularly polarized in the (x, y) plane; (b) bulk electronic states if the wave is linearly polarized along the z axis; (c) surface electronic states if the wave is circularly polarized in the (x, y) plane.

Since the optically-induced band splittings plotted in Fig. 1 are of meV scale for the irradiation intensities around $I \sim$ kW/cm^2, they can be observed experimentally in optical electron transitions induced by another weak (probing) electromagnetic wave. Particularly, such optical transitions between the split bands will lead to fine structure of the optical spectra. Besides the conventional optical measurements, the modern angle-resolved photoemission spectroscopy (ARPES) can also be applied to study the electron energy spectra plotted in Fig. 1. Indeed, ultraviolet laser-based ARPES provides sub-meV resolution [12], which is enough for detecting features of them.

Although the Hamiltonian (1) depends on continuous electron wave vector $\mathbf{k}$, it can also be used to analyze electronic properties of nanostructures, where the electron wave vector is discontinuous. To take into account the size quantization in nanostructures, one has to analyze the Floquet problem with the Hamiltonian $\hat{\mathcal{H}}(\hat{\mathbf{k}}, t) + U(\mathbf{r})$, where $\hat{\mathbf{k}} = -i\partial/\partial\mathbf{r}$ is the electron wave vector operator, $U(\mathbf{r})$ is the quantizing potential of the nanostructure, and the Hamiltonian $\hat{\mathcal{H}}(\hat{\mathbf{k}}, t)$ results from the Hamiltonian (1) with the replacement $\mathbf{k} \to \hat{\mathbf{k}}$.

Acknowledgements

The reported study was funded by RFBR (project number 20-02-00084). I.A.S. thanks Icelandic Science Foundation (project "Hybrid polaritonics") and the Ministry of Science and Higher Education of the Russian Federation (Megagrant number 14.Y26.31.0015).

References

[1] N. Goldman and J. Dalibard, *Phys. Rev. X* **4**, 031027 (2014).
[2] M. Bukov, L. D'Alessio, and A. Polkovnikov, *Adv. Phys.* **64**, 139 (2015).
[3] S. Morina, O.V. Kibis, A.A. Pervishko *et al*, *Phys. Rev. B* **91**, 155312 (2015).
[4] A.A. Pervishko, O.V. Kibis, S. Morina *et al*, *Phys. Rev. B* **92**, 205403 (2015).
[5] O.V. Kibis, K. Dini, I.V. Iorsh *et al*, *Phys. Rev. B* **95**, 125401 (2017).
[6] I.V. Iorsh, K. Dini, O.V. Kibis *et al*, *Phys. Rev. B* **96**, 155432 (2017).
[7] V.K. Kozin, I.V. Iorsh, O.V. Kibis *et al*, *Phys. Rev. B* **97**, 035416 (2018).
[8] V.K. Kozin, I.V. Iorsh, O.V. Kibis *et al*, *Phys. Rev. B* **97**, 035416 (2018).
[9] O. Kyriienko, O.V. Kibis, I.A. Shelykh, *Phys. Rev. B* **99**, 115411 (2019).
[10] J.M. Luttinger, *Phys. Rev.* **102**, 1030 (1956).
[11] G.L. Bir and G.E. Pikus, *Symmetry and Strain-Induced Effects in Semiconductors* (Wiley, New York, 1974).
[12] W. Zhang, *Photoemission Spectroscopy on High Temperature Superconductor* (Springer, Berlin, 2013).

28th Int. Symp. "Nanostructures: Physics and Technology"
Minsk, Belarus, September 2020

Non-abelian properties of charge carriers in a quasirelativistic graphene model

H.V. Grushevskaya and *G.G. Krylov*
Physics Faculty, Belarusian State University, 220030 Minsk, Belarus

Abstract. Charge carrier transport peculiarities stipulated by non-trivial topology of a quasi-relativistic graphene model are investigated. It has been demonstrated that the model predicts additional topological contributions such as Majorana-like mass-term correction to ordinary Ohmic component of current, spin-orbital-coupling and "Zitterbewegung"-effect corrections to conductivity in space and time dispersion regime. Phenomena of negative differential conductivity for graphene have been interpreted based on the proposed approach.

Introduction

Currently, the progress in the development of quantum devices on the graphene-like material platform is connected with the so-called "valleytronics direction" utilizing the valley Hall effect (VHE). VHE for graphene reveals itself as an appearance of an electrical current in the direction orthogonal to an applied electric field (applied bias) $\vec{E}$ in the absence of a magnetic field. The existence of VHE signifies that charge transport for graphene can be topologically nontrivial. Suggested explanations of VHE are model dependent. The effect for monolayer graphene could be due to a non-zero Berry curvature which is non-vanishing at breaking inversion symmetry or(and) time reversal symmetry. But, the gap opening which should accompany such a breaking has not been confirmed experimentally.

Up to now there is no consistent theory of topologically non-trivial graphene conductivity. Graphene belongs to strongly correlated many-body systems, where topologically non-trivial effects, such e.g., as Majorana fermion states can manifest themselves. Experimental signatures of graphene Majorana states in graphene-super conductor junctions without need for spin-orbital coupling (SOC) have been established in [2].

In this paper, we investigate quantum transport of charge carriers with vortex dynamics in a quasi-relativistic graphene model using a high-energy $\vec{k}\cdot\vec{p}$-Hamiltonian. The Wilson non-closed loop method will be used to prove dichroism of the band-structure which leads to valley Hall conductivity.

1. Fundamentals

Quasi-relativistic graphene model has been derived (see, [3] and reference therein) as a consequent account of the effects of relativistic exchange interaction on the ground of truly secondary quantized relativistic consideration of the problem within the known Dirac–Hartree–Fock self-consistent field approximation. It has been established that the model admits a form as Majorana-like system of equations as well as two-dimensional Dirac-like equation with an additional "Majorana-force correction" term [3], and it reads

$$v_F\left[\vec{\sigma}_{2D}^{AB}\cdot\vec{p}_{BA}-c^{-1}M_{BA}\right]\left|\psi_{BA}^{*}\right\rangle = E\left|\psi_{BA}^{*}\right\rangle \qquad (1)$$

and the same equation with labels (AB, BA) exchanged for another sublattice. Here (AB, BA) are related to sublattices and refer to the quantities which are obtained by similar transformations with a relativistic exchange matrix Σ_{rel}^{x} e.g., for the momentum operator $\vec{p}$ one gets $\vec{p}_{BA}=\Sigma_{BA}\vec{p}\;\Sigma_{BA}^{-1}$; v_F is the Fermi velocity. The vector of 2D Pauli matrixes comprises of two matrixes $\sigma_{2D}=(\sigma_x,\sigma_y)$. The term $M_{BA}=-\frac{1}{cv_F}\Sigma_{BA}\Sigma_{AB}$ is a Majorana-like mass term, where c is the speed of light. It turns out to be zero in the Dirac point $K(K')$ and gives a very small momentum dependent correction outside of $K(K')$. The relativistic exchange operator for tight-binding approximation and accounting of nearest lattice neighbors is given by as

$$\Sigma_{rel}^{x}=\begin{pmatrix}0 & \Sigma_{AB}\\ \Sigma_{BA} & 0\end{pmatrix}, \qquad (2)$$

so that its action on secondary quantized wave functions on sublattices $A(B)$ of the system reads

$$\Sigma_{AB}\widehat{\chi}_{\sigma_B}^{\dagger}(\vec{r})\,|0,\sigma\rangle=\sum_{i=1}^{N_v N}\int d\vec{r}_i\,\widehat{\chi}_{\sigma_i B}^{\dagger}(\vec{r})\,|0,\sigma\rangle\,\Delta_{AB} \qquad (3)$$
$$\langle 0,-\sigma_i|\widehat{\chi}_{-\sigma_i^A}^{\dagger}(\vec{r}_i)V(\vec{r}_i-\vec{r})\widehat{\chi}_{-\sigma_B}(\vec{r}_i)|0,-\sigma_{i'}\rangle,$$

$$\Sigma_{BA}\widehat{\chi}_{-\sigma_A}^{\dagger}(\vec{r})\,|0,-\sigma\rangle=\sum_{i'=1}^{N_v N}\int d\vec{r}_{i'}\,\widehat{\chi}_{-\sigma_{i'}^A}^{\dagger}(\vec{r})\,|0,-\sigma\rangle\,\Delta_{BA} \qquad (4)$$
$$\langle 0,\sigma_{i'}|\widehat{\chi}_{\sigma_{i'}^B}^{\dagger}(\vec{r}_{i'})V(\vec{r}_{i'}-\vec{r})\widehat{\chi}_{\sigma_A}(\vec{r}_{i'})|0,\sigma_i\rangle.$$

Here interaction (2×2)-matrices Δ_{AB} and Δ_{BA} are gauge fields (or components of a gauge field). Vector-potentials for these gauge fields are introduced by the phases α_0 and $\alpha_{\pm,k}$, $k=1,2,3$ of $\pi(\mathrm{p}_z)$-electron wave functions $\psi_{\mathrm{p}_z}(\vec{r})$ and $\psi_{\mathrm{p}_z,\pm\vec{\delta}_k}(\vec{r})$ attributed to a given lattice site and its three nearest neighbors (see detail in [3], $V(\vec{r})$ is the three-dimensional (3D) Coulomb potential, summation is performed on all lattice sites and number of electrons. The introduction of these non-abelian gauge fields was stipulated by a requirement of reality of eigenvalues of the Hamiltonian operator as gauge conditions. In this case, the operator of relativistic exchange gains an additional implicit $\vec{k}$-dependence upon momentum in the case of non-zero values of gauge fields.

A global characterization of all Dirac touching with non-abelian Zak phases $\Phi_1,\ldots,\Phi_4$ as arguments of Wilson-loop operator for our model predict the homotopy group Z_{12} with generator $-\pi/6$ in the Dirac points $K(K')$ [3]. It is naturally to assume that such peculiarities would lead also to observable consequences in charge transport in such a system.

2. Non-abelian currents in quasi-relativistic graphene model

Conductivity can be considered as a coefficient linking the current density with an applied electric field in linear regime of

response. To reach the goal, several steps should be performed. First, one has to subject the system by an electromagnetic field, this can be implemented by standard change to canonical momentum $\vec{p} \to \vec{p} - \frac{e}{c}A$ in the Hamiltonian where $\vec{A}$ is a vector-potential of the field. Then, one can find a quasi-relativistic current of charge carriers in graphene as:

$$j_i^{SM} = c^{-1} j_i \equiv j_i^O + j_i^{Zb} + j_i^{so},\ i = 1, 2;$$
$$j_i = e\chi^\dagger_{+\sigma_B}(x^+) v^i_{x^+x^-} \chi_{+\sigma_B}(x^-) - \frac{e^2 A_i}{c\, M_{AB}} \chi^\dagger_{+\sigma_B}(x^+)$$
$$\times \chi_{+\sigma_B}(x^-) + \frac{e\bar{h}}{2M_{AB}} \left[\vec{\nabla} \times \chi^\dagger_{+\sigma_B}(x^+) \vec{\sigma} \chi_{+\sigma_B}(x^-)\right]_i . \quad (5)$$

Here

$$x^\pm = x \pm \epsilon,\ x = \{\vec{r},\ t_0\},\ \vec{r} = \{x, y\},\ t_0 = 0,\ \epsilon \to 0; \quad (6)$$

$v^i_{x^+x^-}$ is the velocity operator determined by a derivative of the Hamiltonian [1], $\chi_{+\sigma_B}(x^+)$ is the secondary quantized fermion field, the terms $j_i^O,\ j_i^{Zb},\ j_i^{so}, i = x, y$ describe an ohmic contribution which satisfies the Ohm law and contributions of the polarization and magneto-electric effects respectively. Potential energy operator V for interaction between the secondary quantized fermionic field $\chi_{+\sigma_B}(x)$ with an electromagnetic field reads

$$V = \chi^\dagger_{+\sigma_B} \Big[-c\vec{\sigma}_{BA} \cdot \frac{e}{c}\vec{A} - M_{BA}(0) - \sum_i \frac{dM_{BA}}{dp_i'}\Big|_{p_i'=0} \quad (7)$$
$$\times \left(p_i^{AB} - \frac{e}{c}A_i\right) - \frac{1}{2}\sum_{i,j} \frac{d^2 M_{BA}}{dp_i' dp_j'}\Big|_{p_i',\ p_j'=0}$$
$$\times \left(p_i^{AB} - \frac{e}{c}A_i\right)\left(p_j^{AB} - \frac{e}{c}A_j\right) + \ldots \Big] \chi_{+\sigma_B}. \quad (8)$$

To perform quantum-statistical averaging for the case of non-zero temperature, we use a quantum field method developed in [4]. After tedious but simple algebra one can find the conductivity in our model:

$$\sigma^O_{ii}(\omega,\ k) = \frac{\imath e^2 \bar{\beta}^2}{(2\pi c)^2} \mathrm{Tr} \int \left(1 - M_{BA}(\vec{p}) \frac{\partial^2 M_{BA}}{\partial p_i^2}\right)$$
$$\times \left(M\vec{v}^i(p), N\vec{v}^i(p)\right) d\vec{p}, \sigma^{Zb}_{ll}(\omega, k) = \frac{\imath e^2 \bar{\beta}^2}{(2\pi c)^2}$$
$$\times \mathrm{Tr} \int \frac{M_{BA}(\vec{p})}{2} \sum_{i=1}^{2} \frac{\partial^2 M_{BA}}{\partial p_i^2} \left(M\vec{v}^i(p),\ N\vec{v}^i(p)\right) d\vec{p}, \quad (9)$$
$$\sigma^{so}_{12(21)}(\omega, k) = (-1)^{1(2)} \frac{\imath}{2} \frac{\imath e^2 \bar{\beta}^2}{(2\pi c)^2}$$
$$\times \mathrm{Tr} \int M_{BA}(\vec{p}) \frac{\partial^2 M_{BA}}{\partial p_1 \partial p_2} \left(M\vec{v}^{1(2)}(p), N\vec{v}^{1(2)}(p)\right) \sigma_z d\vec{p} \quad (10)$$

for the current $j_i^O,\ j_i^{Zb},\ j_i^{so}$ respectively. Here matrices M, N are given by the following expressions:

$$M = \frac{f[\bar{\beta}((H(p^+) - \mu)/\bar{h})] - f[\bar{\beta}(H^\dagger(-p^-) - \mu/\bar{h})]}{\bar{\beta}z - \bar{\beta}(H(p^+)/\bar{h}) + \bar{\beta}(H^\dagger(-p^-)/\bar{h})},$$
$$N = \frac{\delta\,(\bar{h}\omega + \mu)}{(\bar{h}z + H(p^+) - H^\dagger(-p^-))\bar{\beta}}.$$

Here f is the Fermi–Dirac distribution, $z = \omega + i\epsilon$, $\vec{p}^\pm = \vec{p} \pm \vec{k}$, ω is a frequency, μ is a chemical potential, $\bar{\beta}$ is an inverse temperature divided by c.

Total current $\vec{J}$ in graphene are determined by two currents of valleys K, K' as $\vec{J} = \vec{J}_K - \vec{J}_{K'}$. $\vec{J}_K, \vec{J}_{K'}$ are orthogonal to each others due to the homotopy group $\mathbf{Z}_{12}$ of graphene Brillouin zone. Therefore the current directed along an applied electrical field $\vec{E} = (\vec{E}_x,\ \vec{E}_y)$ can be presented as $\vec{J} = \vec{J}_x - \vec{J}_y = \sum_{i=1}^{2}(-1)^{i-1}(\sigma^O_{ii} + \sigma^{Zb}_{ii})\vec{E}_i$. Let us denote the first and the second terms in σ^O_{ii} through σ^o_{ii} and σ^{add}_{ii} respectively: $\sigma^O_{ii} = \sigma^o_{ii} + \sigma^{add}_{ii}$. σ^{add}_{ii} and σ^o_{ii} depends and does not depend on the Majorana-like mass term M_{AB} through respectively. Then, one can determine conductivity σ^{tp}_{ii} for topological currents as $\sigma^{tp}_{ii} = \sigma^{add}_{ii} + \sigma^{Zb}_{ii}$, $\sigma^{tp}_{xx} = -\sigma^{tp}_{yy}$. Fig. 1 demonstrates negative differential differential conductivity for the topological current $j^{tp} = \Re e \sigma^{tp}_{ii}(\omega) U$ assuming the increase of the system energy in a form $\bar{h}\omega \sim U^2$, where U is a bias voltage.

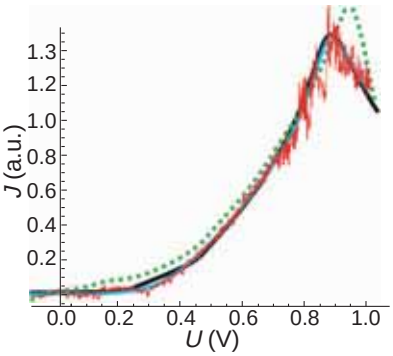

Fig. 1. Dependencies of topological current J on bias voltage U: simulation results (red solid curve) and their fitting (blue solid curve) for negative differential conductivity (NDC) in our quasirelativistic graphene model at temperature $T = 3$ K, chemical potential $\mu = 135$ K; black solid and green dashed curves present experimental data and theoretical calculation for NDC in two graphene flakes twisted approximately at 90° to each other at 1.8° misalignment angle [1]. The bias voltage U is given in volts "V".

A total spin-orbital valley current $\vec{J}_{VHE} = \sigma^{so}_{xy}\vec{B}_y - \sigma^{so}_{yx}\vec{B}_x$ is produced under an action of a magnetic field $\vec{B}_\parallel$ parallel to $\vec{E}$. One can note that $\vec{J}_{VHE}$ is always directed orthogonally to the bias $\vec{E}$ and, accordingly compensates the current $\vec{j}^{tp}$. The current in the direction of the vector $\vec{E}$ increases because of the decrease of "topological current" of leakage $\vec{j}^{tp} - \vec{J}_{VHE}$ in orthogonal to $\vec{E}$ direction signifying that a negative magnetoresistance (NMR) appears at weak magnetic fields parallel to electric ones. NMR is a specific feature of topological materials and presents a phenomenon of chiral anomaly [5].

To conclude we have demonstrated that the $\mathbf{Z}_{12}$ semimetal model as an effective controlling tool due to dichroism of the band structure offers a new class of topological gapless materials. Device construction based on topological currents existing in such materials would provide robust quantum computing.

References

[1] A. Mishchenko *et al*, *Nature Nanotechnology* **9**, 808 (2014).
[2] P. San-Jose *et al*, *Phys. Rev. X* **5**, 041042 (2015).
[3] H. Grushevskaya, G. Krylov, *Symmetry* **12**, 261 (2020).
[4] L.A. Falkovsky, A.A. Varlamov,*Eur. Phys. J.* **56**, 281 (2007).
[5] A.C. Niemann *et al*, *Sci. Rep.* **7**, 43394 (2017).

28th Int. Symp. "Nanostructures: Physics and Technology"
Minsk, Belarus, September 2020

Determination of the quadrupole splitting in bulk n-GaAs by warm-up spectroscopy

V.M. Litvyak[1], R.V. Cherbunin[1] V.K. Kalevich[1,2] and K.V. Kavokin[1]

[1] Spin Optics Laboratory, 1 Ulianovskaya, 198504, St Petersburg, Russia
[2] Ioffe Institute, 26 Politekhnicheskaya, 194021, St Petersburg, Russia

Abstract. We found bulk n-GaAs layers grown by liquid phase epitaxy to be irregularly stressed. Deformation created by this stress causes a small but detectable quadrupole splitting of Zeeman nuclear energy levels. In our work we detected a very weak quadrupole splitting for ^{69}Ga and ^{75}As isotopes in bulk n-GaAs and obtained the value of the sample deformation. To this end, we used a new method that we call warm-up spectroscopy of nuclear spins in weak external magnetic fields.

Introduction

We studied the warm-up of the nuclear spin system (NSS) by the oscillating magnetic field (OMF) in a sample of n-GaAs grown by the liquid phase epitaxy with donor concentration $n = 2\times10^{15}$ cm^{-3}. Due to a small roughness of the surface, each point on the sample had a different magnitude of the quadrupole splitting of nuclear spins. Absorption spectra of OMF by NSS in the external magnetic field were obtained from five-stage experiments, with a varied frequency of the OMF [1].

1. Warm-up spectroscopy

In order to measure absorption spectra, circular polarization of photoluminescence at the wavelength $\lambda = 817$ nm was measured as a function of time, while the external magnetic fields and amplitude of OMF were changed accordingly to the time sequence described below. Experiments were performed at the lattice temperature of about 10 K, with the circularly polarized excitation light focused on different points on the sample. Time sequence at each frequency of the OMF consisted of five stages: 1) dark interval for establishing an equilibrium between nuclear and lattice temperatures during the time of the order of nuclear spin-lattice relaxation time (about 100 s); 2) optical cooling of the NSS in a magnetic field parallel to the pump beam for 120–150 s, when the NSS reaches the nuclear spin temperature of 10^{-3} K; 3) adiabatic demagnetization to zero fields during 20 ms. This time must be shorter than nuclear spin-lattice relaxation time, but longer than the time needed for the establishment of a Boltzmann distribution over NSS energy levels. Adiabatic demagnetization lowers the temperature down to 10^{-5} K; 4) application of the OMF with frequencies $f = 100-50000$ Hz in transverse (relative to the OMF direction) static magnetic fields in the dark during 3–7 s. 5) turning on a weak static magnetic field, transverse to the pump beam, which results in polarization of nuclear spins according to the NSS susceptibility. The electron spin depolarizes in the total field formed by the external and nuclear fields. Thereafter electron spin polarization changes in time, following the relaxation of the nuclear polarization. We measure the time-dependent electron spin polarization from the circular polarization of photoluminescence. From each curve, measured in such a way, we obtained the value of the nuclear field, which remained immediately after the fourth stage. This nuclear field we recalculated to the warmup rate of nuclear spins $1/T_\omega$.

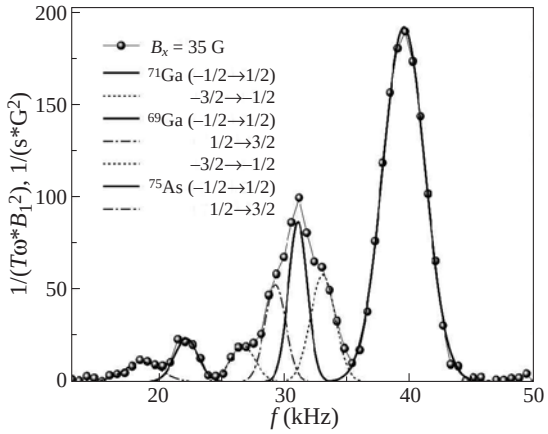

Fig. 1. Absorption spectrum of the NSS by oscillating magnetic field for static transverse magnetic field $B_x = 35$ G. Quadrupole splitting for ^{69}Ga and ^{75}As isotopes is observed. Each peak is fitted by a Gaussian function.

2. Experimental results

For transverse magnetic fields stronger than 20 G, applied on a fourth stage, absorption spectra consist of individual peaks, which correspond to the resonances of ^{71}Ga, ^{69}Ga or ^{75}As nuclei. These peaks have high- and low-frequency satellites shifted to different frequencies, depending on the point on the sample. These satellites correspond to quadrupole splitting (Fig. 1). From the absorption spectrum on Fig. 1, we obtained quadrupole frequency shifts: $\Delta f = 2$ kHz for ^{69}Ga and 4 kHz for ^{75}As. These shifts evidence a very weak quadrupole interaction at this point on the sample. From these frequency shifts we calculated the component ε_b of the deformation tensor (Eq. (1)):

$$\varepsilon_b = \frac{\Delta f 2h}{S_{11} e q_i} \tag{1}$$

where h – Planck constant, e – electron charge, q_i – quadrupole constant for i-th isotope and S_{11} is a component of the gradient-elastic tensor [2,3]. The difference of the quadrupole splitting of different isotopes agrees well with the difference in their quadrupole constants, so that splitting of As and Ga nuclei gives the same estimate of deformation. This deformation was found to be very small, e.g. ten times smaller than in the unstrained QD's where it reaches 30 kHz. Thus, the measurement of absorption spectra using the warm-up rate of the NSS allows one to detect even a very small quadrupole splitting in A_3B_5 crystals under optical pumping conditions.

Acknowledgements

The authors acknowledge Saint Petersburg State University for a research Grant No. 51125686, RFBR for research Grant 19-32-90084 and 19-52-12043.

References

[1] F. Mayer, B. Zakhartchenya, *Optical Orientation*, (Elsevier Science Publishers B.V.) CH.5, 1984.
[2] E.A. Chekhovich, I.M. Griffiths, M.S. Skolnick, *et al*, *Phys. Rev. B*, **97**, 235311 (2018).
[3] I.M. Griffiths, H. Huang, A. Rastelli, *et al*, *Phys. Rev. B*, **99**, 125304 (2019).

28th Int. Symp. “Nanostructures: Physics and Technology”
Minsk, Belarus, September 2020

EMF generation by propagating surface magnetostatic waves in integrated thin-film Pt/YIG structure

Y.V. Nikulin[1,2], M.E. Seleznev[1,2], Y.V. Khivintsev[1,2], V.K. Sakharov[1], E.S. Pavlov[1], S.L. Vysotsky[1,2], A.V. Kozhevnikov, and Y.A. Filimonov[1,2]

[1] Kotel'nikov IRE RAS, Saratov Branch, 410019 Saratov, Russia
[2] Saratov State University, 410012 Saratov, Russia

Abstract. Magnetostatic surface waves (MSSW) propagation and electromotive force (EMF) generation effects in 14.6 μm-thick yttrium iron garnet (YIG) film covered by 8 nm-thick Pt layer was studied. It was found that MSSW dispersion $k = k(f)$ and transmission $S_{21}(f)$ characteristics in YIG/Pt structure are very similar to that of free YIG film. For YIG/Pt structure, we show that EMF (U) demonstrates non-monotonous frequency dependence $U(f)$ and is characterized by two peaks $U_{1,2}$. The first one (U_1) is located near the short-wavelength ($k \to \infty$) cut-off frequency of the MSSW spectra and can be attributed to MSSW drag of electrons in YIG/Pt structure. The second one U_2 is located near the long-wavelength ($k \to 0$) cut-off frequency of the MSSW spectra and can be attributed to the inverse spin Hall effect due to the spin pumping.

Introduction

Development of conductor-magnetic dielectric structures is interesting for information processing systems based on the magnonics and spintronics principles [1,2]. An important task of research aimed to creating an energy-efficient element base is the problem of the effective mutual conversion of the spin and electric currents at the ferrite-conductor interface. The most widely studied structures in this connection are structures based on films of iron-yttrium garnet (YIG) and paramagnetic metals (Pt), where the appearance of a static EMF (U) is explained by the appearance of the inverse spin Hall effect (ISHE) due to spin pumping at the YIG/Pt interface [2–4]. To date, experiments on the detection of static EMF U have been mainly performed under conditions close to excitation of ferromagnetic resonance in the YIG film [1–5]. In this paper, we consider the effect of EMF generation in the YIG/Pt structure due to the drag of electrons in platinum by the field of a propagating MSSW.

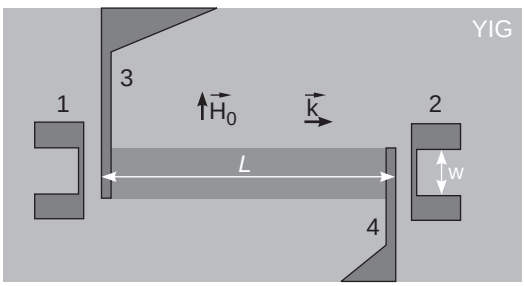

Fig. 1. Photograph of the YIG/Pt structure. The numbers indicate the system of copper microantennas (1,2) and contact pads (3,4) to the Pt microstrip of length L≈630 μm.

1. Experimental

The studied structures were prepared on the base of epitaxial YIG/GGG structure. YIG film has thickness d≈14.6 μm, FMR linewidth ΔH≈0.6 Oe. The Pt film with thickness h≈8 nm and resistivity $\rho \approx 50$ μOhm·m was grown on YIG surface by DC-magnetron sputtering. System of Pt microstrips with length L≈230, 430, 630 and 830 μm and width of w≈110 μm along with the system of copper micro-stripe antennas (1,2) with a width w≈10 μm and length l≈110 μm and contact pads (3,4) were formed on YIG surface by photolithography, ion etching and dc-sputtering (Fig. 1).

The transmission characteristics $S_{21}(f)$ were measured using a vector network analyzer along with a microwave probe station for in-plane magnetic field H≈940 Oe applied along the antennas that corresponds to the excitation of MSSW. It was found that MSSW dispersion $k = k(f)$ and transmission $S_{21}(f)$ characteristics in YIG/Pt structure are very similar to that of free YIG film (Fig. 2). The arrows on frequency axis point positions of low f_0 and high f_s cut-off frequencies of the MSSW bandwidth which corresponds, respectively, to the long-wave-kb lengths ($k \to 0$) and short-wavelength ($k \to \infty$) limits in MSSW spectra $k = k(f)$.

EMF voltage $U(f)$ generated at the edges of the Pt stripes due to the MSSW propagation was measured in carrier modulation (100 kHz) mode in order to separate the thermal voltage induced by the microwave heating of Pt and inertialess effects associated with the transfer of the MSSW impulse to the electrons of Pt.

2. Results

In Fig. 3 the measured dependencies $U(f)$ for YIG/Pt structure with Pt microstripes length L≈230 (1), 430 (2) and 830 (3) μm and for incident pump power $P \approx -5$ dBm are shown. Note that transmission spectra $S_{21}(f)$ for this structures is shown in Fig. 2.

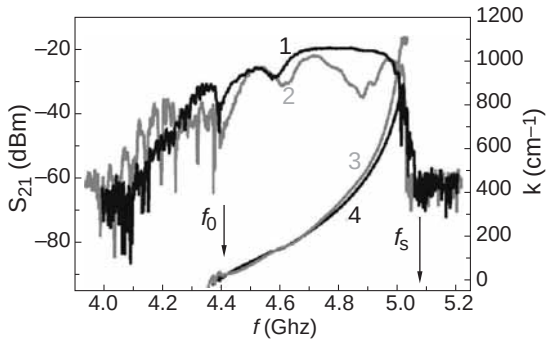

Fig. 2. MSSW transmission $S_{21}(f)$ (1,2) characteristics and dispersion $k(f)$ (3,4) in a free YIG film (1,4) and YIG/Pt structure (2,3) with Pt microstrip of length L≈630 μm.

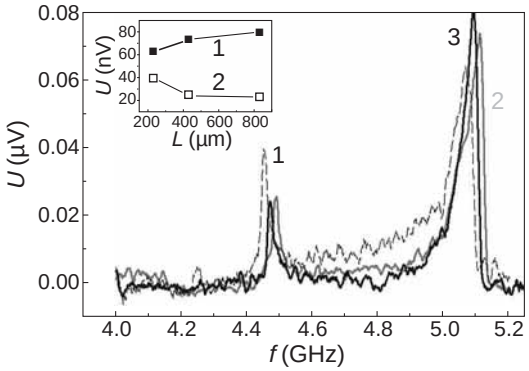

Fig. 3. $U(f)$ dependence for YIG/Pt structure with Pt microstripes length L≈230 (1), 430 (2) and 830 (3) μm. Inset — Dependences of $U(f)$ on the length L of Pt microstrip for peaks at high f_s (1) and low f_0 (2) cut-off frequencies of the MSSW bandwidth.

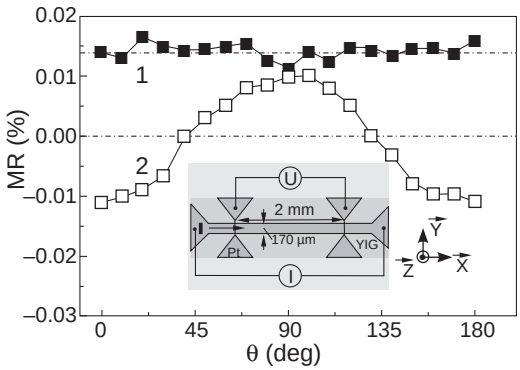

Fig. 4. SHMR values for two cases: 1 — $\vec{H}$ applied in plane and along to the $\vec{I}$ (θ≈0°, 180°) rotates from in-plane direction (θ≈0°, 180°) to out-of-plane (θ≈90°); 2 — $\vec{H}$ rotates in-plane from $\vec{H} \| \vec{I}$ (θ≈0°, 180°) to $\vec{H} \perp \vec{I}$ (θ≈90°). Inset — Hall-bar structure (Pt(8 nm)/YIG(14.6 μm)) for spin Hall magnetoresistance (SHMR) measurements.

One can see, that $U(f)$ dependencies are non-monotonous and can be characterized by two peaks. The first one U_1 is located near short-wavelength frequency limit f_s. The second one U_2 — near the long-wavelength frequency f_0 limit. One can see, that amplitude of peak U_1 increases with Pt length L, while peak U_2 decreases.

For the MSSW power less than the threshold of the parametric instability process, $U(f)$ was proportional to pump power P: $U(f) = G(f) \cdot P(f)$. The sensitivity coefficient G is increased with increasing wave number of the MSW and reached maximum values at frequencies corresponding to the upper boundary of the MSSW zone. The sensitivity for the YIG/Pt structures in the linear mode reaches G≈0.002 V/W at the boundary frequencies $f_{0,S}$ of the MSSW spectra.

The appearance of the two peaks $U_{1,2}$ in studied structure YIG/Pt can be explained by the presence of two mechanisms for generating voltage U. The first mechanism is so-called spin waves drag on electrons [6]. This is "volume" mechanism and acts at any point of Pt layer where MSSW microwave fields can penetrate. It is important that according to this mechanism generated voltage is directly proportional to MSSW wavenumber k. From that point of view one can expect that MSSW drag on electrons is responsible for peak U_1.

The second mechanism, responsible for appearance of the peak U_2, is spin pumping effect at interface YIG/Pt, that leads to generation ISHE. Indeed, the presence of such mechanism in studied structure is proved by spin Hall magnetoresistance (SHMR) measurements, which was done for YIG/Pt structure shown on inset to Fig. 4.

In Fig. 4 curves 1 and 2 shows magnetoresistance (MR) dependences on angle θ between current $\vec{I}$ and magnetic field $\vec{H}$ directions. Curve 1 corresponds $\vec{H}$ rotation in plane $(\vec{x}, \vec{z})$, where $\theta \approx 0°$, 180° corresponds $\vec{H} \parallel \vec{I}$, while $\theta \approx 90°$ corresponds to the out-of-plane orientation ($\vec{H} \parallel \vec{z}$, $\vec{H} \perp \vec{I}$). Curve 2 corresponds to in-plane $(\vec{x}, \vec{y})$ magnetic field rotation from the direction parallel to the current ($I\theta \approx 0°$, 180°) to the direction perpendicular to current I ($\theta \approx 90°$).

From MR(θ) dependence shown by curve 1 on can see, that MR is approximately independent on out-of-plane angle θ, ranging between 0.011% and 0.016%. The MR(θ) dependence for in-plane $\vec{H}$ rotation is close to $sin^2\theta$ dependence, see curve 2. For that case MR(θ) reaches maximal values |MR| $\approx$ 0.012% for $\theta \approx 0°$, 180° ($\vec{H} \parallel \vec{I}$) and $\theta \approx 90°$ ($\vec{H} \perp \vec{I}$), while at $\theta \approx 45°$, 135° MR drops to zero. The in-plane $sin^2\theta$ angular dependence of MR (2) along with out-of-plane dependence MR(θ) $\approx$ const (1) exclude a possible contribution to measured data on Fig. 4 from anisotropic magnetoresistance (as one can expect due to the partial magnetization of Pt atoms near the Pt/YIG interface caused by the proximity effect). This indicates that the observed magnetoresistance mainly come from SHMR induced by the spin current absorption at the YIG/Pt interface.

Acknowledgements

This work has been supported in part by RFBR (projects No. 19-37-90099, No. 20-07-00968).

References

[1] C.W. Sandweg *et al*, *Appl. Phys. Lett.* **97**, 252504 (2010).
[2] H. Kurebayashi *et al*, *Appl. Phys. Lett.* **99**, 162502 (2011).
[3] H. Kurebayashi *et al*, *Nature Materials* **10**, 660 (2011).
[4] C.W. Sandweg *et al*, *Phys. Rev. Lett.* **106**, 216601 (2011).
[5] V. Castel *et al*, *Phys. Rev. B.* **86**, 134419 (2012).
[6] Y.V. Gulyaev *et al*, *J. Comm. Tech. and Electr.* **23**, 897 (1978).

28th Int. Symp. "Nanostructures: Physics and Technology"
Minsk, Belarus, September 2020

Hyperfine interactions in diamond with paramagnetic color centers: Quantum chemistry simulation versus experiment

A.P. Nizovtsev[1,2], S.Ya. Kilin[1], A.L. Pushkarchuk[3,4], S.A. Kuten[4] and F. Jelezko[5]

[1] Institute of Physics, Nat. Acad. Sci. of Belarus, 220072 Minsk, Belarus
[2] National Research Nuclear University "MEPhY", 115409 Moscow, Russia
[3] Institute of Physical-Organic Chemistry, Nat. Acad. Sci. of Belarus, 220072 Minsk, Belarus
[4] Institute for Nuclear Problems, Belarusian State University, 220006 Minsk, Belarus
[5] Institute for Quantum Optics, Ulm University, 89069 Ulm, Germany

Abstract. We are presenting the review of our recent results of computer simulation of spatial and hyperfine characteristics of "nitrogen-vacancy" (NV) and "silicon-vacancy" (SiV) paramagnetic color centers in H-terminated clusters $C_{510}[NV^-]H_{252}$ and $C_{128}[SiV^-]H_{98}$, $C_{128}[SiV^0]H_{98}$. Using the simulated data we have interpreted some available experimental results and did some predictions.

1. Introduction

Hybrid spin systems consisting of the electronic spin of single paramagnetic color centers (PCC) in diamond and neighbor nuclear spins of isotopic ^{13}C atoms are now widely used to implement numerous room-temperature applications in quantum information processing, quantum sensing and metrology (see, e.g. recent reviews [1–5]). In these systems, the 13C nuclear spins with their excellent coherence times serve as quantum memories accessed via the more easily controllable electronic spin of the PCC which, in turn, can be associated with optical photons.

Historically first and most well-studied representative of such hybrid systems is the negatively charged nitrogen-vacancy (NV^-) center in diamond having the electron spin $S = 1$ hyperfine coupled to its intrinsic $^{14}N/^{15}N$ nuclear spin and, as well, to nuclear spins of isotopic ^{13}C atoms in diamond lattice including those disposed rather far from the NV^- center. Such spin systems are currently widely used, in particular, to create small multi-qubit quantum registers and quantum memories or to implement quantum error correction (see, e.g. [6–11]), all at room temperature.

More recently the other PCC in diamond have been identified and studied exhibiting even better optical characteristics in comparison with the NV center. Among them, the vacancy-related group-IV-elements paramagnetic color centers (SiV, GeV, SnV, PbV) have attracted a considerable attention (see e.g. [12] for recent review). The main advantage of these centers over the NV^- center is the fact that most of their fluorescence belongs to a narrow zero-phonon line, allowing for effective optical interfacing their spin state to photons. In particular, for the negatively charged SiV^- center the generation of indistinguishable photons has been obtained [13] and simultaneous microwave control and optical readout of the center spin $S = 1/2$ have been demonstrated [14,15], a key prerequisite for further quantum information processing tasks. Very recently the quantum register [16,17] and quantum repeater [18] were implemented for a first time using *hfi*-coupled electron-nuclear spin systems SiV^--^{13}C. It have been done at very low (mK) temperatures because the SiV^- center exhibits very short spin coherence time of 38 ns [19] even at liquid helium (4 K) temperatures. In turn, the neutral color SiV^0 center has much longer spin coherence time [20] at low temperatures but can be optically bright and stable only in special boron-doped diamond samples. The SiV^0 center is associated with the KUL1 electron paramagnetic resonance center [21,22] with zero-field splitting $D = 942$ MHz.

Essential point for high-fidelity spin manipulation in the above systems with tailored control pulse sequences is a complete knowledge of hyperfine interactions (*hfi*) in them. It is the aim of this report to present the review of our recent results [23–26] concerning simulation of *hfi* characteristics for different hybrid electron-nuclear spin systems in diamond and their comparison with some available experimental data.

2. Basic results

For the NV-^{13}C spin systems we recently found in [23] the *hfi* characteristics by simulation of the NV-hosting H-terminated carbon cluster $C_{510}[NV]^-H_{252}$ where we calculated *hfi* matrices A_{KL} for every possible position of the ^{13}C nuclear spin in the cluster. These matrices have been used in the ground-state spin Hamiltonian of the NV center to calculate the signatures of these *hfi* in optically detected magnetic resonance (ODMR) spectra of various ^{14}NV-^{13}C spin systems. Using the calculated data we were able to identify the ^{13}C atom positions in the specific ^{14}NV-^{13}C spin systems studied experimentally and fit well a wide range of the reported experimental data. More recently our predictions got few direct experimental confirmations [6–8]. Moreover, in [23] we calculated the rates of the ^{13}C spin flip-flops induced by anisotropic *hfi* for all possible locations of ^{13}C atom in the cluster and showed that there are specific positions of nuclear ^{13}C spin, in which it almost does not undergo such flip-flops. Along with the expected stable "NV-axial ^{13}C" systems wherein the ^{13}C nuclear spin is located on the NV axis, we found for the first time new families of positions for the ^{13}C nuclear spin exhibiting negligible *hfi*-induced flipping rates due to near-symmetric local spin density distribution. Spatially, these positions are located in the diamond bilayer passing through the vacancy of the NV center and being perpendicular to the NV axis. Analysis of available publications showed that, apparently, some of the predicted non-axial near-stable systems NV-^{13}C have already been observed experimentally[9–11]. A special experiment [23] done on one of these systems confirmed the prediction made.

Moreover, we used the *hfi* database of the work [23] to predict [24] *hfi* characteristics of various quantum registers NV-

^{13}C in diamond nanocrystals formed by seeding approach from aza-adamantane and methyl-aza-adamantane molecules differing in the position of isotopic ^{13}C nuclear spins in them. Additionally, using the simulated *hfi* database of [23] we predicted optimal characteristics of micro-wave radiation to manipulate effectively (with probability 1) the state of 13C nuclear spins in various coupled spin systems NV-^{13}C [25].

For the coupled SiV^0-^{13}C and SiV^--^{13}C spin systems we also got the full *hfi* matrices simulating neutral [26] and negatively charged clusters $C_{128}[SiV]H_{78}$. We showed that in both cases the completely relaxed clusters exhibited the presence of the inversion center located on the Si atom but the total symmetry of the clusters were D_{3d} and C_{2h}, respectively. Using simulated *hfi* data for SiV^--^{13}C spin systems we were able to identify the position (with respect to the SiV^- center) of the ^{13}C nuclear spin which was recently studied experimentally in [15]. Additionally, we simulated the electronic structure of the cluster $C_{128}[SiV^-]H_{78}$ and analyzed spatial localization of molecular orbitals of the SiV^- center. Detailed results will be presented in few posters at this conference.

Acknowledgements

This work has been supported in part by BRFFI, grants ΦMC-036 and by MEPhY.

References

[1] J.R. Weber *et al*, *PNAS*, **107**, 8513 (2010).
[2] F.J. Heremans, Ch.G. Yale and D.D. Awschalom, *IEEE Proc*, **104**, 2009 (2016).
[3] M.W. Doherty *et al*, *Physics Reports*, **528**, 1 (2113).
[4] D.D. Awschalom *et al*, *Nature Photonics*, **12**, 518 (2018).
[5] J.N. Becker, Ch. Becher., *Phys. Status Solidi A*, **214**, 1700586 (2017).
[6] K. Sasaki, K.K. Itoh and E. Abe, *Phys. Rev. B* , **98**, 121405(R) (2018).
[7] J. Zopes *et al*, *Nat. Communs.* , **9**, 4678 (2018).
[8] M H. Abobeih *et al*, *Nature*, **576**, 411 (2019).
[9] G. Waldherr *et al*, *Nature* **506**, 204-7 (2014).
[10] S. Zaiser *et al*, *Nature Communs.*, **7**, 12279 (2016).
[11] Th. Unden *et al*, *Phys. Rev. Lett.*, **116**, 230502 (2016).
[12] D. Chen, N. Zheludev, W. Gao., *Quantum Technologies*, 1900069 (2019).
[13] A. Sipahigil *et al*, *Phys. Rev. Lett.*, **113**, 113602 (2014).
[14] B. Pingault *et al*, *Phys. Rev. Lett.*, **122**, 190503 (2019).
[15] M.H. Metsch *et al*, *Phys. Rev. Lett.*, **122**, 190503 (2019).
[16] S.T. Nguyen *et al*, *Phys. Rev. Lett.*, **123**, 183602 (2019).
[17] S.T. Nguyen *et al*, *Phys. Rev. B*, **100**, 165428 (2019).
[18] M.K. Bhaskar *et al*, *Nature*, **580**, 60 (2020).
[19] L. Rogers *et al*, *Phys. Rev. Lett.*, **113**, 263602 (2014).
[20] B.C. Rose *et al*, *Science*, **361**, 60 (2018).
[21] A.M. Edmonds *et al*, *Phys. Rev. B*, **77**, 245205 (2008).
[22] U.F.S. D'Haenens-Johansson *et al*, *Phys. Rev. B*, **84**, 245208 (2011).
[23] A.P. Nizovtsev *et al*, *New J. Phys.*, **20**, 023022 (2018).
[24] A.P. Nizovtsev, S.Ya. Kilin and A.L. Pushkarchuk, *Abstracts of XIII Int. workshop on Quantum Optics (IWQO-2019, September 9-14, Vladimir, Russia), p. 87–90*.
[25] A.P. Nizovtsev and S.Ya. Kilin, *Bulletin of the Russian Academy of Sciences: Physics*, **84**, No. 3, 235–240 (2020) (Izvestiya Rossiiskoi Akademii Nauk, Seriya Fizicheskaya, 2020, Vol. 84, No. 3, pp. 310–316).
[26] A.P. Nizovtsev *et al*, *Int. J. of Nanoscience*, **18**, 1940010 (2019).

28th Int. Symp. "Nanostructures: Physics and Technology"
Minsk, Belarus, September 2020

Spin noise of color centers at electron paramagnetic resonance

A.V. Poshakinskiy and S.A. Tarasenko
Ioffe Institute, 194021 St Petersburg, Russia

Abstract. We develop a microscopic theory of spin noise for an ensemble of spin-1/2 and spin-3/2 color centers in the conditions of electron paramagnetic resonance, when the system is subjected to a static magnetic field and driven by a radio-frequency field. The radio-frequency field splits individual peaks in the power spectrum of spin noise into the Mollow-like triplets. Even in systems with strong inhomogeneous broadening, the spin noise spectrum contains narrow lines insensitive to the dispersion of the effective g-factors. Thus, the measurements of spin noise at electron paramagnetic resonance provides an access to the intrinsic spin lifetime of electrons.

Introduction

Optically addressable color centers associated with the defects of crystal lattice, such as NV centers in diamond or silicon vacancies in silicon carbide, are of particular interest for fundamental research in optics and applications in sensorics and spintronics. The centers are characterized by spin-dependent optical cycles: their spin states can be selectively initialized and read-out by optical means and, additionally, efficiently manipulated by a radiofrequency (RF) field [1]. Such color centers can be gathered in the classes depending on their spin in the ground state, $S = 1/2$, $S = 1$, or $S = 3/2$.

Here, we describe a novel method to study the spin and optical properties of color centers: by probing the fluctuations stemming from the interaction of the centers with the environment. The method represents a development of the spin-noise spectroscopy in equilibrium conditions, which has already become a powerful tool for studying the spin dynamics in atomic systems and semiconductors. We develop a microscopic theory of spin fluctuations in an ensemble of half-integer spin centers in the non-equilibrium conditions of paramagnetic resonance, when electrons interacting with environment are subject to a static magnetic field and a weak perpendicular RF magnetic field.

1. Theory

We consider the spin dynamics of an ensemble of color centers in the static magnetic field $\mathbf{B} \parallel z$ and a weak perpendicular magnetic field $\mathbf{B}_{\rm rf}(t)$ that oscillates at frequency $\omega_{\rm rf}$, see Fig. 1(a). We consider the case of rather high temperatures when the average spin polarization is negligible. The spin correlation function, which is a measure of spin fluctuations, is defined by

$$K_{\alpha\beta}(t, t') = \langle s_\alpha(t)\, s_\beta(t')\rangle, \qquad (1)$$

where angle brackets denote averaging over the ensemble. In the equilibrium conditions, the spin correlation function depends on the time difference $t - t'$ only. The presence of an external RF field breaks the time homogeneity in the system. Therefore, the correlation function $\mathbf{K}(t, t')$ depends not only on the time difference $t-t'$ but also on the absolute time $(t+t')/2$. The latter dependence is periodic in $2\pi/\omega_{\rm rf}$ because of the RF field periodicity.

In such conditions, the spin-noise spectrum can be defined as [2]

$$K^{(n)}_{\alpha\beta}(\omega) = \langle s_\alpha(\omega + n\omega_{\rm rf}/2) s_\beta(\omega - n\omega_{\rm rf}/2)\rangle, \qquad (2)$$

where $\mathbf{s}(\omega) = \int \mathbf{s}(t)\, \mathrm{e}^{\mathrm{i}\omega t} dt$ is the Fourier transform of the noise. In a conventional spin noise experiment, one measures the spectral density of the spin noise, which corresponds to $K^{(0)}_{\alpha\beta}(\omega)$. Other harmonics $K^{(n)}_{\alpha\beta}(\omega)$ with $n \neq 0$ arise only in the presence of the RF drive. They correspond to correlation function between the spin-noise signal and the spin-noise signal frequency-shifted by $n\omega_{\rm rf}$ and are accessible by a lock-in technique.

2. Spin-1/2 centers

The dynamics of a spin-1/2 center is governed by the operator equation

$$\frac{d\mathbf{s}}{dt} = [\mathbf{\Omega}_{\rm L} + \mathbf{\Omega}_{\rm rf}(t) + \mathbf{\Omega}_{\rm fl}(t)] \times \mathbf{s}\,, \qquad (3)$$

where $\mathbf{\Omega}_{\rm L} = (0, 0, \Omega_{\rm L})$ and $\mathbf{\Omega}_{\rm rf}(t) = \Omega_{\rm rf}(\cos\omega_{\rm rf} t, \sin\omega_{\rm rf} t, 0)$ are the Larmor frequencies corresponding to the static magnic field fields $\mathbf{B}$ and to the circularly polarized RF field $\mathbf{B}_{\rm rf}(t)$. Interaction with environment for the spin-1/2 center is described in terms of its precession in a rapidly fluctuating magnetic field with frequency $\mathbf{\Omega}_{\rm fl}(t)$ that leads to spin relaxation.

In most of experiments, an ensemble of centers rather than a single center is probed. The ensemble is characterized by some dispersion in the parameters, which leads to inhomogeneous broadening of the peaks in the spin-noise spectra. The application of RF field can suppress this broadening providing an access to the intrinsic spin relaxation time. To illustrate it, we consider the ensemble with a distribution of the effective g-factors resulting in a variation of the Larmor precession frequency $\Omega_{\rm L}$.

Figure 1(b-d) shows the spectra of the spin-noise density $K^{(0)}_{xx}$ calculated for the ensembles with different g-factor dispersions. Panel (b) shows the spin-noise spectra in the absence of the RF field, which feature a single peak at the average Larmor frequency of the ensemble $\Omega_{\rm L}$. The dispersion of the g-factors results in a significant broadening of the peak and a decrease of its amplitude. When the resonant RF field is turned on, the single peak is split into the Mollow triplet, see Fig. 1(c). The evolution of the triplet when the frequency of the RF field is detuned from the resonant condition $\omega_{\rm rf} = \Omega_{\rm L}$ is shown in Fig. 1(d). Importantly, the central peak of the triplet at $\omega = \omega_{\rm rf}$ is not broadened with the increase of the g-factor dispersion while its amplitude exhibits only a slight decrease. The side peaks of the triplet are shifted from the central peak by the frequency $\Omega' = \sqrt{\Omega_{\rm rf}^2 + (\Omega_{\rm L} - \omega_{\rm rf})^2}$. In the ensemble with the dispersion of $\Omega_{\rm L}$, the side peaks are asymmetric: their outer

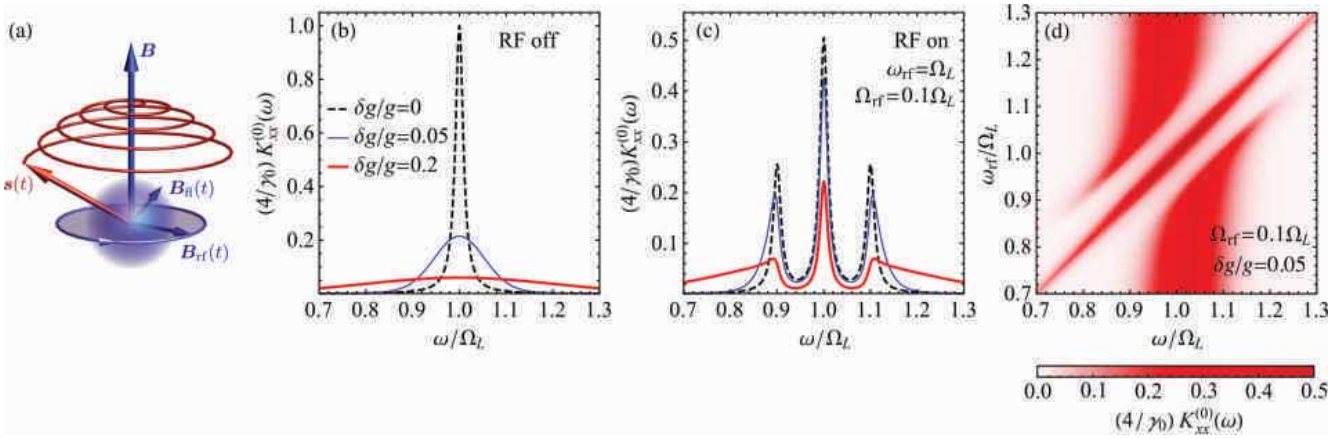

Fig. 1. (a) Dynamics of an electron spin **s** in the presence of static **B**, radio-frequeqncy $\mathbf{B}_{\rm rf}(t)$, and fluctuating $\mathbf{B}_{\rm fl}(t)$ magnetic fields. (b) Spin noise spectra $K_{xx}^{(0)}(\omega)$ in the absence of RF field for various g-factor dispersions δg. (c) The same when the RF field with the frequency $\omega_{\rm rf} = \Omega_{\rm L}$ and the intensity corresponding to the Rabi frequency $\Omega_{\rm rf} = 0.1\Omega_{\rm L}$ is turned on. (d) Evolution of the spectra when the RF field frequency $\omega_{\rm rf}$ is scanned.

wings are broadened while the inner wings, which are shifted from the central peak by $\Omega_{\rm rf}$, remain sharp. Therefore, the narrow peaks with the widths determined by the intrinsic spin relaxation time are resolved in the RF driven noise spectrum even for the ensembles with large dispersions while the noise spectrum in the absence of RF field is completely smeared, cf. thick red lines in Fig. 1(b) and (c).

3. Spin-3/2 centers

The spin state of an ensemble of spin-3/2 centers is described by the 4×4 spin density matrix with 15 real linearly independent components which stand for 3 components of the spin dipole polarization **s**, 5 components of the spin quadrupole polarization **d**, and 7 components of the spin octupole polarization **f** [3]. Due to the spin sensitivity of the optical cycle of Si vacancies in SiC, the photoluminescence intensity depends on whether the center is in the "bright" state with $s_z = \pm 3/2$ or in the "dark" state with $s_z = \pm 1/2$. The jumps of individual centers between these states leads to fluctuations (blinking) of the photoluminescence intensity. The correlation function of the photoluminescence intensity $g^{(2)}$ is determined by the correlation function

$$K_{zz,zz}(t,t') = \langle d_{zz}(t)\, d_{zz}(t')\rangle \tag{4}$$

of the spin quadrupole $d_{zz} = s_z^2 - 5/4$. Application of the RF with the frequency that matches the splitting between the states with $s_z = \pm 1/2$ and $s_z = \pm 3/2$ induces the Rabi oscillations between these levels. Then, the spectral density of the quadrupole polarization fluctuations assumes the form

$$K_{zz,zz}^{(0)}(\omega) \propto \frac{1}{1 + (\omega - \Omega_{\rm R})^2 T_d^2} \tag{5}$$

and can be used to measure the spin-quadrupole relaxation time T_d. In the presence of a static magnetic filed, the RF field can couple the spin quadrupole to the spin dipole and octupole, and their relaxation times T_s and T_f can also be extracted from the noise spectra of the photoluminescence intensity. A more complex technique involving RF drive at two distinct frequencies can be used to eliminate the effect of inhomogeneous broadening [4].

Summary

To summarize, we have studied spin noise of an ensemble of color centers in the non-equilibrium conditions of the magnetic resonance. It is shown that application of a resonant radio-frequency magnetic field splits the peaks in the spin-noise spectra into the Mollow triplets. The central peak of the triplet appears to be robust against inhomogeneous broadening, while the side peaks are smeared in such an asymmetric way that their inner wings remain sharp. Therefore, the measurements of the spin-noise spectra in the presence of radio-frequency field provide an access to the intrinsic spin relaxation time in an inhomogeneous ensemble. The spin fluctuations in an ensemble of spin-3/2 centers can be probed by measuring the correlation function of the luminescence intensity $g^{(2)}$. The spectral density of the photoluminecence intensity fluctuations provides information about the relaxation time of spin multipoles.

Acknowledgements

This work was supported by the Russian President Grant No. MK-599.2019.2 and the Foundation "BASIS".

References

[1] V.A. Soltamov, C. Kasper, A.V. Poshakinskiy *et al*, *Nat. Commun.* **10**, 1678 (2019).

[2] A.V. Poshakinskiy and S.A. Tarasenko, *Phys. Rev. B* **101**, 075403 (2020).

[3] S.A. Tarasenko, A.V. Poshakinskiy, D. Simin *et al*, *Phys. Status Solidi B* **255**, 1700258 (2018).

28th Int. Symp. "Nanostructures: Physics and Technology"
Minsk, Belarus, September 2020

DFT simulation of electronic and spin properties of GeV^- color center in volume and near-surface of nanodiamond for Temperature Sensor applications

A.L. Pushkarchuk[1,2], A.P. Nizovtsev[1,3], S.Ya. Kilin[1], S.A. Kuten[4], V.A. Pushkarchuk[5], D. Michels[6], D. Lyakhov[6] and F. Jelezko[7]

[1] Institute of Physical-Organic Chemistry, Nat. Acad. Sci. of Belarus, 220072 Minsk, Belarus
[2] Institute of Physics, Nat. Acad. Sci. of Belarus, 220072 Minsk, Belarus
[3] National Research Nuclear University "MEPhY", 115409 Moscow, Russia
[4] Institute for Nuclear Problems, Belarusian State University, 220030 Minsk, Belarus
[5] Belarusian State University of Informatics and Radioelectronics,22013 Minsk, Belarus
[6] Computer, Electrical and Mathematical Science and Engineering Division,
4700 King Abdullah University of Science and Technology, Thuwal 23955-6900, Saudi Arabia
[7] Institute for Quantum Optics, Ulm University, 89069.Ulm, Germany

The "germanium-vacancy" (GeV) center in diamond by analogy with the well-known "nitrogen-vacancy" (NV) center can be used for integrated quantum-optical and quantum-information systems including as remarkable Temperature Sensors [1]. The idea of GeV-based thermometry is based on optical measurements of the spectral shift of the zero-phonon line and its spectral width as a function of temperature changes. (see e.g. [2] as recent review). Optical characteristics of GeV center which is located near-surface could be modified by formation of defect states in forbidden zone based on surface dangling bonds. Below we are presenting results of computer simulation for the negatively charged GeV^- color center using density functional theory (DFT) to elucidate spatial structure and electronic properties for the "volume" H-terminated diamond-like cluster $C_{69}[GeV^-]H_{84}$ containing 69 carbon atoms hosting the GeV^- center in its central part and 84 hydrogen atoms which saturate dangling bonds on the surface of volume cluster (Fig. 1a). Beside it, we considered "surface" cluster $C_{64}[GeV^-]H_{68}$-(100)-11H having one dangling bond at the (100) diamond surface (see [3]). "Surface" cluster was obtained from the "volume" H-terminated cluster $C_{69}[GeV^-]H_{84}$ (Fig. 1a) by elimination of five carbon atoms to form the (100) surface consisted in this case of the 6 superficial C atoms, for which 11 of 12 dangling bonds were saturated with hydrogen atoms while one was left to be not saturated. For this cluster denotation (100) 11H means, that 11 hydrogen atoms are adsorbed on surface (100) (Fig. 1b). DFT calculations were performed using the ORCA program package [4]. The spatial structure of the clusters was optimized using the DFT/UKS/PW91/RI/def2-SVP level of theory. As shown in [5] this functional and basis set is large enough to yield good results in the geometry optimization and in the calculation of the electronic structure for the GeV center. The GeV^- center has the spin-doublet ($S = 1/2$) ground state. During geometry optimization the Ge atom moves to new interstitial position as it is substantially larger than the carbon atoms of the diamond lattice (Fig. 1a). The DFT calculations have been done with the fully relaxed "surface" clusters with reconstructed (2×1) symmetry.

Preliminary analysis for the electronic structure of "volume" cluster and possible influence on the electronic structure of cluster of the surface dangling bond on is presented in this paper. Results of electronic structure calculation of the clusters under investigation are presented on the Fig. 2.

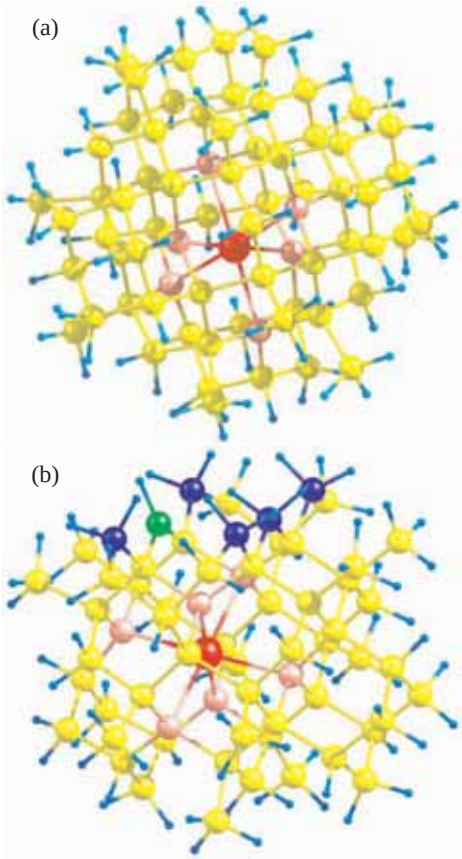

Fig. 1. Structures of the (a) "volume" $C_{69}[GeV]H_{84}$ cluster and (b) "surface" $C_{64}[GeV]H_{68}$-(100)-H11 cluster optimized by DFT/UKS/PW91/RI/def2-SVP level of theory. The colors of the atoms: C — yellow, Ge — red, C nearest neighbors to Ge — pink, surface C — dark blue, C with dangling bond — green, H — blue.

It was shown for the first time that formation of isolated dangling bond on the (100) diamond surface leads to formation of unoccupied state in forbidden zone in vicinity of 1 eV, which is located on the distance of 1.9 eV of conduction band edge.

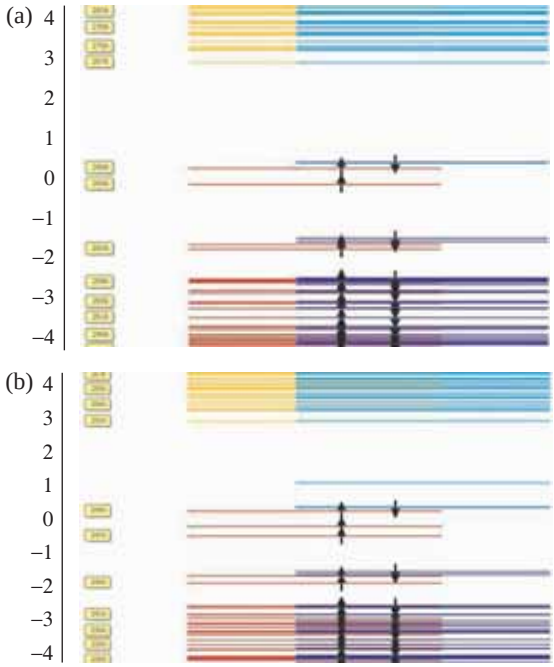

Fig. 2. Electronic Structure of the (a) "volume" C_{69}[GeV]H_{84}cluster and b) "surface" C_{64}[GeV]H_{68}-(100)-H11 clusters are optimized by DFT/PW91/RI/def2-SVP level of theory. Energy is referred in units of eV. Different direction of arrows ↑ and ↓ indicates spin orientation (α and β) for given electronic level. Red color defines occupied levels for α orientation, and blue does for β orientation. While yellow defines unoccupied levels for α orientation and cyan does for β orientation.

We conclude that this state in forbidden zone may influence optical properties of GeV in diamond.

References

[1] P. Siyushev *et al*, *Phys. Rev.*, **B 96**, 081201(R) (2017).
[2] J.-W. Fan *et al*, *ACS Photonics*, **5**, 765 (2018).
[3] V.A. Pushkarchuk *et al*. *Int. Journal of Nanoscience*, **18**, 1940012 (4 pages) (2019)
[4] F. Neese *Wiley Interdiscip. Rev.: Comput. Mol. Sci.*, **2**, 73 (2012).
[5] A. Komarovskikh *et al*, *Diamond and Related Materials*, **76**, 86 (2017).

28th Int. Symp. “Nanostructures: Physics and Technology”
Minsk, Belarus, September 2020

Investigation of magnetic property of $Mn_{0.095}Hg_{0.905}Te$ by ESR method

A.V. Shestakov, I.V. Yatsyk, I.I. Fazlizhanov, M.I. Ibragimova, R.M. Eremina
Zavoisky Physical-Technical Institute, FRC Kazan Scientific Center of RAS, 420029 Kazan, Russia

Abstract. A single crystal of mercury chalcogenide $Mn_{0.095}Hg_{0.905}Te$ was grown by crystallization from a two-phase mixture with replenishment of the melt from tellurium solution and has *n*-type conductivity. The EPR spectra of a single crystal were studied at temperatures from helium to 100 K, angular evolution was completed at a temperature of 5 K and liquid nitrogen. One line with a smaller g-factor is associated with charge carriers localized on defects with a strong exchange interaction with the spins of manganese ions. The second line, the narrowed ESR line, was identified as a signal from Mn^{2+} ions.

Introduction

Narrow-gap MnHgTe semiconductor is an alternative to CdHgTe, because it has better structural properties and higher values of the mobility of charge carriers [1,2]. And therefore this allows the use of MnHgTe instead of CdHgTe [3], especially in applications where stringent requirements are imposed on the stability of a device's parameters. One of the first studies of magnetic properties of solid $Hg_{1-x}Mn_xTe$ solutions was performed by Andrianov *et al* [4]. Magnetic properties strongly depend on the Mn concentration. Strong spin-spin interactions between band electrons and localized magnetic ions lead to many completely new magneto-optical physical phenomena, such as the Faraday giant [5] and photoinduced magnetization effects [6]. The manganese ions are in a bivalent state in solid $Hg_{1-x}Mn_xTe$ solutions with antiferromagnetic exchange interaction between them [7]. At x greater than 0.3, magnetic clusters with antiferromagnetic interaction are formed [8]. Features of Shubnikov-De Haas oscillations for single crystal $Mn_{0.11}Hg_{0.89}Te$ were investigated in [9,10].

The aim of this work was to study the magnetic properties and characteristics of charge carriers in the monocrystals of the *n*-$Mn_{0.095}Hg_{0.905}Te$ compound using magnetic resonance method.

1. Experimental

The *n*-$Hg_{0.905}Mn_{0.095}Te$ monocrystals were grown by crystallization from a two-phase mixture with replenishment of the melt from a tellurium solution. The concentration of Mn ions was refined by SEM[1] method ($x = 0.095 \pm 0.002$). The TEM[2] method has showed that this sample is single-phase and the lattice period is 6.441 Å. The crystal composition was determined from measurements of the Hall coefficient and spectral distribution of photoconductivity. Characteristic of the sample at 77 K were: electron concentration $n_{500} = 9.3\times10^{14}$ cm^{-3} (500 Oe), $n_{15000} = 8.8\times10^{14}$ cm^{-3} (15000 Oe), resistivity $\rho = 5.9\times10^{-2}\Omega\times$ cm, mobility $\mu = 11\times10^5$ cm$^2\cdot V^{-1}\cdot s^{-1}$.

ESR spectra were measured on ER 200 SRC (EMX/plus) spectrometer (Bruker) using temperature controller (Oxford instruments ITC 503S). Measurements of angular dependence were performed at the temperatures 77 K and 5 K at the magnetic fields varying from 0 to 1×10^4 Oe using X-band Varian E12 on frequency (9.15 GHz). The sample ~ 1 mm^3 was placed into the cavity. The microwave absorption power derivative (dP/dH) was registered.

[1] Scanning electron microscope
[2] Transmission electron microscopy

2. Experimental results

The angular evolution of the X-band ESR spectra as a function of the magnetic field for $Hg_{0.905}Mn_{0.095}Te$ single crystal at the temperature 5 K and 77 K are shown in Fig. 1 and 2. Two intensive lines were observed in ESR spectra at 5 K.

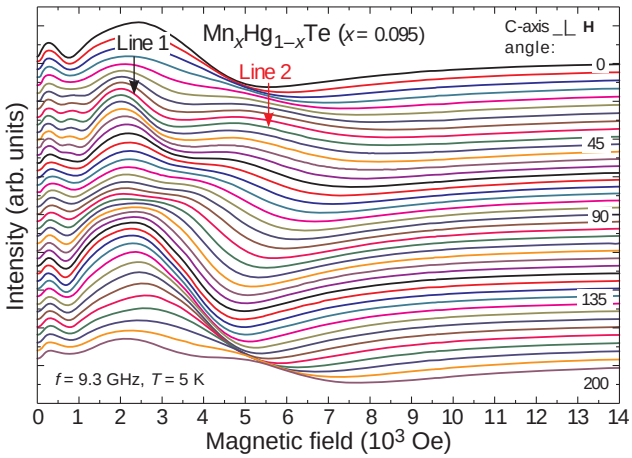

Fig. 1. The angular evolution of the ESR spectra in $Hg_{0.905}Mn_{0.095}Te$ at the 5 K.

The linewidth and position of ESR line were fitted by the Lorentz curve with an asymmetric Dyson coefficient (α) [11]:

$$\frac{dP}{dH} \sim \frac{d}{dH}\left[\frac{\Delta H+\alpha\,(H-H_0)}{4\,(H-H_0)^2+\Delta H^2}+\frac{\Delta H-\alpha\,(H+H_0)}{4\,(H+H_0)^2+\Delta H^2}\right], \quad (1)$$

where ΔH — linewidth, H_0 — resonance magnetic field.

As the temperature increased from 5 to 77 K, the positions of the resonance lines shifted to the region of smaller g-factors, and the shifts for the first and second lines were the same (see Fig. 3).

The temperature evolution of the X-band ESR spectra for $Hg_{0.905}Mn_{0.095}Te$ single crystal from 5 K to 105 K is shown in Fig. 4.

As can be seen, the two high-intensity ESR lines are broadening significantly with temperature increasing. We believe that the strong exchange interaction between the spins of conduction electrons and holes and manganese ions leads to a nontrivial behavior of the temperature dependence of the ESR spectra of single crystal $Hg_{1-x}Mn_xTe$. Estimating the effective g-factor from the resonance relation $h\nu = g_{\text{eff}}\beta H$ shows that the g-factors of the first and second ESR lines are significantly different from $g \simeq 2.0$ and their temperature dependencies

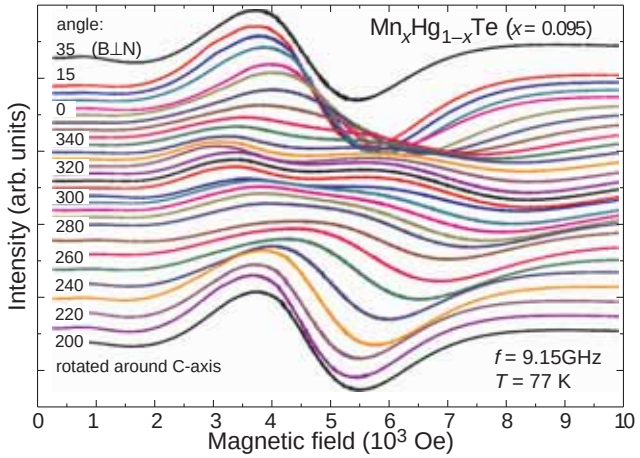

Fig. 2. The angular evolution of the ESR spectra in $Hg_{0.905}Mn_{0.095}Te$ at the 77 K.

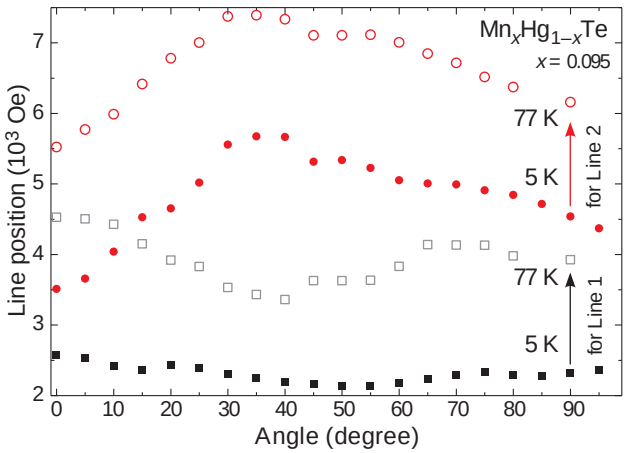

Fig. 3. The angular dependencies of the resonance fields of first and second ESR lines at the 5 and 77 K.

are not characteristic for paramagnetic behavior. In the EPR spectra at temperatures above 75 K in the region 3.4 KOe the third low-intensity line from the spins of manganese ions was registered.

We suppose that the first and second ESR lines are associated with localized charge carriers magnetic moments near defects and spins of manganese ions with strong exchange interaction. The presence of two different types of charges is consistent with the results for p-$Mn_xHg_{1-x}Te$ epitaxial films with $x = 0.12$–0.19 where different types of carriers were observed: heavy (m_1) and light (m_2) holes in p-$Mn_{0.135}Hg_{0.865}Te$: m_1/m_0=0.27, m_2/m_0=0.032 [12].

As can be seen from Fig. 5 the changes in the character of the temperature dependencies of linewidths are observed in region 10 K and 70 K. We suppose that this is due to the presence of phase transitions in this sample. We associate the phase transition observed near 10 K with the metal-semiconductor transition. Presumably the transition at 70 K corresponds to the delocalization of carriers on defects.

Acknowledgements

We are grateful to N.M. Lyadov for the SEM measurements and V.A. Shustov for X-ray diffraction analysis.

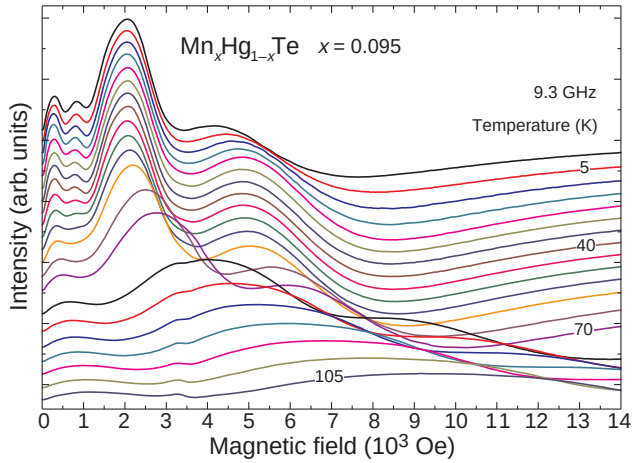

Fig. 4. The temperature evolution of the ESR spectra in $Hg_{0.905}Mn_{0.095}Te$.

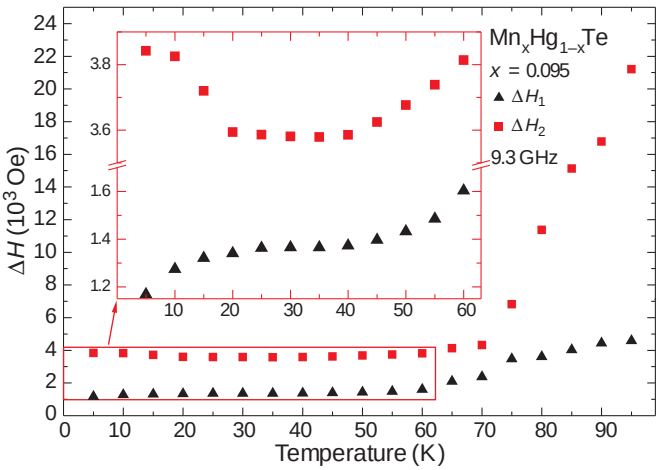

Fig. 5. The temperature dependencies of the linewidth of 1^{st} and 2^{d} ESR lines in $Hg_{0.905}Mn_{0.095}Te$.

References

[1] A. Rogalskii, *Infrared Physics* **31** (2), 117–166 (1991).
[2] A. Rogalskii, *Prog. Quantum Electron.* **13**, 299 (1989).
[3] V.G. Deibuk *et al*, *Semiconductors* **39** (10), 1111–1116 (2005).
[4] D.G. Andrianov *et al*, *Sov. Phys. Semicond.* **10** (1), 66–68 (1976).
[5] J.F. Dillon *et al*, *Journal of Applied Physics* **67**, 4917–4919 (1990).
[6] H. Krenn *et al*, *Phys. Rev. Lett.* **55**, 1510 (1985).
[7] W. Zewen and J. Wanqi, *Journal of Wuhan University of Technology-Mater. Sci. Ed.* **30**, 1130–1133 (2015).
[8] S. Nagata *et al*, *Physical Review B* **22** (7), 3331–3343 (1980).
[9] A.E. Belyaev *et al*, *Sov. Phys. Semicond.* **22** (2), 205–207 (1988).
[10] A.V. Shestakov *et al*, *Semiconductors*, **52** (14), 1817–1821 (2018).
[11] P. Janhavi *et al*, *Journal of Magnetic Resonance* **168**, 284–287 (2004).
[12] I.M. Nesmelova, *Semiconductors*, **37** (11), 1257–1258 (2003).

28th Int. Symp. "Nanostructures: Physics and Technology"
Minsk, Belarus, September 2020

Magnetic resonances in nanoscale particles of ferrihydrite

S.V. Stolyar [1,2,3], V.P. Ladygina[2], D.A. Balaev[1,3], A.I. Pankrats[1,3], Yu.V. Knyazev[1], R.N. Yaroslavtsev[1,2] and R.S. Iskhakov[1]

[1] Kirensky Institute of Physics, SB Russian Academy of Sciences, 660036, Krasnoyarsk, Russia
[2] Krasnoyarsk Scientific Center, Federal Research Center KSC SB RAS, 660036, Krasnoyarsk, Russia
[3] Siberian Federal University, 660041, Krasnoyarsk, Russia

Abstract. Ferromagnetic resonance was used to study three types of ferrihydrite nanoparticles: nanoparticles formed as a result of the cultivation of microorganisms *Klebsiella oxytoca*; chemically ferrihydrite nanoparticles; chemically prepared ferrihydrite nanoparticles doped with Cu. It is established from the ferromagnetic resonance data that the frequency-field dependence (in the temperature range $T_P < T < T^*$) is described by the expression: $2\pi\nu/\gamma = H_R + H^A_{(T=0)} \cdot (1-T/T^*)$, where γ is the gyromagnetic ratio, H_R is the resonance field. The induced anisotropy H^A is due to the spin-glass state of the near-surface regions. T_P temperature characterizes the energy of the interparticle interaction of nanoparticles.

Introduction

The size of the ferrihydrite nanoparticles, which is a magnetic semiconductor, is in a narrow range of up to 8 nm. The transformation $Fe_2O_3{\cdot}nH_2O \rightarrow Fe_2O_3$ occurs as the particle sizes increase. Ferrihydrite plays a huge role in the metabolism of living organisms because it is formed in the core of the protein complex of ferritin. The majority of magnetic studies was performed on ferritins (horse spleen ferritin) and ferrihydrites obtained chemically. According to the results of these studies, ferrihydrite is an antiferromagnet with a Neel temperature $T_N = 340$ K [1]. The superparamagnetic blocking temperature can vary up to ~100 K as a function of the origin of the nanoparticles and their size. At low temperatures, the magnetization curves are characterized by magnetic hysteresis and exchange bias (after cooling in an external field [2–4]. The temperature dependences of the coercive field and the exchange bias field are usually correlated. The resonance properties of ferrihydrite nanoparticles were studied in [5,6]. The resonance curves at low temperatures are characterized by nonmonotonic temperature dependences and additional absorption lines. The purpose of this work is to study ferrihydrite nanoparticles by the method of ferromagnetic resonance. We investigated three types of nanoparticles: nanoparticles formed as a result of the cultivation of microorganisms Klebsiella oxytoca; chemically ferrihydrite nanoparticles; chemically prepared ferrihydrite nanoparticles doped with Cu.

1. Experimental

Nanoparticles of biogenic ferrihydrite are synthesized as a result of the cultivation of microorganisms. The bacterium *Klebsiella oxytoca* under anaerobic conditions can synthesize secretory exopolysaccharide [7–9], which is associated with nanoparticles of ferrihydrite. The synthesized biogenic powders are ferrihydrite nanoparticles coated with polysaccharides. This shell significantly weakens the interactions between ferrihydrite nanoparticles, which makes it possible to assess the contribution of interparticle interactions to the magnetic properties of the material. Synthetic ferrihydrite nanoparticles are synthesized as a result of the reaction of Fe^{3+} iron salt and alkali solution. The addition of Cu salt to the solution in the preparation of ferrihydrite nanoparticles by a chemical method led to the doping of the nanoparticles. Electron microscopic studies of the resulting nanoparticles were carried out on a Hitachi HT7700 transmission electron microscope (accelerating voltage of 100 kV). The sizes of the studied nanoparticles were 2–3 nm. Magnetic resonance studies were carried out using an original setup [10], which makes it possible to obtain frequency–field dependences in a wide range of fields, frequencies and temperatures.

2. Results and discussion

Figure 1 shows the frequency–field dependences for two temperatures: 4.2 and 150 K. The figure shows that at $T = 4.2$ K ν(H) is characterized by a gap, which depends on temperature. This gap indicates the presence of induced rotational anisotropy in the ferrihydrite nanoparticles [11]. Using the values of the resonance fields, the temperature dependences of the anisotropy field were determined, which are shown in Figure 2 for two frequencies of 75 and 52 GHz. Fig. 2 shows that the induced anisotropy field HR linearly depends on temperature in the range $T_P < T < T^*$. At $T^* \approx 60$ K $H_R \rightarrow 0$. The behavior of the anisotropy field at $T < T_P$ indicates the presence of another type of interaction in chemically synthesized nanoparticles of ferrihydrite. This additional interaction mechanism turns off at $T = T_P$. For comparison, the inset in Fig. 2 shows the dependence of the induced anisotropy field $H_A(T)$ of ferrihydrite nanoparticles coated with a polysaccharide shell [12]. For biogenic ferrihydrite nanoparticles, the T_P temperature is absent.

The presence of induced anisotropy indicates the freezing of this subsystem of spins, i.e., the transition to a spin-glass state at a temperature T^* above which the subsystem of surface spins goes into the paramagnetic state. The table shows the results of a study of ferrihydrite nanoparticles by FMR method ($\nu = 75$ GHz). The presence of a large specific surface in magnetic nanoparticles leads to the formation of surface anisotropy due to a violation of the coordination numbers of surface atoms [13]. High values of surface anisotropy in ferrihydrite nanoparticles are also due to structural features consisting of surface depletion of the nanoparticle'[14]. The effect of surface depletion leads to the fact that the density of the surface regions is less than the density of the central part of the particle. The configurations of cation-cation bonds in the surface region should lead to frustration of exchange interactions and the formation of a spin-glass state.

Ferrihydrite nanoparticles with a magnetic moment interact with each other, which can lead to a "collective spin glass" state at low temperatures. We believe that at $T < T_P$, collective

Table 1. Spin-glass transition temperature and anisotropy field of ferrihydrite samples

Sample	BioFerr	SynthFerr	SynthFerr+Cu(5%)
H_A (Oe)	7.66	13.52	14.9
T^* (K)	55	64	56
T_P, (K)	—	14	16

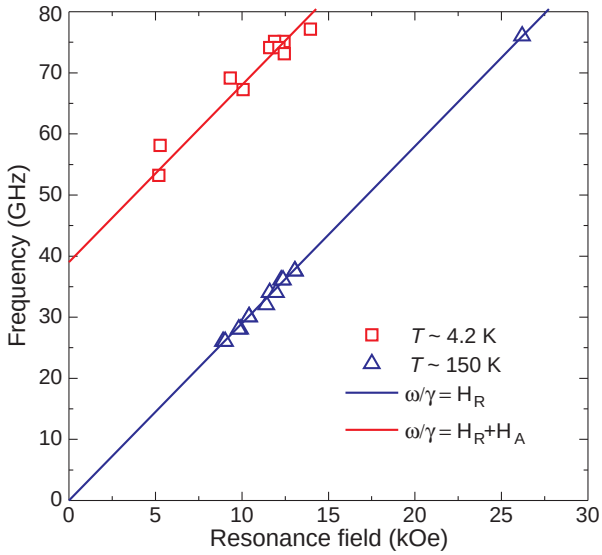

Fig. 1. Frequency-field dependences of synthetic ferrihydrite at temperatures of 4.2 and 150 K.

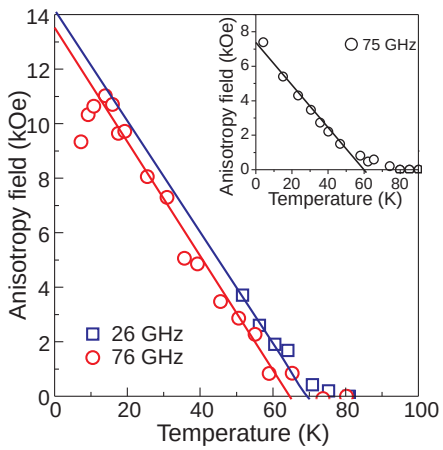

Fig. 2. Temperature dependences of induced anisotropy fields of at frequencies of 26 and 76 GHz. The inset shows the temperature dependence of the anisotropy field for biogenic ferrihydrite.

effects play a decisive role, due to the interaction of chemically synthesized ferrihydrite nanoparticles. In the case of ferrihydrite nanoparticles coated with a polysaccharide coating, this effect is absent.

Acknowledgements

This work was supported by the Russian Foundation for Basic Research, the Government of the Krasnoyarsk Territory, the Krasnoyarsk Regional Fund for the Support of Scientific and Technical Activities (project No. 19-42-240012 r-a "Magnetic resonance in ferrihydrite nanoparticles: Effects associated with the "core-shell" structure). This work was supported by a grant from the President of the Russian Federation for state support of young Russian scientists-candidates of sciences No. MK-1263.2020.3.

References

[1] M.S. Seehra, V.S. Babu, A. Manivannan *et al*, *Phys. Rev. B* **61**, 3513 (2000).
[2] D.A. Balaev, A.A. Krasikov, A.A. Dubrovskiy *et al*, *J. Appl. Phys.* **120**, 183903 (2016).
[3] S.A. Makhlouf, F.T. Parker, and A.E. Berkowitz, *Phys. Rev. B* **55**, R14717 (1997).
[4] A. Punnoose, T. Phanthavady, M.S. Seehra *et al*, *Phys. Rev. B* **69**, 54425 (2004).
[5] A. Punnoose, M.S. Seehra, J. van Tol *et al*, *J. Magn. Magn. Mater.* **288**, 168 (2005).
[6] S.V. Stolyar, R.N. Yaroslavtsev, R.S. Iskhakov *et al*, *Phys. Solid State* **59**, 555 (2017).
[7] F. Baldi, A. Minacci, M. Pepi *et al*, *FEMS Microbiol. Ecol.* **36**, 169 (2001).
[8] S.V. Stolyar, O.A. Bayukov, Y.L. Gurevich *et al*, *Inorg. Mater.* **42**, 763 (2006).
[9] S. Kianpour, A. Ebrahiminezhad, M. Mohkam *et al*, *J. Basic Microbiol.* **57**, 132 (2017).
[10] V.I. Tugarinov, I.Y. Makievskii, and A.I. Pankrats, *Instruments Exp. Tech.* **47**, 472 (2004).
[11] R.J. Prosen, J.O. Holmen, and B.E. Gran, *J. Appl. Phys.* **32**, S91 (1961).
[12] S.V. Stolyar, D.A. Balaev, V.P. Ladygina *et al*, *JETP Lett.* **111**, 183 (2020).
[13] B. MartInez, X. Obradors, L. Balcells *et al*, *Phys. Rev. Lett.* **80**, 181 (1998).
[14] T. Hiemstra, *Geochim. Cosmochim. Acta* **158**, 179 (2015).

28th Int. Symp. "Nanostructures: Physics and Technology"
Minsk, Belarus, September 2020

Ballistic conductance in a topological 1T′ MoS_2 Nanoribbon

V. Sverdlov[1,2], A.-M. El-Sayed[1], H. Kosina[1], and S. Selberherr[1]

[1] Christian Doppler Laboratory for Nonvolatile Magnetoresistive Memory and Logic
Institute for Microelectronics, Technische Universität Wien, 1040 Wien, Austria
[2] Institute for Microelectronics, Technische Universität Wien, 1040 Wien, Austria

Abstract. A MoS_2 sheet in its 1T′ phase is a two-dimensional topological insulator. It possess highly conductive edge states which due to topological protection, are insensitive to back scattering and are suitable for device channels. A transition between the topological and conventional insulator phases in a wide 1T′-MoS_2 sheet is controlled by an electric field orthogonal to the sheet. In order to enhance the current through the channel several narrow nanoribbons are stacked. We evaluate the subbands in a narrow nanoribbon of 1T′-MoS_2 by using an effective $\mathbf{k}\cdot\mathbf{p}$ Hamiltonian. In contrast to a wide channel, a small gap in the spectrum of edge states in a nanoribbon increases with the electric field. It results in a rapid decrease in the nanoribbon conductance with the field, making it potentially suitable for switching.

Edge states in two-dimensional (2D) topological insulators (TI) propagate without backscattering, making them attractive for designing highly conductive transistor channels [1]. However, possessing robust conductive channels is only one requirement for a good transistor. To make a switch it is necessary to suppress the current through the channel as a function of gate voltage. A standard approach is to restore the traditional band order [2]. Recently it was discovered that the 1T′ phase of MoS_2, a well-known 2D material with a high promise for future microelectronic devices [3], is a TI [4]. The inverted band structure is well approximated by parabolas, with the conduction and valence bands having masses of $m_{y(x)}^{d(p)}$ [4]. The spin-orbit interaction opens a gap at the intersection of the valence and conduction bands, which appears at a finite value of the momentum k_y along the quantization axis OY (Fig. 1, solid green lines). A topologically protected highly conductive edge state must exist within the gap. By applying an electric field E_z along the OZ axis perpendicular to the nanoribbon the gap at one of the minima can be reduced, closed (Fig. 1, dotted red lines), and open again (Fig. 1, dashed-dotted blue lines) at large electric fields. The gap at large electric fields becomes a direct gap, so no edge states are allowed within the bulk gap. In order to investigate transport through a nanoribbon, the subband structure and the wave functions must be evaluated first. We parametrize the energy in units of the band inversion gap 2δ at $k_y = 0$, while $k_{y(x)}$ in units of $k_0 = \left(\frac{2\delta}{\hbar^2}\frac{m_y^d m_y^p}{m_y^d + m_y^p}\right)^{1/2}$. By applying a unitary transformation, the 4×4 Hamiltonian [4] is cast in a block-diagonal form [5]:

$$\mathbf{H} = \begin{pmatrix} H(\mathbf{k}) & 0 \\ 0 & H^*(-\mathbf{k}) \end{pmatrix}. \qquad (1)$$

The possibility to express the Hamiltonian in the form (1) is a consequence of the time-reversal symmetry [5]. It then follows that at every edge, if allowed, there are two topologically protected modes propagating in opposite directions with opposite spins. The 2×2 Hamiltonian $H(\mathbf{k})$, $\mathbf{k} = (k_x, k_y)$ in dimensionless units has the form:

$$H(\mathbf{k}) = \begin{pmatrix} \frac{1}{2} - k_y^2 \frac{m}{m_y^p} - k_x^2 \frac{m}{m_x^p} & v_2 k_y + \alpha E_z + i v_1 k_x \\ v_2 k_y + \alpha E_z - i v_1 k_x - \frac{1}{2} + k_y^2 \frac{m}{m_y^d} + k_x^2 \frac{m}{m_x^d}) \end{pmatrix}. \qquad (2)$$

$m = \frac{m_y^d m_y^p}{m_y^d + m_y^p}$ and $v_{1(2)}$ are the Fermi-velocities. We consider a nanoribbon with a width in the OY direction of $d = 40k_0^{-1} \approx 27$ nm. A subband wave function, $\psi_{k_x}(y) = \sum_{j=1}^{4} A_j \exp'(ik_j y)$, where A_j is a two-component spinor, is set to zero at both edges. The dispersion equation is solved numerically, in complete analogy to the problem of finding the eigenenergies and eigenfunctions for a 2-band $\mathbf{k}\cdot\mathbf{p}$ Hamiltonian in silicon films [6]. Figs 2,3, and 4 show the dispersion for several electron and hole subbands. A peculiar feature, which distinguishes the subband structure from that in silicon films, is the presence of the subband with nearly linear dispersion (Fig. 2). The energy of the subband lies in the band gap seen in Fig. 1. The solution corresponds to the topologically protected edge modes. A small gap is opened at $k_x = 0$ reflecting the fact that the topological states located at the two opposite edges interact. By increasing E_z the gap between the subbands electron (hole) subbands minima (maxima) $E_i^{e(h)}$ grows (Fig. 5). It exists (Fig. 3) even when the gap in the bulk is zero (Fig.1, dashed red). The behavior is in sharp contrast to that in a wide ribbon. The nanoribbon ballistic conductance

$$G = \frac{2e^2}{h} \sum_i \left[\frac{1}{1 + \exp'\frac{E_i^e - E_F}{k_B T}} + \frac{1}{1 + \exp\frac{E_F - E_i^h}{k_B T}} \right] \qquad (3)$$

as a function of E_z is shown in Fig.6. Due to the growing gap (Fig.5), G decreases rapidly with the field. This makes 1T′-MoS_2 potentially suitable for transistor applications.

The financial support by the Austrian Federal Ministry for Digital and Economic Affairs and the National Foundation for Research, Technology and Development is gratefully acknowledged. A.-M.E-S. was partly supported by project No. IN 23/2018 "Atom-to-Circuit" modeling technique for exploration of Topological Insulator based ultra-low power electronics — by the Centre for International Cooperation & Mobility (ICM) of the Austrian Agency for International Cooperation in Education and Research (OeAD).

References

[1] L. Kou *et al*, *J. Phys. Chem. Lett.* **8**, 1905 (2017).
[2] W.G. Vandenberghe and M.V. Fischetti, *Nature Comm.* **8**, 14184 (2017).
[3] Yu. Illarionov *et al*, *Nature Electronics* **2**, 230 (2019).
[4] X. Qian *et al*, *Science* **346**, 1344 (2014).
[5] B. Zhou *et al*, *Phys. Rev. Lett.* **101**, 246807 (2008).
[6] V. Sverdlov and S. Selberherr, *Phys. Reports* **585**, 1 (2015).

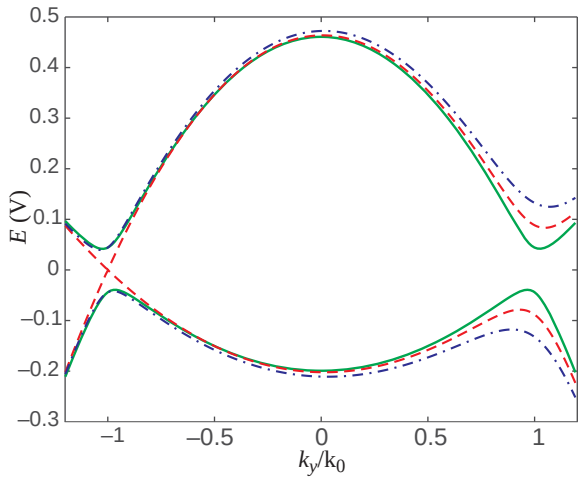

Fig. 1. Bulk bands in 1T′-MoS_2 with an inverted gap at $k_y = -k_0$ at $E_z = 0$ (solid lines), the gape closed at $\alpha E_z = \hbar k_0 v_2$ (dashed lines) and open as a direct gap at ($\alpha E_z = 2\hbar k_0 v_2$, dashed-dotted lines).

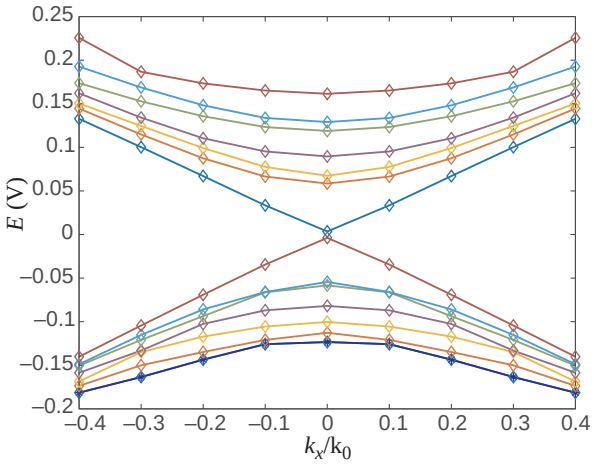

Fig. 2. Subbands in a nanoribbon of the width $d = 40/k_0$ at E_z=0. The subband with an almost linear dispersion corresponding to the topologically protected edge state is clearly seen.

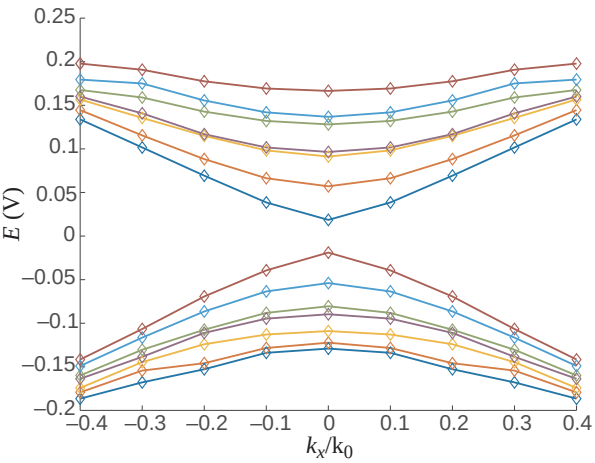

Fig. 3. Subband energies in a nanoribbon of the width $d = 40/k_0$ at $\alpha E_z = \hbar k_0 v_2$, when the gap at $k_y = -k_0$ is closed, see Fig.1, dashed lines.

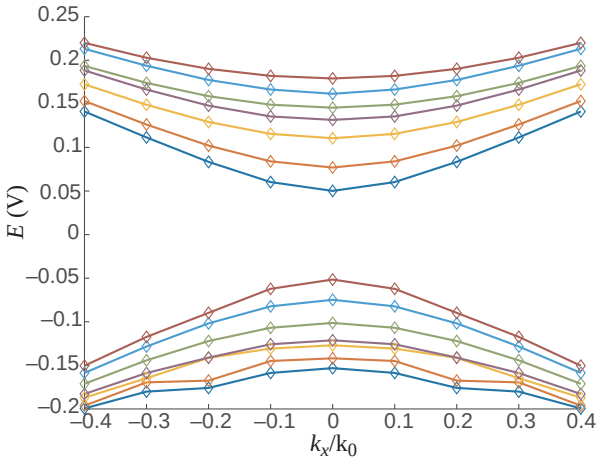

Fig. 4. Subband energies in a nanoribbon of the width $d = 40/k_0$ at $\alpha E_z = 2\hbar k_0 v_2$, when the direct gap opens again at $k_y = -k_0$, see Fig.1, dashed-dotted lines.

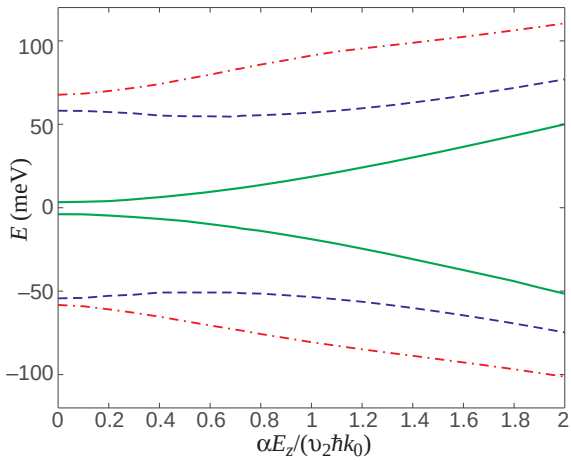

Fig. 5. Dependence of electron (hole) subbands minima (maxima) on the electric field E_z. In contrast to the bulk case, the gap never closes and keeps increasing with E_z growing.

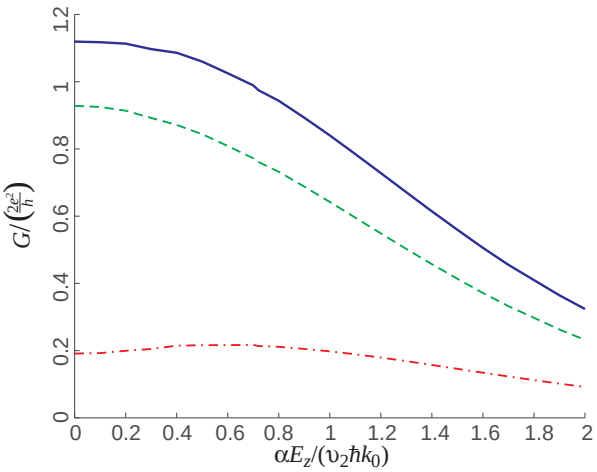

Fig. 6. Ballistic conductance (solid line) of a 1T′-MoS_2 nanoribbon, with the contributions due to the first edge-like states (dashed line), and bulk-like subbands (dashed-dotted line).

28th Int. Symp. "Nanostructures: Physics and Technology"
Minsk, Belarus, September 2020

Effect of strain on voltage generation in Pt-YIG thin film structure under spin wave pumping

S.L. Vysotskii[1,2], A.V. Kozhevnikov[1], Y.V. Khivintsev[1,2], A.S. Dzhumaliev[1,2], V.K. Sakharov[1], Y.V. Nikulin[1,2], M.E. Seleznev[1,2], and Y.A. Filimonov[1,2]

[1] Kotelnikov Institute of Radio-engineering and Electronics of RAS, Saratov Branch, 410019, Saratov, Russia
[2] Chernyshevsky Saratov State University, 410012, Saratov, Russia

Abstract. Effect of a strain applied to a yttrium iron garnet (YIG) — platinum (Pt) layered structure on the electrical voltage induced in Pt by a spin wave propagating in YIG is experimentally explored. It is found that the strain can significantly shift a frequency range where the voltage generation is observed at a fixed bias magnetic field and can boost the generated voltage.

Introduction

Yttrium-iron garnet (YIG) films are considered as one of the main materials for design and development of energy efficient information technologies based on principals of magnonic spintronics and straintronics [1–3]. As YIG films possess the lowest spin wave relaxation and magnetostriction properties, they are used for formation of synthetic multiferroic structures capable effectively control the phase, delay time, filtration bandwidth as well as bistability of spin waves [4,5]. On the other hand, thin-film YIG/Pt structures are actively used to study the effects of mutual transformation of spin and electric currents induced by effects of spin and magnetoelastic pumping at the interface L-magnetic insulator LL paramagnetic metal having strong spin-orbit interactionL [1,6,7].

Experiment

In the experiment we used a monocristalline YIG film grown by a liquid phase epitaxy on a gadolinium gallium garnet substrate of (111) orientation. The YIG film thickness was 3.6 μm. A Pt layer with the thickness of 15 nm was deposited on the YIG film by a direct current magnetron sputtering. The resistivity of the Pt film in our case was $\rho \approx 5\times10^{-7}$ Ohm·m, which is 5 times higher than the ρ value for bulk material. Planar dimensions of the structure were 3 by 10 mm.

The structure was placed on a alumina ceramic plate with microstrip transducers for excitation and detection of spin waves so that the spin waves traveled between the transducers along the long part of the sample. The width of the transducers was 30 μm and length 0–4 mm. The distance between transducers was 5 mm. External bias magnetic field was applied perpendicular to the wave propagation that corresponds to the magenotstaic surface wave (MSSW). The transducers were connected to a vector network analizer in order to excite the MSSW and measure its transmission characteristics.

In order to measure the voltage generated in Pt due to the MSSW propagation inYIG, a lock-in amplifier was used. The voltage was measured between two contacts formed on Pt layer by a conductive glue. The contacts were made so that the voltage generated along the MSSW propagation direction was measured. The voltage measurements were carried out in the pulse mode: a microwave signal coming from the network analyzer was modulated by meander like pulses with a pulse repetition rate of 11.33 kHz and then was applied to the sample.

In order to allow bending deformation for the Pt-YIG structure, a part of the alumuna ceranic plate between the transducers was cut out. A presure was applied in the center of the sample so that the structure bent down in the middle supported by the transducers on sides (see inset to Fig. 1). The pressure was controlled by a mass of the load applied to the structure.

Results

The measurements performed on the YIG film before the Pt deposition showed quite effective conversion of the microwave signal to the MSSW, its transmission between transducers and conversion back (see Fig. 1). In the MSSW transmission band, we observed notches corresponding to the so called "dipole-exchange" resonances [8].

For the Pt–YIG structure, the MSSW propagation was significantly suppressed so that only a narrow band transmission was observed close to the longwave limit of the MSSW spectrum. As a result, the voltage induced in the Pt layer was also observed in a narrow frequency range of about 20 MHz.

This effect can be attributed to the strong influence of the Pt conductivity on the MSSW at-tenuation at the chosen Pt thickness [9]. Figures 2(a) and 2(b) show the results of dispersion $q'(f) = \mathrm{Re}\,(q(f))$ and spatial decrement $q''(f) = \mathrm{Im}\,(q(f))$ calculation (here q is the wave number at frequency f), respectively, for MSSW propagating in the considered structure. In

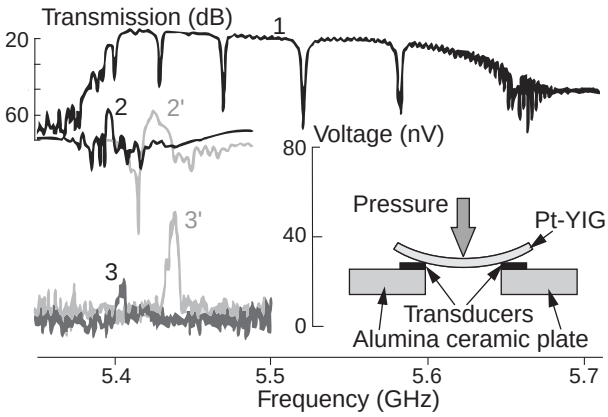

Fig. 1. Curve 1 is the microwave transmission versus a frequency for the YIG film before the Pt deposition. Curves 2 and 2' are the microwave transmission versus a frequency for the Pt-YIG structure with and without the strain, respectively. Curves 3 and 3' are the induced voltage versus a frequency for the Pt-YIG structure with and without the strain, respectively.

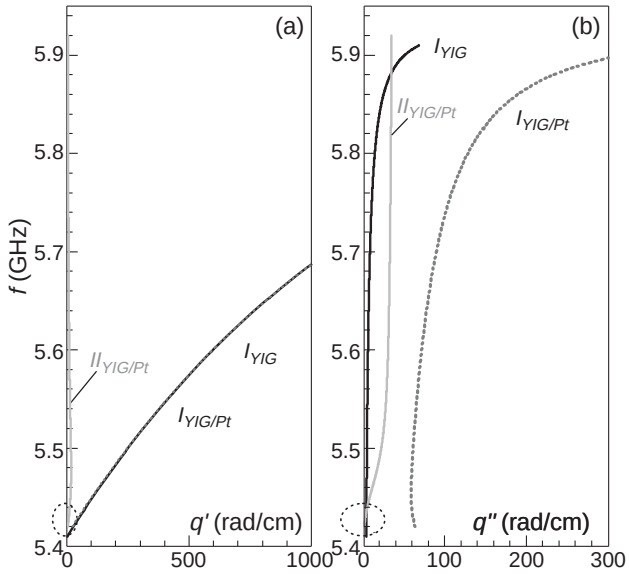

Fig. 2. Calculated dispersion dependence $q'(f) = \mathrm{Re}\, q(f)$ (a) and frequency dependence of spatial decrement $q''(f) = \mathrm{Im}\, q(f)$ (b) for YIG film and YIG/Pt structures.

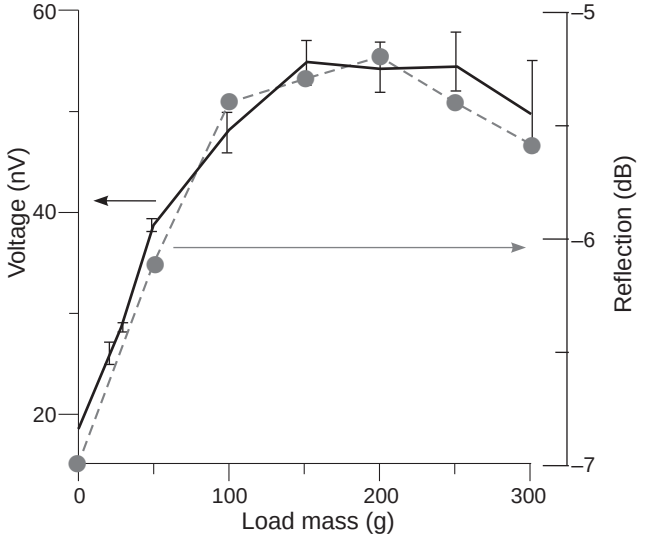

Fig. 3. The voltage induced in the Pt and the reflection coefficient for the input pransducer as a function of the load mass.

Fig. 2, for the dispersion branch $II_{\mathrm{YIG/Pt}}$, we marked the frequency range 20 MHz where the relation $q' \geq q''$ is fulfilled and MSSW propagation in the considered structure is possible. For any other frequency belonging to $II_{\mathrm{YIG/Pt}}$ branch, real and imaginary parts of MSSW are related as $q' < q''$ that corresponds to non-propagating waves. Dispersion branch $I_{\mathrm{YIG/Pt}}$ is rather close to the MSSW dispersion in a single YIG film, see curves I_{YIG} and $I_{\mathrm{YIG/Pt}}$ in Fig. 2(a). However, imaginary part of MSSW wave number for I branch in YIG/Pt structure have values $q''(f) \geq 60\ \mathrm{cm}^{-1}$ that is significantly higher than in the single YIG film, see curves I_{YIG} and $I_{\mathrm{YIG/Pt}}$ in Fig. 2(a). Besides, in YIG/Pt structure, losses of MSSW with the dispersion $I_{\mathrm{YIG/Pt}}$ are ≥ 100 dB at the path length of 3 mm.

When the strain was applied to the Pt-YIG structure both the MSSW transmission band and the frequency range for observation of the induced voltage shifted up in the frequency. This shift is caused by a magnetostriction effect [10].

Also, an increase in the induced voltage was observed as the strain increased. The last might be related with the change in the MSSW excitation efficiency. We believe that the transducers are not in perfect matching conditions for the MSSW excitation. By applying the strain we bend the sample and slightly change the YIG film position relatively to the transducer. In turn, this can change matching the transducer with the YIG film and boost the MSSW excitation efficiency. This explanation is supported by identical behavior of the generated voltage and a reflection coefficient for the input trancder versus the load mass (see Fig. 3).

Acknowledgements

This work has been supported in part by Russian Foundation for Basic Research (projects 19-37-90099 and 20-07-00968).

References

[1] A.V. Chumak *et al*, *Nat. Phys.* **11**, 4530 (2015).
[2] S.A. Nikitov *et al*, *Phys.Usp.* **58**, 1002 (2015).
[3] A.A. Bucharaev *et al*, *Phys.Usp.* **61**, 1175 (2018) .
[4] Y.K. Fetisov *et al*, *Appl. Phys. Lett.* **88**, 143503 (2006).
[5] A.B. Ustinov *et al*, *Tech. Phys. Lett.* **36**, 166 (2010).
[6] Y. Kajiwara *et al*, *Nature* **464**, 262 (2010).
[7] N.I. Polzikova *et al*, *AIP Advan.* **6**, 056306 (2016).
[8] Yu.V. Gulyaev *et al*, *Sov. Phys.-JETP Lett* **30**, 565 (1979).
[9] A.G. Veselov *et al*, *Radiotekh. Elektron.* **39**, 2067 (1994).
[10] S.L. Vysotskii *et al*, *J. Comm. Tech. Electron.* **64**, 1398 (2019).

28th Int. Symp. "Nanostructures: Physics and Technology"
Minsk, Belarus, September 2020

Nonlinear optical response of the colloidal CdSe nanoplatelets under one-photon stationary excitation of excitons

A.M. Smirnov[1,2], *A.D. Golinskaya*[1], M.V. Kozlova[1], E.V. Zharkova[1] and B.M. Saidzhonov[1], R.B. Vasiliev[1] and V.S. Dneprovskii[1]

[1] M.V. Lomonosov Moscow State University, 1-2 Leninskie Gory, 119991, Moscow, Russia
[2] Kotel'nikov IRE RAS, Mokhovaya 11-7, Moscow 125009, Russia

Abstract. Nonlinear change in transmission and photoluminescence of the colloidal CdSe nanoplatelets in the case of stationary exciton excitation by the third harmonic of mode-locked Nd^{3+}:YAP laser pulses allowed to identify peculiarities of the exciton dynamics. The values of saturation intensity were determined from the measured differential transmission spectra. The revealed broadening and red shift of the photoluminescence spectra can be the evidence of the formation of trions and their radiative recombination at room temperature.

Introduction

The advanced methods of colloidal synthesis allow to prepare nanocrystals with a precise control of size, crystal structure, composition and shapes. Among them, two-dimensional colloidal planar crystal, also termed as nanoplatelets, recently emerged as a novel class of material with novel electronic and optical properties [1–6]. The nanoplatelets are semiconductor planar nanocrystals with lateral size of tens nanometers and thickness controlled at the atomic scale. The absorption and emission spectra of the ensemble of nanoplatelets can be tuned by the thickness control owing to size quantization in one (z ∥ [001]) direction [7–8]. These ultrathin planar nanocrystals attract a great deal of attention due to their simplicity synthesis techniques and the set of potential applications in optoelectronic devices such as light emitting diodes [9–11], lasers [12–13], solar concentrations [14] and field effect transistor [15]. Their potential in such applications originates from their unique physical properties, including extremely narrow emission line (full width at half maximum about several meV) and the absence of inhomogeneous broadening as a result of their uniform thickness, high exciton binding energy (up to several hundred meV) owing dielectric confined effect and fast radiative lifetimes (more than one nanosecond) related to the giant oscillator strength effect [16–18]. The nanoplatelets also demonstrate large magnitude of nonlinearities at the room temperature owing to the excitonic resonances enhancement in the spectral vicinity of the fundamental absorption edge [16–21]. The peculiarities of the nonlinear absorption of heterostructured core/shell nanoplatelets in the case of one-photon excitation of the excitons are well understood [22–25] but the exciton dynamic in core-only nanoplatelets has not been extensively studied yet.

In this work, we report the nonlinear optical response of the colloidal CdSe core-only nanoplatelets under the one-photon excitons excitation by means of 10-nanosecond laser pulses.

1. Experimental details

The studied population of 3.5 monolayer thick CdSe nanoplatelets with the lowest energy of exciton absorption band at 463 nm have been synthesized according to [26]. Briefly, 0.5 mmol of $Cd(CH_3COO)*H_2O$, 0.2 mmol of oleic acid (OA) and 10 mL of octadecene (ODE) were loaded into a reaction flask. Then, the mixture was heated to 170 °C and degassed under argon for 30 min. After that, the temperature was increased to 210 °C, and a mixture of 100 μL 1M trioctylphosphine selenide and 350 μL of ODE was injected into the reaction flask. The growth was allowed to proceed for 40 min at 210 °C and was then cooled to room temperature using a water bath. During the cooling process, 0.5 ml of OA was added to the mixture. As-grown nanoplatelets were washed twice by the addition of acetone and centrifugation at 6000 rpm. Finally, the nanoplatelets were dispersed in 6 ml of hexane. The concentration of the nanoplatelets in solution was about 10^{15} cm^{-3}. The morphology of the nanoplatelets was investigated using a LEO912 AB OMEGA transmission electron microscope (TEM) operating at an accelerating voltage of 100 kV (Figure 1a). Dilute solutions of the nanoplatelets were used for optical measurements. The lateral dimension is about 20×100 nm.

The measured transmission spectrum of the colloidal solution of CdSe nanoplatelets (see Figure 1b) is characterized by two well-resolved excitonic minima corresponding to light- and heavy-hole excitons transitions (1lh-1e and 1hh-1e, correspondently).

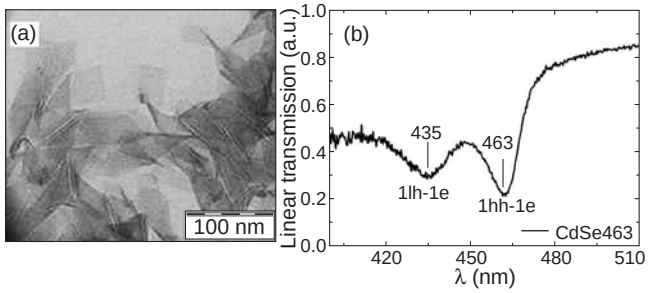

Fig. 1. TEM (a) and linear transmission spectrum (b) of the colloidal CdSe nanoplatelets.

The nonlinear properties of the colloidal CdSe nanoplatelets were investigated by means of modification of pump and probe technique described in ref. [27]. The measurement of nonlinear transmission spectra was realized by the means of the third harmonic pulses of the Nd^{3+}:YAP laser. ($\lambda = 360$ nm, duration is 9 ns). Laser radiation was split into two beams half of which was utilized for the colloidal nanoplatelets excitation. The second half of the third harmonic radiation excited Coumarin-120 dye whose broadband photoluminescence was used to probe

the changes in absorption of the solution. The pump and the probe beams are space-combined and time-synchronised. The radiative recombination time in the nanoplatelets is about 1 ns [1] thus stationary one-photon excitation of excitons was realized. The photoluminescence spectrum of specially chosen dye coincides with the exciton absorption band of the nanoplatelets. All the measurements were carried out at the room temperature.

2. Results and discussions

The linear and nonlinear transmission (under the different pump intensities) were measured. The intensity of laser radiation varied within the range of 0.05 MW/cm^2 to 2.5 MW/cm^2. By the measured linear and nonlinear transmission spectra, the differential transmission spectra were plotted:

$$DT = \frac{T(\lambda, I) - T_0(\lambda)}{T_0(\lambda)}, \qquad (1)$$

where $T_0(\lambda)$ is the linear transmission spectrum and $T(\lambda, I)$ is the transmission spectrum of the sample excited by laser pulses.

The differential transmission spectra of the studied nanoplatelets as function of pump intensity are demonstrated in Fig.2. The significant changes of absorption and saturation

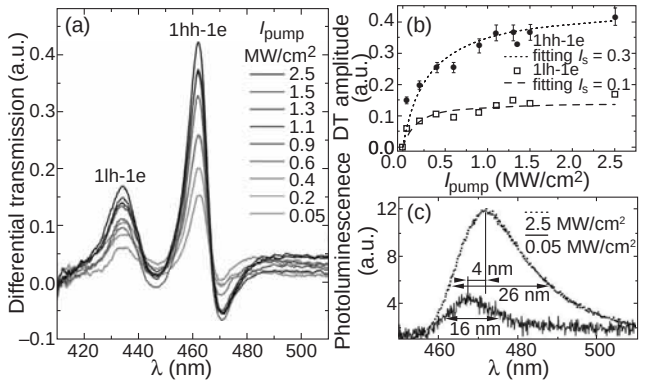

Fig. 2. (a) The differential transmission spectra of the colloidal CdSe nanoplatelets at the different pump intensities. The wavelength of the laser third harmonic was 360 nm. (b) The amplitude of the differential transmission (DT) spectra maxima as a function of pump intensity for light-hole (dots) and heavy-hole (squares) exciton transitions. (c) Photoluminescence spectra at the high (dot line) and the low (solid line) pump intensities.

at the wavelengths of 1hh-1e and 1lh-1e exciton transitions was observed that can be explained by the dominant exciton phase filling effect in the case of excitation regime with photon energy significantly higher than exciton edge of absorption. The exciton absorption was found to saturate with the increasing pump intensity (Figure 2b). For the colloidal solution of CdSe nanoplatelets the pump intensity of 2.5 MW/cm^2 corresponds to the creation on average of about 30 excitons in each nanoplatelet what is enough to exciton phase space filling. Taking into account the Pauli exclusion effect, the probability for the optical creation of more excitons is reduced with increasing excitation power because the free electron and hole states are decreasing. The measured saturation intensity of 1hh-1e and 1lh-1e exciton transitions was about 0.3 MW/cm^2 and 0.1 MW/cm^2, correspondently. The bleaching simultaneously of both exciton transition is also associated with energy exchange between exciton states in two-dimensional structures [22–24]. The negative values of differential transmission were observed in the wavelength region about 470 nm that can be caused by the broadening of absorption peaks due to exciton-exciton interaction [28,29]. We have also revealed the broadening and the red shift of the colloidal CdSe nanoplatelets photoluminescence (Figure 2c). These photoluminescence features can be associated with the emission of charged excitons (trions) [30-31] although other phenomena such as the longitudinal optical phonon assisted exciton recombination [32] and recombination of excited exciton states [33] also can playing a role. In ref. [30–31] it was found that the red shift of trions binding energy with respect to excitons has been determined by the thickness of the nanoplatelets and is about 18–30 meV that corresponds well to our experimental results (23 meV$\Leftrightarrow$ $\Delta\lambda = 4$ nm).

This work was supported by the state task and the Russian Foundation for Basic Research (project number 18-02-00719 and 19-03-00481(sample synthesis)).

References

[1] S. Ithurria *et al, Nature Materials* **10**, 936 (2011).
[2] S. Ithurria *et al, J. Am. Chem. Soc.* **130**, 16504 (2008).
[3] B.M. Saidzhonov *et al, J. Luminescence* **222**, 117134 (2020).
[4] D.A. Kurtina *et al, Chem. Mat.* **31**, 9652 (2019).
[5] B.M. Saidzhonov *et al, J. Luminescence* **209**, 170 (2019).
[6] N.N. Shlenskaya *et al, Chem. Mat.* **29**, 579 (2017).
[7] W. Cho *et al, Chem. Mat.* **30**, 6957 (2018).
[8] S. Christodoulou *et al, Nano Lett.* **18**, 6248 (2018).
[9] Z. Wen *et al, IEEE J. Quantum Electron.* **56**, 1 (2019).
[10] Z. Chen *et al, Adv. Funct. Mater.* **24**, 295 (2014).
[11] A.G. Vitukhnovsky *et al, J. Luminescence* **186**, 194 (2017).
[12] B. Guzelturk *et al, ACS Nano* **8**, 6599 (2014).
[13] C. She *et al, Nano Lett.* **14**, 2772 (2014).
[14] M. Sharma *et al, Adv. Mater.* **29**, 1700821 (2017).
[15] E. Lhuillier *et al, ACS Nano* **8**, 3813 (2014).
[16] I. Maksimovic *et al, ACS Nano* **6**, 6751 (2012).
[17] R. Benchamekh *et al, Phys. Rev. B* **89**, 035307-1 (2014).
[18] L.T. Kunneman *et al, Nano Lett.* **14**, 7039 (2014).
[19] R. Scott *et al, Nano Lett.* **15** , 4985 (2015).
[20] J. Heckmann *et al, Nano Lett.* **17**, 6321 (2017).
[21] A.S. Selyukova *et al, J. Semicond.* **50**, 947 (2016).
[22] A.M. Smirnov *et al, JETP Lett.* **109**, 372 (2019).
[23] A.M. Smirnov *et al, J. Semicond.* **52**, 1798 (2018).
[24] A.M. Smirnov *et al, Solid State Commun.* **299**, 113651 (2019).
[25] A.M. Smirnov *et al, JETP Lett.* **109**(7), 454 (2019).
[26] B.M. Saidzhonov *et al, J. Luminescence* **222**, 117134 (2020).
[27] A.M. Smirnov *et al, JETP* **125**, 890 (2017).
[28] S. Schmitt-Rink *et al, Adv. Phys.* **38**(2), 89 (1989).
[29] M. Pelton *et al, Nano Lett.* **12**(12), 6158 (2012).
[30] E.V. Shornikova *et al, Nanoscale* **10**(2), 646 (2018).
[31] E.V. Shornikova *et al, Nano Lett.* **20**(2), 1370 (2020).
[32] M.D. Tessier *et al, ACS Nano* **7**(4), 3332 (2013).
[33] A.W. Achtstein *et al, Phys. Rev. Lett.* **116**, 116802 (2016).

28th Int. Symp. "Nanostructures: Physics and Technology"
Minsk, Belarus, September 2020

Electronic states in nanowires with hexagonal cross-section

I.A. Kokurin
Mordovia State University, 430005 Saransk, Russia

Abstract. The electron spectrum in a uniform nanowire with a hexagonal cross-section is calculated by means of a numerical diagonalization of the effective-mass Hamiltonian. Two basis sets are utilized. The wave-functions of low-lying states are calculated and visualized. The approach has an advantage over mesh methods based on finite-differences (or finite-elements) schemes: non-physical solutions do not arise. Our scheme can be easily generalized to the case of multi-band (Luttinger or Kane) $\mathbf{k}\cdot\mathbf{p}$ Hamiltonians. The external fields (electrical, magnetic or strain) can be consistently introduced into the problem as well.

Introduction

Semiconductor nanowires (NWs) are currently of great interest due to the possibility of their application in electronics. NWs can be used as a work item of field-effect transistors [1,2] or photodetectors [3]. Usually, NWs of III-V materials with a zinc-blende lattice are grown in [111] crystal direction, that leads to the hexagonal shape of NW's cross-section (Fig. 1a). Early, simple models of NW with circular or square cross-sections were used for the calculation of the charge carrier spectrum and wave functions. However, for optical and transport applications it is a necessary to know the carrier subband spectrum with higher precision, i.e., take into account a real NW's shape.

The NW's translation invariance in longitudinal direction simplifies the problem: one needs simply to solve the spectral problem for a two-dimensional electron bounded in a hexagon. Usually, the finite-difference (or finite elements) method is used for this purpose [4,5]. This problem is nontrivial even for the case of the electron in a non-degenerate band described by the scalar effective mass. We propose an alternative approach based on the numerical diagonalization of the matrix Hamiltonian written in an appropriate basis.

1. Hamiltonian and basis functions

The effective potential barrier bounding an electron in NW is equal to the electron affinity χ (several eV). Within the effective mass approximation, such a height is equivalent to an infinite barrier. To find electronic states in NW with a hexagonal cross-section we propose to use the matrix mechanics. It is convenient to choose as basis functions the eigenfunctions of the Hamiltonian H_0, which describes electrons in NW with a circular or rectangular cross-section. The corresponding circle or rectangle is chosen to be circumscribed around the hexagon (see Fig. 1b,c). The spectral problem is reduced to the problem with the Hamiltonian $H = H_0 + V(\mathbf{r})$, where $V(\mathbf{r})$ is nonzero in shaded areas of Fig. 1b,c. The height of this potential cannot be chosen infinite at calculation, however, we do not make a big mistake putting it to be finite but high, e.g. $V_0 \sim \chi$. The envelope function approximation in a single band with scalar effective mass m^* is used. The spin-dependent terms are excluded from consideration.

The eigenfunctions and eigenenergies for the electron in the infinite circular potential well of radius R are well-known

$$\Psi^0_{mn}(r,\varphi) = \frac{\sqrt{2}}{R J_{|m|+1}(j_{mn})} J_{|m|}\left(j_{mn}\frac{r}{R}\right)\frac{1}{\sqrt{2\pi}} e^{im\varphi}, \quad (1)$$

$$E^0_{mn} = \frac{\hbar^2 j^2_{mn}}{2m^* R^2}, \quad (2)$$

where $m = 0, \pm1, \pm2, ..., n = 1, 2, ...$; $J_m(x)$ is the first kind Bessel function, and j_{mn} is the n-th zero of $J_m(x)$.

In the case of a potential well of rectangular shape circumscribing the same hexagon, the eigenfunctions and energies are given by

$$\Psi^0_{mn}(x,y) = \frac{\sqrt{2}}{3^{1/4}R}\sin\left(\frac{\pi m x}{2R}\right)\sin\left(\frac{\pi n y}{\sqrt{3}R}\right), \quad (3)$$

$$E^0_{mn} = \frac{\pi^2\hbar^2}{8m^*R^2}\left(m^2 + \frac{4}{3}n^2\right) \quad (4)$$

with $m, n = 1, 2, ...$.

We will search for the electron wavefunctions in hexagonal NW (h-NW) as a series in above basis sets

$$\Psi_j(\mathbf{r}) = \sum_{mn} C^j_{mn}\Psi^0_{mn}(\mathbf{r}). \quad (5)$$

The spectral problem is reduced to finding the eigenvalues of the Hamiltonian $H = H_0 + V(\mathbf{r})$ matrix. For the matrix elements we have, $\langle m'n'|H|mn\rangle = E^0_{mn}\delta_{m'm}\delta_{n'n} + \langle m'n'|V(\mathbf{r})|mn\rangle$. The latter term is proportional to the overlap integral $I_{m'n';mn}$ of the basis functions in the single barrier segment.

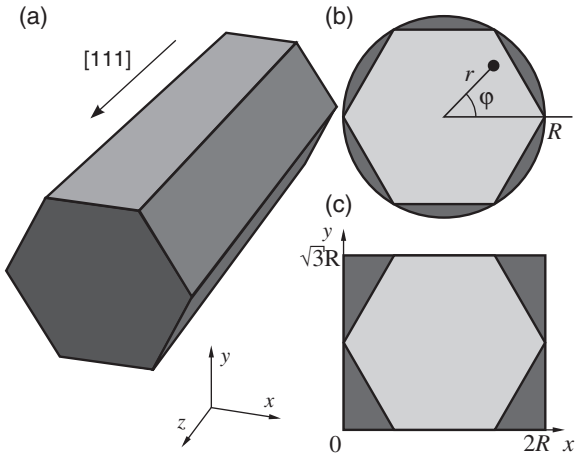

Fig. 1. (a) The sketch of NW with a hexagonal cross-section. (b) The use of circular basis set (1). The shaded areas between the circle and the hexagon serve as additional potential barriers. (c) The same as in (b) for the rectangular basis (3).

We can use some symmetry arguments for the matrix elements calculation. They are given by

$$\langle m'n'|V(\mathbf{r})|mn\rangle = 6V_0\delta_{m',m+6M}I_{m'n';mn}, \qquad (6)$$

and

$$\langle m'n'|V(\mathbf{r})|mn\rangle = 4V_0\delta_{m',m+2M}\delta_{n',n+2N}I_{m'n';mn}, \qquad (7)$$

for the case of circular and rectangular basis, respectively. Here $M, N = 0, \pm1, \pm2, ...$ In the latter case overlap integral can be found analytically, but in the former, only numerically.

2. Numerical diagonalization

For the numerical diagonalization of derived matrix Hamiltonians one needs to truncate the matrix dimension. At the same time, we have to choose a matrix size so as to ensure acceptable accuracy. The maximal values of $m_{\max}$ and $n_{\max}$ determine the size of truncated matrix. In the circular basis the matrix dimension is $(2m_{\max}+1)n_{\max}$, while in rectangular one we have $m_{\max}n_{\max}$. The position of calculated subband bottoms in h-NW is depicted in central section of Fig. 2a. The results are depicted for the truncated matrix of dimension 775×775 and 1000×1000 for circular and rectangular bases, respectively. This corresponds to the choice of $m_{\max} = 15$, $n_{\max} = 25$ and $m_{\max} = 40$, $n_{\max} = 25$, respectively. The energies are scaled to the value $E_0 = \hbar^2/2m^*R^2$, that for the case of GaAs NW ($m^* = 0.067m_0$) with $R = 20$ nm is equal to 1.41 meV. The barrier height V_0 was set to 10^3E_0.

The energy levels are a single or twofold degenerate (excluding spin). This is especially easy to trace when considering a circular basis. In this case degenerate states arise even at diagonalization of the Hamiltonian matrix of low size, which does not give a good precision. In this sense the use of Cartesian basis is more appropriate (there are no degenerate states) in order to track the convergence of the method with growing matrix dimension. Nonetheless, the use of a Cartesian basis requires a larger matrix size to attain the same precision as for a circular basis. Moreover, for the case of a non-degenerate Cartesian basis, the real twofold degeneracy of states is reached only in the limit of $V_0 \to \infty$, $m_{\max}, n_{\max} \to \infty$. This is due to the lack of 6-th order symmetry axis in the model described in Fig. 1c compared to that in Fig. 1b.

The calculated coefficients C^j_{mn} give us the opportunity to find the spatial behavior of wave functions [see Eq. (5)]. The electron distributions $|\Psi|^2$ corresponding to energy levels of Fig. 1a (central panel) are depicted in Figs. 2b–j The wave functions of degenerate states calculated in the Cartesian basis, in general, do not possess hexagonal symmetry. However, the total electron density at degenerate levels has this property.

3. Conclusions

In conclusion, the electronic states in h-NW are calculated. Corresponding wave functions are numerically found and visualized. The given approach can be generalized onto the case of the hole quantization in NWs or the more general case of a multi-band Hamiltonian. In the same manner the external fields can be introduced into the problem. The core-shell (or core-multi-shell) structures with a hexagonal cross-section of the core and shells can be considered by analogy with circular ones [6,7]. This approach is attractive in that there is no need

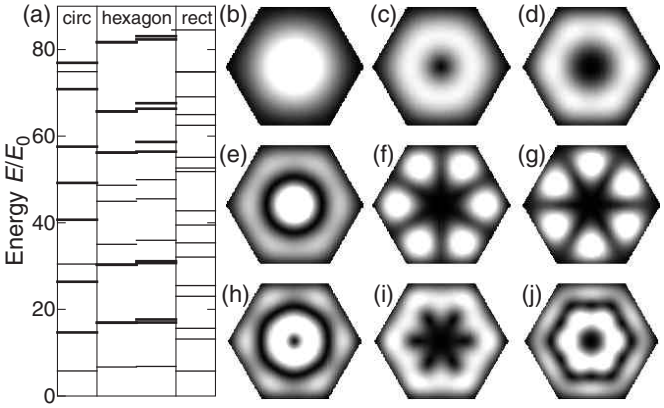

Fig. 2. (a) Subband energies of the circular (left), rectangular (right) and hexagonal (center) NWs. The energy levels for h-NW are calculated using numerical diagonalization of Hamiltonians in both circular and rectangular basis sets. Thick lines denote twofold degenerate (quasi-degenerate) levels. (b)-(j) The spatial distribution of the electron density $|\psi|^2$ in h-NW for 1, 2(3), 4(5), 6, 7, 8, 9(10), 11(12), 13(14)-th subband, respectively.

to impose boundary conditions at the heterointerfaces, which is usually the case when calculating electronic and hole states in heterostructures using wave mechanics [8]. Moreover, nonphysical solutions do not arise in our approach compared to other ones.

References

[1] S.A. Dayeh, D.P.R. Aplin, X. Zhou *et al*, *Small* **3**, 326 (2007).
[2] S. Chuang, Q. Gao, R. Kapadia *et al*, *Nano Lett.* **13**, 555 (2013).
[3] X. Dai, S. Zhang, Z. Wang *et al*, *Nano Lett.* **14**, 2688 (2014).
[4] V.E. Degtyarev, S.V. Khazanova, N.V. Demarina, *Sci. Rep.* **7**, 3411 (2017).
[5] A. Sitek, M. Urbaneja Torres, K. Torfason *et al*, *Nano Lett.* **18**, 2581 (2018).
[6] V.V. Ravi Kishore, B. Partoens, F.M. Peeters, *Phys. Rev. B* **82**, 235425 (2010).
[7] A.O. Rudakov, I.A. Kokurin, *Semiconductors* **53**, 2137 (2019).
[8] G. Bastard, *Wave Mechanics Applied to Semiconductor Heterostructures*, Les Ulis: Les Editions des Physique, 1988.

28th Int. Symp. "Nanostructures: Physics and Technology"
Minsk, Belarus, September 2020

Two-photon exciton absorption in CdSe/CdS nanoplatelets colloidal solution

I.D. Laktaev[1], D.V. Przhiyalkovskii[1], B.M. Saidzhonov[2], R.B. Vasiliev[2], A.M. Smirnov[1,2] and O.V. Butov[1]

[1] Kotelnikov Institute of Radioengineering and Electronics, 125009 Moscow, Russia
[2] M.V. Lomonosov Moscow State University, 119991 Moscow, Russia

Abstract. This work devotes to investigation of two-photon absorption in a colloidal solution of nanoplatelets CdSe/CdS (3.5 and 2 monolayers of CdSe core and CdS shell respectively) in the case of light- and heavy-hole exciton excitation (1lh-1e, 536) and (1hh-1e, 578 nm) by femtosecond laser radiation (1035 nm, 100 kHz). An open-aperture z-scan technique was utilized to measure nonlinear two-photon absorption coefficient which was found as $\beta = 0.15 \pm 0.02$ cm/GW, two-photon absorption cross sections $\sigma^{(2)} \approx 3\times10^4$ GM and nonlinear refraction index $\gamma \approx -1\times10^{-15}$ cm^2/W. The revealed features of the measured z-scan dependencies can be the evidence of stimulated emission in the colloidal solution of CdSe/CdS nanoplatelets at high intensity of two-photon excitation.

Introduction

In recent years, two-photon absorption in nanocrystals is current of interest for practical applications in photonics, medical research and imaging. Two-photon absorber nanostructures can be used as bio-markers [1], photodynamic cancer therapy [2], lithography, polymerization and spectrosco-py [3]. The semiconductor nanostructures combine a high cross section, stability, and frequency tunability through confinement [4]. Among semiconductor colloidal nanocrystals with different morphology CdSe nanoplatelets are very promising structure for using as two-photon absorbers. Typically nano-]lb crystals like CdSe quantum dots [5–7] and nano-wires [8], CdS or typical organic dyes have cross sections of two-photon absorption up to 10^3–10^5 GM (where 1 GM = 1 Göppert-Mayer = 10^{-50} cm^4 s photon^{-1}) [9,10]. Cross section of CdSe nanoplatelets can reach several of 10^7 GM [3]. These nanostructures possess a narrow luminescence band (10–20 nm) [11] and a short luminescence decay time (about 1 ns) in comparison with quantum dots as well [12]. However, two-photon absorption peculiarities in CdSe nano-platelets remains not widely studied [3,13].

In this work we focus on experimental studies of the nonlinear absorption of CdSe/CdS nanoplatelets under two-photon excitation by femtosecond laser pulses.

1. Sample and experimental setup

The studied population of 3.5 monolayer thick CdSe nanoplatelets with the lowest energy of exciton absorption band at 463 nm have been synthesized according to [14]. Briefly, 0.5 mmol of $Cd(CH_3COO)_2 2H_2O$, 0.2 mmol of oleic acid (OA) and 10 mL of octadecene (ODE) were loaded into a reaction flask. Then, the mixture was heated to 170 °C and degassed under argon for 30 min. After that, the temperature was increased to 210 °C, and a mixture of 100 μL 1M trioctylphosphine selenide and 350 μL of ODE was injected into the reaction flask. The reaction was allowed to proceed for 40 min at 210 °C and then the mixture was cooled to room temperature using a water bath. During the cooling process, 0.5 ml of OA was injected into the reaction flask. As-grown nanoplatelets were washed with acetone several times. Preparation of CdSe/CdS core-shell NPLs with two monolayers of CdS shell was realized according to the procedure described in Ref. [15]. Linear absorption spectrum of the synthesized sample is presented in Fig.1. The spectrum has three peaks — at 467 nm (2.66 eV), 536 nm (2.31 eV) and 578 nm (2.14 eV) which correspond to the exciton transition from the spin-orbital to the conduction subband (1so-1e), from the light hole subband to the conduction subband (1lh-1e) and from the heavy hole subband to the conduction subband (1hh-1e) respectively. Three distinct exciton peaks indicate a high quality of the sample (high monodispersity in the thickness and low quantity of defects in nanoplatelets).

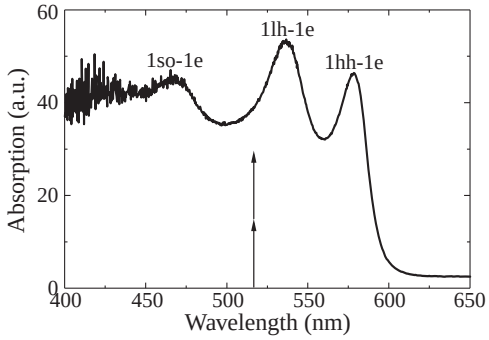

Fig. 1. Linear absorption spectrum of CdSe/CdS nanoplatelets colloidal solution in 1-mm cell.

To determine the nonlinear two-photon absorption of the CdSe/CdS nanoplatelets an open-aperture z-scan technique was utilized. An OptoSystems FL-300 fiber laser was used as a radiation source with a pulse duration of 320 fs and a pulse repetition rate of 100 kHz. The radiation wavelength is 1035 nm (1.2 eV). So the absorption in CdSe/CdS nanoplatelets was realized by means of two-photon interaction of laser radiation with the excitons (arrows on Fig. 1). The radiation was focused on the sample using a lens with a focal length of 10 cm. The sample was mounted on a mechanical linear translator. The incident and transmitted laser radiation power was measured by two power meters.

2. Experimental results and discussion

The result of an open-aperture z-scan of nanoplatelets CdSe/CdS is showed in Fig. 2(a). The 13% decrease of norma-lized transmission about $z = 0$ mm is explained by the process of two-photon absorption in nanoplateletes. The dependence was approximated according to the law [16] by its first six members,

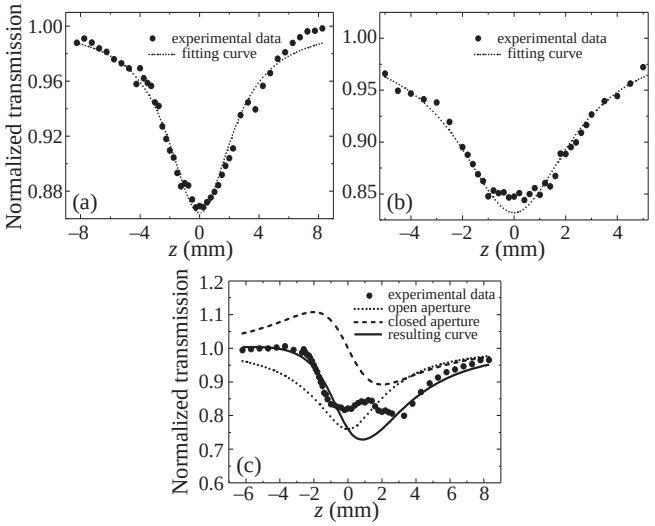

Fig. 2. Dependence of the normalized transmission of CdSe/CdSnoplatelets colloidal solution in 1-mm cell on the detuning of the sample from the focus of the lens. (a) $I_{\text{focus}} = 36.4$ GW/cm^2, (b) $I_{\text{focus}} = 39.2$ GW/cm^2,(c) $I_{\text{focus}} = 122.8$ GW/cm^2. Dotted curve for open aperture z-scan calculation, dashed curve for closed aperture and solid curve for simultaneous action of open and closed aperture.

which make the most significant contribution:

$$T_{\text{open}}(z) = \sum_0^n \frac{(-\beta I_0 L)^n}{(n+1)^{3/2}(1+x^2)^n}, \qquad (1)$$

where β is the two-photon absorption coefficient, I_0 is the intensity in focus of the lens, L is the sample length, $x = z/z_0$, where z_0-diffraction length of a Gaussian beam.

When approximating the experimental data by above expression two-photon absorption coefficient was found and=lb equal to 0.15±0.02 cm/GW. A cross section of two-photon absorption was calculated using formula $\sigma^{(2)} = \frac{\beta h\nu}{n}$, where $h\nu$-photon energy, n-concentration of nanoplatelets (n is about 10^{17} cm^{-3} for the sample under investigation) and cross section was about 3×10^4 GM. The deviation of experimental data from the fitting curve can be explained by Tyndall scattering of incident radiation in colloidal solution.

The dependence measured with higher accuracy is presented in Fig. 2(b). This dependence was approximated by expression (1) and found the same value of β and $\sigma^{(2)}$ as in Fig. 2(a). Fitting curve in Fig. 2(b) lies below the experimental data near zero of z-scan as well as three point in Fig. 2(a). The experimental data in Fig. 2(c) demonstrates even greater deviation from approximation by open aperture z-scan fiting curve. The dependence of transmission has maximum about focus and asymmetric form. To explain these effects, we investigated the dependence in Fig. 2(c) in details. First of all, it was noted that assymetric behavior can be explained by the influence of a closed (limited) aperture z-scan and related to self-focusing or defocusing of passed through a sample radiation. In our case of an open aperture z-scan, the limitation of the aperture determined by the finite size of power meter's sensor. At high intensity the impact of self-focusing/defocusing becomes significant for open aperture z-scan without collecting lens after the sample. Thus, the experimental result at high intensity can be explained by simultaneous accounting of open and closed aperture z-scan peculiarities. The dependence in Fig. 2(c) was approximated by multiplication of functions of both z-scan described by formula (1) and expression (2):

$$T_{\text{closed}}(z) = 1 + \frac{4x\langle\Phi\rangle}{(1+x^2)(9+x^2)}, \qquad (2)$$

where $\langle\Phi\rangle$-the on-axis phase shift at the focus, $x = z/z_0$.

Calculations for open and closed aperture z-scan which constitute the resulting curve was plotted in Fig. 2(c). The form of closed aperture's fitting curve corresponds to self-defocusing, which was thermally induced by the high intensity incident laser pulses due to its high repetition rate [17]. Nonlinear refraction index $\gamma \approx -1\times10^{-15}$ cm^2/W was found from this approximation. The resulting function well approximates the wings of the experimental dependence and its minimum of transmission shifts on right. However, in the range of the maximum intensity the resulting curve lies lower than the experimentally measured values. Such deviation can be explained by contribution of stimulated emission at 580 nm. Minimum of resulting curve (maximum nonli-near two-photon absorption) and maximum of experimental plot coincides that can be also the evidence of stimulated emission presence at highest value of excitation intensities. The same way the plateau about focus can be explained in Fig. 2(a,b).

Thus, nonlinear absorption under two-photon excitation of excitons in colloidal CdSe/CdS nanoplatelets was investigated. The two-photon absorption coefficient 0.15±0.02 cm/GW, cross section of two-photon absorption $\sigma^{(2)} \approx 3\times10^4$ GM, nonlinear refractive index $\gamma \approx -1\times10^{-15}$ cm^2/W of the CdSe/CdS nanoplatelets were found. Also we revealed the percularities of the z-scan experimental results and explained them by the stimulated emission in the sample at the high two-photon excitation intensity.

Acknowledgement

This work was supported by the state task and the Russian Foundation for Basic Research (project number 19-32-90240 and 19-03-00481(sample synthesis)).

References

[1] F. Wang *et al*, *Analyst.* **135**, 1839 (2010).
[2] K.-L. Chou *et al*, *J. Mater. Chem. B* **1**, 4584 (2013).
[3] M.T. Quick *et al*, *Nanoscale* **11**, 17293 (2019).
[4] E. Peteryayeva *et al*, *Appl. Spectrosc.* **67**, 215 (2013).
[5] V. Dneprovskii *et al*, *Physica E* **44**, 1920 (2012).
[6] V. Dneprovskii *et al*, *Quantum Electronics* **43**, 927 (2013).
[7] A.M. Smirnov *et al*, *Opt. and Spectr.* **120**, 472 (2016).
[8] X. Wang *et al*, *Laser Photonics Rev.* **10**, 835 (2016).
[9] M. Nyk *et al*, *Appl. Phys. Lett.* **100**, 041102 (2012).
[10] A. W. Achtstein *et al*, *Phys. Chem. C* **119**, 1260 (2015).
[11] M. Pelton *et al*, *Nano Letters* **12**, 6158 (2012).
[12] S. Ithurria *et al*, *Nature materials* **10**, 936 (2011).
[13] V. Krivenkov *et al*, *ACS Photonics* **7**, 831 (2020).
[14] B.M.Saidzhonov *et al*, *J. Lumin.* **222**, 117134 (2020).
[15] B.M.Saidzhonov *et al*, *J. Lumin.* **209**, 170 (2019).
[16] M. Sheik-Bahae *et al*, *J. of Quant. Electron.* **26**, 760 (1990).
[17] A. Gnoli *et al*, *Opt. Express* **23**, 7976 (2005).

28th Int. Symp. “Nanostructures: Physics and Technology”
Minsk, Belarus, September 2020

Geometrical effects on exchange coupling in system of near-surface donors and quantum dots

E.A. Levchuk, L.F. Makarenko
Belarusian State University, Minsk, Belarus

Abstract. The value of exchange energy for near-surface double-donor and double-quantum dot structures under the effect of external electric field has been calculated using unrestricted Hartree-Fock method. The dependences of exchange energy on geometric parameters have been obtained. It has been found that the location of donor centers near the surface of the semiconductor leads to an increase in the exchange energy. Approximation formulas for the dependence of the exchange energy on the distance between the centers of the gates are obtained. It has been shown that exchange coupling control in such systems differs significantly from the case of bulk donors.

Introduction

A solid-state quantum computer based on electronic or nuclear spins is one of the promising directions for the development of nanoscale electronics. Such devices can be implemented both on the basis of single donors in semiconductors [1–2], and using arrays of quantum dots [3].

According to Kane's proposal [1], quantum calculations are realized using the nuclear spins of phosphorus donors in silicon (Fig. 1). The bound electron of a single donor is affected by the electric field of the main control gate (the gate A), which provides the electron density relocation to semiconductor surface. Two-qubit operations are implemented using the exchange interaction of two neighbouring electrons, regulated by the electric field of the additional gate (the gate J), located between A-gates. In this case, the value of the permissible exchange energy (K) can be estimated due to the limited exposure time of the additional gate: for a pulse duration of 30 ps the exchange energy should be $\sim 8 \cdot 10^{-5}$ eV [4]. To be able to correct errors, the exchange energy K should be less than 10^{-5} eV for zero potential at the auxiliary gate ($\Phi_J = 0$). These values of the exchange energy impose restrictions both on the parameters of the J-gate and on the geometric parameters of the system (for example, the distance between donors, distance from donors to semiconductor surface). When modeling the effect of an electric field on a donor pair, it is usually assumed that the external electric field is homogeneous [4,5], however, the values of the exchange energy for homogeneous and inhomogeneous external fields differ significantly, which had been shown in [4] for the case when the exchange interaction is controlled by external parabolic electric potential. Thus, it becomes necessary to study the effect of an inhomogeneous electric field created by a metal gate on both a pair of donor centers and a pair of electrically induced quantum dots.

In this paper, we study the effect of the electric field of the disk-shaped additional gate J on the value of the exchange interaction of the surface system of two donors, as well as two quantum dots (QDs) induced by the electric field of the main disk-shaped gates A.

1. Formulation of the problem

In the general, the Hamiltonian of the system takes the form

$$\hat{H}(\vec{r}_1, \vec{r}_2) = \hat{H}_1(\vec{r}_1) + \hat{H}_1(\vec{r}_2) + \frac{2}{|\vec{r}_1 - \vec{r}_2|}, \qquad (1)$$

$$\hat{H}_1(\vec{r}) = -\nabla^2 + \hat{V}_R(\vec{r}) + \hat{V}_L(\vec{r}), \qquad (2)$$

where $\hat{V}_R$, $\hat{V}_L$ are donor or QD potentials. To approximate the potential created by the thin disk-shaped gate an expression of the form

$$\hat{V}_G = -\Phi_0 \exp\left(-a\rho^2 - bz\right) \qquad (3)$$

has been used. Parameters a and b have been chosen so that the dependence of ground state energy on gate potential Φ_0 have been close to the dependence in the field created by a real disk-shaped metal gate. Then, a disk-shaped gate of diameter d corresponds to parameter values $a \approx 1.098/d^2$, $b \approx 1.268/d$. With this choice of approximation, the value of the critical potential (the potential at which the maximum electron density of the ground state passes from the donor to the gate) remains unchanged compared to the exact value of the potential.

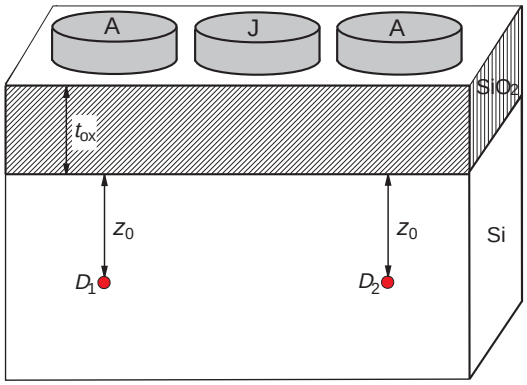

Fig. 1. Schematic view of the system under study.

2. Numerical method

To solve the problem (1)–(2) unrestricted Hartree–Fock (UHF) method based on variational approach has been used. Trial functions have been chosen in the form [7]:

$$\varphi_{ij}^{(1)}(x, y, z) = e^{-\alpha_i (x \pm R/2)^2 - \alpha_i y^2 - \alpha_j (z - z_0)^2},$$
$$\varphi_{ij}^{(2)}(x, y, z) = z e^{-\beta_i (x \pm R/2)^2 - \beta_i y^2 - \beta_j (z - z_0)^2},$$
$$\varphi_{ij}^{(3)}(x, y, z) = z e^{-\beta_i x^2 - \beta_i y^2 - \beta_j (z - z_0)^2},$$
$$i, j = 1..M,$$

where R is the distance between donors (QDs' centers), z_0 is the distance between donors and semiconductor surface (Fig. 1).

Parameters α_i have been chosen so that a linear combination of functions $\exp(-\alpha_i r^2)$ delivered minimum value for ground state energy of the electron in the field of an isolated donor, and $\beta_i = (d/2)^{-1/2}\alpha_i$. The problem for the Poisson equation arising in the UHF method has been reduced to two-dimensional problem using Fourier transform, and then solved using the finite element method.

3. Calculation results

The calculation results for the case when the potential at A-gates is zero for large distances between donors are in good agreement with the corresponding asymptotic expressions [4]:

$$K = 1.64\frac{e^2}{\epsilon\epsilon_0 a^*}\left(\frac{R}{a^*}\right)^{5/2}\exp\left(\frac{-2R}{a^*}\right). \qquad (4)$$

Calculations showed that a formula similar to (4) holds for a system consisting of two electrically induced quantum dots of diameter $d = 2a^*$:

$$K = f(\Phi_0)R^{5/2}\exp(-2R), \qquad (5)$$

where f is a function of A-gate potential. The expression (5) and the form of approximate values of a and b show that the exchange energy values for a system with an arbitrary gate diameter can be obtained from the known values of the exchange energy for a single gate diameter $d = 2a^*$ using scaling, i.e. choosing not the effective Bohr radius (a^*) as the unit of length, but the gate diameter (d).

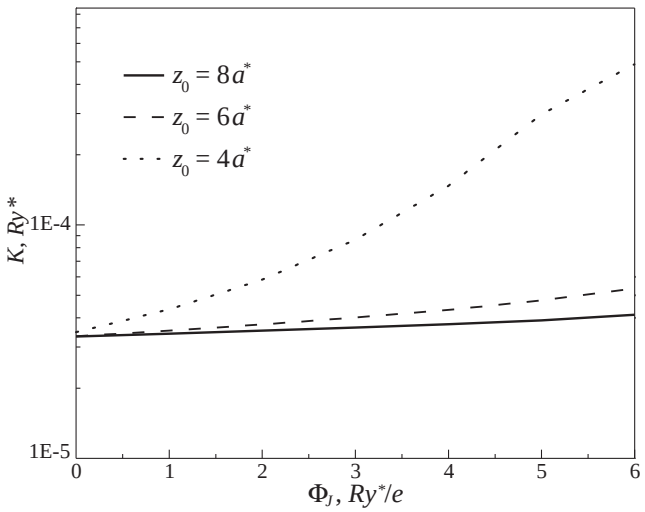

Fig. 2. The dependence of exchange energy on J-gate potential for different distances from donors to semiconductor surface, J-gate diameter $d = 2a^*$, distance between donors $R = 8a^*$.

The calculations showed that for distances from donors to semiconductor surface greater than $6a^*$, the exchange energy changes by no more than 1% and corresponds to the value of the exchange energy for the system of donor centers in the semiconductor bulk. At smaller distances to the surface, an increase of the exchange energy takes place.

As one can see from Fig. 2, exchange energy becomes more sensitive to potential change of the J-gate with decreasing z_0, which means that switching spin exchange coupling between neighbouring qubits can be performed more efficiently for smaller z_0. Electron density relocation, which takes place with growing gate potential, is less abrupt when donors are closer to the surface. This means that overlap of electron wave functions is larger for smaller z_0, which results in larger exchange coupling. For larger d, exchange energy varies over a wider range, but the gate diameter can not be used for improving the system efficiently, as its value is limited with by the distance between the neighbouring qubits.

Conclusions

In conclusion, we have calculated the exchange splitting for electrons in the system of near-surface donors and quantum dots. It has been found that positioning donors closer to semiconductor surface is more preferable for exchange coupling control. Based on the calculation results, optimal system configurations can be proposed for more efficient exchange energy control.

References

[1] B.E. Kane, *Nature (London)* **393**, 133–137 (1998).
[2] Y. He, S.K. Gorman ... and M.Y. Simmons, *Nature* **571**, 371–375 (2019).
[3] D. Loss and D.P. DiVincenzo, *Phys. Rev. A* **57**, 120 (1998).
[4] A. Fang, *Phys. Rev. B* **66**, 155331 (2002).
[5] Y. Wang, A. Tankasala *et al*, *Quantum Information* **2**, 16008 (2016).
[6] Q. Li, L. Cywinski *et al*, *Phys. Rev. B* **81**, 085313 (2010).
[7] G.D.J. Smit, S. Rogge *et al*, *Phys. Rev. B* **68**, 193302 (2003).

28th Int. Symp. "Nanostructures: Physics and Technology"
Minsk, Belarus, September 2020

Growth of thin silicon carbide layers by rapid thermal treatment of silicon wafers

M.V. Lobanok[1], S.L. Prakopyeu[1], M.A. Makhavikou[2], P.I. Gaiduk[1]

[1] Department of Physical electronics and nanotechnology, Belarusian State University, Belarus
[2] Sevchenko Institute of Applied Physics Problems, Belarusian State University, Belarus

Abstract. Thin epitaxial layers of SiC were grown on (100) Si by rapid thermal processing (RTP) in a vacuum of $1 \cdot 10^{-2}$ Pa with a residual carbon atmosphere. A formation of two-phase system of single- and polycrystalline cubic SiC was investigated by transmission electron microscopy and diffraction as a function of the temperature and duration of the RTP. 3C-SiC layers of thickness 13.5 and 25 nm were obtained after RTP at 1100 °C for 30 s and 3 min respectively. A defect evolution both in SiC layers and in Si substrate was investigated and documented as well.

Introduction

Silicon Carbide (SiC) and its polytypes are of huge interest for the power and opto-electronic devices. The SiC properties (wide bandgap, attractive thermal and chemical properties, elevated electron drift velocity and high break-down voltage) make the material suitable for devices operating at extreme power and termal conditions [1,2]. An important task is the integration of SiC devices and silicon circuits within the traditional VLSI technology [1,3]. Technologically efficient and inexpensive methods of silicon carbide growth should be developed. The growth of SiC/Si structures faces the problems of large lattice mismatch and very different thermal expansion constants which result in formation of dislocations, twins and stacking faults [2,4]. SiC films are usually grown by the multistage CVD method [2]. The most important step in the CVD process is the formation of a buffer layer, which is necessary to reduce the stresses associated with the lattice mismatch. A thin cubic SiC layer (3C-SiC) can be used as a buffer layer. Thin 3C-SiC layers are typically grown by carbonation at high temperature. We note here that the growth of a predominantly cubic SiC polytype depends on the crystalline properties of single-crystal silicon. In [4,5], stress relaxation was achieved due to the use of point defects as an interaction, as well as the presence of voids near the interface caused by tensile mechanical stresses. The formation of voids depends on the competition between the Kirkendall and Frenkel effects associated with vacancies. Further, CVD-SiC thick film growth leads to the formation of three-dimensional defects that partly depend on voids at the boundary of SiC / Si [6]. The core of these defects consists of nanocrystals paired with respect to the substrate orientation and is located near the SiC/Si interface [6]. Therefore, for the growth of the SiC buffer layer, it is necessary to reduce the formation of twins and intermediate layers of polytypes. In the present work, the formation of thin layers of SiC during rapid thermal treatment of silicon wafers in the residual carbon atmosphere is investigated.

1. Experimental

The rapid thermal processing (RTP) system used in this study is a modified Jipelec JetFirst-100 unit. The reaction chamber enables vacuum operation and large-area treatment (up to 100 mm diameter substrate) while efficiently utilizing the infrared output of lamps placed on top side of the chamber. A typical procedure chamber pressure achievable is about $1 \cdot 10^{-2}$ Pa. The substrates were standard (100) Si wafers. All samples were 5% HF:H_2O solution dipped and deionized water rinsed just prior to being loaded into the chamber. The procedure for rapid thermal treatment (RTT) of Si wafers was following: ramp-up to temperature 1100 °C at pressure $1 \cdot 10{-}2$ Pa and carbonization at 1100 °C for 30 s–3 min. The structural properties of SiC thin fims were investigated by scanning electron microscopy (SEM), in planar geometry (X-SEM), transmission electron microscopy (TEM), and transmission electron diffraction (TED). The SEM Hitachi S-4800 and TEM Hitachi H-800 microscopes are used for SEM and TEM investigations respectively. The samples are prepared for plan-view TEM investigation by using routine chemical etching from the back side of Si wafer.

2. Result and discussion

Figure 1 (a-b) shows the X-SEM images of silicon wafers after carbonization. Figure 1a shows the continuous thin (13.5 nm) layer (silicon carbide 3C-SiC, TED data see Fig. 2a below) that was grown during carbonization for 30 s. Figure 1b shows the continuous thin (25.5 nm) layer (silicon carbide, TED data see Fig. 2a below) that was grown during carbonization for 3 min. As example, Fig. 1a shows the void formed under the grown SiC layer. Voids are $\sim 0.1{-}1$ μm of width and 0.1–0.3 μm of depth, are well visible below silicon carbide. The void formation is probably controlled by the Kirkendall effect. The regular location of voids let us confirm the formation of continuous porous layer. There is a high lattice mismatch between SiC and Si and in general the elastic strain increases during SiC on Si growth. Taking into account the small thickness of the top SiC layer around 20 nm we suggest that SiC layer is of high cryslal quality partially due to the elastic strain relaxation within the porous layer.

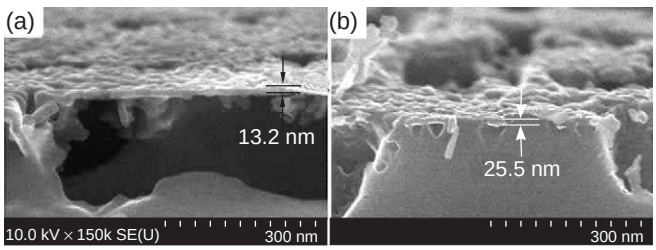

Fig. 1. X-SEM images of epitaxial SiC layers, grown on the top of Si (100) substrate: (a) at 1100 °C for 30 s; (b) at 1100 °C for 3 min

As concluded from SEM data the voids does not contain SiC nanocrystals (Fig. 1 (a,b)). In previous work [7] nanocrystalline SiC was growth on porous-Si/SiC interface. The absence of grains in the pores on SiC/Si structure without porous layer confirm the results of simulation [8]. In this work, the formation of silicon carbide nanocrystals during the high-temperature carbonization of a single crystal and a porous silicon substrate was simulated.

Fig. 2 shows the TED-pattern (a) and bright field TEM image (b) of SiC/Si structure grown by RTT at 1100 °C for 30 seconds. In the TED pattern (Fig. 2a) the two groups of dot reflexes are clearly resolved: the reflexes (200) correspond to the silicon substrate and the reflexes (111), (220) and (311) correspond to 3C-SiC layer. The set of concentric rings in TED image (Fig. 2a) indicate the presence of polycrystalline SiC phase in the SiC layer. The relative intensity of the rings with respect to the dot reflexes is visually much lower that indicates the predominant formation of single-crystal SiC. Consequently, it is clear from TED pattern, that SiC layer has high crystal quality because of weak intensity of concentric rings. However, reflexes marked as “twins”. in Fig. 2a indicate secondary twins for (111) SiC. Fig. 2b shows the bright field TEM image of the corresponding area for TED pattern (Fig.2a). There are bright void related areas at the SiC/Si interface (see Fig. 1). These areas are mostly of rectangular shape and its size varies from 10 to 100 nm. The small in size polycrystalline grains are located near the voids, that proves the presence both monocrystalline and polycryslalline phase in TED pattern (Fig. 2a).

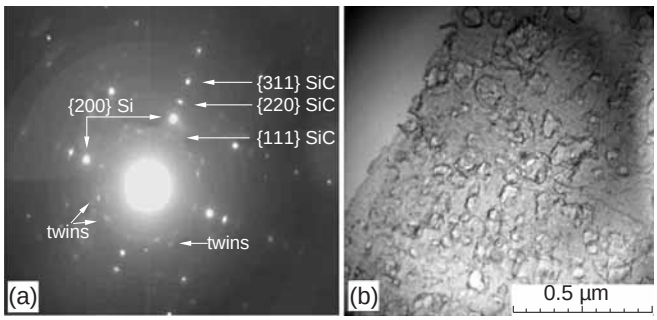

Fig. 2. TED pattern (a), bright field TEM image (b) of epitaxial SiC layer, grown on the top of Si (100) substrate at 110 °C for 30 s

In Fig. 3 (a–b) shows TEM images in dark and bright fields characterizing the structure of 3C-SiC films formed in 3 min.

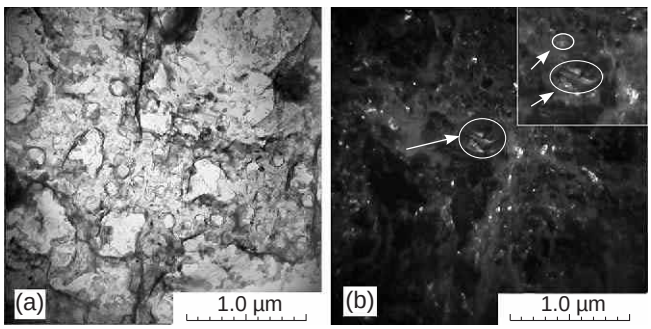

Fig. 3. Plan-view TEM images (a-d) of epitaxial SiC layers, grown on the top of Si (100) substrate at 1100 °C for 3 min.

The presence of void related bright areas at the SiC/Si interface is similar to Fig2b. The rectangular shape of the voids due to (100) orientation of the substrate. The size of the voids varies from 20 to 300 nm. In the dark-field image mode (on the 3C-SiC (111) ring), separate grains are visible as bright light spots. The grains are small in size and located near voids. Striped contrast, magnified in fig. 3b indicates the presence of deformation microtwins.

In conclusion, thin epitaxial films of cubic silicon carbide were grown. These films consist of two-phases (mono- and polycrystalline), as shown by electron microscopy. The polycrystalline SiC phase is characterized by a small grain size. The Si and SiC twins observed in the grown structure. The pore size varies from 20 to 300 nm. Monocrystalline silicon 13.5 nm thick silicon carbide film was grown during rapid thermal carbonization at 1100 °C for 30 s.

Acknowledgement

This work is supported by GPNI “Photonics, opto- and microelectronics” (program 3.2.04, registration number 20190644).

References

[1] D.R. Yakovlev *et al*, *Appl. Phys. Lett.* **78**, 1870 (2001).
[2] D.R. Yakovlev *et al*, *Proc. 26th ICPS*, Edinburgh, UK 2002, publication on CD.
[3] H.J. Lugauer *et al*, *J. Crystal Growth* **175/176**, 619 (1997).
[4] L.Hansen *et al*, *Appl. Phys. Lett.* **79**, 3125 (2001).
[5] W.Y. Yu *et al*, *Phys. Rev. B* **51**, 9722 (1995).
[6] J.A. Gaj *et al*, *Solid State Commun.* **29**, 435 (1979).
[7] B.E. Larson *et al*, *Phys. Rev. B* **37**, 4137 (1988).
[8] D.R. Yakovlev *et al*, *Phys. Rev. Lett.* **88**, 257401 (2002).

28th Int. Symp. "Nanostructures: Physics and Technology"
Minsk, Belarus, September 2020

Strain relaxation in MOVPE grown AlGaN multilayer structures on Si(111)

A.V. Sakharov[1,3], W.V. Lundin[1], E.E. Zavarin[1], D.A. Zakheim[1], M.A. Yagovkina[1], N.A. Cherkashin[2] and A.F. Tsatsulnikov[3]

[1] Ioffe Institute, St Petersburg, Russia
[2] CEMES-CNRS, 29 rue Jeanne Marvig, Toulouse, France
[3] Submicron Heterostructures for Microelectronics Research and Engineering Center RAS, St Petersburg, Russia

Abstract. A key element for the growth of GaN-based device structures on Si is accurate management of strain state of all layers during growth. Here we present a complex study of strain relaxation in multilayer (Al,Ga)N grown by MOVPE, including in-situ reflectometry, XRD and TEM investigations. Optimization of buffer layers and InAlN layers allows fabricating structures without cracks and realize strctures for high electron mobility transistors (HEMTs).

Introduction

Over recent decades GaN has moved from the research laboratory scale and is now widely used in a range of commercial products, including light-emitting diodes, lasers and HEMTs. As a result of commercialization, much attention has recently been focused on reducing the cost of devices, which means cheaper and larger wafers. Demonstration of device growth on Si wafers [1] makes possible to use existing processing techniques developed for Si integrated circuits. Unfortunately, large GaN-Si thermal and lattice mismatch introduces high stress leading to significant wafer-bow or even epilayer cracking [2]. Most techniques used for growth of GaN on Si structures involve the use of AlN and AlGaN. There are several reasons for that: firstly, the use of AlN at initial stage prevents the 'melt back' reaction between Ga and Si; secondly, because AlGaN has a smaller lattice parameter than GaN, compressive strain can be introduced during growth to compensate tensile strain arising on cooling from difference in thermal expansion of III-N layers and Si wafer. A key challenge is the careful control of the AlGaN layers growth to balance strain and avoid generation of new dislocations.

Experimental

Samples were grown by MOVPE on silicon (111) substrates using standard precursors. Samples consisted of thin low-temperature AlN followed by high-T AlN buffer layer, a 0.7–1.5 μm thick AlGaN multilayer structure, 0.5–1 μm thick GaN layer and capped with standard for HEMT 1 nm AlN/23 nm AlGaN barrier layer.

Strain evolution during growth was controlled by *in-situ* multiple points reflectometry/deflectometry system which allows measurements of wafer curvature as well as growth rate and surface roughness. The structural properties of the samples were studied by tranmission electron microscopy and X-ray diffraction using a high-resolution Bruker D8 Discover diffractometer (Bruker AXS, Germany). Reciprocal space maps (RSM) were measured using (11.4) reflection. The electrical parameters, i.e., the sheet resistivity, sheet electron concentration and the electron mobility were measured using the contactless resistivity and Hall effect.

TEM image of structure consisting of 200 nm AlN, three AlGaN layers (thicness 120, 200, 350 nm; Al content 53, 38, 22% respectively) and 1100 nm of GaN is shown on Fig. 1 below.

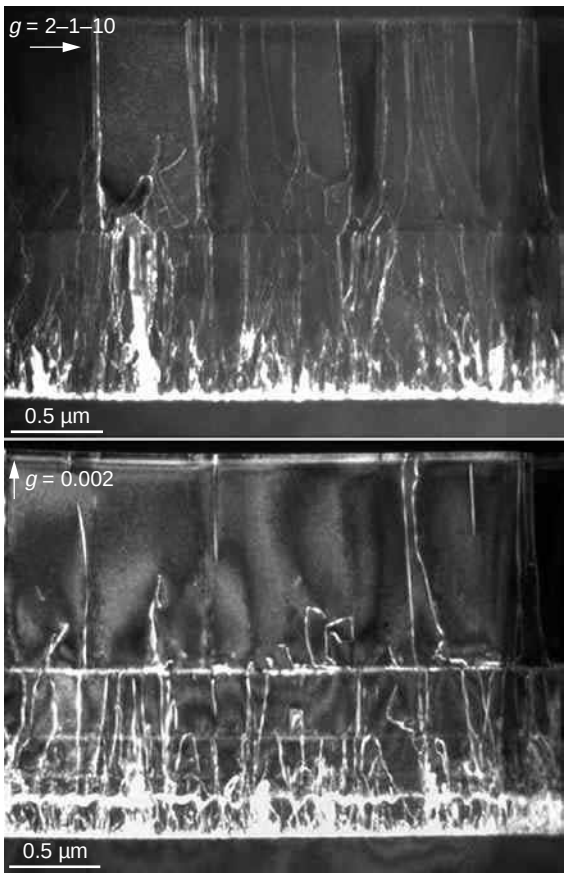

Fig. 1. Cross-section weak beam dark field TEM image of AlGaN/GaN structure on Si

Dislocation density changes from $\sim 3 \times 10^{10}$ cm^{-2} at bottom interfaces to $\sim 4 \times 10^{9}$ cm^{-2} at top of structure. Screw dislocation is absent, edge and mixed dislocations distributed in 60:40 proportions. Dislocation density is nearly one order higher than typical for structures grown on SiC or sapphire in optimal conditions, but reasonable for device applications.

Figure 2 shows reciprocal space map of the same structure measured using asymmetrical (11.4) reflection. Spots on a map have an elliptical form with long axe nearly parallel with relax-

ation line. We can assume that strain in the AlGaN layers varies from layer to layer, with increasing relaxation from bottom to top AlGaN. From several samples study we can conclude that relaxation strongly increases for layers with Al content less than 50%. Intensity spot for thick GaN has not pure elliptical form, and we can assume partial strain relaxation in it or even two layers with different strain state. Top barrier AlGaN layer is totally strained, which means it was coherently grown on GaN and no additional dislocations were generated in transistor channel area.

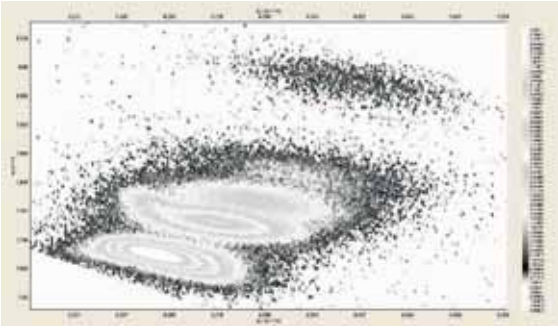

Fig. 2. (11.4) reciprocal space map.

In-situ measurements of wafer curvature during growth shows that each (AlGa)N layer introduce compressive strain during growth, but wafer curvature develops non-linearly during growth of each layer, with faster bowing in the beginning and slowing with layer thickness increase, indicating partial strain relaxation during growth. After cooling grown structure has a concave surface, indicating tensile stress in GaN layer, but has no cracks.

Hall measurements for standart HEMT barrier structure grown on such (AlGa)N buffer on Si(111) gives values of carrier concentration and mobility of $1.1-1.2\times10^{13}$ cm^{-2} and 1400 cm^2/Vs at room temperature. Sheet resistance map measurement shows good uniformity of parameters over whole wafer (see Fig. 3) making such structures suitable for transistor processing.

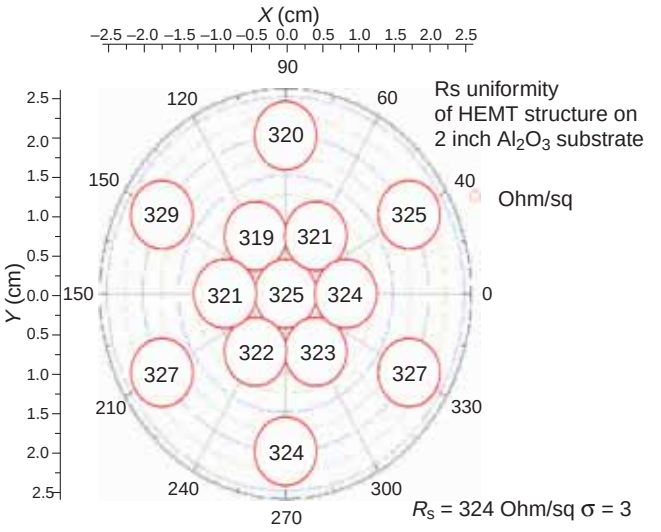

Fig. 3. Sheet resistance map for HEMT structure on Si(111).

Acknowledgement

The X-Ray characterizations were performed using equipment owned by the Joint Research Center "Material science and characterization in advanced technology" (Ioffe Institute, St Petersburg, Russia).

References

[1] A.Krost, A. Dadgar, Phys. Stat. Sol. (a), **194**, 361 (2002).
[2] E. Arslan, *et al*, *J. Phys. D: Appl. Phys.*, **41**, 155317 (2008).

28th Int. Symp. "Nanostructures: Physics and Technology"
Minsk, Belarus, September 2020

The study of the properties of AlN/Si(111) epitaxial structures grown by PA MBE via coalescence overgrowth of AlN nanocolumns

K.Yu. Shubina, D.V. Mokhov, T.N. Berezovskaya, A.M. Mizerov, E.V. Nikitina and A.D. Bouravleuv
Alferov University, St Petersburg, Russia

Abstract. The AlN/Si(111) epitaxial structures were synthesized by coalescence overgrowth of AlN nanocolumns using PA MBE technique. Such epitaxial structures can be used as a buffer layer for obtaining high quality AlN and GaN layers. Structural, chemical and electrical properties of these samples were studied. It was found that the etching of such type of AlN/Si(111) structures in KOH can become a promising method for obtaining high quality free-standing AlN and GaN.

Introduction

Wide bandgap semiconductors, especially III-N compounds, are one of the most prospective materials for the development of modern electronics. III-nitrides have unique electrical, optical and mechanical properties, which are of importance for optoelecronics, high-power and high frequency electronics and microelectromechanical system (MEMS) industry [1]. Among III-N materials, AlN has the largest band gap (6.2 eV). Since it is direct-bandgap semiconductor, AlN is a promising material for deep-ultraviolet light sources [2]. Morover, it has attracted a huge attention due to its giant piezoelectric properties, which are important for surface and bulk acoustic wave devices [3]. However, there is well-known problem for further development of nitride electronics connected with the lack of natural substrates. Since AlN and GaN substrates are very expensive, low-cost A^3N-on-Si epitaxial structures attract more and more attention.

On the other hand, one of the key technological problems of A^3N heteroepitaxy on silicon substrates is large lattice mismatch (16.9% for GaN/Si(111) and 19% for AlN/Si(111)), and large difference in their thermal expansion coefficients. Nonetheless, it is well-known that AlN is often used as a buffer layer for heteroepitaxy of GaN on silicon. However, it is reported that the crystalline quality of AlN buffer layer is not good enough, and its surface is quite rough [4]. One of the promising approaches to improve the crystalline quality of AlN grown on Si(111) substrates is the use of AlN nanocolumn arrays as a seed layers.

Here we report on the results of the studies of AlN/Si(111) structures synthesized by coalescence overgrowth of AlN nanocolumns using plasma-assisted molecular beam epitaxy (PA MBE) technique.

1. Experimental details and results

The AlN/Si(111) samples were obtained by PA-MBE using Veeco Gen 200 MBE system equipped with RF (13.56 MHz) plasma source. The growth procedure was similar to the described in paper [5]. AlN was grown on the semi-insulating ($R > 10000$ Ohm·cm) silicon substrates with (111) crystallographic orientation. Substrates were prepared according to modified Shiraki method [6]. Before the growth, the Si(111) substrates were annealed for 30 min at $T_{sub} = 850$ °C in order to remove SiO_2 layer. The growth procedure began with the deposition of several Al monolayers onto the silicon surface to prevent Si_xN_y formation. Then, an array of AlN nanocolumns was formed on the substrate surface under Al-rich conditions (flux ratio $F_{Al}/F_N \approx 1.7$) at $T_{sub} = 850$ °C. In order to provide the coalescence of AlN nanocolumns the temperature was decreased down to $T_{sub} = 750$ °C and the Al flux was decreased down to the ratio $F_{Al}/F_N \approx 1.3$.

The morphology of the samples grown was studied using scanning electron microscope (SEM) Supra 25 Zeiss. As it can be seen in Fig. 1, an array of AlN nanocolumns about 200 nm height was formed.

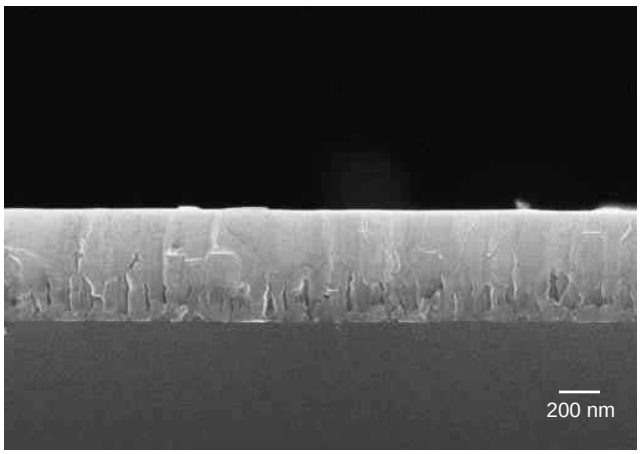

Fig. 1. SEM image of AlN/Si(111) epitaxial structure.

Moreover, it is evident in the micrograph that described changes in growth parameters led to the AlN nanocolumn coalescence that allowed the formation of the continuous AlN epitaxial layer about 300 nm thick. The samples obtained have quite smooth surface morphology with RMS roughness of 6.2 nm. Thus, it is shown that indeed the coalescence overgrowth can be used to obtain quite smooth AlN layers.

Crystallographic polarity of the AlN epitaxial layers was identified by wet chemical etching in 40 °C KOH solution for 5 min. It was found that all the samples have Al-polarity, because after etching the surface of the AlN layer remained unchanged. At the same time, it was found that AlN nanocolumns were etched in accordance with their crystallographic orientation, and the pyramid-like structures were formed (see Fig. 2).

However, after 10 min etching in KOH the AlN layer was partially destroyed at the edge of the sample. So the thickness of the AlN continuous layer should be higher in order to avoid overetching.

Furthermore, the electrical properties of the samples were investigated by Hall effect measurements based on four-probe Van der Pauw method using Ecopia HMS-3000 measurement

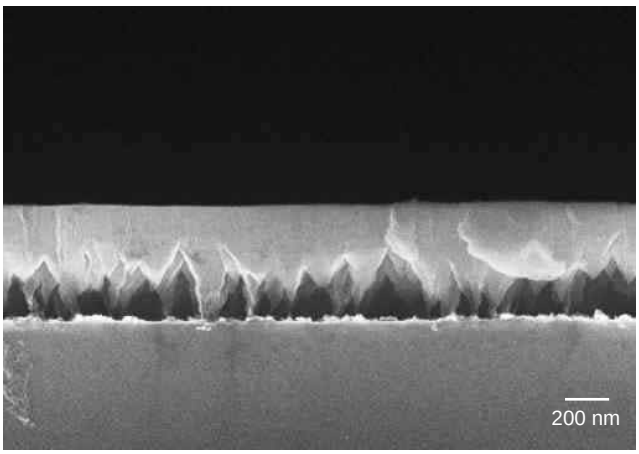

Fig. 2. SEM image of AlN/Si(111) epitaxial structure after etching in KOH solution.

system. It was found that despite all samples were grown undoped, AlN epitaxial layers have n-type conductivity with a carrier concentration $n \approx 2.1\times10^{18}$ cm^{-3}. It can be due to the presence of deep-level defects [7].

These results can be useful for obtaining free-standing AlN, and potentially, free-standing GaN. It is known that there are some attempts to separate GaN and AlN layers from the substrates using pre-growth modified by wet etching GaN buffer layer [8], or porous SiC layer [9]. At the same time, as it was mentioned above, AlN is often used as a buffer layer for GaN heteroepitaxy on silicon substrates. Proposed design of AlN/Si(111) epitaxial structures can be used as a buffer layer for obtaining high quality AlN and GaN layers. Moreover, it is shown that the etching of the obtained type of AlN/Si(111) structures in KOH can become a promising method for obtaining high quality free-standing AlN and GaN.

Acknowledgement

This work was supported by the the Ministry of Education and Science of the Russian Federation (grant No. FSRM-2020-0008).

References

[1] H. Amano *et al*, *J. Phys. D: Appl. Phys.* **51**, 163001 (2018).
[2] Y. Taniyasu *et al*, *Diamond and Related Materials* **17**, 1273 (2008).
[3] S. Tamariz *et al*, *J. Cryst. Growth* **476**, 58 (2017).
[4] Y. Lin *et al*, *CrystEngComm* **18**, 2446 (2016).
[5] A.M. Mizerov *et al*, *Semiconductors* **49**, 274 (2015).
[6] A. Ishizaka *et al*, *J. Eltrochem. Soc.* **133**, 666 (1986).
[7] P.G. Baranov *et al*, *Magnetic Resonance of Semiconductors and Their Nanostructures: Basic and Advanced Applications*, (Wien: Springer-Verlag) 524 (2017).
[8] R. Yu *et al*, *Crystals* **9**, 547 (2019).
[9] A. Redkov *et al*, *J. Phys. Conf.* **741**, 012034 (2016).

28th Int. Symp. "Nanostructures: Physics and Technology"
Minsk, Belarus, September 2020

Strained induced circular photogalvanic effect in zinc-blende-structure semiconductors

G.V. Budkin[1], S. Hubmann[2], M. Otteneder[2], D. But[3], D. Sacré[2], I. Yahniuk[3],K. Diendorfer[2], V.V. Belkov[1], D.A. Kozlov[4], N.N. Mikhailov[4], S.A. Dvoretsky[4], V.S. Varavin[4], V.G. Remesnik[4], S.A. Tarasenko[1], W. Knap[3], and S.D. Ganichev[2]

[1] Ioffe Institute, 194021 St Petersburg, Russia
[2] Terahertz Center, University of Regensburg, 93040 Regensburg, Germany
[3] International Research Centre CENTERA, Institute of High Pressure Physics, PL-02346 Warsaw, Poland
[4] Rzhanov Institute of Semiconductor Physics, 630090 Novosibirsk, Russia

Abstract. We report on the theoretical and experimental study of the circular photogalvanic effect in zinc-blende-structure semiconductors caused by local symmetry breaking by strain. Microscopic theory of the circular photogalvanic effects is developed for indirect optical transitions. We demonstrate the photocurrent results from the quantum interference of different pathways contributing to the free-carrier radiation absorption. The circular photocurrent is experimentally observed in strained $Cd_xHg_{1-x}Te$ epilayers with non-inverted band structure and well described by the developed theory.

Introduction

Circular photogalvanic effect, namely the generation of a photocurrent sensitive to the circular polarization, is typically observed in gyrotropic crystals. We demonstrate both theoretically and experimentally that it can emerge in the nongyrotropic crystals due to symmetry reduction under static deformation. We develop a microscopic theory and calculate circular photocurrent arising due to intraband indirect absorption of radiation in strained zinc-blende crystals. Experimentally, photocurrents sensitive to circular polarization were observed in (013)-oriented $Cd_xHg_{1-x}Te$ layers under terahertz radiation excitation. We demonstrate that theory describe well all experimental features.

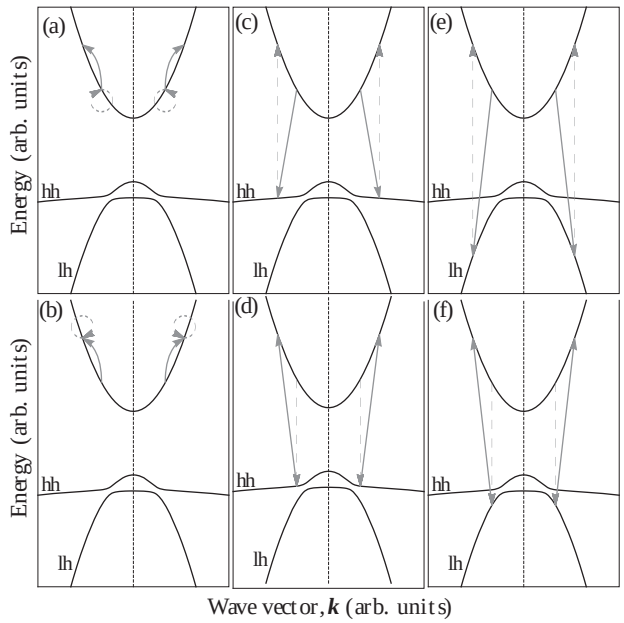

Fig. 1. Panels (a) and (b) show intraband optical transitions with intermediate states in the conduction band. Panels (c)-(f) demonstrate intraband optical transitions with intermediate states in the heavy-hole and light-hole subbands. Gray solid and dashed lines correspond to electron-phonon and electron-photon interaction, respectively.

1. Symmetry analysis

Bulk zinc-blende-structure crystals are described by the T_d point group symmetry. Despite the fact that it lacks the center of space inversion, this symmetry forbids the circular photogalvanic effect due to the presence of 6 σ_d mirror planes. However, if the deformation in the crystal reduces symmetry, the circular photogalvanic effect may emerge. Non-zero components of the circular photocurrent can be determined from the theory of irreducible representations. To the first order in strain the circular current density **j** is given by

$$\begin{aligned} j_{x'} &= [\chi_1(u_{yy}-u_{zz})\hat{o}_x + \chi_2(u_{xy}\hat{o}_y - u_{xz}\hat{o}_{z'})]I\,P_{\rm circ}, \\ j_{y'} &= [\chi_1(u_{zz}-u_{xx'})\hat{o}_y + \chi_2(u_{yz}\hat{o}_z - u_{xy}\hat{o}_{x'})]I\,P_{\rm circ}, \\ j_{z'} &= [\chi_1(u_{xx}-u_{yy})\hat{o}_z + \chi_2(u_{xz}\hat{o}_x - u_{yz}\hat{o}_{y'})]I\,P_{\rm circ}, \end{aligned} \quad (1)$$

where **o** is the unit vector pointing along the photon wave vector, $P_{\rm circ}$ is the degree of circular polarization, I is the radiation intensity, u_{ij} are the strain tensor components, and $x \parallel [100]$, $y \parallel [010]$ and $z \parallel [001]$ are main crystallographic axes. The photocurrent induced by normal and shear strain are described by the independent parameters χ_1 and χ_2, respectively. Equation (2) also shows that the circular photocurrent vanishes in the case of hydrostatic strain that does not disturb the crystal symmetry.

2. Microscopic theory

Now we turn to the microscopic origin of photocurrent generation. Conduction band electrons absorb radiation due to indirect optical transitions (Drude-like). These intraband transitions are assisted by the scattering of electrons by phonons or static defects of the structure in order to simultaneously satisfy the laws of energy and momentum conservation. As additional process of scattering here we consider either absorption or emission of longitudinal acoustic phonons caused by deformation interaction. The total scattering probability is obtained by summing over virtual intermediate states in all bands, see Fig. 1. The main contribution to the scattering probability is made by the processes with intermediate states in the conduction band see Figs. 1 (a–b). These processes describe the Drude absorption, but they are not sensitive to circular polarization.

To obtain circular photocurrent, one should also take into account the virtual transitions with intermediate states in the light- and heavy-hole bands Figs. 1 (c–f). The circular photocurrent arises to the extent of static strain. Therefore, we also take into account the mixing of the states by the static strain, which schematically shown in Fig. 1 as an energy splitting and non-parabolicity in the valence band spectrum. In the relaxation time approximation the photocurrent is given by

$$\mathbf{j} = e\tau \sum_{\mathbf{k}\mathbf{k}'s,\pm} \frac{2\pi}{\hbar} |M^{(c,\pm)}_{\mathbf{k}'s,\mathbf{k}s} + M^{(v,\pm)}_{\mathbf{k}'s,\mathbf{k}s}|^2 \times (\mathbf{v}_{\mathbf{k}'} - \mathbf{v}_{\mathbf{k}})[f(\varepsilon_{ck}) - f(\varepsilon_{ck'})]\delta(\varepsilon_{ck'} - \varepsilon_{ck} - \hbar\omega)\,, \quad (2)$$

$M^{(c,\pm)}_{\mathbf{k}'s,\mathbf{k}s} = V^{(\pm)}_{\mathbf{k}'s,\mathbf{k}s}(R_{\mathbf{k}n,\mathbf{k}s} - R_{\mathbf{k}'n,\mathbf{k}'s})/\hbar\omega$ is the matrix element of scattering with the virtual intermediate state in the conduction band. The contribution with the virtual intermediate state in the valence band which leads to the photocurrent generation is found using third-order perturbation theory and is given by

$$M^{(v,\pm)}_{\mathbf{k}'s',\mathbf{k}s} = \sum_{m,n}\Bigg\{ \frac{V^{(\pm)}_{\mathbf{k}'s',\mathbf{k}m} U_{\mathbf{k}m,\mathbf{k}n} R_{\mathbf{k}n,\mathbf{k}s}}{(\varepsilon_{ck} + \hbar\omega - \varepsilon_{mk})(\varepsilon_{ck} + \hbar\omega - \varepsilon_{nk})} + \frac{R_{\mathbf{k}'s',\mathbf{k}'m} U_{\mathbf{k}'m,\mathbf{k}'n} V^{(\pm)}_{\mathbf{k}'n,\mathbf{k}s}}{(\varepsilon_{ck} - \varepsilon_{mk'})(\varepsilon_{ck} - \varepsilon_{nk'})} + \frac{V^{(\pm)}_{\mathbf{k}'s',\mathbf{k}m} R_{\mathbf{k}m,\mathbf{k}n} U_{\mathbf{k}n,\mathbf{k}s}}{(\varepsilon_{ck} + \hbar\omega - \varepsilon_{mk})(\varepsilon_{ck} - \varepsilon_{nk})}$$
$$+ \frac{U_{\mathbf{k}'s,\mathbf{k}'m} V^{(\pm)}_{\mathbf{k}'m,\mathbf{k}n} R_{\mathbf{k}n,\mathbf{k}s}}{(\varepsilon_{ck} + \hbar\omega - \varepsilon'_{mk})(\varepsilon_{ck} + \hbar\omega - \varepsilon_{nk})} + \frac{U_{\mathbf{k}'s,\mathbf{k}'m} R_{\mathbf{k}'m,\mathbf{k}'n} V^{(\pm)}_{\mathbf{k}'n,\mathbf{k}cs}}{(\varepsilon_{ck} + \hbar\omega - \varepsilon_{nk'})(\varepsilon_{ck} - \varepsilon_{mk'})} + \frac{R_{\mathbf{k}'s,\mathbf{k}'m} V^{(\pm)}_{\mathbf{k}'m,\mathbf{k}n} U_{\mathbf{k}n,\mathbf{k}s}}{(\varepsilon_{ck} - \varepsilon_{mk'})(\varepsilon_{ck} - \varepsilon_{nk})} \Bigg\}, \quad (3)$$

where the indexes m and n run over the valence subbands. Here, $R_{\mathbf{k}'s',\mathbf{k}s}$ is the matrix element of electron-photon interaction, $V^{(\pm)}_{\mathbf{k}'s',\mathbf{k}s}$ is the matrix elements of electron scattering with the emission or absorption of a LA phonon, and $U_{\mathbf{k}s',\mathbf{k}s}$ is the matrix elements of heavy-hole–light-hole mixing by the static strain.

Calculation of the photocurrent after Eq. (2) leads to

$$\chi_1 = -\frac{64\pi}{35} \frac{e^3 N_e b}{\hbar^2 \omega\, c\, n_\omega} \frac{\Xi_{\mathrm{CV}}}{\Xi_{\mathrm{C}}} \frac{P^3}{E_g^4}\,, \quad (4)$$

and $\chi_2 = -(5/3)\chi_1$ [1], where N_e is electron density, n_ω refractive index, E_g is the band gap, P is the Kane parameter, b is the valence band deformation potential, Ξ_c is the conduction band deformation potential and Ξ_{cv} is the interband deformation potential, latter takes into absence of inversion symmetry in zinc-blende crystals.

3. Experiment

The experiments were carried on $Cd_xHg_{1-x}Te$ layers with (013)-orientation grown by molecular beam epitaxy on a CdTe substrate. Static strain in the samples is caused by the lattice mismatch of the CdHgTe layer with the substrate. As a radiation source for the photocurrent measurements molecular gas THz lasers were used. Photocurrents sensitive to the circular polarization were obtained for samples with different Cd contents x and temperatures, which characterized by substantially different energy gaps. In accordance with Eq. (4) ($J_c \propto 1/E_g^4$) the photocurrent magnitude drastically decreases with the increase of the band gap. Figure 2 presents the dependence of circular photocurrent normalized by the radiation power on the radiation frequency. It demonstrates that the photocurrent J_c is proportional to $1/\omega$, which again agrees with Eq. (4). Finally, theoretical predictions of the photocurrent magnitude using known parameters for CdTe and HgTe semiconductors are in a good agreement with the experiment.

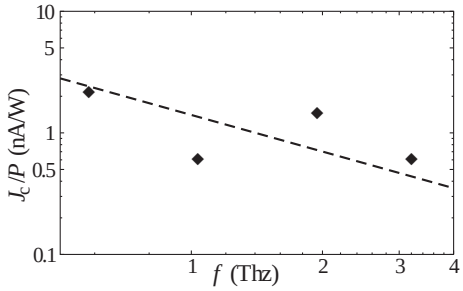

Fig. 2. The dependence of the normalized circular photocurrent J_c/P on the radiation frequency for sample with $x = 0.15$ and $E_g = 83$ meV at temperature $T = 300$ K (black diamonds). Dashed line indicate a fit according to $J_c/P \propto 1/\omega$.

Acknowledgements

The support from the Russian Science Foundation (project 17-12-01265) and "BASIS" foundation is gratefully acknowledged.

References

[1] S. Hubmann, G.V. Budkin *et al*, arXiv:1911.01936

28th Int. Symp. "Nanostructures: Physics and Technology"
Minsk, Belarus, September 2020

Phase analysis of quantum oscillations in HgTe quantum well with an inverted band structure

S.V. Gudina[1], V.N. Neverov[1], K.V. Turutkin[1], N.G. Shelushinina[1], M.V. Yakunin[1], N.N. Mikhailov[2], and S.A. Dvoretsky[2]

[1] M.N. Miheev Institute of Metal Physics of Ural Branch of Russian Academy of Sciences, 18 S. Kovalevskaya Str., Ekaterinburg 620108, Russia
[2] A.V. Rzhanov Institute of Semiconductor Physics of Siberian Branch of Russian Academy of Sciences, 13 Lavrentyev Ave., Novosibirsk 630090, Russia

Abstract. The results of the longitudinal and Hall magnetoresistivity measurements in the Shubnikov–de Haas oscillation regime for the HgCdTe/HgTe/HgCdTe heterostructures with a wide (20.3 nm) HgTe quantum well are presented. An anomalous phase shift of magneto-oscillations is detected in the region of spin-unsplit peaks in contradiction with a conventional situation in 2D systems. It is shown that the observed features are associated with the inverted nature of the spectrum in the size-quantized $H1$ subband of the investigated HgTe quantum well. The results obtained are compared with the phase shift effects of both magneto-oscillations and plateaus of the quantum Hall effect in monolayer graphene and in semimagnetic HgMnTe quantum wells.

Introduction

A characteristic feature of the band structure of systems with Cd(Hg)Te/HgTe/Cd(Hg)Te quantum wells (QW) which makes it possible to obtain several transitions between interesting electronic phases from band insulator (BI) to topological insulator (TI) and then to semimetal (SM) consists in the fact that when the width of the quantum well changes, the sequence of the bands switches from normal to inverted at critical thickness $d_c \approx 6.3$ nm where the conduction and valence bands touch each other and a single-valley gapless 2D Dirac-fermion system is realized [1].

In HgTe QW of the critical thickness, the two-dimensional single-valley gapless Dirac fermion system is formed. The band structure of the system is very similar to that of a graphene [2] but with the Dirac point located in the center of the Brillouin zone, therefore, without a valley degeneracy.

2D topological insulators are electronic materials that have a bulk band gap like an ordinary insulator but they support conducting states on their edges, the so-called quantum spin Hall states. The edge states in these materials can be described by the Dirac equation with a linear in energy zero-gap dispersion of the Dirac fermions.

The Dirac fermions have a massless nature with the nontrivial phase acquired by the cyclotron orbit (Berry phase) due to a degeneracy at Dirac point. The notion of the Berry phase is important when discussing topological phases: theoretically, it means the accumulated phase factor of a quantum-mechanical system after it completes a closed path [2,3].

In transport experiments on a system with a Dirac spectrum (monolayer graphene, zero-gap HgTe QW, edge 2D TI states, etc.), the presence of the Berry phase is manifested in a phase shift of magneto-oscillations by π or in shifted positions of the quantum Hall plateaus We emphasize that the remarkable consequence of the Berry phase due to the Dirac point is the existence of a zero-energy Landau level in graphene [4].

The gap between the conduction and valence subbands in the bulk of HgTe QW (and hence a 2D TI state) exists only for $d \leq 18$ nm. In wider HgTe/Cd(Hg)Te QWs with an inverted energy band structure, a new 2D electron system has been shown to exist: a 2D SM.

For the inverted energy spectrum of the HgTe QW, the first size-quantized heavy-hole $H1$ subband becomes the lowest conduction subband [5,6]. Thus, the $H1$ sublevel belongs to the heavy-hole branch of the $\Gamma 8$ band with the z-component of the total momentum $J_z = \pm 3/2$, but the theory [5,6] predicts an electron-like effective mass for it.

Results and discussion

We investigated the regime of Shubnikov– de Haas oscillations (SHO) in the longitudinal, ρ_{xx}, and Hall, ρ_{xy}, resistivities in magnetic fields B up to 2.5T at temperatures T = (2.2–10)K for the sample with a 20.3-nm-wide HgTe quantum well between $Hg_{0.35}Cd_{0.65}Te$ barriers grown on the (013) GaAs substrate, symmetrically modulation doped with In at both sides at distances of about 10 nm spacers. The electron gas density is $n_s = 1.5\times10^{15}\mathrm{m}^{-2}$ with the mobility of 22 m^2/Vs.

We note an important peculiarity in the region of doubly degenerate peaks of $\rho_{xx}(B < B^*)$: the peaks of $\rho_{xx}(B)$ are observed for even filling factors and the minima correspond to odd $\nu = (7-21)$. It is contrary to the conventional situation with the spin-degenerate LLs.

The spin splitting for the case investigated is comparable with the cyclotron splitting, $g\mu_B B \geq \hbar\omega_c$ (and there is a reason for this, namely, the ratio of γ-parameters of the Γ_8 band in HgTe (see details in [7])). Then, the region of spin-unsplit peaks at $B < B^*$ corresponds to the condition $|g\mu_B B - \hbar\omega_c| < \Gamma$, Γ being the Landau level broadening. In this case, the two-fold degeneracy of the ρ_{xx} peaks is due to the proximity of the energies for the adjacent Landau levels (LL) with the oppositely directed spins, $N\downarrow$ and $(N-1)\uparrow$. Thus, we have a system of doubly degenerate Landau levels with an "extra" non-degenerate level for $N = 0\downarrow$.

The situation is similar to a monolayer graphene [2,3]; the difference being in that the peaks in graphene are fourfold degenerate. In graphene, the lowest LL with $N = 0$ appears at $E = 0$ and each level, including zero LL, has the 4-fold degeneracy (2 spins×2 pseudospins). The origin of the latter is associated with the presence of two carbon sublattices. The zero LL in the Dirac-like spectrum of graphene is half-

populated by electrons (2-fold degeneracy) and half-populated by holes (2-fold degeneracy) [3].

If you focus only on one (e.g., electronic) branch of the spectrum, then this property implies that the degeneracy for $N = 0 \downarrow$ is half that for any other N. This explains the "half-integer" QHE plateau [2] $\rho_{xy}^{-1} = g_s(i+1/2)e^2/h$ at the filling factors $\nu = g_s(i+1/2)$ (with $g_s = 4$ and $i = 0, 1, 2$ — for graphene) and, at the same time an anomalous phase of SHO (ρ_{xx} minima correspond to ρ_{xy} plateau and ρ_{xx} maxima correspond to transitions between the plateau).

In our system, these considerations are applicable for $g_s = 2$ (in the region where there is no spin splitting, $\nu > 7$) and, thus, minima of ρ_{xx} should be at the odd $\nu = 2(i+1/2)$ (with $i \geq 3$) and maxima of ρ_{xx}, at the even $\nu = 2i$ (with $i \geq 4$), as it is actually observed in the experiment.

However, it is worth emphasizing that while the behavior of $\rho_{xx}(B)$ and $\rho_{xy}(B)$ both in the field of oscillations and in the QHE regime for graphene is due to fundamental physical reasons, the features observed by us have a "technical" origin: it is due to a specific ratio of parameters (γ and κ parameters) in a specific band (Γ_8 band) of a specific material (HgTe).

In our system, the double degeneracy of levels is lifted at fields $B > B^*$, which corresponds to the condition $|g\mu_B B - \hbar\omega_c| > \Gamma$, and the LL spectrum becomes "normal": all Landau levels are equally non-degenerate. Therefore, at this range of fields there is no anomalous phase shift, and the conventional QHE with the integer plateaus of $i = 1, 2, 3$ and the peaks of $\rho_{xx}(B)$ at $\nu = 1.5$; 2.5; and 3.5 is observed (see [8]).

On the other hand, in graphene, because of a small value of the g-factor ($g \cong 2$), the spin degeneracy is not lifted even in the field of 14T at which the QHE data are presented [2]. Thus, the difference in the degree of degeneracy for LL with $N = 0$ (2-fold) and the remaining LLs (4-fold) is also preserved in the QHE regime, which leads to an abnormal phase shift and, as a result, to the half-integer QHE plateaus.

It is also of interest to match our results with the data of Buhmann *et al* [9] on the quantum Hall effect and the Shubnikov–de Haas oscillations in Mn-doped HgTe quantum wells, which exhibit the anomalous sequence of the QHE plateaus with the odd filling factors. This anomaly originates from the very large spin splitting in this material, which exceeds the cyclotron energy even at moderate magnetic fields.

The "giant Zeeman splitting" in dilute magnetic semiconductor $Hg_{1y}Mn_yTe$ is observed due to a strong sp–d exchange interaction between the local magnetic moments of Mn ions and conduction electrons [9 and references therein] The exchange interaction modifies the energy-band structure of a semimagnetic semiconductor and causes a temperature-dependent and magnetic-field-dependent effective g-factor.

The spin splitting due to the sp-d exchange interaction is described by a Brillouin function-type dependence and its saturation leads to LL subband crossings in the vicinity of the Fermi energy at sufficiently strong magnetic fields. Just the spin-split Laudau-sublevel crossings in conjunction with LL broadening are responsible for the suppression of even filling factor quantum Hall states.

The speciality of our situation is that the large spin splitting of the Landau levels is due to a large value of the intrinsic quasi-spin of conduction electrons in the $H1$ subband, $|J_z| = 3/2$, without any magnetic impurities.

The phase shift of SHO and, at the same time, the half-integer QHE in "ideal" graphene is considered as the manifestation of Berry's phase acquired by Dirac fermions moving in magnetic field [2,3]. The Berry plot, a plot of the position, $1/B$, of the n-th minimum (maximum) depending on its number $n(n+1/2)$, is widely used for a direct probe of Berry phase in the magneto-oscillation of systems with a topologically non-trivial energy spectrum, which is the case of graphene, as well as of 2D- or 3D-topological insulators (see [3] and references therein).

For graphene, the extrapolation of the straight line $1/B(n)$ to a half integer (!) value $n^* = 1/2$ with $1/B \to 0$ (see Fig. 3b in [2]) is considered a manifestation of the non-trivial Berry phase due to the peculiar topology of the graphene band structure with a linear dispersion relation and vanishing mass near the Dirac point.

Büttner *et al* [10] studied the transport properties of zero-gap HgTe quantum wells grown at the critical thickness $d_c \cong 6.3$ nm. The presence of a single valley Dirac point in this system was demonstrated by the Berry plot with the numbers of SHO deep minima positioned on a straight line extrapolated to $n^* = 1/2$.

To identify a nontrivial phase shift, it is necessary to use the dependence of $1/B$ just on the number n of the ρ_{xx} minimum, regardless of the degree of the peak degeneracy [3]. It is easy to find that for partial lifting of degeneracy (LLs are degenerate for $\nu > \nu^*$, and degeneracy lifted for $\nu < \nu^*$) the minimum number, n, is related to the filling factor, ν, as follows $n = (\nu + \nu^*)/2$, that is, for $1/B \longrightarrow 0 (\nu \longrightarrow 0)$ $n \longrightarrow n^* = \nu^*/2$. Thus, if the resistivity minima are counted, there are two possibilities for the values of the $1/B(n)$ offset: integer n^*(if there is no extra zeroth LL, ν^* is even) and half-integer (if such a LL exists and ν^* is odd).

Extrapolating the dependence of $1/B$ on n to $1/B \to 0$ from the region of unsplit peaks ($B < B^*$) in our sample yields the limit $n^* \cong 3.5$, i.e. a half integer (!) cutoff value. The specific value of $n^* = 3.5$ is due to the fact that the spin degeneracy is retained only to $\nu = 7$.

Let us emphasize that the half-integer values of n^* found by us have nothing to do with the genuine Berry phase for topologically nontrivial systems. Here, it is a simple consequence of the fact that for $B < B^*$ in the system of doubly degenerate Landau levels there is an "extra" non-degenerate level for $N = 0$ due to the special relation $g\mu_B B \cong \hbar\omega_c$ for HgTe QW with an inverted energy spectrum.

Acknowledgements

The research was carried out within the state assignment of FASO of Russia (theme Electron No. AAAA-A18-118020190098-5), supported in part by RFBR (project No. 18-02-00172).

References

[1] B.A. Bernevig *et al*, *Science* **314**, 1757 (2006).
[2] K.S. Novoselov *et al*, *Nature* **438**, 197 (2005).
[3] A.Yu. Kuntsevich *et al*, *Phys.Rev.B* **97**, 195431 (2018).
[4] G.M. Gusev *et al*, *Phys. Rev. B* **96**, 045304 (2017).
[5] M.I. Dyakonov, A.V. Khaetskii, *JETP* **55**, 917 (1982).
[6] E.G. Novik *et al*, *Phys. Rev. B* **72**, 035321 (2005).
[7] V.N. Neverov *et al*, *cond-mat* **2002.02283** .
[8] S.V. Gudina *et al*, *Low Temp. Phys.* **45** , 412 (2019).
[9] H. Buhmann *et al*, *Appl. Phys. Lett.* **86**, 212104 (2005).
[10] B. Büttner *et al*, *Nature Phys.* **7**, 418 (2011).

28th Int. Symp. “Nanostructures: Physics and Technology”
Minsk, Belarus, September 2020

Superlattice in carbon nanotubes

Z.Ya. Kosakovskaya, Yu.V. Gulyaev, A.M. Smolovich, G.G. Kosakovskii
Kotel’nikov Institute of Radio Engineering and Electronics (IRE) of the RAS

The ballistic model of charge transfer along the whole length of a carbon nanotube (CNT) does not allow explaining the emission effects observed during applying an electric field to CNT. The mentioned effects include low voltage field emission (LVFE), optical emission, oscillatory processes, resonance nature of LVFE, and areas with negative differential conductivity on it, etc. The purpose of this work was to study the conditions in which the charge transfer along the UNT takes place. For this purpose, a huge array of SEM, AFM and STM images of CNT obtained during almost 30 years of CNT study both by us and other researchers was analyzed. It was found that the SEM and AFM images of CNT show periodic deformation of its walls. In other words, a superlattice (SL) is observed (Fig. 1 a,b). The analysis of the images allowed us to identify two different types of deformation of the CNT: periodic change of the CNT diameter along its axis (“beads”) and twisting of the CNT like a spring with a constant pitch and deformation of the walls (Fig. 1c). SL can be formed both in the process of CNT growth and in the process of experiment as a result of external electric, magnetic and electromagnetic fields. We have proposed 3 possible mechanisms of SL formation, which will be discussed.

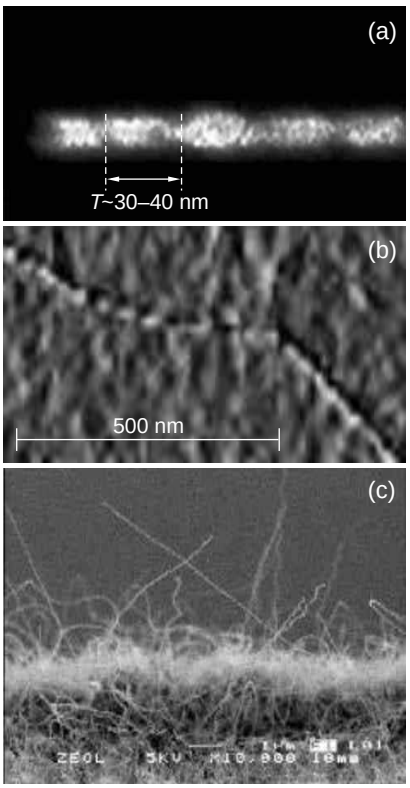

Fig. 1. The SEM image (a) and AFM image (b) of CNT superlattice (period $\sim$ 30−40 nm). REM image of differ type of CNT superlattice (c).

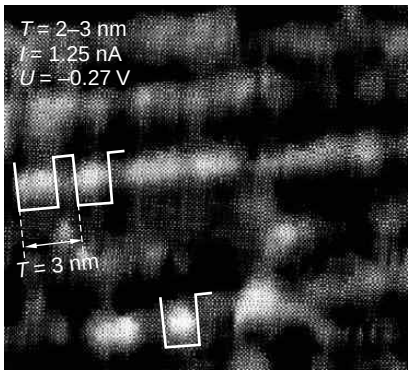

Fig. 2. The STM image the electron gas superlattice in CNT (period $\sim$ 3 nm at $U = -0.27$ V).

Thus, the charge transfer in ST is carried out under SL conditions. In other words, the charge transfer is carried out along the chain of sequentially connected quantum wells separated by potential barriers. It is interesting that the STM image of the CNT indicates a periodic change in the density of electron gas along the length of the CNT. However, its period is by an order of magnitude smaller than the period of CNT SL (Fig. 2). In these conditions, the mechanisms of occurrence of all the above effects can be explained. Their relationship to the external field effect becomes clear. We hope that this will help to create new room temperature nanodevices, for example, a room temperature detector or tunable generator of electromagnetic radiation with a wide range of frequencies.

Acknowledgement

This work is supported by RFBR grant No. 20-07-01062.

28th Int. Symp. "Nanostructures: Physics and Technology"
Minsk, Belarus, September 2020

Percolation transport of two-dimensional topological insulator of critical width

M.M. Mahmoodian[1,2], M.V. Entin[1,2]

[1] Rzhanov Institute of Semiconductor Physics, Siberian Branch, Russian Academy of Sciences, Novosibirsk, 630090 Russia
[2] Novosibirsk State University, Novosibirsk, 630090 Russia

We study the conductivity of a two-dimensional topological insulator (2D-TI) HgTe with a width close to the critical 6.3 nm. In this case, random width fluctuations turn the sample into a mixture of topological and ordinary insulators, at the boundary of which edge states are formed. These states arise along the lines where the energy gap vanishes (zero gap lines (ZGL)). Edge states energies overlap the forbidden band (see Fig. 1 which shows the spectrum of edge states of 2D-TI obtained in the two-dimensional Volkov–Pankratov model [1,2]). The problem is studied on the basis of a percolation model taking into account the spatial overlapping of edge states with finite width.

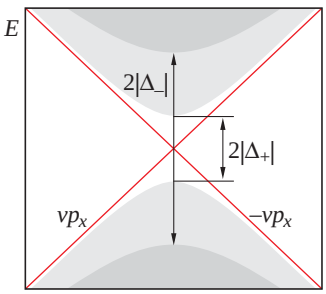

Fig. 1. Spectra of two-dimensional (shaded) and edge (red lines) states of 2D-TI. Edge states are formed along zero gap lines. Δ_+ and Δ_- are the asymptotics of the gap at large distances from the ZGL.

If the HgTe layer width approaches the threshold value of 6.3 nm, the overlapping of the edge states produces the network covering the entire sample. When the Fermi level falls into the common forbidden band, the only possibility for low-temperature transport is the collisionless motion of electrons along the edge states (Fig. 2).

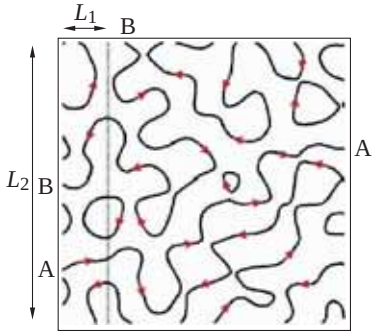

Fig. 2. The motion of electrons on the edge state along the ZGL occurs at a constant velocicty v, the sign of which depends on the electron spin.

ZGLs arise at the transition threshold, passing from one edge of a large sample to the opposite edge. The sample conductance was analyzed on the basis of percolation theory. At near-threshold widths, all the ZGLs turn out to be closed and the conductance tends to zero. With the finiteness of the width of the edge state taken into account, the low-temperature conductivity of an infinite sample was found when the Fermi level falls into the forbidden band [3]:

$$\sigma \sim (e^2/h) \cdot (\alpha w a/\hbar v)^{0.149}$$

Here $\alpha \approx 0.09$ meV/nm; a and w are the spatial scale and mean-square width fluctuation, respectively.

Fig. 3. A net of edge states taking into account their finite width. When electrons move, jumps between ZGLs occur.

Acknowledgement

This research was supported in part by the RFBR, grant No. 20-02-00622.

References

[1] B.A. Volkov, O.A. Pankratov, *JETP Lett.*, **42**, 178 (1985).
[2] M.V. Entin, M.M. Mahmoodian, L.I. Magarill, *EPL* **118**, 57002 (2017).
[3] [3] M.M. Mahmoodian, M.V. Entin, a rxiv.org/abs/1911.09455 [accepted for publication in *Phys.Rev. B* (2020)].

28th Int. Symp. "Nanostructures: Physics and Technology"
Minsk, Belarus, September 2020

Thermodynamics of the ideal two-dimensional magnetoexciton gas with linear dispersion law

S.A. Moskalenko[1], I.V. Podlesny[1], I.A. Zubac[1], B.V. Novikov[2]

[1] Institute of Applied Physics, Academiei str. 5, Chisinau, MD-2028, Republic of Moldova
[2] Department of Solid State Physics, Institute of Physics, St Petersburg State University, 1, Ulyanovskaya str., Petrodvorets, 198504, St Petersburg, Russia

Abstract. The Bose–Einstein condensation of the two-dimensional magnetoexciton gas with Dirac cone dispersion law is possible at different from zero critical temperature. The partition function, the thermodynamic functions such as the free and full energies, entropy and heat capacity were calculated in both gaseous and degenerate phases. The second order phase transition takes place. The jump of the heat capacity at critical temperature does not exist.

Introduction

As was mentioned in the Ref. [1] the two-dimensional (2D) ideal Bose gas with linear dispersion law can undergo the Bose–Einstein condensation (BEC) event with critical temperature $T_c \neq 0$ different from zero. It happens because to excite quantum fluctuations in the form of the particles with linear dispersion law and to enforce them to live the condensate with small wave vectors is necessary to spend more energy than in the case of the quadratic dispersion law. The number of such particles is infinitesimal; they cannot destroy the long range order established in the system in spite of its lower dimensionality and increased density of states. The BEC becomes possible.

In the present time there are two known cases of the 2D excitons with linear dispersion law. One of them concerns the Wannier–Mott valley excitons discovered recently in the monolayers of the transition metal dichalcogenides (TMDCs) [2], the energy band structure of which contains the direct band gaps situated in the corner points $\vec{k}$ and $-\vec{k}$ of the 2D hexagonal Brillouin zone. Another case is the 2D magnetoexcitons with the resultant spin projections of the electron–hole (e–h) pairs $F = \pm 1$; with electric dipole structure, the arm of the dipole $\vec{d}$ being perpendicular to the center-of-mass in plane wave vector $\vec{k}_\parallel$ and proportional to its modulus $|\vec{d}| = |\vec{k}_\parallel| l_0^2$, where l_0 is the magnetic length. The direct e–h Coulomb interaction determines the ionization potential of these bare magnetoexcitons with $F = \pm 1$ and degenerate energy levels.

1. The exchange electron-hole Coulomb interaction

The diagrams representing the direct, exchange and mixed electron–hole (e–h) Coulomb interaction are represented in the Fig. 1. During the direct Coulomb scattering the particles are moving separately without changing of their origins. In the exchange scattering process the e-h pairs are created and annihilated. In the mixed scattering process one particle conserves his origin, whereas the another one changes it, transiting, for example, from the valence in the conduction band. The exchange e–h Coulomb interaction leads to the formation of the superposition states, one of them with symmetric and another one with asymmetric combinations of the bare exciton wave functions. The symmetric state acquires a linear dispersion law in the range of the small wave vectors. The asymmetric state has the same dispersion law as the bare magnetoexciton states. It has a quadratic dispersion law in the range of small wave vectors characterized by the magnetic mass and the saturation trend in the range of higher wave vectors, where the free electron and hole in their Landau quantization states appear, but without Coulomb interaction. The optical and the quantum statistical properties of the magnetoexcitons in these two superposition states are different.

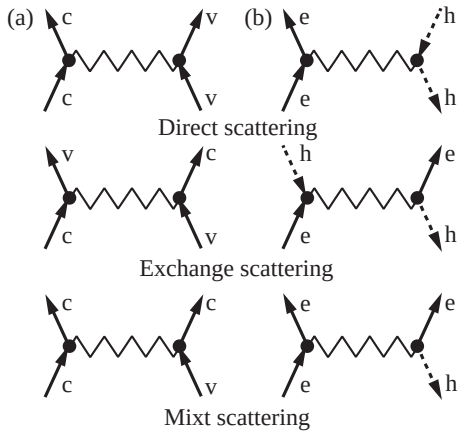

Fig. 1. The electron–hole Coulomb scattering processes: (a) in two-band representation and (b) in electron-hole description. The figure is reproduced from the Ref. [4].

2. Bose–Einstein condensation of the 2D Bose gas with linear dispersion law

The statistical thermodynamics of the ideal 2D Bose gas with Dirac cone dispersion law is described below following the model elaborated by Lee and Yang [3] in the case of the weakly nonideal 3D Bose gas with quadratic dispersion law.

We are considering the energy spectrum of the type $T_k = \hbar \upsilon_g k_\parallel$, depending on the modulus $k_\parallel = \sqrt{k_x^2 + k_y^2}$, which is the same as in the gaseous as well as in the degenerate phases, because the interaction between the particles is not taken in to account. We have deal with the plane layer with the surface area S and the exciton number N_{ex} and with their concentration $\sigma = \frac{N_{\text{ex}}}{S}$. The group velocity υ_g of the symmetric superposition state was calculated in the Ref. [4]. It is proportional to the square of the relation $\left(\left|\frac{\rho_{c-v}}{l_0}\right|\right)$, where ρ_{c-v} is the matrix element of the coordinate calculated with the periodic parts of the electron Bloch functions corresponding to the conduction and to the valence bands. It is different from zero in the case of dipole active quantum transition from the ground state of the

crystal in the symmetric magnetoexciton state The relations between the critical temperature, T_c the group velocity υ_g and the interband dipole moment are [1,4]

$$k_B T_c = \left[\frac{2\pi\hbar^2\upsilon_g^2\sigma}{g_2(1)}\right]^{1/2}; \quad \upsilon_g \approx \left|\frac{\rho_{c-v}}{l_0}\right|^2;$$
$$l_0^2 = \frac{\hbar c}{eB}; \quad T_c \sim \upsilon_g \sim B.$$

where B is the magnetic field strength, and $g_2(\xi)$ is the generalized Riemann function. The critical temperature as well as the group velocity increase with the increasing of the magnetic field strength B. The partition function the thermodynamic functions such as the free and full energies, the entropy and the heat capacity were calculated. The second order phase transition takes place. The jump of the heat capacity in the point of the phase transition is absent. In the frame of the degenerate phase the heat capacity has quadratic temperature dependence.

Conclusions

The influence of the electron–hole exchange Coulomb interaction on the superposition states formed by two 2D magnetoexciton with quantum numbers $F = \pm 1$, as well as by two valley Wannier–Mott excitons created in the TMDCs monolayers leads to the arising of these new superposition exciton states with Dirac cone dispersion laws. The necessary condition for the realization of this property is the interdependence between the center-of-mass and the relative electronhole motions. In the case of the magnetoexcitons such interdependence is induced by the Lorentz force, whereas in the case of TMDCs by the existence and the superposition of the exciton states in two equivalent valleys $\vec{K}$ and $-\vec{K}$ of the hexagonal Brillouin zone.

The statistical thermodynamic functions of the ideal two-dimensional (2D) Bose gas with linear dispersion law in the degenerate and gaseous phases lower and upper the critical temperature of the Bose–Einstein condensation were deduced. They are continuous in the critical temperature point showing the second order phase transmission. The jump of the heat capacity of the gas in this point does not exist.

References

[1] S.A. Moskalenko and D.W. Snoke. *Bose-Einstein condensation of excitons and biexcitons and the coherent nonlinear optics with excitons*. Cambridge Univesity Press, 2000, U.K., New York.

[2] Y. Hongyi, L. Gui-Bin, G. Pu, *et al*, *Nature Commun.*, **5**, 3876 (2014).

[3] T.D. Lee and C.N. Yang, *Phys. Rev.*, **112**, 1419 (1958).

[4] S. Moskalenko, I. Podlesny, I. Zubac and B. Novikov, *Solid State Commun.*, **308**, 113714 (2020).

Author Index